

**FOIA/PA: 2012-0231**

**GROUP A**

**RECORDS BEING RELEASED IN PART**

**SANDIA LETTER REPORT**

Draft Completed: April 2006

# **Analysis of Emergency Spray Mitigation of Spent Fuel Pool Loss-of-Coolant Inventory Accidents**

K. C. Wagner  
R. O. Gauntt

Prepared by  
Sandia National Laboratories  
Albuquerque, New Mexico 87185 and Livermore, California 94550

Sandia is a multiprogram laboratory operated by Sandia Corporation,  
a Lockheed Martin Company, for the United States Department of Energy's  
National Nuclear Security Administration under Contract DE-AC04-94AL85000.



Issued by Sandia National Laboratories, operated for the United States Department of Energy by Sandia Corporation.

**NOTICE:** This report was prepared as an account of work sponsored by an agency of the United States Government. Neither the United States Government, nor any agency thereof, nor any of their employees, nor any of their contractors, subcontractors, or their employees, make any warranty, express or implied, or assume any legal liability or responsibility for the accuracy, completeness, or usefulness of any information, apparatus, product, or process disclosed, or represent that its use would not infringe privately owned rights. Reference herein to any specific commercial product, process, or service by trade name, trademark, manufacturer, or otherwise, does not necessarily constitute or imply its endorsement, recommendation, or favoring by the United States Government, any agency thereof, or any of their contractors or subcontractors. The views and opinions expressed herein do not necessarily state or reflect those of the United States Government, any agency thereof, or any of their contractors.



SANDIA Letter Report  
Draft, April 2006

# Analysis of Emergency Spray Mitigation of Spent Fuel Pool Loss-of-Coolant Inventory Accidents

K. C. Wagner  
R. O. Gauntt

Analysis and Modeling Division  
Sandia National Laboratories  
P.O. Box 5800  
Albuquerque, New Mexico 87185-MS-0748

## Abstract

This report describes calculations to analyze the effectiveness of emergency spray mitigation of spent fuel pool (SFP) loss-of-coolant inventory accidents. The data used to perform these calculations were developed from an operating boiling water reactor. This report is a supplement to earlier studies, which also examined the BWR SFP accident response without spray mitigation. The MELCOR 1.8.5 severe accident computer code was the primary tool used to simulate the SFP accident response. The emergency spray mitigation calculations include separate effects calculations of one or a few assemblies in the spent fuel pool and the whole pool response. Some hand calculations are also included to illustrate the basic energy balances.

## EXECUTIVE SUMMARY

In 2001, United State Nuclear Regulatory Commission (NRC) staff performed an evaluation of the potential accident risk in a spent fuel pool (SFP) at decommissioning plants in the United States [NUREG-1738]. The study was prepared to provide a technical basis for decommissioning rulemaking for permanently shutdown nuclear power plants. The study described a modeling approach of a typical decommissioning plant with design assumptions and industry commitments; the thermal-hydraulic analyses performed to evaluate spent fuel stored in the spent fuel pool at decommissioning plants; the risk assessment of spent fuel pool accidents; the consequence calculations; and the implications for decommissioning regulatory requirements. It was known that some of the assumptions in the accident progression in NUREG-1738 were necessarily conservative, especially the estimation of the fuel damage. Subsequently, the NRC desired to expand the study to include accidents in the spent fuel pools of operating power plants. Consequently, the NRC has continued spent fuel pool accident research by applying best-estimate computer codes to predict the severe accident progression following various postulated accident initiators. This report describes the effectiveness of emergency sprays systems for mitigating spent fuel pool accidents.

FE 4  
The data used to perform these calculations were developed from an operating boiling water reactor (BWR). The reference plant is typical of many BWRs with fuel in the SFP from several decades old to the most recent offload. This reference plant has a two-year fuel cycle and roughly discharges one-third of the reactor fuel (b)(7)(F) each outage. The plant removes an equivalent amount of various aged fuel between outages for storage in dry casks, thereby maintaining a relatively constant number of assemblies in the SFP. Hence, the SFP has a wide variety of different aged fuel. In addition, the SFP racks have enough empty cell locations (b)(7)(F) to permit a complete emergency reactor offload as well as store all the refueling blade guides. A schematic of the reference BWR spent fuel pool storage building is shown in Figure ES-1.

The MELCOR 1.8.5 severe accident computer code [Gauntt] with enhancements through Version RP was used to simulate the SFP accident response. MELCOR includes fuel degradation models for pressurized water reactor (PWR) and BWR fuel, radiation, convection, and conduction heat transfer models, air and steam oxidation models, hydrogen burn models, two-phase thermal-hydraulic models, and fission product release and transport models. Therefore, it contains the basic models to address questions and phenomena expected during a spent fuel pool accident.

Version RP includes three recent modeling enhancements applicable to BWR SFP modeling, (1) a new rack component, which permits better modeling of a SFP rack, (2) a new oxidation kinetics model, and (3) a simplified flow regime model. The new BWR spent fuel pool rack component permits proper radiative modeling of the SFP rack between groups of different assemblies. The new oxidation kinetics model predicts the transition to breakaway oxidation in air environments on a node-by-node basis. The simplified flow regime model permitted simulation of liquid films draining down the BWR fuel assemblies during spray operation.

Ex 7F  
Ex 7F

The purpose of the study is to evaluate the effectiveness of emergency spray mitigation during a loss-of-coolant inventory accident. The accidents are initiated with a leak in the SFP. Once the water level (b)(7)(F) the fuel, there can be inadequate cooling. Most calculations assumed a (b)(7)(F) until an emergency spray system could be activated. In a complete loss-of-coolant inventory accident, the leak is located at the bottom of the SFP on the side wall. An air natural circulation pattern can be established through the assemblies if the level drains below the bottom of the racks. If the fuel heats to high temperatures, then rapid exothermic oxidation of the zirconium cladding and canisters occurs using the oxygen in the air. If water from the spray system fills the bottom of the pool above the bottom of the racks, the accident will progress without convective air cooling.

Two sets of hand calculations were performed to estimate the heat removal required from the spray system in the reference BWR spent fuel pool. The hand calculations represent simple straight-forward energy balances that are useful for estimating the required flowrate for a spray system. In the first calculation, the spray system was initiated prior to uncover of the fuel and the water leakage location is above the top of the racks. (b)(7)(F)

Ex 7F

Ex 7F

(b)(7)(F) Since the fuel is covered, a spray system is not technically needed. Rather any water injection system would be sufficient. In the second hand calculation, it is assumed that the fuel is uncovered. (b)(7)(F)

Ex 7F

(b)(7)(F)

(b)(7)(F) Since the fuel is uncovered, a spray system is required to distribute the water to the individual assemblies. The flowrate estimate includes factors to account for inefficiencies due to overlap from the adjacent nozzles and flow into the region between the fuel canister and rack walls.

A series of separate effects calculations were performed to assess the effectiveness of a spray system at providing cooling. Table E-1 summarizes the highlights of separate effects spray calculations. Calculations were performed for the uniform, checkerboard, and 1x4 configurations. For each configuration, parametric calculations were performed with variations in one or more of the scenario or modeling attributes. The variations in the calculations included fuel configuration (uniform, checkerboard, and 1x4), aging time of the peak powered assembly,

Ex 7F

(b)(7)(F) spray flow rate (b)(7)(F) air flow (b)(7)(F)

Ex 7F

(b)(7)(F) and a modeling parameter (b)(7)(F)

(b)(7)(F) Ex 7F

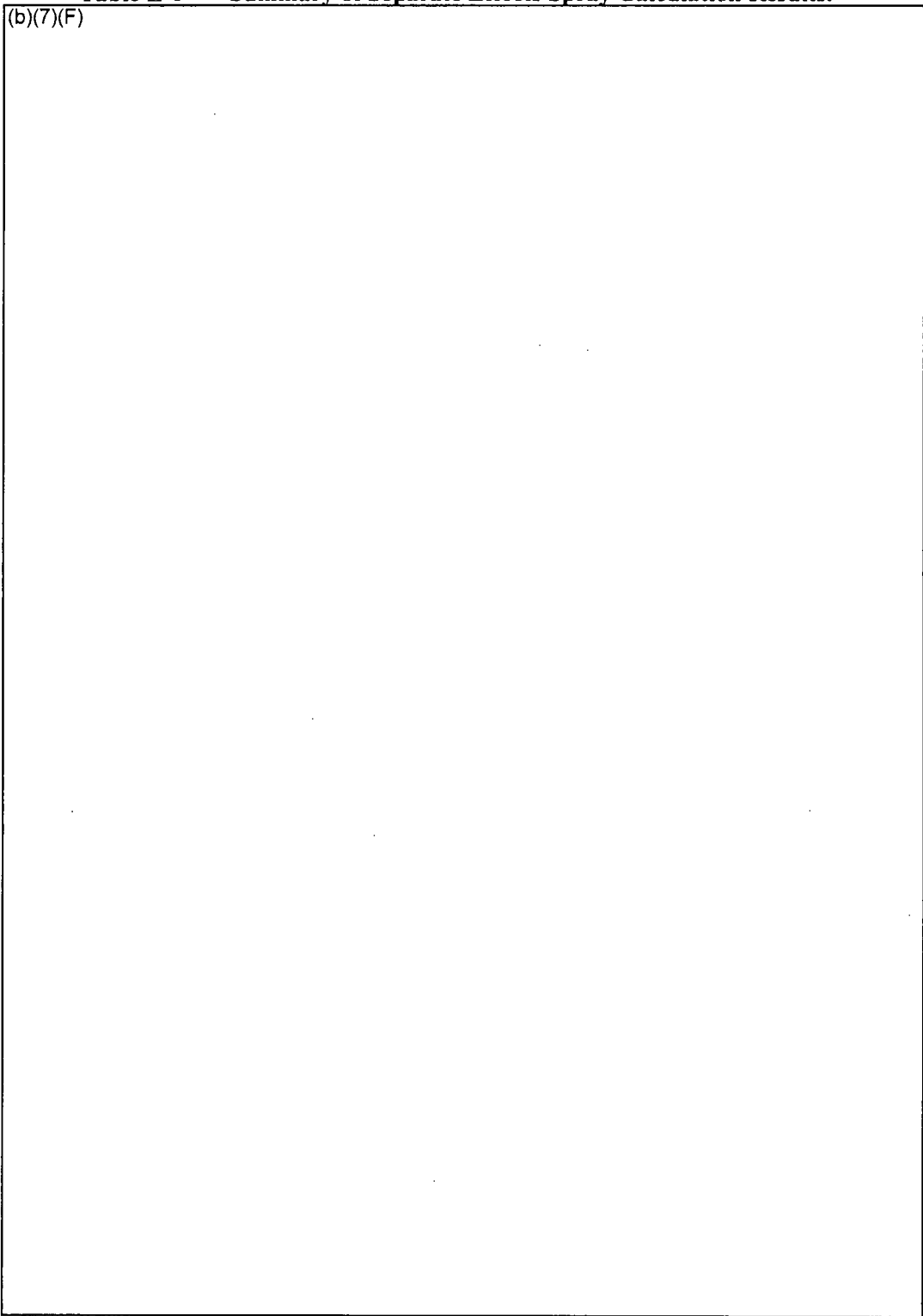
For fuel which has been favorably configured (i.e., a 1x4 or checkerboard pattern), a spray flow rate of (b)(7)(F) (b)(7)(F)

Ex 7F

(b)(7)(F)

**Table E-1 Summary of Separate Effects Spray Calculation Results.**

(b)(7)(F)



Ex 7F

Finally, a short-term task was performed to estimate the effectiveness of an emergency spray system at reducing fission product releases for a configuration and scenario that had inadequate cooling. (b)(7)(F)

EX 7F

A series of separate effects, hybrid<sup>1</sup>, and whole pool calculations were performed to estimate the scrubbing efficiency. (b)(7)(F)

(b)(7)(F)

(b)(7)(F) Each approach had aspects that were judged to be calculated well whereas other aspects were judged not to be calculated properly.

Nevertheless, the following observations are made from the available results.

1. (b)(7)(F)

EX 7F

(b)(7)(F) Both the separate effect and hybrid calculations only showed slightly smaller releases than the cases without spray.

2. (b)(7)(F)

EX 7F

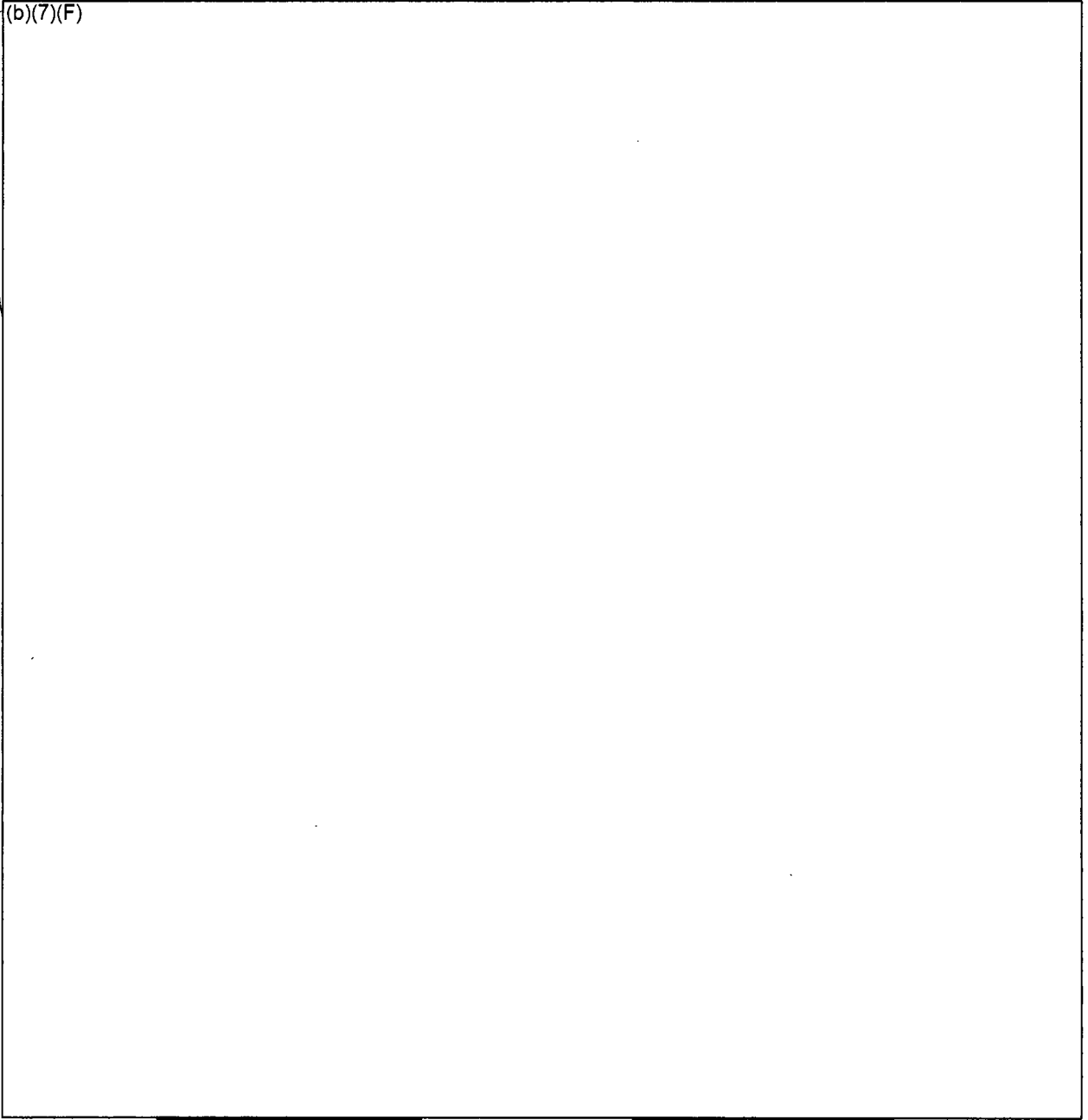
(b)(7)(F) This conclusion, however, is based on very low fission product releases in the spray cases. The impact of scrubbing efficiency in a high release case is unknown.

<sup>1</sup> The hybrid model was based on the detailed separate effects model of a single assembly with scaled control volumes to represent the gas space above the racks and the refueling room.

**Table E-2 Summary of Spray and Building Decontamination Factors in the Whole Pool Calculations.**

<i>F27F</i>	(b)(7)(F)	
<b>Notes:</b>		
1.	(b)(7)(F)	<i>1F</i>
2.	(b)(7)(F)	<i>1F</i>

(b)(7)(F)



EX 4

**Figure E-1 Schematic of a BWR Reactor Building Showing the Refueling Room and Spent Fuel Pool.**

E x 7/F

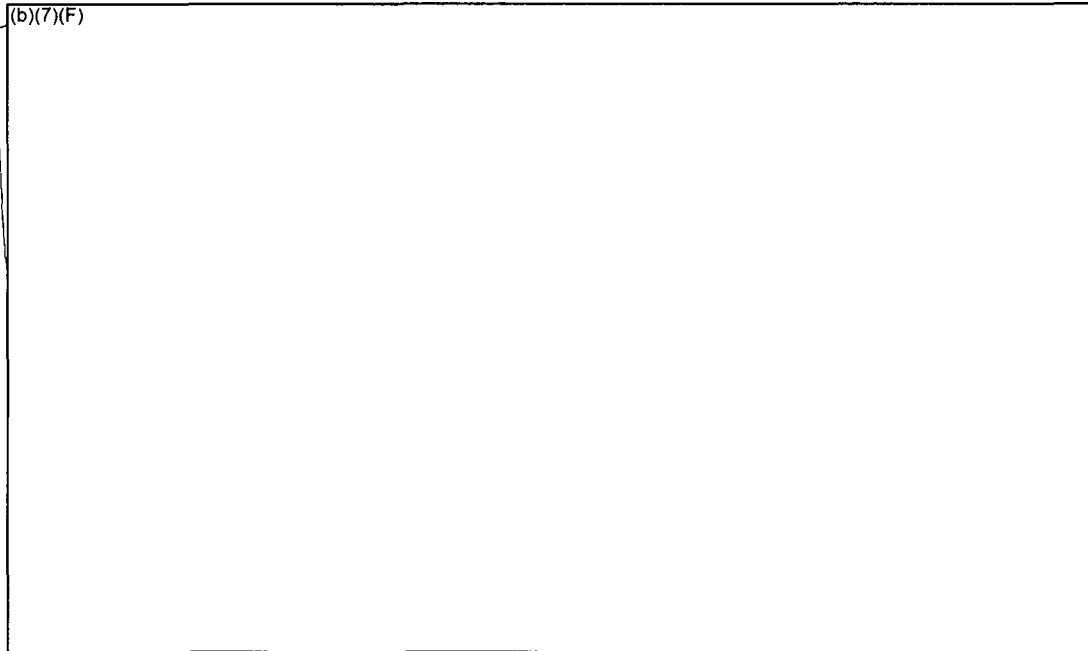


**Figure E-2 Hand Calculations to Estimate Spray Heat Removal Requirements for Leaks Above and Below the Top of the Racks.**

E x 7/F

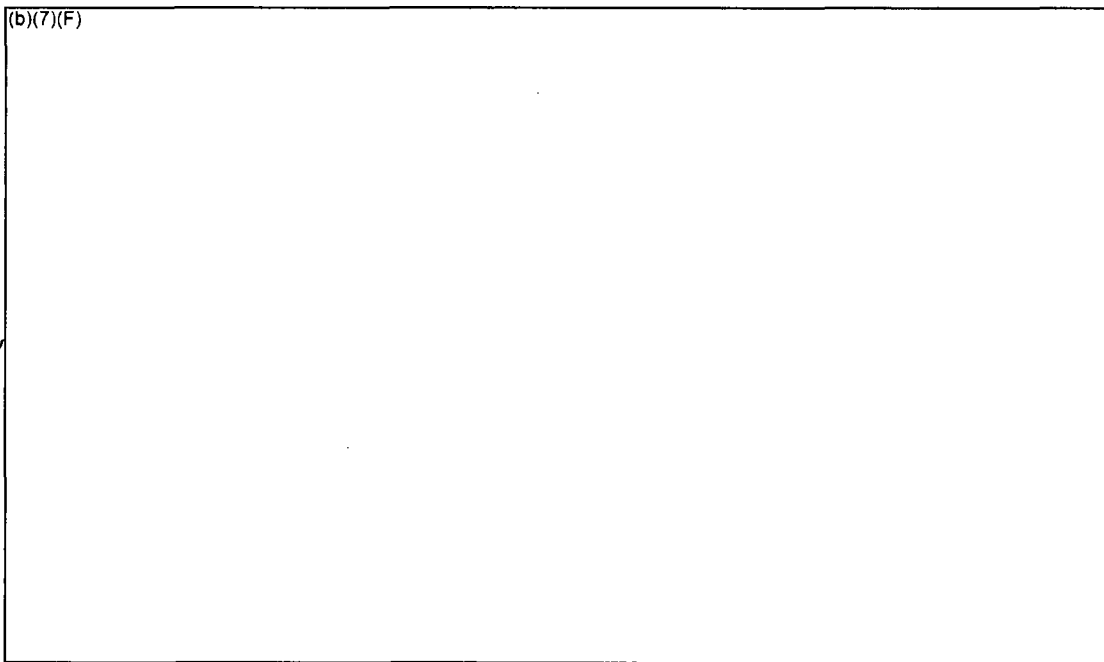


**Figure E-3 Comparison of the Peak Cladding Temperatures for the Uniform Configuration with Various Aging Periods and a Whole Pool Spray Flow of**

E x 7/F

(b)(7)(F)

TABLE OF CONTENTS

1. INTRODUCTION..... 1

2. BACKGROUND ..... 2

    2.1 Description of the Spent Fuel Pool..... 2

    2.2 SFP Accident Scenarios..... 5

        2.2.1 Complete Loss-of-Coolant Inventory Accident..... 5

        2.2.2 Partial Loss-of-Coolant Accident..... 6

3. ANALYSIS METHODOLOGY ..... 8

    3.1 New BWR SFP Modeling..... 8

        3.1.1 New BWR SFP Model..... 8

        3.1.2 Breakaway Air Oxidation Model..... 12

        3.1.3 New Hydraulic Resistance Model ..... 16

        3.1.4 Spray Flow Modeling in MELCOR..... 22

    3.2 MELCOR Separate Effects Model..... 25

        3.2.1 Separate Effects Model ..... 25

        3.2.2 Hybrid Spray Model ..... 30

    3.3 Whole Pool Models ..... 33

        3.3.1 Original BWR Whole Pool Model..... 33

        3.3.2 New Whole Pool Nodalization ..... 39

            3.3.2.1 Radial Thermal Coupling..... 41

            3.3.2.2 Simplified Refueling Room Model..... 45

    3.4 Description of the Initial and Boundary Conditions ..... 49

4. SPRAY MITIGATION HAND CALCULATIONS ..... 51

    4.1 Leak Above the Top of the Racks..... 51

    4.2 Leak Below the Top of the Racks..... 53

        4.2.1 Calculations for One Point on the BWR Spray Chart..... 55

        4.2.2 Calculations for Counter-Current Flow Limitation (CCFL)..... 56

        4.2.3 Impact of Assembly Sensible Heat ..... 58

5. WHOLE POOL MODEL BOUNDARY CONDITION CALCULATIONS..... 60

    5.1 (b)(7)(F) Spray Flow Rate ..... 61

6. MELCOR SEPARATE EFFECTS MODEL RESULTS..... 66

    6.1 Summary of Separate Effect Spray Calculations ..... 66

    6.2 Separate Effects Spray Model Results for the Uniform Configuration..... 71

        6.2.1 Base Calculations for (b)(7)(F) Spray..... 71

        6.2.2 Energy Balance on Base Calculation for (b)(7)(F) Spray ..... 77

        6.2.3 Coolability Analysis for (b)(7)(F) Spray Flowrate ..... 80

        6.2.4 Coolability Analysis for (b)(7)(F) Spray Flowrate ..... 81

Ex 7 F

Ex 7 F  
Ex 7 F  
Ex 7 F  
Ex 7 F

6.2.5 Coolability Analysis for (b)(7)(F) Spray Flowrate ..... 82 <sup>Ex 1F</sup>

**6.3 Separate Effects Spray Model Results for the Checkerboard Configuration..... 83**

6.3.1 Base Calculations for (b)(7)(F) Spray ..... 83 <sup>Ex 1F</sup>

6.3.2 Energy Balance on Base Calculation for (b)(7)(F) Spray ..... 91 <sup>Ex 1F</sup>

**6.4 Separate Effects Spray Model Results for the 1x4 Configuration Cases..... 94**

6.4.1 Base Calculations for (b)(7)(F) Spray ..... 94 <sup>Ex n =</sup>

6.4.2 Energy Balance on Base Calculation for (b)(7)(F) Spray ..... 102 <sup>Ex 1F</sup>

**7. SPRAY SCRUBBING CALCULATIONS ..... 105**

7.1 Calculations with Original Whole Pool Model..... 108

7.2 Hybrid Calculations..... 118

7.3 Summary of the Findings from the Fission Product Scrubbing Cases..... 122

**8. REFERENCES..... 124**

**List of Tables**

**Table 2-1 Spent Fuel Pool Data. .... 3**

**Table 2-2 Fuel Assembly Data. .... 4**

**Table 2-3 Spent Fuel Pool Rack Data..... 4**

**Table 3-1 MELCOR Fit of the Timings for Transition from Pre-Breakaway to Post-Breakaway Oxidation Reaction Kinetics for Zirlo and Zircaloy-4 in the ANL Experiments [Natesan, 2004]. .... 14**

**Table 3-2 S<sub>LAM</sub> And k Coefficients for the Unblocked Water Rod Assembly Assuming All Flow Passes Through the Bundle. .... 18**

**Table 3-3 Summary of Regions in the MELCOR Whole Pool Model..... 44**

**Table 3-4 Summary of Base Case SFP Model Initial Conditions for BWR SFP Emergency Spray Calculations..... 49**

**Table 3-5 Summary of Base Case SFP Model Boundary Conditions for BWR SFP Emergency Spray Calculations..... 50**

**Table 5-1 Summary of the Steady-State Water Levels as a Function of Leakage Hole Size and Spray Flow Rate..... 60**

**Table 6-1 Summary of the Spray Calculations ..... 67**

**Table 6-2 Energy Balance for the Uniform Assembly Configuration in SFP with (b)(7)(F) Spray..... 79** <sup>Ex 1F</sup>

**Table 6-3 Energy Balance for the Checkerboard Assembly Configuration in SFP with (b)(7)(F) Spray..... 93** <sup>Ex 1F</sup>

**Table 6-4 Energy Balance for 1x4 Assembly Configuration in SFP with (b)(7)(F) Spray. .... 104** <sup>Ex 1F</sup>

**Table 7-1 Summary of Whole Pool Calculations. .... 108**

**Table 7-2 Summary of Spray and Building Decontamination Factors in the Whole Pool Calculations. .... 110**

**Table 7-3 Summary of Hybrid Calculations..... 118**

### List of Figures

Figure 2-1	Spent Fuel Pool Rack Layout.....	3
Figure 2-2	Typical Spent Fuel Pool Rack Cut-away Cross-Section Showing the Fuel Assembly.....	5
Figure 3-1	MELCOR Modeling of a BWR Assembly in the Reactor Core.....	9
Figure 3-2	Original MELCOR Modeling of BWR Assemblies in a 1x4 SFP Configuration.....	10
Figure 3-3	Heat Flow for the Original MELCOR Modeling of a BWR Assemblies in a 1x4 SFP Configuration.....	10
Figure 3-4	New MELCOR Modeling of BWR Assemblies in a 1x4 SFP Configuration.....	11
Figure 3-5	Heat Flow for the New MELCOR Modeling of BWR Assemblies in a 1x4 SFP Configuration.....	12
Figure 3-6	Comparison of the MELCOR Breakaway Timing Fit to the Zirlo and Zr-4 Data from the ANL Air Oxidation Tests.....	13
Figure 3-7	Parabolic Reaction Kinetics Coefficients for Zr-4 Oxidation.....	15
Figure 3-8	BWR Assembly Experimental Apparatus used in the Hydraulic Resistance Testing.....	19
Figure 3-9	Measured Pressure Drop over the Full, Partial, and Total Assembly Regions.....	20
Figure 3-10	Comparison of the Calculated and Measured Bypass Flow.....	21
Figure 3-11	Axial Temperature Profile in the Assembly with Spray Flow.....	23
Figure 3-12	Core Package Representation of a Spray Flow.....	24
Figure 3-13	CVH Package Representation of a Spray Flow.....	24
Figure 3-14	Repeating Patterns Found in the MELCOR Separate Effects Models.....	25
Figure 3-15	Schematic of the 1x4 Configuration.....	28
Figure 3-16	MELCOR Nodalization of the 5 Assembly Separate Effects Model.....	29
Figure 3-17	Hybrid Separate Effects Schematic with Emergency Spray Operation.....	31
Figure 3-18	Comparison of Reactor Building Leak Rates from BWR Whole Pool Complete Loss-of-Coolant Inventory Calculations [Wagner, 2004] with and without Failure of the Blowout Panel.....	32
Figure 3-19	Original BWR Whole Pool Nodalization.....	36
Figure 3-20	Spent Fuel Locations Colored by Decay Heat Level at 1 Month after the Large Discharge to the SFP.....	37
Figure 3-21	MELCOR Axial Levels of Spent Fuel Assembly in Rack.....	38
Figure 3-22	Schematic of the Whole Pool Model Configuration.....	40
Figure 3-23	Example of Alternating and Repeating 1x4 Patterns.....	43
Figure 3-24	The Radial Coupling Scheme as Implemented in MELCOR SFP Model.....	44
Figure 3-25	MELCOR Reactor Building Model.....	47
Figure 3-26	Example of Pressurized Water Reactor SFP Building Flow Patterns From FLUENT Calculations With An Open Roll Door.....	48
Figure 4-1	Total Decay Heat Power in the Reference BWR SFP.....	52
Figure 4-2	Make-up Flowrate for the Reference BWR SFP.....	53
Figure 4-3	Comparison of the Peak, Median, and Minimum Assembly Decay Heat Power in the Reference BWR SFP.....	54
Figure 4-4	Make-up Flowrate for the Reference BWR SFP.....	55

Figure 4-5 Timing Impact of Sensible Heat on Assembly Cooling at (b)(7)(F) for a Uniform Configuration..... 59 Ex 7F

Figure 4-6 Timing Impact of Sensible Heat on Assembly Cooling at (b)(7)(F) for a Uniform Configuration..... 59 Ex 7F

Figure 5-1 Water Level Boundary Condition from the BWR Whole Pool Model with (b)(7)(F) and a Spray Flow of (b)(7)(F) ..... 62 Ex 7F

Figure 5-2 Vapor and Liquid Temperature Boundary Condition from the BWR Whole Pool Model with (b)(7)(F) and a Spray Flow of (b)(7)(F) ..... 62 Ex 7F

Figure 5-3 Steam Partial Pressure Boundary Condition from the BWR Whole Pool Model with (b)(7)(F) and a Spray Flow of (b)(7)(F) ..... 63 Ex 7F

Figure 5-4 Whole Pool Level Response from a (b)(7)(F) of the Pool with (b)(7)(F) and a Spray Flow of (b)(7)(F) ..... 63 Ex 7F

Figure 5-5 Gas Concentration in the Refueling Room above the SFP for (b)(7)(F) and a Spray Flow of (b)(7)(F) ..... 64

Figure 5-6 Comparison of the Leak Rate and Spray Flowrate Response from a (b)(7)(F) at the Bottom of the Pool with (b)(7)(F) and a Spray Flow of (b)(7)(F) ..... 64 Ex 7F

Figure 5-7 Total Injection Spray Flow for (b)(7)(F) Make-up Case. .... 65

Figure 6-1 Comparison of the Peak Cladding Temperatures for the (b)(7)(F) with a Uniform Configuration with (b)(7)(F) and a Whole Pool Spray Flow of (b)(7)(F) ..... 73 Ex 7F

Figure 6-2 Comparison of the Peak Cladding Temperatures for the (b)(7)(F) with a Uniform Configuration with (b)(7)(F) and a Whole Pool Spray Flow of (b)(7)(F) ..... 73 Ex 7F

Figure 6-3 Assembly Cladding Temperatures for the Uniform Configuration with (b)(7)(F) and (b)(7)(F) Spray Flow (Case S1)..... 74 Ex 7F

Figure 6-4 Assembly Cladding Temperatures for the Uniform Configuration with (b)(7)(F) Spray Flow, and the Flow Regime Model Inactive (Case S1a). .... 74 Ex 7F

Figure 6-5 Assembly Cladding Temperatures for the Uniform Configuration with (b)(7)(F) and No Spray Flow (Case S1b). .... 75 Ex 7F

Figure 6-6 Assembly Cladding Temperatures for the Uniform Configuration with (b)(7)(F) and (b)(7)(F) Spray Flow and Plugged Inlet (Case S1p). .... 75 Ex 7F

Figure 6-7 Axial Cladding Temperature Profiles for the Uniform Configuration with 20 days Aging and (b)(7)(F) Spray Flow. .... 76 Ex 7F

Figure 6-8 Time-averaged Energy Flow in the Uniform Configuration with 20 days Aging and (b)(7)(F) Spray Flow. .... 78

Figure 6-9 Comparison of the Peak Cladding Temperatures for the Uniform Configuration with Various Aging Periods and a Whole Pool Spray Flow of (b)(7)(F) ..... 80

Figure 6-10 Comparison of the Peak Cladding Temperatures for the Uniform Configuration with Various Aging Periods and a Whole Pool Spray Flow of (b)(7)(F) ..... 81 Ex 7F

Figure 6-11 Comparison of the Peak Cladding Temperatures for the Uniform Configuration with Various Aging Periods and a Whole Pool Spray Flow of (b)(7)(F) ..... 82 Ex 7F

Figure 6-12 Comparison of the Peak Cladding Temperatures for the (b)(7)(F) with a Checkerboard Configuration with (b)(7)(F) and a Whole Pool Spray Flow of (b)(7)(F) ..... 85 *Ex 7 F*

Figure 6-13 Comparison of the Peak Cladding Temperatures for the (b)(7)(F) with a Checkerboard Configuration with (b)(7)(F) and a Whole Pool Spray Flow of (b)(7)(F) ..... 85 *Ex 7 F*

Figure 6-14 High-Powered Assembly Cladding Temperatures for the Checkerboard Configuration with (b)(7)(F) and (b)(7)(F) Spray Flow (Case S3)..... 86 *Ex 7 F*

Figure 6-15 Low-Powered Assembly Cladding Temperatures for the Checkerboard Configuration with (b)(7)(F) and (b)(7)(F) Spray Flow (Case S3)..... 86 *Ex 7 F*

Figure 6-16 High-Powered Assembly Cladding Temperatures for the Checkerboard Configuration with (b)(7)(F) and (b)(7)(F) Spray Flow and the Flow Regime Model Inactive (S3a). ..... 87 *Ex 7 F*

Figure 6-17 Low-Powered Assembly Cladding Temperatures for the Checkerboard Configuration with (b)(7)(F) and (b)(7)(F) Spray Flow and the Flow Regime Model Inactive (S3a). ..... 87 *Ex 7 F*

Figure 6-18 High-Powered Assembly Cladding Temperatures for the Checkerboard Configuration with (b)(7)(F) and No Spray Flow (Case S3b). ..... 88 *Ex 7 F*

Figure 6-19 Low-Powered Assembly Cladding Temperatures for the Checkerboard Configuration with (b)(7)(F) and No Spray Flow (Case S3b). ..... 88 *Ex 7 F*

Figure 6-20 High-Powered Assembly Cladding Temperatures for the Checkerboard Configuration with (b)(7)(F) and (b)(7)(F) Spray Flow and Plugged Inlet (Case S3p). ..... 89 *Ex 7 F*

Figure 6-21 Low-Powered Assembly Cladding Temperatures for the Checkerboard Configuration with (b)(7)(F) and (b)(7)(F) Spray Flow and Plugged Inlet (Case S3p). ..... 89 *Ex 7 F*

Figure 6-22 High-Powered Assembly Cladding Temperature Profiles for the Checkerboard Configuration with (b)(7)(F) and (b)(7)(F) Spray Flow. .... 90 *Ex 7 F*

Figure 6-23 Low-Powered Assembly Cladding Temperature Profiles for the Checkerboard Configuration with (b)(7)(F) and (b)(7)(F) Spray Flow. .... 90 *Ex 7 F*

Figure 6-24 Time-average Energy Flow in the Checkerboard Configuration with (b)(7)(F) and a Whole Pool Spray Flow of (b)(7)(F) ..... 92 *Ex 7 F*

Figure 6-25 Comparison of the Peak Cladding Temperatures for the (b)(7)(F) with a 1x4 Configuration with (b)(7)(F) and a Whole Pool Spray Flow of (b)(7)(F) ..... 96 *Ex 7 F*

Figure 6-26 Comparison of the Peak Cladding Temperatures for the 10" Leak with a 1x4 Configuration with (b)(7)(F) and a Whole Pool Spray Flow of (b)(7)(F) ..... 96 *Ex 7 F*

Figure 6-27 Center Assembly Cladding Temperatures for the 1x4 Configuration with (b)(7)(F) and (b)(7)(F) Spray Flow (Case S4)..... 97 *Ex 7 F*

Figure 6-28 Peripheral Assembly Cladding Temperatures for the 1x4 Configuration with (b)(7)(F) and (b)(7)(F) Spray Flow (Case S4)..... 97 *Ex 7 F*

*Ex 7 F*  
*Ex 7 F*



Figure 7-14 Cesium Aerosol Decontamination Factor for Whole Pool for the (b)(7)(F) Ex 7F  
(b)(7)(F) Spray Case (WP8). ..... 115

Figure 7-15 Peak Ring Temperature Response for Whole Pool for the (b)(7)(F) Ex 7F  
Spray Case (WP9). ..... 116

Figure 7-16 Cesium Aerosol Release and Distribution for Whole Pool for the (b)(7)(F) Ex 7F  
(b)(7)(F) Spray Case (WP9). ..... 116

Figure 7-17 Cesium Aerosol Decontamination Factor for Whole Pool for the (b)(7)(F) Ex 7F  
(b)(7)(F) Spray Case (WP9). ..... 117

Figure 7-18 Comparison of Peak Cladding Temperatures from the Hybrid Calculations. .... 119

Figure 7-19 Comparison of Fission Product Releases from Fuel for the Hybrid Calculations. .... 119

Figure 7-20 Comparison of Fission Product Releases to the Environment for the Hybrid Calculations. .... 120

Figure 7-21 Comparison of Fission Product Releases through the Break Location for the Hybrid Calculations. .... 120

Figure 7-22 Comparison of Reactor Building Decontamination Factors for the Hybrid Calculations. .... 121

## Analysis of Emergency Spray Mitigation of Spent Fuel Pool Loss-of-Coolant Inventory Accidents

### 1. INTRODUCTION

In 2001, United State Nuclear Regulatory Commission (NRC) staff performed an evaluation of the potential accident risk in a spent fuel pool (SFP) at decommissioning plants in the United States [NUREG-1738]. The study was prepared to provide a technical basis for decommissioning rulemaking for permanently shutdown nuclear power plants. The study described a modeling approach of a typical decommissioning plant with design assumptions and industry commitments; the thermal-hydraulic analyses performed to evaluate spent fuel stored in the spent fuel pool at decommissioning plants; the risk assessment of spent fuel pool accidents; the consequence calculations; and the implications for decommissioning regulatory requirements. It was known that some of the assumptions in the accident progression in NUREG-1738 were necessarily conservative, especially the estimation of the fuel damage. Subsequently, the NRC desired to expand the study to include accidents in the spent fuel pools of operating power plants. Consequently, the NRC has continued spent fuel pool accident research by applying best-estimate computer codes to predict the severe accident progression following various postulated accident initiators. This report describes the effectiveness of emergency sprays systems for mitigating spent fuel pool accidents.

The data used to perform these calculations were developed from an operating boiling water reactor (BWR). The reference plant is typical of many BWRs with fuel in the SFP from several decades old to the most recent offload. This reference plant has a two-year fuel cycle and roughly discharges one-third of the reactor fuel (b)(7)(F) each outage. The plant removes an equivalent amount of various aged fuel between outages for storage in dry casks, thereby maintaining a relatively constant number of assemblies in the SFP. Hence, the SFP has a wide variety of different aged fuel. In addition, the SFP racks have enough empty cell locations (b)(7)(F) to permit a complete emergency reactor offload as well as store all the refueling blade guides.

The MELCOR 1.8.5 severe accident computer code [Gauntt] with enhancements through Version RP is used to simulate the SFP accident response. MELCOR includes fuel degradation models for pressurized water reactor (PWR) and BWR fuel, radiation, convection, and conduction heat transfer models, air and steam oxidation models, hydrogen burn models, two-phase thermal-hydraulic models, and fission product release and transport models. Therefore, it contains the basic models to address questions and phenomena expected during a spent fuel pool accident.

Version RP includes three recent modeling enhancements applicable to BWR SFP modeling, (1) a new rack component, which permits better modeling of a SFP rack, (2) a new oxidation kinetics model, and (3) a simplified flow regime model. The new BWR spent fuel pool rack component permits proper radiative modeling of the SFP rack between groups of different assemblies. The new oxidation kinetics model predicts the transition to breakaway oxidation in

air environments on a node-by-node basis.<sup>2</sup> The simplified flow regime model permitted simulation of liquid films draining down the BWR fuel assemblies during spray operation.

## 2. BACKGROUND

The reference plant for the SFP analysis is a large BWR. Like most other nuclear plants, the reference plant has installed high-density racks to maximize the storage of fuel in the SFP. A description of the reference plant SFP is given in 2.1. The accidents considered in the present study consist of a loss-of-coolant inventory. A description of the accident progression is provided in Section 2.2.

### 2.1 Description of the Spent Fuel Pool

*Ex 7F*  
The spent fuel pool, 40 feet wide by 35.3 feet long by 38 feet deep, is located on the refueling floor of (b)(7)(F) of the reactor building. The pool is constructed of reinforced concrete with a wall and floor lining of 1/4-inch thick stainless steel. The walls and the floor of the spent fuel pool are approximately 6'. In the northeast corner of the SFP is a cask area of 10' square (see Figure 2-1). The general attributes of the spent fuel pool, the BWR fuel assemblies, and the spent fuel pool racks are described in Table 2-1, Table 2-2, and Table 2-3, respectively.

The high density SFP racks provide spent fuel storage at the bottom of the fuel pool. The fuel storage racks are normally covered with about 23 ft of water for radiation shielding. The SFP racks are freestanding, full length, top entry and are designed to maintain the spent fuel in a spaced geometry, which precludes the possibility of criticality under any condition.

*Ex 7F*  
The high-density SFP racks are of the "poison" type utilizing a neutron absorbing material to maintain a subcritical fuel array. The racks are rectilinear in shape and are of nine different sizes. A total of (b)(7)(F) locations are provided in the pool. The racks are constructed of stainless steel materials and each rack module is composed of cell assemblies, a base plate, and base support assemblies. Each cell is composed of (a) a full-length enclosure constructed of 0.075" thick stainless steel, (b) sections of Bisco Boraflex, which is a neutron absorbing material, and (c) wrapper plates constructed of 0.020" tick stainless steel. The inside square dimension of a cell enclosure is 6.07". The cell pitch is 6.28".

The base plate is a 0.5" thick stainless steel with 3.8" chamfered through holes centered at each storage location, which provides a seating surface for the fuel assemblies. These holes also provide passage for coolant flow.

Each rack module has base support assemblies (i.e., 'rack feet') located at the center of the corner cells within the module and at interior locations<sup>3</sup> to distribute the pool floor loading (e.g., see Figure 2-2). Each base assembly is composed of a level block assembly, a leveling screw, and a support pad. The top of the leveling block assembly is welded to the bottom of the base plate. SFP fuel cells are located above each rack foot. Four 1" holes are drilled into the side of

<sup>2</sup> It should be noted that the steam oxidation model does not use a breakaway kinetics model. Steam-zircaloy oxidation is based on the default Urbanic-Heidrich model [Gauntt].

<sup>3</sup> There are several different rack sizes in the SFP. However, for a 19x10 size rack, there are 18 base support assemblies, 14 on the perimeter and 4 in the interior.

the support pad. The interior of the support pad is hollow and permits flow to the opening in the base plate.

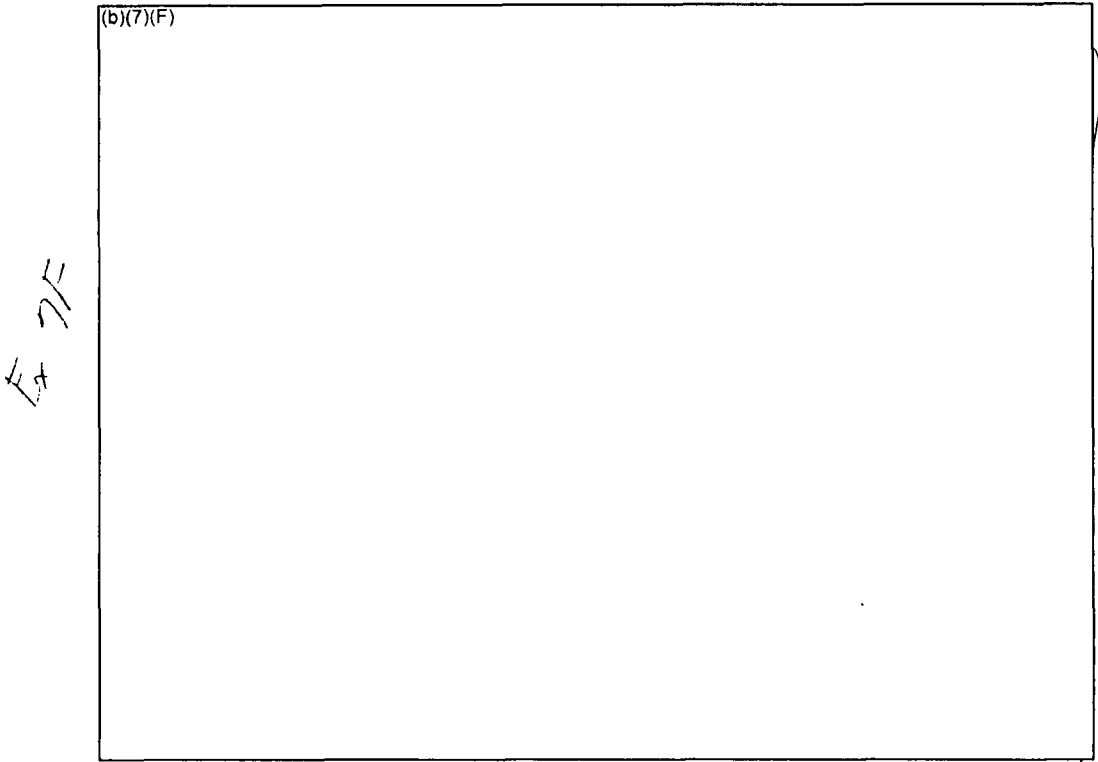


**Figure 2-1 Spent Fuel Pool Rack Layout.**

**Table 2-1 Spent Fuel Pool Data.**

<b>SFP Pool Characteristics</b>	<b>Description or Dimensions</b>	
Dimensions	480" x 424" 10 ft square Cask Area in NW corner 39' high walls	
Concrete thickness	~6 feet	
SFP Volume	53,350 ft <sup>3</sup> (399,000 gal)	
Number of storage locations	(b)(7)(F)	Ex 7F

**Table 2-2 Fuel Assembly Data.**

<b>Assembly Characteristics</b>	<b>Description or Dimensions</b>
Fuel Type	GE 9x9
Number of Fuel Rods	74
Fuel Pitch	0.566"
Fuel Rod Dimensions	0.44" OD 0.028" Cladding 146" Active Length
Maximum Initial Enrichment	4% U-235 by weight
Number of Water Rods	2
Water Rod Dimensions	0.98" OD Zircaloy

**Table 2-3 Spent Fuel Pool Rack Data.**

<b>SFP Rack Characteristics</b>	<b>Description or Dimensions</b>
Rack Height Above the Base Plate	169"
Baseplate Thickness	0.5"
Support Leg Height	7.25"
Poison Material	Boraflex
Cell Pitch	6.28
Cell Construction	0.075" (Gage 14) 304 stainless steel walls with Bisco Boraflex B <sub>4</sub> C particles clad in a non-metallic binder (0.081") with 0.020" stainless wrapper

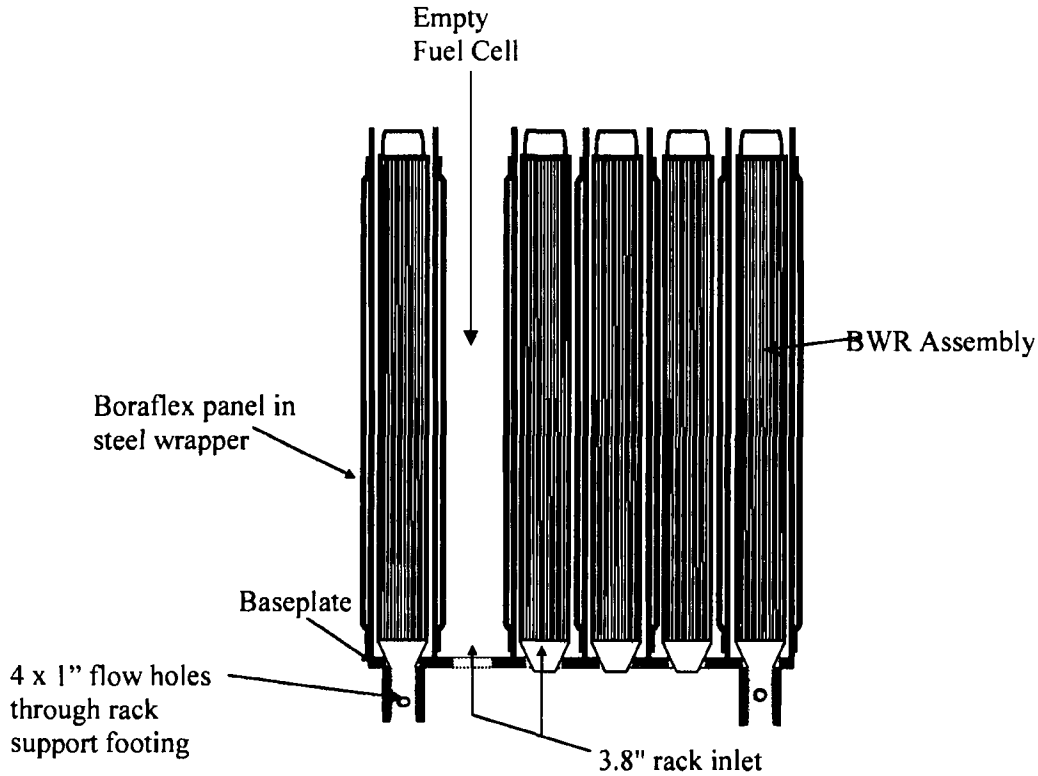


**Figure 2-2 Typical Spent Fuel Pool Rack Cut-away Cross-Section Showing the Fuel Assembly.**

## 2.2 SFP Accident Scenarios

From a natural circulation flow perspective, the SFP accidents are broken down into two categories; scenarios with water above the base plate of the racks and scenarios with a completely drained SFP. Each accident is described next.

### 2.2.1 Complete Loss-of-Coolant Inventory Accident

In the "air" flow case, the accident is initiated with a complete loss-of-coolant accident (see Figure E-1 for pre-accident building configuration and Figure 2-2 for the rack configuration). Due to the removal of the water, a heat-up of the fuel rods ensues. The fuel rods heat the air in the assemblies, which creates a natural circulation pattern. Complex flow patterns develop above and around the SFP racks and in the refueling room due to the interaction between the hot rising plume and descending cool air. After the hot plume exits the SFP, the plume will rise to the ceiling and spread radially within the hot gas layer at the top of the refueling room. The degree of heating in the spent fuel storage building and behavior of the hot gas layer depends on many factors including the rate of ventilation (e.g., ventilation system operation, openings or

leakage, and/or structural failures), the heat loss through the building walls and ceiling, and other accident thermal effects (e.g., fire).

The flow patterns of the gases under the racks are also complicated. The regions of down flow include the space between the rack and walls, some of the empty rack slots, and the cask region or other open areas. If a high speed flow region develops under the racks, then there can be a Bernoulli Effect. For example, if the air to the SFP cells is preferentially provided through the cask area, a high speed flow (i.e., 3 m/s) can develop under the rack cells adjacent to the cask area. The high speed flow reduces the upflow of gases into the affected assemblies, which leads to less heat removal and a faster heat-up (e.g., see [Wagner, 2000]).

If inadequate cooling is provided, then the fuel cladding will heat up and the Zircaloy cladding will rapidly oxidize (i.e., burn) and to a lesser extent, nitride (i.e., combine with nitrogen if no oxygen or steam are available). Since the oxidation and nitride processes are exothermic, the fuel rods could heat to melting conditions and structurally degrade. Meanwhile, the steel racks supporting the fuel assemblies will also heat due to convection and radiation from the fuel assemblies. The timing of the degradation of the specific fuel assemblies and racks are affected by the decay heat level (i.e., burn-up, power history, enrichment, and time since discharge), the assembly inlet temperature, convective and conductive heat removal rates, and the heat transfer rate from/to adjacent assemblies. Finally, and most importantly, the degradation of the fuel rods can lead to fission product releases.

An accurate analysis of the SFP response requires consideration of the aforementioned phenomena. As evidenced by the accident description, there is a large range of geometric length scales and modeling requirements. The length scales range from details of the individual assembly heat generation and flow patterns (e.g., also including multi-dimensional flow within an assembly, see [Ross, 2003]), intra-assembly heat transfer, large scale flow patterns above, below, and through the racks, and the building response (e.g., ventilation, heat loss, structural failures, etc.). The relevant physics and phenomena include heat transfer (convection, conduction, and radiation), fluid flow (small scale to large scale), chemical reactions (i.e., oxidation), severe accident fuel degradation behavior, and fission product release and transport.

### **2.2.2 Partial Loss-of-Coolant Accident**

In the second type of accident, the SFP is partially drained (i.e., due to partial drain or boil-off) and does not include recirculation of hot gases through the bottom of racks. Consequently, the gas in the fuel assemblies above the pool level is relatively stagnant (i.e., except for steam flow from boiling). In this condition, steam cooling and/or a level swell from the boiling will keep the fuel rods cool unless the pool level drops too far. However, once the level drops below roughly one-half of the fuel height, the top of the fuel rods will heat-up and degrade.

If the top of the fuel is uncovered, then several new phenomena occur in a partial loss-of-coolant accident. First, the convective flows are much smaller than a complete loss-of-coolant accident. In the complete loss-of-coolant accident, there was ample air flow as the assembly heated. However, in a partial loss-of-coolant accident, the fluid in the assembly is relatively stagnant because the pool blocks the bottom of the racks. The primary source of cooling comes from

steam flow due to boiling below the water level. Hence, there are competing effects of the lack of a strong convective flow versus the benefits of some steam cooling and axial conduction to the water. In summary, the scenarios with water include (a) two-phase boiling, (b) an assembly flow rate that is strongly affected by the amount of boiling below the water surface, and (c) gas inlet temperature that is limited to the boiling point of water (i.e., the air cases are not similarly constrained).

The rate of oxidation of the Zircaloy cladding is the second key difference expected in a partial loss-of-coolant accident. In particular, the fluid next to the Zircaloy cladding will be steam rather than air. Steam also reacts exothermically with Zircaloy but at a slower rate than with air. Furthermore, the byproduct of this reaction is hydrogen. The hydrogen will replace the steam and retard or stop the Zircaloy/steam reaction. Consequently, the reaction could become "steam starved" and controlled by the rate of steam production by boiling below the pool level, which is expected to be very low for aged spent fuel. If there is adequate steam when the Zircaloy reaches high temperatures (i.e., >1500 K), the power from metal water reactions can be much larger than decay heat. Therefore, there are two competing effects on the rate of fuel degradation relative to the complete loss-of-inventory accident scenario (i.e., as described in Section 2.2.1), (1) a lower, controlled oxidation effect (i.e., due to steam starvation) and (2) a much lower convective cooling rate (i.e., because the bottom of the racks are "plugged" with water).

Finally, a third new difference in the partial loss-of-coolant accident is the behavior of the hydrogen. As hydrogen is produced during fuel degradation, the hydrogen may collect and mix with oxygen in the air above the pool. Given the appropriate conditions, the hydrogen could ignite and possibly cause structural damage to the reactor building. Any damage or enhanced leakage caused by the pressurization from the hydrogen burn could increase the release of fission products and their associated adverse consequences.

As will be discussed in Section 5, spray operation complicates the potential for water plugging the inlet to the racks. For appropriate combinations of leakage and sprays rates and leakage location, the spray flow can maintain a water level above the base plate of the racks. Consequently, spray operation in some circumstances will stop air natural circulation. Depending upon the relative magnitudes of the spray flow and decay heat power, the resultant configuration may be less effectively cooled.

### 3. ANALYSIS METHODOLOGY

Based on the information supplied by the reference plant staff, MELCOR models were developed to perform accident analyses (e.g., see [Wagner, 2003] and [Wagner, 2004]). Since those analyses were performed, there have been several significant improvements in the modeling of the SFPs. Section 3.1 summarizes those improvements. Several different models were used for the detailed evaluations of the fuel response to emergency spray. A description of the MELCOR separate effects models are presented in Section 3.2. The separate effects models were used to simulate the details of the spray penetration into the assemblies. Next, the whole pool models are described in Section 3.3. The whole pool models were used to calculate boundary conditions for the separate effects models as well as calculate the spray scrubbing efficiency and the source term behavior.

#### 3.1 New BWR SFP Modeling

Since the last report on BWR SFP modeling, there have been a number of improvements in MELCOR's modeling capabilities. Section 3.1.1 describes the new BWR-SFP Core Package model with the new Rack component. Next, Section 3.1.2 describes the new breakaway oxidation kinetics model based on experiments at Argonne National Laboratory. The fuel geometric model was completely updated to include partial fuel rods, the hydraulic effects of water rod flow, and other detailed weight and geometric information from GNF hardware used in the SNL SFP experiments. In addition, a new flow resistance model was implemented based on detailed flow tests. The pertinent results from the SNL experimental program are described in Section 3.1.3. Finally, a technique to model the spray thermal-hydraulic response in MELCOR was developed and is described in Section 3.1.4.

##### 3.1.1 New BWR SFP Model

Previous MELCOR BWR SFP calculations were performed using the "BWR" model designation in the CORE Package input (i.e., [Wagner, 2003] and [Wagner 2004]). Once the model designation is selected, certain fixed geometry specifications are made. At the time of the original calculations, only the BWR and PWR model designations were available. The BWR designation assumes the BWR fuel rods are surrounded by a BWR canister. Outside the canister is a control blade (see Figure 3-1). Typically in a MELCOR reactor application, concentric rings are used to model the fuel in the core. Ring 1 would represent the center of the core and successive, concentric rings would represent annular regions of assemblies with increasing radii to the edge of the core.

MELCOR 1.8.5 BWR Model  
("Blade" is enclosed inside the ring)

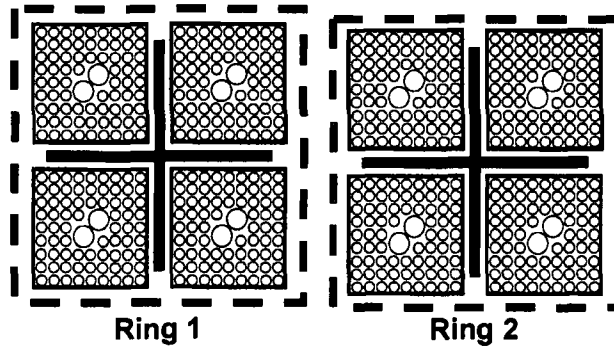
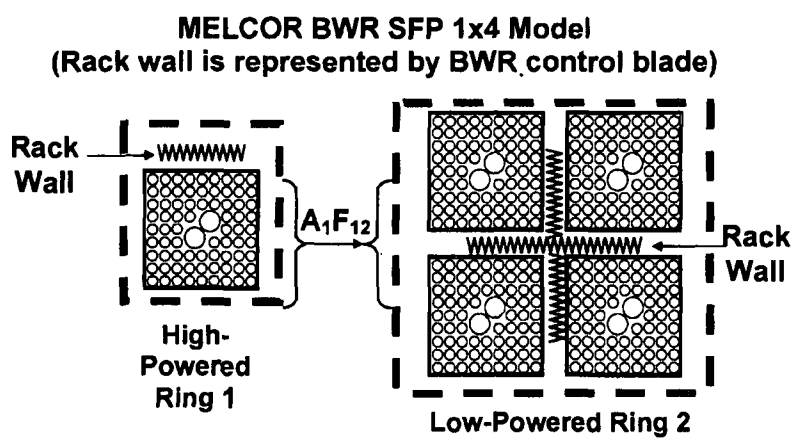


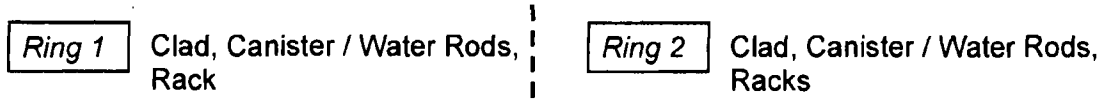
Figure 3-1 MELCOR Modeling of a BWR Assembly in the Reactor Core.

For application to the SFP geometry, it was not possible to explicitly model the SFP rack. The only components available are those shown Figure 3-1, i.e., the fuel and cladding, the canister, and the control blade. For the original SFP BWR calculations, the control blade component was used to model the rack. The SFP BWR 1x4 configuration is shown in Figure 3-2. Although the rack walls are contained internally within a ring, the appropriate surface area and mass was properly conserved. From a radiation heat transfer perspective, heat flows from adjacent rings between the canister walls. In particular, the radiation heat transfer from Ring 1 to Ring 2 in Figure 3-2 occurs from the canister of Ring 1 to the canister of Ring 2 (i.e., see Figure 3-3). Simultaneously, radiative exchange is also calculated within each ring from the canister wall to the rack wall (i.e., see summary in Figure 3-3). Consequently, from a radiation perspective, the rack wall is not correctly represented between the adjacent rings of fuel assemblies. Similarly, the surface areas for convection are preserved. However, the adjacent fluid temperature for the racks is characteristic of the region within a ring (i.e., the bypass fluid region outside the canister) rather than the Ring 1 bypass on interior side and the Ring 2 bypass on the exterior side.

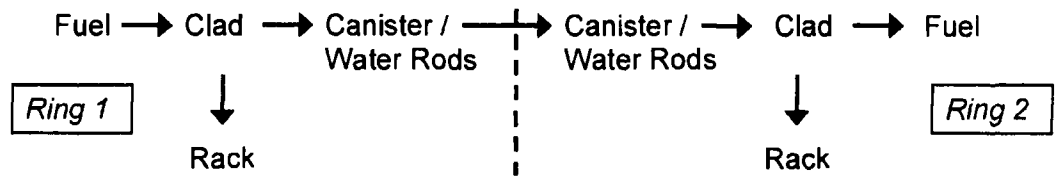


**Figure 3-2 Original MELCOR Modeling of BWR Assemblies in a 1x4 SFP Configuration.<sup>4</sup>**

**Convective Heat Transfer Surfaces:**



**Radiative Heat Transfer Flow Path:**



- Rack is modeled via a Control Rod Blade component

**Figure 3-3 Heat Flow for the Original MELCOR Modeling of a BWR Assemblies in a 1x4 SFP Configuration.**

During and subsequent to the original BWR SFP separate effects calculations, additional scoping work was done to estimate the impact of the aforementioned heat transfer limitation. For the configuration of a single assembly in a uniform decay heat region (i.e., the configuration for many of the calculation), the heat transfer rate from the fuel would be too high prior to achieving steady state conditions because heat was simultaneously transferring directly to the rack wall and the canister. However, due to the efficiency of high temperature radiation from thin structures with large surface areas the thermal coupling between the fuel rods and the rack wall was

<sup>4</sup> The rack wall is shown in a zigzag pattern to only emphasize the correct surface and mass was preserved while wholly containing the rack wall on the inside of Rings 1 and 2.

expected to be very close<sup>5</sup>. The greatest impact was expected to occur in a 1x4 configuration where radiative heat transfer from a high-powered center assembly to four adjacent peripheral assemblies. In this configuration, the rack wall would be a radiation barrier between the center assembly and the peripheral assemblies. Hence, the thermal coupling shown in Figure 3-2 and Figure 3-3 would be over-estimated.

Subsequent to the release of the original MELCOR BWR separate effects report ([Wagner, 2003]), MELCOR was modified to include "SFP-BWR" and "SFP-PWR" model types. The new designator specified the geometry as shown in Figure 3-4 for the 1x4 configuration and the radiation and convection solution as shown in Figure 3-5. Consequently, the rack wall around Ring 1 is properly placed between the Ring 1 and Ring 2 assemblies. The remaining rack walls for the four peripheral assemblies in Ring 2 is placed at the outer boundary of Ring 2, which is an adiabatic boundary condition for the 1x4 simulations. Similar to previous models, the rack wall was comprised of steel and control material. The MELCOR models described in Section 3.2 and 3.3.2 used this designation.

**Introduced in MELCOR 1.8.5 Version RO  
"SFP-BWR" Model Representation of 1x4 Model  
(Cell wall is represented by new rack component)**

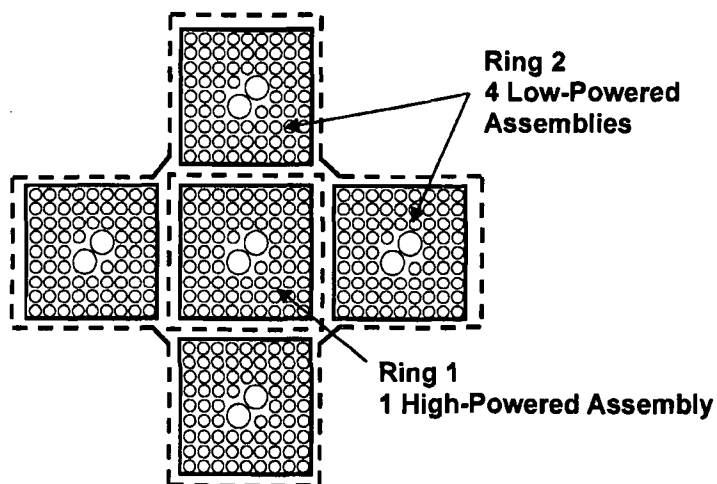


**Figure 3-4 New MELCOR Modeling of BWR Assemblies in a 1x4 SFP Configuration.**

<sup>5</sup> These limitations were recognized early and have been steadily examined with increasingly sophisticated approaches. Initially, the MELCOR heat structure components were used to examine the heat flow for a uniform configuration. Subsequently, three-dimensional COBRA-SFS calculations were performed for the 1x4 configuration. Next, MELCOR was modified as described in this section to properly represent the geometric location of the rack wall and the radiative exchange in a 1x4 configuration. Most recently, analysis of experimental work is being done with the new SFP-BWR configuration. Each of the complimentary analyses has confirmed the goodness of this assumption. The more accurate SFP-BWR 1x4 model only shows a minor degradation of radial radiative heat transfer at high temperatures.

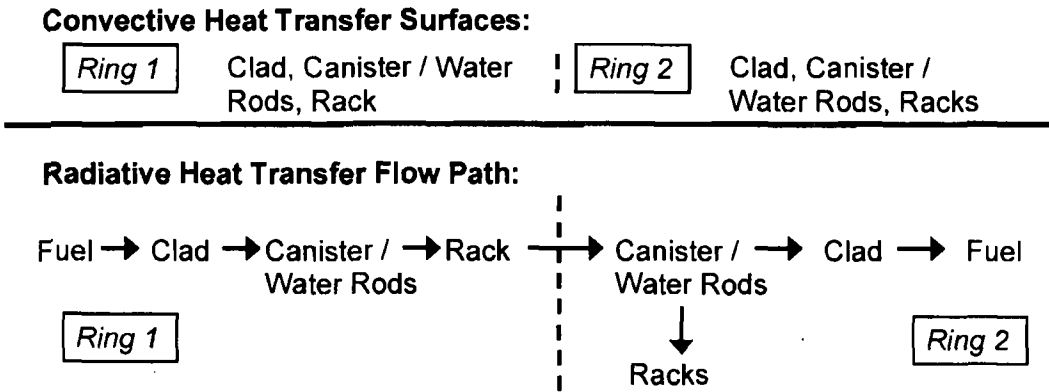


**Figure 3-5 Heat Flow for the New MELCOR Modeling of BWR Assemblies in a 1x4 SFP Configuration.**

Finally, as implied in Figure 3-3, MELCOR does not include explicit modeling of the water rods. The two large water rods in the center of a 9x9 GNF assembly are modeled indirectly as additional mass and surface area on the canister component. As a new feature in the “SFP-BWR” model, the inside and outside surface area of the canister component can be specified independently. The water rod masses and surface areas were added to the canister mass and canister inside surface area, respectively. Hence, the proper outer canister surface to the rack was preserved as well as the thermal coupling from the fuel rods to the canister and the water rods. Previously, the surface area of the water rods was ignored but the mass was included as part of the canister.

**3.1.2 Breakaway Air Oxidation Model**

Argonne National Laboratory (ANL) has performed oxidation kinetics testing on Zr-based alloys including Zircaloy-4, which is similar to the Zircaloy-2 alloy used in the reference BWR plant assemblies. The testing showed that air oxidation can be observed at temperatures as low as 600 K. In the tests, a specimen was held at constant temperature and the weight gain due to oxidation as a function of time was measured. The reaction rates for air oxidation are described by parabolic kinetics similar to the ones used to describe steam oxidation. The general form of the equation is,

$$\frac{dw^2}{dt} = K(T) \tag{Eqn. 2.1}$$

where, w is oxide scale thickness or, alternatively, in the MELCOR convention, reacted metal mass. The rate of oxidation was initially steady versus the square root of time at a particular temperature. However, the rate of oxidation increased after some time and persisted for the remainder of the test.

A new oxidation model was implemented in MELCOR by adding a breakaway lifetime calculation. The model calculates an oxidation "lifetime" value for Zircaloy components in each cell using the local Zircaloy cladding temperature. Figure 3-6 shows the breakaway timing data from the ANL tests. As the specimen temperature increased, the amount of time until breakaway became shorter.

For implementation into MELCOR, the ANL data was curve fit as follows,

$$LF = \int_0^{t'} \frac{t'}{\tau(T)} \quad (\text{Eqn. 2.2})$$

where,  $\tau(T)$  is

$$\tau(T) = 10^{P_{LOX}} \quad (\text{Eqn. 2.3})$$

and  $P_{LOX}$

$$P_{LOX} = -12.528 \cdot \log_{10} T + 42.038 \quad (\text{Eqn. 2.4})$$

A comparison of the data with Equation 2.4 is shown in Figure 3-6. For reference, specific values of the breakaway timing are provided in Table 3-1.

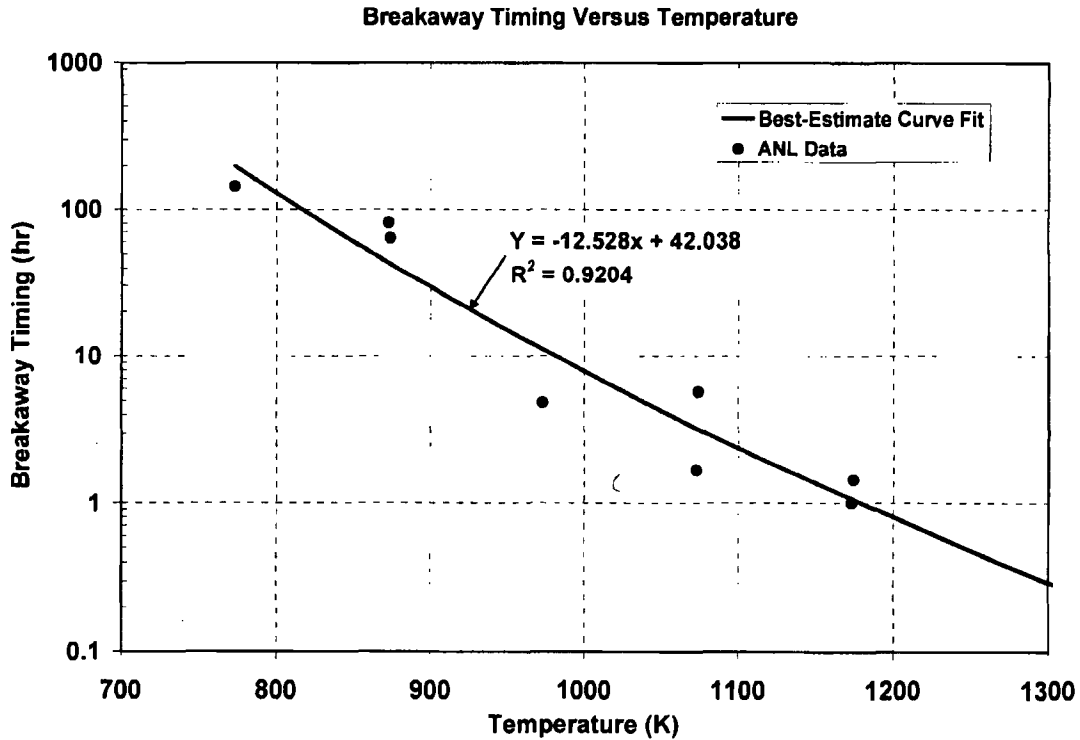


**Figure 3-6 Comparison of the MELCOR Breakaway Timing Fit to the Zirlo and Zr-4 Data from the ANL Air Oxidation Tests.**

The new MELCOR breakaway oxidation model calculates the lifetime function at every node in the MELCOR model with Zircaloy cladding. The oxidation kinetics linearly transitions from the pre-breakaway correlation at  $LF = 1$  to post-breakaway kinetics at  $LF = 1.25$ . Hence, only nodes that have exceeded the lifetime function will have the higher post-breakaway oxidation kinetics.

The ANL pre- and post-breakaway Zr-4 oxidation correlations<sup>6</sup> are summarized below,

- Steam pre-oxidized, wide-temperature pre-breakaway Zr-4 oxidation correlation (red line on Figure 3-7)

$$K(T) = 26.7 \exp (-17,490 / T) \text{ [kg}^2/\text{m}^4\text{-s]} \quad (\text{Eqn 6.6 in [Natesan, 2004]})$$

- Steam pre-oxidized, wide-temperature post-breakaway Zr-4 oxidation correlation (black line on Figure 3-7)

$$K(T) = 2.97e4 \exp (-19,680 / T) \text{ [kg}^2/\text{m}^4\text{-s]} \quad (\text{Eqn 6.7 in [Natesan, 2004]})$$

**Table 3-1 MELCOR Fit of the Timings for Transition from Pre-Breakaway to Post-Breakaway Oxidation Reaction Kinetics for Zirlo and Zircaloy-4 in the ANL Experiments [Natesan, 2004].**

Specimen Temperature	Breakaway Timing (Eqn. 2.4)	ANL Data Used in Curve Fit (See Figure 3-6)
400°C (673 K)	1125 hr (Extrapolated)	-
450°C (723 K)	458 hr (Extrapolated)	-
500°C (773 K)	198 hr	144 hr
550°C (823 K)	90 hr	-
600°C (873 K)	43 hr	64 and 81hr
650°C (923 K)	22 hr	-
700°C (973 K)	11 hr	4.8 hr
750°C (1023 K)	5.9 hr	-
800°C (1073 K)	3.3 hr	1.7 hr and 5.8 hr
850°C (1123 K)	1.8 hr	-
900°C (1173 K)	1.1 hr	1 hr and 1.4 hr

<sup>6</sup> Note that the form of the leading coefficient of these correlations were adjusted to MELCOR input requirements, which uses  $K(T)$  is a function of Zircaloy oxidized versus oxide weight gain.

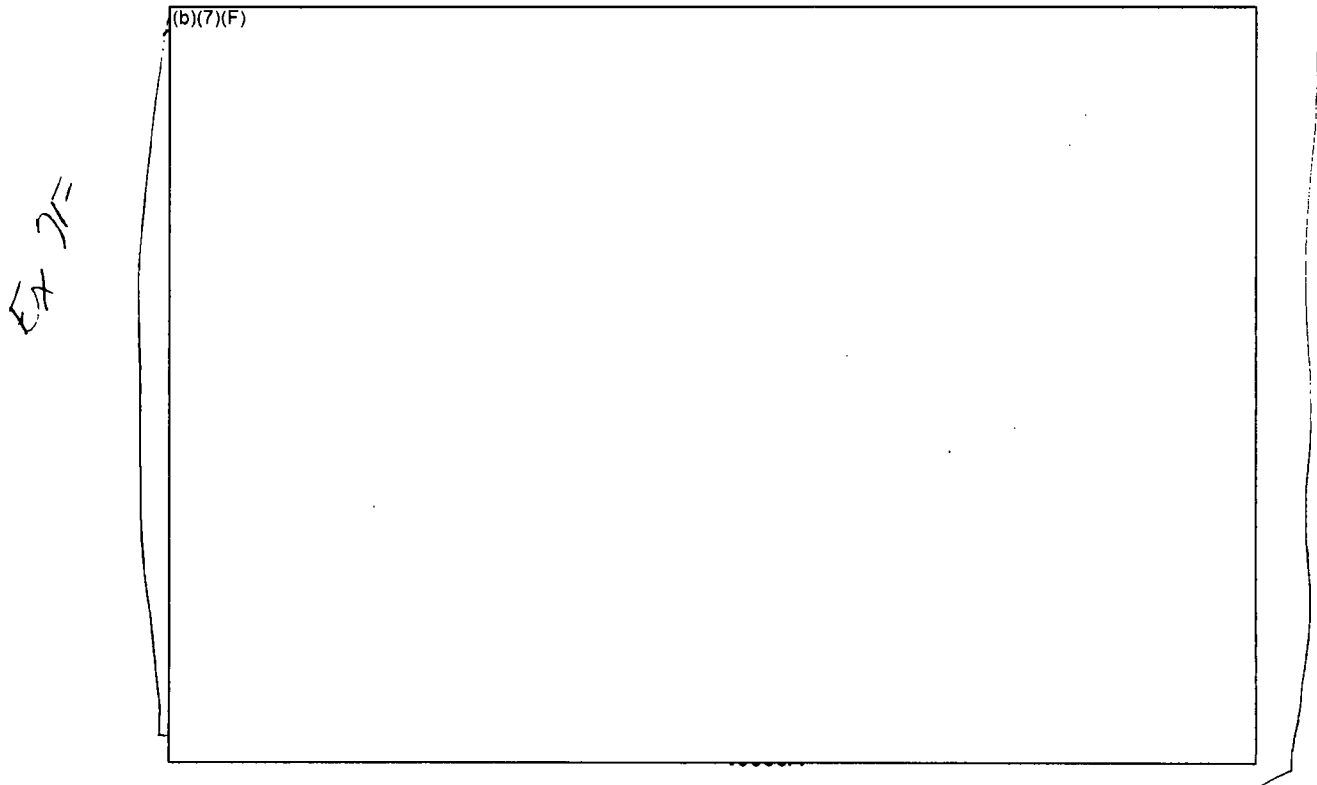


**Figure 3-7 Parabolic Reaction Kinetics Coefficients for Zr-4 Oxidation.**

### 3.1.3 New Hydraulic Resistance Model

Recently, hydraulic resistance measurements were performed on a Global Nuclear Fuel (GNF) 9x9 BWR assembly at Sandia National Laboratories [Durbin]. Commercial components were purchased to create the assembly including the top and bottom tie plates, spacers, water rods, channel box, and all related assembly hardware. Stainless steel conduit was substituted for the fuel pins for hydraulic testing. The stainless steel mock fuel pins were fabricated based on drawings and physical examples supplied by GNF.

Figure 3-8 shows the layout of the BWR pressure drop experimental assembly, including the 18 pressure port locations. Two Paroscientific Digiquartz differential pressure transducers were plumbed directly to the desired pressure ports. These pressure gauges use a highly sensitive quartz crystal to measure slight changes in differential pressure (resolution ~ 0.02 Pa). Measurements were recorded directly to the hard drive of a PC based data acquisition system every 3 seconds using a LabView 7.1 interface. These measurements included the air flow rate through the assembly, ambient air temperature, ambient air pressure, and the assembly pressure drops.

Three primary series of experimental runs were performed. In the first two sets of experimental runs, the flow holes in the water rods were either blocked or unblocked. The bypass holes on the inlet nozzle assembly were blocked for these tests. In the final tests, the bypass holes were opened. In the assembly's prototypical configuration, the water rods are un-blocked and the bypass holes are unplugged. The subsequent analysis of the data calculated a wide range of parameters including the flow through the water rods and bypass holes as well as the corresponding local and total pressure drops for a Reynolds Numbers range of 70 to 900

Ex 7F

(b)(7)(F) In all configurations, the tests were repeated several times and alternate primary measurements were performed to verify the assembly flowrate and overall pressure drop. From the pressure drop data, the laminar flow resistance terms were processed in terms of inputs for the MELCOR code (i.e., see below,  $S_{LAM}$  and  $k$ ). An error analysis of the measurements revealed an uncertainty of hydraulic resistance values for input into MELCOR to be very small (b)(7)(F)

(b)(7)(F) Ex 7F

MELCOR, like other control volume codes, includes constitutive relationships to specify form losses (i.e., minor losses) and wall friction losses (i.e., major or viscous) along a flow path as a hydraulic flow loss term to the momentum equation. The format of the user-specified input for MELCOR is defined from the sum of the local viscous and major pressure drops,

$$\Delta P = \frac{1}{2} \rho v^2 (fL/D + k) \quad \text{Eqn. 3.1}$$

The laminar friction factor ( $f$ ) for laminar flow is written explicitly as,

$$f = S_{LAM} / Re \quad \text{Eqn. 3.2}$$

where,

$S_{LAM} = 64$  for pipe flow (and  $S_{LAM} = 100$  for bundle flow in the BWR SFP model in [Boyd], [Wagner, 2003], and [Wagner, 2004])

$Re$  = Reynolds Number or  $(\rho v d_H) / \mu$

$\rho$  = local density

$v$  = local velocity

$\mu$  = local fluid viscosity

$d_H$  = local hydraulic diameter (defined as  $4 A / P_w$ )

$A$  = local flow area

$P_w$  = wetted perimeter

EX 7F

As shown in Figure 3-8, the BWR fuel assembly (b)(7)(F) grid spacers, upper and lower tie-plates, full and partial rod regions, two water rods, and an inlet nozzle. It is not practical to include a detailed representation of all the geometry changes in the MELCOR model. In addition, the MELCOR code includes some hard-wired geometry models that further limit the modeling of the two large water rods inside the assembly and their associated flow. Consequently, modeling choices are required to represent the geometry of the BWR assembly. Relative to the hydraulic modeling in the BWR SFP MELCOR model, the experimental data are used in the following manner,

- Based on the hydraulic impact of the fully populated versus the partial regions, the control volume boundaries were specified to span uniform geometry regions. Control volume boundaries were placed at the bottom of the lower tieplate, the transition from the fully populated rod region to the partial region, and at the top of the upper tieplate. By spatially dividing the two regions, the distinct flow loss effects can be extended to heated conditions, where the flow will accelerate along the length of the assembly.
- The flow resistance in a flow path spans the region from cell-center of the lower control volume to cell-center of the upper control volume. Hence, the pressure in a given control volume represents the pressure in the center of the control volume. A single flow path may span more than one grid spacer and perhaps a tieplate. Segment data on a particular flow path defines the form and wall friction losses along the geometric regions encompassed in the flow path length. Several flow paths had multiple flow segments due to geometry changes within the flow path range. The net effects of varying flow resistance are calculated by the code.
- For the application to the emergency BWR SFP spray analysis, the results from Table 3-2 were used, which includes prototypical water rod flow effects. For the flow segments in the fully populated tube region, a  $S_{LAM}$  of (b)(7)(F) was used and  $k$  losses of (b)(7)(F) were used for each spacer included in the range of the flow path. The flow area and hydraulic diameters were preserved. The total length across all flow paths in the fully populated region (b)(7)(F) and the total  $k$  was 19. Therefore, the total flow losses (b)(7)(F) were exactly preserved, including the effect of flow within the water rods. Similarly, the partially populated tube region used a  $S_{LAM}$  of (b)(7)(F) per spacer in the range of the flow path. The total length across all flow paths in the fully populated region (b)(7)(F) and the total  $k$  was

(b)(7)(F)

EX 7F  
(b)(7)(F)

EX 7F

EX 7F

EX 7 (b)(7)(F) The flow path segments in the partial rod region used the larger flow area and hydraulic diameter as specified in 2-8 from Table 3-2. For reference, the overall resistance was of a SLAM of (b)(7)(F) and k losses of (b)(7)(F). In comparison, the previous BWR analysis used SLAM of (b)(7)(F) and k losses of (b)(7)(F) across the same region (i.e., not including the inlet nozzle). EX 7 F

- Table 3-2 was also used to specify the pressure drop across the upper tieplate (1-2) and lower tieplates and the inlet region (b)(7)(F). Similar to above, the appropriate flow areas and hydraulic diameters for these regions were used.
- Finally, the results from Figure 3-10 were used to specify the flow loss terms for the inlet nozzle leakage to the interstitial bypass region. The form losses in the MELCOR model were adjusted to match the measured total to bypass flow split.

Until this hydraulic data was available, the previous BWR SFP MELCOR analyses did not include the sophistication of separate flow resistances for the partial and fully populated regions of the BWR bundle.

It is worth noting that while the experimental analysis could not separately discern the contribution of wall friction distinct from form losses, the results analysis in Table 3-2 precisely satisfies the model input requirements for MELCOR, as well as other control volume codes, where the overall hydraulic losses are averaged across larger regions. The linear (i.e.,  $S_{LAM}$ ) and quadratic (i.e., the k term) hydraulic loss coefficients are easily put into the MELCOR input format and will replicate the measured flow losses across the Reynolds number range of 70 to 900, including the overall nonlinear hydraulic effects from (a) flow development regions, (b) the grid spacer entrance, internal, and exit effects, (c) the inlet and exit flows to the water rods, and (d) the transition from the fully to partially populated tubes regions.

**Table 3-2  $S_{LAM}$  And k Coefficients for the Unblocked Water Rod Assembly Assuming All Flow Passes Through the Bundle.**

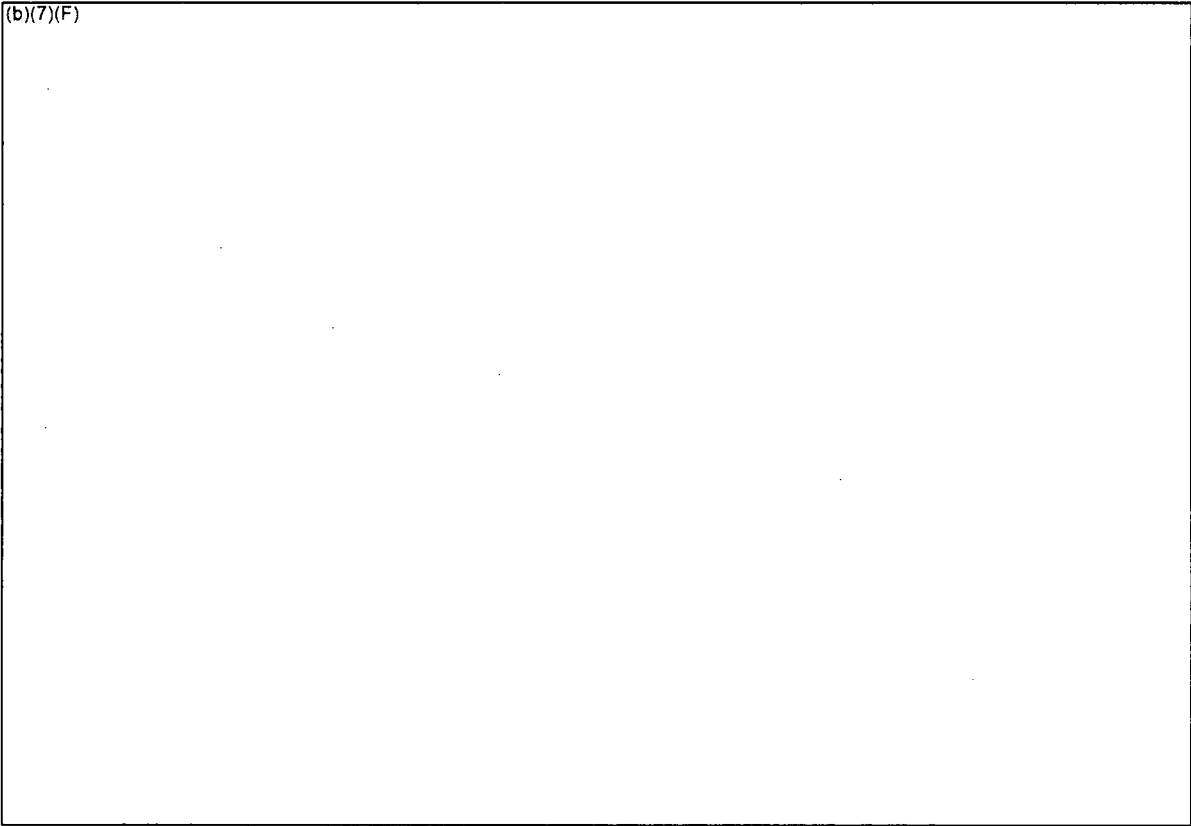
EX 4

(b)(7)(F)

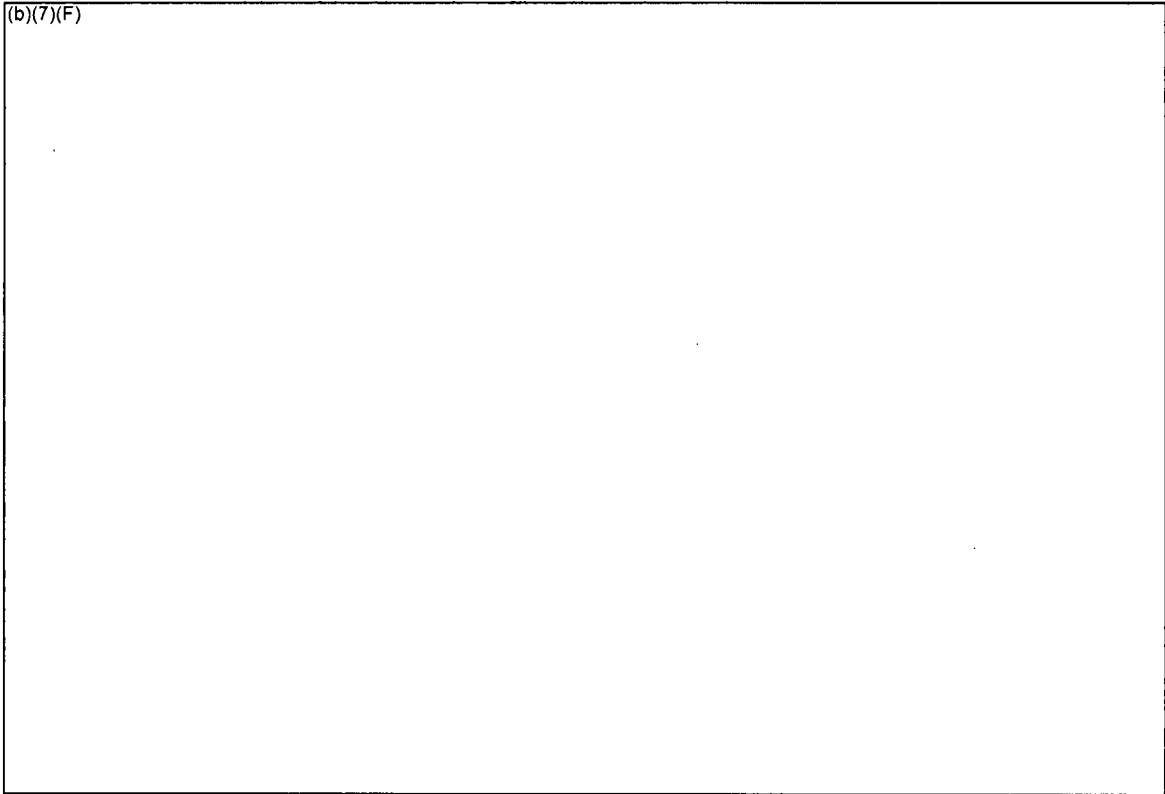
(b)(7)(F)
-----------



Figure 3-8 BWR Assembly Experimental Apparatus used in the Hydraulic Resistance Testing.



**Figure 3-9 Measured Pressure Drop over the Full, Partial, and Total Assembly Regions.**



**Figure 3-10 Comparison of the Calculated and Measured Bypass Flow.**

### 3.1.4 Spray Flow Modeling in MELCOR

The spray flow modeling was performed in two ways. For the whole pool calculations, the MELCOR containment spray model was used. The MELCOR containment spray package includes calculations for spray droplet heat and mass transfer and fission product removal [Gauntt]. A droplet size of 1250 microns was used unless otherwise noted. The droplets were directed into the assemblies and open spaces based on their respective cross-sectional areas. Upon entering the assemblies, the thermal-hydraulic calculations were performed by MELCOR's CVH package as described below.

Generally, the separate effects models were used to resolve the spray performance. Boundary conditions for the inlet and exit of the separate assembly model were provided by whole pool calculations (see Section 3.3 for a description of the models). A spray water source was specified to the top of the assembly according to the relative cross-sectional area. For example, spray water was added to CV-119, CV-129, CV-219, and CV-229 in the 1x4 SE model (see Figure 3-16). The flow area and resistance representing the upper tie-plate is represented in the next downward flowpath. The penetration of the spray water into the assembly is controlled by MELCOR's interphase momentum model, which replicates the Wallis flooding curve [Gauntt].

Once the spray water enters the assembly, the spray is assumed to form a thin film on the fuel structures in the assembly, which drains downward. The new CORE Package simplified flow regime model identifies the spray flow as a film in contact with the fuel rods (see Figure 3-12). Heat transfer takes place between the fuel rods and water in core cells where the flow regime model is active. Nucleate or film boiling heats the water film to saturation conditions as it drains down the assembly. Simultaneous heat transfer from the rods and surrounding gas causes the spray flow to boil. The spray film travels downward in contact with the fuel rods until the local CVH void fraction becomes greater than 99.8% (i.e.,  $\alpha > 0.998$ ). Due to numerical considerations, the residual water is converted into a shallow pool where the liquid heat transfer area is apportioned by the depth of the pool in the control volume.<sup>7</sup> Typically, the remaining water boils away in the first core cell after the flow regime model is disabled.

A relatively detailed CVH/CORE nodalization was used to track the water as it penetrates into the assembly (see Figure 3-15). The detailed nodalization permits a better local representation of the fluid conditions and the location of the spray dryout. The calculated results show a steadily decreasing flowrate and increasing void fraction as the liquid spray penetrates into the assembly. For example, Figure 3-11 shows the axial temperature response in an assembly with spray cooling using the new flow regime model. In this case, the top of the assembly is cooled to near saturation conditions and is in nucleate boiling heat transfer. (b)(7)(F)

(b)(7)(F)

(b)(7)(F)

Ex 7/1

<sup>7</sup> If the flow regime model was used until the flow disappears, very small timesteps are needed to resolve the large heat transfer rates to negligible water mass. When the surface area in contact with water is partitioned by the pool depth, a larger timestep can be used which just boils the water dry in the first or next CVH volume. The residual heat removal for void fractions greater than 0.998 is relatively small.

It should be noted that the CVH package interprets the liquid film as small pools at the bottom of each CVH volume (see Figure 3-13). Due to the high void fraction, the phasic resistance of the steam or air flowing through the pool is relatively insignificant, which is the expected impact of a liquid film. Similarly, the depth of the spray water penetration is controlled by the CORE heat transfer rate rather than the momentum solution. Axial, stepwise heat transfer from the core cells limits how far the spray water penetrates into the assembly.

A possible limitation of the CVH representation is the relatively small heat transfer area between the two phases (i.e., only heat transfer through the pool and the surface versus a film). However, the rate of heat transfer from the gas to the water film is minor in comparison to the nucleate and film boiling heat transfer on the surface of the fuel rods. In addition, MELCOR's quenching model is relatively ineffective. The model accurately calculates separate quenched and un-quenched temperatures in each CORE cell that is in film boiling. However, it assumes the unquenched portion is at the top of the cell. Hence, any axial condition benefit from a downward moving quench front is not realized. The impact from this limitation is not expected to be too significant due to the relative magnitudes of the surface heat transfer rate relative to any axial conduction effects.

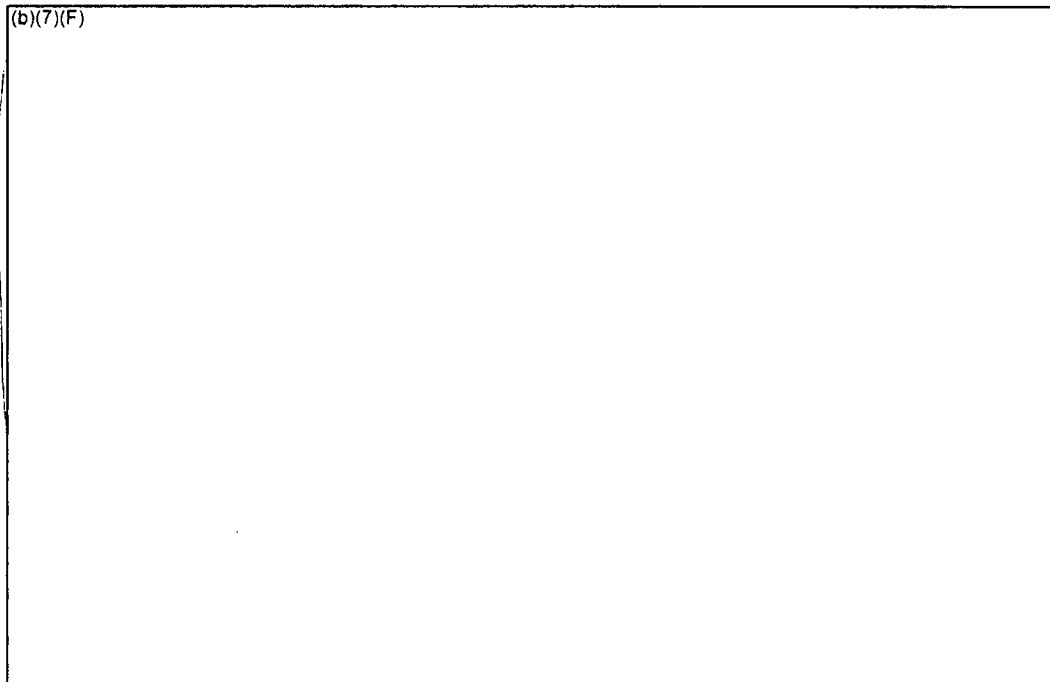


**Figure 3-11 Axial Temperature Profile in the Assembly with Spray Flow.**

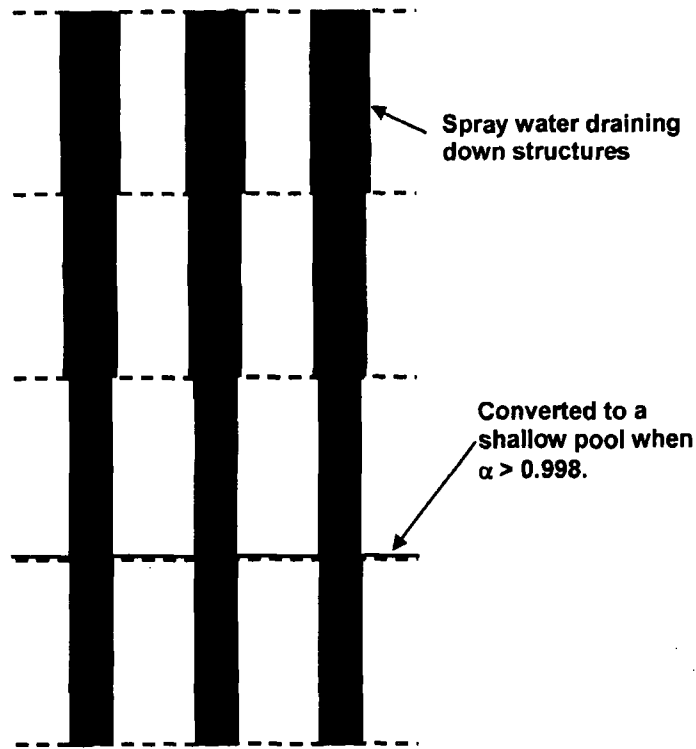


Figure 3-12 Core Package Representation of a Spray Flow.

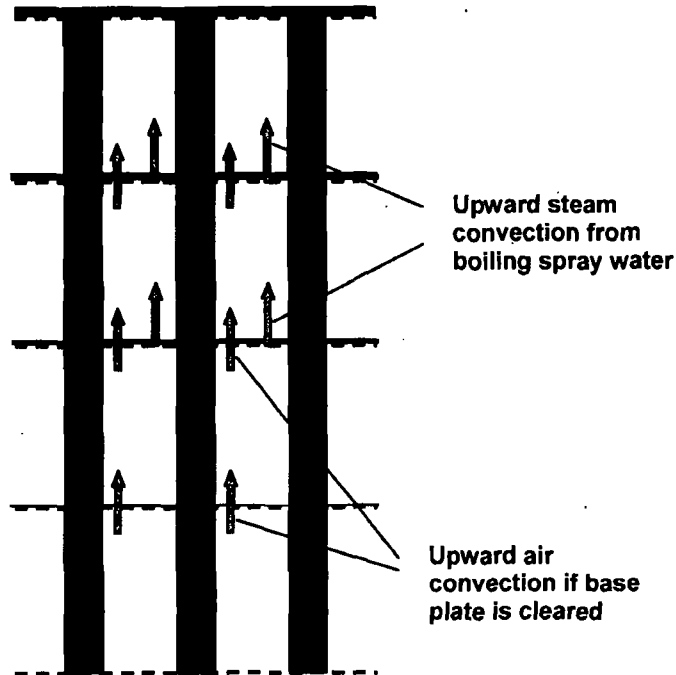


Figure 3-13 CVH Package Representation of a Spray Flow.

### 3.2 MELCOR Separate Effects Model

Several different models were used for the detailed evaluations of the fuel response to emergency spray. The uniform, checkerboard, and 1x4 fuel configurations with spray operation were simulated with these models. Section 3.2.1 describes the separate effect nodalizations. A variant of the separate model called the hybrid model was developed to calculate the spray scrubbing efficiency. The hybrid model is described Section 3.2.2.

#### 3.2.1 Separate Effects Model

Three intact configuration separate effect models were developed to analyze the spent fuel pool response to emergency spray mitigation of loss-of-coolant inventory accident conditions. The models simulate uniform, checkerboard, and 1x4 patterns. For implementation into MELCOR, the uniform pattern model was represented by a single, high-powered assembly with an adiabatic radial boundary or a 1x4 model with equal power in all five assemblies. The checkerboard pattern was represented with a high-powered and a low-powered assembly (i.e., taken as having the median assembly on the reference BWR spent fuel pool) with the appropriate adjoining wall area. Hence, radial heat transfer was possible from the high-powered assembly to the low-powered assembly. Similarly, a 1x4 pattern model was developed, which had one high-powered assembly surrounded by four low-powered assemblies. The MELCOR models represent the coupled thermal response of repeating pattern for each configuration (e.g., see Figure 3-23 for an example of a repeat 1x4 pattern). An adiabatic boundary was specified on the outer radial face of each model.

For reference purposes, the 1x4 intact configuration separate effects model will be described. The checkerboard model was a variation of the 1x4 model. However, the number of low-powered assemblies was reduced to one and the adjoining area between the two assemblies was adjusted accordingly. Finally, two types of uniform pattern models were used. First, the 1x4 model was used; however, all assemblies were specified to have the same power. However, to improve runtime on more difficult calculations, a dedicated separate effects model was developed with only one assembly and an adiabatic outer boundary.

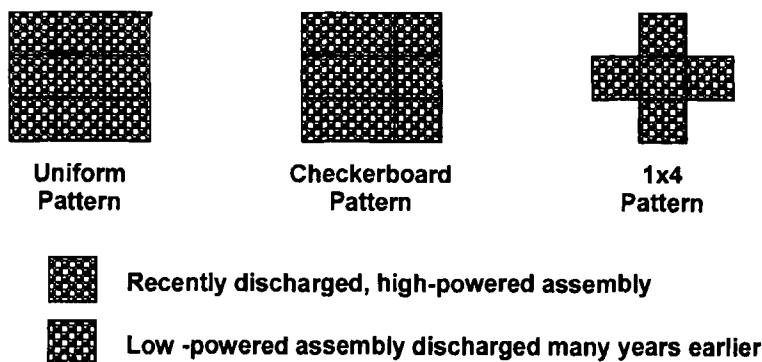


Figure 3-14 Repeating Patterns Found in the MELCOR Separate Effects Models.

As described above, the 1x4 separate effects model contains 5 spent fuel assemblies (see Figure 3-15). The five assemblies are divided into two radial rings and are modeled using the MELCOR “SFP-BWR” designation (see Section 3.1.1 for further discussion). The inner assembly is in Ring 1 and the four adjacent assemblies are in Ring 2 (see Figure 3-15). The outer boundary of Ring 2 is modeled as adiabatic. In the various calculations, the power is sometimes varied independently from Ring 1 and Ring 2. Each ring has 9 axial control volumes, which represent the fluid volume within the fuel assembly.

The interstitial area between the canister wall and the rack wall is modeled as the BWR bypass region. The bypass uses the same 9 control volume axial nodalization as the channel region. Nine radial cross-flow paths are located between the bypass and channel region. The cross-flow paths are controlled by the CORE package and open if the canister wall should fail. A control volume represents the region below the assemblies. Another control volume represents the bulk pool conditions above the separate effects model.

The hydraulic resistance was specified using the results from the SNL experimental test program (see Section 3.1.3). The flow resistance under the racks was represented using typical contraction inertial loss coefficients and viscous losses consistent with a flow length to the center of the SFP.<sup>8</sup>

The BWR assembly canister is modeled with the MELCOR canister component. The rack walls are modeled with the new rack component (see Section 3.1.1) with stainless steel and Boraflex. MELCOR does not include an option to model the two large water rods in the assembly. Consequently, the water rod mass and surface area was included in the canister wall.

The axial and canister wall blockage models were active and controlled the resistance in the respective flow paths. The blockage model monitors the porosity of the materials in the various core regions. If a debris bed forms, the flow resistance is adjusted via an Ergun flow resistance model [Gauntt]. The canister wall radial blockage model controls flow paths between the bypass region and the assembly. Initially, the canister wall precludes flow. However, if the canister fails, a radial flow path is activated that permits flow between the two regions. Similar to the axial blockage model, the flow resistance is adjusted based on the local debris porosity.

The BWR fuel assembly is represented by 14 axial levels in the CORE Package,

- Level 1 is the region below the core,
- Level 2 is the base plate
- Level 3 is the inlet region between the inlet nozzle and the lower tieplate
- Level 4 is the start of the active fuel region
- Level 8 is the top of the partial rod active fuel region
- Level 9 represents the region of the plenum of partial rods
- Level 12 is the top of the full length rod active fuel region
- Level 13 represents the plenum region of the full-length rods
- Level 14 represents the region between the upper tieplate and the top of the racks

---

<sup>8</sup> CFD calculations show the flow resistance under the racks is relatively small [Chiffelle].

The upper and lower tieplates are modeled as supporting plate structures, made of stainless steel. The 0.5" rack support plate at Level 2 is also modeled as a stainless-steel supporting structure.

The assembly ring-to-ring radiation is modeled (described in Section 3.1.1) between the outer surfaces of the Ring 1 rack wall to the outer surface of the canister in the adjacent ring. Radiative coupling was enabled for all calculations. In cases of a uniform configuration (i.e., a region where all assemblies have the same power), the ring-to-ring thermal radiative coupling did not have an effect because all 5 assemblies had the same decay power and thermal response.

(b)(7)(F)

The assembly decay heat is specified separately for each core ring. The decay heat load is primarily deposited in the fuel. However, as calculated by the gamma heating model, a small fraction of the decay heat is deposited directly in the cladding, canister, and surrounding structures (i.e., the rack wall). The outer boundary heat structures (i.e., ordinarily modeling the core barrel) outside Ring 2 were modeled as adiabatic (i.e., do not absorb any energy from Ring 2).

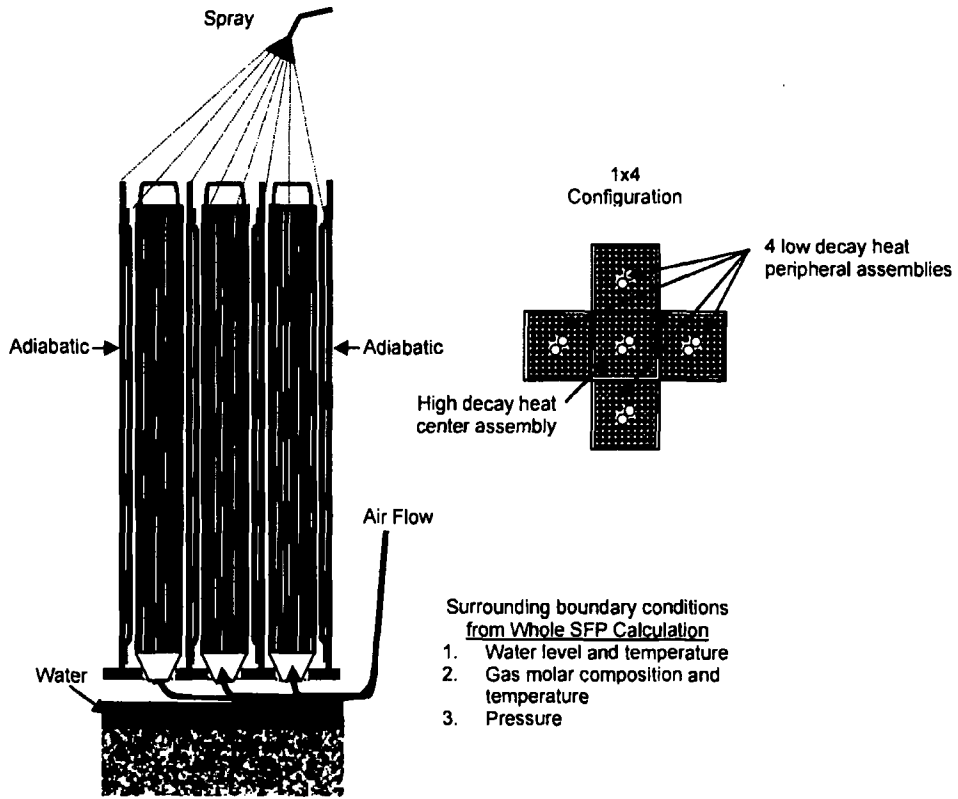
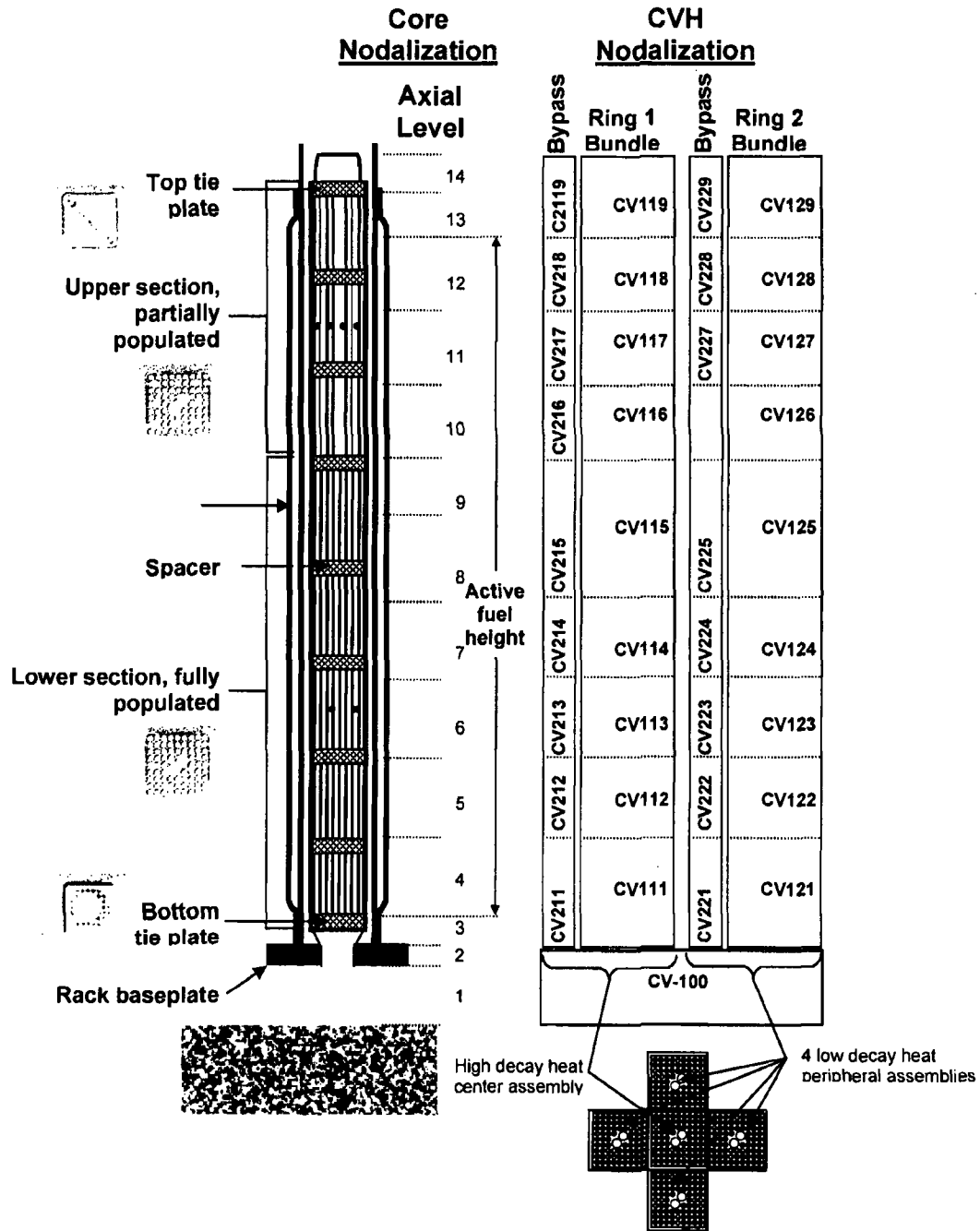


Figure 3-15 Schematic of the 1x4 Configuration.



**Figure 3-16 MELCOR Nodalization of the 5 Assembly Separate Effects Model.<sup>9</sup>**

<sup>9</sup> Only the center assembly is shown for the Core Package nodalization shown in the left-hand side of this figure. However, the four peripheral assemblies are lumped together and have an identical 14 level axial nodalization. Both the CVH nodalizations for the center (Ring 1) and four peripheral assemblies (Ring 2) are shown on the right-hand side.

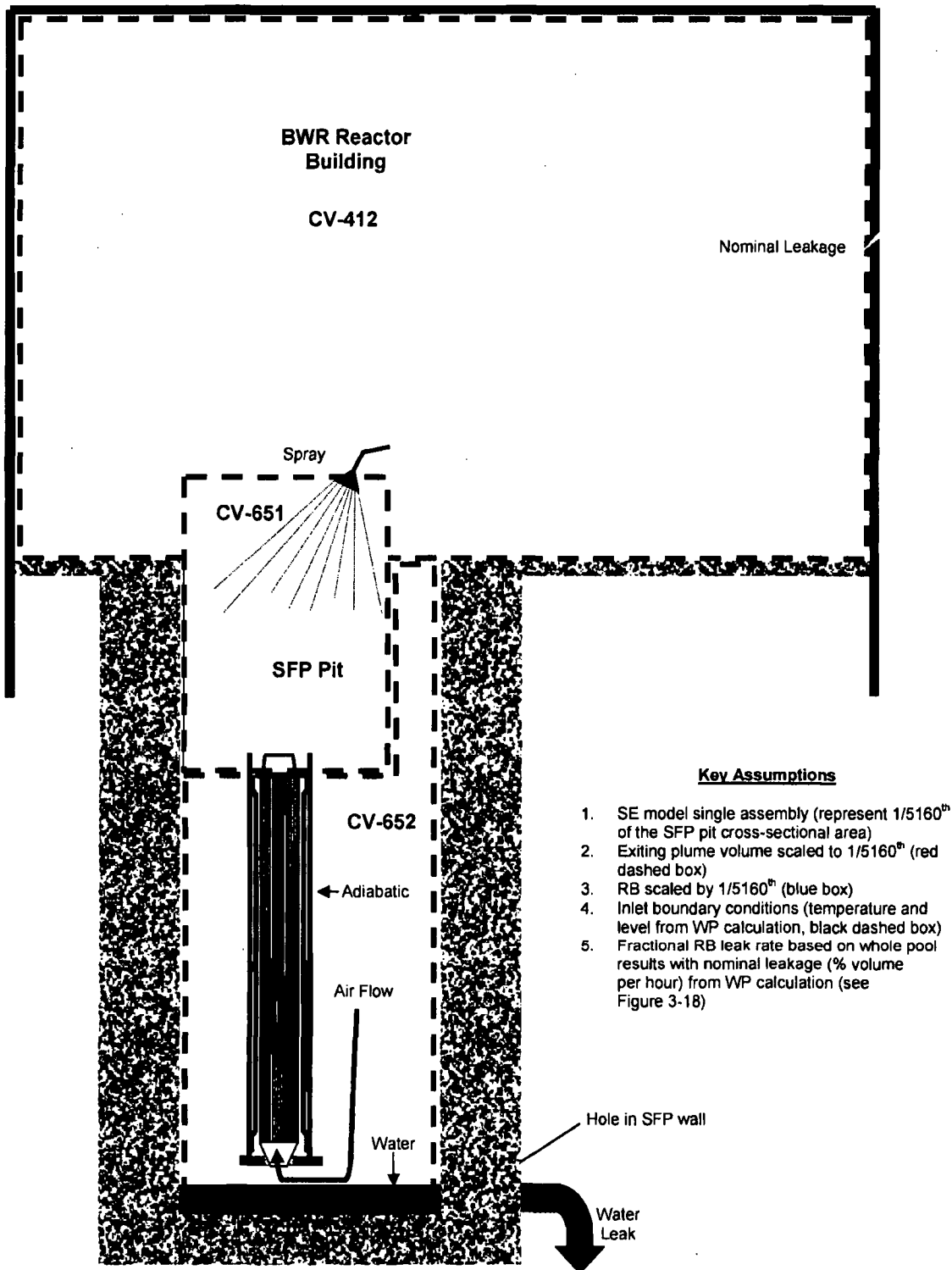


Figure 3-17 Hybrid Separate Effects Schematic with Emergency Spray Operation.

### 3.2.2 Hybrid Spray Model

For some of the source term calculations, a hybrid model was developed, which was a single assembly separate effects model with additional control volumes to represent the gas space above the racks and the refueling room. The gas space above the assembly and the refueling room were scaled by 1/5160, the ratio of a single assembly area in the SFP to the total SFP cross-sectional area (see Section 4.2.1 for the calculation). Figure 3-17 shows a schematic of the hybrid model. The MELCOR containment spray model was used to introduce the spray flow into the SFP. The spray was added to the CV-651 control volume represented by the red box. The blue box (i.e., CV-412) represented the refueling room and the black box (i.e., CV-652) represented a downcomer region. The assembly had the detailed nodalization represented in Figure 3-16 but for only one assembly.

The hybrid nodalization was used in a source term calculation, which assumed normal building leakage. Previous whole pool source term calculations were reviewed, which had normal building leakage and leakage through a failed blowout panel [Wagner, 2004]. The volumetric leakage rate was normalized to the refueling room volume and represented as a percentage room leakage per second (see Figure 3-18). (b)(7)(F)

F-715

(b)(7)(F) In this manner, the scaled room leakage was similar to the detailed reactor building model. (b)(7)(F)  
(b)(7)(F)

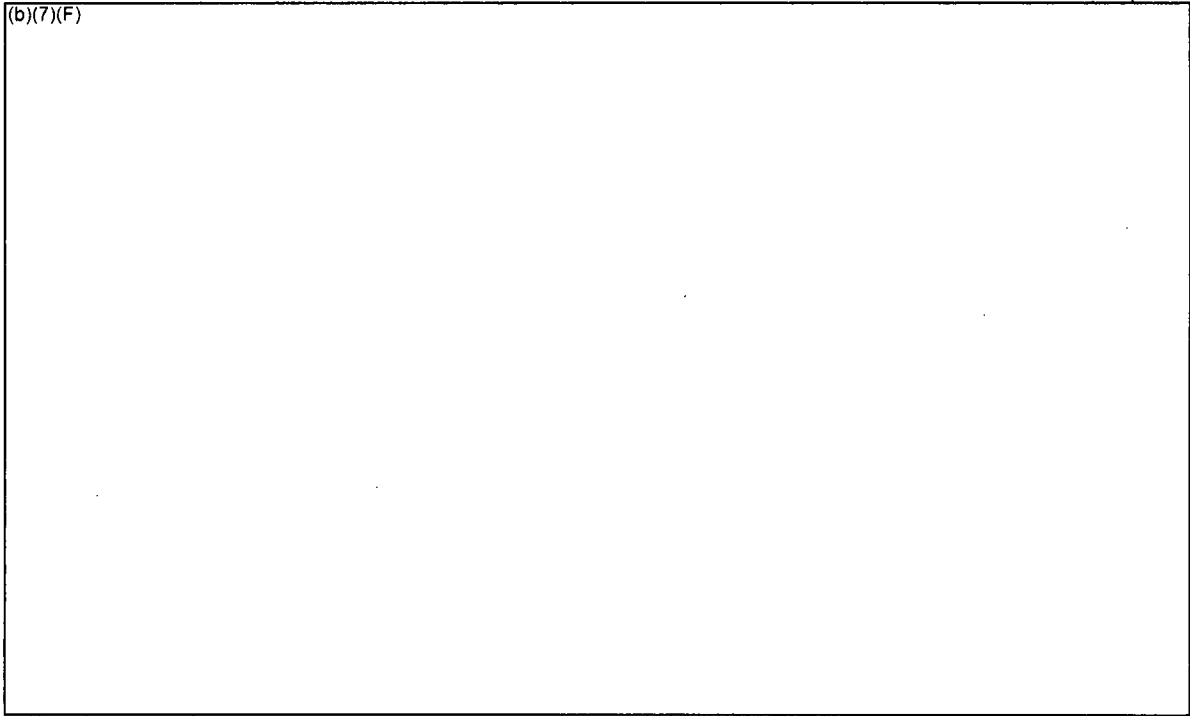
F-715

As will be discussed in Section 7.2, the hybrid calculations had some problems. In particular, there was only one pressure boundary condition for the model. (b)(7)(F)

(b)(7)(F) The specified leakage flow was generally too low to balance the pressure in the model. In particular, the scaled volume for the refueling room was connected to an assembly that represented the highest powered assembly in the SFP. It perhaps would have been more accurate to use power scaling. (b)(7)(F)

E-7F

(b)(7)(F) Furthermore, some type of additional pressure control would be needed to account for the initial heating and volumetric expansion of the refueling room gas, heat loss through the walls and ceiling, and pressurization into the bulk of the reactor building. The unfortunate consequence of this modeling issue for the hybrid model was higher than expected gas and fission product flow out the SFP water leakage location. Nevertheless, the hybrid calculations offered some insights into the source term response and are therefore included in Section 7.3.



Ex 7F

**Figure 3-18 Comparison of Reactor Building Leak Rates from BWR Whole Pool Complete Loss-of-Coolant Inventory Calculations [Wagner, 2004]**

(b)(7)(F)

(b)(7)(F)

Ex 7F

### 3.3 Whole Pool Models

Two whole pool models were used to specify the boundary conditions for the separate effect calculations and the spray scrubbing calculations. For expediency, the original BWR Whole Pool model was used for some source term scrubbing calculations (see [Wagner, 2004] for a description). The original BWR whole pool model did not include the new features described in Section 3.1. However, it was upgraded for the calculations represented in this report to include the new breakaway oxidation kinetics (see Section 3.1.2).

A new simplified whole pool model was used to specify the boundary conditions for the separate effects model. The new BWR whole pool model includes all the new features described in Section 3.1 except the more detailed CORE/CVH nodalization for tracking spray front.<sup>10</sup> The fuel assemblies and empty rack cells are represented in 9 rings in the MELCOR model. The new whole pool model uses the same 14-axial level CORE Package described in separate effect model (see Section 3.2.1). However, for improved computational runtime, only one control is used for the bundle region and one for the bypass region per CORE package ring.

#### 3.3.1 Original BWR Whole Pool Model

The original BWR Whole Pool model was used for some source term scrubbing calculations (see [Wagner, 2004] for a complete description). The model was used to estimate the scrubbing benefit from emergency spray operation during a complete loss-of-coolant accident. Since the development of the model, there have been several upgrades in SFP modeling as described in Section 3.1. A separate effort was started to develop a new whole pool model with all the cited modeling upgrades. However, the new whole pool model described in Section 3.3.2 was not sufficiently upgraded for source term calculations to meet the schedules of this project. Consequently, the original BWR whole pool model was used with limited upgrades to add an emergency spray model, the breakaway oxidation kinetics model (see Section 3.2.1), and a new decay heat and source term option for (b)(7)(F).

The original BWR model was developed to closely represent an actual BWR SFP configuration in 2003. At the reference plant, the fuel was discharged in a somewhat random pattern governed by available empty rack cells after the dry cask loadings. Figure 3-20 shows the corresponding decay heat levels at (b)(7)(F) the last reactor shutdown. The high decay heat levels from the most recently discharged fuel are readily evident. However, the fuel from the second most recent offload and older somewhat blend together. Following the rapid decrease in decay heat of the assemblies in the first two years, there are smaller differences in assembly decay heats.

The model nodalization is shown in Figure 3-19. The large geometry and range of fuel ages and decay heats makes the SFP assembly layout difficult to represent. It is neither possible nor practical to model each of the (b)(7)(F). A seven ring model was used to represent the layout of the highest powered assemblies and their proximity to lower powered

<sup>10</sup> A detailed CORE/CVH nodalization in the framework of a multi-ring model is too computationally intensive for the present application. The simplified whole pool model is used to calculate global boundary conditions for the more detailed separate effect models described in Section 3.1.

Ex 7F assemblies. The fuel assemblies from the two most recent offloads (i.e., 1999 and 2001) were broken into three regions; high, medium, and low connectivity to lower powered assemblies. The connectivity refers to how many sides of a high-powered assembly are immediately adjacent to a low-powered assembly (i.e., assemblies from fuel discharges in 1995 or earlier). The average assembly decay power levels and effective view factor between the high-powered assemblies to the adjacent lower-powered assemblies for each group were calculated. The results of the grouping show that Rings 1, 3, and 5 had average view factors of 0.94, 0.46, and 0.04. For the (b)(7)(F) which were treated in a separate MELCOR region (i.e., Ring 7), the average view factor to low-powered assemblies was 0.1. Rings 2, 4, and 6 represented the low-powered regions (i.e., fuel discharged prior to 1997). The present calculations use factor of 10 reductions in thermal coupling from the base value to reflect a more uniform distribution of assemblies. Consequently, the radiation view factor values for Rings 1, 3, 5, and 7 were 0.09, 0.05, 0.004, and 0.01, respectively.

The BWR fuel assembly is represented by 16 axial levels in the MELCOR Core Package (see Figure 3-21). The 16 axial levels are specified as follows.

- Level 1 is the region below the rack base plate.
- Level 2 is the base plate.
- Level 3 is the inlet region in the assembly between the inlet nozzle and the lower tieplate.
- Levels 4 through 15 are the active fuel region (b)(7)(F) Ex 7F
- Level 16 is the unfueled plenum and the upper tieplate at the top of the fuel rods.

The upper and lower tieplates are modeled as supporting plate structures and are made of stainless steel. The 0.5" rack support plate at Level 2 is also modeled as a stainless-steel supporting structure.

The MELCOR Control Volume Hydrodynamics (CVH) nodalization is indicated in Figure 3-19. Each of the seven "COR" rings and the empty rack cells are modeled using groupings of CVH control volumes. Each "COR" ring includes CVH volumes for the channel region, the bypass region (i.e., the region between the canister and the SFP rack wall), and the region below the racks. Variable area and resistance flow paths are specified to connect the channel region and the bypass if the canister wall melts or collapses. In addition, variable area and resistance vertical flow paths are specified to represent changes in the hydraulics as the fuel rod and bypass areas degrade or collapse (i.e., via the MELCOR Core Package blockage model).

As noted previously, the original whole pool model does not include the complex geometry sophistication of partial length fuel rods, the new hydraulic resistance model, and the BWR-SFP new rack and radiation model. However, the new breakaway oxidation model was activated (see Section 3.1.2).

The reactor building was modeled on a level-by-level basis, beginning in the basement (i.e., torus room) and sequentially rising up through the main floors to the refueling bay. The torus room elevation is modeled with two control volumes. The first represents the room volume excluding the isolated corner rooms. This floor is connected to the next higher floor by two flow paths representing grated hatches. The second represents a single corner room (in the NE) where the

secondary containment-wetwell vacuum breaker terminates. This corner room is connected to the next higher floor by a flow path, which represents the stairwell between the two. The three intermediate floors of the building are each sub-divided into from two to four control volumes based on the flow connectivity of each level (basement level – 2 CVs, first floor level – 3 CVs, second floor level – 4 CVs). A single control volume models the refueling bay. An open hatch in the southeast quadrant (via flow paths) interconnects the three intermediate floors and the refueling bay. Nominal reactor building leakage is modeled at the center elevation of each control volume. These leakage flow paths have been modeled to match the 100% design in-leakage rate of the reactor building.

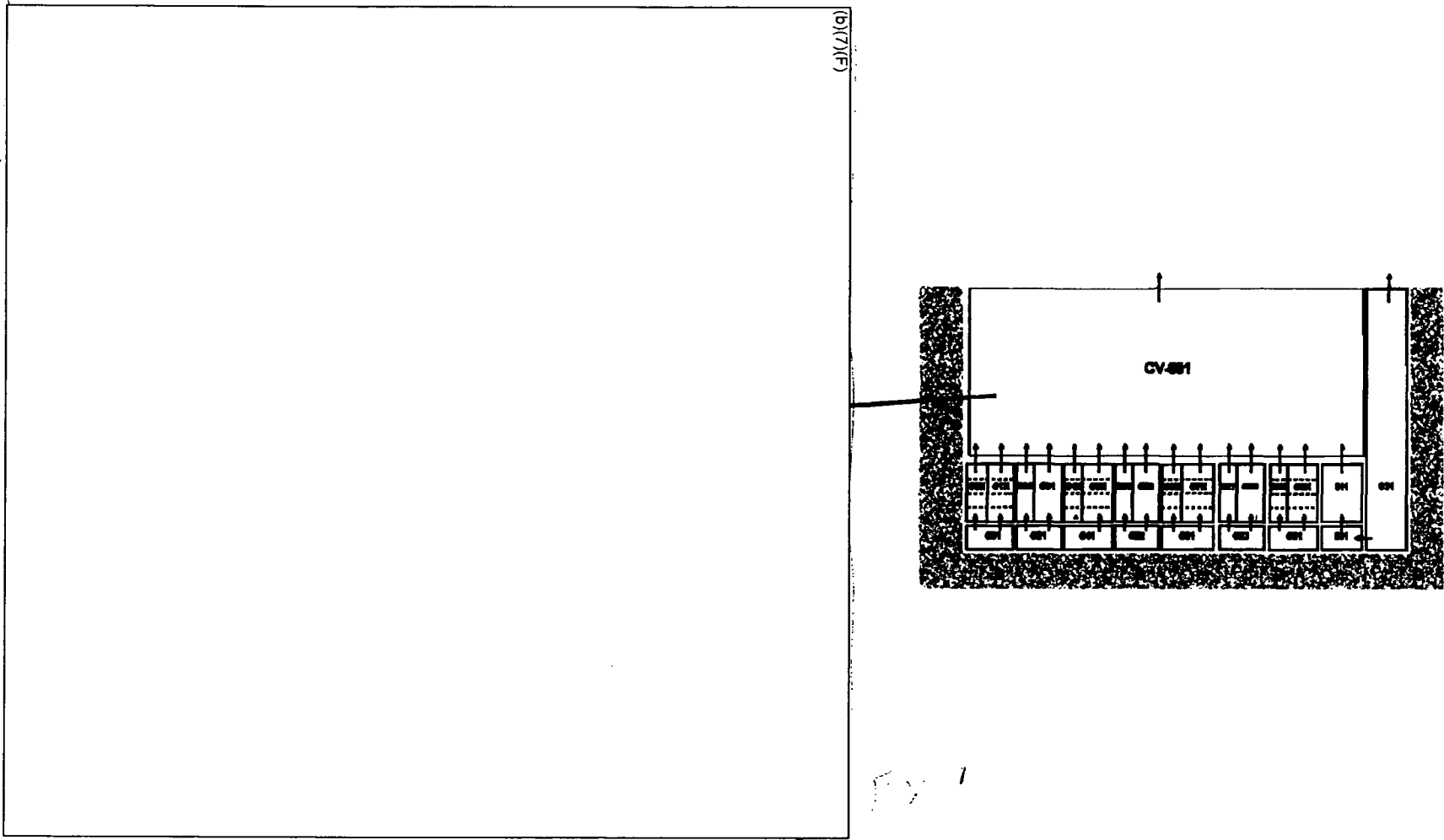
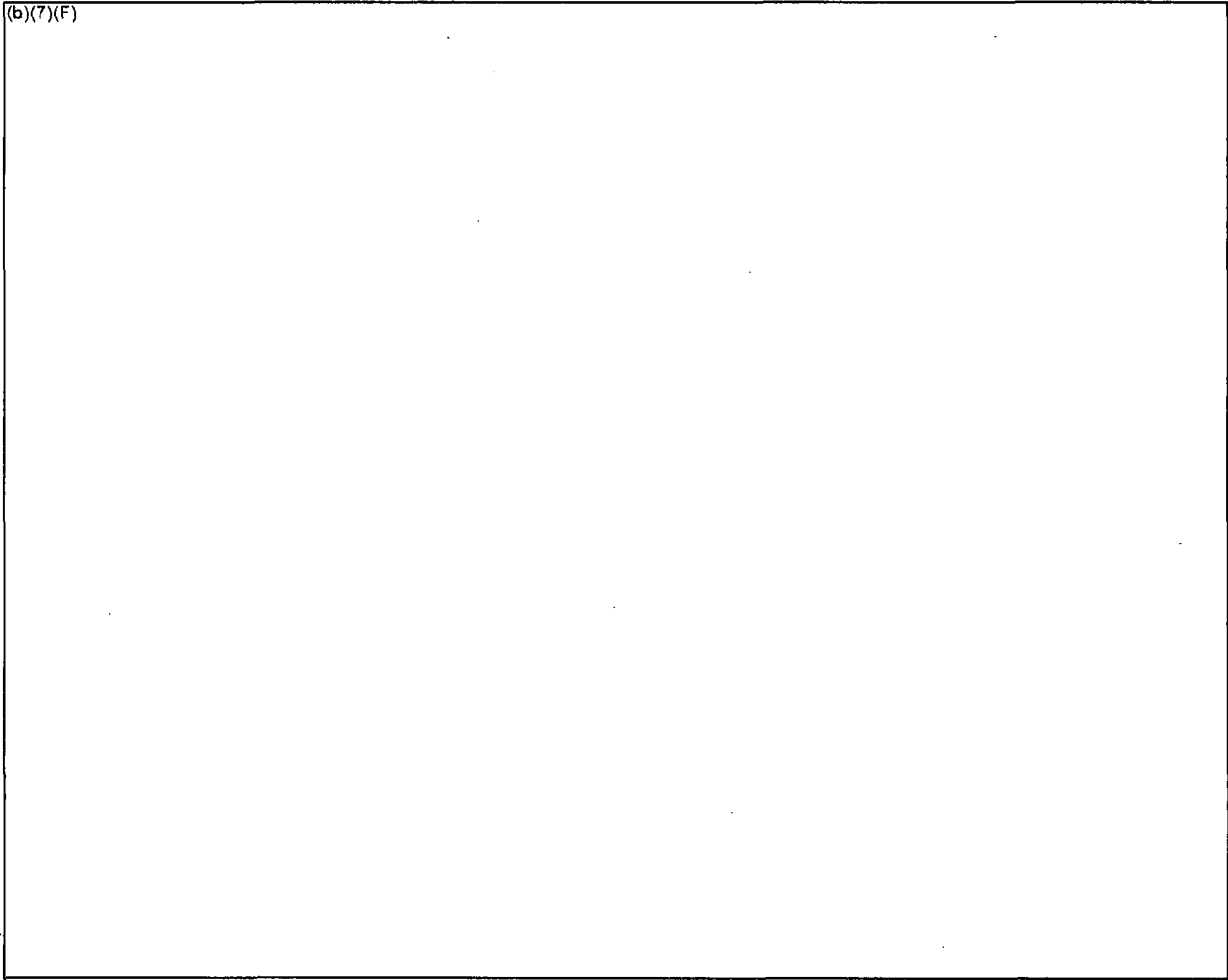


Figure 3-19 Original BWR Whole Pool Nodalization.



**Figure 3-20 Spent Fuel Locations Colored by Decay Heat Level at (b)(7)(F) the Large Discharge to the SFP.**

Ex 7F

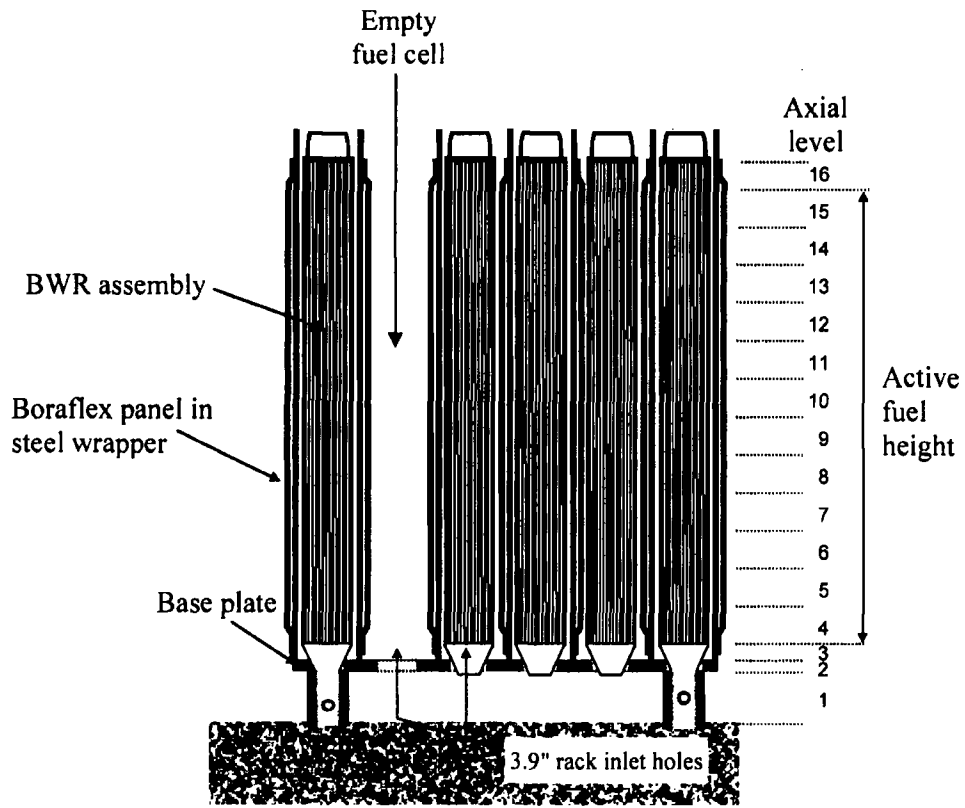


Figure 3-21 MELCOR Axial Levels of Spent Fuel Assembly in Rack.

### 3.3.2 New Whole Pool Nodalization

Figure 3-22 shows the CVH nodalization of the SFP region of the simplified whole pool model. The lower SFP was divided into ten regions. CV-299 represents all the open regions in the SFP around the racks and including the cask area. The racks are divided into 9 regions. CV-110 and CV-210 represent the assembly and bypass regions of the first ring. Similarly, CORE Rings 2 through 8 contain assembly and bypass regions. Ring 9 represents the (b)(7)(F) Ex 7F. Hence, CV-190 only contains empty cells (i.e., no assemblies or bypass regions). The axial volume, flow area, and resistance are represented as described in Section 3.1.3. The region above the pool is divided into two control volumes. Typically, flow goes down CV-301 and CV-299 and rises through CV-300. The flow enters the bottom of the racks through CV-100. A 14 level CORE nodalization is used as described in Section 3.2.1.

EX 7F

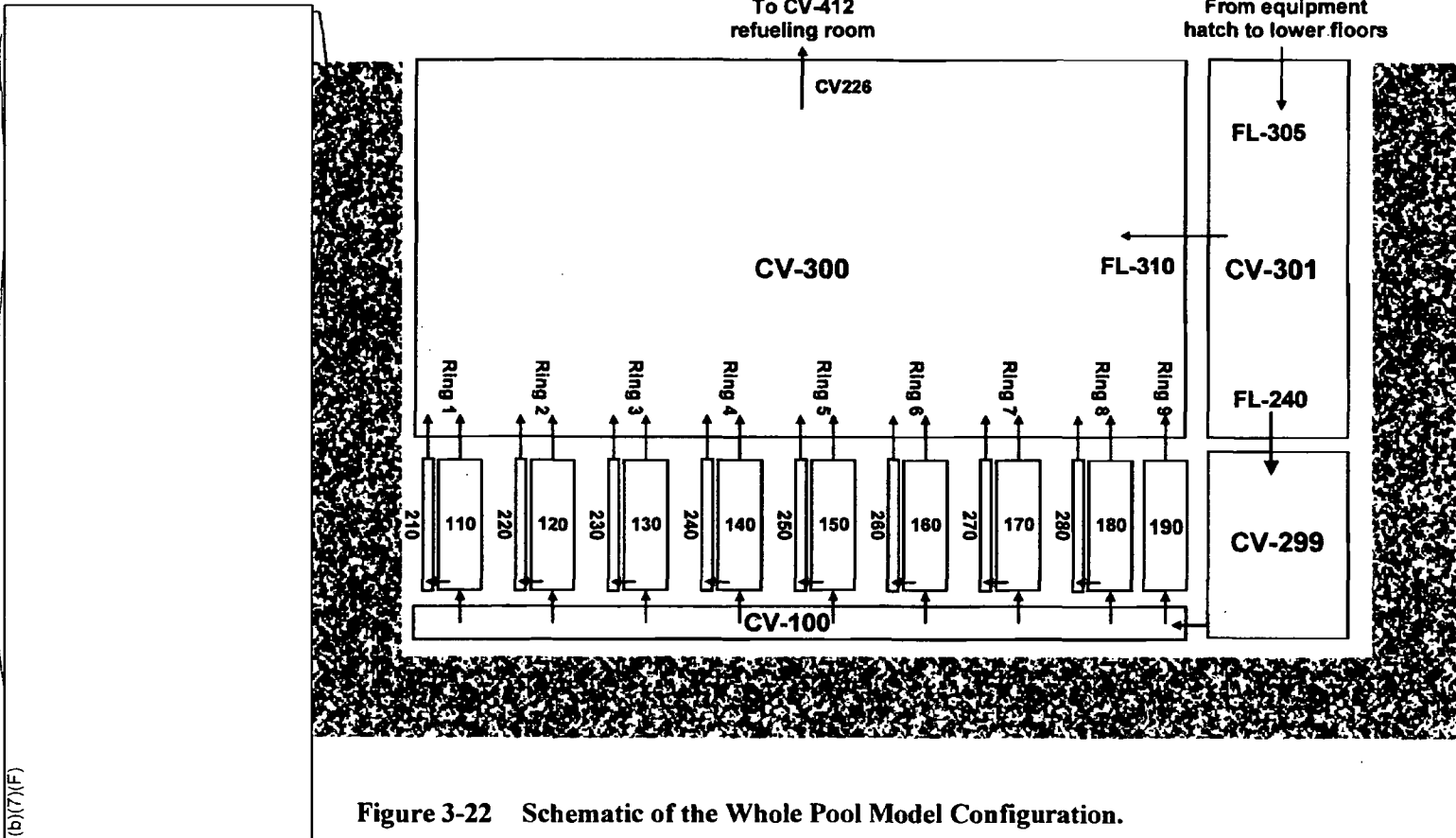


Figure 3-22 Schematic of the Whole Pool Model Configuration.

### 3.3.2.1 Radial Thermal Coupling

The reference plant for the SFP analysis is a large BWR. The SFP is representative of a modern, high-density SFP. The plant has begun a dry or off-site fuel storage program. As fuel assemblies are added to the SFP, a similar number are removed for dry storage. Consequently, the number of assemblies in the SFP is kept approximately constant. For the present analyses, the layout of the fuel was specified to be representative of a well-configured SFP. In particular, the assembly layout was specified to enhance radial heat transfer from recently discharged, high-powered assemblies to low-powered assemblies. Figure 3-23 shows an example of a well-configured SFP layout. The most recently discharged "orange" and "red" assemblies are surrounded by the older "blue" assemblies in the SFP in 1x4 patterns. (b)(7)(F)

(b)(7)(F)

Ex 7F

The layout of the assemblies from the last offload for the new MELCOR whole pool model conceptually followed the example shown in Figure 3-23.<sup>11</sup> The assemblies in the reference PWR SFP were grouped into 9 types or "rings" by decay heat power and time of discharge.<sup>12</sup> The ring layout assumed in this analysis is shown in Table 3-3. The last assembly offload from the reference plant (b)(7)(F) assemblies. (b)(7)(F) assemblies were subdivided into Rings 1, 3, and 5. By using three rings to represent the last core offload, the relative powers of the assemblies were accurately characterized into high, medium, and low-powered groups. Surrounding each of those groups in Rings 2, 4, and 6 were the lowest-powered assemblies in the SFP. There were four low-powered assemblies in Rings 2, 4, and 6 for each high-powered assembly in Rings 1, 3, and 5, respectively. This 1x4 pattern utilized (b)(7)(F) of the lowest powered assemblies. The remaining mid-powered assemblies were placed in an approximate checkerboard pattern with the next lowest powered (b)(7)(F) Ring 7 interspersed amongst (b)(7)(F) Ring 8. Finally, (b)(7)(F) empty cells were placed around the outside of the SFP to ensure open air downflow regions into the SFP in the event of a complete loss-of-coolant inventory accident.

Ex 7F

Ex 7F

Ex 7F

Ex 7F

Figure 3-24 shows the cell-wall radiation view factors between the various rings. The resultant view factor specifies the amount of coupling from each region to another. For example, the Ring 1 cells are completely surrounded by Ring 2 cells. Hence, the view factor from Ring 1 to Ring 2 is 1.0. Similarly, Rings 3 and 4 and Rings 5 and 6 are coupled in 1x4 patterns. Due to limitations in the MELCOR radial radiation scheme, only adjacent rings can be thermally coupled. Consequently, the inter-dependent coupling between adjacent rings can not be represented. The resultant assembly patterns only couple the 1x4 patterns in Rings 1 through 6,

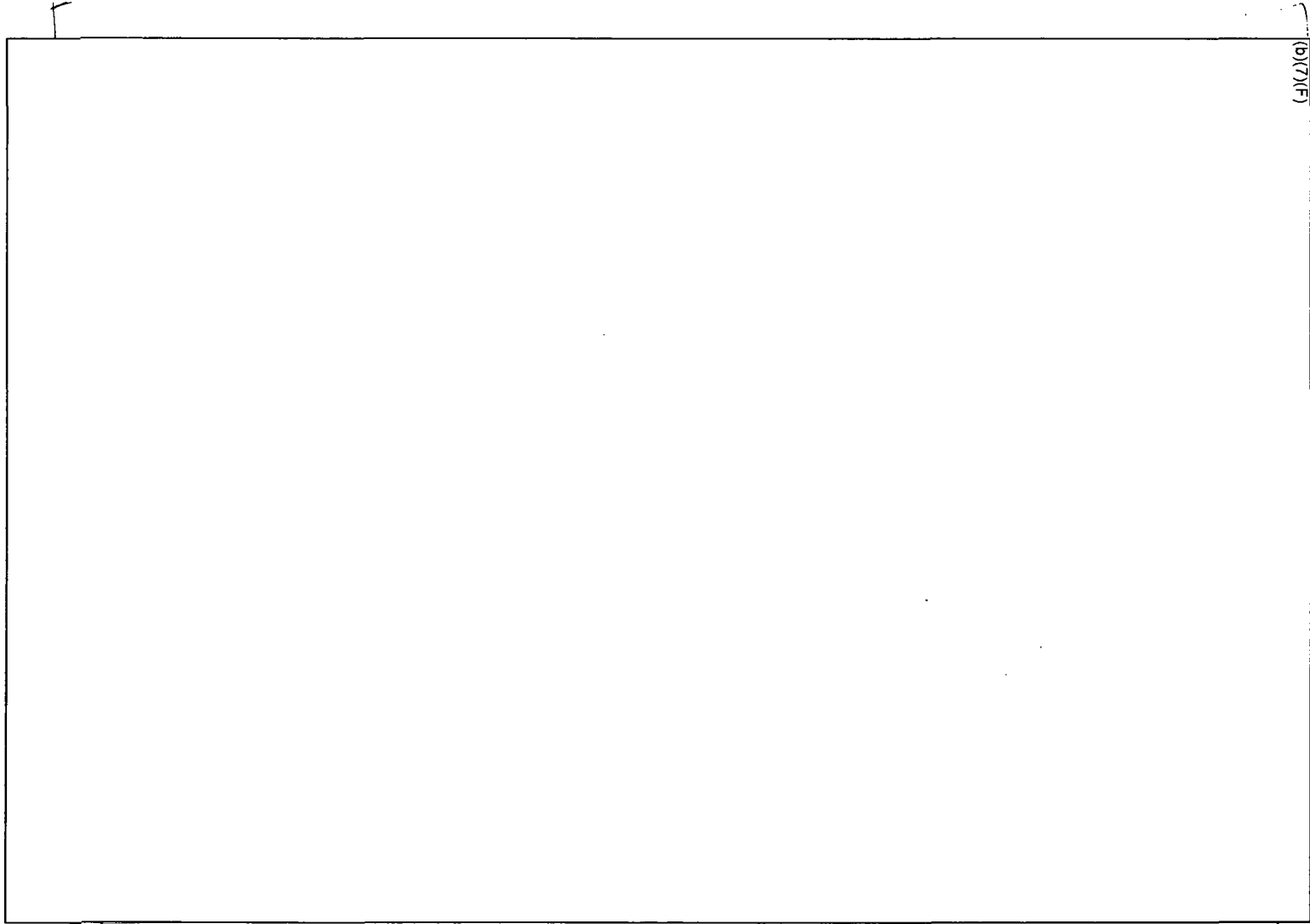
<sup>11</sup> Figure 3-23 is an illustration of a well-configured SFP. Similarly, the layout used in the present analysis uses 1x4 patterns with the last offload surrounded by the lowest decay heat assemblies. However, the layout of the (b)(7)(F) assemblies was a simply a checkerboard pattern. Since the new whole pool model was only used to establish inlet boundary conditions for the separate effects models, no further refinement of the assembly or ring layout was performed. It would be relatively straight-forward to change the number of assemblies in each ring and their coupling to adjacent rings.

Ex 7F

<sup>12</sup> "Ring" is a MELCOR term for a grouping of assemblies. In MELCOR's typical reactor configuration, the core is geometrically divided into a group of concentric rings. Each assembly in a ring has the same decay heat and thermo-physical properties.

a checkerboard pattern in Rings 7 and 8 and empty cells around the periphery in Ring 9. No other inter-ring couplings are considered.

Within each MELCOR ring, the assembly decay heat is uniform. Table 3-3 summarizes the average assembly decay power in each ring from the individual batches. Consequently, for any given scenario, the decay heat in each ring is adjusted to give the average assembly power. Due to the variable decay factors in the assembly decay heat, the assembly power is conservatively assumed to remain constant for the duration of the scenario.



(b)(7)(F)

Ex 1F

**Figure 3-23 Example of Alternating and Repeating 1x4 Patterns.**

Table 3-3 Summary of Regions in the MELCOR Whole Pool Model.

(b)(7)(F)

Ex 4F

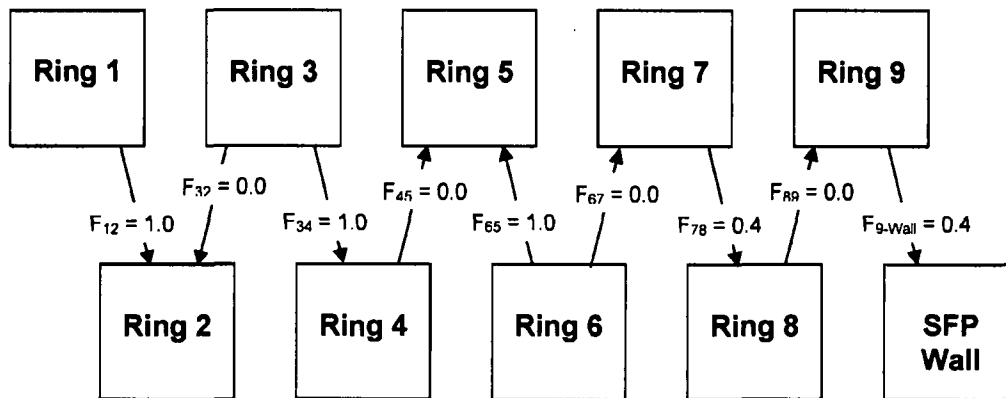


Figure 3-24 The Radial Coupling Scheme as Implemented in MELCOR SFP Model.

### 3.3.2.2 Simplified Refueling Room Model

A complete reactor building was developed as part of the BWR reference plant accident progression model. However, for the present analysis, the reactor building model was simplified to only model the refueling room (i.e., within the red dashed line on Figure 3-25). The SFP nodalization (see Section 3.3.2) was coupled to the SFP model as shown in Figure 3-25.

A single control volume models the refueling bay. An open hatch in the southeast quadrant (via flow paths) connects the refueling bay to a boundary condition volume representing the lower sections of the building. Nominal reactor building leakage is modeled at the center elevation of the refueling bay. The leakage flow in the simplified model was tuned to match the 100% design in-leakage rate of the detailed reactor building model.

The detailed reactor building model represented many over-pressure failure flow paths within the reactor building. The two most important flow paths for the present calculations were added to the simplified refueling floor model, (1) the blowout panels on the refueling room walls and (2) a pathway representing the structural failure of the reactor building roof. (b)(7)(F)

(b)(7)(F)

Ex 9F

Recently, computational fluid dynamic (CFD) simulations of the air flow patterns in a PWR fuel storage building during a complete loss-of-coolant inventory accident guided the development of the model nodalization [Khalil]. The CFD results show a flow pattern of hot air exiting from the assemblies at the top of the racks (see Figure 3-26). The hot gases form a plume which that rises to the building ceiling. Once the plume hits the ceiling, it spreads radially and mixes within the hot gas layer at the top of the room. The room remains thermally stratified as hot gases preferentially leak out the large, open ceiling ventilation units. Meanwhile, cool air enters (b)(7)(F) to replace the exiting hot gases. The cool air fills the lower regions of the building, overflows to the SFP floor elevation, and sinks into the SFP to replace exiting hot gases. The cool air flows underneath the racks from the cask area and then spreads radially under the racks. The hydrostatic pressure difference between the cold gases outside the racks and the hot gases inside the assemblies drives the airflow through the racks.

Ex 10F

This flow pattern is similar to that expected in the reference BWR refueling room<sup>13</sup>. By comparing Figure 3-25 and Figure 3-26, (b)(7)(F)

(b)(7)(F)

Ex 11F

MELCOR does not include models for stratification of hot gases. Each control volume is assumed to be well-mixed and have a single temperature. Large-scale natural circulation flow patterns can be predicted where the bulk temperature differences between adjacent rooms create mixing flows. However, it would be awkward or perhaps impossible to predict complex plume

<sup>13</sup> The PWR refueling building is shown because the CFD code used in that analysis provides superior visualization of the resultant flow patterns than the figures available from the comparable BWR CFD study.

behavior within regions typically modeled with a single control volume (e.g., the room above the SFP). Consequently, the MELCOR calculations are expected to over-predict the amount of thermal mixing within the building. Based on insights from the CFD calculations, the MELCOR refueling room model nodalization included modeling features to minimize excessive mixing.

The refueling room is modeled as a single control volume. (b)(7)(F)

(b)(7)(F)

left-hand side of Figure 3-25). In this manner, the cool gases leaving the lower regions of the building are not brought into thermal equilibrium with gases above the SFP. Cross-flow is simulated between CV-300 and CV-301 as observed in Figure 3-26.

Finally, no counter-current flow was modeled between CV-301 (see Figure 3-22) and the refueling room (CV-412). CV-301 is connected to the refueling room via flow into the SFP pit. The detailed FLUENT CFD solution shows a hot gas layer near the ceiling of the room above the SFP pit. If the heat removal through the ventilation unit is inadequate, the hot gas layer fills the room (i.e., CV-320) and extends down into the lower rooms in the building. MELCOR can not calculate the formation and movement of a hot gas layer. However, when the gas flow into the refueling room (i.e., via FL-300 from the SFP pit) exceeds the leakage from the building, hot air circulates into lower floors through the hatch.<sup>14</sup>

<sup>14</sup> For the present boundary condition calculations, the temperature feedback from the hot gas layer filling the refueling room was not adequately modeled. If the refueling room filled with hot gas, there was not a mechanism to heat the lower floors and draw hotter gas into the SFP. This deficiency will be addressed in future calculations by including a heated gas recirculation path into the SFP.

(b)(7)(F)

Fix 4

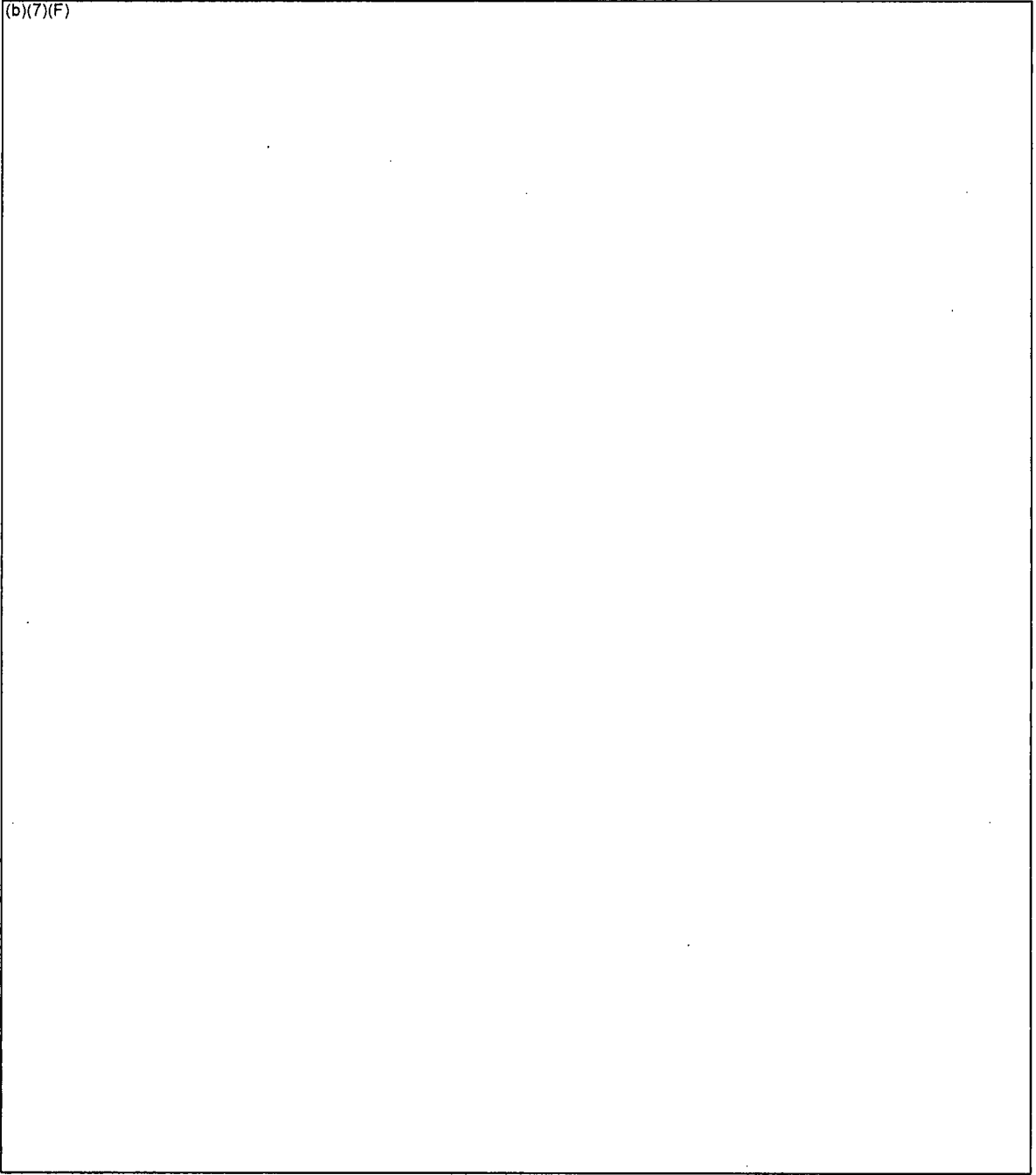


Figure 3-25 MELCOR Reactor Building Model.

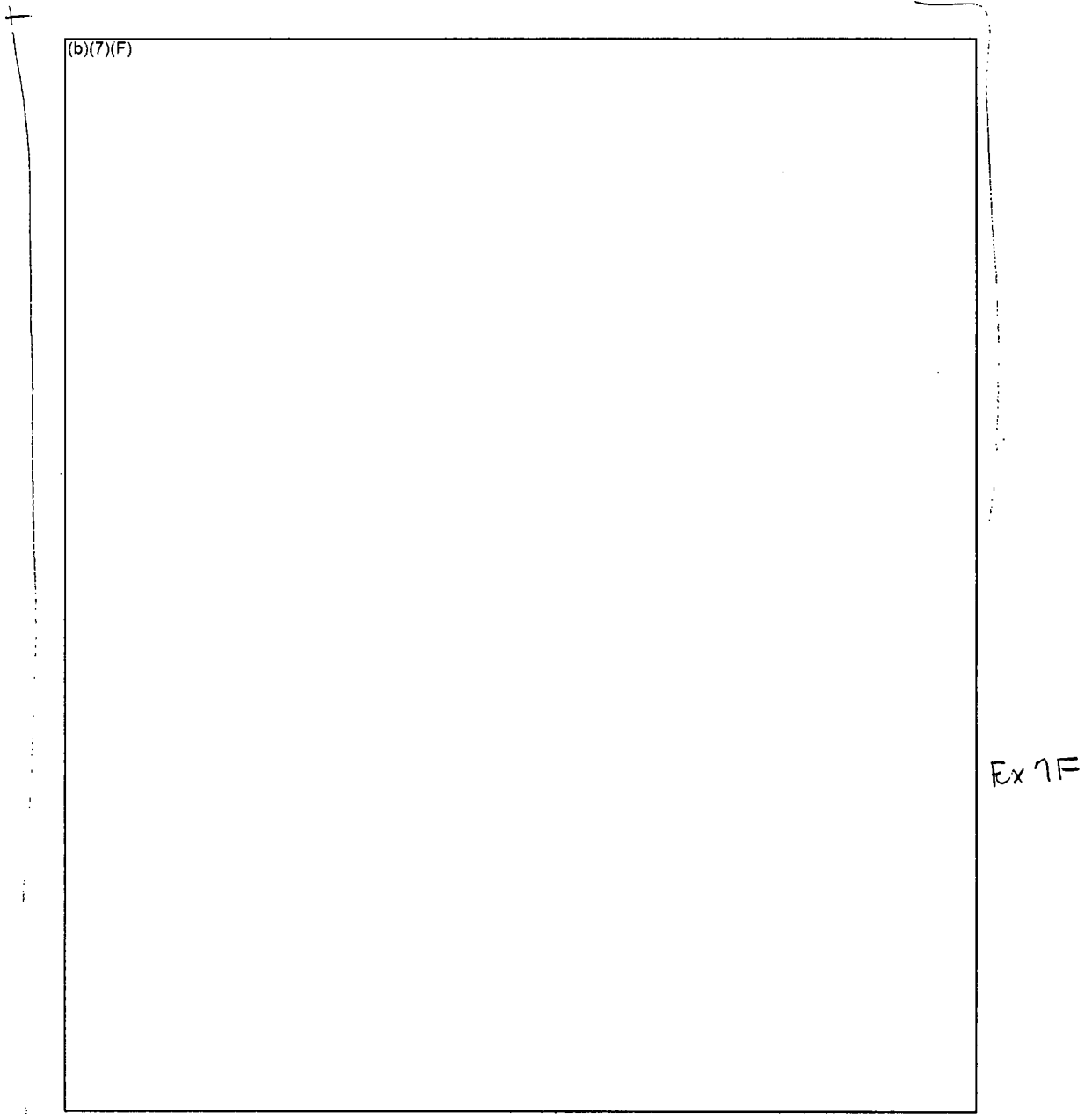


Figure 3-26 Example of Pressurized Water Reactor SFP Building Flow Patterns From FLUENT Calculations With (b)(7)(F) Ex 1F

### 3.4 Description of the Initial and Boundary Conditions

In most cases, the separate effect BWR SFP models described in Section 3.2 were used to evaluate the fuel thermal response to emergency spray operation. The initial conditions are summarized in Table 3-4. The model was initiated from normal conditions (i.e., 300 K and normal water level). However, the pool heat removal and the building ventilation were assumed disabled. The emergency spray flowrate (b)(7)(F) across the pool cross-section. *Ex 7F* The spray system response above the SFP racks was modeled in the whole pool model and used MELCOR's spray model.

The focus of the present study was to characterize the fuel response to spray operation. Other uncertainties affecting the response have been examined in a previous BWR separate effects study [Wagner, 2003]. Table 3-5 summarizes the base values of the uncertain and variable values used in the present study. These base modeling parameters were similar to the base values used previously. The last boundary condition was the emergency spray source. It was assumed that the emergency SFP spray system evenly covered the cross-sectional area of the SFP. Once it hit the assemblies in the SFP racks, the water drained into the SFP assemblies. The spray water was introduced as a water source into the control volume representing the upper tieplate.

**Table 3-4 Summary of Base Case SFP Model Initial Conditions for BWR SFP Emergency Spray Calculations.**

Parameter	Value
Pool temperature	300 K
Water level	Normal, 37.75 ft
Pool heat removal	Deactivated
Building ventilation	Deactivated
Spray injection flowrate	<span style="border: 1px solid black; padding: 0 20px;">(b)(7)(F)</span> <i>Ex 7F</i>
Spray water temperature	300 K
Spray droplet size	Usually 1250 $\mu\text{m}$
Spray initiation time	<span style="border: 1px solid black; padding: 0 20px;">(b)(7)(F)</span> <i>Ex 7F</i>
Spray nozzle overlap inefficiencies	None
Spray nozzle delivery inefficiencies	None
Notes:	
1.	The spray system is assumed to <span style="border: 1px solid black; padding: 0 20px;">(b)(7)(F)</span> uniformly across the entire SFP cross-section.
2.	Any inefficiencies due to overlap from adjacent spray nozzles or droplets hitting the walls or missing the SFP are not included. To <span style="border: 1px solid black; padding: 0 20px;">(b)(7)(F)</span> <i>Ex 7F</i> into the pool, the overall system flowrate must be increased.
3.	Only the hybrid and whole pool models simulated the falling spray droplets. The separate effects model simulated the spray as a water pool forming on the upper tieplate of the assembly.

**Table 3-5 Summary of Base Case SFP Model Boundary Conditions for BWR SFP Emergency Spray Calculations.**

Parameter	Value
Decay Heat	Peak assembly power from utility calculation using ANSI/ANS-95 decay heat standard. Low-powered assemblies were at the reference BWR SFP median value <span style="border: 1px solid black; padding: 0 5px;">(b)(7)(F)</span> <span style="float: right; margin-left: 20px;">Ex 7F</span>
Bernoulli Effect	Not explicitly included
Inlet Temperature and water level	Specified from whole pool model (see Section 5)
Initial Oxide Layer Thickness	25 $\mu\text{m}$ [Lanning]
Viscous Wall Friction Correlation	As measured in SNL experiments.
Flow Restrictions	None unless noted.
Rod Ballooning	No modeled. <sup>15</sup>
Oxidation Correlation	ANL zircaloy-4 air oxidation kinetics model with breakaway <sup>16</sup> and Urbanic-Heidrich steam oxidation model.
Heat Transfer to surrounding cells or assemblies	Adiabatic boundary in the radial direction. Radial heat transfer was calculated within the checkerboard and 1x4 models between the low- and high-powered assemblies.
Spray water source	Specified as a liquid source to the control volume above the upper tie-plate. For the whole pool and hybrid models, the spray source was modeled using MELCOR's containment spray model [Gauntt].

Ex 7F(b)(7)(F)

<sup>16</sup> The pre- and post-breakaway air oxidation kinetics models were based on Zircaloy-4 cladding. The reference BWR assemblies have Zircaloy-2 cladding. It is assumed (and believed) that Zircaloy-4 and Zircaloy-2 will oxidize at the same rate. Due to limited data, MELCOR's breakaway timing model is based data from both Zircaloy-4 and Zirlo samples.

#### 4. SPRAY MITIGATION HAND CALCULATIONS

Two sets of hand calculations were performed to estimate the heat removal required from the spray system in the reference BWR spent fuel pool. In the first calculation, the spray system was initiated prior to uncover of the fuel and the water leakage location is above the top of the racks. In the second hand calculation, it is assumed that the fuel is uncovered. The hand calculations represent simple straight-forward energy balances that are useful for estimating the required flowrate for a spray system. The hand calculations do not address the complications of radial heat transfer between low- and high-powered assemblies, the effectiveness of heat removal through the bypass region between the canister and the rack wall, or the response when the assumptions are violated (e.g., inadequate cooling). The MELCOR calculations in Sections 6 and 7 address those phenomena and conditions.

##### 4.1 Leak Above the Top of the Racks

In the first calculation, the spray system was initiated prior to uncover of the fuel and the water leakage location is above the top of the racks. It is assumed that the accident has disabled the SFP heat removal capabilities and the decay heat from the SFP is boiling away the remaining inventory. Depending on the time of the accident, the decay heat varies. Close to the most recent offload of fuel into the SFP, the decay heat is highest (see whole pool decay heat for the reference BWR in Figure 4-1). Figure 4-2 shows the required flow rate to maintain the SFP level.

The calculations for the heat removal requirements at (b)(7)(F) are shown below. (b)(7)(F) a  $10^7$  relatively modest amount of (b)(7)(F) is required. Since the fuel is covered, a spray system is not technically needed. Rather any water injection system would be sufficient.

##### Assumptions:

1. Reference BWR SFP decay heat data
2. Last offload had (b)(7)(F) since reactor shutdown  $F \times 11$
3. 80°F spray water
4. Decay heat removal is provided by boiling spray (injection) water
5. Other modes of heat transfer are ignored.

$$\rho = 62.1 \text{ lbm/ft}^3 = 996 \text{ kg/m}^3$$

$$h_{fg} = 970.3 \text{ BTU/lbm} = 2.257 \times 10^6 \text{ J/kg}$$

$$h_{80^\circ\text{F} \rightarrow 212^\circ\text{F}} = 180.18 \text{ BTU/lbm} - 48.13 \text{ BTU/lbm} = 132.05 \text{ BTU/lbm} = 3.072 \times 10^5 \text{ J/kg}$$

$$\Delta h = h_{fg} + h_{80^\circ\text{F} \rightarrow 212^\circ\text{F}} = 1102 \text{ BTU/lbm} = 2.56 \times 10^6 \text{ J/kg}$$

Whole pool decay heat at (b)(7)(F)

Spray Flowrate = (b)(7)(F) / ((996 kg/m<sup>3</sup> \* 2.56x10<sup>6</sup> J/kg) \* (60 sec/min) \* (264.2 gal/m<sup>3</sup>))

(b)(7)(F)

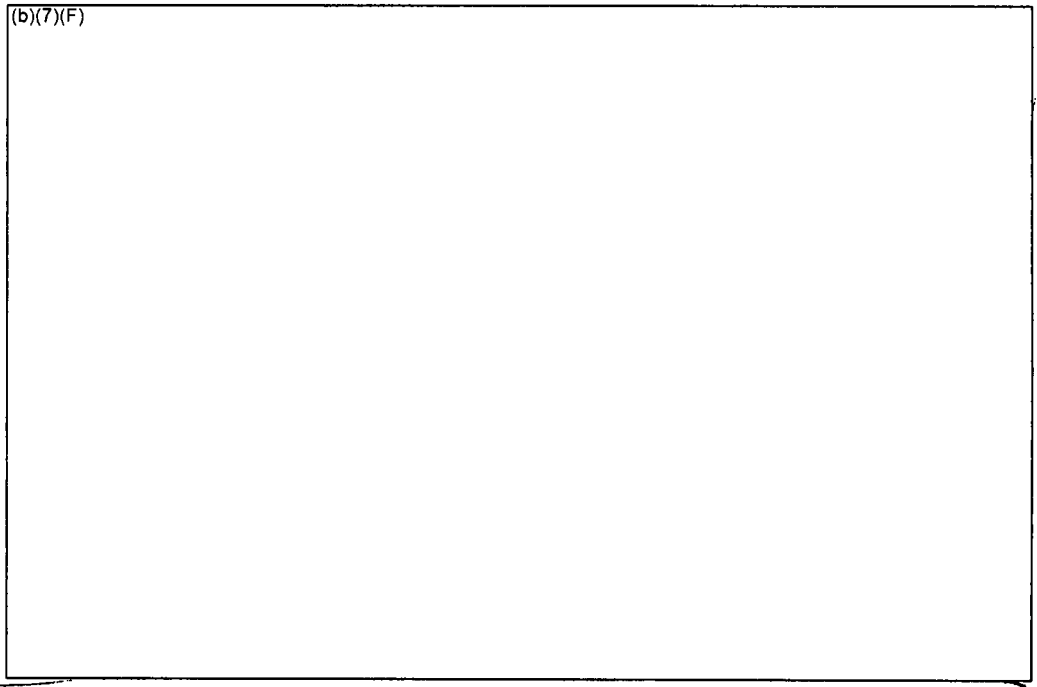
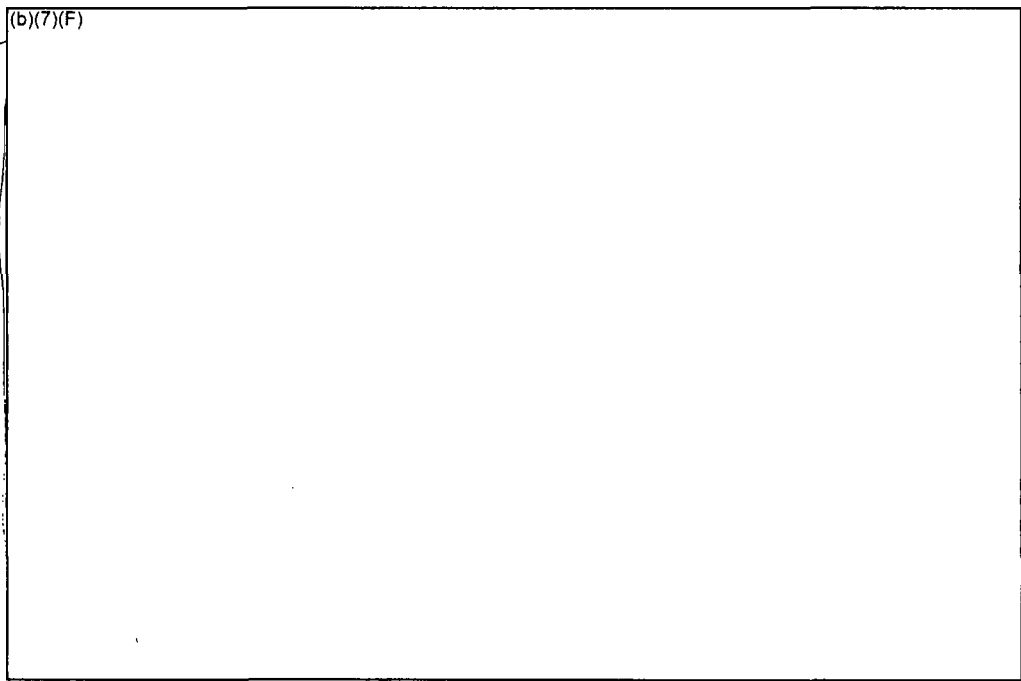


Figure 4-1 Total Decay Heat Power in the Reference BWR SFP.



**Figure 4-2 Make-up Flowrate for the Reference BWR SFP.**

**4.2 Leak Below the Top of the Racks**

In the second calculation, the spray system was not initiated prior to uncover of the fuel and/or the water leakage location is below the top of the racks. Similar to the previous calculation, the accident has disabled the SFP heat removal capabilities and the decay heat from the SFP is boiling away the remaining inventory. It is assumed that the spray system is initiated before the fuel becomes uncovered. If not, additional spray would be required to remove the sensible heat from the regions of the assembly which has heated (e.g., see Section 4.2.3). Furthermore, if the fuel rods are at high temperature, then the initial mode of spray heat removal would be film boiling, which is less effective than nucleate boiling.

There are several other assumptions that were applied for these calculations. Since the fuel is uncovered, a spray system is required to distribute the water to the individual assemblies. To achieve a uniform coverage, the spray systems would have some inefficiencies due to overlap from the adjacent nozzles and inaccurate delivery (e.g., hitting walls or missing the pool). The magnitude of the total SFP spray flow assumes a 33% spray overlap factor to account for these two inefficiencies. However, the hand calculations assume that the most limiting assembly is not within a zone that has spray overlap. Furthermore, only the spray which enters the assembly canister was considered as effective (i.e., neglect spray into the space between the assembly canister and the rack cell wall). In addition, all other modes of heat transfer are conservatively

neglected. For example, radial heat transfer to adjacent lower powered assemblies was neglected.

Figure 4-3 shows the peak, median, and minimum assembly power in the reference BWR SFP as a function of time after the last offload. (b)(7)(F)

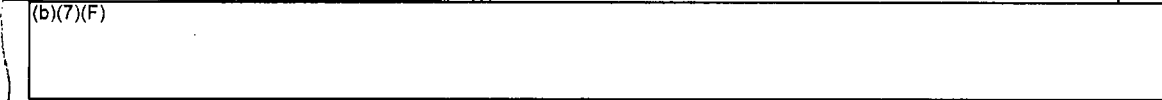
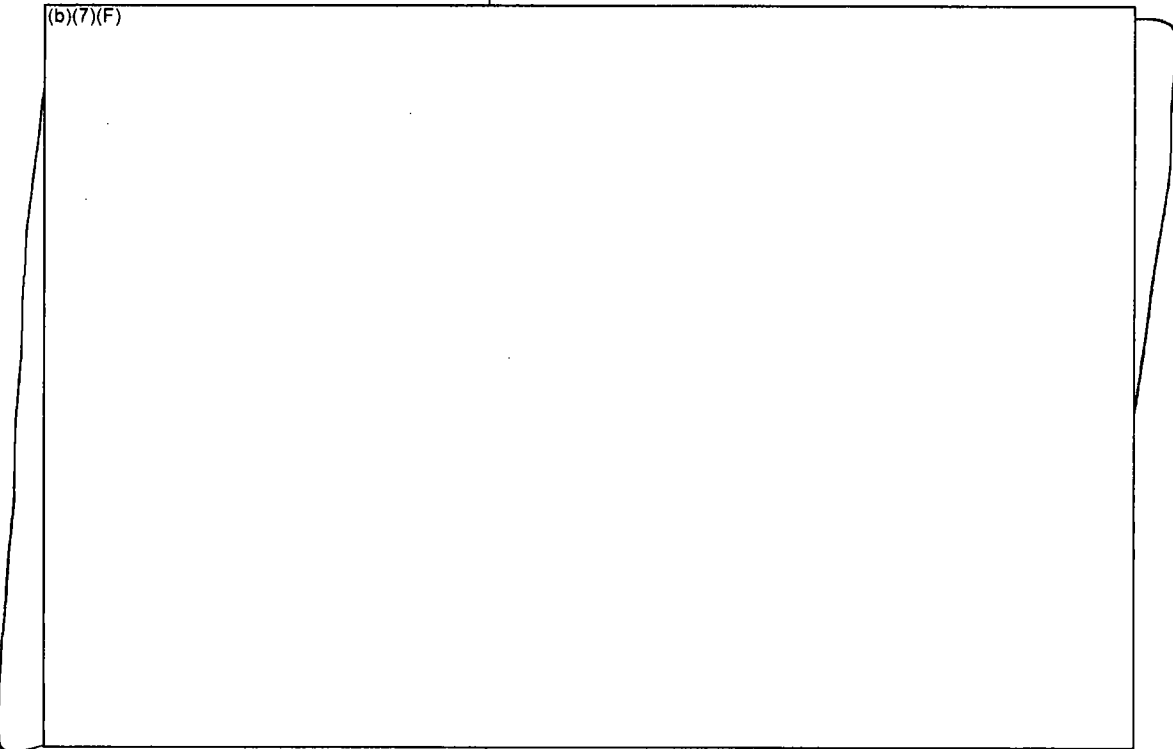


Figure 4-4 shows the required spray rate to provide adequate heat removal from the peak decay heat assembly. For example, (b)(7)(F) Furthermore, a spray system is required to direct the flow into the assemblies. Sample calculations for the heat removal requirements (b)(7)(F) are shown in Section 4.2.1. Some scoping hand calculations suggest that the spray water will be able to penetrate into the assembly (b)(7)(F) (see Section 4.2.2). Finally, the impact of the assembly sensible heat upon the initial spray effectiveness is discussed in Section 4.2.3. Ex 1F



**Figure 4-3 Comparison of the Peak, Median, and Minimum Assembly Decay Heat Power in the Reference BWR SFP.**

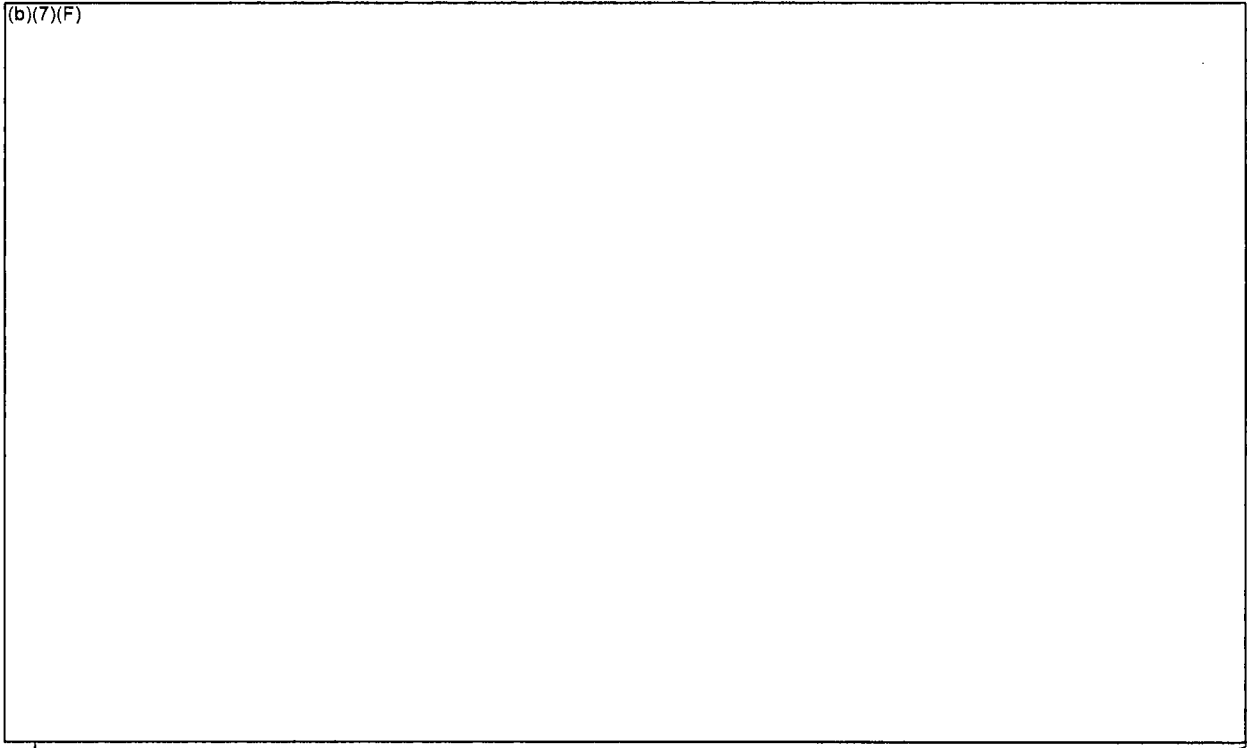


Figure 4-4 Make-up Flowrate for the Reference BWR SFP.

#### 4.2.1 Calculations for One Point on the BWR Spray Chart

Assumptions:

1. Reference BWR SFP data
2. Peak assembly (b)(7)(F) Ex 7F
3. 80°F spray water
4. 33% spray coverage inefficiency/overlap
5. Only flow within the canister cross-section is effective
6. Make-up based on peak assembly decay heat projected across entire pool

$$\rho = 62.1 \text{ lbm/ft}^3 = 996 \text{ kg/m}^3$$

$$h_{fg} = 970.3 \text{ BTU/lbm} = 2.257 \times 10^6 \text{ J/kg}$$

$$h_{80^\circ\text{F} \rightarrow 212^\circ\text{F}} = 180.18 \text{ BTU/lbm} - 48.13 \text{ BTU/lbm} = 132.05 \text{ BTU/lbm} = 3.072 \times 10^6 \text{ J/kg}$$

$$\Delta h = h_{fg} + h_{80^\circ\text{F} \rightarrow 212^\circ\text{F}} = 1102 \text{ BTU/lbm} = 2.56 \times 10^6 \text{ J/kg}$$

Peak assembly power  $\frac{(b)(7)(F)}{(b)(7)(F)}$

BWR SFP Assembly Pitch = 6.28"  
BWR SFP Canister ID = 5.4

Inside canister area to cell pitch ratio =  $(5.4'' \times 5.4'') / (6.28'' \times 6.28'') = 0.739$

Whole Pool Size =  $480'' \times 424'' = 203,520 \text{ in}^2 = 131.3 \text{ m}^2$  (Cross-sectional area)

Equivalent number of SFP rack cells in entire SFP cross-section  
=  $203,520 \text{ in}^2 / (6.28'' \times 6.28'') = 5160$  equivalent cells

Spray Flowrate =  $\frac{(b)(7)(F)}{(996 \text{ kg/m}^3 \times 2.56 \times 10^6 \text{ J/kg}) \times (60 \text{ sec/min})}$   
 $\times (264.2 \text{ gal/m}^3) \times 1.33 \text{ (overlap)} \times 1.35 \text{ (chan ratio)} \times 5160 \text{ equiv. cells}$

$\frac{(b)(7)(F)}{(b)(7)(F)}$

#### 4.2.2 Calculations for Counter-Current Flow Limitation (CCFL)

$(b)(7)(F)$

Ex 7F

$(b)(7)(F)$  Consequently, counter-current flow limiting (CCFL) of water down into the assembly due to the shear forces from the upward steam flow is a concern.

The following terms are needed to calculate the Wallis non-dimensional flooding velocities to evaluate whether CCFL is a concern, assuming a downward liquid velocity  $(b)(7)(F)$  water and steam properties, and the reference BWR geometry  $(b)(7)(F)$

Ex 1F

$(b)(7)(F)$  First, calculate the phasic volumetric fluxes [Wallis],

$$J_i = Q_i / A$$

where,

$J_i$  is the phasic volumetric flux

$Q_i$  is the volumetric flow

$$Q_L = \frac{(b)(7)(F)}{(b)(7)(F)} \quad \text{Ex 1F}$$

$$Q_G = \frac{(b)(7)(F)}{(b)(7)(F)}$$

A is the cross-sectional flow area  $(b)(7)(F)$  Ex 1F

So,

$$J_L = \frac{(b)(7)(F)}{(b)(7)(F)} \quad \text{Ex 7F}$$

$$J_G = \frac{(b)(7)(F)}{(b)(7)(F)}$$

Next calculate  $J_i^*$  terms,

$$J_i^* = J_i \cdot (\rho_i)^{1/2} / [g \cdot D_H \cdot (\rho_L - \rho_G)]^{1/2}$$

where,

$Q_i$  is the phasic volumetric flux

$$Q_L = \frac{(b)(7)(F)}{(b)(7)(F)} \quad Ex 1F$$

$$Q_G = \frac{(b)(7)(F)}{(b)(7)(F)}$$

$g$  is gravity ( $9.81 \text{ m/s}^2$ )

$D_H$  is the hydraulic diameter of the upper assembly  $(b)(7)(F)$   $F \times 1F$

$\rho_L$  is the water density ( $996 \text{ kg/m}^3$ )

$\rho_G$  is the steam density ( $0.598 \text{ kg/m}^3$ )

So,

$Ex 1F$

$$J_G^* = \frac{(b)(7)(F)}{(b)(7)(F)} \cdot 0.5 / [9.81 \text{ m/s}^2 \cdot (b)(7)(F) \cdot (996 \text{ kg/m}^3 - 0.598 \text{ kg/m}^3)]^{0.5}$$

$Ex 1F$

$$J_L^* = \frac{(b)(7)(F)}{(b)(7)(F)} \cdot 0.5 / [9.81 \text{ m/s}^2 \cdot (b)(7)(F) \cdot (996 \text{ kg/m}^3 - 0.598 \text{ kg/m}^3)]^{0.5}$$

Next Grashof Number is calculated as follows,

$$N_L = [ \rho_L g D^3 (\rho_L - \rho_G) / \mu_L^2 ]^{1/4}$$

$$N_L = [ 996 \text{ kg/m}^3 \cdot 9.81 \text{ m/s}^2 \cdot (b)(7)(F)^3 \cdot (996 \text{ kg/m}^3 - 0.598 \text{ kg/m}^3) / (2.82 \times 10^{-4} \text{ kg/m-s}) ]^{1/4}$$

$Ex 1F$

From the Wallis flooding curve with  $N_L = \frac{(b)(7)(F)}{(F)}$

$$m = 1$$

$$C = 0.8$$

The flooding (CCFL) limit is,

$$(J_G^*)^{0.5} + (J_L^*)^{0.5} \cdot \frac{(b)(7)(F)}{(b)(7)(F)}$$

$$\frac{(b)(7)(F)}{(b)(7)(F)}^{0.5} + \frac{(b)(7)(F)}{(b)(7)(F)}^{0.5} = 0.8$$

$Ex 1F$

$$\frac{(b)(7)(F)}{(F)} < 0.8, \text{ which is below the flooding limit}$$

Another criterion by Wallis also suggests that the flow conditions are well below the flow reversal limitation,

$$J_G^* = 0.5 \text{ for flow reversal.}$$

In our case,

$$\frac{(b)(7)(F)}{(b)(7)(F)}^{0.5} < 0.5?$$

$Ex 1F$

Ex 7F  $\frac{(b)(7)(F)}{(F)} \approx 0.5$ , which is also below the flooding limit

It has been acknowledged that the classical Wallis correlations have some limitations due to the diameter effect [Bergles]. Using an alternate Kutaleadze relationship, which represents the ratio of the gas inertial forces acting on the capillary waves,

$$Ku = (J_g) * (\rho_g)^{1/2} / [g \sigma (\rho_L - \rho_G)]^{1/4}$$

where,

Ku is the Kutaleadze Number

$\sigma$  is surface tension between steam and water (0.072 kg/s<sup>2</sup>)

Ex 7F  $Ku = \frac{(b)(7)(F)}{(F)} * (0.598 \text{ kg/m}^3)^{1/2} / [9.81 \text{ m/s}^2 * 0.073 \text{ kg/s}^2 * (996 \text{ kg/m}^3 - 0.598 \text{ kg/m}^3)]^{1/4}$

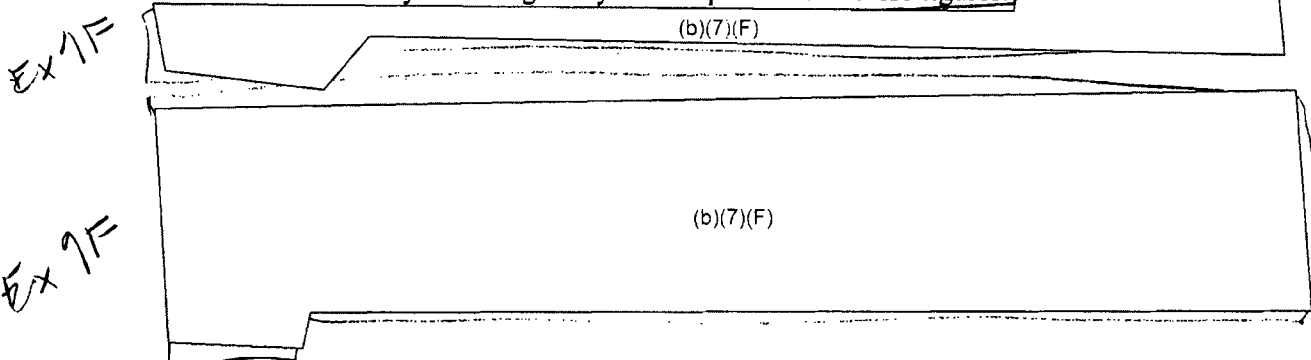
Ex 7F  $Ku = \frac{(b)(7)(F)}{(F)} \ll 3.2$

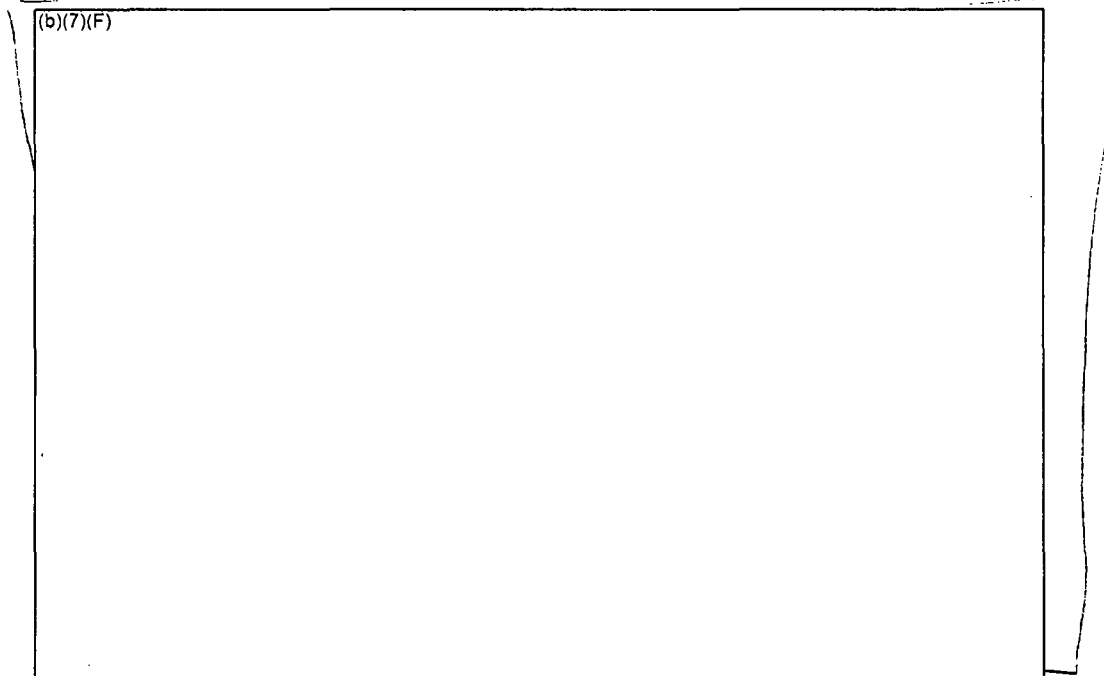
If the Kutaleadze number is less than 3.2, then there is no CCFL. Hence, all three flooding correlations show CCFL is not expected to be a concern  $\frac{(b)(7)(F)}{(F)}$

#### 4.2.3 Impact of Assembly Sensible Heat

The assembly sensible heat has an effect on the spray heat removal effectiveness. If the sprays are started after the assembly begins heating, then a portion of the water's cooling potential removes the sensible heat from the assembly. A high amount of sensible energy (i.e., high temperature) also transitions the rod heat transfer from nucleate boiling to less effective film boiling. If film boiling is not effective, then the fuel would continue to heat.

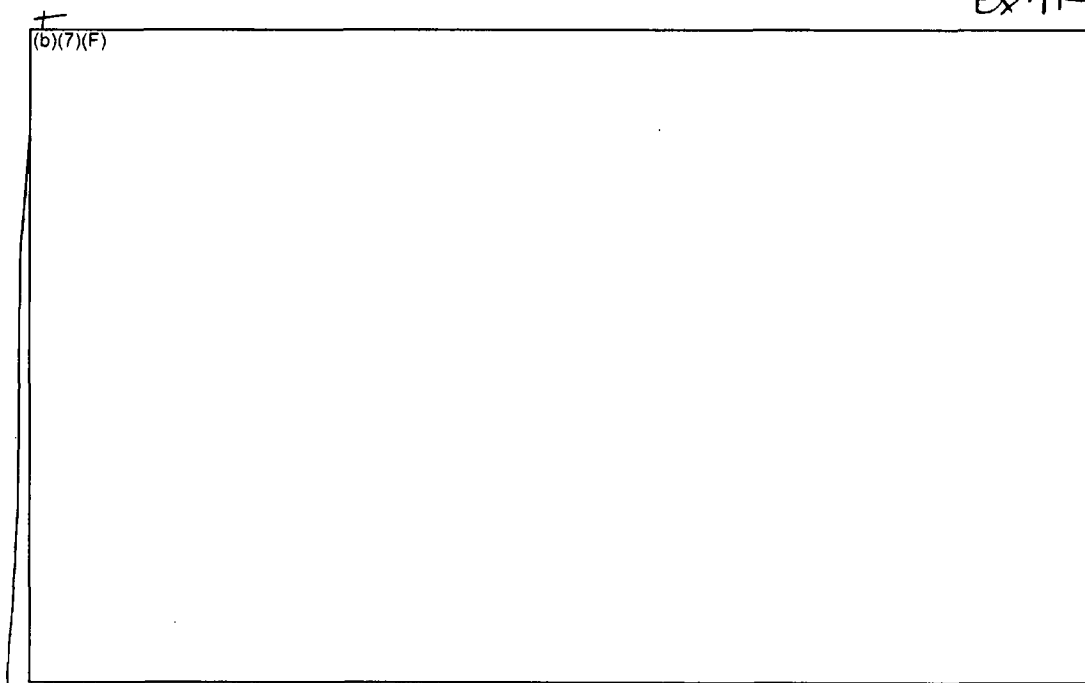
Assuming that the heat transfer (i.e., whether film or nucleate boiling) is effective enough to boil all the spray water entering the limiting assembly, the impact on the cooling time is shown in Figure 4-5 and Figure 4-6 for  $\frac{(b)(7)(F)}{(F)}$  spray flow, respectively. The amount of time required to cool the assembly to near saturation conditions from various initial temperatures while simultaneously removing decay heat is quantified in these figures.





Ex 7F

**Figure 4-5** Timing Impact of Sensible Heat on Assembly Cooling at (b)(7)(F) for a Uniform Configuration.



Ex 7F

Ex 1F

**Figure 4-6** Timing Impact of Sensible Heat on Assembly Cooling at (b)(7)(F) for a Uniform Configuration.

Ex 7F

### 5. WHOLE POOL MODEL BOUNDARY CONDITION CALCULATIONS

An assortment of whole pool calculations was run using the new whole pool model (see Section 3.3.2) to establish boundary conditions for the separate effects calculations. Section 5.1 shows typical results from a (b)(7)(F) [redacted]. The detailed responses from other cases are not shown but were similar.

Ex 7F

Ex 7F

The most interesting of these boundary condition values was the resultant water level. (b)(7)(F) [redacted]

Ex 7F

(b)(7)(F) [redacted]  
(b)(7)(F) [redacted] Table 5-1 summarizes the results

from the whole pool calculations. For the range of hole sizes and spray flow rates considered in this study, the long-term water level spanned conditions that would allow air flow (i.e., the inlet is not plugged) versus cases where the inlet would be plugged. (b)(7)(F) [redacted] hole cases had a relatively high level that would partially cover the bottom of the fuel (a water level of >16"). In contrast, (b)(7)(F) [redacted] hole had a very low water level and would be ensured to have air natural circulation flow. As discussed in Section 2.2, the phenomena and thermal response for cases with the inlet plugged by the water level is much different than the response when there is air flow in the assembly. Furthermore, it is expected that (b)(7)(F) [redacted] case with (b)(7)(F) [redacted] hole might have characteristics of both types of accidents.

Ex 7F

Ex 7F

Ex 7F

**Table 5-1 Summary of the Steady-State Water Levels as a Function of Leakage Hole Size and Spray Flow Rate.**

(b)(7)(F) [redacted]

Ex 7F

5.1 (b)(7)(F) Spray Flow Rate

*Ex 7F*  
*Ex 7F* Figure 5-1 through Figure 5-4 show the boundary conditions taken from the (b)(7)(F) of the (b)(7)(F) emergency spray flow. A special boundary condition control volume was created to specify fluid boundary conditions for the separate effects model. The time-dependent data consisted of water level (Figure 5-1), water and gas temperature (Figure 5-2), steam partial pressure (Figure 5-3), non-condensable gas concentrations (Figure 5-5<sup>17</sup>, actually reflects normal atmospheric concentrations of nitrogen and oxygen), and gas pressure (not shown, approximately atmospheric pressure). The blue points on each figure represent the data transferred to the separate effects model.

The whole pool results show expected trends. The water level drops in response to the leakage. Since the boundary condition control volume is only 5 m, Figure 5-1 only shows the level response below 5 m. Figure 5-4 shows the overall model level response. (b)(7)(F)

(b)(7)(F)  
(b)(7)(F) Since the base plate of the racks is 7.25" off the SFP floor, there was a circulation of natural air into the racks. *Ex 7F*

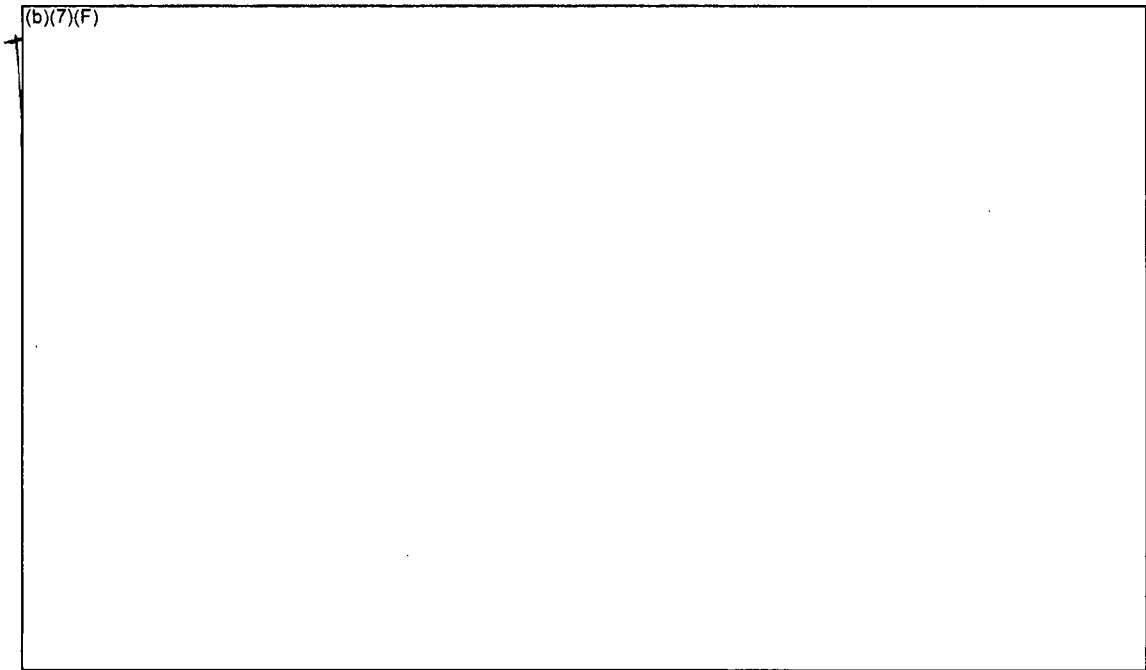
The water temperatures initially heated in response to the loss of SFP heat removal. Once the rack uncovered, separate gas and water temperatures are calculated. However, due to spray cooling, the pool under the racks and the gas temperatures remained relatively low. (b)(7)(F) *Ex 7F*

*Ex 7F* (b)(7)(F) Due to boiling of the spray water in the hot assemblies and evaporation, the partial pressure of the steam in the room also steadily increased (Figure 5-3). (b)(7)(F) the equivalent steam molar concentration was (b)(7)(F) (see Figure 5-5).

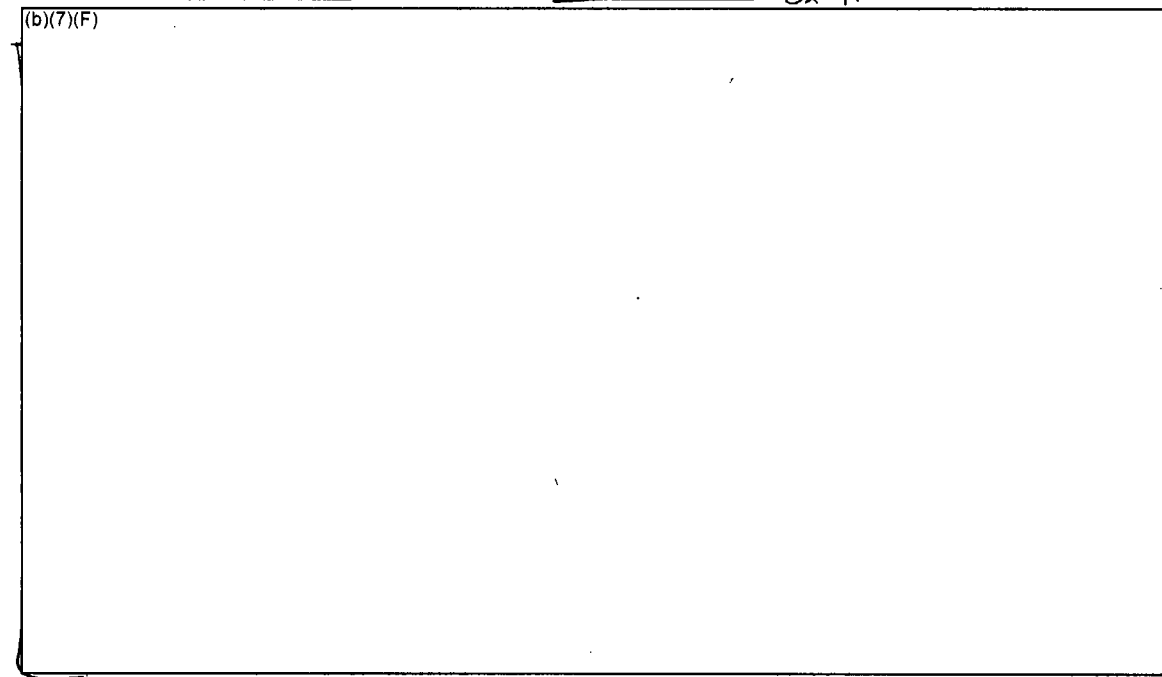
Figure 5-6 shows the flow balance between the water leakage flow from the SFP and the emergency spray flow. Initially the water leakage flow was very high due to the large head of water above the leakage location. As the water level dropped, the water leakage flow steadily decreased. (b)(7)(F) emergency spray system was started. However, due to the high leakage flow rate, emergency spray had little impact in slowing the level drop. (b)(7)(F) *Ex 7F*  
the water level (b)(7)(F) and the leakage flow is equal to the spray flow. The level remained at this value for the remainder of the calculation.

Figure 5-7 shows the integrated water flow over 48 hours. Approximately, 551,000 gallons of water has been sprayed into the SFP. The water volume corresponds to 73,800 ft<sup>3</sup>, which may be a concern for flooding equipment in lower rooms.

<sup>17</sup> The data from Figure 5-5 was not used directly. However, it was included to show the relative molar concentrations of steam, oxygen, and nitrogen. To define the gas composition, the steam partial pressure (Figure 5-3) was used with constant non-condensable molar concentrations of oxygen (20%) and nitrogen (80%).



**Figure 5-1** Water Level Boundary Condition from the BWR Whole Pool Model with (b)(7)(F) and a Spray Flow of (b)(7)(F) Ex 7F



**Figure 5-2** Vapor and Liquid Temperature Boundary Condition from the BWR Whole Pool Model with (b)(7)(F) and a Spray Flow of (b)(7)(F)

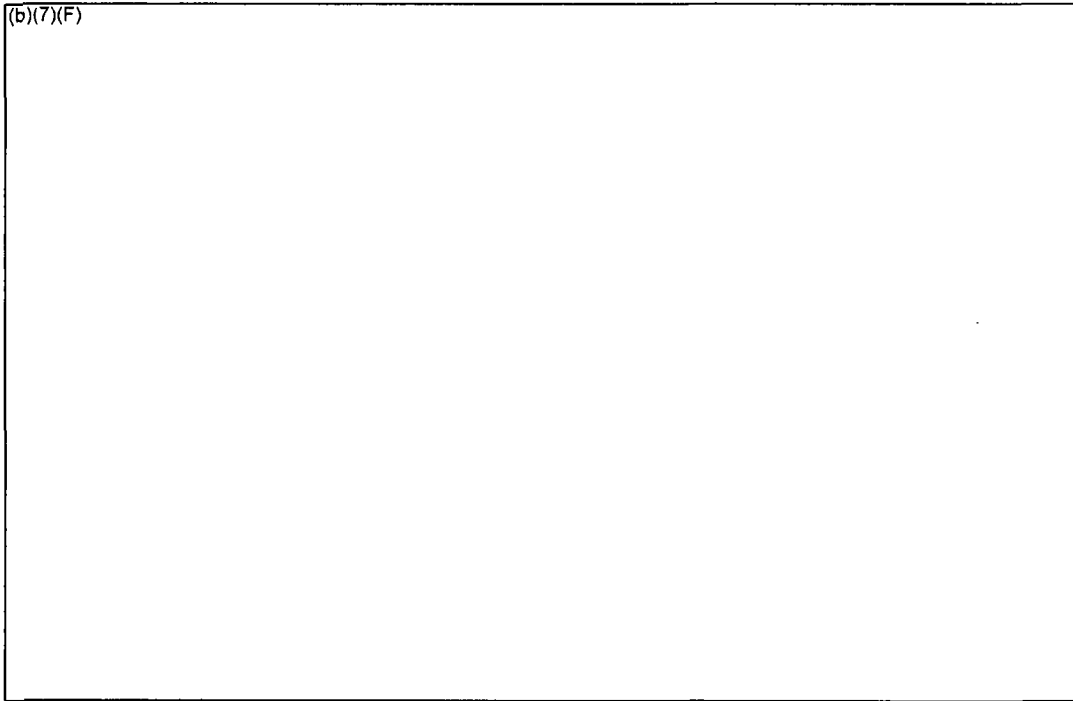


**Figure 5-3** Steam Partial Pressure Boundary Condition from the BWR Whole Pool Model with (b)(7)(F) and a Spray Flow of (b)(7)(F)

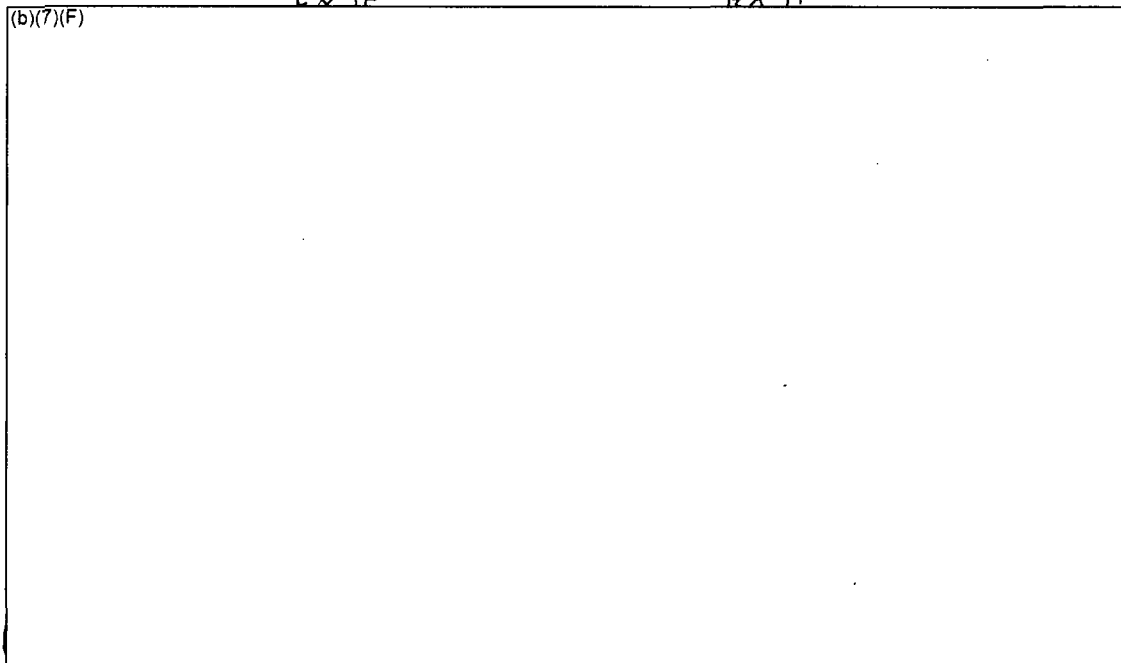


**Figure 5-4** Whole Pool Level Response from a (b)(7)(F) at the Bottom of the Pool with (b)(7)(F) and a Spray Flow of (b)(7)(F)

Ex 7F

Ex 7F

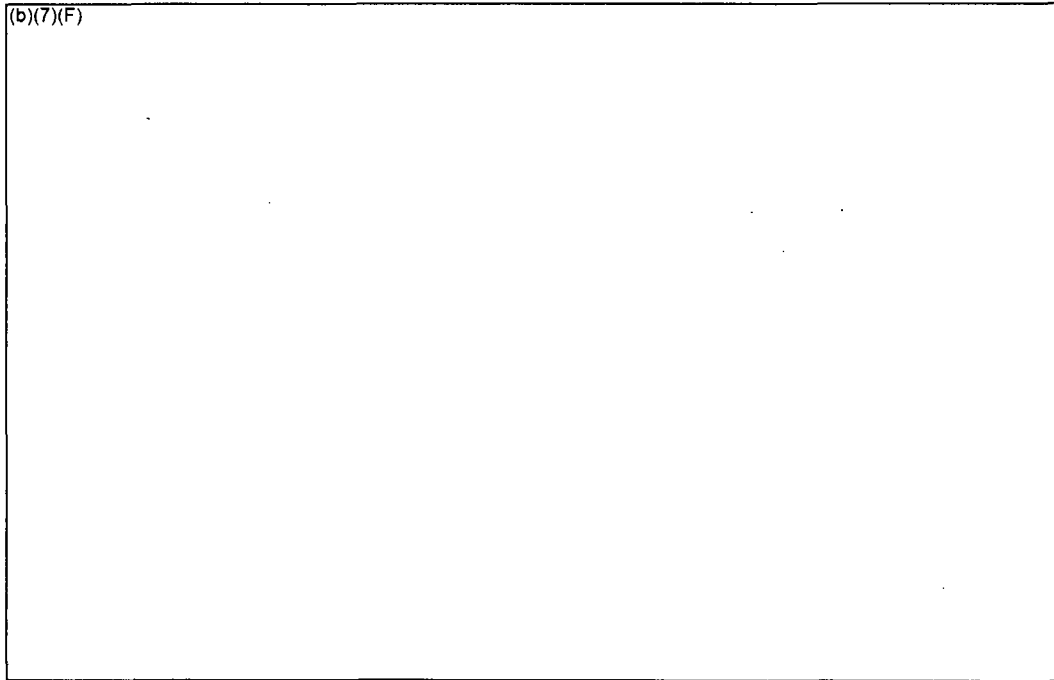


**Figure 5-5 Gas Concentration in the Refueling Room above the SFP for (b)(7)(F) and a Spray Flow of (b)(7)(F)**

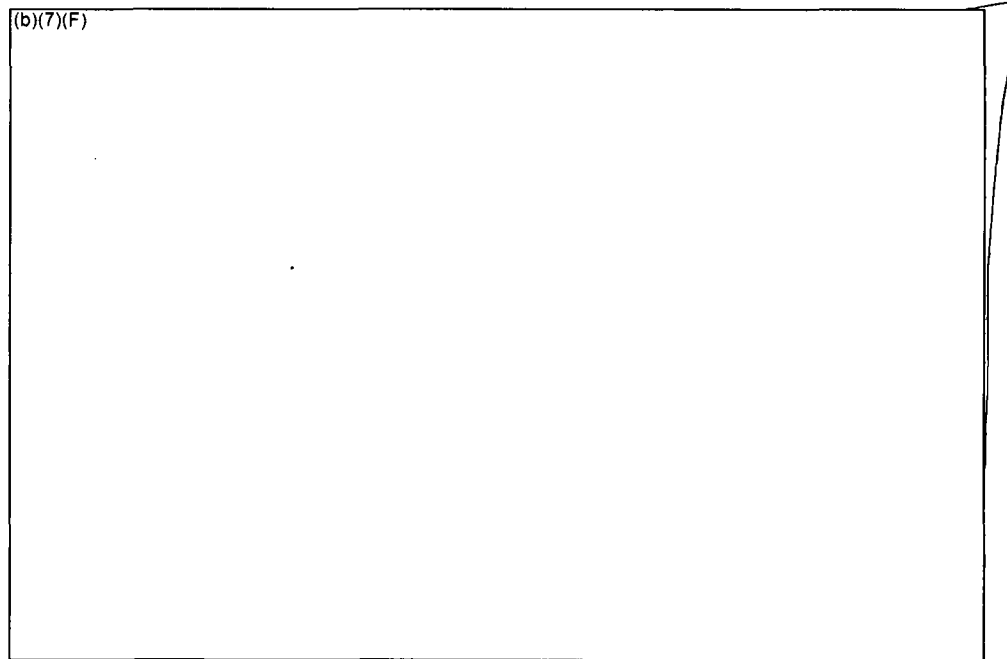


**Figure 5-6 Comparison of the Leak Rate and Spray Flowrate Response from a (b)(7)(F) at the Bottom of the Pool with (b)(7)(F) and a Spray Flow of (b)(7)(F)**

Ex 7F

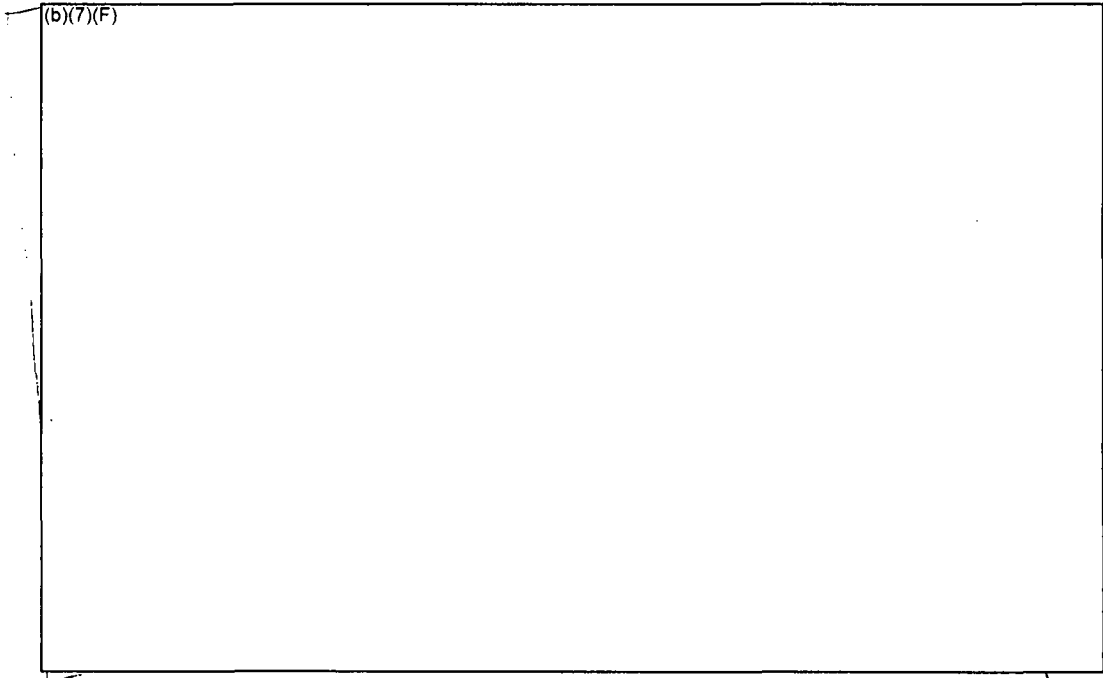
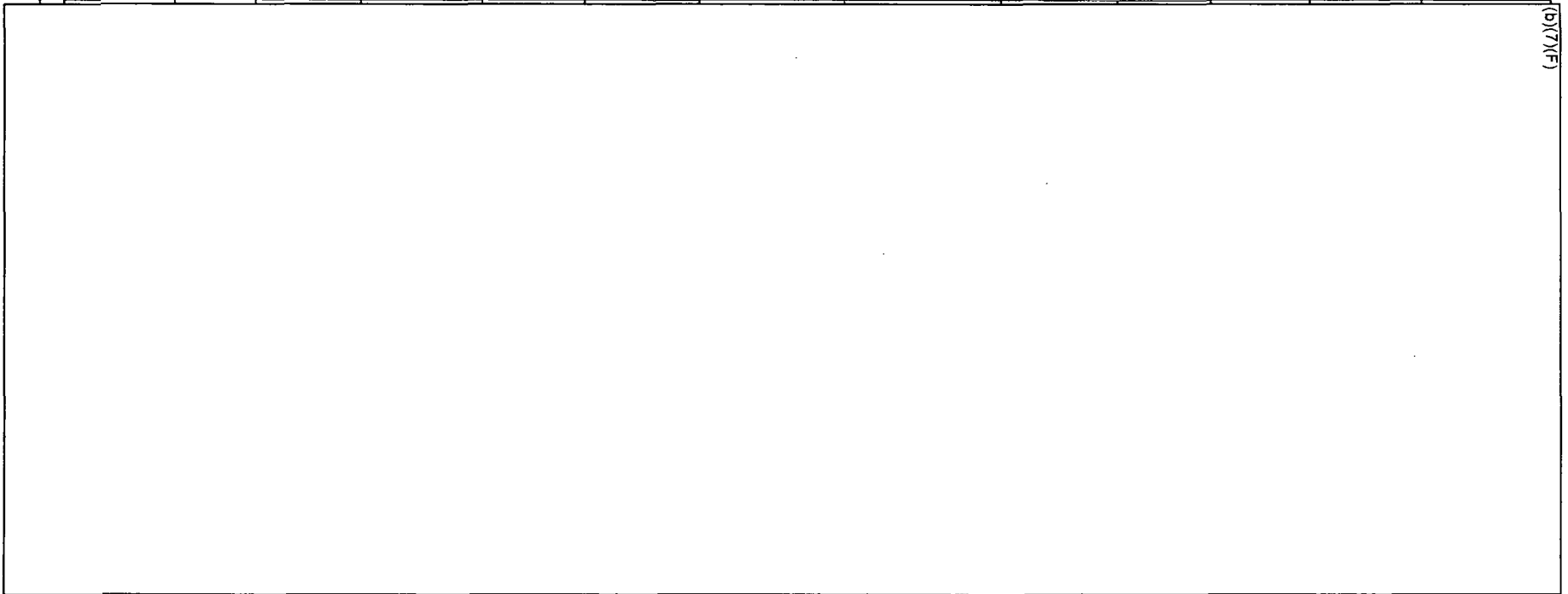


Figure 5-7 Total Injection Spray Flow for (b)(7)(F) Make-up Case.

Ex 7F

Table 6-1 Summary of the Spray Calculations



(b)(7)(F)

E+2/E

## 6. MELCOR SEPARATE EFFECTS MODEL RESULTS

Section 6.1 provides a table with a coolability summary of all the separate effects spray calculation. Additional details about the uniform, checkerboard, and 1x4 configuration calculations are provided in Sections 6.2, 6.3, and 6.4, respectively.

### 6.1 Summary of Separate Effect Spray Calculations

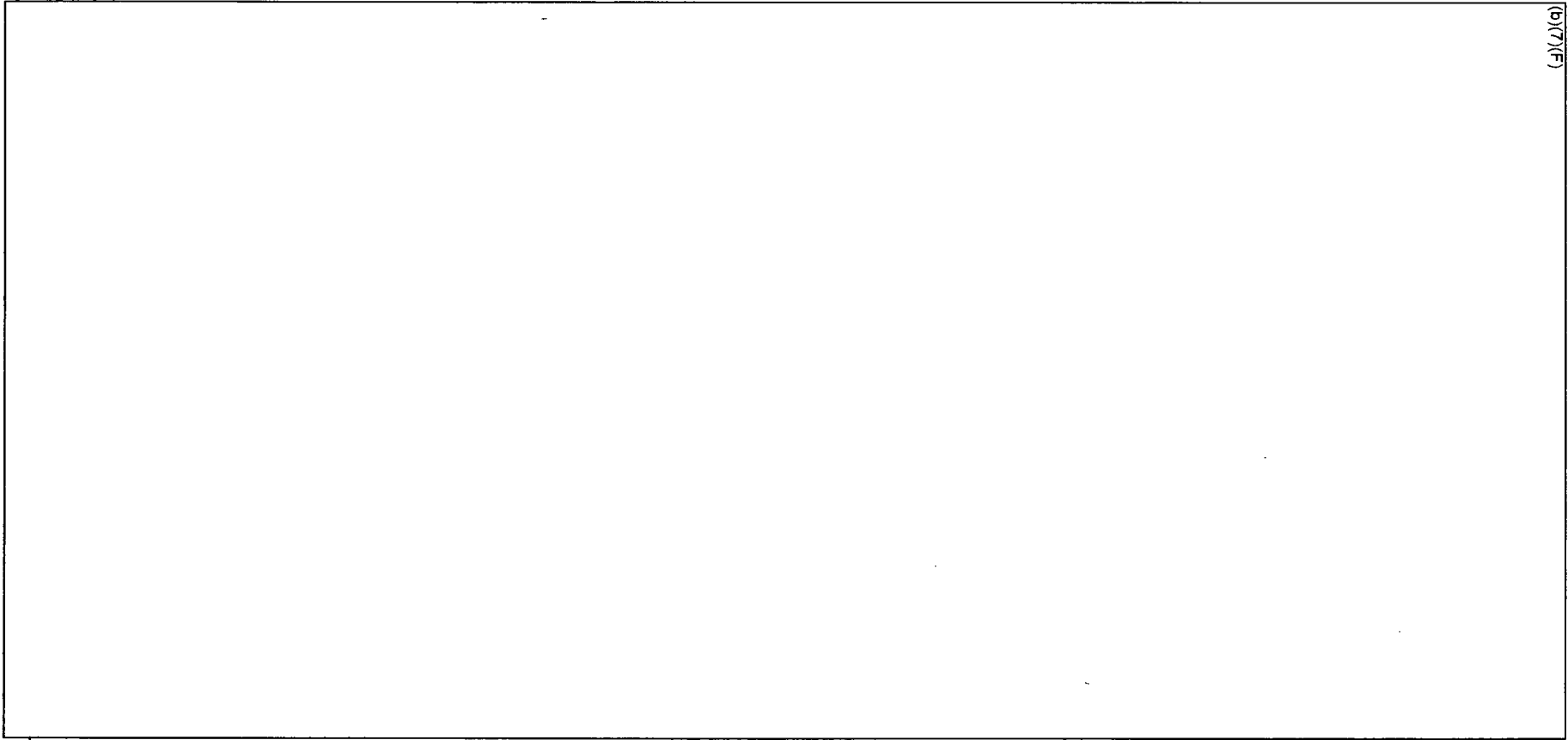
Table 6-1 summarizes the results of the spray separate effects calculations. Calculations were performed for the uniform, checkerboard, and 1x4 configurations. For each configuration, parametric calculations were performed with variations in one of the scenario or modeling attributes. The various groups of calculations are separated by bold horizontal lines in the table. The table was intended to provide a quick quantitative summary of the coolability results from the various cases. The variations in the calculations included fuel configuration (uniform, checkerboard, and 1x4), aging time of the peak powered assembly, leak size (b)(7)(F) Ex 7F, spray flow rate (b)(7)(F) Ex 7F, air flow (some configurations that were expected to have air flow had a sensitivity study where the inlet was plugged with water), and a modeling parameter (MELCOR's flow regime model active or inactive).

The high level results are presented in the last two columns of the table. (b)(7)(F) Ex 7F

(b)(7)(F)

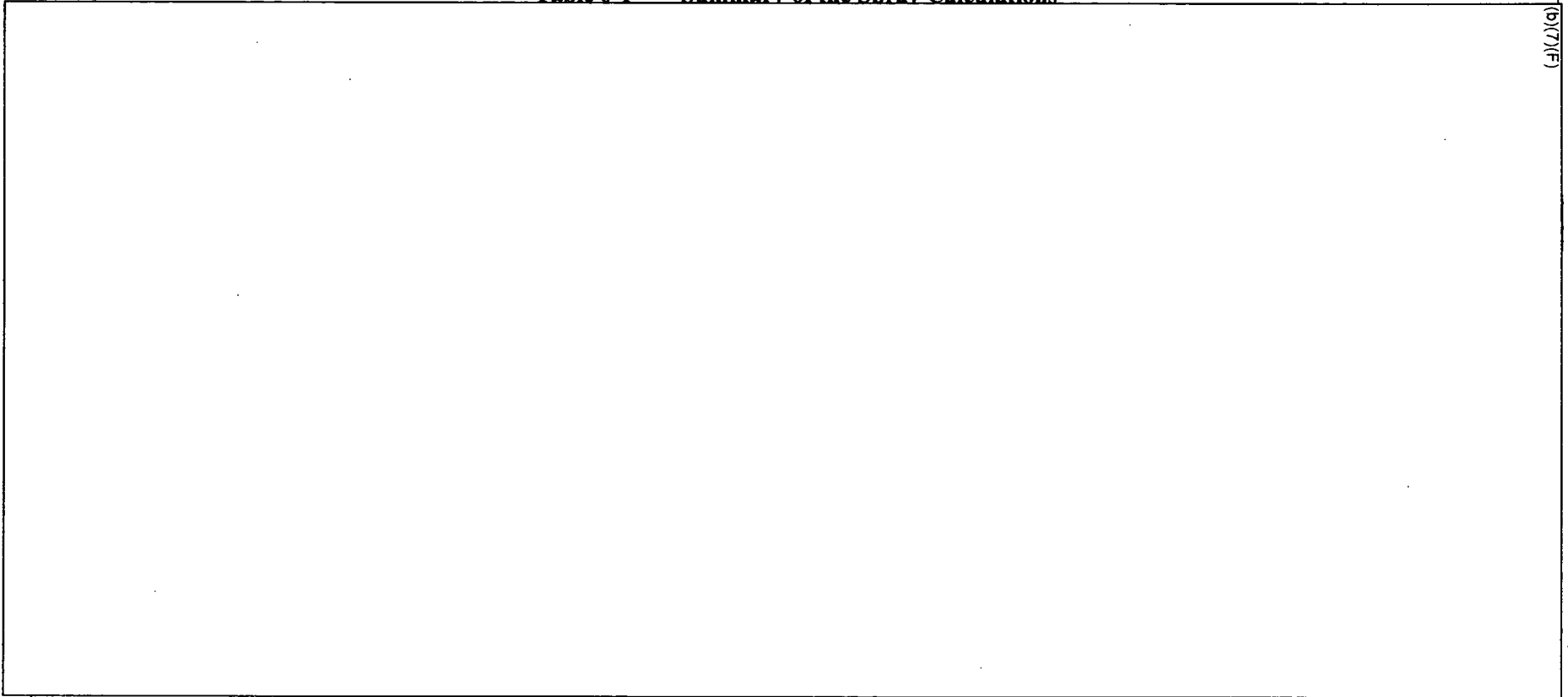
(b)(7)(F) Additional details about the uniform, checkerboard, and 1x4 configurations are provided in Sections 6.2, 6.3, and 6.4, respectively.

**Table 6-1 Summary of the Spray Calculations**



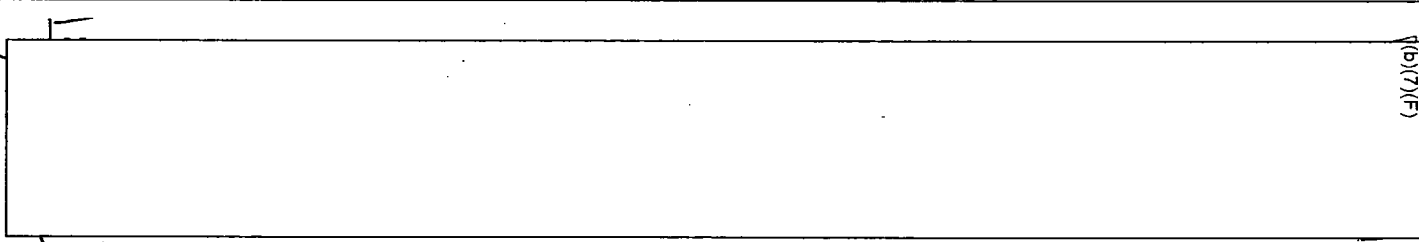
(b)(7)(F)

**Table 6-1 Summary of the Sprav Calculations**

A large rectangular area that has been completely redacted, leaving it blank. It is outlined by a black border. In the top right corner, there is a vertical label (b)(7)(F). In the bottom right corner, there is a handwritten label Ex 11F.

(b)(7)(F)

Ex 11F

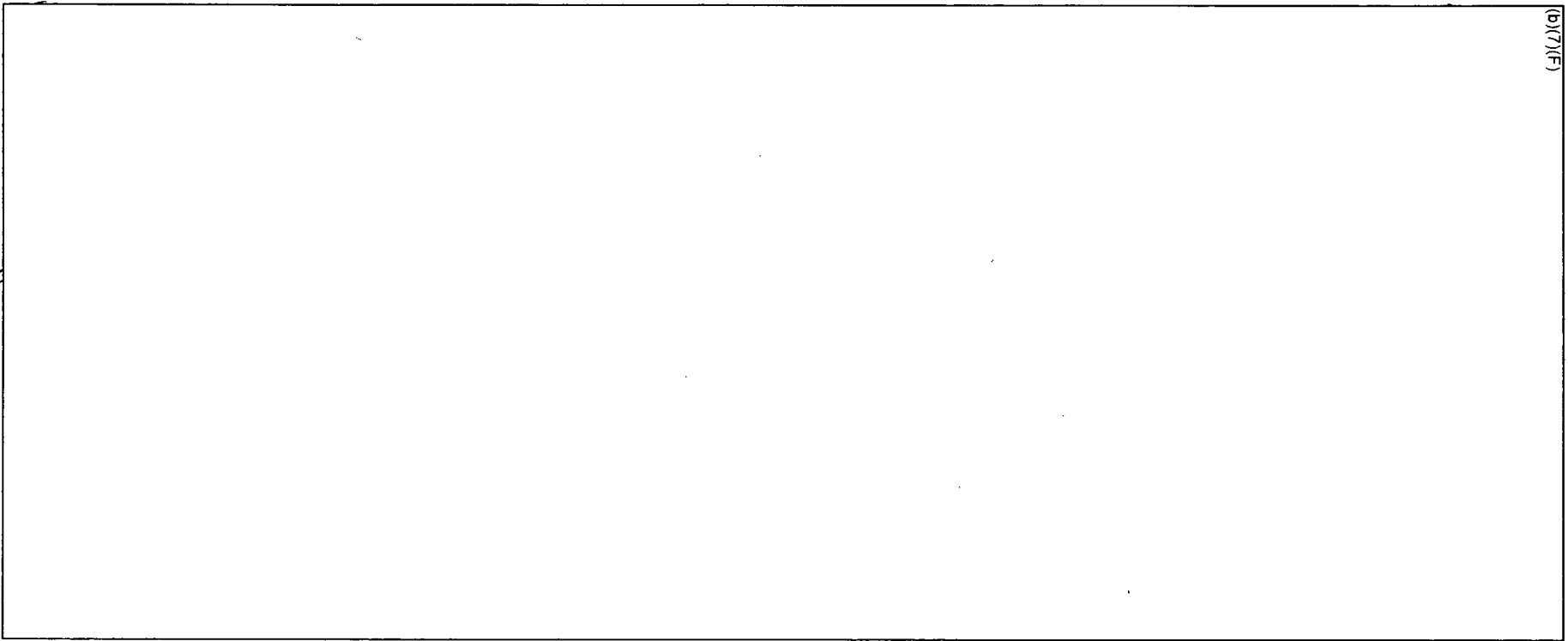
A smaller rectangular area that has been completely redacted, leaving it blank. It is outlined by a black border. In the top right corner, there is a vertical label (b)(7)(F). To the right of the table, there is a handwritten label Ex 7F.

(b)(7)(F)

Ex 7F

(b)(7)(F)

Ex 7F



## 6.2 Separate Effects Spray Model Results for the Uniform Configuration

Section 6.2.1 gives a summary of the 4 cases with (b)(7)(F) (b)(7)(F) leakage hole in a uniform fuel configuration. The four cases examine differences in the response with and without sprays and with and without the flow regime model active (see Section 3.1.4 for a more complete discussion). Section 6.2.2 shows the results of an energy balance on (b)(7)(F) case to illustrate the heat flows. Finally, Sections 6.2.3, 6.2.4, and 6.2.5 show the coolability results as a function of aging for different leakage rates and spray flow rates.

### 6.2.1 Base Calculations for (b)(7)(F) Spray

The S1 and S5 base case configuration calculations simulated a uniform configuration of the highest powered assemblies discharged into the spent fuel pool with (b)(7)(F) since reactor shutdown. The uniform configuration represents the response of an assembly in the center of a region of high-powered assemblies, such that there is negligible radial heat transfer (i.e., an adiabatic condition in the radial direction). (b)(7)(F)

(b)(7)(F)

Ex 7F

(b)(7)(F) examined differences in the response with and without sprays and with and without the flow regime model active. When the flow regime model was deactivated, the spray water has a relatively small surface contact area with the cladding. Due to the reduction of heat transfer, the spray flow penetrates more deeply into the assembly before completely evaporating. In addition, a S1 case was run where the inlet of the assembly was plugged by water. As discussed in Section 5, depending upon the hole size and the spray rate, cases were identified where the inlet to the racks could be covered. Consequently, Case S1 and S1p parametrically investigated both conditions. However, it should be noted that the best-estimate level responses (b)(7)(F) (b)(7)(F) sprays were well below the bottom of the rack baseplate.

Ex 7F

Ex 7F

(b)(7)(F)

Ex 7F

The axial temperature profiles for the four cases are shown in Figure 6-3 through Figure 6-6.

(b)(7)(F)  
(b)(7)(F) The designators in the figure legend

Ex 7F

correspond to the CORE Package nodalization shown in Figure 3-16. For example, COR-TCL.104 corresponds to the CORE Package cladding temperature in Ring 1 and Level 4. Level 4 is the bottom of the active fuel and Level 12 is the top of the active fuel. Level 13 is the gas plenum at the top of the fuel rods.

The axial temperature response for the case with the flow regime model inactive is shown in Figure 6-4. (b)(7)(F)

(b)(7)(F)

Ex 7F

The plugged case (S1p) did not have air cooling. As shown in Figure 6-1 and Figure 6-6, the peak temperature response was similar to Case S1. However, the absence of air in the assembly led to less oxidation heating and a slower heatup at high temperatures. (b)(7)(F) Ex 7F

Finally, the axial temperature profiles (b)(7)(F) Ex 7F are shown in Figure 6-7 for all four cases. It is interesting to observe that the peak cladding temperature somewhat follows the axial power profile in the case without spray.<sup>18</sup> In contrast, the cases with spray flow are much cooler at the top of the assembly. Both the base case (S1) and the plugged case (S1p) used the flow regime model, which enhanced heat removal at the top of the assembly. However, due to the large mismatch between the heat generation rate and the heat removal (also see Section 6.2.2), the region at the top of the assembly still oscillated between film and nucleate boiling (e.g., see temperature responses in Figure 6-3 and Figure 6-6). Conversely, the non-flow regime case spray was less effective at the top but penetrated deep into the assembly. (b)(7)(F) Ex 7F

(b)(7)(F) The net effect was to slightly delay heatup relative to the other cases.

<sup>18</sup> This axial profile trend will change if the assembly reached a steady state temperature profile or was the heating rate was lower. In a lower-power steady state calculation, the peak temperature is closer to the top of the assembly.

Ex 7F

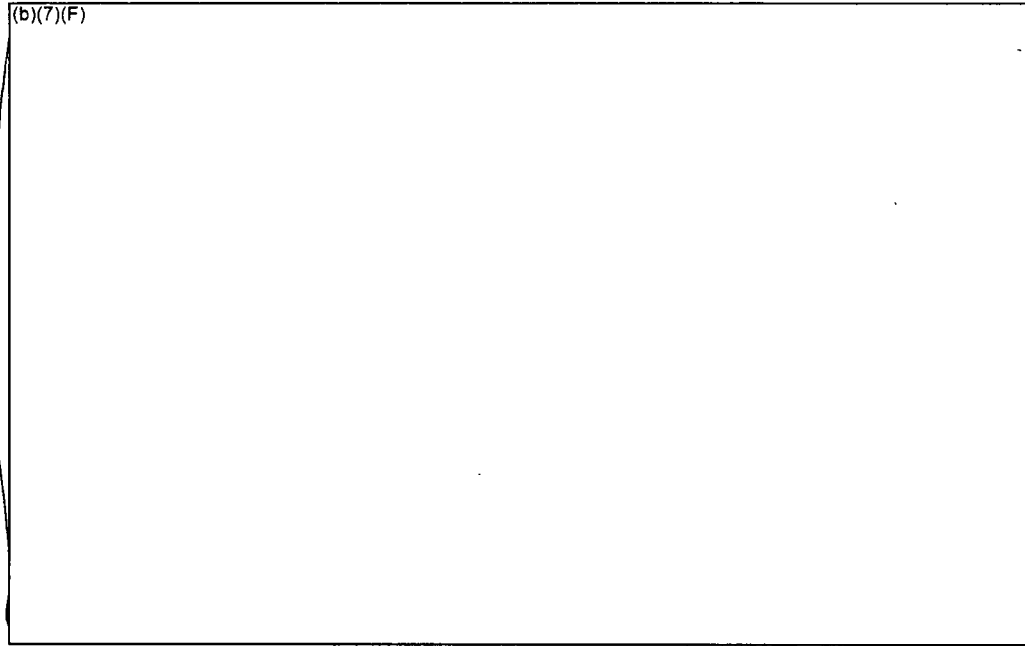


Figure 6-1 Comparison of the Peak Cladding Temperatures for the (b)(7)(F) with a Uniform Configuration with (b)(7)(F) and a Whole Pool Spray Flow of (b)(7)(F)

(b)(7)(F)

Ex 7F

Ex 7F

Ex 7F

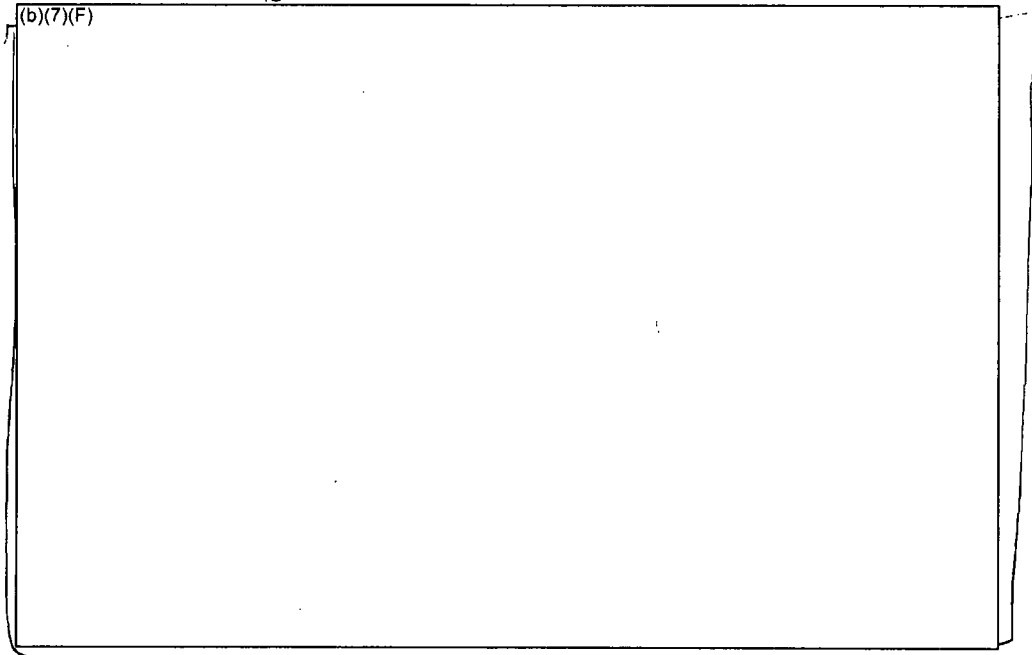
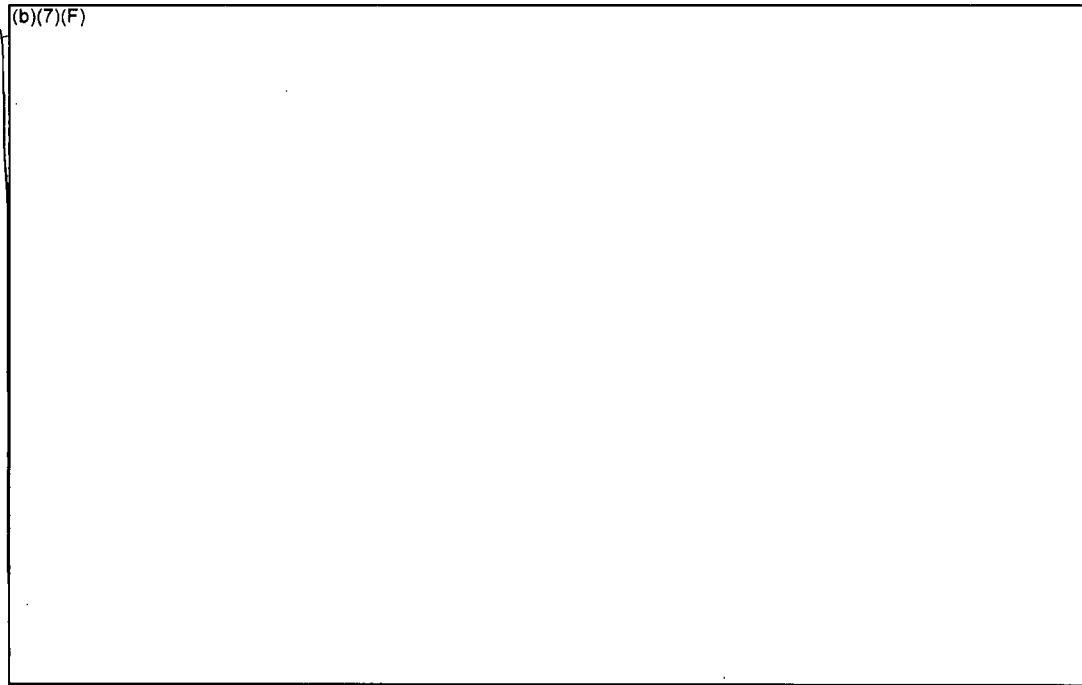


Figure 6-2 Comparison of the Peak Cladding Temperatures for the (b)(7)(F) with a Uniform Configuration with (b)(7)(F) and a Whole Pool Spray Flow of (b)(7)(F)

(b)(7)(F)

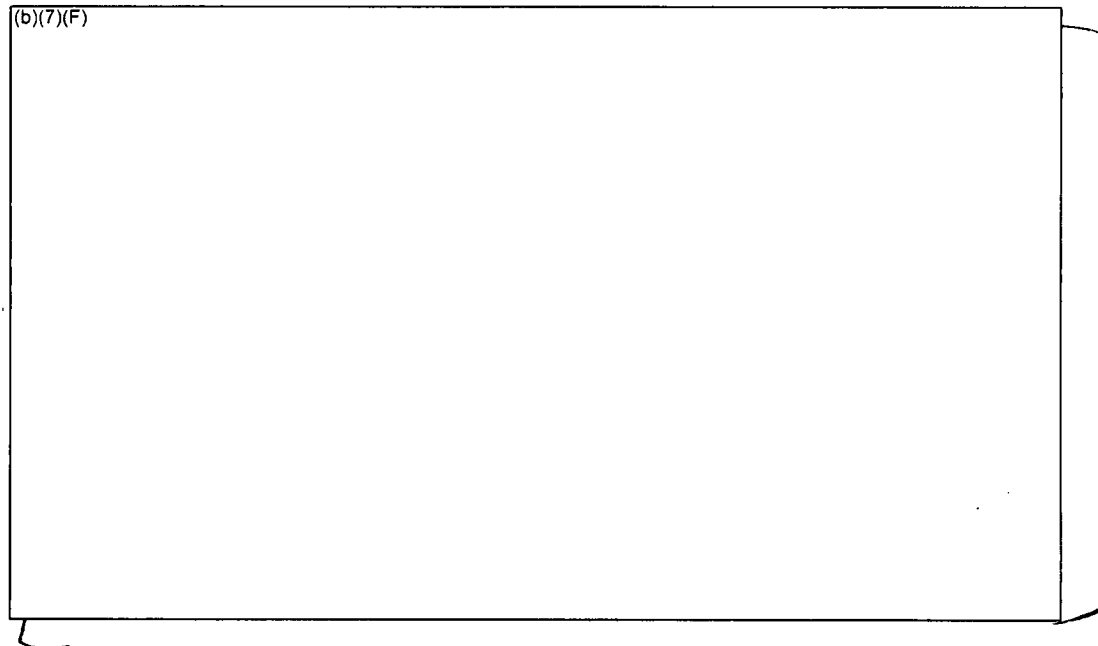
Ex 7F

Ex 7F



Ex 7F

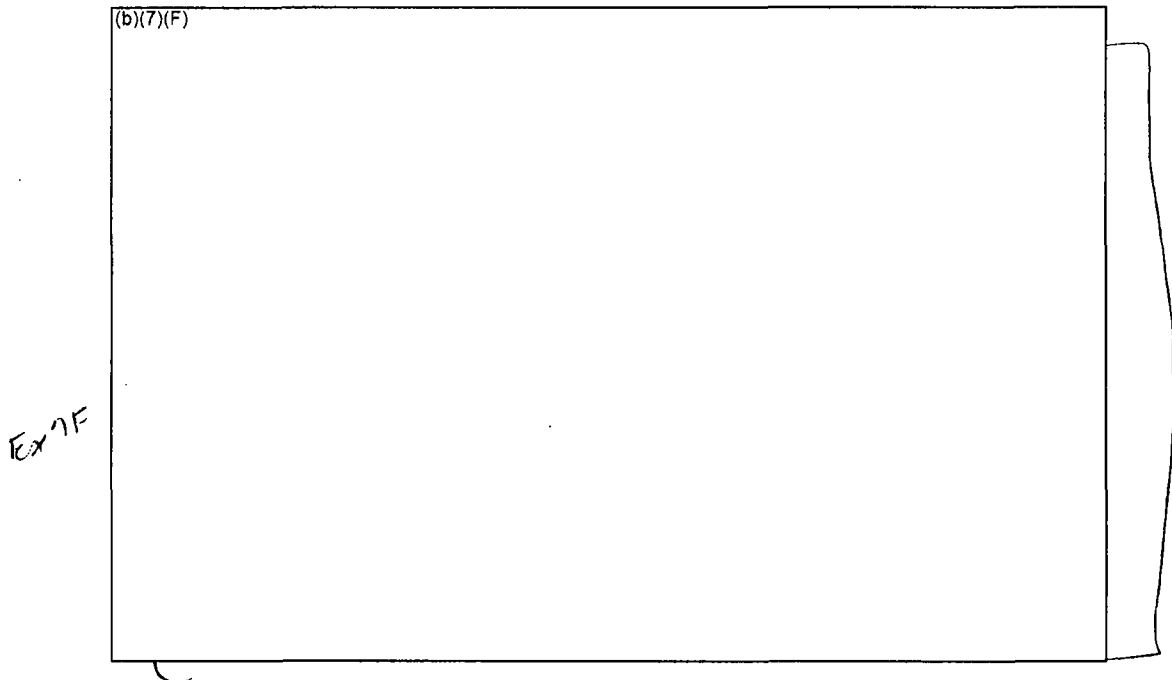
Figure 6-3 **Assembly Cladding Temperatures for the Uniform Configuration with**  
**(b)(7)(F) Spray Flow (Case S1).**



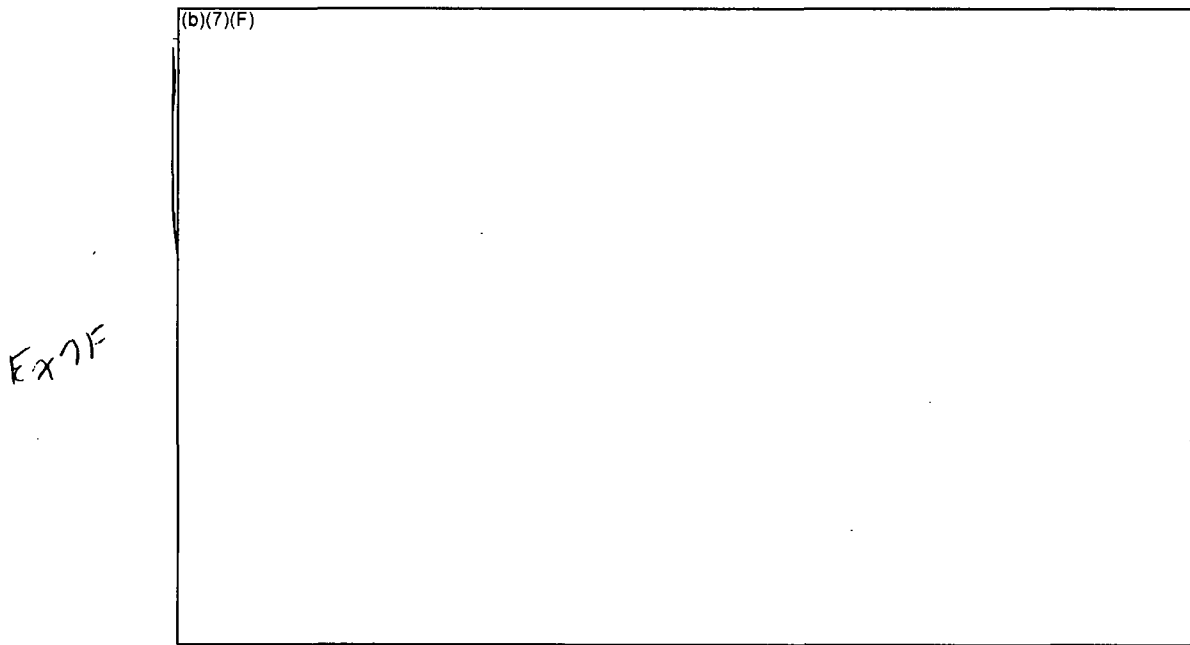
Ex 7F

Figure 6-4 **Assembly Cladding Temperatures for the Uniform Configuration with**  
**(b)(7)(F) Spray Flow, and the Flow Regime Model Inactive**  
**(Case S1a).**

Ex 7F

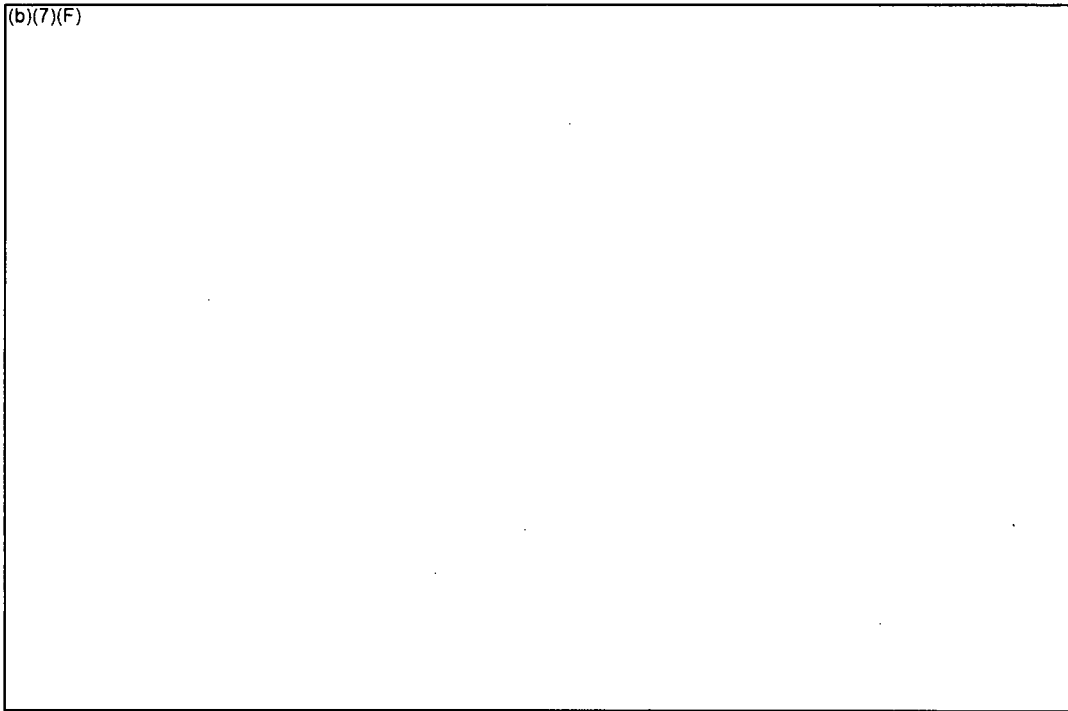


**Figure 6-5** Assembly Cladding Temperatures for the Uniform Configuration with (b)(7)(F) and No Spray Flow (Case S1b).



**Figure 6-6** Assembly Cladding Temperatures for the Uniform Configuration with (b)(7)(F) Spray Flow and Plugged Inlet (Case S1p).

Ex 7F                      Ex 7F



Ex 7F

Figure 6-7 Axial Cladding Temperature Profiles for the Uniform Configuration with (b)(7)(F) Spray Flow.

(b)(7)(F) Ex 7F Ex 7F

**6.2.2 Energy Balance on Base Calculation for** (b)(7)(F) **Spray**

An energy balance was performed on the S1 case with the flow regime model operating. This energy balance is somewhat less useful than the ones done for the checkerboard and 1x4 configurations because the assembly did not reach steady conditions. (b)(7)(F)

(b)(7)(F) Figure 6-8 graphically shows the key heat flows in the model.

(b)(7)(F) Meanwhile, the structure energy is increasing thereby

signifying a steady increase in its temperature. The net heat removal by the gas (b)(7)(F)

(b)(7)(F) when the exit enthalpy flow diminishes due to the rapid consumption of oxygen and a slight cooling of the exit gases<sup>19</sup>. The net heat balance is the sum of the heat flow terms besides the decay power (i.e., it should be approximately equal to the decay heat power<sup>20</sup>).

The energy balance is reported in Table (b)(7)(F) during a period before rapid oxidation (see Figure 6-3). The total power put into the assembly is a combination of the decay heat (b)(7)(F) and oxidation power (b)(7)(F)

The resultant distribution of that power (b)(7)(F) of the energy going into the structures and (b)(7)(F) being removed by the gas (i.e., the combination of air flow and steam from boiled spray water).

Since the liquid spray flow entering the assembly was completely boiled to steam, liquid component is only adding energy from a phasic enthalpy removal perspective. In summary, there was a large difference between the heat removal (b)(7)(F) and the total heat generation (b)(7)(F)

<sup>19</sup> The oxygen concentration exiting the center assembly (b)(7)(F) and all other gas component mass flows (i.e., nitrogen and steam) remained approximately the same. The exit gas temperature (b)(7)(F) because of slightly more effective cooling by the spray flow (i.e., slower gas velocity). The spray cooling effect was more effective than the increased heating near the high oxidation location. Since more mass was entering than leaving and the exit gases were cooled by the spray flow, the net enthalpy decreased.

<sup>20</sup> The small transient differences between the net energy balance and the decay power is attributed to limitations in the access of plot quantities of all the subcomponents of the energy flow. However, the major components are shown on the figure. The MELCOR CORE Package calculations have very high fidelity. For example, Case S1 had a total energy error of 0.02%.

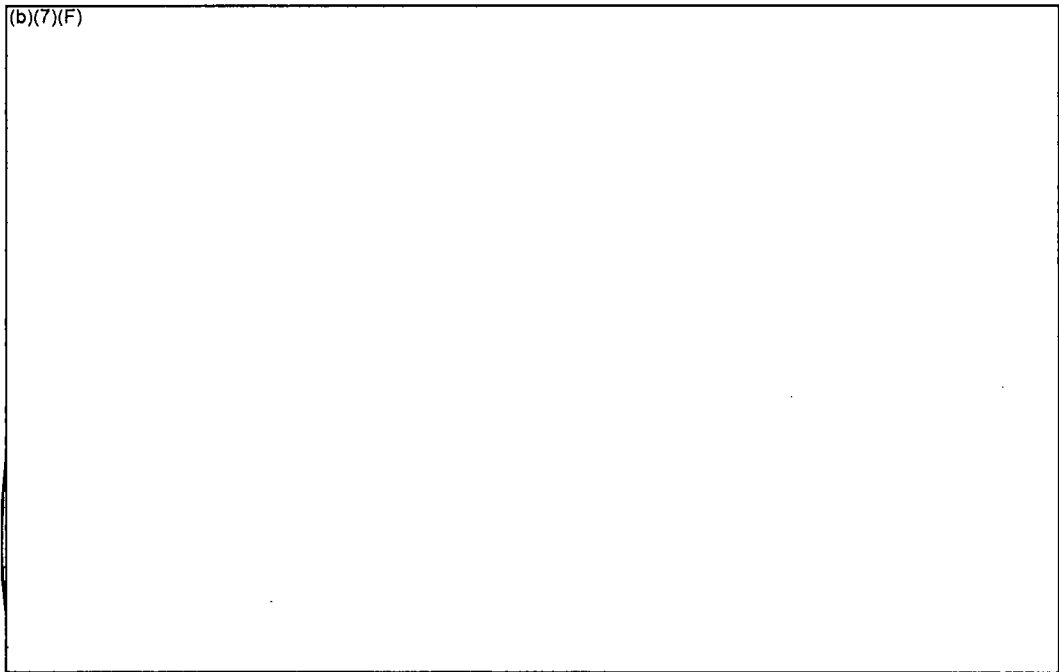


**Figure 6-8** Time-averaged Energy Flow in the Uniform Configuration with (b)(7)(F) (b)(7)(F) Spray Flow.

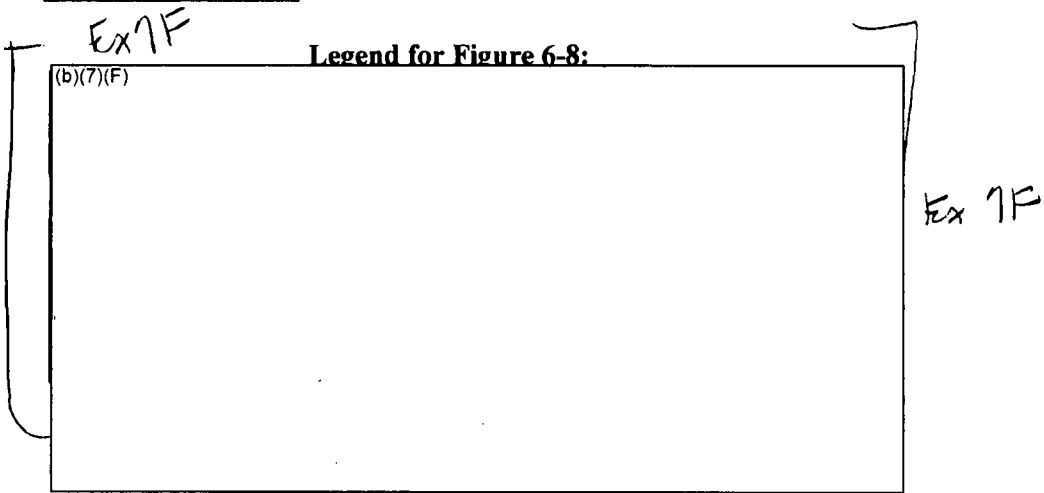
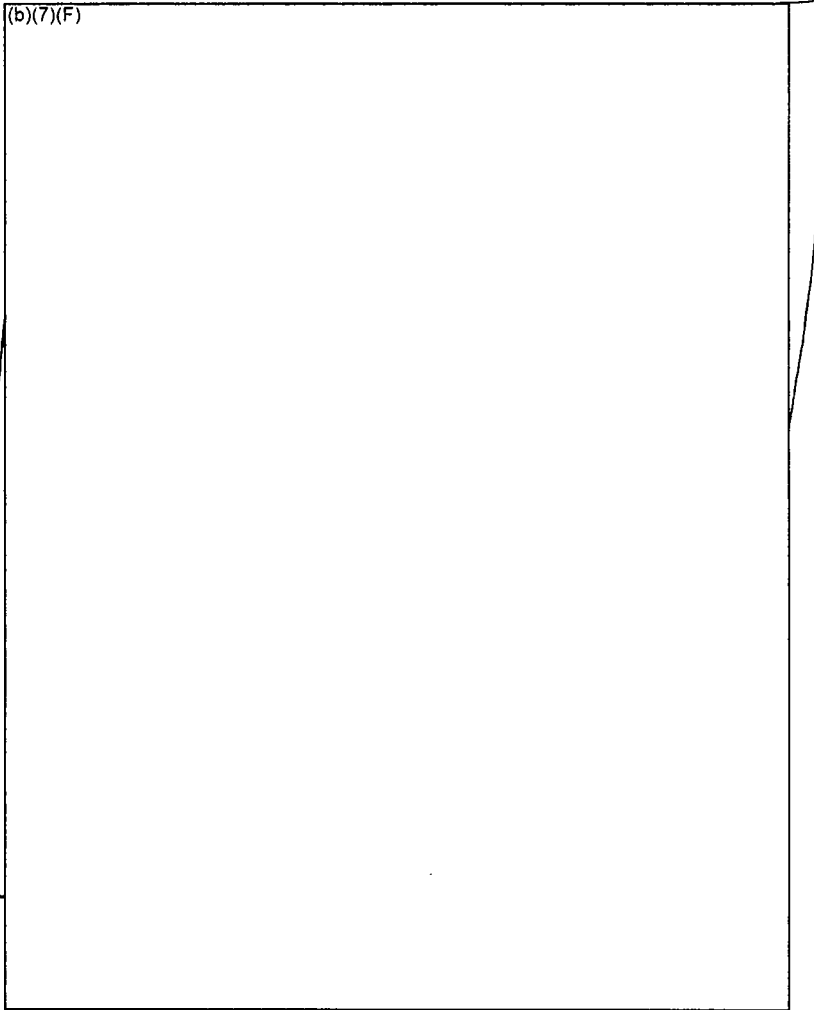


Table 6-2 Energy Balance for the Uniform Assembly Configuration in SFP with

(b)(7)(F) Spray.

Ex 7F

(b)(7)(F)



Ex 7F

Ex 7F

6.2.3 Coolability Analysis for (b)(7)(F) Spray Flowrate

Ex 7F

A coolability analysis was done for the uniform configuration with a (b)(7)(F) spray. A set of parametric calculations was performed with aging ranging (b)(7)(F) to (b)(7)(F). As shown previously in Section 6.2.1, an aging time (b)(7)(F)

Ex 7F

(b)(7)(F) In previous separate effects calculations for the uniform configuration with air flow but no spray flow [Wagner, 2003] (b)(7)(F)

Ex 7F



Ex 7F

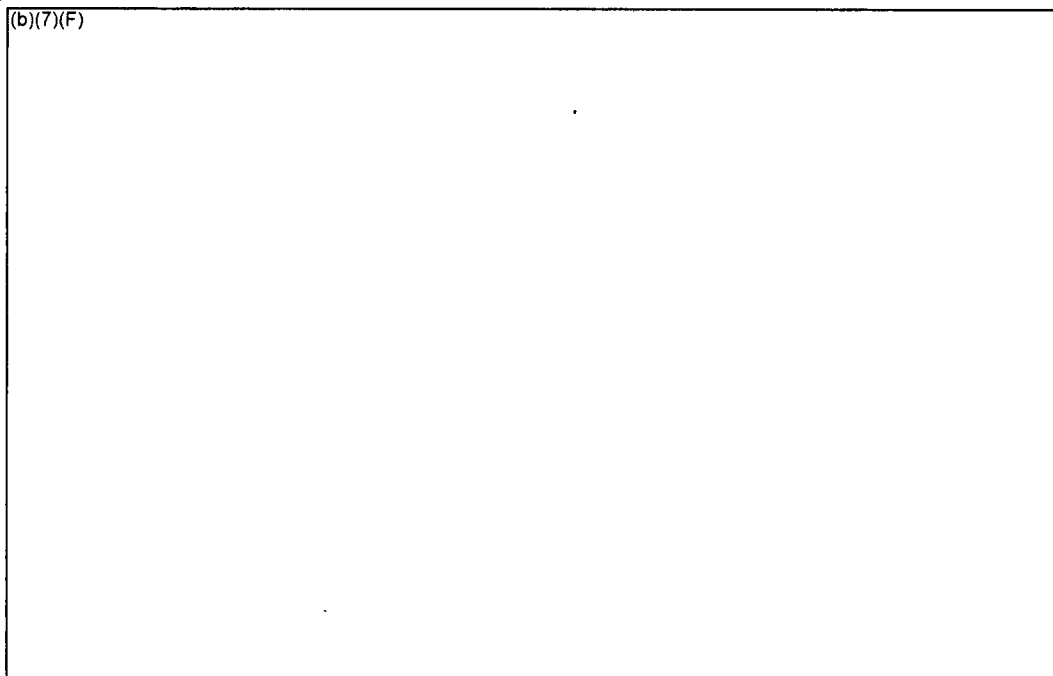
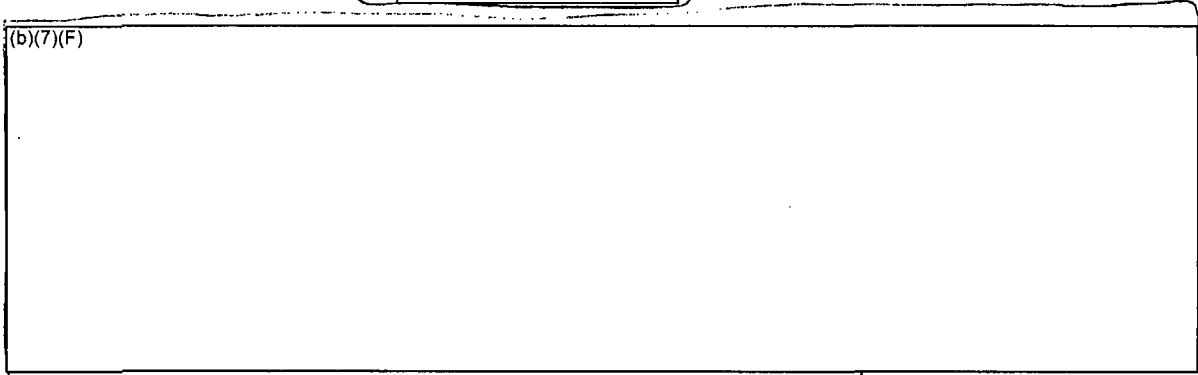


Figure 6-9 Comparison of the Peak Cladding Temperatures for the Uniform Configuration with Various Aging Periods and a Whole Pool Spray Flow of

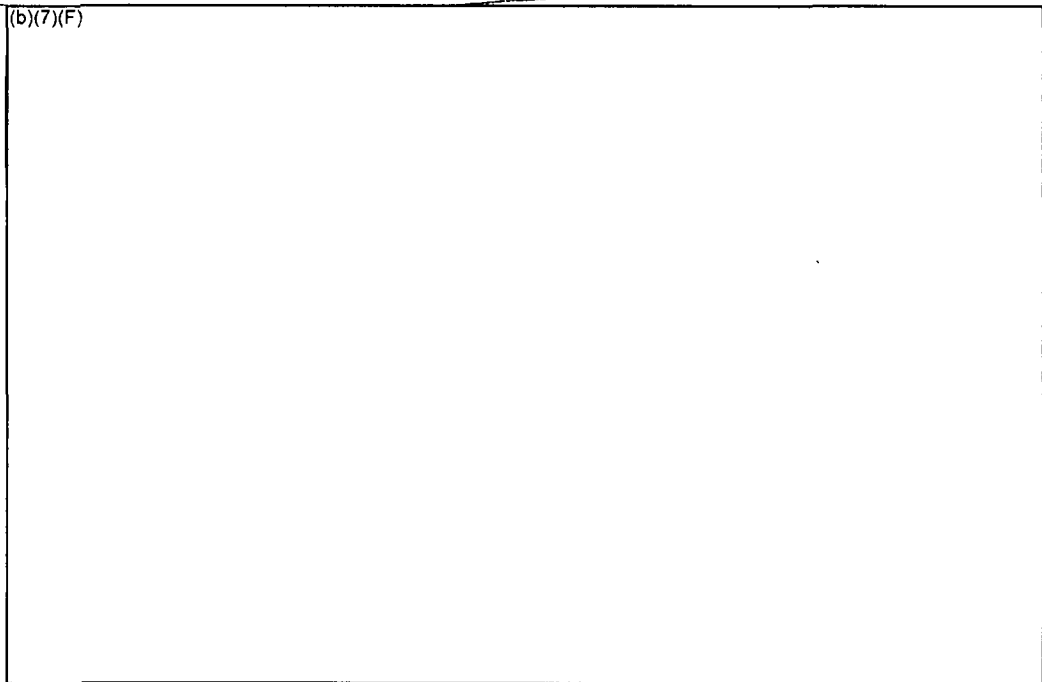
(b)(7)(F)

Ex 7F

6.2.4 Coolability Analysis for (b)(7)(F) Spray Flowrate



Ex 7E



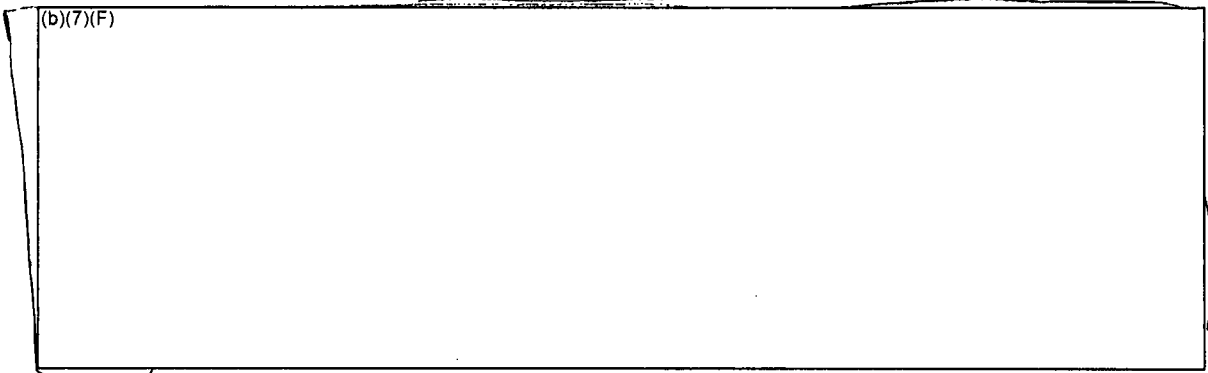
Ex 7E

Figure 6-10 Comparison of the Peak Cladding Temperatures for the Uniform Configuration with Various Aging Periods and a Whole Pool Spray Flow of (b)(7)(F)

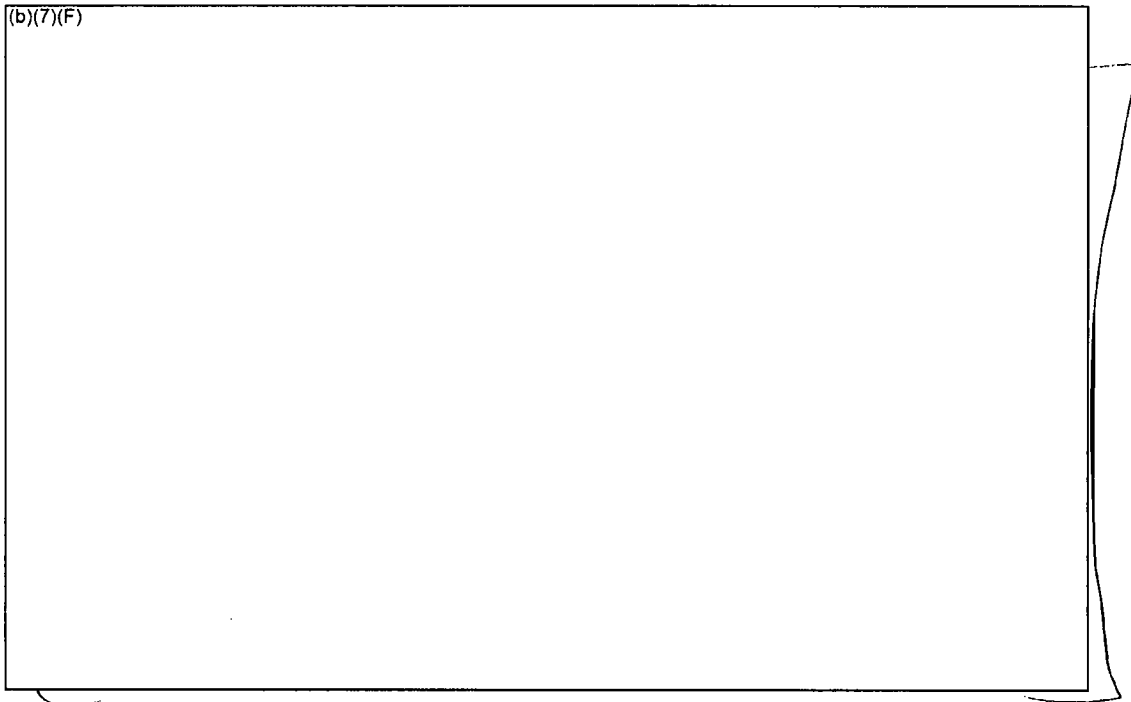
Ex 7E

(b)(7)(F)

6.2.5 Coolability Analysis for (b)(7)(F) Spray Flowrate



Ex 7F



Ex 7F

Figure 6-11 Comparison of the Peak Cladding Temperatures for the Uniform Configuration with Various Aging Periods and a Whole Pool Spray Flow of (b)(7)(F)

(b)(7)(F)

Ex 7F

### 6.3 Separate Effects Spray Model Results for the Checkerboard Configuration

Ex 7F

Section 6.3.1 gives a summary of the 4 cases with (b)(7)(F) in a uniform fuel configuration. The four cases examine differences in the response with and without sprays and with and without the flow regime model active (see Section 3.1.4 for a more complete discussion). Section 6.3.2 shows the results of an energy balance (b)(7)(F) spray case to illustrate the heat flows.

Ex 7F

#### 6.3.1 Base Calculations for (b)(7)(F) Spray

The S3 and S7 configuration calculations simulated a checkerboard configuration of the highest powered assemblies discharged into the spent fuel pool with (b)(7)(F) since reactor shutdown and low-powered assemblies at the median power of the reference BWR SFP

Ex 7F

(b)(7)(F) The limiting response in a checkerboard configuration represents the response of the high-powered assembly in a region of alternating high- and low-powered assemblies. Unlike the uniform configuration, the high-powered assemblies benefit from radial heat transfer to adjacent low-powered assemblies. (b)(7)(F)

Ex 7F

(b)(7)(F)

Ex 7F

The four (b)(7)(F) (i.e., see S3 calculations in Table 6-1) examined differences in the response with and without sprays and with and without the flow regime model active. When the flow regime model was deactivated, the spray water has a relatively small surface contact area with the cladding. Due to the reduction of heat transfer, the spray flow penetrates more deeply into the assembly before completely evaporating. In addition, a S3 case was run where the inlet of the assembly was plugged by water. (b)(7)(F)

Ex 7F

(b)(7)(F)

Figure 6-12 and Figure 6-13 show the temperature responses (b)(7)(F)

Ex 7F

(b)(7)(F)

Ex 7F

For completeness, the high- and low-powered cladding temperature responses from Cases S3b and S3p are shown in Figure 6-18 through Figure 6-21. In a checkerboard configuration, convective heat removal in the low-powered assemblies is particularly important. Due to radial heat transfer, (b)(7)(F) heat from the high-powered assembly in Case S3 was transferred to the peripheral assembly (see the energy balance in Section 6.3.2 for a full discussion). If the inlet is plugged, the benefit of the peripheral assembly to remove heat is greatly diminished. The peripheral assembly initially stores some of the heat from the center assembly but gradually becomes ineffective as an energy sink without simultaneous convective heat removal. In contrast, the impact of plugging in the uniform assembly configuration is less important because there is no radial heat transfer.

In previous separate effects calculations for the checkerboard configuration with air flow but no spray flow [Wagner, 2003], (b)(7)(F) Subsequent refinements to the BWR SFP modeling (i.e., see Section 3.1) will likely increase that value but have not yet been quantified. (b)(7)(F)

Ex 7F

(b)(7)(F) However, if water blocks or limits the air flow through the bottom of the racks, additional spray flow would be necessary to provide cooling.

Finally, the high- and low-powered assembly axial temperature profiles are shown in Figure 6-22 and Figure 6-23 for all four cases, respectively. As observed in the axial temperature profiles for the uniform cases, the impact of the spray flow at the top of the assembly is clearly seen. The cases with the flow regime model active have cooler temperatures until the spray flow is depleted. The case without the flow regime model shows less heat removal at the top of the assembly but more heat removal at the bottom. In general, the temperatures are lower in the low-powered assembly and the spray penetrates deeper. Consequently, there is radial heat transfer is from the high-powered assembly to the low-powered assembly. (b)(7)(F)

Ex 7F

(b)(7)(F)

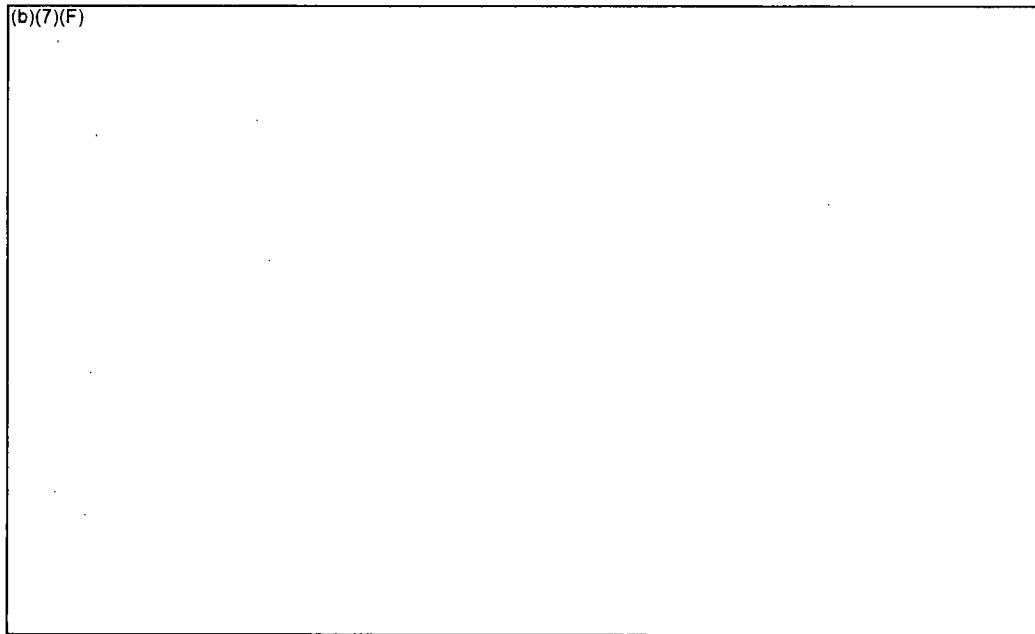


Figure 6-12 Comparison of the Peak Cladding Temperatures for the (b)(7)(F) with a Checkerboard Configuration with (b)(7)(F) and a Whole Pool Spray Flow of (b)(7)(F)

Ex 7F Ex 7F

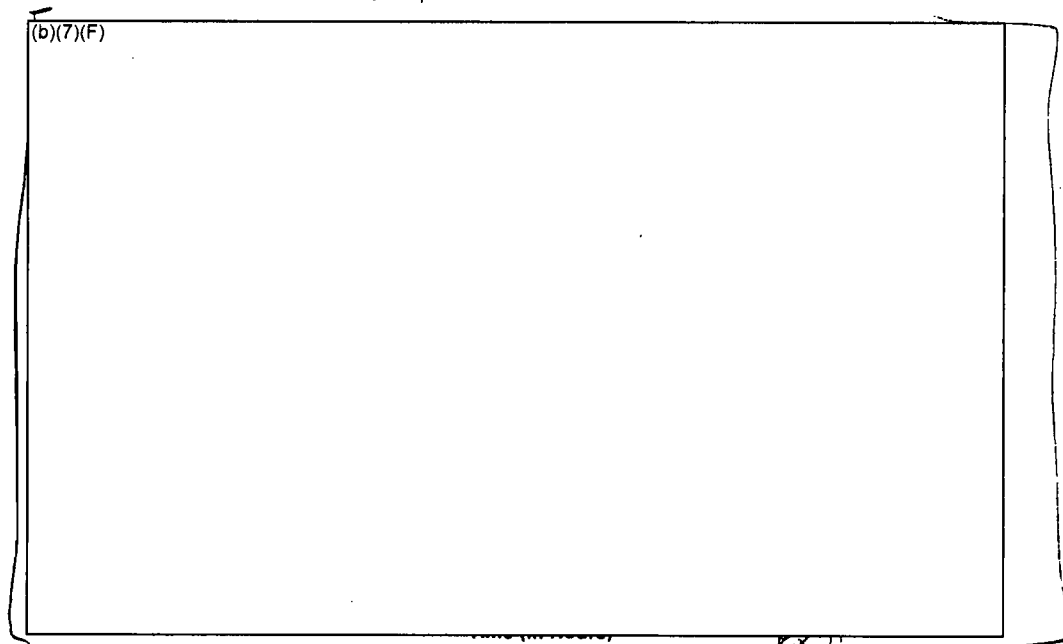


Figure 6-13 Comparison of the Peak Cladding Temperatures for the (b)(7)(F) with a Checkerboard Configuration with (b)(7)(F) and a Whole Pool Spray Flow of (b)(7)(F)

Ex 7F Ex 7F

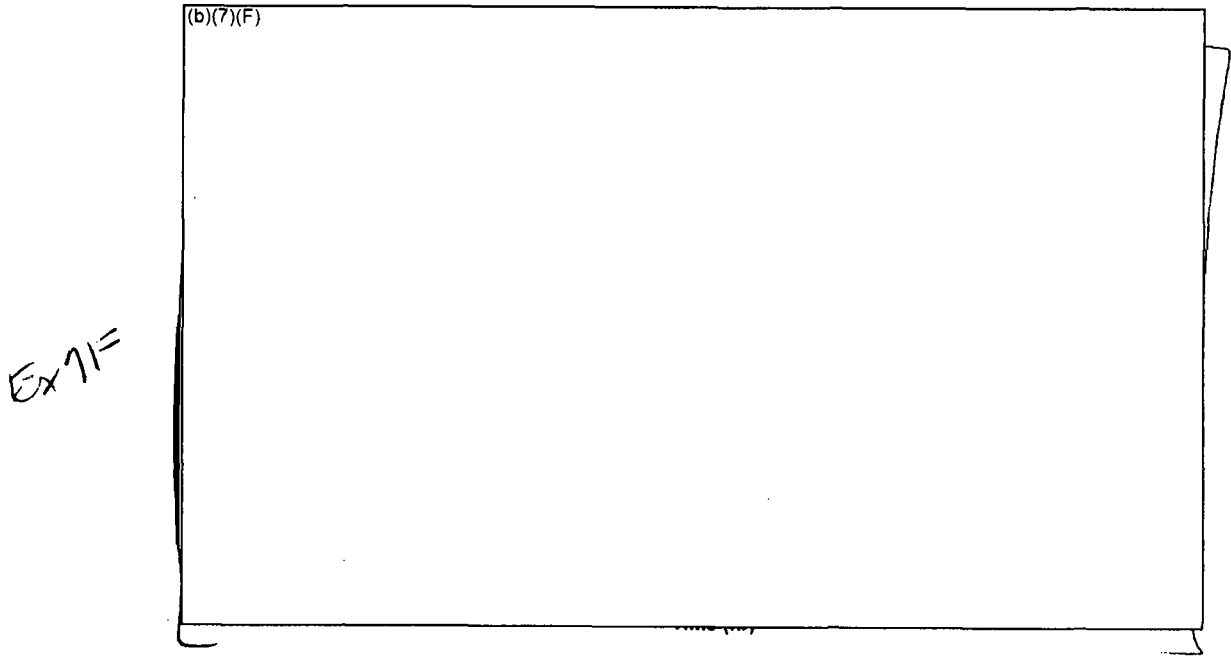


Figure 6-14 High-Powered Assembly Cladding Temperatures for the Checkerboard Configuration with (b)(7)(F) Spray Flow (Case S3).

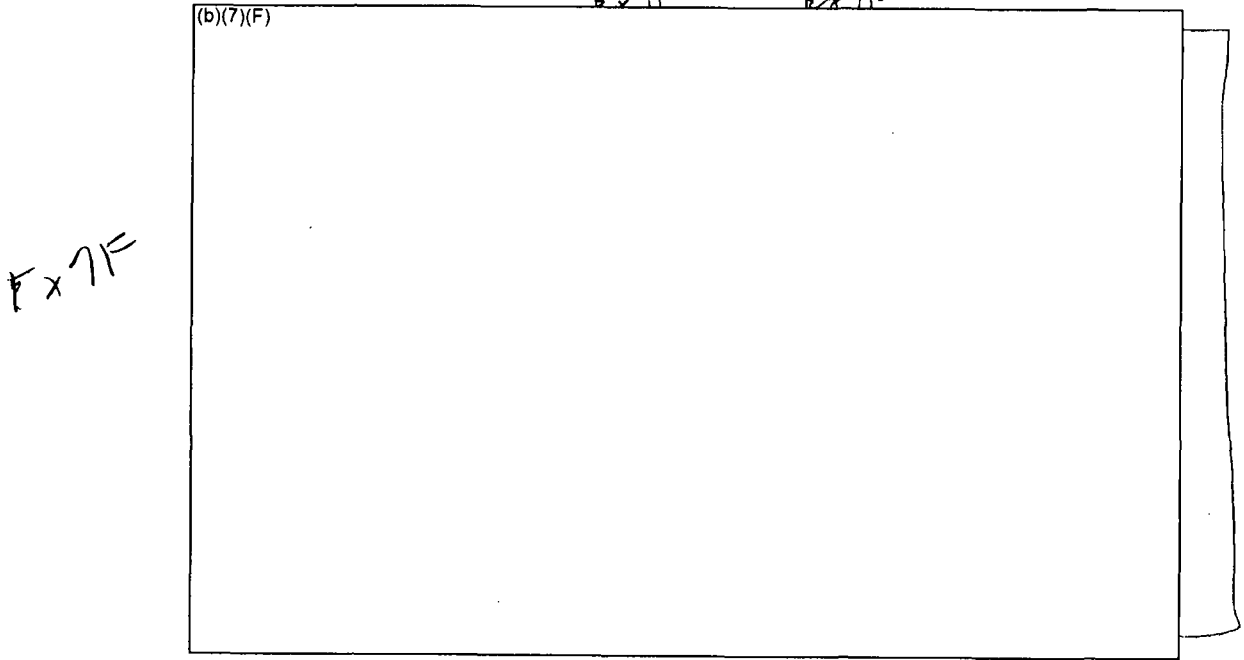
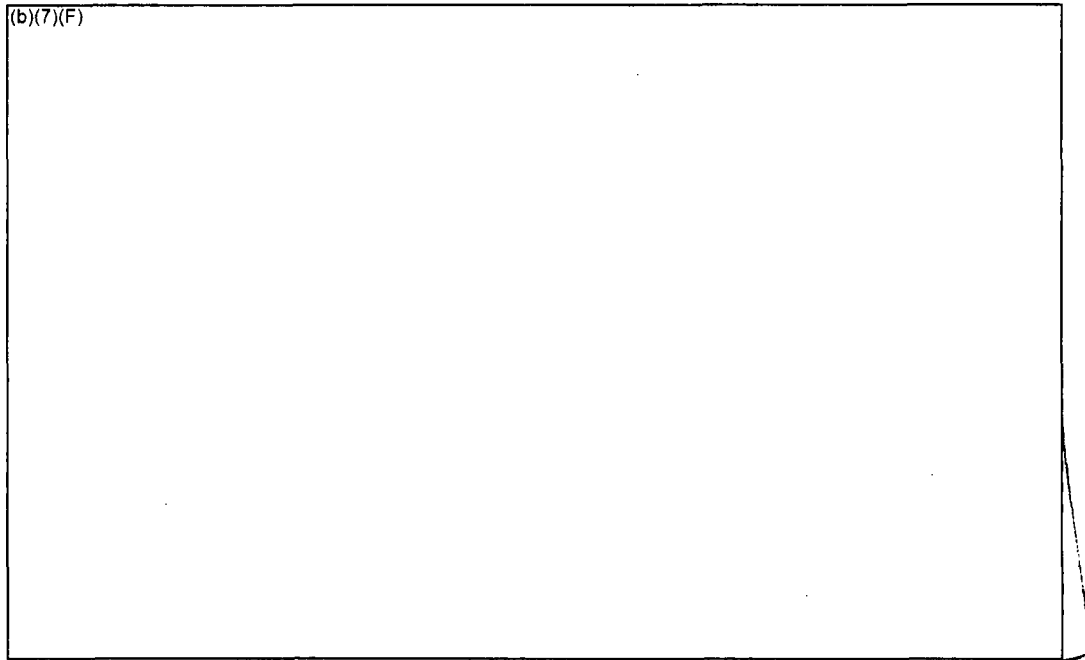
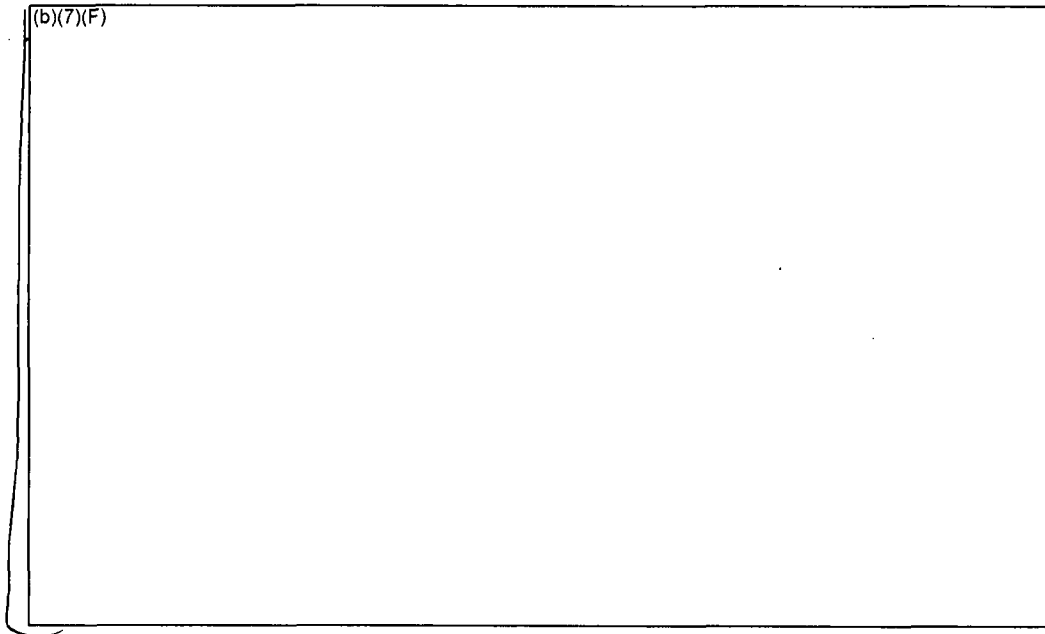


Figure 6-15 Low-Powered Assembly Cladding Temperatures for the Checkerboard Configuration with (b)(7)(F) Spray Flow (Case S3).



**Figure 6-16 High-Powered Assembly Cladding Temperatures for the Checkerboard Configuration with (b)(7)(F) Spray Flow and the Flow Regime Model Inactive (S3a).**

Ex 7F



**Figure 6-17 Low-Powered Assembly Cladding Temperatures for the Checkerboard Configuration with (b)(7)(F) Spray Flow and the Flow Regime Model Inactive (S3a).**

Ex 7F

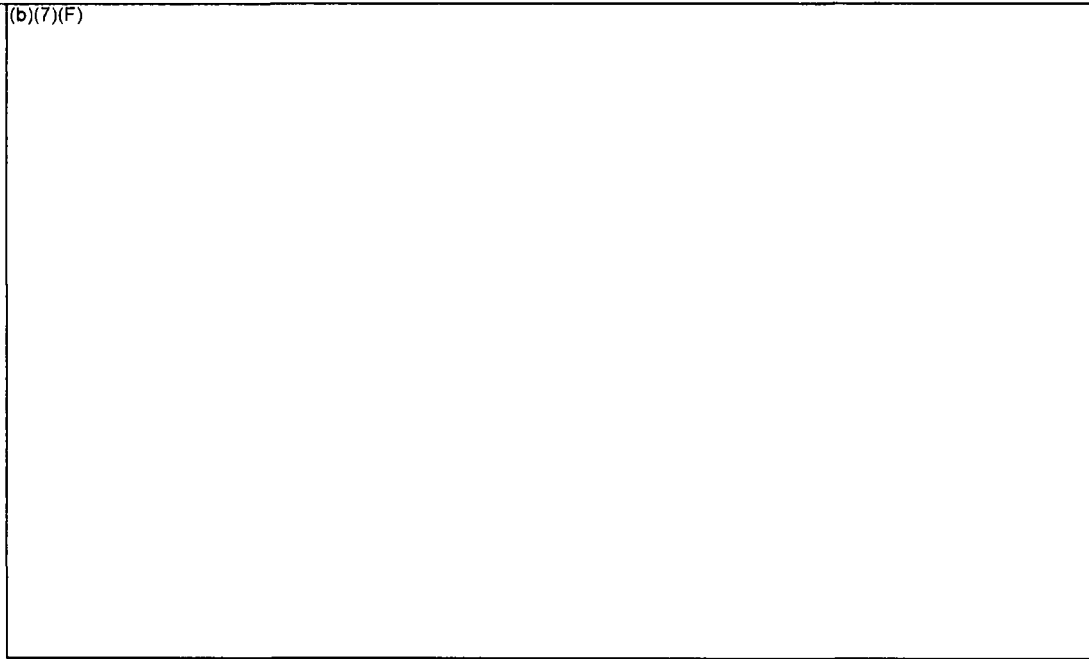


Figure 6-18 High-Powered Assembly Cladding Temperatures for the Checkerboard Configuration with (b)(7)(F) and No Spray Flow (Case S3b).

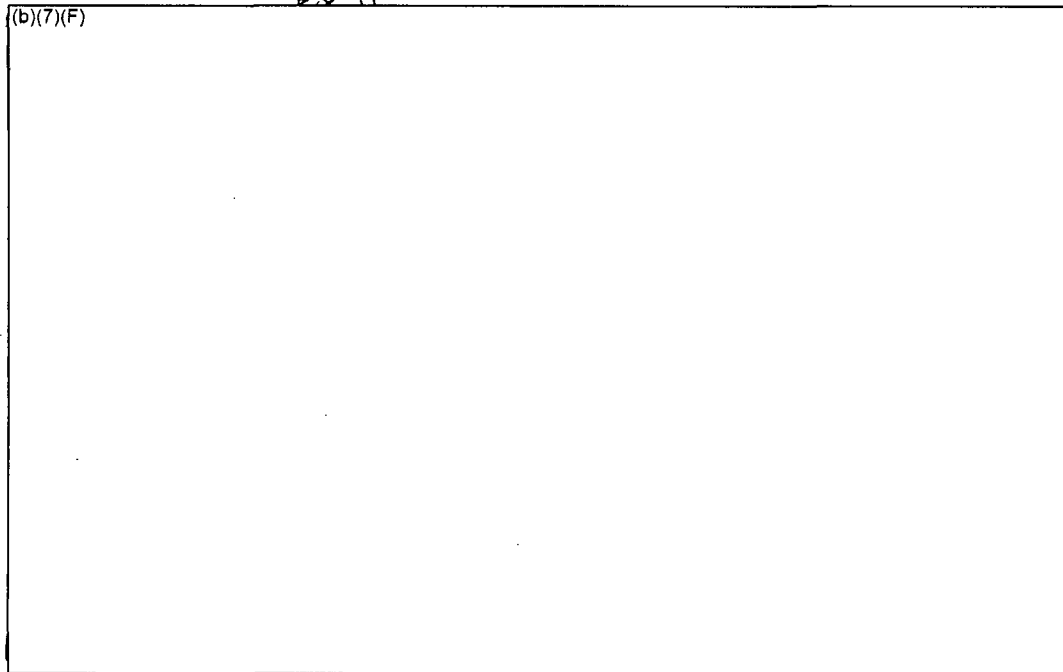


Figure 6-19 Low-Powered Assembly Cladding Temperatures for the Checkerboard Configuration with (b)(7)(F) and No Spray Flow (Case S3b).

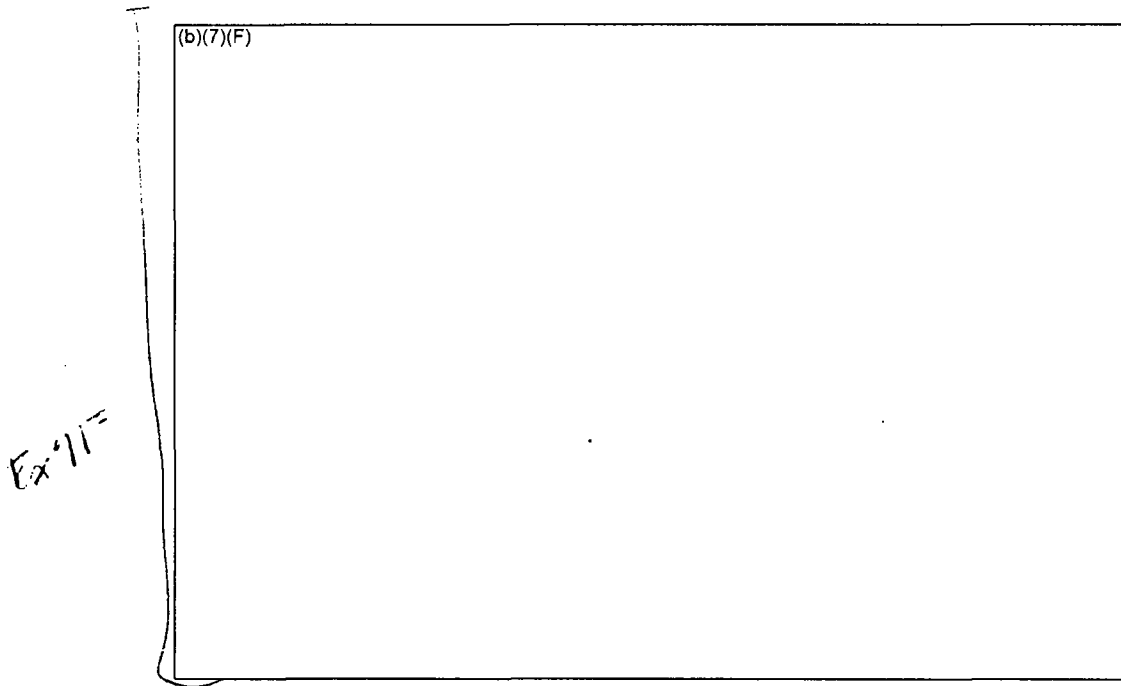


Figure 6-20 High-Powered Assembly Cladding Temperatures for the Checkerboard Configuration with (b)(7)(F) Spray Flow and Plugged Inlet (Case S3p).

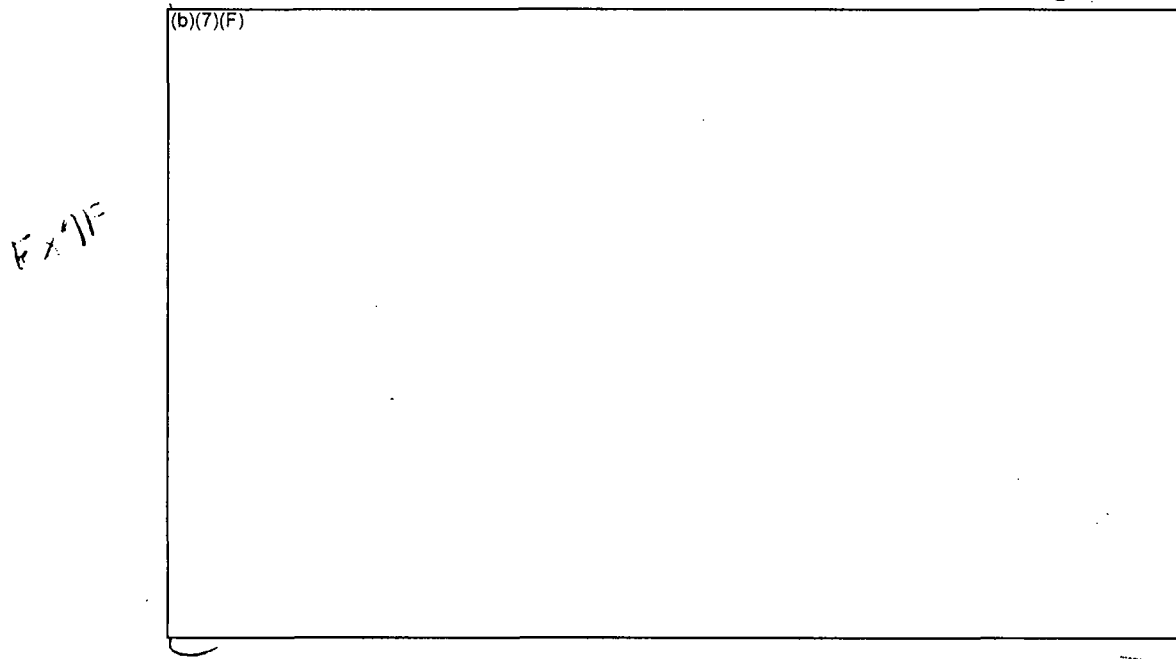
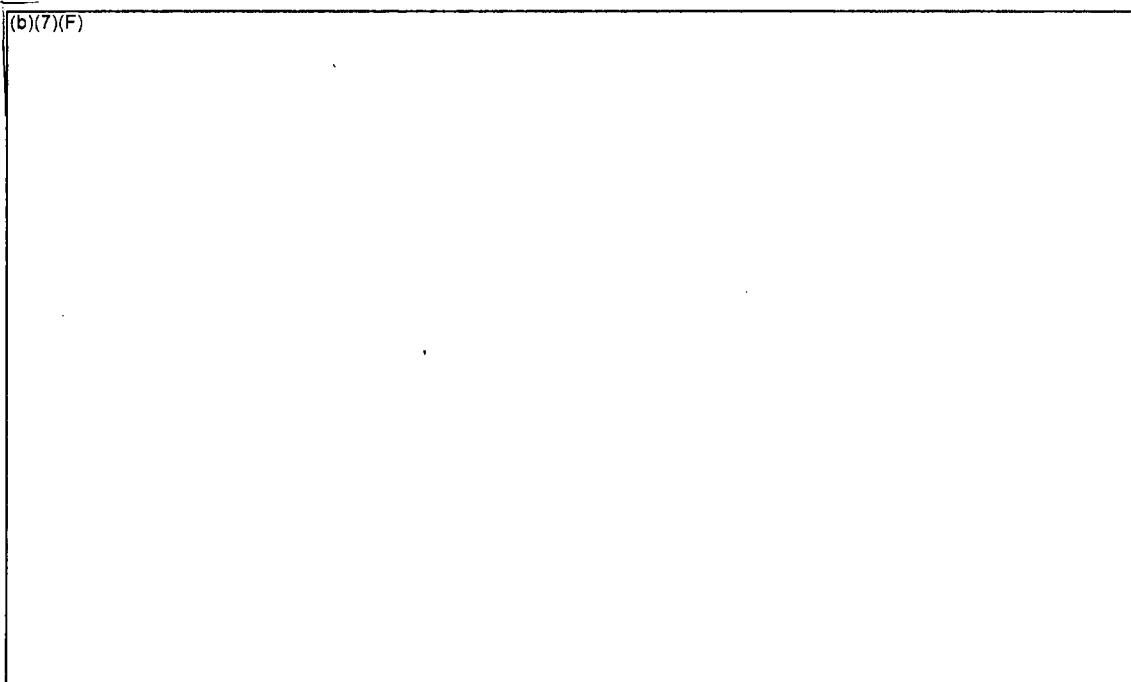
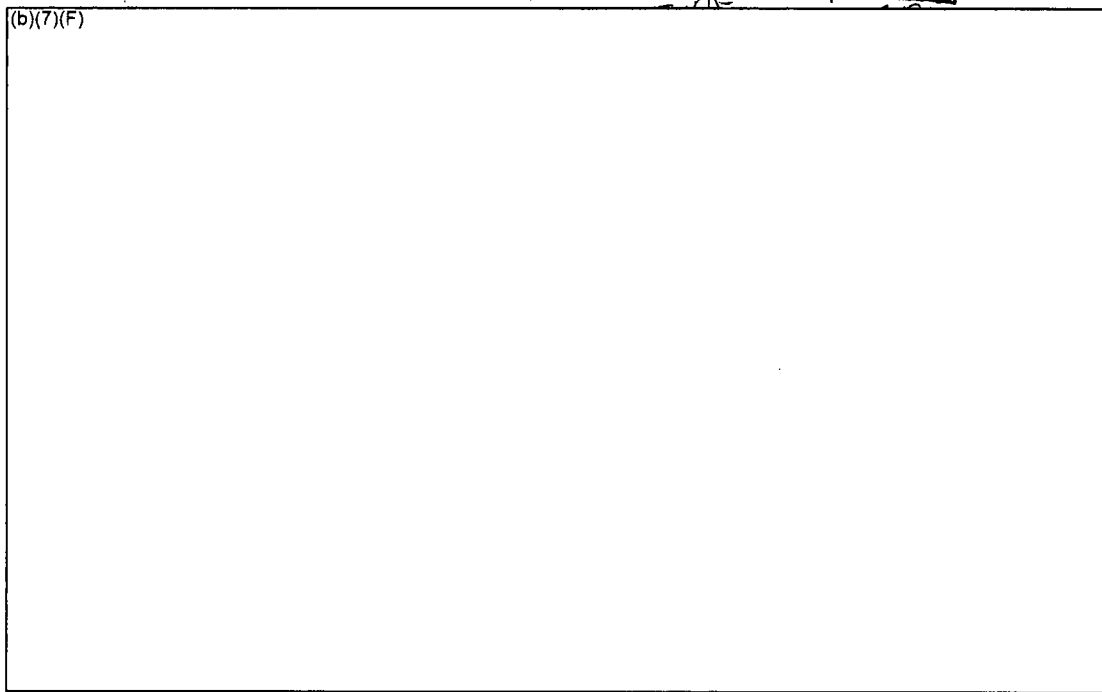


Figure 6-21 Low-Powered Assembly Cladding Temperatures for the Checkerboard Configuration with (b)(7)(F) Spray Flow and Plugged Inlet (Case S3p).



Ex 11=

**Figure 6-22 High-Powered Assembly Cladding Temperature Profiles for the Checkerboard Configuration with (b)(7)(F) Spray Flow.**



Ex 1F

**Figure 6-23 Low-Powered Assembly Cladding Temperature Profiles for the Checkerboard Configuration with (b)(7)(F) Spray Flow.**

Ex 7F

6.3.2 Energy Balance on Base Calculation for (b)(7)(F) Spray

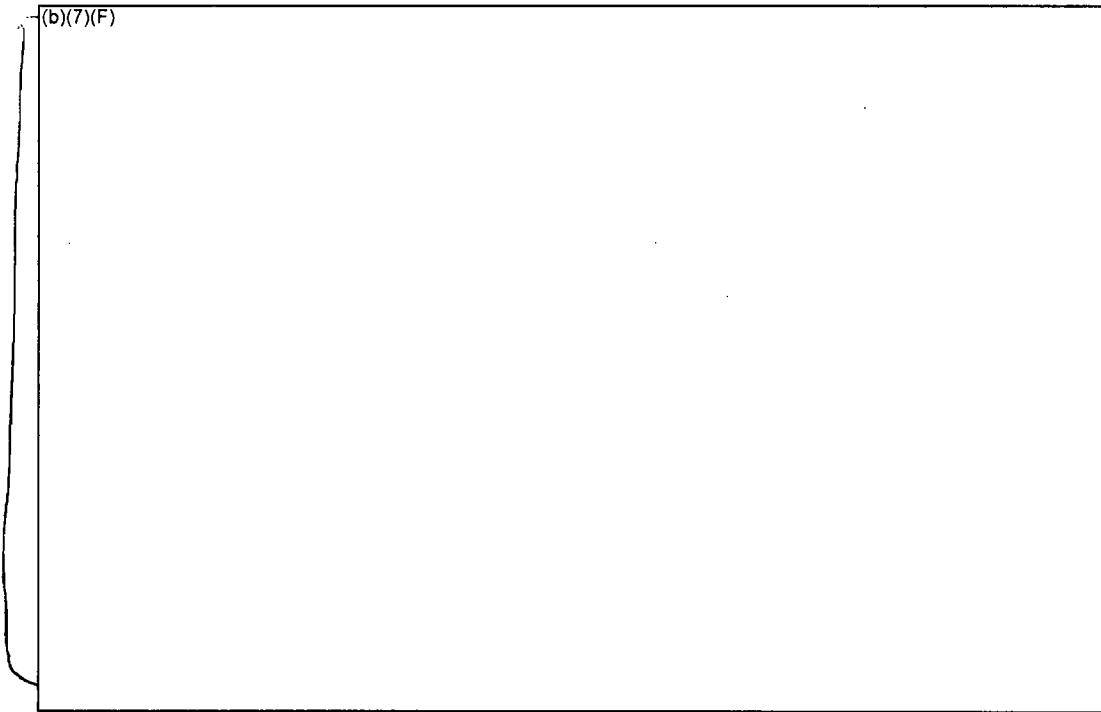
An energy balance was performed on the S3 case with the flow regime model operating. Figure 6-34 graphically shows the key heat flows in the model. After water level drops below the base plate, the power going into the structure steadily decreases to near zero. Meanwhile, due to air and steam convection, the heat removed by the gas in the peripheral assembly gradually increases. The convective heat removal by the center assembly gas is relatively constant after the base plate clearing. In this figure, the decay power includes both the low- and high-powered assemblies. The net heat balance is the sum of the heat flow terms besides the decay power (i.e., it should be approximately equal to the decay heat power<sup>21</sup>).

Ex 7F

The energy balance is reported in Table 6-2 based on average conditions (b)(7)(F). The total power put into the checkerboard configuration is a combination of the decay heat for both the high- and low-powered assemblies (b)(7)(F) and oxidation power

(b)(7)(F) The resultant distribution of energy generated in the center represented (b)(7)(F) of the decay power and (b)(7)(F) oxidation energy. (b)(7)(F) of the power in the high-powered assembly is removed by convective gas flow and the remaining (b)(7)(F) of the energy is radially transferred to the peripheral assembly. The decay heat power in the peripheral assembly is relatively small (b)(7)(F). However, the addition of the radial heat load from the center assembly increases the effective peripheral assembly heat load (b)(7)(F) of that heat load is convectively removed by the gas and a small amount (b)(7)(F) goes into slowly heating portions of the assembly and heat removal by spray water out of the bottom.

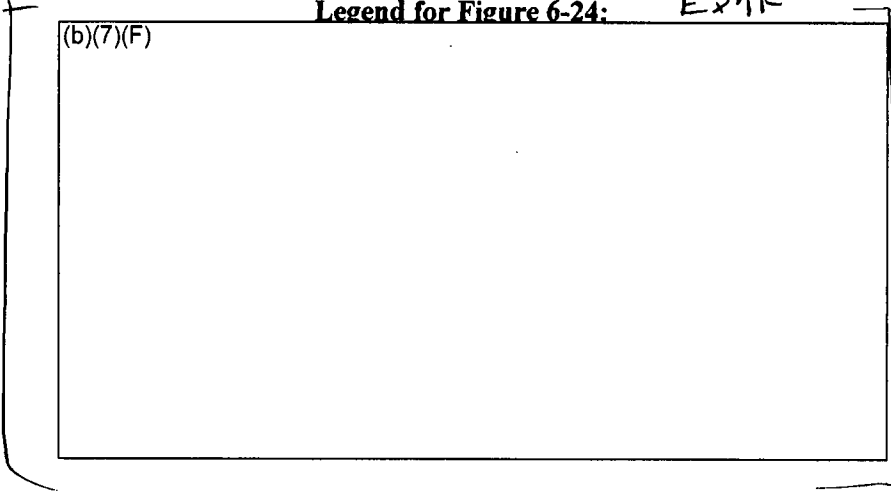
<sup>21</sup> The small transient differences between the net energy balance and the decay power is attributed to limitations in the access of plot quantities available to the user to access all the subcomponents of the energy flow. However, the major components are shown on the figure. The internal MELCOR core calculations have very high fidelity.



Ex 7F

Figure 6-24 Time-average Energy Flow in the Checkerboard Configuration with (b)(7)(F) and a Whole Pool Spray Flow of (b)(7)(F)

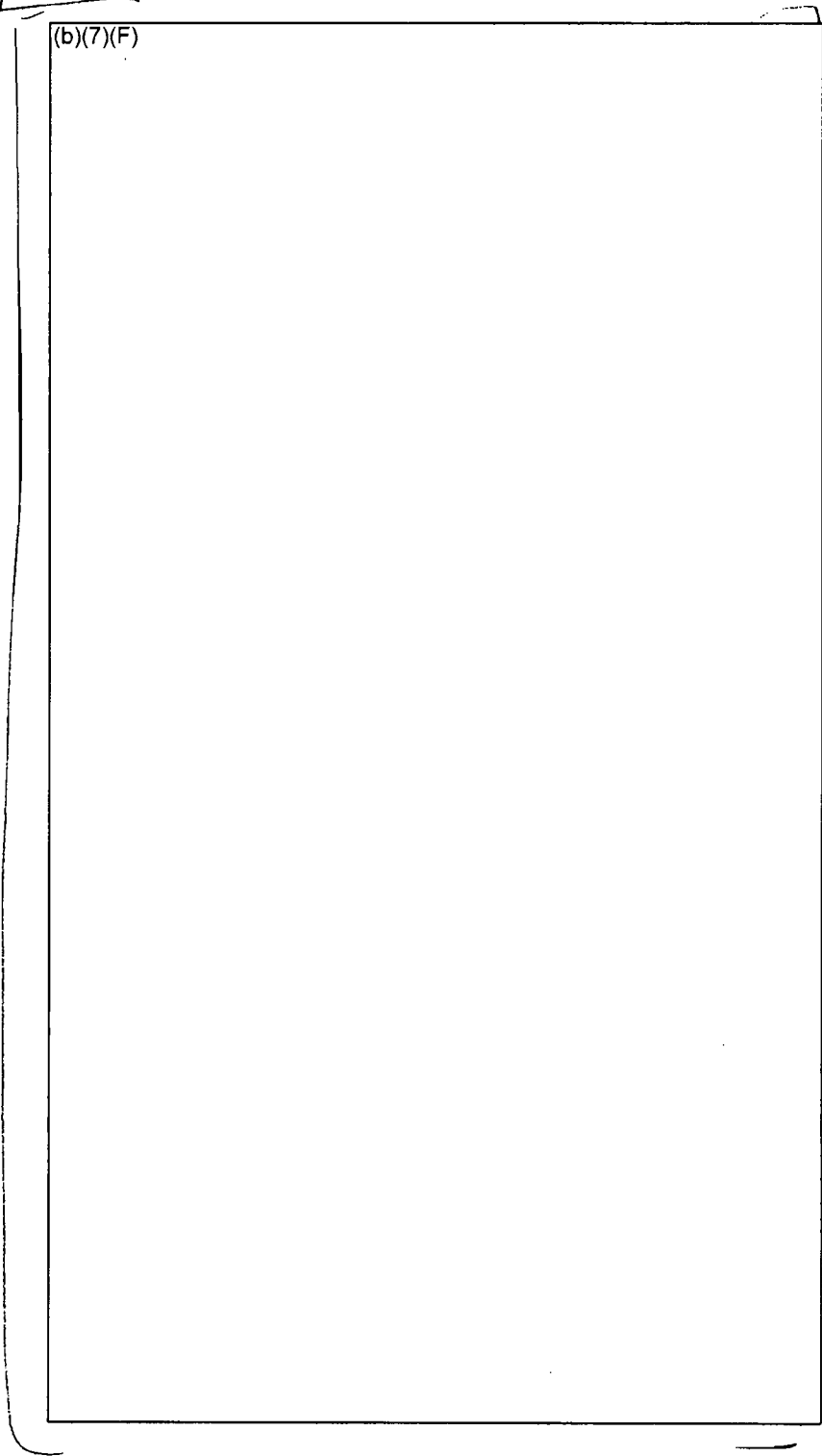
Legend for Figure 6-24: Ex 7F



Ex 7F

Table 6-3 Energy Balance for the Checkerboard Assembly Configuration in SFP with (b)(7)(F) Spray.

(b)(7)(F)



*F x 1F*

#### 6.4 Separate Effects Spray Model Results for the 1x4 Configuration Cases

Section 6.4.1 gives a summary of the 4 cases with (b)(7)(F) and (b)(7)(F) leakage hole in a 1x4 fuel configuration. The four cases examine differences in the response with and without sprays and with and without the flow regime model active (see Section 3.1.4 for a more complete discussion). Finally, Section 6.3.2 shows the results of an energy balance on (b)(7)(F) case with sprays to illustrate the heat flows.

(b)(7)(F)

##### 6.4.1 Base Calculations for (b)(7)(F) Spray

The S4 and S8 configuration calculations simulated a 1x4 configuration of the highest powered assemblies discharged into the spent fuel pool with (b)(7)(F) since reactor shutdown surrounded by four low-powered assemblies at the median power with the reference BWR SFP (b)(7)(F). The limiting response in a 1x4 configuration represents the response of a repeating pattern of 1x4 assemblies (e.g., see Figure 3-23). Similar to the checkerboard configuration, the high-powered assemblies benefit from radial heat transfer to adjacent low-powered assemblies. The transient is initiated with

Ex 7F

Ex 7F

(b)(7)(F)

The four (b)(7)(F) (i.e., see S4 calculations in Table 6-1) examined differences in the response with and without sprays and with and without the flow regime model active. When the flow regime model was deactivated, the spray water has a relatively small surface contact area with the cladding. Due to the reduction of heat transfer, the spray flow penetrates more deeply into the assembly before completely evaporating. In addition, a S4 case was run where the inlet of the assembly was plugged by water. As discussed in Section 5, depending upon the size hole and the spray rate, cases were identified where the inlet to the racks could be covered.

Consequently, Case S4 and S4p parametrically investigated both conditions. (b)(7)(F)

Ex 7F

(b)(7)(F)

(b)(7)(F)

Figure 6-25 and Figure 6-26 show the temperature responses for the (b)(7)(F) respectively. (b)(7)(F)

Ex 7F

(b)(7)(F) Similar to the uniform and checkerboard results, the disabled flow regime model cases were more effective at providing spray cooling to the middle of the assembly. (b)(7)(F) with the flow regime model off were (b)(7)(F) cooler than when the model was active. The effect was more dramatic in the checkerboard cases at (b)(7)(F) because the peak cladding temperatures in the flow regime cases were more greatly affected by the breakaway oxidation kinetics. In the cases with flow regime model active, there is very effective cooling of the top region of the fuel. (b)(7)(F)

(b)(7)(F) Ex 7F

(b)(7)(F)

Ex 7F

Ex 7F

(b)(7)(F) In both cases, the peripheral assemblies were well cooled.

Ex 7F

Figure 6-27 and Figure 6-28 show the axial temperature response in the center and peripheral assemblies for Case S4 with the flow regime model. (b)(7)(F)

(b)(7)(F) The center assembly is cooled by gas convection, which is enhanced by the spray flow and radial heat transfer (b)(4) see the energy balance in Section 6.4.2 for a full discussion). In the peripheral assemblies, gas convection out the top of the assembly removed most of the effective heat load from the peripheral assembly decay heat power and the radial heat flow from the center assembly. In addition, spray water flows out the bottom of the peripheral assemblies (b)(7)(F) of the total decay heat power.

Similar to the previous configurations, the calculation with the flow regime model inactive (i.e., Case 4a in Figure 6-29 and Figure 6-30) had a slightly lower peak temperature than when the flow regime model was active.

The high- and low-powered cladding temperature responses from Cases S4b and S4p are shown in Figure 6-31 through Figure 6-34. (b)(7)(F)

Ex 7F

(b)(7)(F) In previous separate effects calculations for the 1x4 configuration with air flow but no spray flow [Wagner, 2003], (b)(7)(F)

(b)(7)(F)

Ex 7F

Ex 7F

(b)(7)(F) Similar to the checkerboard configuration, the convective heat removal in the low-powered assemblies is important. However, the 1x4 configuration has four low-powered assemblies surrounding the high-powered assembly. Although the convective gas flow was limited, the convective removal in the center assembly by boiling the spray water as well as removal in the liquid flow out the bottom of the four peripheral assemblies provided sufficient heat removal to keep the configuration cool.

Finally, the center and peripheral assembly axial temperature profiles are shown in Figure 6-35 and Figure 6-36 for all four cases, respectively. As observed in the axial temperature profiles for the uniform and checkerboard cases, the impact of the spray flow at the top of the assembly is clearly seen. The cases with the flow regime model active have cooler temperatures until the spray flow is depleted. The case without the flow regime model shows less heat removal at the top of the assembly but more heat removal at the bottom. (b)(7)(F)

Ex 7F

(b)(7)(F)

water at lower regions (esp., 1.2 to 2.5 m) removed the configuration's decay heat power. Consequently, the center assembly spray flow removed much of the decay heat at the top of the assembly whereas the spray flow in the peripheral assemblies helped removed the decay power in the lower portion of the assembly for the plugged case.

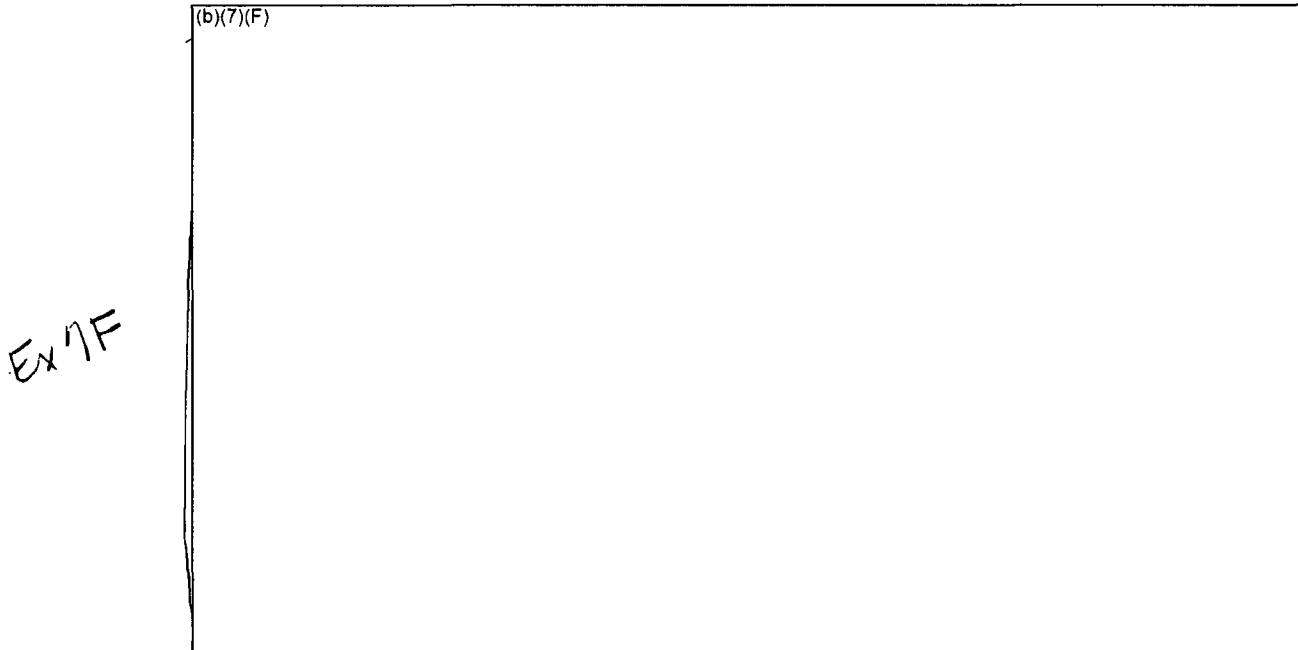


Figure 6-25 Comparison of the Peak Cladding Temperatures for the (b)(7)(F) with a 1x4 Configuration with (b)(7)(F) and a Whole Pool Spray Flow of (b)(7)(F)

Ex 7F

Ex 7F

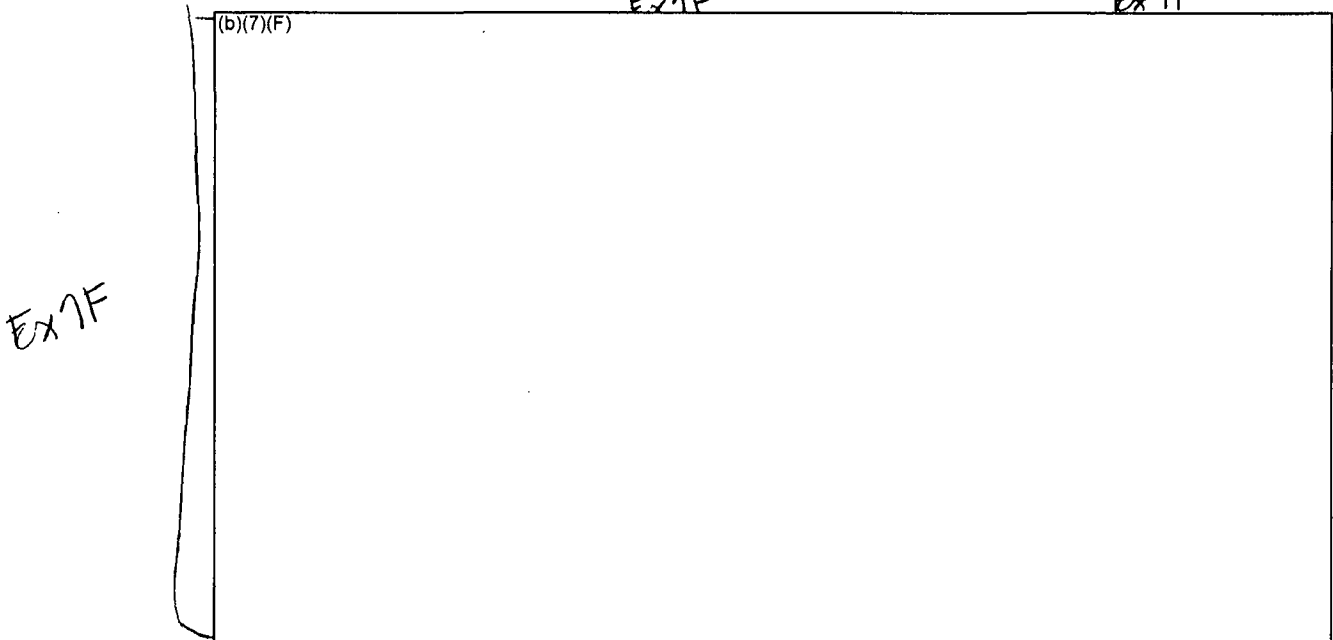


Figure 6-26 Comparison of the Peak Cladding Temperatures for the (b)(7)(F) with a 1x4 Configuration with (b)(7)(F) and a Whole Pool Spray Flow of (b)(7)(F)

Ex 7F

Ex 7F

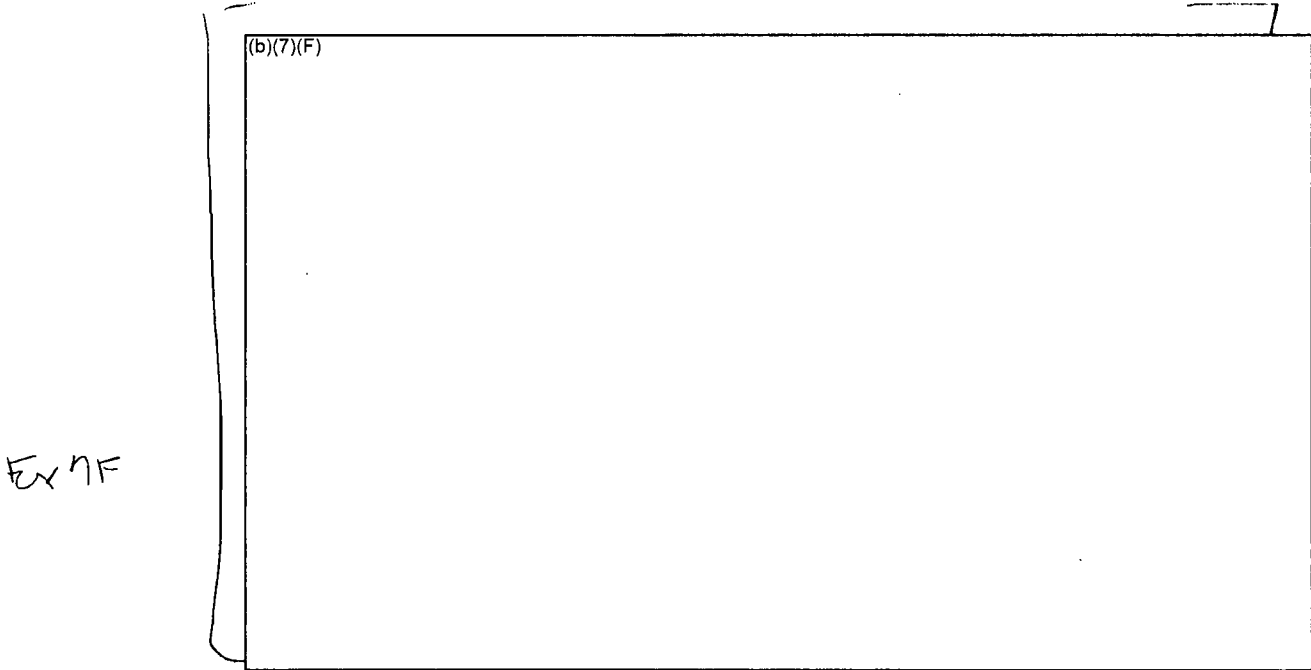


Figure 6-27 Center Assembly Cladding Temperatures for the 1x4 Configuration with (b)(7)(F) and (b)(7)(F) Spray Flow (Case S4).

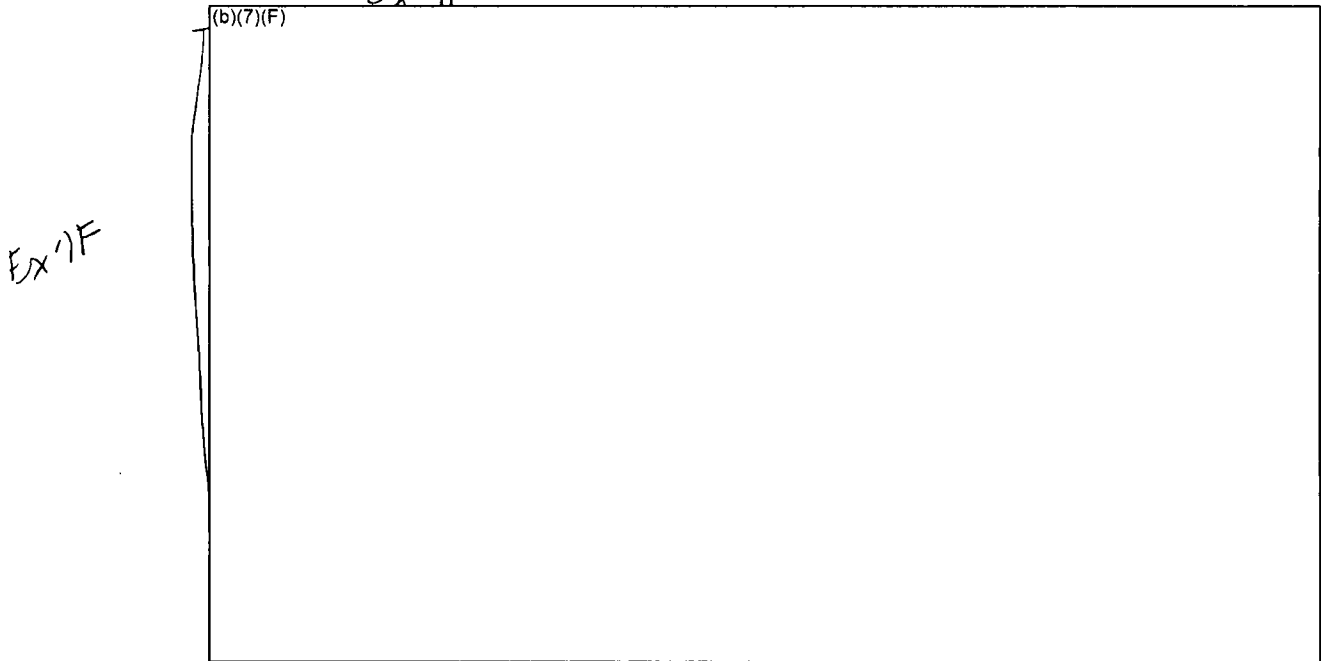
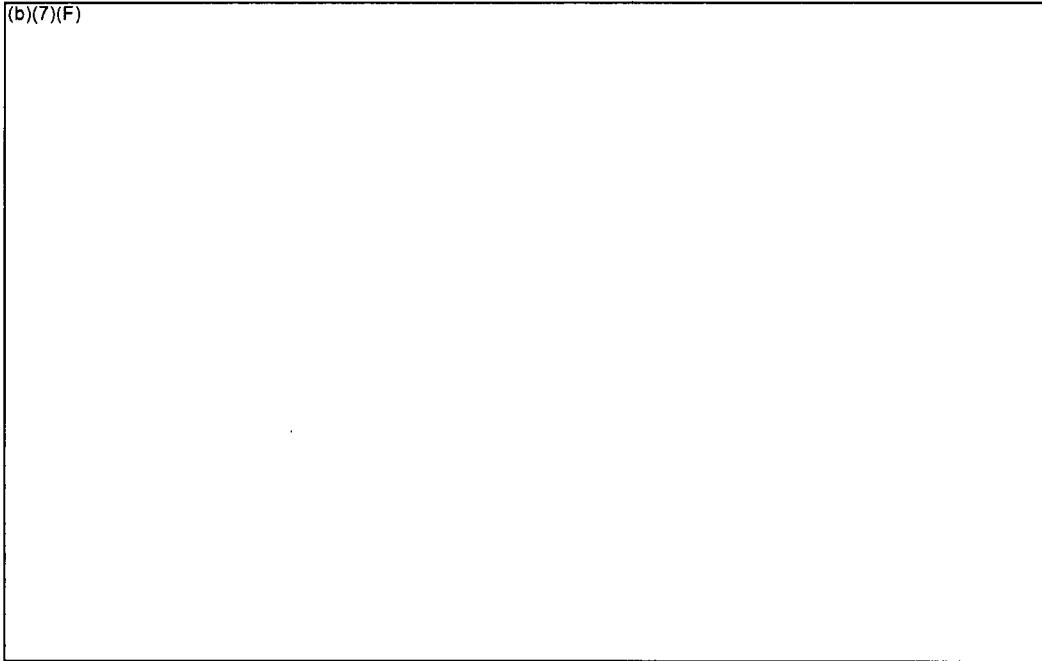


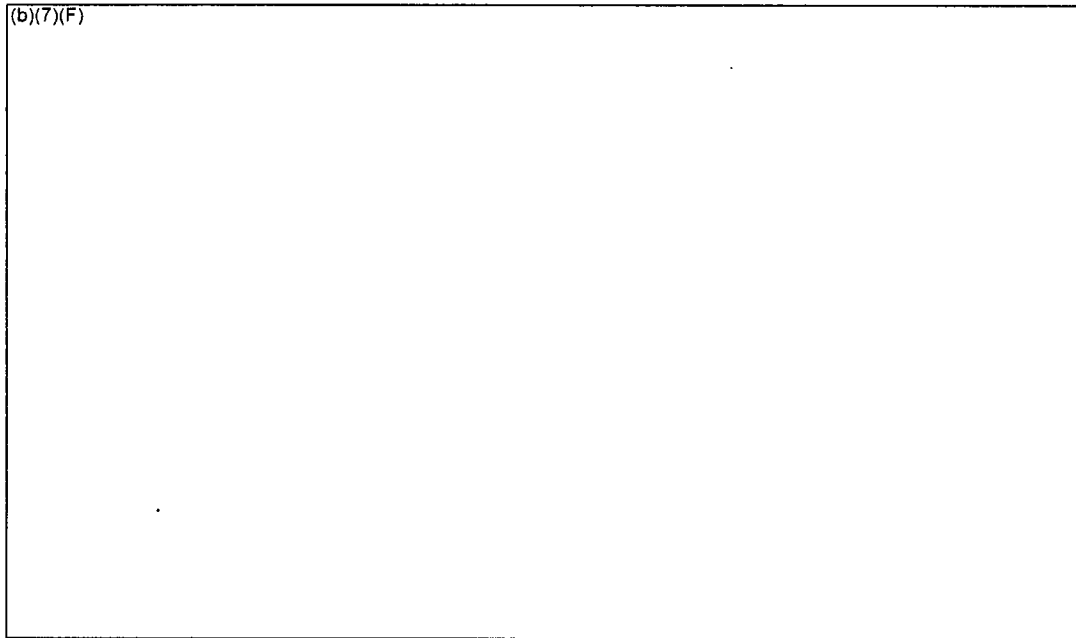
Figure 6-28 Peripheral Assembly Cladding Temperatures for the 1x4 Configuration with (b)(7)(F) and (b)(7)(F) Spray Flow (Case S4).



Ex 7F

**Figure 6-29 Center Assembly Cladding Temperatures for the 1x4 Configuration with**  
**Spray and the Flow Regime Model Inactive**  
**(Case S4a).**

Ex 7F



Ex 7F

**Figure 6-30 Peripheral Assembly Cladding Temperatures for the 1x4 Configuration with**  
**Spray and the Flow Regime Model Inactive**  
**(Case S4a).**

Ex 7F

Ex 7F

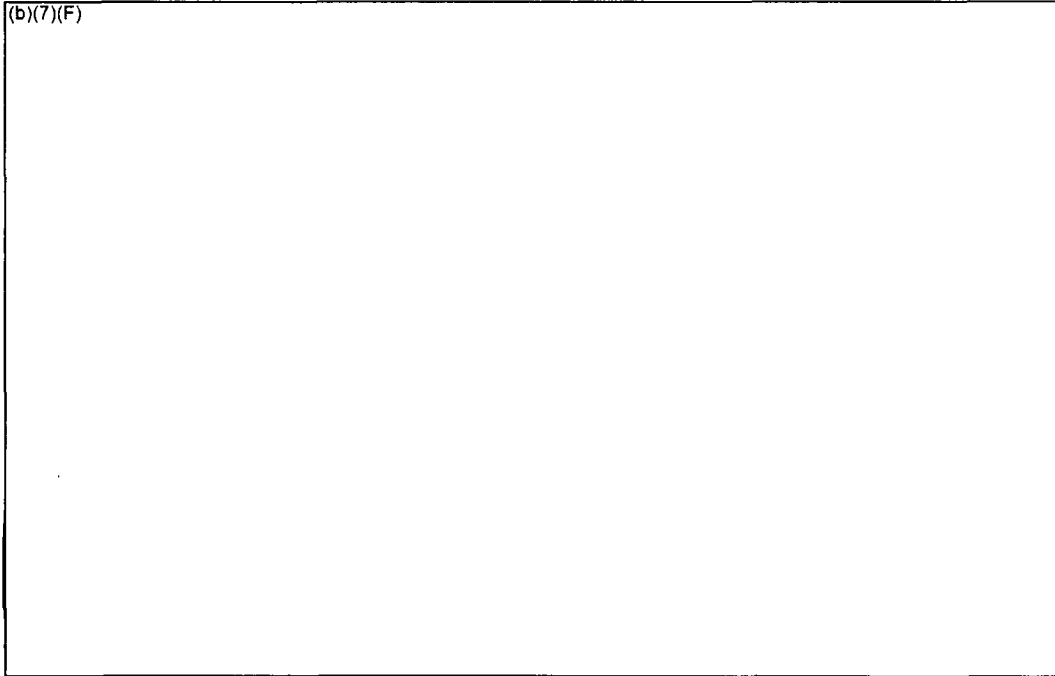


Figure 6-31 Center Assembly Cladding Temperatures for the 1x4 Configuration with (b)(7)(F) and No Sprays (Case S4b).

Ex 7F

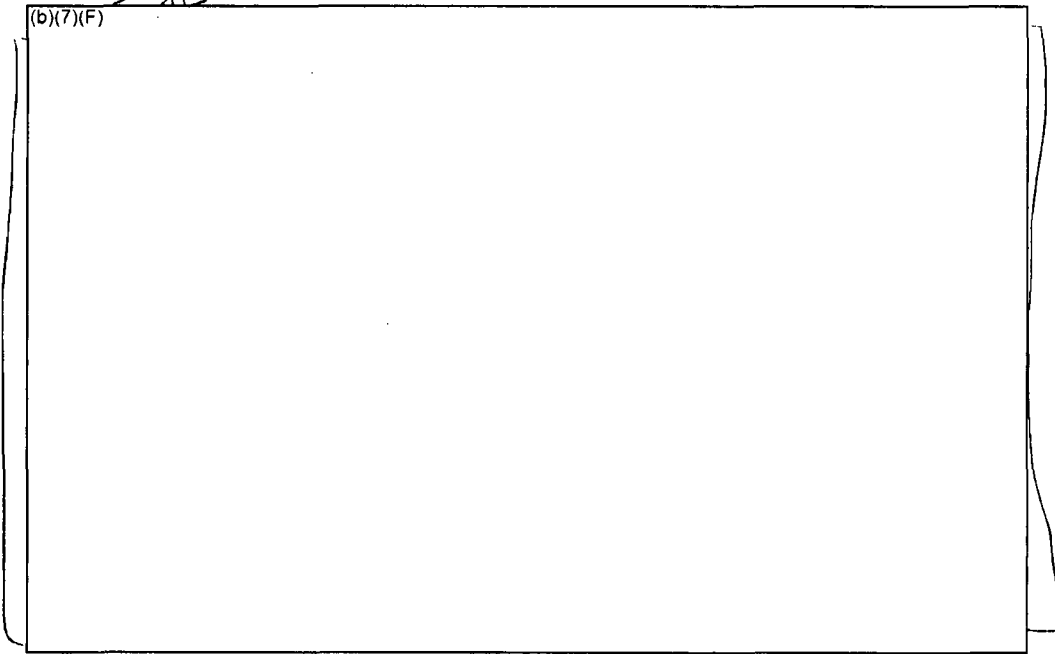


Figure 6-32 Peripheral Assembly Cladding Temperatures for the 1x4 Configuration with (b)(7)(F) and No Spray Flow (Case S4b).

Ex 7F

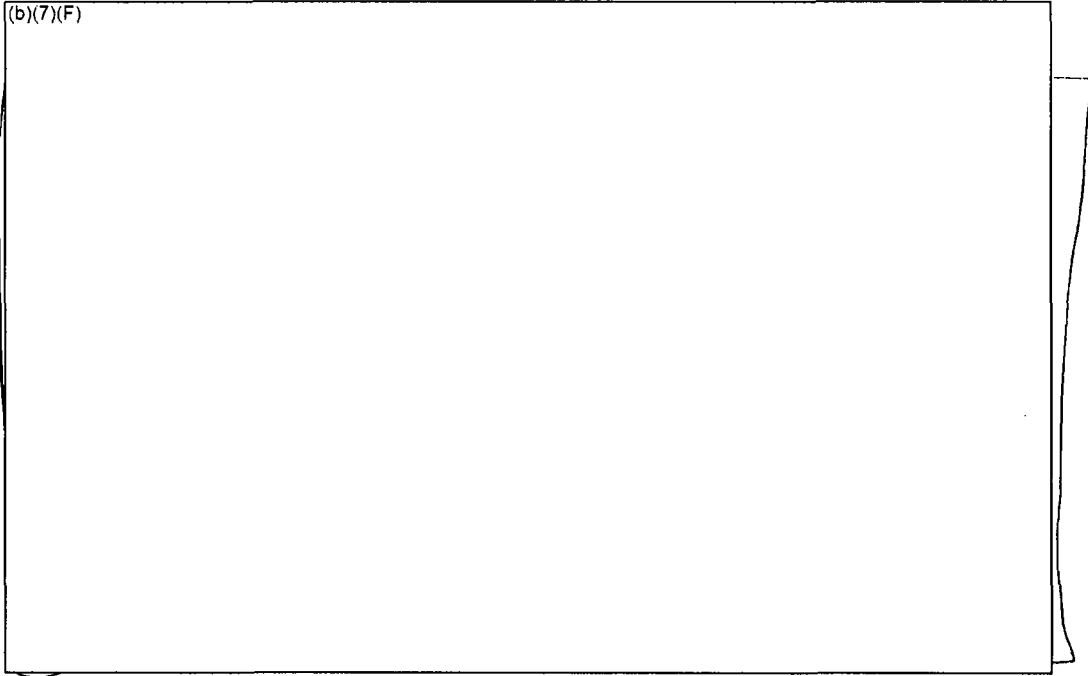


Figure 6-33 Center Assembly Cladding Temperatures for the 1x4 Configuration with (b)(7)(F) Spray Flow and Plugged Inlet (Case S4p).

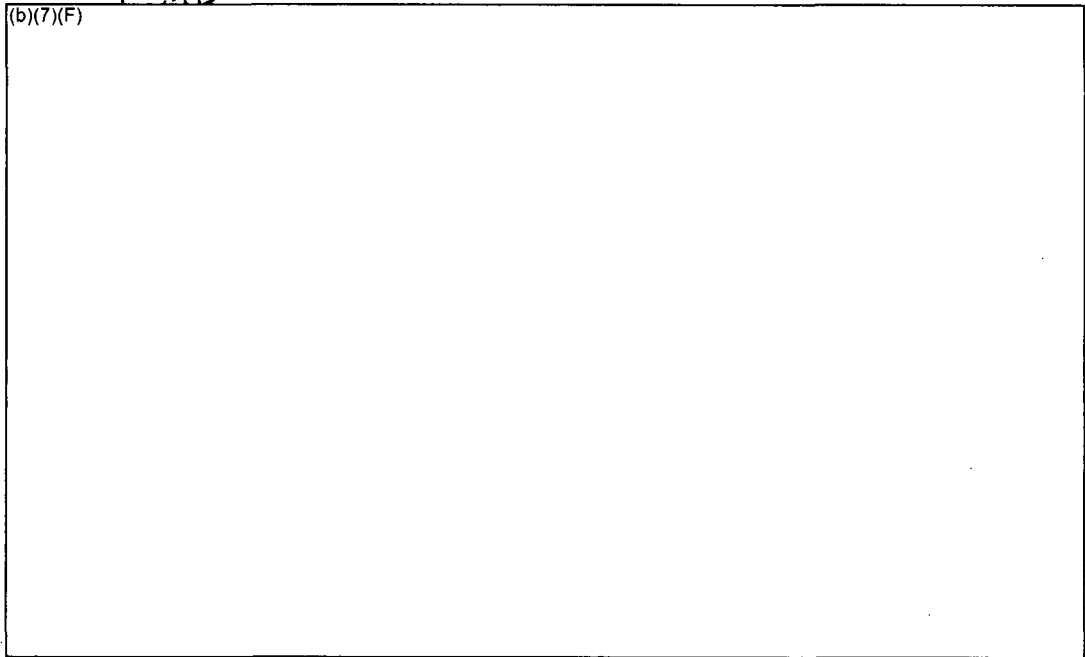
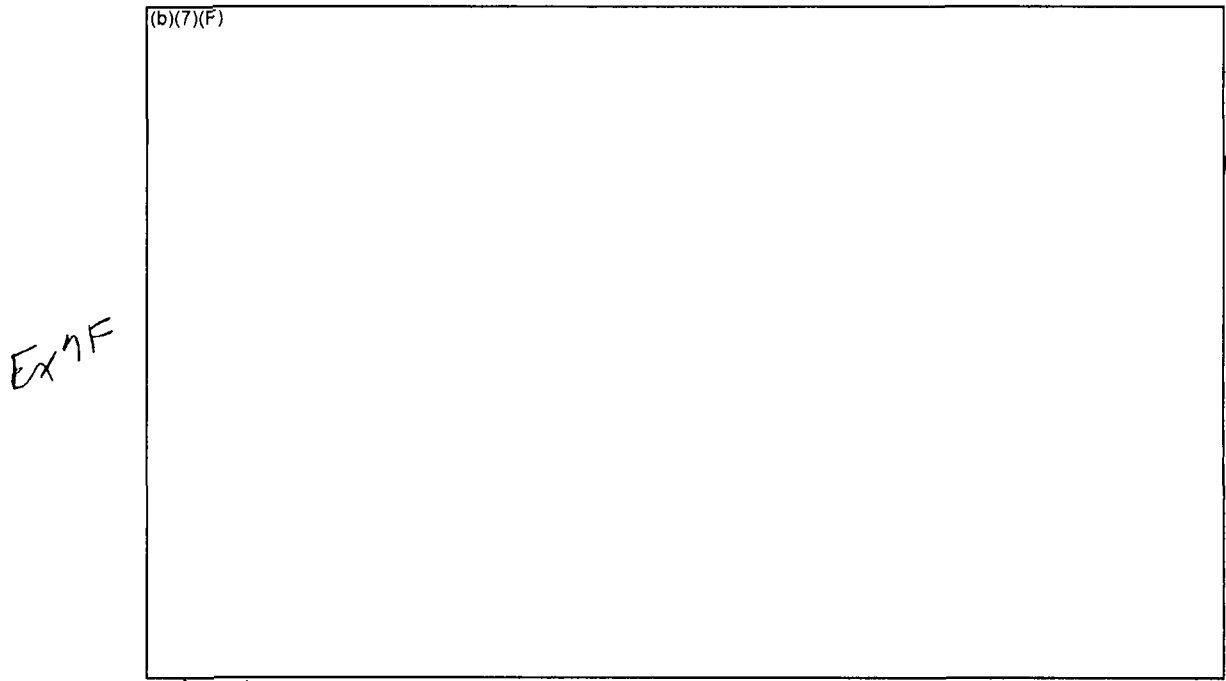
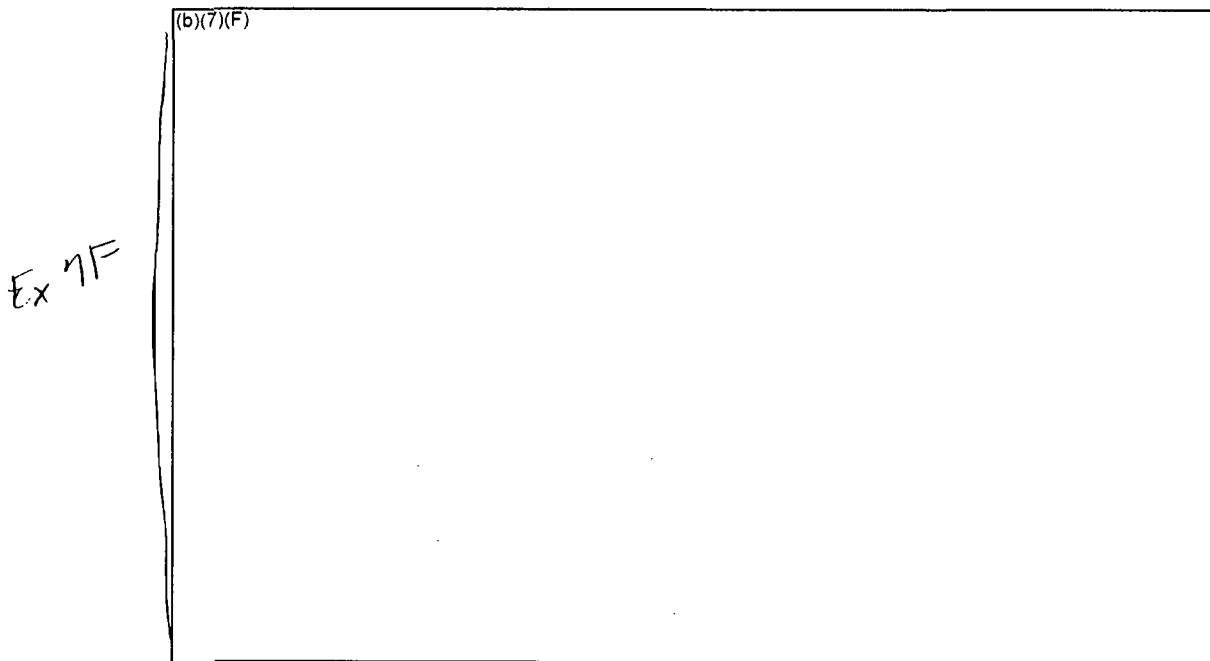


Figure 6-34 Peripheral Assembly Cladding Temperatures for the 1x4 Configuration with (b)(7)(F) Spray Flow and Plugged Inlet (Case S4p).



**Figure 6-35 Center Assembly Axial Cladding Temperatures for the 1x4 Configuration with (b)(7)(F) Spray Flow.**



**Figure 6-36 Peripheral Assembly Axial Cladding Temperatures for the 1x4 Configuration with (b)(7)(F) Spray Flow.**

Ex 7F

**6.4.2 Energy Balance on Base Calculation for** (b)(7)(F)  
**Spray**

EX 7 F

An energy balance was performed on the S4 case with the flow regime model operating (Case S4). Figure 6-37 graphically shows the key heat flows in the model. After water level drops below the base plate, the power going into the structure steadily decreases to near zero. Meanwhile, due to air and steam convection, the heat removed by the gas in the peripheral assembly gradually increases. The convective heat removal by the center assembly gas is relatively constant after the base plate clearing. In this figure, the decay power includes both the low- and high-powered assemblies. The net heat balance is the sum of the heat flow terms besides the decay power (i.e., it should be approximately equal to the decay heat power<sup>22</sup>).

The energy balance is reported in Table 6-4. The total power put into the 1x4 configuration is a combination of the decay heat for both the high- and low-powered assemblies (b)(7)(F)

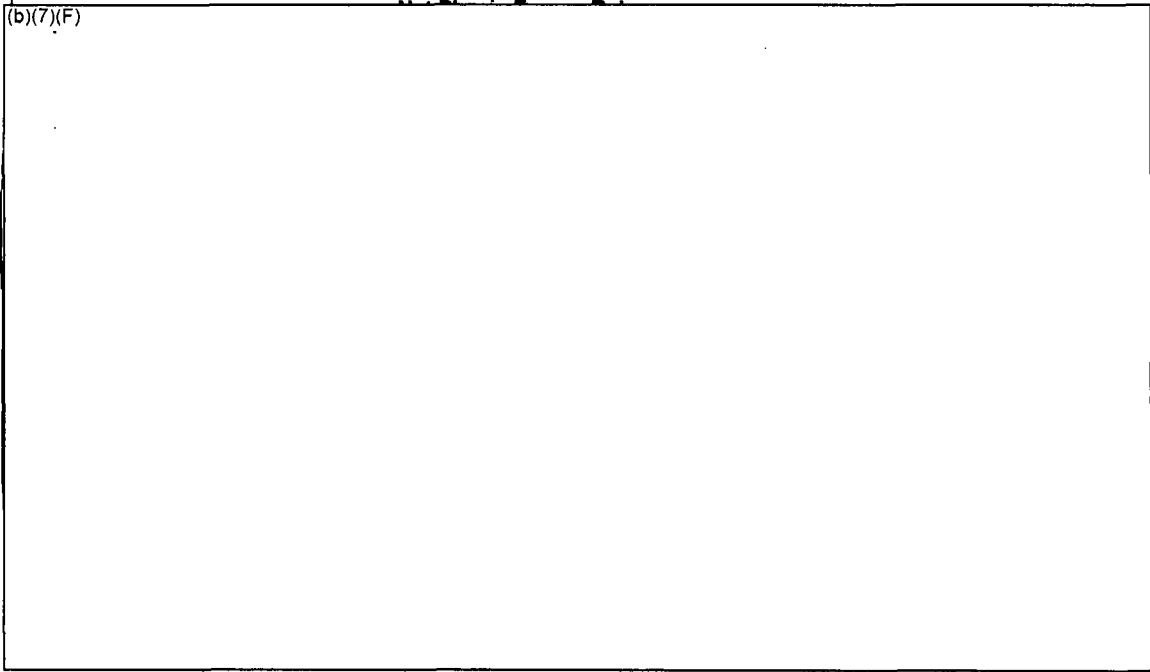
EX 7 F

(b)(7)(F)  
(b)(7)(F)  
(b)(7)(F)

(b)(7)(F) Due to the relatively low temperatures in all five assemblies, there was negligible oxidation power.   of the power in the center assembly was removed by convection and   by radial heat transfer to the peripheral assemblies. In the peripheral assemblies,   of the net heat load from the peripheral assembly decay powers and the radial heat transfer was removed by gas convection out the top of the assembly.   of the power in the peripheral assemblies was carried away by liquid spray flow out the bottom of the assembly.

(b)(7)(F)

<sup>22</sup> The small transient differences between the net energy balance and the decay power is attributed to limitations in the access of plot quantities available to the user to access all the subcomponents of the energy flow. However, the major components are shown on the figure. The internal MELCOR core calculations have very high fidelity.



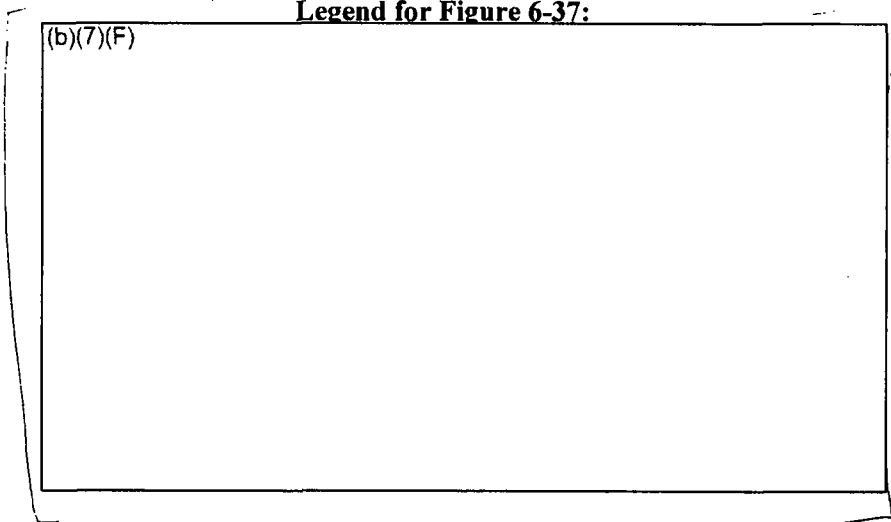
Ex 7F

**Figure 6-37** Time-averaged Energy Flow in the 1x4 Configuration with (b)(7)(F) and a Whole Pool Spray Flow of (b)(7)(F)

Ex 7F

Ex 7F

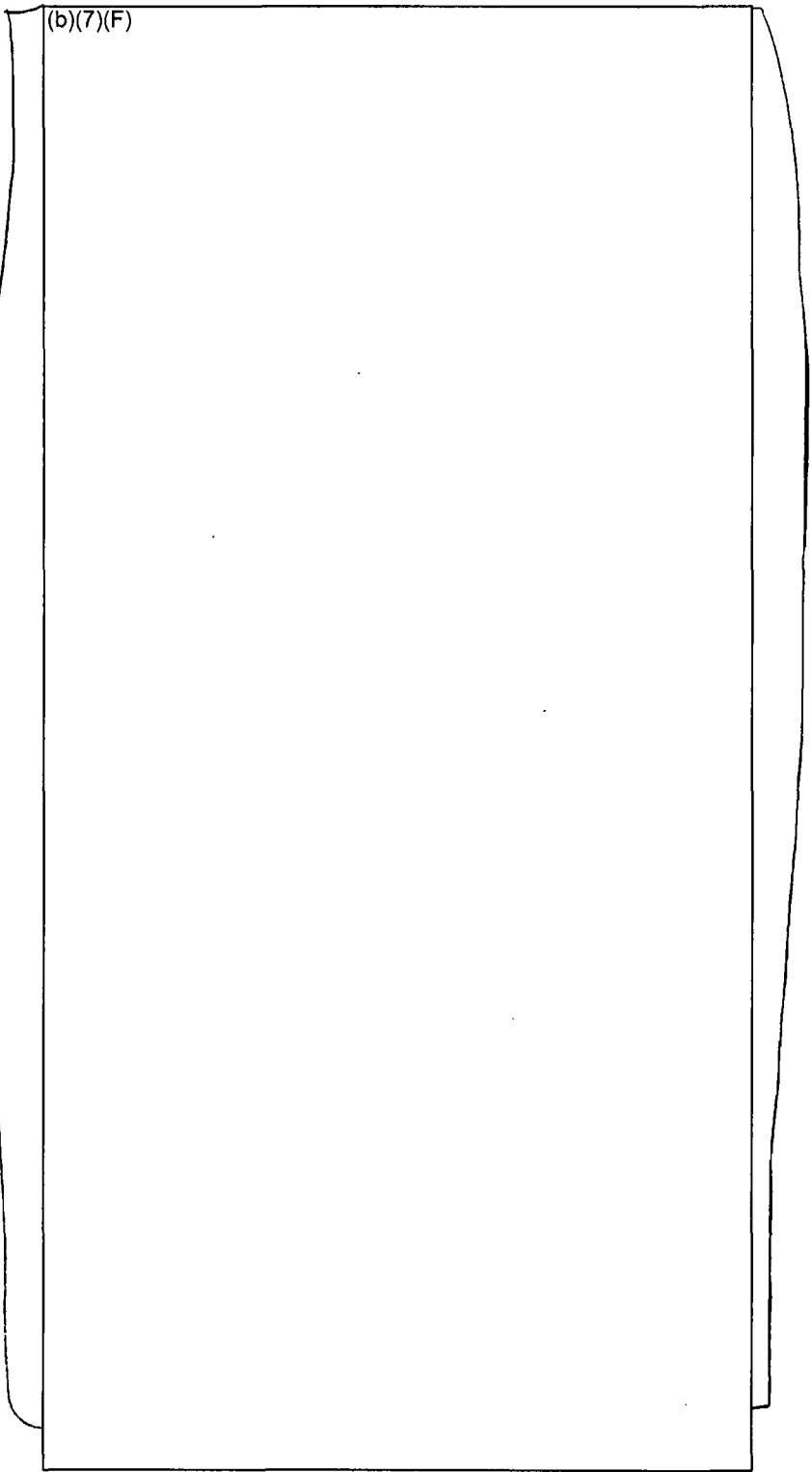
**Legend for Figure 6-37:**



Ex 7F

Table 6-4 Energy Balance for 1x4 Assembly Configuration in SFP with (b)(7)(F) Spray.

(b)(7)(F)



Ex 7F

## 7. SPRAY SCRUBBING CALCULATIONS

A short-term task was performed to estimate the effectiveness of an emergency spray system at reducing fission product releases for a configuration and scenario that had inadequate cooling. A

(b)(7)(F) and uniform configuration for the most recent offload was selected.

(b)(7)(F) emergency spray system was initiated at (b)(7)(F) after the start of the leak. Ex 7F (b)(7)(F)

Previously, the separate effect calculations in Section 6.2.1 suggested this configuration would heat to ignition conditions in less (b)(7)(F) Ex 7F

As a first step, the separate effects model S5 calculation was continued through fuel degradation and fission product releases (see Figure 7-1 and Figure 7-2). The peak cladding and debris temperatures were very high (i.e., peak cladding temperature (b)(7)(F) and peak debris (b)(7)(F)

(b)(7)(F) and the volatile fission product releases<sup>23</sup> were very high (b)(7)(F) Ex 7F

(b)(7)(F) However, the peak temperatures and fission product releases were

even more severe without sprays (see Figure 7-3 and Figure 7-4). At (b)(7)(F) (i.e., the end of the spray calculation), the peak debris temperature was (b)(7)(F) and the volatile fission product (b)(7)(F)

releases were (b)(7)(F) It appeared further releases would occur in the spray case; however, further releases were slowly evolving because of the lower debris temperatures at most axial levels (i.e., from a robust fission product release condition).

As well as the magnitude of the release from the fuel, it was desired to know the scrubbing benefit of the sprays and other possible retention enhancements (e.g., lower building leakage due to cooling of the refueling room air by the sprays). Two approaches and several calculations were performed in an attempt to quantify these effects. In Section 7.1, the original BWR whole pool model was used to simulate the accident progression (see model description in Section 3.3.1). However, due to the relatively coarse CVH nodalization, there were some problems in achieving the desired conditions. Consequently, a parallel effort was initiated using the detailed separate effects model with additional control volumes to represent the gas space above the SFP rack and the refueling room. The results from those calculations are discussed in Section 7.2. Due to the limited resources and time for this task, both sets of calculations had limitations. Section 7.3 provides some interpretation of the results and some more important qualitative conclusions.

<sup>23</sup> For the purposes of this discussion, the volatile fission products include the MELCOR radionuclide classes representing (the noble gases, cesium, iodine, and tellurium.) Ex 7F

Ex 7F

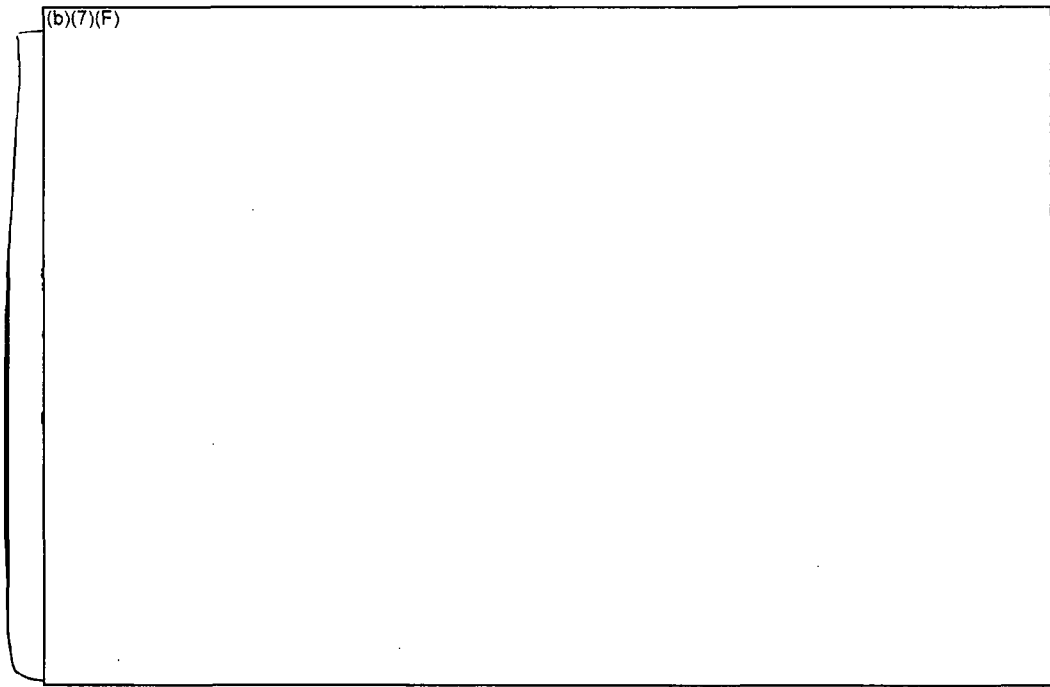


Figure 7-1 Cladding and Debris Temperature Response for the Separate Effects Model with (b)(7)(F) Spray (S5).

Ex 7F

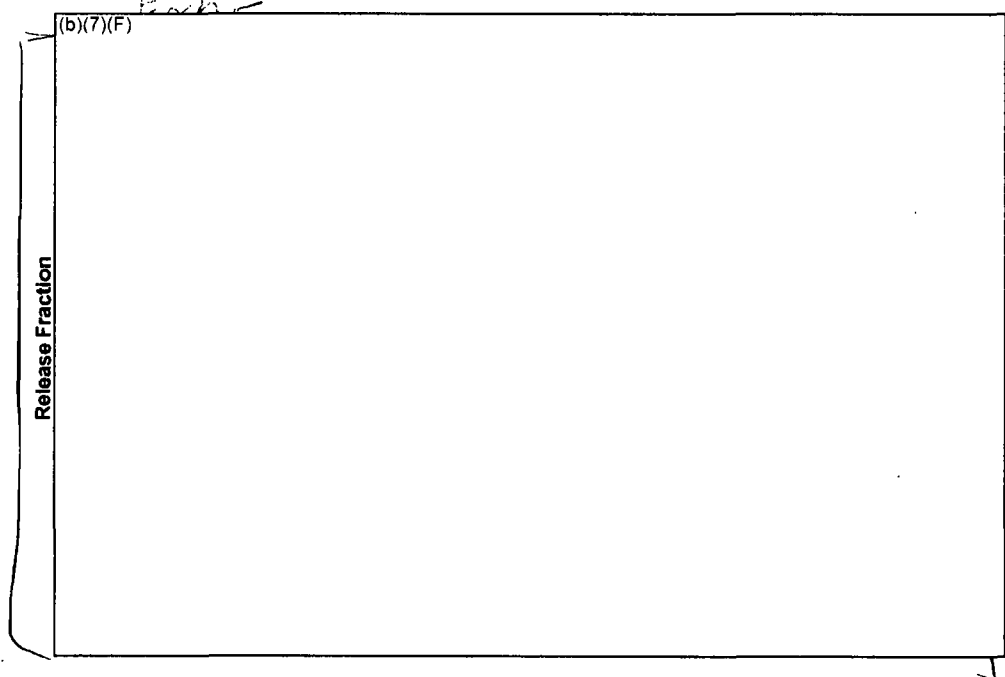
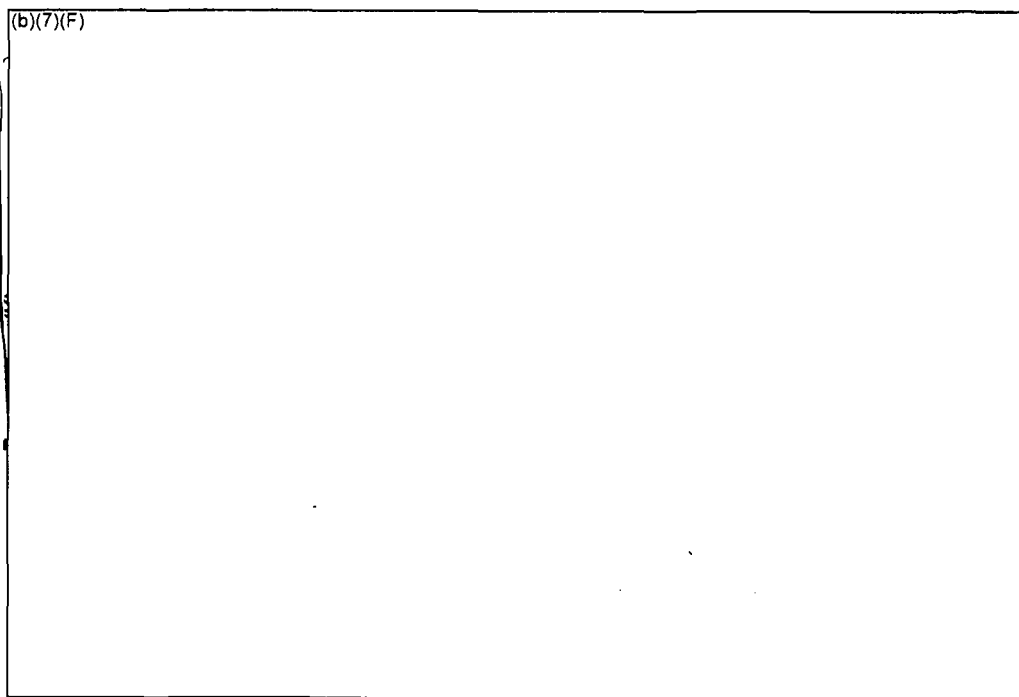


Figure 7-2 Fission Product for the Separate Effects Model with (b)(7)(F) Spray (S5).

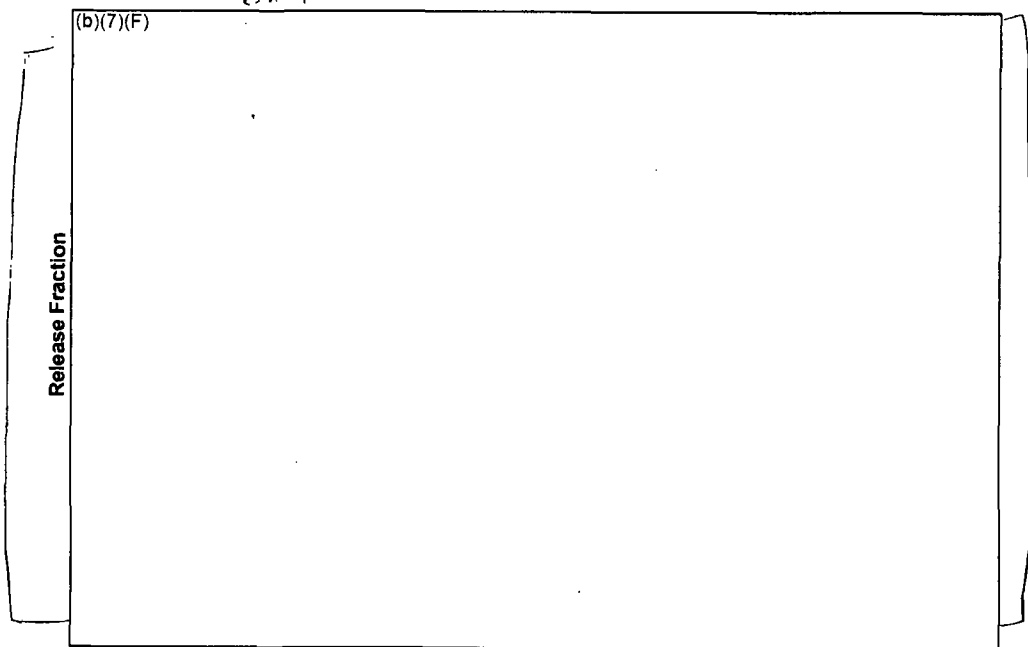
Ex 7F

Ex 7F



**Figure 7-3 Cladding and Debris Temperature Response for the Separate Effects Model with (b)(7)(F) and No Sprays (S5\_No).**

Ex 7F



Ex 7F

**Figure 7-4 Fission Product for the Separate Effects Model with (b)(7)(F) and No Sprays (S5\_No).**

Ex 7F

7.1 Calculations with Original Whole Pool Model

Ex 7F

The original BWR whole spent fuel pool model was upgraded to include a (b)(7)(F) decay heat profile and a rearrangement of the (b)(7)(F) assemblies from the last offload into Ring 1. The average power of an assembly in Ring 1 was (b)(7)(F) of the peak value used in the separate effects calculations. The remaining (b)(7)(F) from the last offload were placed in Ring 3 and had an average power of (b)(7)(F) of the peak value. The previous two offloads were reconfigured into Rings 5 (b)(7)(F) and Ring 7 (b)(7)(F). All the other assemblies were evenly distributed in Rings 2, 4, and 6 with an average power of only (b)(7)(F). The radial communication between Ring 1 and the low-powered rings was degraded by a factor of 10 (i.e., the low radial thermal coupling scheme (RTCS) as described in a previous whole pool calculation report [Wagner, 2004]. This technique was previously used to degrade the thermal coupling in the relatively well-configured pool to a coupling which would be more representative of a uniform configuration. After decreasing the RTCS by a factor of 10, the radial coupling for the hottest assemblies from the last offload was (b)(7)(F) effective thermal coupling with the low-powered assemblies. A (b)(7)(F) emergency spray was initiated at (b)(7)(F) after the start of a (b)(7)(F) on the bottom of the SFP.

Ex 7F \*

Ex 7F

Ex 7F

Ex 7F

A set of four calculations were performed as described in Table 7-1. The droplet size was varied from (b)(7)(F). Case WP\_S10 did not have sprays.

Ex 7F

Table 7-1 Summary of Whole Pool Calculations.

(b)(7)(F)
-----------

Ex 7F

Figure 7-5 shows the temperature response of the hottest fuel (i.e., Ring 1) for the case without sprays. Following the uncovering of the fuel at (b)(7)(F) the fuel heat rapidly proceeds to ignition conditions. The hottest location near the exit first goes through a rapid, breakaway oxidation transient. However, the fire moves downward as lower cladding regions successively heat up and consume all the available oxygen. The regions above the fire location somewhat cool off due to the absence of local oxidation heating and the presence of radial heat transfer. The fire reaches the bottom location and consumes most of the Zircaloy before moving upward. A second sustained heatup occurs (b)(7)(F) before the rack base plate yields due to high temperature at (b)(7)(F).

Ex 7F

The midplane temperatures for all 7 rings are shown in Figure 7-6. The highest decay power fuel from the most recent offload (i.e., Rings 1 and 3) led the heatups. Although the coupling to the adjacent rings was degraded, the radial radiative heat transfer at high temperatures is still

significant. The behavior of Rings 2 and 4 are in contrast to Ring 6 (i.e., with identical decay heat properties), which remained at a much lower temperature until between (b)(7)(F) Ex 7 F

Figure 7-7 shows the release and distribution of the cesium from the fuel (i.e., characteristic of a volatile fission product aerosol). Most of the releases occur from (b)(7)(F) when the fuel was on the second sustained heatup. By the end of the calculation, (b)(7)(F) of the cesium from Rings 1 and 3 had been released. Overall, (b)(7)(F) of the cesium was released from all fuel locations. The released fission products slowly leak from the building (b)(7)(F) when there is a hydrogen burn. The burn opens the refueling room blowout panels and rapidly blows out (b)(7)(F) of the airborne cesium in the reactor building. The subsequent environmental release rate is much higher due to the failed blowout panels. The building decontamination factor was (b)(7)(F) prior to the hydrogen burn (b)(7)(F) at the end of the calculation (see Figure 7-8). Ex 7 F

(b)(7)(F) Ex 7 F

Next, the spray case WP\_S7 is shown. Figure 7-9 shows the temperature response of Ring 1. The peak fuel temperatures were greater than (b)(7)(F) which is the criterion for the fuel cladding pressure boundary failure and release of the gap fission products. The peak cladding temperature was (b)(7)(F) 3 near the bottom of the active fuel. However, by (b)(7)(F) the fuel had cooled down to (b)(7)(F). Most of the fuel was between (b)(7)(F). Due to their lower power levels, the other rings were cooler. However, Ring 3 also exceeded the gap fission product release criterion at (b)(7)(F).

(b)(7)(F)

The cesium release and distribution behavior is shown in Figure 7-10. Due to the relatively low temperatures, only gap fission products releases from Rings 1 and 3 were predicted through the duration of the calculation. Most of the released fission products quickly moved from the SFP into the refueling room of the reactor building.<sup>24</sup> However, the release to the environment is relatively slow. There were no hydrogen burns in the calculation and none would be expected due to the low amount of Zircaloy oxidation.

Figure 7-11 shows two decontamination factors for the released cesium. The spray system decontamination factor is the ratio of the released cesium to the amount in the reactor building. The long-term spray system decontamination factor is (b)(7)(F). Unfortunately, the parameter includes airborne aerosols as well as ones in the water. A review of the final output shows that (b)(7)(F) of the released cesium aerosols are in the water, presumably either captured by the spray system or otherwise settled in the pool. Hence, a better internal building spray decontamination factor is the total released mass divided by the total mass not in pools in the reactor building. The information necessary to plot this factor is not available but a review of the final edit shows this value: (b)(7)(F) (see Table 7-2). In comparison, the case without sprays had only (b)(7)(F) of the released cesium aerosols settled in pools of water at the end of the calculation. However, the value of the overall building decontamination factor at the end of the calculation (i.e., 26) was approximately the same as the case without sprays (i.e., negligible fission product scrubbing benefit from the spray system).

(b)(7)(F)

(b)(7)(F)

(b)(7)(F)

<sup>24</sup> The fission products in the reactor building represented all regions in the reactor building except the SFP. It includes both airborne aerosols and aerosols in the water. The necessary plot variables to separate the two quantities were not specified. However, examination of the final output edit shows the relative distribution.

Figure 7-12 through Figure 7-17 show the corresponding results for Cases WP\_S8 and WP\_S9. The temperature response in these cases was essentially the same as Case WP\_S7. The most notable differences are the building and corrected spray decontamination factors shown in Table 7-2. The cases with smaller spray droplets were more effective at capturing the released cesium aerosol in water pools. There is approximately a factor [redacted] improvement in the gain in the decontamination efficiency from [redacted] spray case to the smaller [redacted] cases. Whereas the overall building decontamination factor was similar between the case without sprays (WP\_S10) and the [redacted] spray case (WP\_S7), the [redacted] (WP\_S8) and [redacted] (WP\_S9) cases were a factor [redacted] better (i.e., showing some fission product scrubbing benefit).

(b)(7)(F)

(b)(7)(F)  
Ex 7F

**Table 7-2 Summary of Spray and Building Decontamination Factors in the Whole Pool Calculations.**

(b)(7)(F)
(b)(7)(F)

Ex 7F

Ex 7F

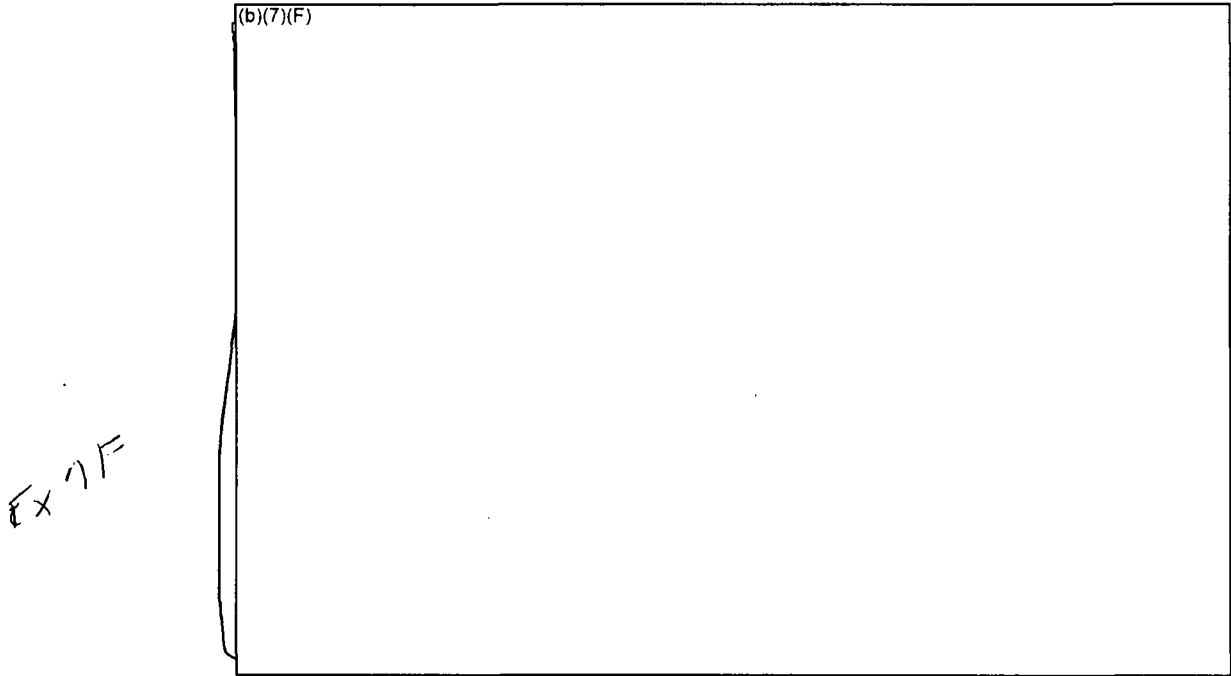


**Figure 7-5 Ring 1 Temperature Response for Whole Pool for the No Spray Case (WP10).**

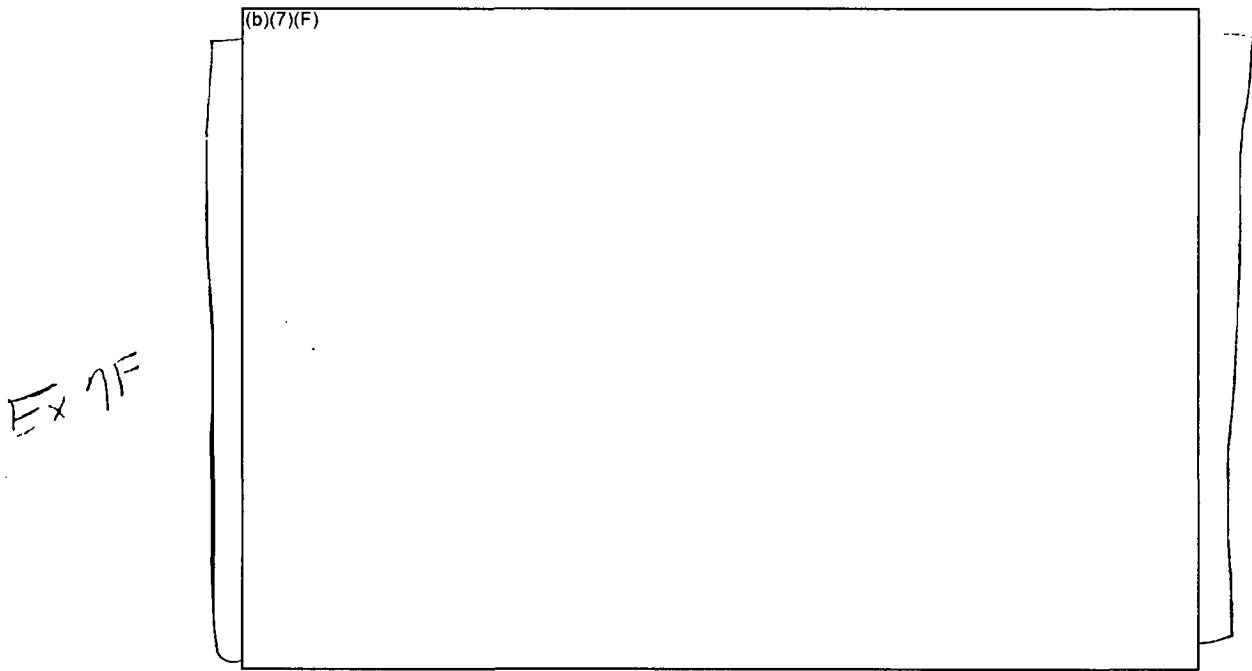


**Figure 7-6 Midplane Temperature Response for all 7 Rings for the Whole Pool No Spray Case (WP10).**

Ex 7F

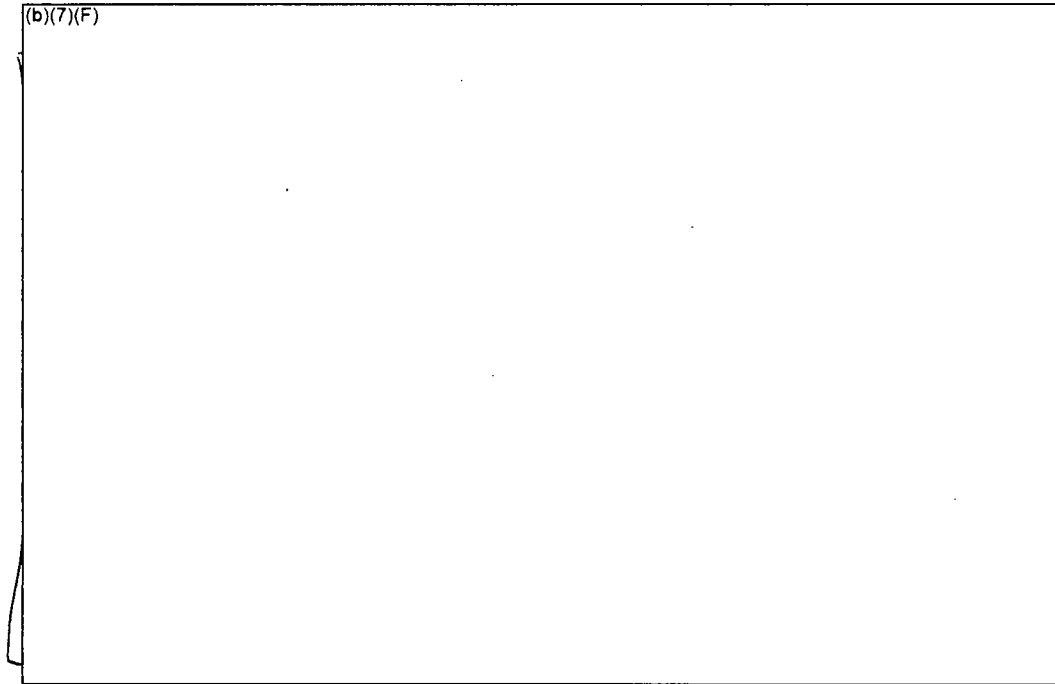


**Figure 7-7 Cesium Aerosol Release and Distribution for Whole Pool for the No Spray Case (WP10).**

Ex 7F

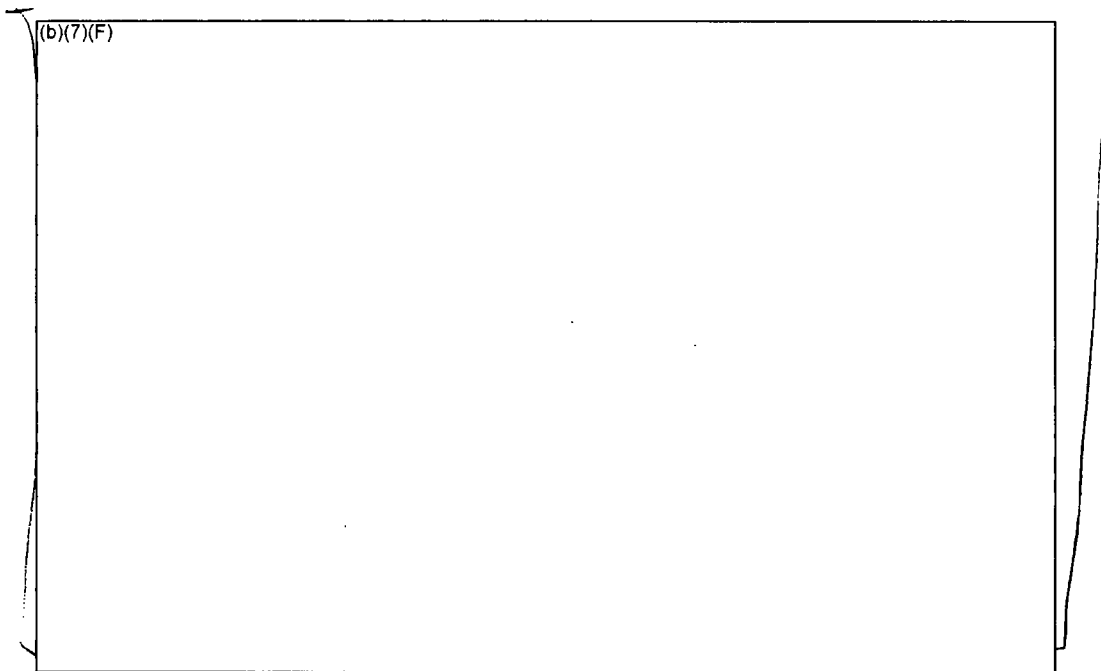


**Figure 7-8 Cesium Aerosol Decontamination Factor for Whole Pool for the No Spray Case (WP10).**

Ex 7F

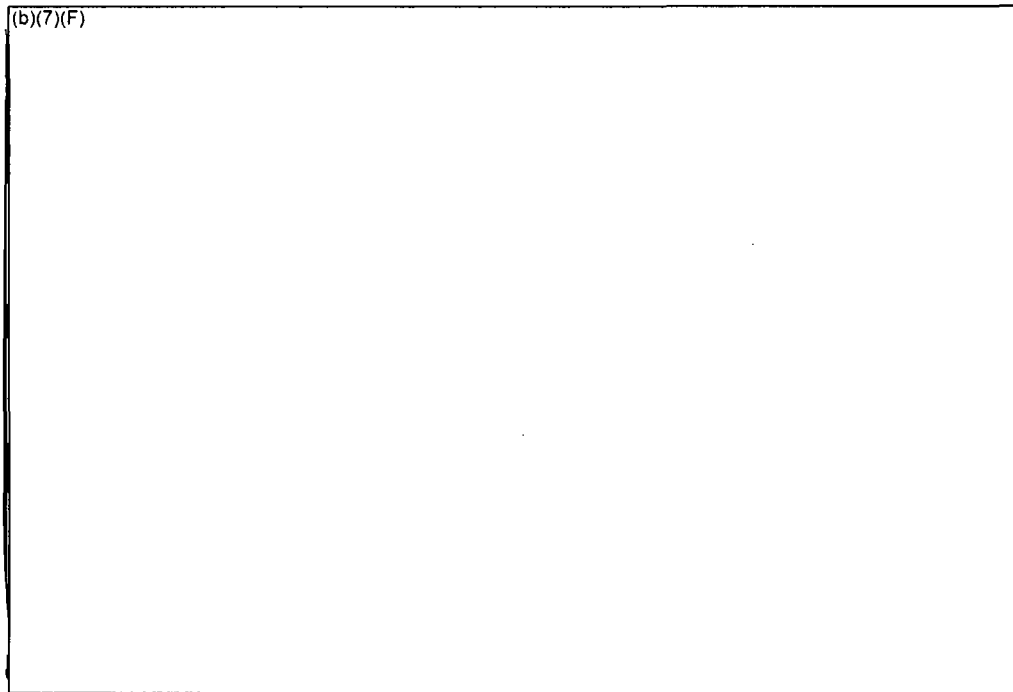


Figure 7-9 Peak Ring Temperature Response for Whole Pool for the (b)(7)(F) Spray Case (WP7).

Ex 7F

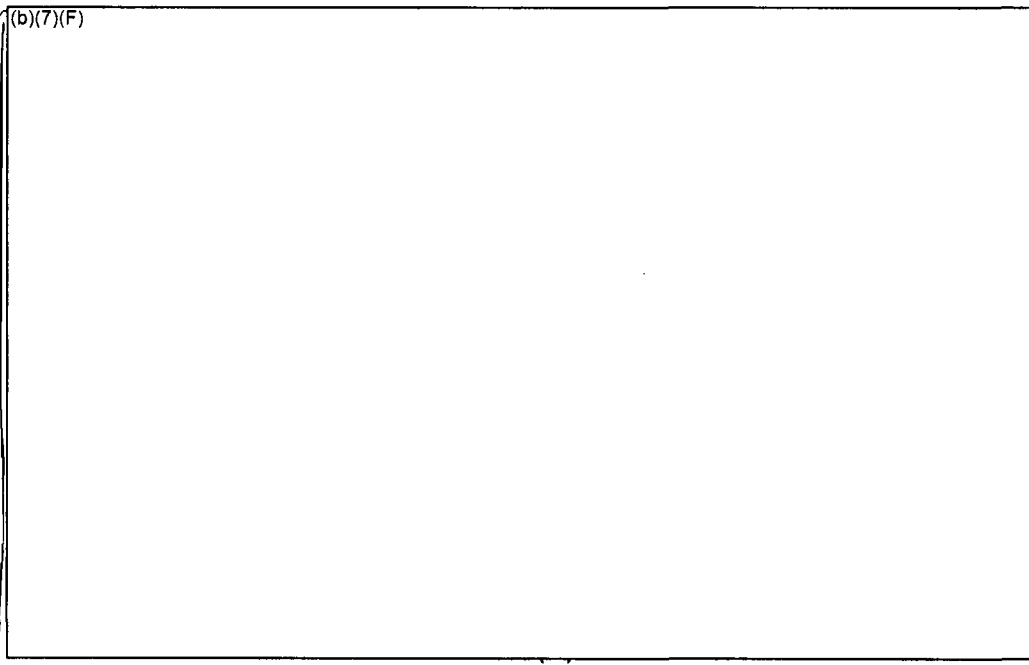
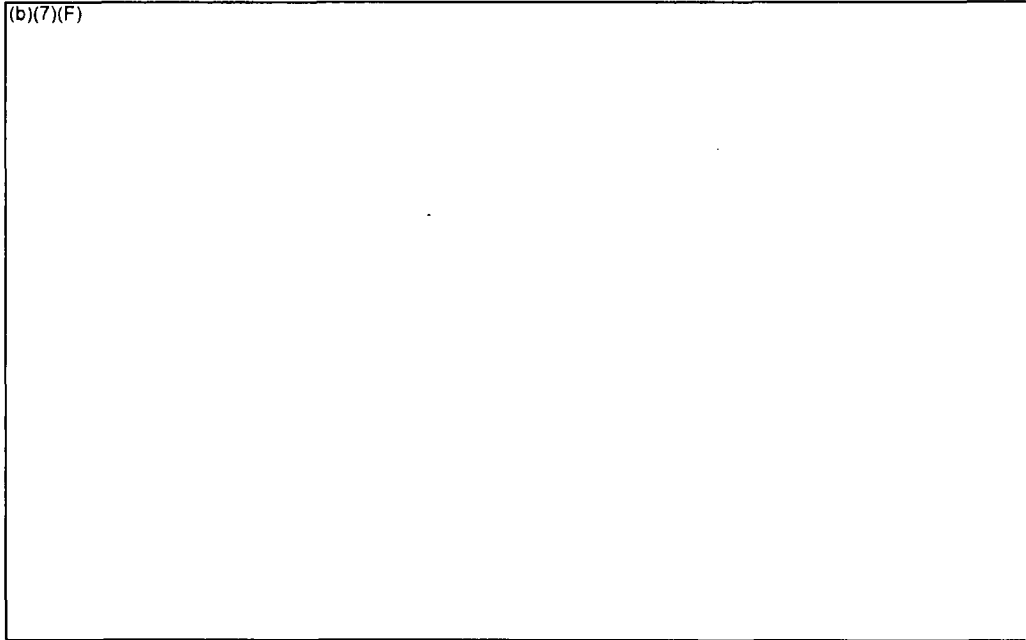
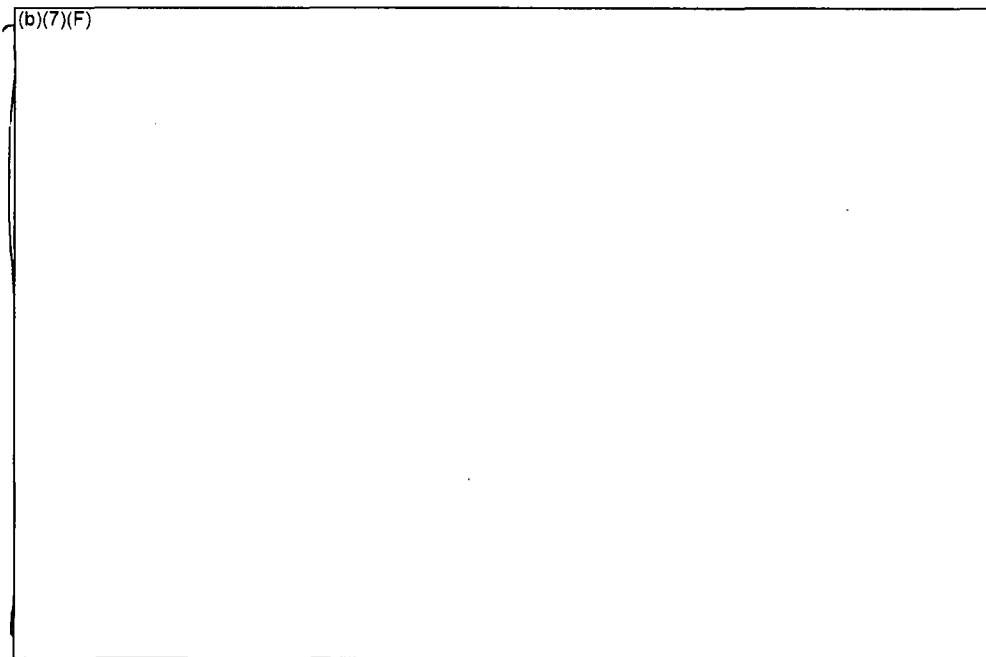


Figure 7-10 Cesium Aerosol Distribution for Whole Pool for the (b)(7)(F) Spray Case (WP7).



Ex 7F

**Figure 7-11 Cesium Aerosol Decontamination Factors for Whole Pool for the (b)(7)(F) (b)(7)(F) Spray Case (WP7).<sup>25</sup>**



Ex 7F

**Figure 7-12 Peak Ring Temperature Response for Whole Pool for the (b)(7)(F) (b)(7)(F) Spray Case (WP8).**

Ex 7F

<sup>25</sup> See discussion in Table 7-2 concerning the spray system DF.

Ex 11

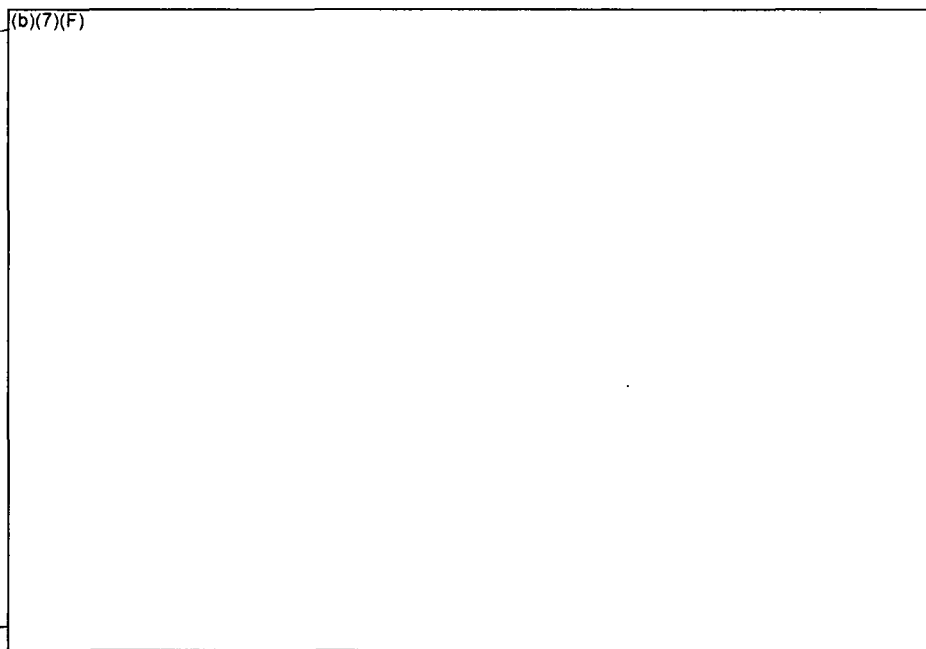
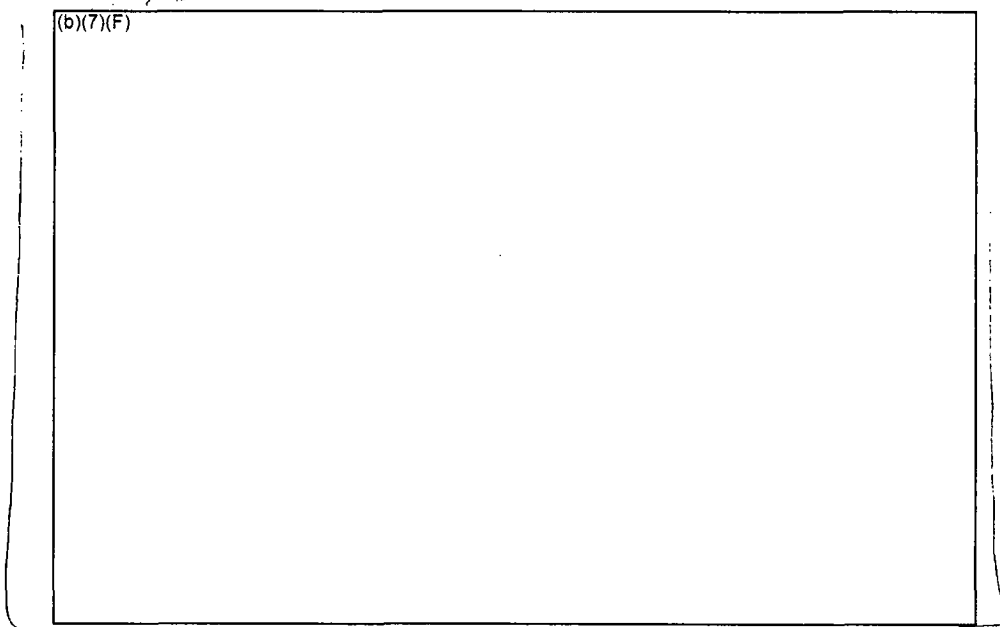


**Figure 7-13 Cesium Aerosol Release and Distribution for Whole Pool for the (b)(7)(F) (b)(7)(F) Spray Case (WP8).**



Ex 11

**Figure 7-14 Cesium Aerosol Decontamination Factor for Whole Pool for the (b)(7)(F) (b)(7)(F) Spray Case (WP8).<sup>26</sup>**

Ex 11

<sup>26</sup> See discussion in Table 7-2 concerning the spray system DF.

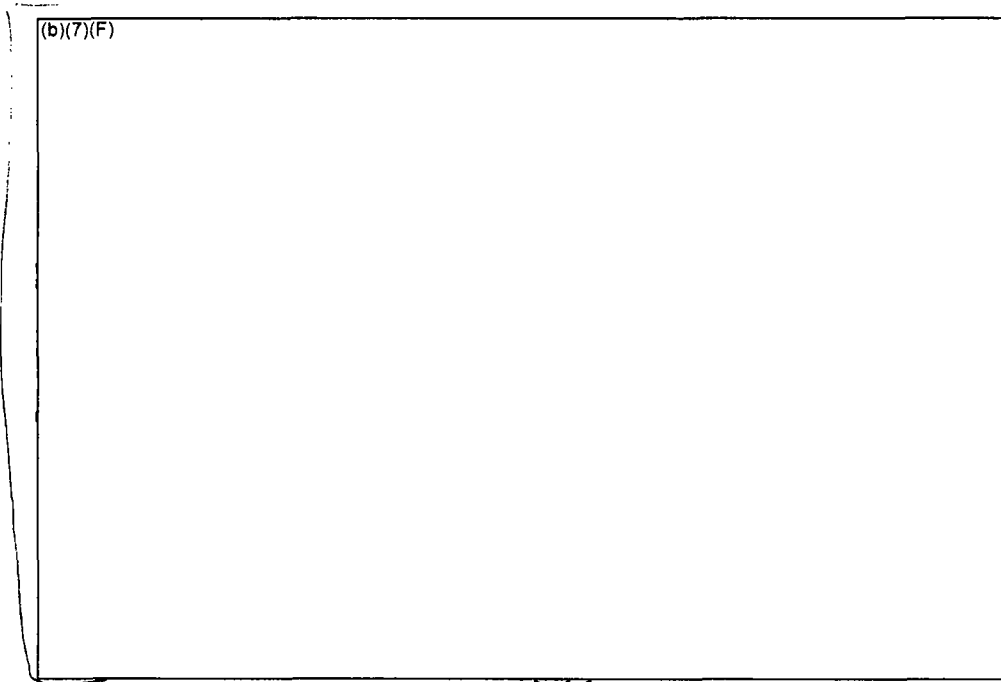


Figure 7-15 Peak Ring Temperature Response for Whole Pool (b)(7)(F)  
Spray Case (WP9).

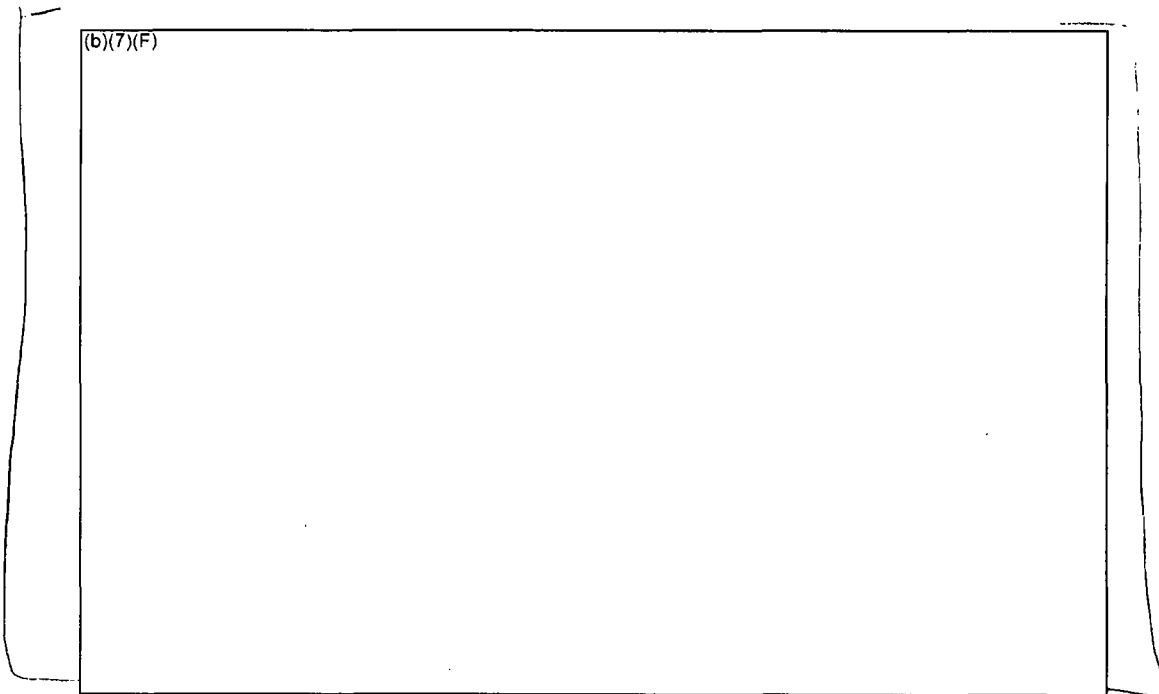


Figure 7-16 Cesium Aerosol Release and Distribution for Whole Pool for (b)(7)(F)  
(b)(7)(F) Spray Case (WP9).

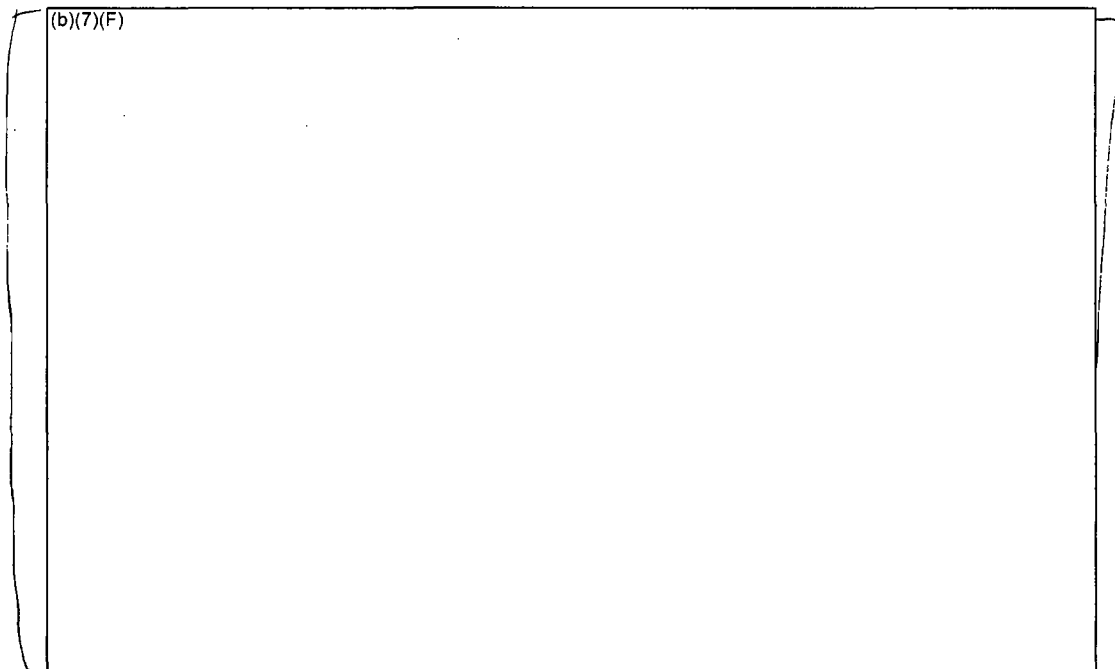


Figure 7-17 Cesium Aerosol Decontamination Factor for Whole Pool for the (b)(7)(F) (b)(7)(F) Spray Case (WP9).

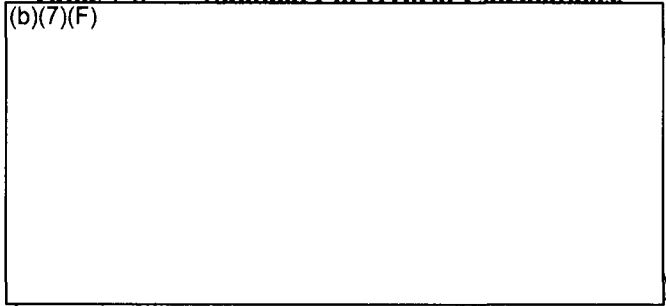
Ex 7F

## 7.2 Hybrid Calculations

The hybrid calculations simulated the hottest assembly from the last fuel offload with (b)(7)(F) aging since the shutdown of the reactor. The radial boundaries of the assembly are adiabatic. The configuration is consistent with an assembly in the center of a group of assemblies with similar decay heat powers. (b)(7)(F) emergency spray was initiated (b)(7)(F) the start of (b)(7)(F) on the bottom of the SFP. Similar to the whole pool calculations, a set of four calculations were performed as described in Table 7-3. The spray droplet size was varied from (b)(7)(F). Case HM9 did not have sprays. Details about the hybrid model are presented in Section 3.2.2.

**Table 7-3 Summary of Hybrid Calculations**

(b)(7)(F)



The results from the hybrid calculations are shown in Figure 7-18 through Figure 7-22. Similar to the separate effects model shown in Section 6, the peak cladding temperatures and the fission product releases were very high whether the sprays were active or not. In general, (b)(7)(F) and (b)(7)(F) cases responded very similarly. The temperature and fission product response of the (b)(7)(F) case slightly lagged the other two cases because of less effective heat and mass transfer from the large drops providing more subcooling as the droplets entered the assembly. However, the effect had a relatively small impact on the longer term results. (b)(7)(F)

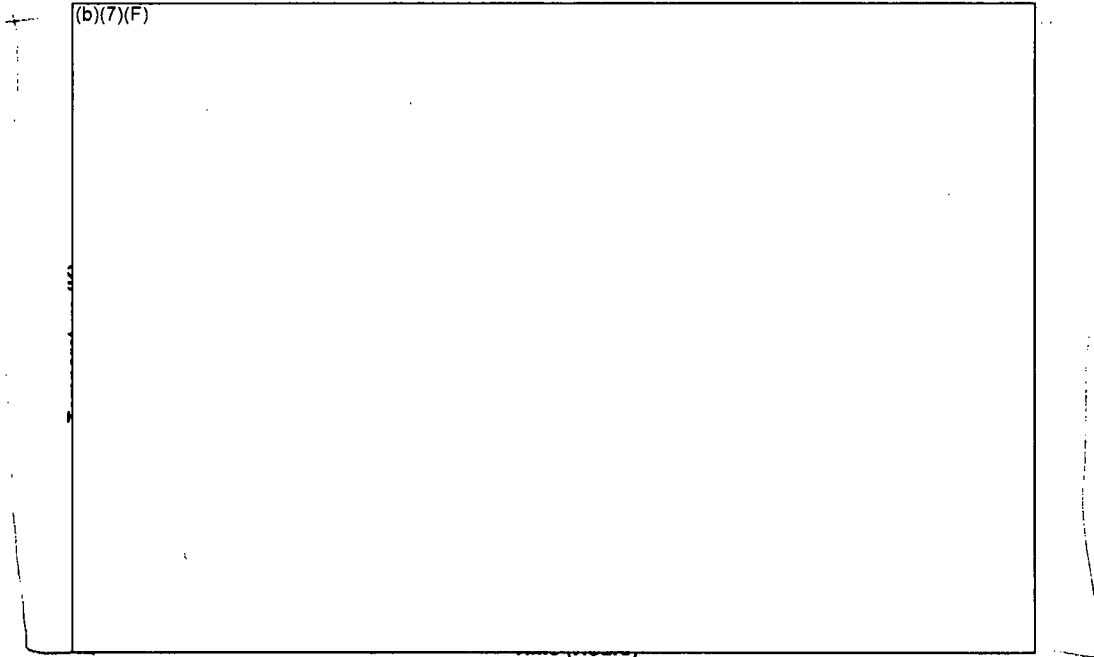
(b)(7)(F)  
(b)(7)(F)

Figure 7-22 shows the overall building decontamination factor. The decontamination factors for the spray cases ranged from (b)(7)(F). It is difficult to discern any difference between the spray cases. However, the difference between the spray and non-spray cases suggests a factor of two benefit from the spray system. (b)(7)(F)

(b)(7)(F)



Hence, although the fuel heat and overall fission product release looked reasonable, it is difficult to draw further conclusions of the distribution of the fission products once they were released.



**Figure 7-18 Comparison of Peak Cladding Temperatures from the Hybrid Calculations.**

*Ex-117*

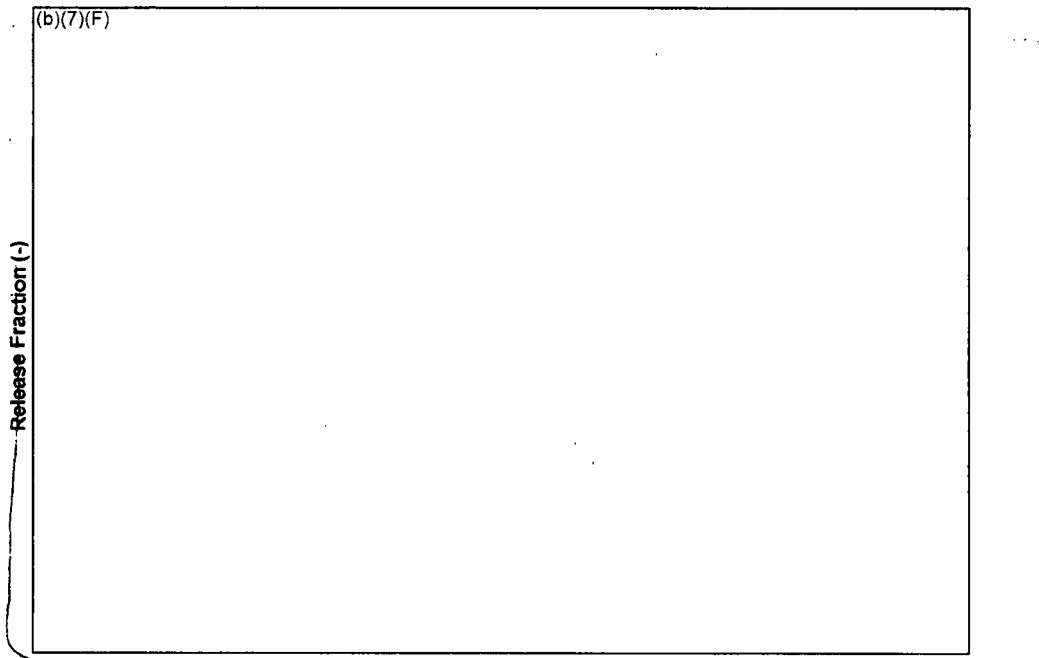


**Figure 7-19 Comparison of Fission Product Releases from Fuel for the Hybrid Calculations.**

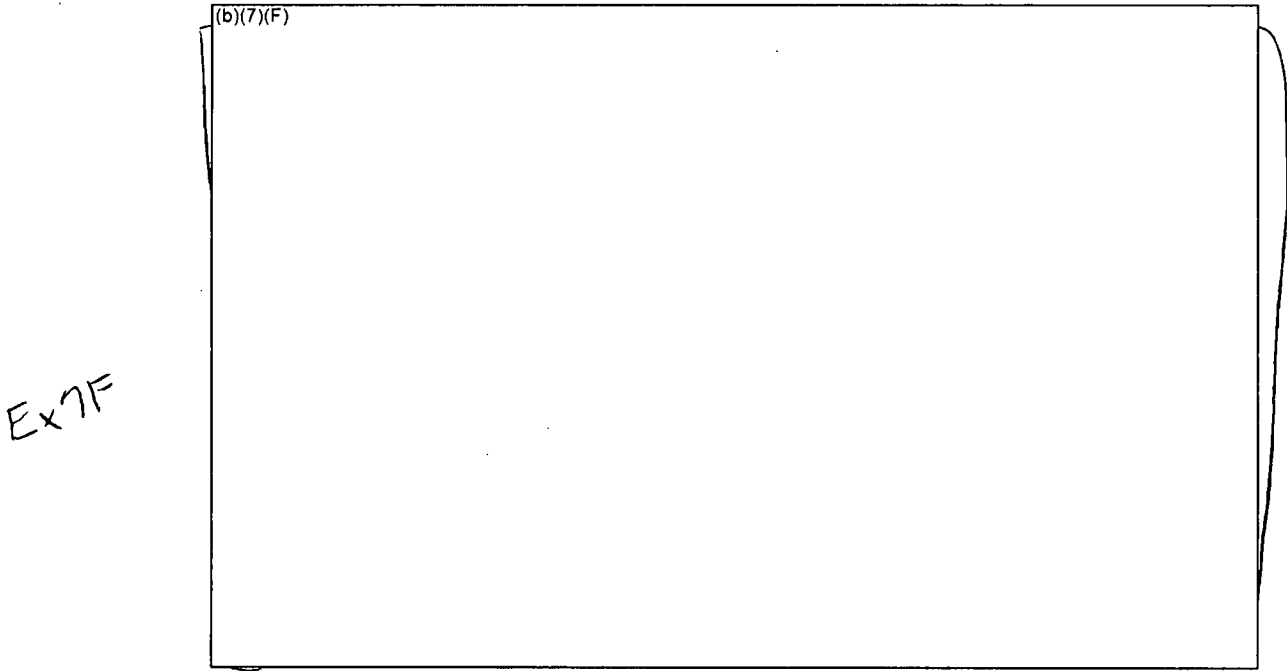


**Figure 7-20 Comparison of Fission Product Releases to the Environment for the Hybrid Calculations.**

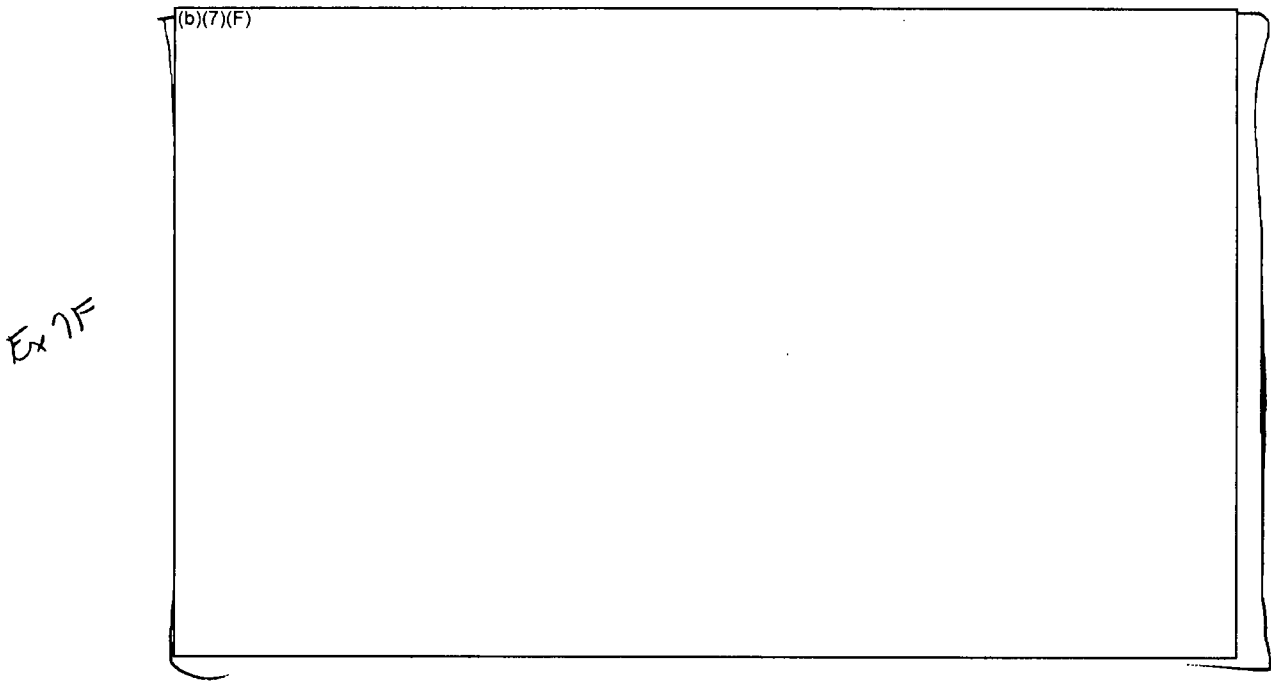


**Figure 7-21 Comparison of Fission Product Releases through the Break Location for the Hybrid Calculations.**

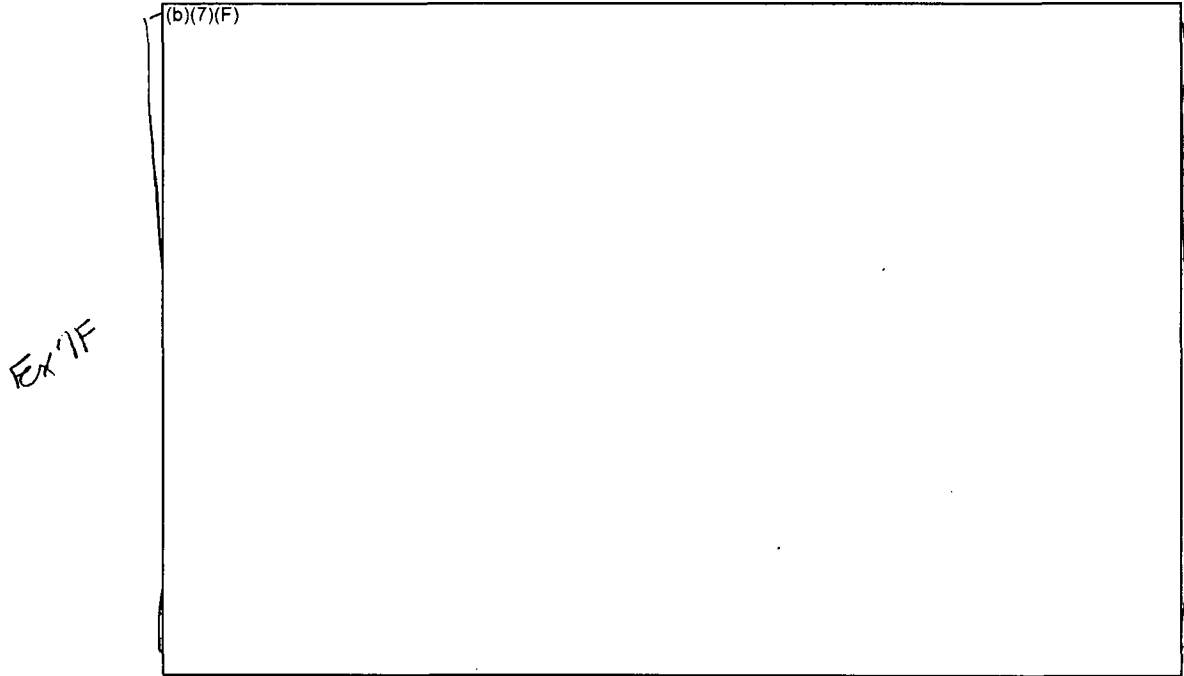


**Figure 7-22 Comparison of Reactor Building Decontamination Factors for the Hybrid Calculations.**

**OFFICIAL USE ONLY – SECURITY-RELATED INFORMATION**

**7.3 Summary of the Findings from the Fission Product Scrubbing Cases**

None of the separate effects, whole pool, and hybrid calculations adequately calculated scrubbing efficiency from the (b)(7)(F) emergency spray system during accident conditions with fission product releases. Each approach had aspects that were judged to be calculated well whereas other aspects were judged not to be calculated properly. In general, the strengths of the separate or hybrid calculations were a weakness in the whole pool calculations and visa versa. It is believed that the deficiencies in each approach could be addressed with the lessons learned from these initial calculations. However, the resources available for this task did not permit any further investigations. Nevertheless, the following observations are made from the available results.

Judged as a Reasonable Response

1. For the case (b)(7)(F) on the bottom of the pool with (b)(7)(F) spray (b)(7)(F) the separate effects and hybrid calculations both showed large releases of volatile fission products from the fuel in spite of the spray. Both the separate effect and hybrid calculations only showed slightly smaller releases than the cases without spray.

The hybrid model which included a falling spray droplet from above the racks yielded similar responses as the separate effects model, which only modeled the water penetration after the droplets contacted the assembly.

2. The whole pool model results showed little benefit of the spray scrubbing for the large droplet spray (b)(7)(F) versus a case without sprays (see Table E-2). The smaller spray droplet (b)(7)(F) showed a factor (b)(7)(F) better retention of released aerosols into the water versus (b)(7)(F) spray case and a factor of three better building retention versus the case without sprays. This conclusion, however, is based on very low fission product releases in the spray cases. The impact of scrubbing efficiency in a high release case is unknown.

Judged as Incorrect in the Calculations

1. The whole pool calculations with spray operation showed relatively low peak temperatures and very small fission product releases relative to the separate effects and hybrid cases. The whole pool responses were judged to be incorrect. Two factors seemed to cause this behavior. First, the CVH and CORE nodalizations were inadequately refined due to computational constraints to track the penetration of the spray flow. More detailed separate effects and hybrid spray flow calculations show the spray water is completely boiled away before reaching the middle and lower sections of the fuel rods. In the detailed separate effects calculations, the cladding ignition was calculated to start below the dryout of the spray flow and then propagate axially. The whole pool calculations benefited from spray penetration and cooling all the way to the bottom of the assembly.

Second, even though the radial heat transfer was degraded in the whole pool calculations, the responses of the (b)(7)(F) adjacent to (b)(7)(F) in Ex 7F Ring 1 and (b)(7)(F) in Ring 3 from the last offload show a relatively strong impact. In particular, the low-powered assemblies in Rings 2 and 4 heated more quickly and to much higher temperatures than the higher powered assemblies in Rings 5 and 7. Since the mass of the assemblies in Rings 2 and 4 is much larger than Rings 1 and 3, they had a significant impact on limiting the temperature rise of the last offload in Rings 2 and 4. The separate effects and hybrid calculations conservatively model an adiabatic radial boundary to the rack, which is judged to better reflect the most limiting assembly behavior in the center of a region of uniformly powered assemblies.

2. The hybrid model needs improvement to the scaling of the reactor building volume and boundary conditions for water level and building pressure. Due to pressure imbalances, airborne aerosols flowed downward and out the break.

3. The similar fission product scrubbing results for all droplet sizes in the hybrid model were judged incorrect. (b)(7)(F)

Ex 7F

(b)(7)(F)  
(b)(7)(F) A scaled gas space above the assembly likely does not adequately represent the gas concentration or spray contact volume above the racks. For example, once the gas and fission products exit the highest powered assembly (i.e., the one modeled in the hybrid model), (b)(7)(F)

(b)(7)(F)

Ex 7F

## 8. REFERENCES

Bergles, A. E., et al., Two-Phase Flow and Heat Transfer in the Power and Process Industries, McGraw-Hill Book Company, 1981.

Boyd, C., "Predictions of Spent Fuel Heatup after a Complete Loss-of-Coolant Accident," NUREG-1726, July 2000.

Collins, T. E., and Hubbard, G., "Technical Study of Spent Fuel Pool Accident Risk at Decommissioning Nuclear Power Plants," NUREG-1738, February, 2001.

Durbin, S., "Hydraulic Analysis of the Spent Fuel Pool Experiment," Revision 4, Sandia National Laboratories Internal Memo dated 11/21/05.

Ex 7F

Gauntt, R. O. et al, "MELCOR Computer Code Manuals, Reference Manual, Version 1.8.5, Vol. 2, Rev. 2", Sandia National Laboratories, NUREG/CR-6119, SAND2000-2417/1.

Khalil, I., and Webb, S., "Simulations of Natural Convection Airflow in a Completely Drained Pressurized Water Reactor Spent Fuel Pool using FLUENT," Sandia National Laboratories, Letter Report, Revision 1, October 2005.

Ex 7F

Lanning, D. D., Beyer, C. E., Geelhood, and K.J., FRAPCON-3 Updates, Including Mixed-Oxide Fuel Properties," NUREG/CR-6534, Vol. 4, PNNL-11513, Pacific Northwest National Laboratory, May 2005.

Natesan, K., and Soppet, W.K., "Air Oxidation Kinetics for Zr-Based Alloys," NUREG/CR-6846, Argonne National Laboratories, June 2004.

Nuclear Regulatory Commission, "Accident Source Terms for Light-Water Nuclear Power Plants," NUREG-1465, February 1995.

Ross, K. W., Wagner, KC, and Gauntt, R. O., "Analysis of Spent Fuel Pool Flow Patterns Using Computational Fluid Dynamics: Part 2 - Partial Water Cases," Sandia National Laboratories, Informal Report, April 2003.

Wagner, K. C., and Gauntt, R. O., "MELCOR 1.8.5 Separate Effect Analyses of Spent Fuel Pool Assembly Accident Response," Sandia National Laboratories, Draft Informal Report, Revision 0, June 2003.

Wagner, K. C., and Gauntt, R. O., "Evaluation of a BWR Spent Fuel Pool Accident Response to Loss-of-Coolant Inventory Scenarios Using MELCOR 1.8.5," Sandia National Laboratories, Draft Informal Report, Revision 2, December 2004.

Wagner, K. C., and Gauntt, R. O., "Analysis of BWR Spent Fuel Pool Flow Patterns Using Computation Fluid Dynamics: Supplemental Air Cases," Sandia National Laboratories, Draft Informal Report, Revision 2, October 2005.

Wagner, K. C. , Dallman, R. J., and Annon, M.C., "Best-Estimate Evaluation Of Loss-Of-Coolant Inventory In A Nuclear Power Plant Spent Fuel Pool," *International Meeting on Best-Estimate Methods in Nuclear Installation Safety Analysis (BE-2000)*, Washington, DC, November, 2000.

Wallis, G. B., One-Dimensional Two-phase Flow, McGraw-Hill Book Company, 1969.

## SANDIA LETTER REPORT

Draft Completed: April 2006  
Revision 1: May 2006

# Analysis of Emergency Spray Mitigation of Spent Fuel Pool Loss-of-Coolant Inventory Accidents

K. C. Wagner  
R. O. Gauntt

Prepared by  
Sandia National Laboratories  
Albuquerque, New Mexico 87185 and Livermore, California 94550

Sandia is a multiprogram laboratory operated by Sandia Corporation,  
a Lockheed Martin Company, for the United States Department of Energy's  
National Nuclear Security Administration under Contract DE-AC04-94AL85000.



**Sandia National Laboratories**

Issued by Sandia National Laboratories, operated for the United States Department of Energy by Sandia Corporation.

**NOTICE:** This report was prepared as an account of work sponsored by an agency of the United States Government. Neither the United States Government, nor any agency thereof, nor any of their employees, nor any of their contractors, subcontractors, or their employees, make any warranty, express or implied, or assume any legal liability or responsibility for the accuracy, completeness, or usefulness of any information, apparatus, product, or process disclosed, or represent that its use would not infringe privately owned rights. Reference herein to any specific commercial product, process, or service by trade name, trademark, manufacturer, or otherwise, does not necessarily constitute or imply its endorsement, recommendation, or favoring by the United States Government, any agency thereof, or any of their contractors or subcontractors. The views and opinions expressed herein do not necessarily state or reflect those of the United States Government, any agency thereof, or any of their contractors.



SANDIA Letter Report  
Draft, April 2006

# Analysis of Emergency Spray Mitigation of Spent Fuel Pool Loss-of-Coolant Inventory Accidents

K. C. Wagner  
R. O. Gauntt

Analysis and Modeling Division  
Sandia National Laboratories  
P.O. Box 5800  
Albuquerque, New Mexico 87185-MS-0748

## Abstract

This report describes calculations to analyze the effectiveness of emergency spray mitigation of spent fuel pool (SFP) loss-of-coolant inventory accidents. The data used to perform these calculations were developed from an operating boiling water reactor. This report is a supplement to earlier studies, which also examined the BWR SFP accident response without spray mitigation. The MELCOR 1.8.5 severe accident computer code was the primary tool used to simulate the SFP accident response. The emergency spray mitigation calculations include separate effects calculations of one or a few assemblies in the spent fuel pool and the whole pool response. Some hand calculations are also included to illustrate the basic energy balances.

## EXECUTIVE SUMMARY

In 2001, United State Nuclear Regulatory Commission (NRC) staff performed an evaluation of the potential accident risk in a spent fuel pool (SFP) at decommissioning plants in the United States [NUREG-1738]. The study was prepared to provide a technical basis for decommissioning rulemaking for permanently shutdown nuclear power plants. The study described a modeling approach of a typical decommissioning plant with design assumptions and industry commitments; the thermal-hydraulic analyses performed to evaluate spent fuel stored in the spent fuel pool at decommissioning plants; the risk assessment of spent fuel pool accidents; the consequence calculations; and the implications for decommissioning regulatory requirements. It was known that some of the assumptions in the accident progression in NUREG-1738 were necessarily conservative, especially the estimation of the fuel damage. Subsequently, the NRC desired to expand the study to include accidents in the spent fuel pools of operating power plants. Consequently, the NRC has continued spent fuel pool accident research by applying best-estimate computer codes to predict the severe accident progression following various postulated accident initiators. This report describes the effectiveness of emergency sprays systems for mitigating spent fuel pool accidents.

The data used to perform these calculations were developed from an operating boiling water reactor (BWR). The reference plant is typical of many BWRs with fuel in the SFP from several decades old to the most recent offload. This reference plant has a two-year fuel cycle and roughly discharges one-third of the reactor fuel (b)(7)(F) each outage. The plant removes an equivalent amount of various aged fuel between outages for storage in dry casks, thereby maintaining a relatively constant number of assemblies in the SFP. Hence, the SFP has a wide variety of different aged fuel. In addition, the SFP racks have enough empty cell locations (b)(7)(F) to permit a complete emergency reactor offload as well as store all the refueling blade guides. A schematic of the reference BWR spent fuel pool storage building is shown in Figure ES-1.

The MELCOR 1.8.5 severe accident computer code [Gauntt] with enhancements through Version RP was used to simulate the SFP accident response. MELCOR includes fuel degradation models for pressurized water reactor (PWR) and BWR fuel, radiation, convection, and conduction heat transfer models, air and steam oxidation models, hydrogen burn models, two-phase thermal-hydraulic models, and fission product release and transport models. Therefore, it contains the basic models to address questions and phenomena expected during a spent fuel pool accident.

Version RP includes three recent modeling enhancements applicable to BWR SFP modeling, (1) a new rack component, which permits better modeling of a SFP rack, (2) a new oxidation kinetics model, and (3) a simplified flow regime model. The new BWR spent fuel pool rack component permits proper radiative modeling of the SFP rack between groups of different assemblies. The new oxidation kinetics model predicts the transition to breakaway oxidation in air environments on a node-by-node basis. The simplified flow regime model and an expanded axial CVH nodalization corresponding to a 1:1 matching of the COR nodalization permitted simulation of liquid films draining down the BWR fuel assemblies during spray operation.

Ex 7F  
Ex 7F  
The purpose of the study is to evaluate the effectiveness of emergency spray mitigation during a loss-of-coolant inventory accident. The accidents are initiated with a leak in the SFP. Once the water level has reached roughly the fuel (b)(7)(F) there would be inadequate cooling. Most calculations assumed a (b)(7)(F) until an emergency spray system could be activated. In a complete loss-of-coolant inventory accident, the leak is located at the bottom of the SFP on the side wall. An air natural circulation pattern can be established through the assemblies if the level drains below the bottom of the racks. If the fuel heats to high temperatures, then rapid exothermic oxidation of the zirconium cladding and canisters occurs using the oxygen in the air. If water from the spray system fills the bottom of the pool above the bottom of the racks, the accident will progress without convective air cooling.

Two sets of hand calculations were performed to estimate the heat removal required from the spray system in the reference BWR spent fuel pool. The hand calculations represent simple straight-forward energy balances that are useful for estimating the required flowrate for a spray system. In the first calculation, the spray system was initiated prior to uncovering of the fuel and the water leakage location is above the top of the racks. (b)(7)(F)

(b)(7)(F) Since the fuel is covered, a spray system is not technically needed. Rather any water injection system would be sufficient. In the second hand calculation, it is assumed that the fuel is substantially uncovered. (b)(7)(F)

(b)(7)(F)  
Ex 7F  
(b)(7)(F) Since the fuel is uncovered, a spray system is required to distribute the water to the individual assemblies. The flowrate estimate includes factors to account for inefficiencies due to overlap from the adjacent nozzles and flow into the region between the fuel canister and rack walls. The hand calculations also assume no radial heat transfer between assemblies, which effectively represents conditions corresponding to uniform loading of the most recently discharged fuel.

Recognizing that the above hand calculations for an uncovered pool were potentially conservative, a series of whole pool and detailed separate effects MELCOR calculations were performed. First, a BWR whole pool model was developed to establish boundary conditions for the separate effects calculations.<sup>1</sup> The most important output from the whole pool calculations was the steady state water level. For the range of hole sizes and spray flow rates considered in this study, the long-term water level spanned conditions that would allow air flow (i.e., the water level is not above the inlet to the racks or "plugged" by the water) versus cases where the inlet would be plugged. (b)(7)(F)

(b)(7)(F) Ex 7F  
Previous calculations have shown that the phenomena and thermal response for cases with the inlet plugged by the water level are different than the response when there is air flow in the assembly. Most importantly, the blocked inlet configuration substantially decreases the assembly heat removal. However, the spray calculations with a plugged inlet showed a much

<sup>1</sup> As will be discussed in the report, it was computationally impractical to include a sufficiently detailed nodalization to track spray behavior within the fuel assemblies in the whole spent pool and building model. Hence, the whole pool model was used to establish global boundary conditions for the separate effects calculations.

less significant impact after the spray initiation. The spray flow source provided an active heat removal mechanism that reduced the necessity of convective air flow.

Table ES-1 summarizes the highlights of separate effects spray calculations. Calculations were performed for the uniform, checkerboard, and 1x4 configurations. For each configuration, parametric calculations were performed with variations in one or more of the scenario or modeling attributes. The variations in the calculations included fuel configuration (uniform, checkerboard, and 1x4), aging time of the peak powered assembly, leak size (b)(7)(F) Ex 7F  
spray flow rate (b)(7)(F), air flow (some configurations that were expected to have air flow had a sensitivity study where the inlet was plugged with water), and a modeling parameter (MELCOR's flow regime model active or inactive).

Ex 7F

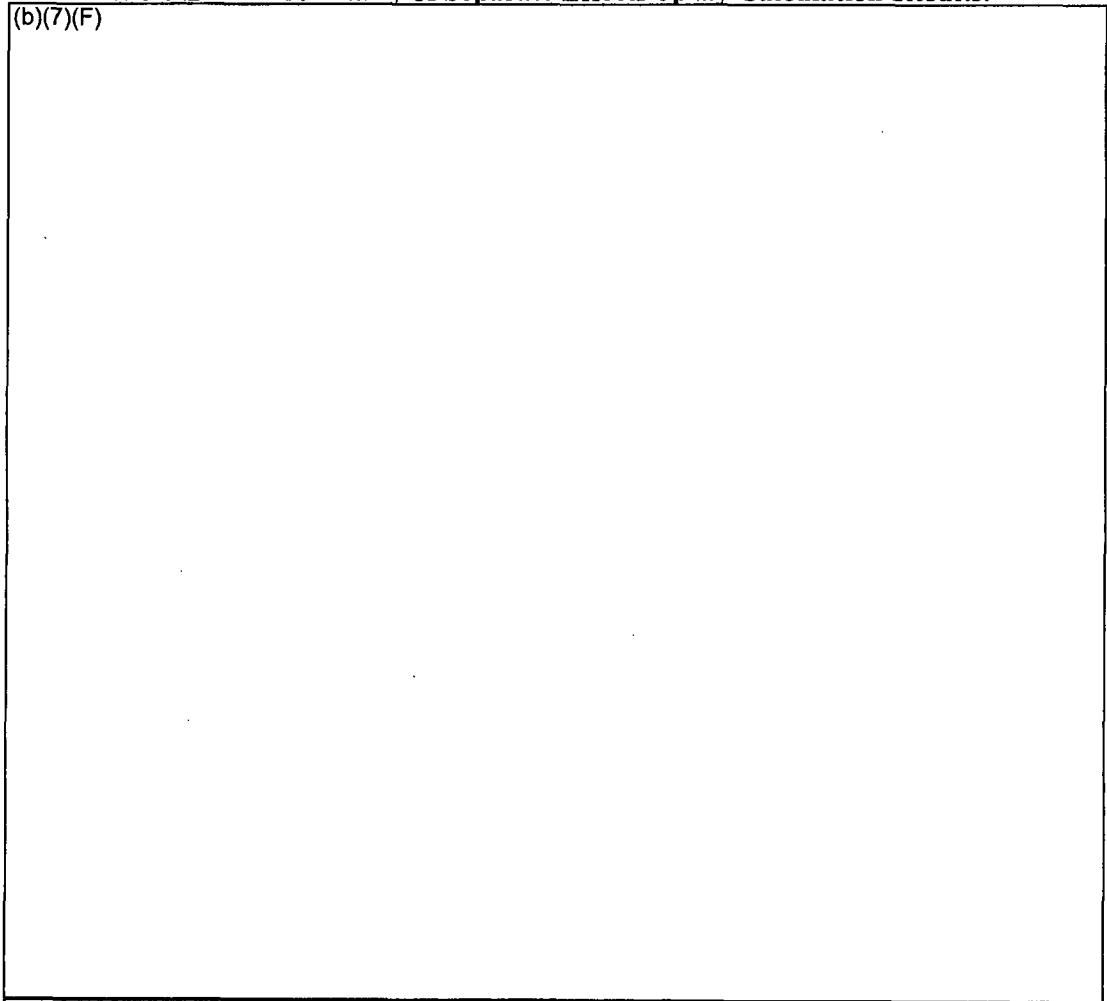
For fuel which has been favorably configured (i.e., a 1x4 or checkerboard pattern), a spray flow rate (b)(7)(F) is adequate for cooling the fuel at (b)(7)(F) (b)(7)(F) Ex 7F

Ex 7F

(b)(7)(F)

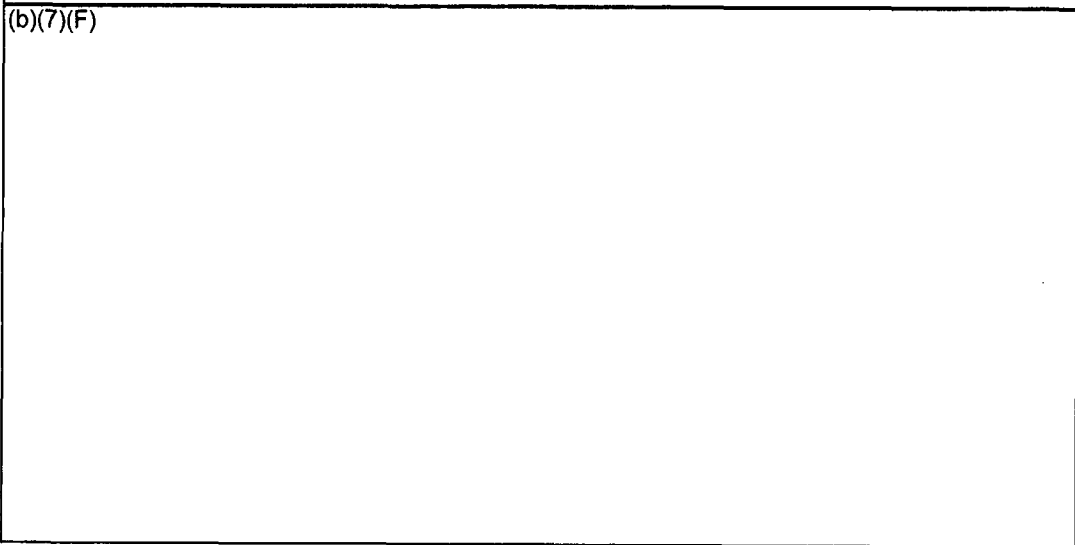
**Table ES-1 Summary of Separate Effects Spray Calculation Results.**

(b)(7)(F)



Ex 7F

(b)(7)(F)



7F

Ex 7F

(b)(7)(F)

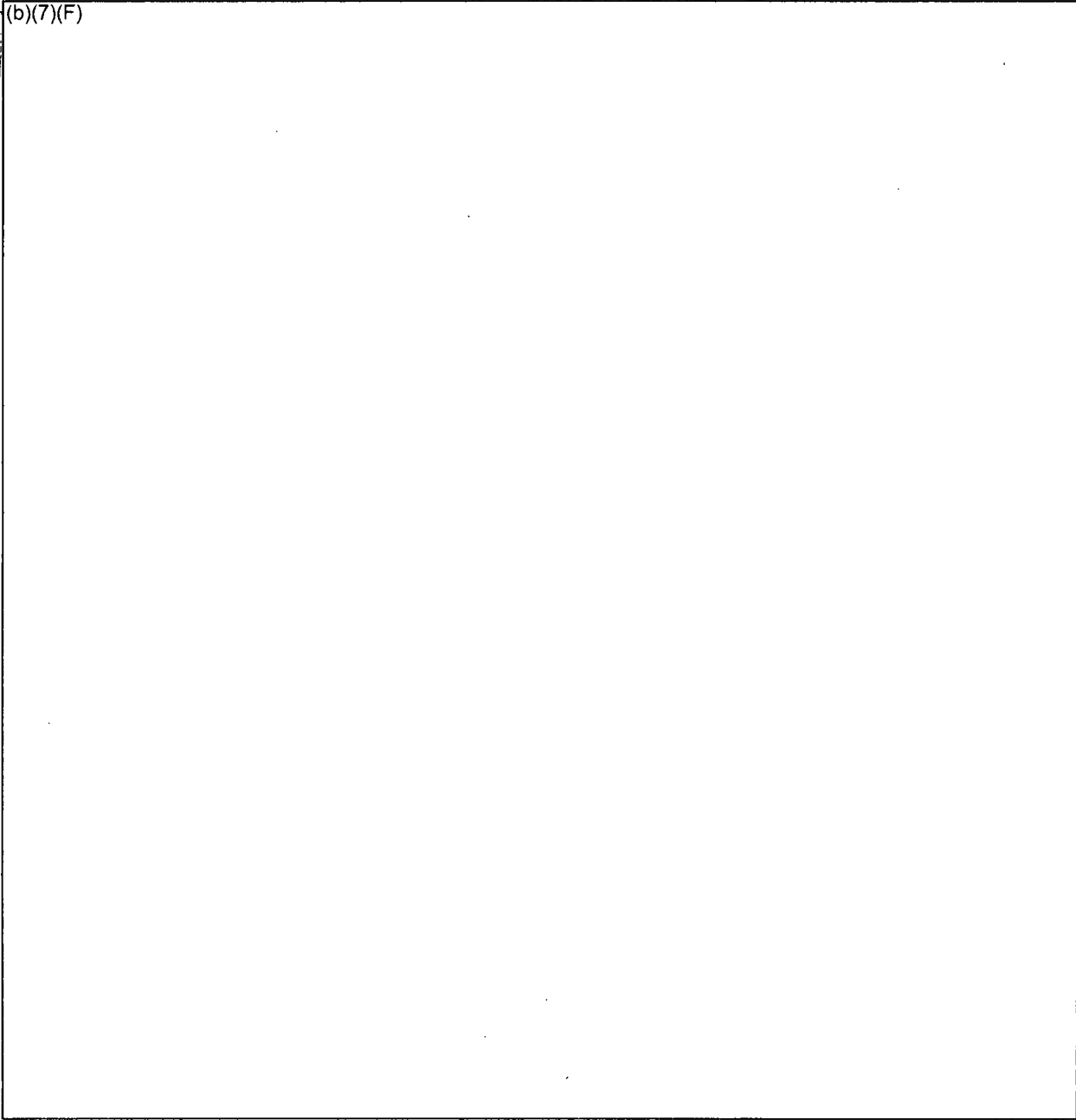


**Figure ES-1 Schematic of a BWR Reactor Building Showing the Refueling Room and Spent Fuel Pool.**

*Ex'*

Make-up Flowrate for Reference BWR SFP

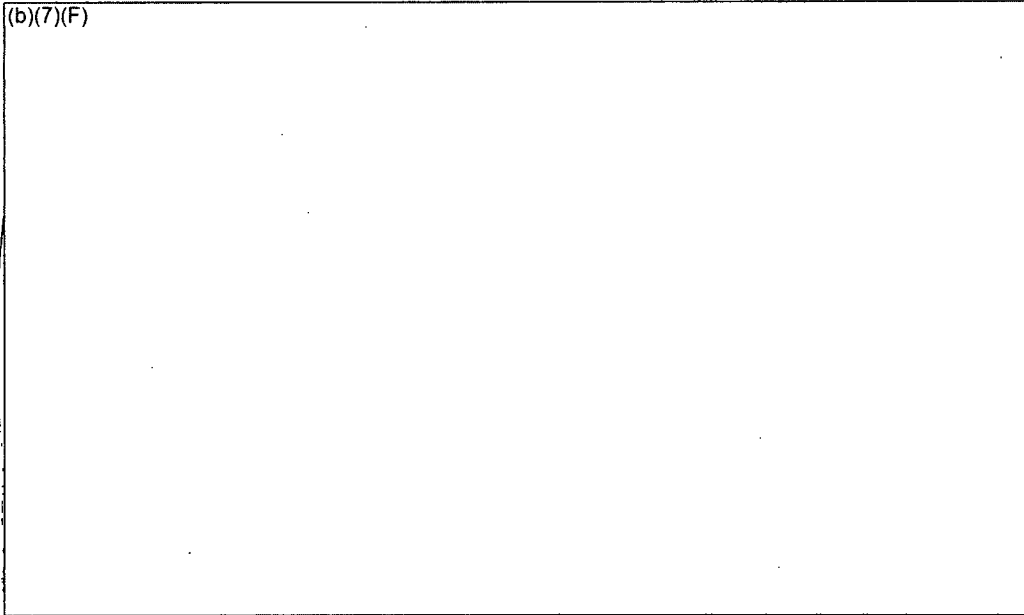


Figure ES-2 Hand Calculations to Estimate Spray Heat Removal Requirements for Leaks Above and Below the Top of the Racks.

Comparison of Peak Cladding Temperatures in a Uniform Pattern with Spray

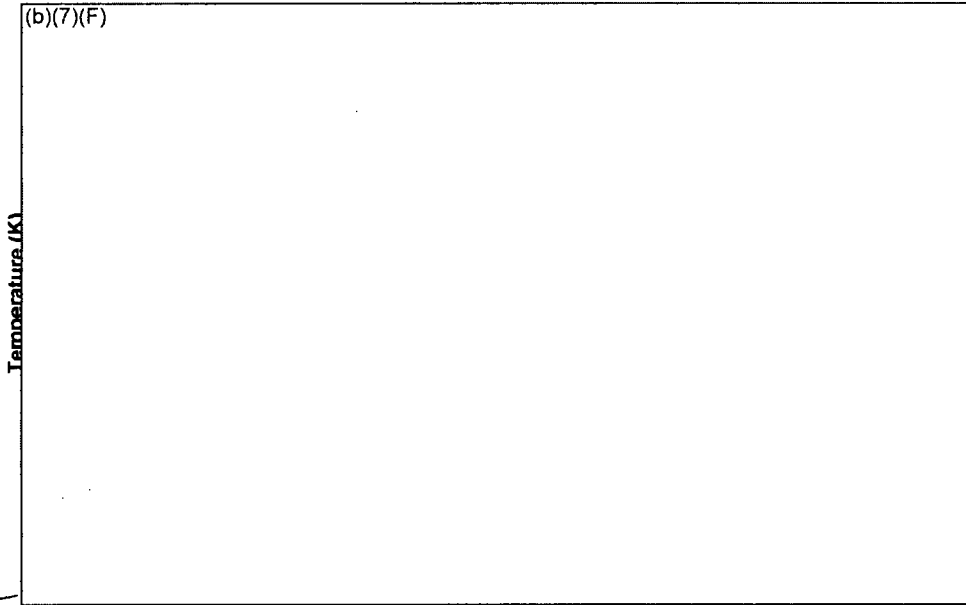


Figure ES-3 Comparison of the Peak Cladding Temperatures for the Uniform Configuration with Various Aging Periods and a Whole Pool Spray Flow of

Ex 7F (b)(7)(F)

TABLE OF CONTENTS

1. INTRODUCTION..... 1

2. BACKGROUND ..... 2

    2.1 Description of the Spent Fuel Pool ..... 2

    2.2 SFP Accident Scenarios..... 6

        2.2.1 Complete Loss-of-Coolant Inventory Accident..... 6

        2.2.2 Partial Loss-of-Coolant Accident..... 7

3. ANALYSIS METHODOLOGY ..... 9

    3.1 New BWR SFP Modeling ..... 9

        3.1.1 New BWR SFP Model..... 9

        3.1.2 Breakaway Air Oxidation Model..... 13

        3.1.3 New Hydraulic Resistance Model ..... 17

        3.1.4 Spray Modeling in MELCOR ..... 23

    3.2 MELCOR Separate Effects Model..... 26

    3.3 Whole Pool Model..... 31

        3.3.1.1 Radial Thermal Coupling..... 33

        3.3.1.2 Simplified Refueling Room Model..... 37

    3.4 Description of the Initial and Boundary Conditions ..... 41

4. SPRAY MITIGATION HAND CALCULATIONS ..... 43

    4.1 Leak Above the Top of the Racks..... 43

    4.2 Leak Below the Top of the Racks ..... 45

        4.2.1 Calculations for One Point on the BWR Spray Chart..... 47

        4.2.2 Calculations for Counter-Current Flow Limitation (CCFL)..... 48

        4.2.3 Impact of Assembly Sensible Heat ..... 50

5. WHOLE POOL MODEL BOUNDARY CONDITION CALCULATIONS..... 52

    5.1 (b)(7)(F) Spray Flow Rate..... 53

6. MELCOR SEPARATE EFFECTS MODEL RESULTS..... 57

    6.1 Summary of Separate Effect Spray Calculations ..... 57

    6.2 Separate Effects Spray Model Results for the Uniform Configuration..... 62

        6.2.1 Base Calculations for (b)(7)(F) Spray..... 62

        6.2.2 Energy Balance on Base Calculation for (b)(7)(F) Spray ..... 69

        6.2.3 Coolability Analysis for (b)(7)(F) Spray Flowrate ..... 72 Ex 7F

        6.2.4 Coolability Analysis for (b)(7)(F) Spray Flowrate ..... 73 Ex 7F

        6.2.5 Coolability Analysis for (b)(7)(F) Spray Flowrate ..... 74 Ex 7F

    6.3 Separate Effects Spray Model Results for the Checkerboard Configuration..... 75

        6.3.1 Base Calculations for (b)(7)(F) Spray..... 75 Ex 7F

6.3.2 Energy Balance on Base Calculation for (b)(7)(F) Spray ..... Ex 7F 83

6.4 Separate Effects Spray Model Results for the 1x4 Configuration Cases..... 86 Ex 7F

6.4.1 Base Calculations (b)(7)(F) Spray ..... 86

6.4.2 Energy Balance on Base Calculation for (b)(7)(F) Spray ..... Ex 7F 94

7. REFERENCES..... 97

List of Tables

Table 2-1 Spent Fuel Pool Data. .... 4

Table 2-2 Fuel Assembly Data. .... 4

Table 2-3 Spent Fuel Pool Rack Data..... 4

Table 2-4 Fuel Assembly and Rack Flow Area Data. .... 5

Table 3-1 MELCOR Fit of the Timings for Transition from Pre-Breakaway to Post-Breakaway Oxidation Reaction Kinetics for Zirlo and Zircaloy-4 in the ANL Experiments [Natesan, 2004]. .... 15

Table 3-2 S<sub>LAM</sub> And k Coefficients for the Unblocked Water Rod Assembly Assuming All Flow Passes Through the Bundle. .... 19

Table 3-3 Summary of Regions in the MELCOR Whole Pool Model..... 36

Table 3-4 Summary of Base Case SFP Model Initial Conditions for BWR SFP Emergency Spray Calculations..... 41

Table 3-5 Summary of Base Case SFP Model Boundary Conditions for BWR SFP Emergency Spray Calculations..... 42

Table 5-1 Summary of the Steady-State Water Levels as a Function of Leakage Hole Size and Spray Flow Rate..... 52

Table 6-1 Summary of the Spray Calculations ..... 58

Table 6-2 Energy Balance for the Uniform Assembly Configuration in SFP with (b)(7)(F) Spray..... Ex 7F 71

Table 6-3 Energy Balance for the Checkerboard Assembly Configuration in SFP with (b)(7)(F) Spray..... Ex 7F 85

Table 6-4 Energy Balance for 1x4 Assembly Configuration in SFP with (b)(7)(F) Spray. Ex 7F 96

**List of Figures**

Figure 2-1	Spent Fuel Pool Rack Layout.....	3
Figure 2-2	Typical Spent Fuel Pool Rack Cut-away Cross-Section Showing the Fuel Assembly.....	6
Figure 3-1	MELCOR Modeling of a BWR Assembly in the Reactor Core.....	10
Figure 3-2	Original MELCOR Modeling of BWR Assemblies in a 1x4 SFP Configuration.....	11
Figure 3-3	Heat Flow for the Original MELCOR Modeling of a BWR Assemblies in a 1x4 SFP Configuration.....	11
Figure 3-4	New MELCOR Modeling of BWR Assemblies in a 1x4 SFP Configuration.....	12
Figure 3-5	Heat Flow for the New MELCOR Modeling of BWR Assemblies in a 1x4 SFP Configuration.....	13
Figure 3-6	Comparison of the MELCOR Breakaway Timing Fit to the Zirlo and Zr-4 Data from the ANL Air Oxidation Tests.....	14
Figure 3-7	Parabolic Reaction Kinetics Coefficients for Zr-4 Oxidation.....	16
Figure 3-8	BWR Assembly Experimental Apparatus used in the Hydraulic Resistance Testing.....	20
Figure 3-9	Measured Pressure Drop over the Full, Partial, and Total Assembly Regions.....	21
Figure 3-10	Comparison of the Calculated and Measured Bypass Flow.....	22
Figure 3-11	Axial Temperature Profile in the Assembly with Spray Flow.....	24
Figure 3-12	Core Package Representation of Spray Flow.....	25
Figure 3-13	CVH Package Representation of Spray Flow.....	25
Figure 3-14	Repeating Patterns Found in the MELCOR Separate Effects Models.....	26
Figure 3-15	Schematic of the 1x4 Configuration.....	29
Figure 3-16	MELCOR Nodalization of the 5 Assembly Separate Effects Model.....	30
Figure 3-17	Schematic of the Whole Pool Model Configuration.....	32
Figure 3-18	Example of Alternating and Repeating 1x4 Patterns.....	35
Figure 3-19	The Radial Coupling Scheme as Implemented in MELCOR SFP Model.....	36
Figure 3-20	MELCOR Reactor Building Model.....	39
Figure 3-21	Example of Pressurized Water Reactor SFP Building Flow Patterns From FLUENT Calculations With An Open Roll Door.....	40
Figure 4-1	Total Decay Heat Power in the Reference BWR SFP.....	44
Figure 4-2	Make-up Flowrate for the Reference BWR SFP.....	45
Figure 4-3	Comparison of the Peak, Median, and Minimum Assembly Decay Heat Power in the Reference BWR SFP.....	46
Figure 4-4	Make-up Flowrate for the Reference BWR SFP.....	47
Figure 4-5	Timing Impact of Sensible Heat on Assembly Cooling <span style="border: 1px solid black; padding: 2px;">(b)(7)(F)</span> for a $E_x \uparrow F$ Uniform Configuration.....	51
Figure 4-6	Timing Impact of Sensible Heat on Assembly Cooling <span style="border: 1px solid black; padding: 2px;">(b)(7)(F)</span> for a $E_x \uparrow F$ Uniform Configuration.....	51
Figure 5-1	$E_x \uparrow F$ Water Level Boundary Condition from the BWR Whole Pool Model with <span style="border: 1px solid black; padding: 2px;">(b)(7)(F)</span> and a Spray Flow <span style="border: 1px solid black; padding: 2px;">(b)(7)(F)</span> .....	54
Figure 5-2	Vapor and Liquid Temperature Boundary Condition from the BWR Whole Pool Model with <span style="border: 1px solid black; padding: 2px;">(b)(7)(F)</span> and a Spray Flow <span style="border: 1px solid black; padding: 2px;">(b)(7)(F)</span> .....	54 $E_x \uparrow F$

Figure 5-3 Steam Partial Pressure Boundary Condition from the BWR Whole Pool Model with (b)(7)(F) ..... 55 Ex 7F

Figure 5-4 Whole Pool Level Response from a (b)(7)(F) with (b)(7)(F) and a Spray Flow of (b)(7)(F) ..... 55 Ex 7F

Figure 5-5 Gas Concentration in the Refueling Room above the SFP (b)(7)(F) and a Spray Flow of (b)(7)(F) ..... 56 Ex 7F

Figure 5-6 Comparison of the Leak Rate and Spray Flowrate Response from a (b)(7)(F) and a Spray Flow of (b)(7)(F) ..... 56 Ex 7F

Figure 6-1 Comparison of the Peak Cladding Temperatures for the (b)(7)(F) with a Uniform Configuration with (b)(7)(F) Spray Flow of (b)(7)(F) ..... 64 Ex 7F

Figure 6-2 Comparison of the Peak Cladding Temperatures for (b)(7)(F) with a Uniform Configuration with (b)(7)(F) Spray Flow of (b)(7)(F) ..... 65 Ex 7F

Figure 6-3 Assembly Cladding Temperatures for the Uniform Configuration with (b)(7)(F) Spray Flow (Case S1)..... 65 Ex 7F

Figure 6-4 Assembly Cladding Temperatures for the Uniform Configuration with (b)(7)(F) Spray Flow, and the Flow Regime Model Inactive (Case S1a). ..... 66 Ex 7F

Figure 6-5 Assembly Cladding Temperatures for the Uniform Configuration with (b)(7)(F) and No Spray Flow (Case S1b). ..... 66 Ex 7F

Figure 6-6 Assembly Cladding Temperatures for the Uniform Configuration with (b)(7)(F) Spray Flow and Plugged Inlet (Case S1p). ..... 67 Ex 7F

Figure 6-7 Axial Cladding Temperature Profiles for the (b)(7)(F) Uniform Configuration, (b)(7)(F) Spray Flow at (b)(7)(F) ..... 67 Ex 7F

Figure 6-8 Axial Temperature Profiles for the (b)(7)(F) Uniform Configuration, (b)(7)(F) Spray Flow as a Function of Time..... 68 Ex 7F

Figure 6-9 Axial Temperature Profiles for the (b)(7)(F) Uniform Configuration, (b)(7)(F) and No Spray Flow as a Function of Time. .... 68 Ex 7F

Figure 6-10 Time-averaged Energy Flow in the Uniform Configuration with (b)(7)(F) (F) and (b)(7)(F) Spray Flow..... 70 Ex 7F

Figure 6-11 Comparison of the Peak Cladding Temperatures for the Uniform Configuration with Various Aging Periods and a Whole Pool Spray Flow of (b)(7)(F) ..... 72 Ex 7F

Figure 6-12 Comparison of the Peak Cladding Temperatures for the Uniform Configuration with Various Aging Periods and a Whole Pool Spray Flow of (b)(7)(F) ..... 73 Ex 7F

Figure 6-13 Comparison of the Peak Cladding Temperatures for the Uniform Configuration with Various Aging Periods and a Whole Pool Spray Flow of (b)(7)(F) ..... 74 Ex 7F

Figure 6-14 Comparison of the Peak Cladding Temperatures for the (b)(7)(F) with a Checkerboard Configuration (b)(7)(F) and a Whole Pool Spray Flow of (b)(7)(F) ..... 77 Ex 7F

Figure 6-15	Comparison of the Peak Cladding Temperatures for the (b)(7)(F) with a Checkerboard Configuration (b)(7)(F) and a Whole Pool Spray Flow (b)(7)(F).....	77	Ex 7F
Figure 6-16	High-Powered Assembly Cladding Temperatures for the Checkerboard Configuration (b)(7)(F) Spray Flow (Case S3).....	78	Ex 7F
Figure 6-17	Low-Powered Assembly Cladding Temperatures for the Checkerboard Configuration (b)(7)(F) Spray Flow (Case S3).....	78	Ex 7F
Figure 6-18	High-Powered Assembly Cladding Temperatures for the Checkerboard Configuration (b)(7)(F) Spray Flow and the Flow Regime Model Inactive (S3a).....	79	Ex 7F
Figure 6-19	Low-Powered Assembly Cladding Temperatures for the Checkerboard Configuration (b)(7)(F) Spray Flow and the Flow Regime Model Inactive (S3a).....	79	Ex 7F
Figure 6-20	High-Powered Assembly Cladding Temperatures for the Checkerboard Configuration (b)(7)(F) and No Spray Flow (Case S3b).....	80	Ex 7F
Figure 6-21	Low-Powered Assembly Cladding Temperatures for the Checkerboard Configuration (b)(7)(F) and No Spray Flow (Case S3b).....	80	Ex 7F
Figure 6-22	High-Powered Assembly Cladding Temperatures for the Checkerboard Configuration (b)(7)(F) Spray Flow and Plugged Inlet (Case S3p).....	81	Ex 7F
Figure 6-23	Low-Powered Assembly Cladding Temperatures for the Checkerboard Configuration (b)(7)(F) Spray Flow and Plugged Inlet (Case S3p).....	81	Ex 7F
Figure 6-24	High-Powered Assembly Cladding Temperature Profiles for the Checkerboard Configuration with (b)(7)(F) and (b)(7)(F) Spray Flow.....	82	Ex 7F
Figure 6-25	Low-Powered Assembly Cladding Temperature Profiles for the Checkerboard Configuration with (b)(7)(F) and (b)(7)(F) Spray Flow.....	82	Ex 7F
Figure 6-26	Time-average Energy Flow in the Checkerboard Configuration (b)(7)(F) (b)(7)(F) and a Whole Pool Spray Flow (b)(7)(F).....	84	Ex 7F
Figure 6-27	Comparison of the Peak Cladding Temperatures for the (b)(7)(F) with a 1x4 Configuration with (b)(7)(F) and a Whole Pool Spray Flow (b)(7)(F).....	88	Ex 7F
Figure 6-28	Comparison of the Peak Cladding Temperatures for (b)(7)(F) with a 1x4 Configuration (b)(7)(F) and a Whole Pool Spray Flow (b)(7)(F).....	88	Ex 7F
Figure 6-29	Center Assembly Cladding Temperatures for the 1x4 Configuration with (b)(7)(F) Spray Flow (Case S4).....	89	Ex 7F
Figure 6-30	Peripheral Assembly Cladding Temperatures for the 1x4 Configuration with (b)(7)(F) Spray Flow (Case S4).....	89	Ex 7F
Figure 6-31	Center Assembly Cladding Temperatures for the 1x4 Configuration with (b)(7)(F) Spray and the Flow Regime Model Inactive (Case S4a).....	90	Ex 7F

Ex 7F

Figure 6-32 **Peripheral Assembly Cladding Temperatures for the 1x4 Configuration with** (b)(7)(F) **Spray and the Flow Regime Model Inactive**  
(Case S4a). ..... 90

Ex 7F

Figure 6-33 **Center Assembly Cladding Temperatures for the 1x4 Configuration with** (b)(7)(F) **and No Sprays (Case S4b).** ..... 91

Ex 7F

Figure 6-34 **Peripheral Assembly Cladding Temperatures for the 1x4 Configuration with** (b)(7)(F) **and No Spray Flow (Case S4b).** ..... 91

E 7F

Figure 6-35 **Center Assembly Cladding Temperatures for the 1x4 Configuration with** (b)(7)(F) **Spray Flow and Plugged Inlet (Case S4p).** ..... 92

Ex 7F

Figure 6-36 **Peripheral Assembly Cladding Temperatures for the 1x4 Configuration with** (b)(7)(F) **Spray Flow and Plugged Inlet (Case S4p).** ..... 92

Ex 7F

Figure 6-37 **Center Assembly Axial Cladding Temperatures for the 1x4 Configuration** (b)(7)(F) **Spray Flow.** ..... 93

Figure 6-38 **Peripheral Assembly Axial Cladding Temperatures for the 1x4**  
**Configuration with a** (b)(7)(F) **Spray Flow.** ..... 93

Ex 7F

Figure 6-39 **Time-averaged Energy Flow in the 1x4 Configuration with** (b)(7)(F) **and a Whole Pool Spray Flow** (b)(7)(F) ..... 95

Ex 7F

## Analysis of Emergency Spray Mitigation of Spent Fuel Pool Loss-of-Coolant Inventory Accidents

### 1. INTRODUCTION

In 2001, United State Nuclear Regulatory Commission (NRC) staff performed an evaluation of the potential accident risk in a spent fuel pool (SFP) at decommissioning plants in the United States [NUREG-1738]. The study was prepared to provide a technical basis for decommissioning rulemaking for permanently shutdown nuclear power plants. The study described a modeling approach of a typical decommissioning plant with design assumptions and industry commitments; the thermal-hydraulic analyses performed to evaluate spent fuel stored in the spent fuel pool at decommissioning plants; the risk assessment of spent fuel pool accidents; the consequence calculations; and the implications for decommissioning regulatory requirements. It was known that some of the assumptions in the accident progression in NUREG-1738 were necessarily conservative, especially the estimation of the fuel damage. Subsequently, the NRC desired to expand the study to include accidents in the spent fuel pools of operating power plants. Consequently, the NRC has continued spent fuel pool accident research by applying best-estimate computer codes to predict the severe accident progression following various postulated accident initiators. This report describes the effectiveness of emergency sprays systems for mitigating spent fuel pool accidents.

The data used to perform these calculations were developed from an operating boiling water reactor (BWR). The reference plant is typical of many BWRs with fuel in the SFP from several decades old to the most recent offload. This reference plant has a two-year fuel cycle and roughly discharges one-third of the reactor fuel <sup>(b)(7)(F)</sup> each outage. The plant removes an equivalent amount of various aged fuel between outages for storage in dry casks, thereby maintaining a relatively constant number of assemblies in the SFP. Hence, the SFP has a wide variety of different aged fuel. In addition, the SFP racks have enough empty cell locations <sup>(b)(7)(F)</sup> to permit a complete emergency reactor offload as well as store all the refueling blade guides.

The MELCOR 1.8.5 severe accident computer code [Gauntt] with enhancements through Version RP is used to simulate the SFP accident response. MELCOR includes fuel degradation models for pressurized water reactor (PWR) and BWR fuel, radiation, convection, and conduction heat transfer models, air and steam oxidation models, hydrogen burn models, two-phase thermal-hydraulic models, and fission product release and transport models. Therefore, it contains the basic models to address questions and phenomena expected during a spent fuel pool accident.

Version RP includes three recent modeling enhancements applicable to BWR SFP modeling, (1) a new rack component, which permits better modeling of a SFP rack, (2) a new oxidation kinetics model, and (3) a simplified flow regime model. The new BWR spent fuel pool rack component permits proper radiative modeling of the SFP rack between groups of different assemblies. The new oxidation kinetics model predicts the transition to breakaway oxidation in

air environments on a node-by-node basis.<sup>2</sup> The simplified flow regime model and an expanded axial CVH nodalization corresponding to a 1:1 matching of the COR nodalization permitted simulation of liquid films draining down the BWR fuel assemblies during spray operation.

## 2. BACKGROUND

The reference plant for the SFP analysis is a large BWR. Like most other nuclear plants, the reference plant has installed high-density racks to maximize the storage of fuel in the SFP. A description of the reference plant SFP is given in 2.1. The accidents considered in the present study consist of a loss-of-coolant inventory. A description of the accident progression is provided in Section 2.2.

### 2.1 Description of the Spent Fuel Pool

The spent fuel pool, 40 feet wide by 35.3 feet long by 38 feet deep, is located on the refueling floor (b)(7)(F) of the reactor building. The pool is constructed of reinforced concrete with a wall and floor lining of 1/4-inch thick stainless steel. The walls and the floor of the spent fuel pool are approximately 6'. In the northeast corner of the SFP is a cask area of 10' square (see Figure 2-1). The general attributes of the spent fuel pool, the BWR fuel assemblies, the spent fuel pool racks, and the assembly and rack flow areas are described in Table 2-1, Table 2-2, Table 2-3, and Table 2-4, respectively.

The high density SFP racks provide spent fuel storage at the bottom of the fuel pool. The fuel storage racks are normally covered with about 23 ft of water for radiation shielding. The SFP racks are freestanding, full length, top entry and are designed to maintain the spent fuel in a spaced geometry, which precludes the possibility of criticality under any condition.

The high-density SFP racks are of the "poison" type utilizing a neutron absorbing material to maintain a subcritical fuel array. The racks are rectilinear in shape and are of nine different sizes. A total (b)(7)(F) storage locations are provided in the pool. The racks are constructed of stainless steel materials and each rack module is composed of cell assemblies, a base plate, and base support assemblies. Each cell is composed of (a) a full-length enclosure constructed of 0.075" thick stainless steel, (b) sections of Bisco Boraflex, which is a neutron absorbing material, and (c) wrapper plates constructed of 0.020" tick stainless steel. The inside square dimension of a cell enclosure is 6.07". The cell pitch is 6.28".

The base plate is a 0.5" thick stainless steel with 3.8" chamfered through holes centered at each storage location, which provides a seating surface for the fuel assemblies. These holes also provide passage for coolant flow.

Each rack module has base support assemblies (i.e., 'rack feet') located at the center of the corner cells within the module and at interior locations<sup>3</sup> to distribute the pool floor loading (e.g., see Figure 2-2). Each base assembly is composed of a level block assembly, a leveling screw,

<sup>2</sup> It should be noted that the steam oxidation model does not use a breakaway kinetics model. Steam-zircaloy oxidation is based on the default Urbanic-Heidrich model [Gauntt].

<sup>3</sup> There are several different rack sizes in the SFP. However, for a 19x10 size rack, there are 18 base support assemblies, 14 on the perimeter and 4 in the interior.

and a support pad. The top of the leveling block assembly is welded to the bottom of the base plate. SFP fuel cells are located above each rack foot. Four 1" holes are drilled into the side of the support pad. The interior of the support pad is hollow and permits flow to the opening in the base plate.

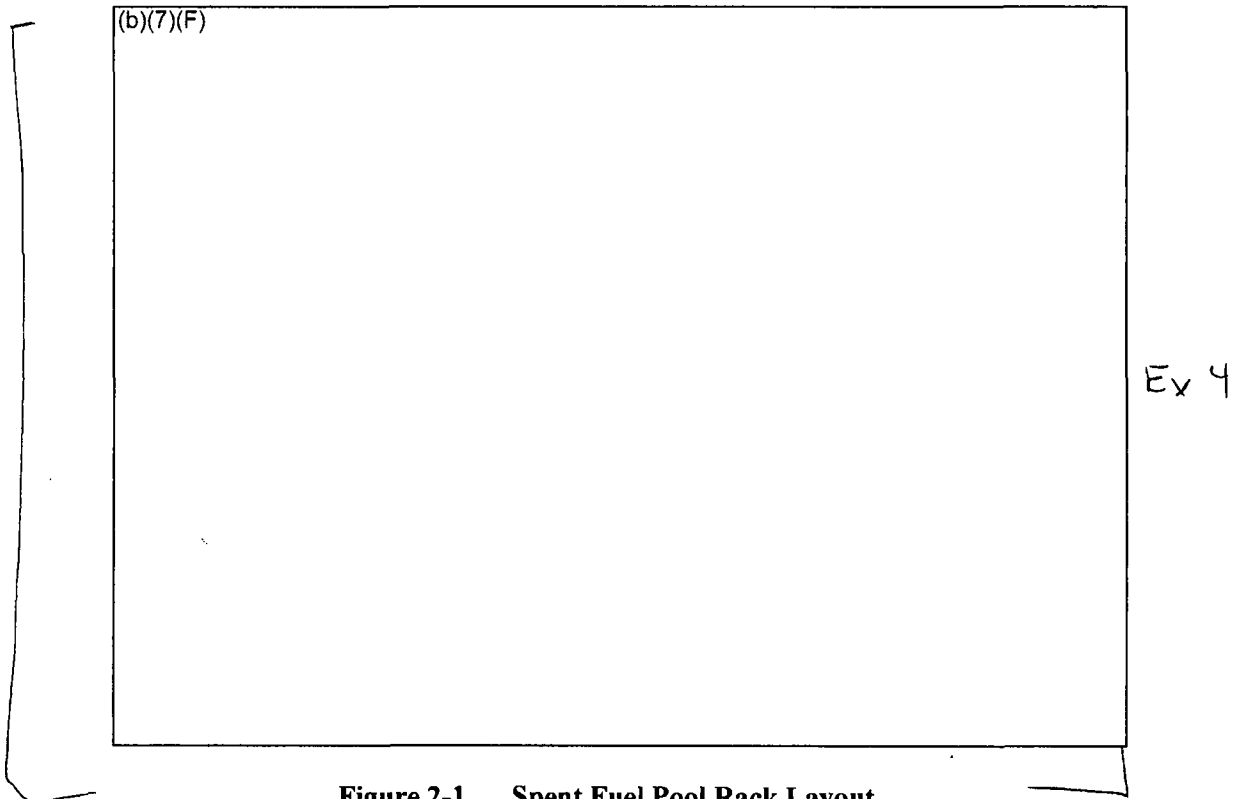


**Figure 2-1 Spent Fuel Pool Rack Layout.**

Table 2-1 Spent Fuel Pool Data.

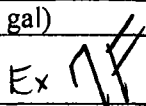
SFP Pool Characteristics	Description or Dimensions
Dimensions	480" x 424" 10 ft square Cask Area in NW corner 39' high walls
Concrete thickness	~6 feet
SFP Volume	53,350 ft <sup>3</sup> (399,000 gal)
Number of storage locations	(b)(7)(F) Ex 

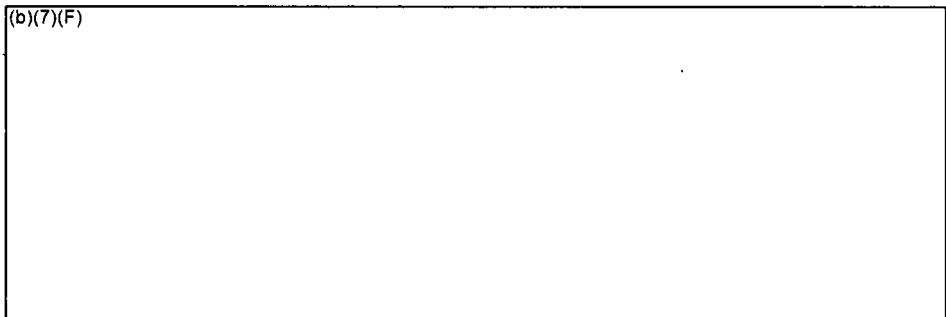
Table 2-2 Fuel Assembly Data.

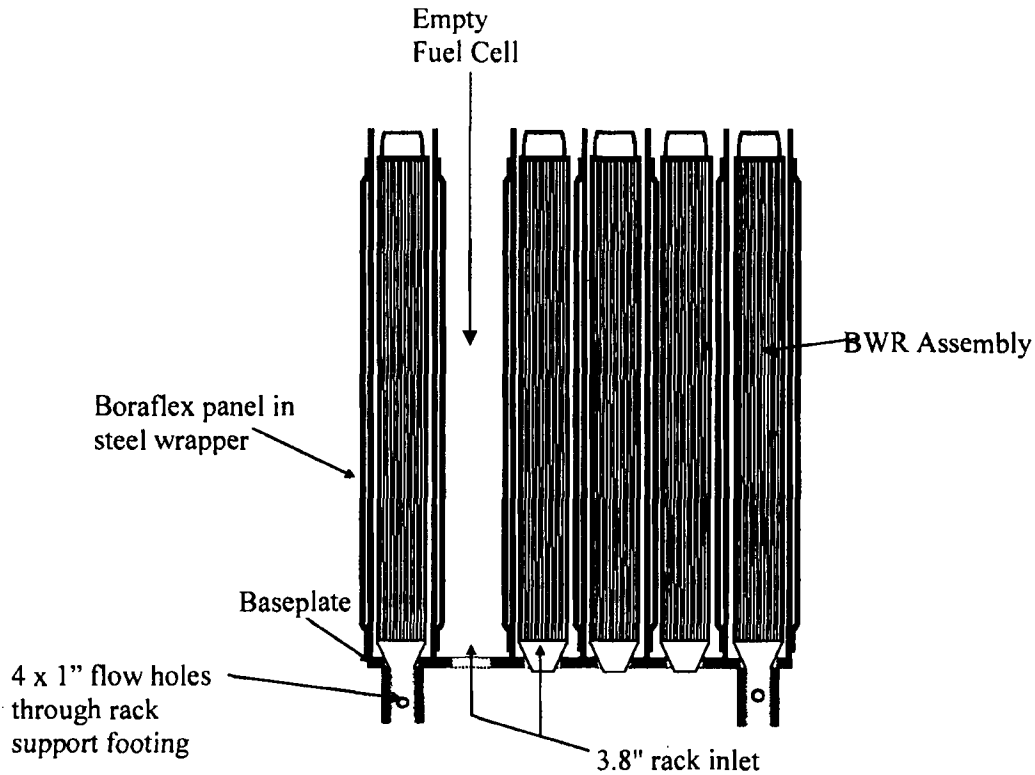
Assembly Characteristics	Description or Dimensions
Fuel Type	GE 9x9
Number of Fuel Rods	74
Fuel Pitch	0.566"
Fuel Rod Dimensions	0.44" OD 0.028" Cladding 146" Active Length
Maximum Initial Enrichment	4% U-235 by weight
Number of Water Rods	2
Water Rod Dimensions	0.98" OD Zircaloy

Table 2-3 Spent Fuel Pool Rack Data.

SFP Rack Characteristics	Description or Dimensions
Rack Height Above the Base Plate	169"
Baseplate Thickness	0.5"
Support Leg Height	7.25"
Poison Material	Boraflex
Cell Pitch	6.28
Cell Construction	0.075" (Gage 14) 304 stainless steel walls with Bisco Boraflex B <sub>4</sub> C particles clad in a non-metallic binder (0.081") with 0.020" stainless wrapper

(b)(7)(F)





**Figure 2-2** Typical Spent Fuel Pool Rack Cut-away Cross-Section Showing the Fuel Assembly.

## 2.2 SFP Accident Scenarios

From a natural circulation flow perspective, the SFP accidents are broken down into two categories; scenarios with water above the base plate of the racks and scenarios with a completely drained SFP. Each accident is described next.

### 2.2.1 Complete Loss-of-Coolant Inventory Accident

In the "air" flow case, the accident is initiated with a complete loss-of-coolant accident (see Figure ES-1 for pre-accident building configuration and Figure 2-2 for the rack configuration). Due to the removal of the water, a heat-up of the fuel rods ensues. The fuel rods heat the air in the assemblies, which creates a natural circulation pattern. Complex flow patterns develop above and around the SFP racks and in the refueling room due to the interaction between the hot rising plume and descending cool air. After the hot plume exits the SFP, the plume will rise to the ceiling and spread radially within the hot gas layer at the top of the refueling room. The degree of heating in the spent fuel storage building and behavior of the hot gas layer depends on many factors including the rate of ventilation (e.g., ventilation system operation, openings or

leakage, and/or structural failures), the heat loss through the building walls and ceiling, and other accident thermal effects (e.g., fire).

The flow patterns of the gases under the racks are also complicated. The regions of down flow include the space between the rack and walls, some of the empty rack slots, and the cask region or other open areas. If a high speed flow region develops under the racks, then there can be a Bernoulli Effect. For example, if the air to the SFP cells is preferentially provided through the cask area, a high speed flow (i.e., 3 m/s) can develop under the rack cells adjacent to the cask area. The high speed flow reduces the upflow of gases into the affected assemblies, which leads to less heat removal and a faster heat-up (e.g., see [Wagner, 2000]).

If inadequate cooling is provided, then the fuel cladding will heat up and the Zircaloy cladding will rapidly oxidize (i.e., burn) and to a lesser extent, nitride (i.e., combine with nitrogen if no oxygen or steam are available). Since the oxidation and nitride processes are exothermic, the fuel rods could heat to melting conditions and structurally degrade. Meanwhile, the steel racks supporting the fuel assemblies will also heat due to convection and radiation from the fuel assemblies. The timing of the degradation of the specific fuel assemblies and racks are affected by the decay heat level (i.e., burn-up, power history, enrichment, and time since discharge), the assembly inlet temperature, convective and conductive heat removal rates, and the heat transfer rate from/to adjacent assemblies. Finally, and most importantly, the degradation of the fuel rods can lead to fission product releases.

An accurate analysis of the SFP response requires consideration of the aforementioned phenomena. As evidenced by the accident description, there is a large range of geometric length scales and modeling requirements. The length scales range from details of the individual assembly heat generation and flow patterns (e.g., also including multi-dimensional flow within an assembly, see [Ross, 2003]), intra-assembly heat transfer, large scale flow patterns above, below, and through the racks, and the building response (e.g., ventilation, heat loss, structural failures, etc.). The relevant physics and phenomena include heat transfer (convection, conduction, and radiation), fluid flow (small scale to large scale), chemical reactions (i.e., oxidation), severe accident fuel degradation behavior, and fission product release and transport.

### **2.2.2 Partial Loss-of-Coolant Accident**

In the second type of accident, the SFP is partially drained (i.e., due to partial drain or boil-off) and does not include recirculation of hot gases through the bottom of racks. Consequently, the gas in the fuel assemblies above the pool level is relatively stagnant (i.e., except for steam flow from boiling). In this condition, steam cooling and/or a level swell from the boiling will keep the fuel rods cool unless the pool level drops too far. However, once the level drops below roughly one-half of the fuel height, the top of the fuel rods will heat-up and degrade.

If the top of the fuel is uncovered, then several new phenomena occur in a partial loss-of-coolant accident. First, the convective flows are much smaller than a complete loss-of-coolant accident. In the complete loss-of-coolant accident, there was ample air flow as the assembly heated. However, in a partial loss-of-coolant accident, the fluid in the assembly is relatively stagnant because the pool blocks the bottom of the racks. The primary source of cooling comes from

steam flow due to boiling below the water level. Hence, there are competing effects of the lack of a strong convective flow versus the benefits of some steam cooling and axial conduction to the water. In summary, the scenarios with water include (a) two-phase boiling, (b) an assembly flow rate that is strongly affected by the amount of boiling below the water surface, and (c) gas inlet temperature that is limited to the boiling point of water (i.e., the air cases are not similarly constrained).

The rate of oxidation of the Zircaloy cladding is the second key difference expected in a partial loss-of-coolant accident. In particular, the fluid next to the Zircaloy cladding will be steam rather than air. Steam also reacts exothermically with Zircaloy but at a slower rate than with air. Furthermore, the byproduct of this reaction is hydrogen. The hydrogen will replace the steam and retard or stop the Zircaloy/steam reaction. Consequently, the reaction could become "steam starved" and controlled by the rate of steam production by boiling below the pool level, which is expected to be very low for aged spent fuel. If there is adequate steam when the Zircaloy reaches high temperatures (i.e., >1500 K), the power from metal water reactions can be much larger than decay heat. Therefore, there are two competing effects on the rate of fuel degradation relative to the complete loss-of-inventory accident scenario (i.e., as described in Section 2.2.1), (1) a lower, controlled oxidation effect (i.e., due to steam starvation) and (2) a much lower convective cooling rate (i.e., because the bottom of the racks are "plugged" with water).

Finally, a third new difference in the partial loss-of-coolant accident is the behavior of the hydrogen. As hydrogen is produced during fuel degradation, the hydrogen may collect and mix with oxygen in the air above the pool. Given the appropriate conditions, the hydrogen could ignite and possibly cause structural damage to the reactor building. Any damage or enhanced leakage caused by the pressurization from the hydrogen burn could increase the release of fission products and their associated adverse consequences.

As will be discussed in Section 5, spray operation complicates the potential for water plugging the inlet to the racks. For appropriate combinations of leakage and sprays rates and leakage location, the spray flow can maintain a water level above the base plate of the racks. Consequently, spray operation in some circumstances will stop air natural circulation. Depending upon the relative magnitudes of the spray flow and decay heat power, the resultant configuration may be less effectively cooled.

### **3. ANALYSIS METHODOLOGY**

Based on the information supplied by the reference plant staff, MELCOR models were developed to perform accident analyses (e.g., see [Wagner, 2003] and [Wagner, 2004]). Since those analyses were performed, there have been several significant improvements in the modeling of the SFPs. Section 3.1 summarizes those improvements. Several different models were used for the detailed evaluations of the fuel response to emergency spray. A description of the MELCOR separate effects models are presented in Section 3.2. The separate effects models were used to simulate the details of the spray penetration into the assemblies. Next, the whole pool models are described in Section 3.3. The whole pool models were used to calculate boundary conditions for the separate effects models as well as calculate the spray scrubbing efficiency and the source term behavior.

#### **3.1 New BWR SFP Modeling**

Since the last report on BWR SFP modeling, there have been a number of improvements in MELCOR's modeling capabilities. Section 3.1.1 describes the new BWR-SFP Core Package model with the new Rack component. Next, Section 3.1.2 describes the new breakaway oxidation kinetics model based on experiments at Argonne National Laboratory. The fuel geometric model was completely updated to include partial fuel rods, the hydraulic effects of water rod flow, and other detailed weight and geometric information from GNF hardware used in the SNL SFP experiments. In addition, a new flow resistance model was implemented based on detailed flow tests. The pertinent results from the SNL experimental program are described in Section 3.1.3. Finally, a technique to model the spray thermal-hydraulic response in MELCOR was developed and is described in Section 3.1.4.

##### **3.1.1 New BWR SFP Model**

Previous MELCOR BWR SFP calculations were performed using the "BWR" model designation in the COR Package input (i.e., [Wagner, 2003] and [Wagner 2004]). Once the model designation is selected, certain fixed geometry specifications are made. At the time of the original calculations, only the BWR and PWR model designations were available. The BWR designation assumes the BWR fuel rods are surrounded by a BWR canister. Outside the canister is a control blade (see Figure 3-1). Typically in a MELCOR reactor application, concentric rings are used to model the fuel in the core. Ring 1 would represent the center of the core and successive, concentric rings would represent annular regions of assemblies with increasing radii to the edge of the core.

MELCOR 1.8.5 BWR Model  
("Blade" is enclosed inside the ring)

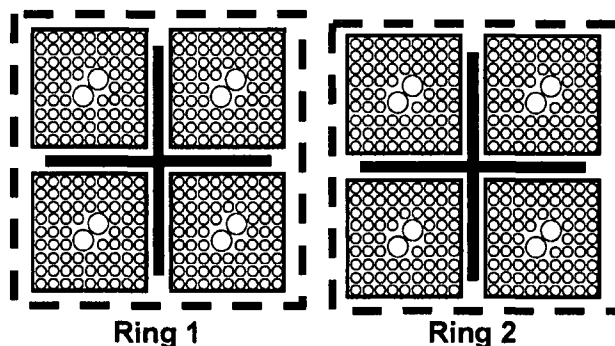
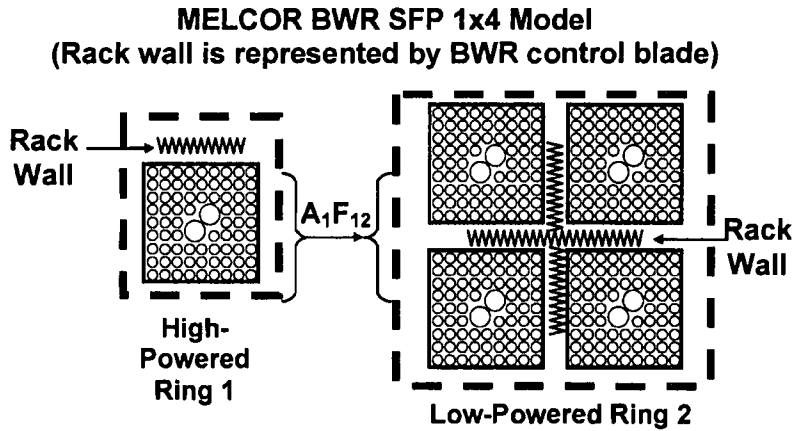


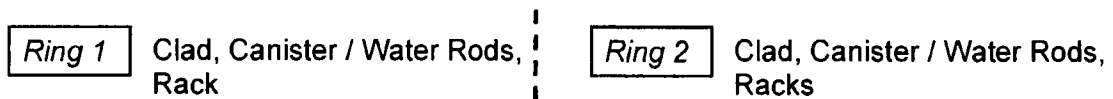
Figure 3-1 MELCOR Modeling of a BWR Assembly in the Reactor Core.

For application to the SFP geometry, it was not possible to explicitly model the SFP rack. The only components available are those shown Figure 3-1, i.e., the fuel and cladding, the canister, and the control blade. For the original SFP BWR calculations, the control blade component was used to model the rack. The SFP BWR 1x4 configuration is shown in Figure 3-2. Although the rack walls are contained internally within a ring, the appropriate surface area and mass was properly conserved. From a radiation heat transfer perspective, heat flows from adjacent rings between the canister walls. In particular, the radiation heat transfer from Ring 1 to Ring 2 in Figure 3-2 occurs from the canister of Ring 1 to the canister of Ring 2 (i.e., see Figure 3-3). Simultaneously, radiative exchange is also calculated within each ring from the canister wall to the rack wall (i.e., see summary in Figure 3-3). Consequently, from a radiation perspective, the rack wall is not correctly represented between the adjacent rings of fuel assemblies. Similarly, the surface areas for convection are preserved. However, the adjacent fluid temperature for the racks is characteristic of the region within a ring (i.e., the bypass fluid region outside the canister) rather than the Ring 1 bypass on interior side and the Ring 2 bypass on the exterior side.

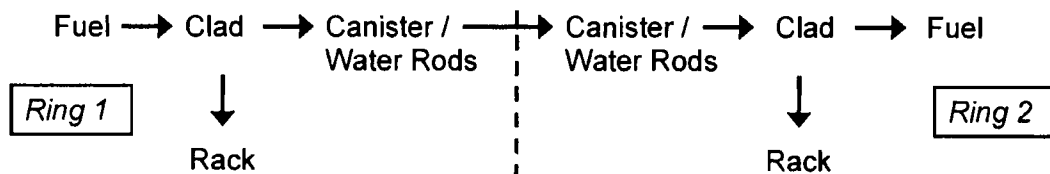


**Figure 3-2 Original MELCOR Modeling of BWR Assemblies in a 1x4 SFP Configuration.<sup>4</sup>**

**Convective Heat Transfer Surfaces:**



**Radiative Heat Transfer Flow Path:**



- Rack is modeled via a Control Rod Blade component

**Figure 3-3 Heat Flow for the Original MELCOR Modeling of a BWR Assemblies in a 1x4 SFP Configuration.**

During and subsequent to the original BWR SFP separate effects calculations, additional scoping work was done to estimate the impact of the aforementioned heat transfer limitation. For the configuration of a single assembly in a uniform decay heat region (i.e., the configuration for many of the calculation), the heat transfer rate from the fuel would be too high prior to achieving steady state conditions because heat was simultaneously transferring directly to the rack wall and the canister. However, due to the efficiency of high temperature radiation from thin structures with large surface areas the thermal coupling between the fuel rods and the rack wall was

<sup>4</sup> The rack wall is shown in a zigzag pattern to only emphasize the correct surface and mass was preserved while wholly containing the rack wall on the inside of Rings 1 and 2.

expected to be very close<sup>5</sup>. The greatest impact was expected to occur in a 1x4 configuration where radiative heat transfer from a high-powered center assembly to four adjacent peripheral assemblies. In this configuration, the rack wall would be a radiation barrier between the center assembly and the peripheral assemblies. Hence, the thermal coupling shown in Figure 3-2 and Figure 3-3 would be over-estimated.

Subsequent to the release of the original MELCOR BWR separate effects report ([Wagner, 2003]), MELCOR was modified to include "SFP-BWR" and "SFP-PWR" model types. The new designator specified the geometry as shown in Figure 3-4 for the 1x4 configuration and the radiation and convection solution as shown in Figure 3-5. Consequently, the rack wall around Ring 1 is properly placed between the Ring 1 and Ring 2 assemblies. The remaining rack walls for the four peripheral assemblies in Ring 2 is placed at the outer boundary of Ring 2, which is an adiabatic boundary condition for the 1x4 simulations. Similar to previous models, the rack wall was comprised of steel and control material. The MELCOR models described in Section 3.2 and 3.3 used this designation.

**Introduced in MELCOR 1.8.5 Version RO  
"SFP-BWR" Model Representation of 1x4 Model  
(Cell wall is represented by new rack component)**

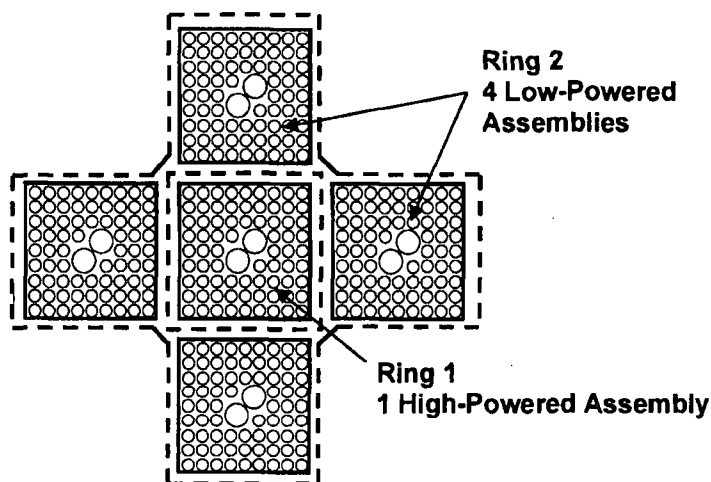
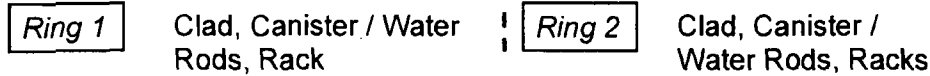


**Figure 3-4 New MELCOR Modeling of BWR Assemblies in a 1x4 SFP Configuration.**

<sup>5</sup> These limitations were recognized early and have been steadily examined with increasingly sophisticated approaches. Initially, the MELCOR heat structure components were used to examine the heat flow for a uniform configuration. Subsequently, three-dimensional COBRA-SFS calculations were performed for the 1x4 configuration. Next, MELCOR was modified as described in this section to properly represent the geometric location of the rack wall and the radiative exchange in a 1x4 configuration. Most recently, analysis of experimental work is being done with the new SFP-BWR configuration. Each of the complimentary analyses has confirmed the goodness of this assumption. The more accurate SFP-BWR 1x4 model only shows a minor degradation of radial radiative heat transfer at high temperatures.

**Convective Heat Transfer Surfaces:**



**Radiative Heat Transfer Flow Path:**

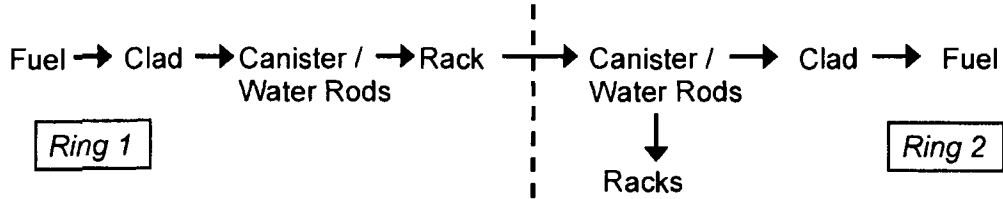


**Figure 3-5 Heat Flow for the New MELCOR Modeling of BWR Assemblies in a 1x4 SFP Configuration.**

Finally, as implied in Figure 3-5, MELCOR does not include explicit modeling of the water rods. The two large water rods in the center of a 9x9 GNF assembly are modeled indirectly as additional mass and surface area on the canister component. As a new feature in the “SFP-BWR” model, the inside and outside surface area of the canister component can be specified independently. The water rod masses and surface areas were added to the canister mass and canister inside surface area, respectively. Hence, the proper outer canister surface to the rack was preserved as well as the thermal coupling from the fuel rods to the canister and the water rods. Previously, the surface area of the water rods was ignored but the mass was included as part of the canister.

**3.1.2 Breakaway Air Oxidation Model**

Argonne National Laboratory (ANL) has performed oxidation kinetics testing on Zr-based alloys including Zircaloy-4, which is similar to the Zircaloy-2 alloy used in the reference BWR plant assemblies. The testing showed that air oxidation can be observed at temperatures as low as 600 K. In the tests, a specimen was held at constant temperature and the weight gain due to oxidation as a function of time was measured. The reaction rates for air oxidation are described by parabolic kinetics similar to the ones used to describe steam oxidation. The general form of the equation is,

$$\frac{dw^2}{dt} = K(T) \tag{Eqn. 2.1}$$

where, w is oxide scale thickness or, alternatively, in the MELCOR convention, reacted metal mass. The rate of oxidation was initially steady versus the square root of time at a particular temperature. However, the rate of oxidation increased after some time and persisted for the remainder of the test.

A new oxidation model was implemented in MELCOR by adding a breakaway lifetime calculation. The model calculates an oxidation "lifetime" value for Zircaloy components in each cell using the local Zircaloy cladding temperature. Figure 3-6 shows the breakaway timing data from the ANL tests. As the specimen temperature increased, the amount of time until breakaway became shorter.

For implementation into MELCOR, the ANL data was curve fit as follows,

$$LF = \int_0^t \frac{t'}{\tau(T)} \quad (\text{Eqn. 2.2})$$

where,  $\tau(T)$  is

$$\tau(T) = 10^{P_{LOX}} \quad (\text{Eqn. 2.3})$$

and  $P_{LOX}$

$$P_{LOX} = -12.528 \cdot \log_{10} T + 42.038 \quad (\text{Eqn. 2.4})$$

A comparison of the data with Equation 2.4 is shown in Figure 3-6. For reference, specific values of the breakaway timing are provided in Table 3-1.

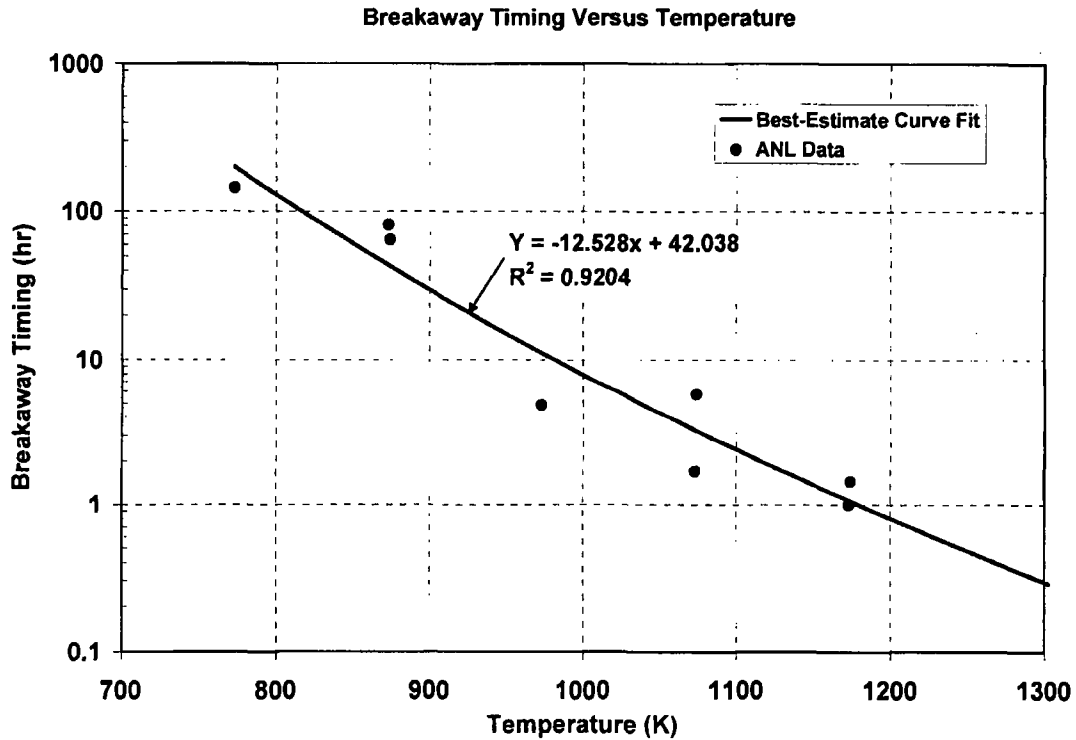


**Figure 3-6 Comparison of the MELCOR Breakaway Timing Fit to the Zirlo and Zr-4 Data from the ANL Air Oxidation Tests.**

The new MELCOR breakaway oxidation model calculates the lifetime function at every node in the MELCOR model with Zircaloy cladding. The oxidation kinetics linearly transitions from the pre-breakaway correlation at  $LF = 1$  to post-breakaway kinetics at  $LF = 1.25$ . Hence, only nodes that have exceeded the lifetime function will have the higher post-breakaway oxidation kinetics.

The ANL pre- and post-breakaway Zr-4 oxidation correlations<sup>6</sup> are summarized below,

- Steam pre-oxidized, wide-temperature pre-breakaway Zr-4 oxidation correlation (red line on Figure 3-7)

$$K(T) = 26.7 \exp(-17,490 / T) \text{ [kg}^2/\text{m}^4\text{-s]} \quad (\text{Eqn 6.6 in [Natesan, 2004]})$$

- Steam pre-oxidized, wide-temperature post-breakaway Zr-4 oxidation correlation (black line on Figure 3-7)

$$K(T) = 2.97e4 \exp(-19,680 / T) \text{ [kg}^2/\text{m}^4\text{-s]} \quad (\text{Eqn 6.7 in [Natesan, 2004]})$$

**Table 3-1 MELCOR Fit of the Timings for Transition from Pre-Breakaway to Post-Breakaway Oxidation Reaction Kinetics for Zirlo and Zircaloy-4 in the ANL Experiments [Natesan, 2004].**

Specimen Temperature	Breakaway Timing (Eqn. 2.4)	ANL Data Used in Curve Fit (See Figure 3-6)
400°C (673 K)	1125 hr (Extrapolated)	-
450°C (723 K)	458 hr (Extrapolated)	-
500°C (773 K)	198 hr	144 hr
550°C (823 K)	90 hr	-
600°C (873 K)	43 hr	64 and 81 hr
650°C (923 K)	22 hr	-
700°C (973 K)	11 hr	4.8 hr
750°C (1023 K)	5.9 hr	-
800°C (1073 K)	3.3 hr	1.7 hr and 5.8 hr
850°C (1123 K)	1.8 hr	-
900°C (1173 K)	1.1 hr	1 hr and 1.4 hr

<sup>6</sup> Note that the form of the leading coefficient of these correlations were adjusted to MELCOR input requirements, which uses  $K(T)$  is a function of Zircaloy oxidized versus oxide weight gain.

(b)(7)(F)

Ex 7F

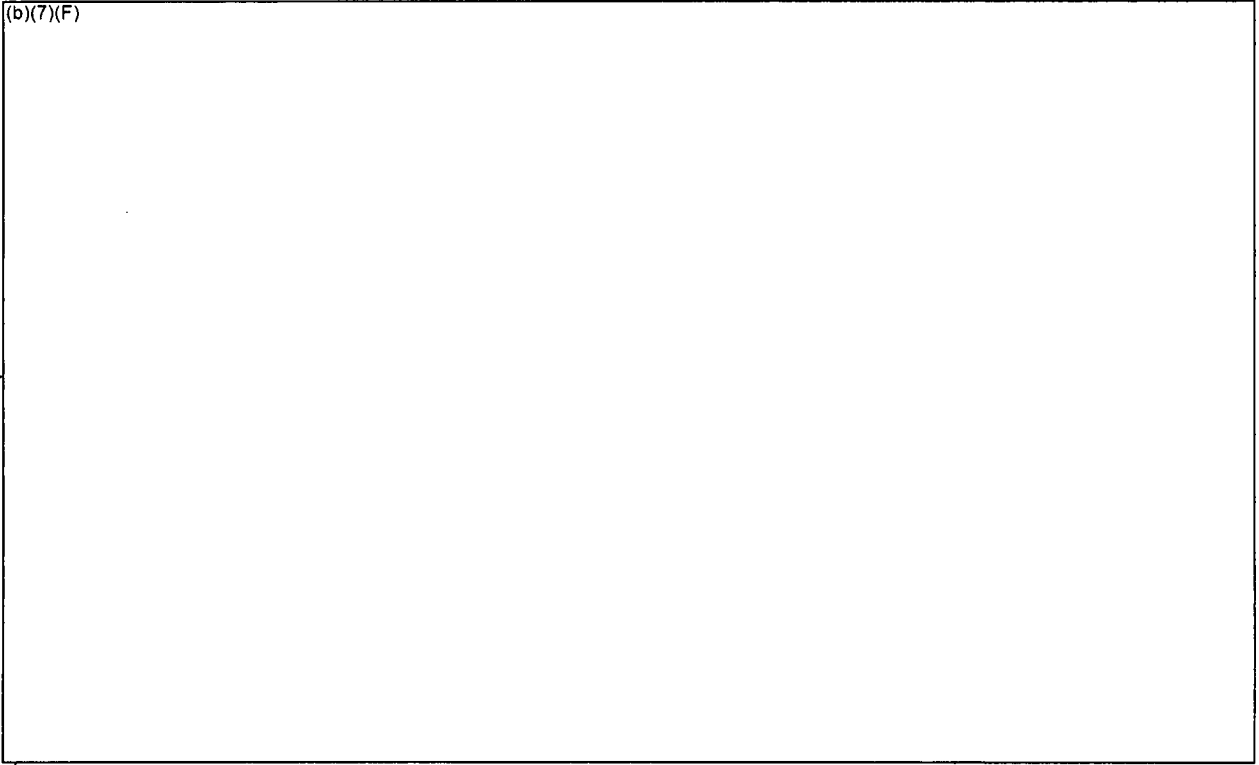


Figure 3-7 Parabolic Reaction Kinetics Coefficients for Zr-4 Oxidation.

### 3.1.3 New Hydraulic Resistance Model

Recently, hydraulic resistance measurements were performed on a Global Nuclear Fuel (GNF) 9x9 BWR assembly at Sandia National Laboratories [Durbin]. Commercial components were purchased to create the assembly including the top and bottom tie plates, spacers, water rods, channel box, and all related assembly hardware. Stainless steel conduit was substituted for the fuel pins for hydraulic testing. The stainless steel mock fuel pins were fabricated based on drawings and physical examples supplied by GNF.

Figure 3-8 shows the layout of the BWR pressure drop experimental assembly, including the 18 pressure port locations. Two Paroscientific Digiquartz differential pressure transducers were plumbed directly to the desired pressure ports. These pressure gauges use a highly sensitive quartz crystal to measure slight changes in differential pressure (resolution ~ 0.02 Pa). Measurements were recorded directly to the hard drive of a PC-based data acquisition system every 3 seconds using a LabView 7.1 interface. These measurements included the air flow rate through the assembly, ambient air temperature, ambient air pressure, and the assembly pressure drops.

Three primary series of experimental runs were performed. In the first two sets of experimental runs, the flow holes in the water rods were either blocked or unblocked. The bypass holes on the inlet nozzle assembly were blocked for these tests. In the final tests, the bypass holes were opened. In the assembly's prototypical configuration, the water rods are un-blocked and the bypass holes are unplugged. The subsequent analysis of the data calculated a wide range of parameters including the flow through the water rods and bypass holes as well as the corresponding local and total pressure drops for a Reynolds Numbers range of 70 to 900

Ex 7F

(b)(7)(F) In all configurations, the tests were repeated several times and alternate primary measurements were performed to verify the assembly flowrate and overall pressure drop. From the pressure drop data, the laminar flow resistance terms were processed in terms of inputs for the MELCOR code (i.e., see below,  $S_{LAM}$  and  $k$ ). An error analysis of the measurements revealed an uncertainty of hydraulic resistance values for input into MELCOR to be very small (b)(7)(F)

Ex 7F

MELCOR, like other control volume codes, includes constitutive relationships to specify form losses (i.e., minor losses) and wall friction losses (i.e., major or viscous) along a flow path as a hydraulic flow loss term to the momentum equation. The format of the user-specified input for MELCOR is defined from the sum of the local viscous and major pressure drops,

$$\Delta P = \frac{1}{2} \rho v^2 (fL/D + k) \quad \text{Eqn. 3.1}$$

The laminar friction factor ( $f$ ) for laminar flow is written explicitly as,

$$f = S_{LAM} / Re \quad \text{Eqn. 3.2}$$

where,

$S_{LAM} = 64$  for pipe flow (and  $S_{LAM} = 100$  for bundle flow in the BWR SFP model in [Boyd], [Wagner, 2003], and [Wagner, 2004])

$Re =$  Reynolds Number or  $(\rho v d_H) / \mu$

$\rho =$  local density

$v =$  local velocity

$\mu =$  local fluid viscosity

$d_H =$  local hydraulic diameter (defined as  $4 A / P_w$ )

$A =$  local flow area

$P_w =$  wetted perimeter

Ex 7F

As shown in Figure 3-8, the BWR fuel assembly (b)(7)(F) grid spacers, upper and lower tie-plates, full and partial rod regions, two water rods, and an inlet nozzle. It is not practical to include a detailed representation of all the geometry changes in the MELCOR model. In addition, the MELCOR code includes some hard-wired geometry models that further limit the modeling of the two large water rods inside the assembly and their associated flow. Consequently, modeling choices are required to represent the geometry of the BWR assembly. Relative to the hydraulic modeling in the BWR SFP MELCOR model, the experimental data are used in the following manner,

- Based on the hydraulic impact of the fully populated versus the partial regions, the control volume boundaries were specified to span uniform geometry regions. Control volume boundaries were placed at the bottom of the lower tieplate, the transition from the fully populated rod region to the partial region, and at the top of the upper tieplate. By spatially dividing the two regions, the distinct flow loss effects can be extended to heated conditions, where the flow will accelerate along the length of the assembly.
- The flow resistance in a flow path spans the region from cell-center of the lower control volume to cell-center of the upper control volume. Hence, the pressure in a given control volume represents the pressure in the center of the control volume. A single flow path may span more than one grid spacer and perhaps a tieplate. Segment data on a particular flow path defines the form and wall friction losses along the geometric regions encompassed in the flow path length. Several flow paths had multiple flow segments due to geometry changes within the flow path range. The net effects of varying flow resistance are calculated by the code.

(b)(7)(F)

- For the application to the emergency BWR SFP spray analysis, the results from Table 3-2 were used, which includes prototypical water rod flow effects. For the flow segments in the fully populated tube region, a  $S_{LAM}$  of (b)(7)(F) was used and k losses of (b)(7)(F) were used for each spacer included in the range of the flow path. The flow area and hydraulic diameters were preserved. The total length across all flow paths in the fully populated region (b)(7)(F) and the total k was 19. Therefore, the total flow losses (b)(7)(F) were exactly preserved, including the effect of flow within the water rods. Similarly, the partially populated tube region used a  $S_{LAM}$  of (b)(7)(F) per spacer in the range of the flow path. The total length across all flow paths in the fully populated region (b)(7)(F) and the total k (b)(7)(F)

Ex 7F  
Ex 7F  
Ex 7F

*Ex 71F* (b)(7)(F) The flow path segments in the partial rod region used the larger flow area and hydraulic diameter as specified in 2-8 from Table 3-2. For reference, the overall resistance was of a *Ex 71F*  $S_{LAM}$  of (b)(7)(F) and  $k$  losses of (b)(7)(F). In comparison, the previous BWR analysis used  $S_{LAM}$  of (b)(7)(F) and  $k$  losses of (b)(7)(F) across the same region (i.e., not including the inlet nozzle).

- Table 3-2 was also used to specify the pressure drop across the upper tieplate (1-2) and lower tieplates and the inlet region (b)(7)(F). Similar to above, the appropriate flow areas and hydraulic diameters for these regions were used.
- Finally, the results from Figure 3-10 were used to specify the flow loss terms for the inlet nozzle leakage to the interstitial bypass region. The form losses in the MELCOR model were adjusted to match the measured total to bypass flow split.

Until this hydraulic data was available, the previous BWR SFP MELCOR analyses did not include the sophistication of separate flow resistances for the partial and fully populated regions of the BWR bundle.

The results analysis in Table 3-2 precisely satisfies the model input requirements for MELCOR, as well as other control volume codes. The linear (i.e.,  $S_{LAM}$ ) and quadratic (i.e., the  $k$  term) hydraulic loss coefficients are easily put into the MELCOR input format and will replicate the measured flow losses across the Reynolds number range of 70 to 900, including the overall nonlinear hydraulic effects from (a) flow development regions, (b) the grid spacer entrance, internal, and exit effects, (c) the inlet and exit flows to the water rods, and (d) the transition from the fully to partially populated tubes regions.

**Table 3-2  $S_{LAM}$  And  $k$  Coefficients for the Unblocked Water Rod Assembly Assuming All Flow Passes Through the Bundle.**

*Ex 4*

(b)(7)(F)
-----------

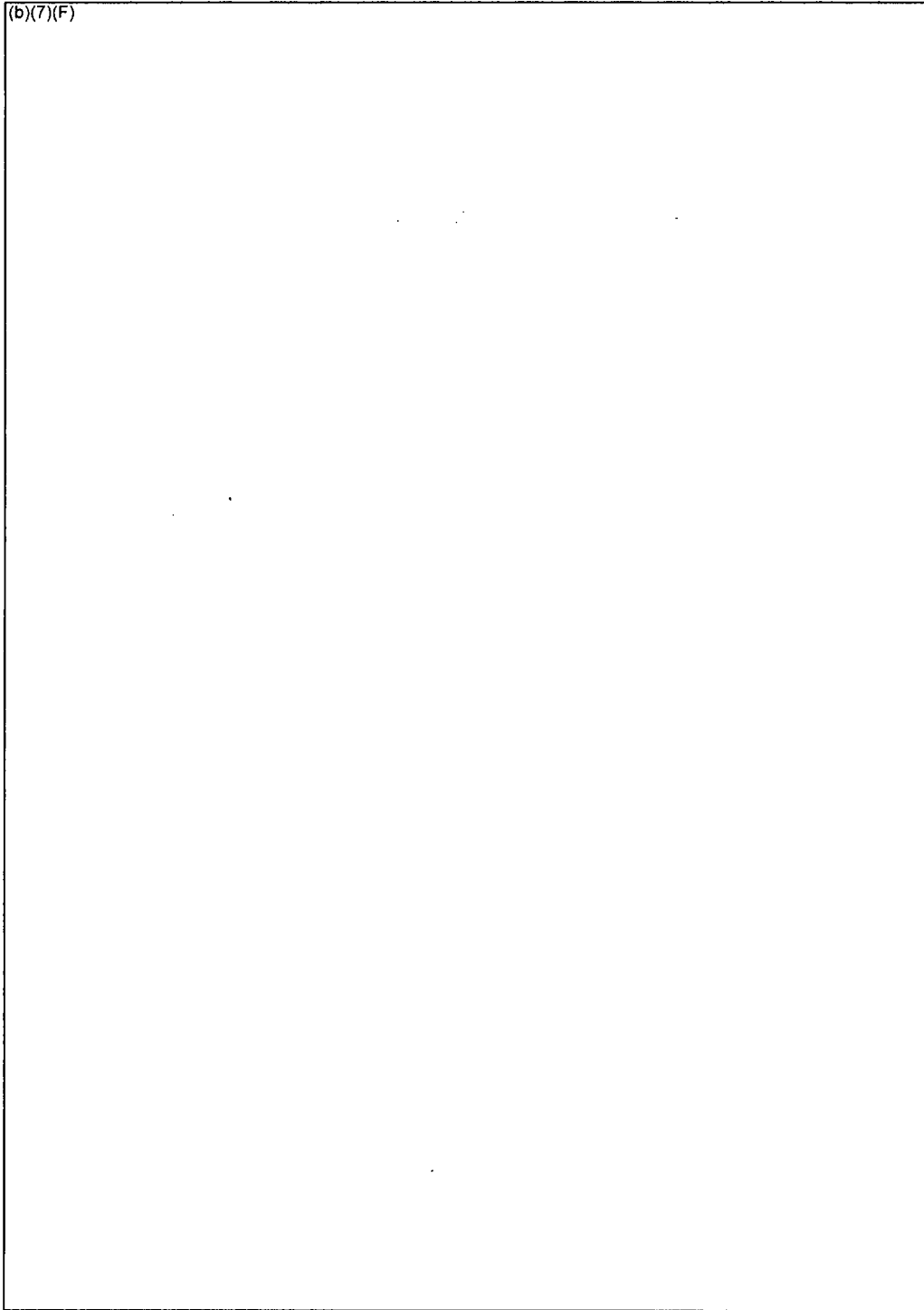
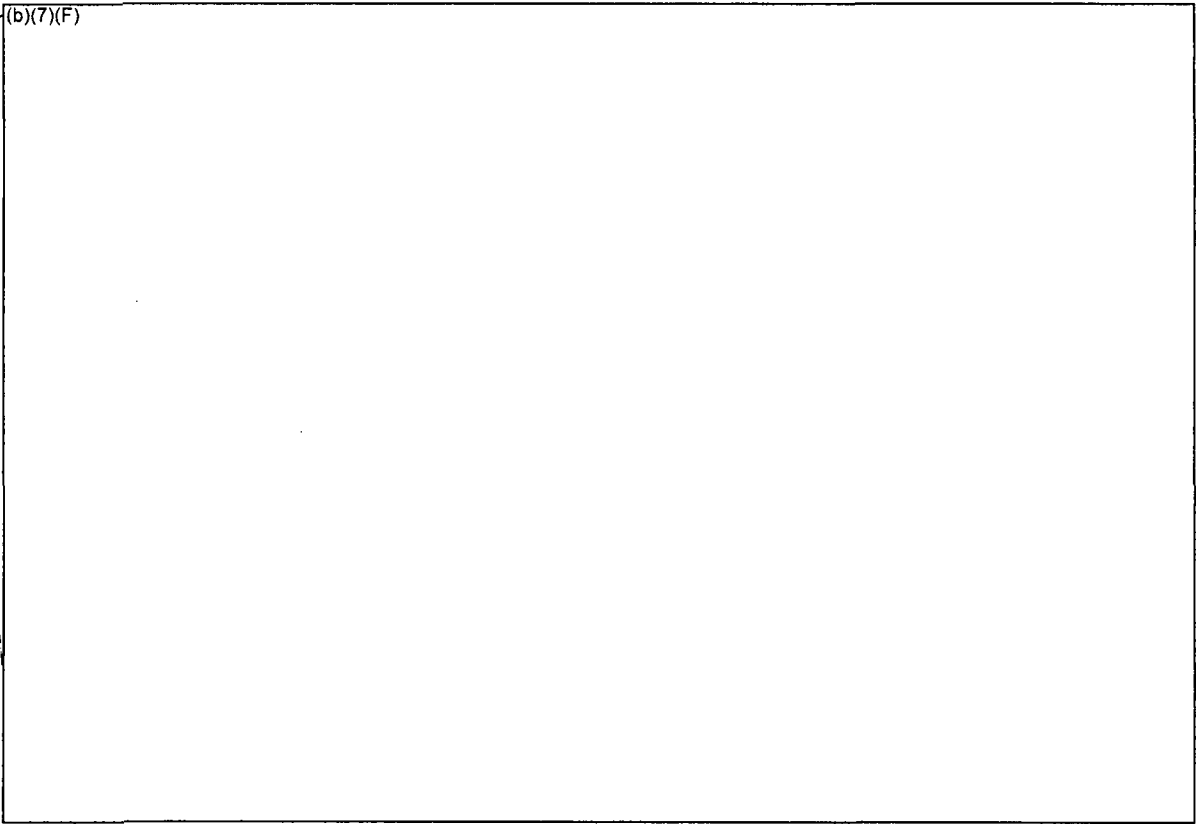


**Figure 3-8 BWR Assembly Experimental Apparatus used in the Hydraulic Resistance Testing.**



EX-71E

**Figure 3-9 Measured Pressure Drop over the Full, Partial, and Total Assembly Regions.**

(b)(7)(F)

Ex 7F

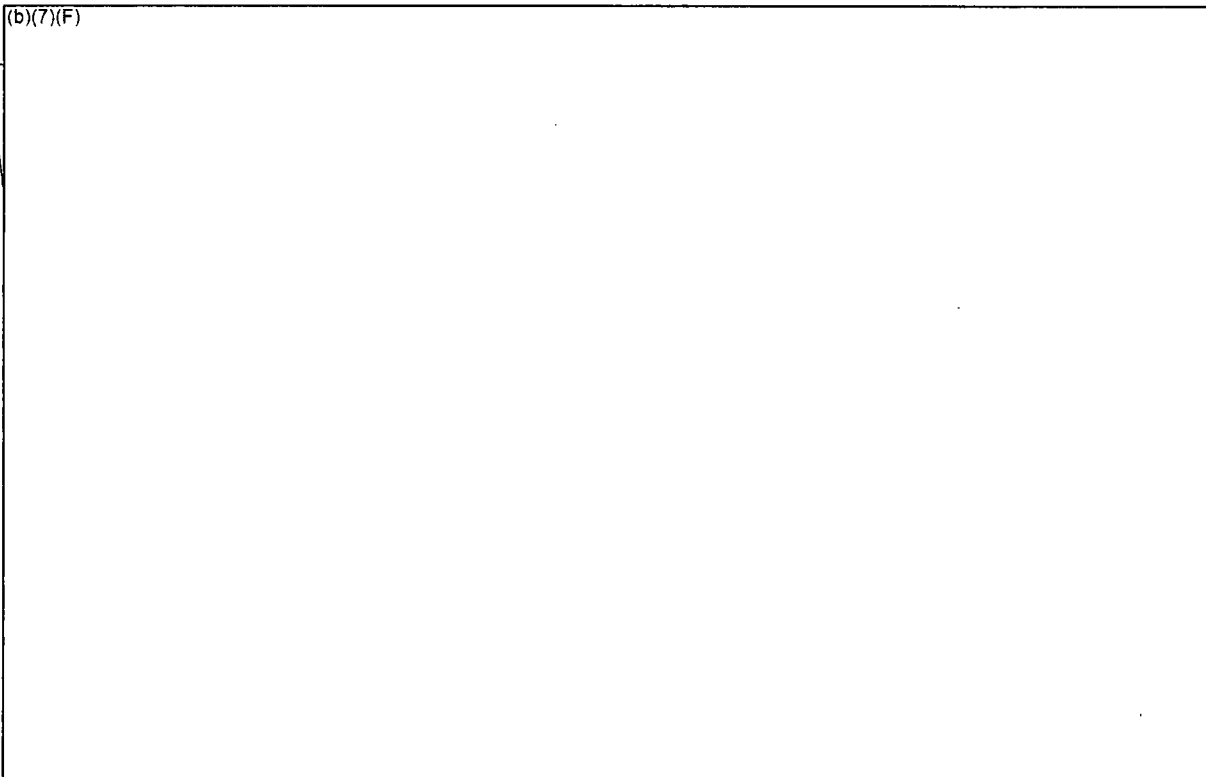


**Figure 3-10 Comparison of the Calculated and Measured Bypass Flow.**

### 3.1.4 Spray Modeling in MELCOR

The spray modeling was performed in two ways. For the whole pool calculations, the MELCOR containment spray model was used. The MELCOR containment spray package includes calculations for spray droplet heat and mass transfer and fission product removal [Gauntt]. A droplet size of 1250 microns was used unless otherwise noted.<sup>7</sup> The droplets were directed into the assemblies and open spaces based on their respective cross-sectional areas. Upon entering the assemblies, the thermal-hydraulic calculations were performed by MELCOR's CVH package as described below.

Generally, the separate effects models were used to resolve the spray performance. Boundary conditions for the inlet and exit of the separate assembly model were provided by whole pool calculations (see Section 3.3 for a description of the models). A spray water source was specified to the top of the assembly according to the relative cross-sectional area. For example, spray water was added to CV-119, CV-129, CV-219, and CV-229 in the 1x4 SE model (see Figure 3-16). The flow area and resistance representing the upper tie-plate is represented in the next downward flowpath. The penetration of the spray water into the assembly is controlled by MELCOR's interphase momentum model, which replicates the Wallis flooding curve [Gauntt].

Once the spray water enters the assembly, the spray is assumed to form a thin film on the fuel structures in the assembly, which drains downward. The new COR Package simplified flow regime model identifies the spray flow as a film in contact with the fuel rods (see Figure 3-12). Heat transfer takes place between the fuel rods and water in core cells where the flow regime model is active. Nucleate or film boiling heats the water film to saturation conditions as it drains down the assembly. Simultaneous heat transfer from the rods and surrounding gas causes the spray flow to boil. The spray film travels downward in contact with the fuel rods until the local CVH void fraction becomes greater than 99.8% (i.e.,  $\alpha > 0.998$ ). Due to numerical considerations, the residual water is converted into a shallow pool where the liquid heat transfer area is apportioned by the depth of the pool in the control volume.<sup>8</sup> Typically, the remaining water boils away in the first core cell after the flow regime model is disabled.

A detailed CVH/COR nodalization was used to track the water as it penetrates into the assembly (see Figure 3-15). The detailed nodalization permits a better local representation of the fluid conditions and the location of the spray dryout. The calculated results show a steadily decreasing flowrate and increasing void fraction as the liquid spray penetrates into the assembly. For example, Figure 3-11 shows the axial temperature response in an assembly with spray cooling using the new flow regime model. (b)(7)(F)

(b)(7)(F)

Ex 7F

<sup>8</sup> If the flow regime model was used until the flow disappears, very small timesteps are needed to resolve the large heat transfer rates to negligible water mass. When the surface area in contact with water is partitioned by the pool depth, a larger timestep can be used which just boils the water dry in the first or next CVH volume. The residual heat removal for void fractions greater than 0.998 is relatively small.

(b)(7)(F)

7F

It should be noted that the CVH package interprets the liquid film as small pools at the bottom of each CVH volume (see Figure 3-13). Due to the high void fraction, the phasic resistance of the steam or air flowing through the pool is relatively insignificant, which is the expected impact of a liquid film. Similarly, the depth of the spray water penetration is controlled by the COR heat transfer rate rather than the momentum solution. Axial, stepwise heat transfer from the core cells limits how far the spray water penetrates into the assembly.

A possible limitation of the CVH representation is the relatively small heat transfer area between the two phases (i.e., heat transfer through the pool and the surface versus a film). However, the rate of heat transfer from the gas to the water film is minor in comparison to the nucleate and film boiling heat transfer on the surface of the fuel rods. In addition, MELCOR's quenching model is relatively ineffective. The model accurately calculates separate quenched and un-quenched temperatures in each COR cell that is in film boiling. However, it assumes the unquenched portion is at the top of the cell. Hence, any axial condition benefit from a downward moving quench front is not realized. The impact from this limitation is not expected to be too significant due to the relative magnitudes of the surface heat transfer rate relative to any axial conduction effects.

(b)(7)(F)

10x 7F

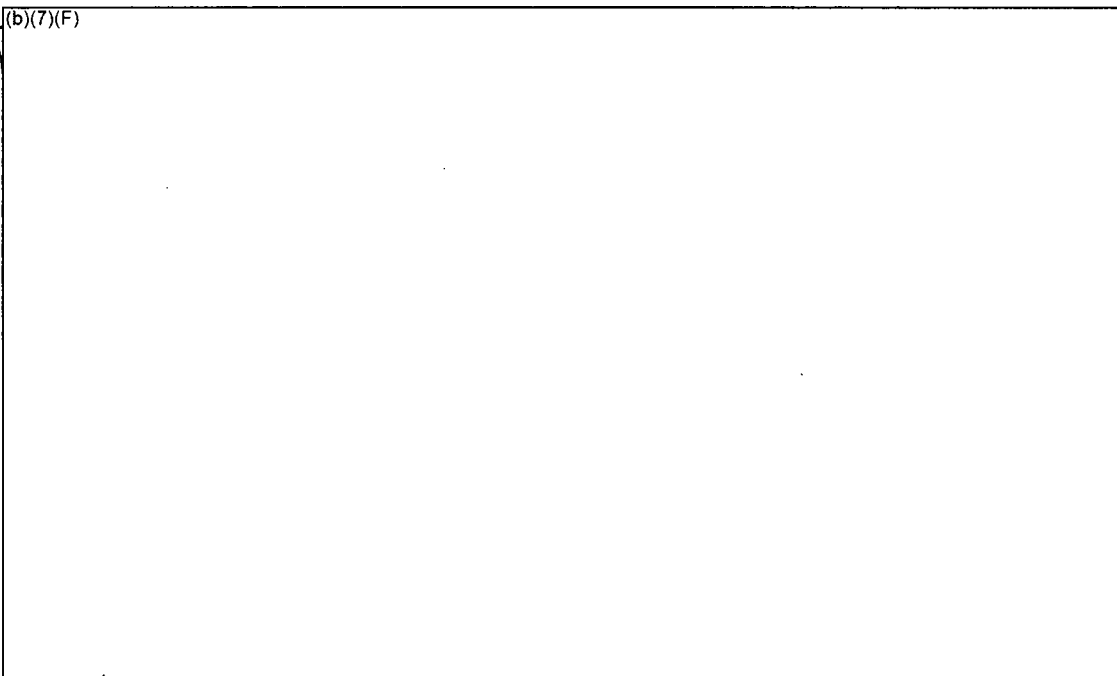


Figure 3-11 Axial Temperature Profile in the Assembly with Spray Flow.

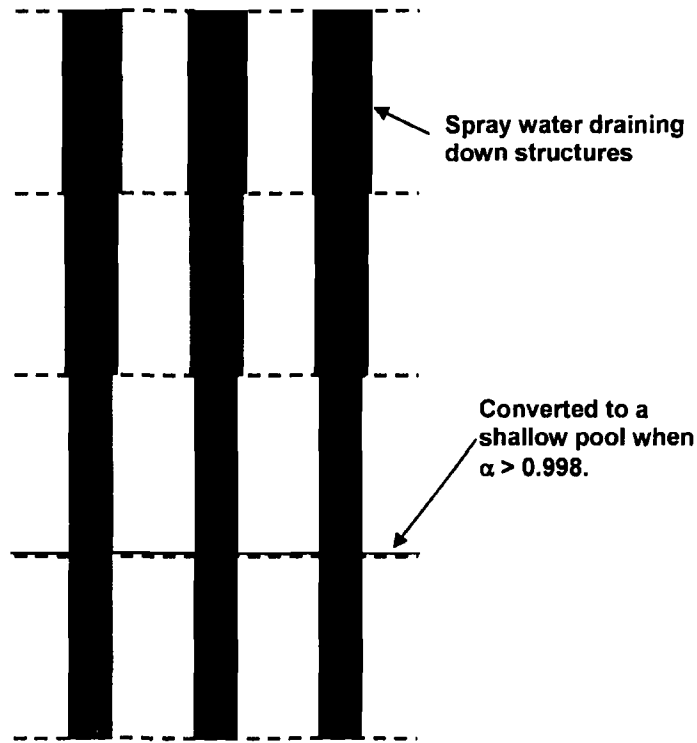


Figure 3-12 Core Package Representation of Spray Flow.

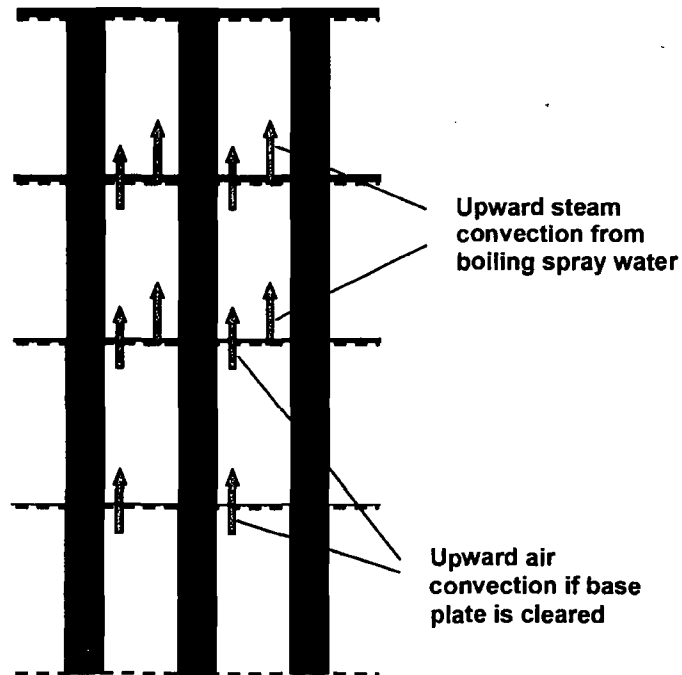
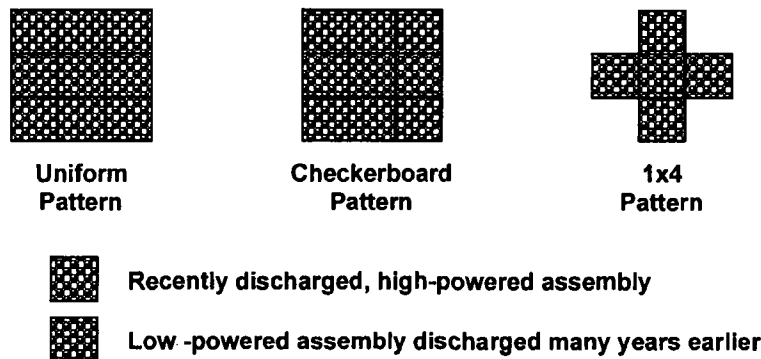


Figure 3-13 CVH Package Representation of Spray Flow.

### 3.2 MELCOR Separate Effects Model

Three intact configuration separate effect models were developed to analyze the spent fuel pool response to emergency spray mitigation of loss-of-coolant inventory accident conditions. The models simulate uniform, checkerboard, and 1x4 patterns. For implementation into MELCOR, the uniform pattern model was represented by a single, high-powered assembly with an adiabatic radial boundary or a 1x4 model with equal power in all five assemblies. The checkerboard pattern was represented with a high-powered and a low-powered assembly (i.e., taken as having the median assembly on the reference BWR spent fuel pool) with the appropriate adjoining wall area. Hence, radial heat transfer was possible from the high-powered assembly to the low-powered assembly. Similarly, a 1x4 pattern model was developed, which had one high-powered assembly surrounded by four low-powered assemblies. The MELCOR models represent the coupled thermal response of repeating pattern for each configuration (e.g., see Figure 3-18 for an example of a repeat 1x4 pattern). An adiabatic boundary was specified on the outer radial face of each model.

For reference purposes, the 1x4 intact configuration separate effects model will be described. The checkerboard model was a variation of the 1x4 model. However, the number of low-powered assemblies was reduced to one and the adjoining area between the two assemblies was adjusted accordingly. Finally, two types of uniform pattern models were used. First, the 1x4 model was used; however, all assemblies were specified to have the same power. However, to improve runtime on more difficult calculations, a dedicated separate effects model was developed with one assembly and an adiabatic outer boundary.



**Figure 3-14 Repeating Patterns Found in the MELCOR Separate Effects Models.**

As described above, the 1x4 separate effects model contains 5 spent fuel assemblies (see Figure 3-15). The five assemblies are divided into two radial rings and are modeled using the MELCOR “SFP-BWR” designation (see Section 3.1.1 for further discussion). The inner assembly is in Ring 1 and the four adjacent assemblies are in Ring 2 (see Figure 3-15). The outer boundary of Ring 2 is modeled as adiabatic. In the various calculations, the power is sometimes varied independently from Ring 1 and Ring 2. Each ring has 9 axial control volumes, which represent the fluid volume within the fuel assembly.

The interstitial area between the canister wall and the rack wall is modeled as the BWR bypass region. The bypass uses the same 9 control volume axial nodalization as the channel region. Nine radial cross-flow paths are located between the bypass and channel region. The cross-flow paths are controlled by the COR package and open if the canister wall should fail. A control volume represents the region below the assemblies. Another control volume represents the bulk pool conditions above the separate effects model.

The hydraulic resistance was specified using the results from the SNL experimental test program (see Section 3.1.3). The flow resistance under the racks was represented using typical contraction inertial loss coefficients and viscous losses consistent with a flow length to the center of the SFP.<sup>9</sup>

The BWR assembly canister is modeled with the MELCOR canister component. The rack walls are modeled with the new rack component (see Section 3.1.1) with stainless steel and Boraflex. MELCOR does not include an option to model the two large water rods in the assembly. Consequently, the water rod mass and surface area was included in the canister wall.

The axial and canister wall blockage models were active and controlled the resistance in the respective flow paths. The blockage model monitors the porosity of the materials in the various core regions. If a debris bed forms, the flow resistance is adjusted via an Ergun flow resistance model [Gauntt]. The canister wall radial blockage model controls flow paths between the bypass region and the assembly. Initially, the canister wall precludes flow. However, if the canister fails, a radial flow path is activated that permits flow between the two regions. Similar to the axial blockage model, the flow resistance is adjusted based on the local debris porosity.

The BWR fuel assembly is represented by 14 axial levels in the COR Package,

- Level 1 is the region below the core,
- Level 2 is the base plate
- Level 3 is the inlet region between the inlet nozzle and the lower tieplate
- Level 4 is the start of the active fuel region
- Level 8 is the top of the partial rod active fuel region
- Level 9 represents the region of the plenum of partial rods
- Level 12 is the top of the full length rod active fuel region
- Level 13 represents the plenum region of the full-length rods
- Level 14 represents the region between the upper tieplate and the top of the racks

The upper and lower tieplates are modeled as supporting plate structures, made of stainless steel. The 0.5" rack support plate at Level 2 is also modeled as a stainless-steel supporting structure.

The assembly ring-to-ring radiation is modeled (described in Section 3.1.1) between the outer surfaces of the Ring 1 rack wall to the outer surface of the canister in the adjacent ring. Radiative coupling was enabled for all calculations. In cases of a uniform configuration (i.e., a region where all assemblies have the same power), the ring-to-ring thermal radiative coupling did not have an effect because all 5 assemblies had the same decay power and thermal response.

---

<sup>9</sup> CFD calculations show the flow resistance under the racks is relatively small [Chiffelle].

(b)(7)(F)

Ex 7F

The assembly decay heat is specified separately for each core ring. The decay heat load is primarily deposited in the fuel. However, as calculated by the gamma heating model, a small fraction of the decay heat is deposited directly in the cladding, canister, and surrounding structures (i.e., the rack wall). The outer boundary heat structures (i.e., ordinarily modeling the core barrel) outside Ring 2 were modeled as adiabatic (i.e., do not absorb any energy from Ring 2).

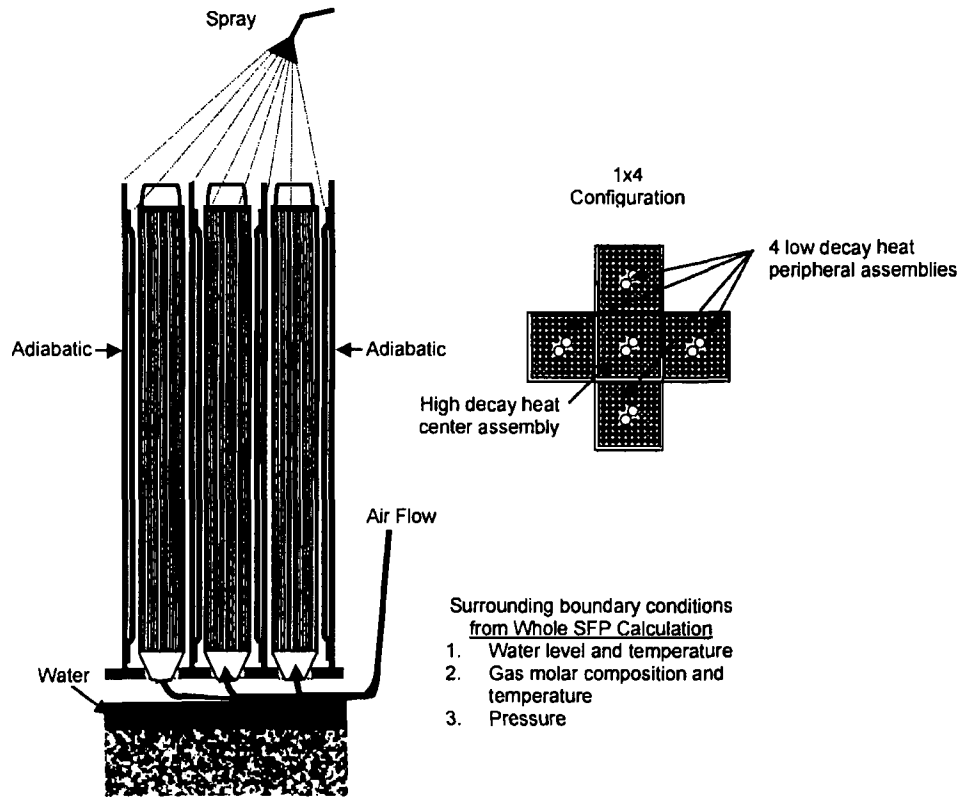


Figure 3-15 Schematic of the 1x4 Configuration.

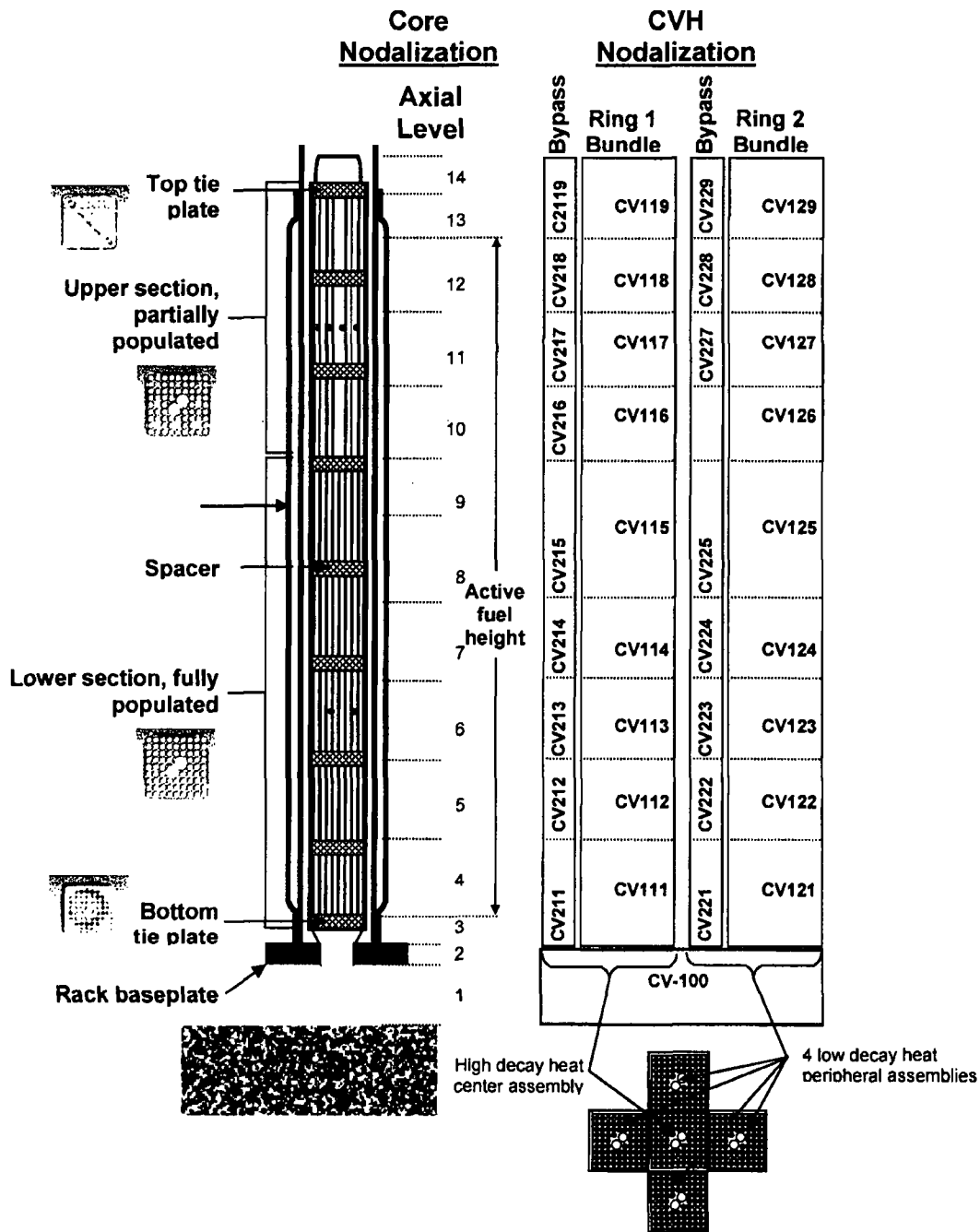


Figure 3-16 MELCOR Nodalization of the 5 Assembly Separate Effects Model.<sup>10</sup>

<sup>10</sup> Only the center assembly is shown for the Core Package nodalization shown in the left-hand side of this figure. However, the four peripheral assemblies are lumped together and have an identical 14 level axial nodalization. Both the CVH nodalizations for the center (Ring 1) and four peripheral assemblies (Ring 2) are shown on the right-hand side.

### 3.3 Whole Pool Model

A whole pool model was previously developed to perform source term calculations (see [Wagner, 2004] for a description). The scope of the whole pool model included the entire spent fuel pool including all the assemblies and the surrounding reactor building. However, the original BWR whole pool model did not include the new features described in Section 3.1. Consequently, a new simplified whole pool model was used to specify the boundary conditions for the separate effects model. The new BWR whole pool model includes all the new features described in Section 3.1 except the more detailed COR/CVH nodalization for tracking spray front.<sup>11</sup> The fuel assemblies and empty rack cells are represented in 9 rings in the MELCOR model. The new whole pool model uses the same 14-axial level COR Package described in the separate effects model (see Section 3.3). However, for improved computational runtime, only one control is used for the bundle region and one for the bypass region per COR package ring.

Figure 3-17 shows the CVH nodalization of the SFP region of the new simplified whole pool model. The lower SFP was divided into ten regions. CV-299 represents all the open regions in the SFP around the racks and including the cask area. The racks are divided into 9 regions. CV-110 and CV-210 represent the assembly and bypass regions of the first ring. Similarly, COR Rings 2 through 8 contain assembly and bypass regions. Ring 9 represents   empty rack cells. Hence, CV-190 only contains empty cells (i.e., no assemblies or bypass regions). The axial volume, flow area, and resistance are represented as described in Section 3.1.3. The region above the pool is divided into two control volumes. Typically, flow goes down CV-301 and CV-299 and rises through CV-300. The flow enters the bottom of the racks through CV-100. A 14 level COR nodalization is used as described in Section 3.2.

Ex AF (b)(7)(F)

---

<sup>11</sup> A detailed COR/CVH nodalization in the framework of a multi-ring model is too computationally intensive for the present application. The simplified whole pool model is used to calculate global boundary conditions for the more detailed separate effect models described in Section 3.1.

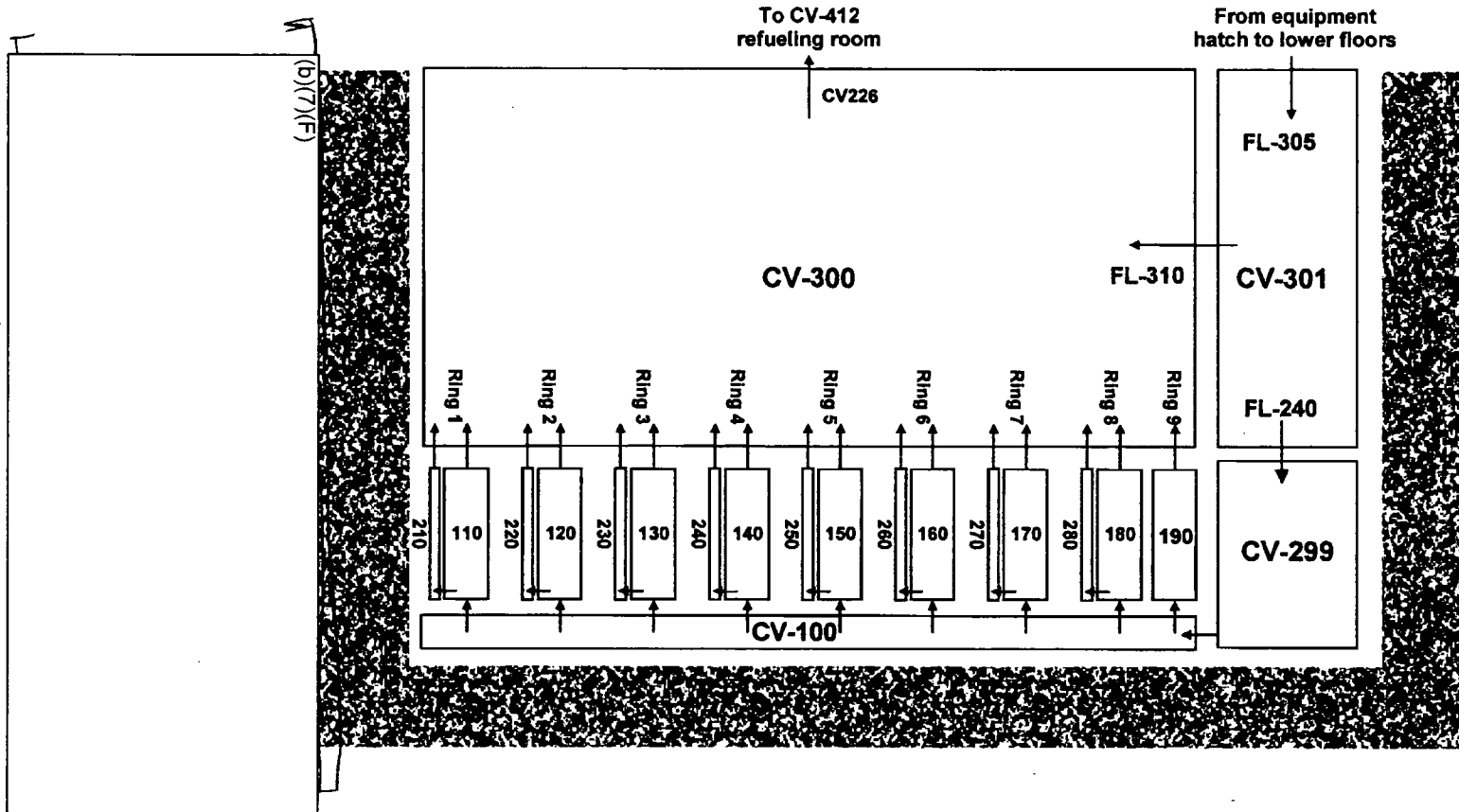


Figure 3-17 Schematic of the Whole Pool Model Configuration.

### 3.3.1.1 Radial Thermal Coupling

The reference plant for the SFP analysis is a large BWR. The SFP is representative of a modern, high-density SFP. The plant has begun a dry or off-site fuel storage program. As fuel assemblies are added to the SFP, a similar number are removed for dry storage. Consequently, the number of assemblies in the SFP is kept approximately constant. For the present analyses, the layout of the fuel was specified to be representative of a well-configured SFP. In particular, the assembly layout was specified to enhance radial heat transfer from recently discharged, high-powered assemblies to low-powered assemblies. Figure 3-18 shows an example of a well-configured SFP layout. The most recently discharged "orange" and "red" assemblies are surrounded by the older "blue" assemblies in 1x4 patterns.

(b)(7)(F)

The layout of the assemblies from the last offload for the new MELCOR whole pool model conceptually followed the example shown in Figure 3-18.<sup>12</sup> The assemblies in the reference PWR SFP were grouped into 9 types or "rings" by decay heat power and time of discharge.<sup>13</sup> The ring layout assumed in this analysis is shown in Table 3-3. The last assembly offload from the reference plant (b)(7)(F) assemblies. The (b)(7)(F) assemblies were subdivided into Rings 1, 3, and 5. By using three rings to represent the last core offload, the relative powers of the assemblies were accurately characterized into high, medium, and low-powered groups. Surrounding each of those groups in Rings 2, 4, and 6 were the lowest-powered assemblies in the SFP. There were four low-powered assemblies in Rings 2, 4, and 6 for each high-powered assembly in Rings 1, 3, and 5, respectively. This 1x4 pattern utilized (b)(7)(F) of the lowest powered assemblies. The remaining mid-powered assemblies were placed in an approximate checkerboard pattern with the next lowest powered (b)(7)(F)

Ring 7 interspersed amongst (b)(7)(F) Ring 8. Finally, (b)(7)(F) empty cells were placed around the outside of the SFP to ensure open air downflow regions into the SFP in the event of a complete loss-of-coolant inventory accident.

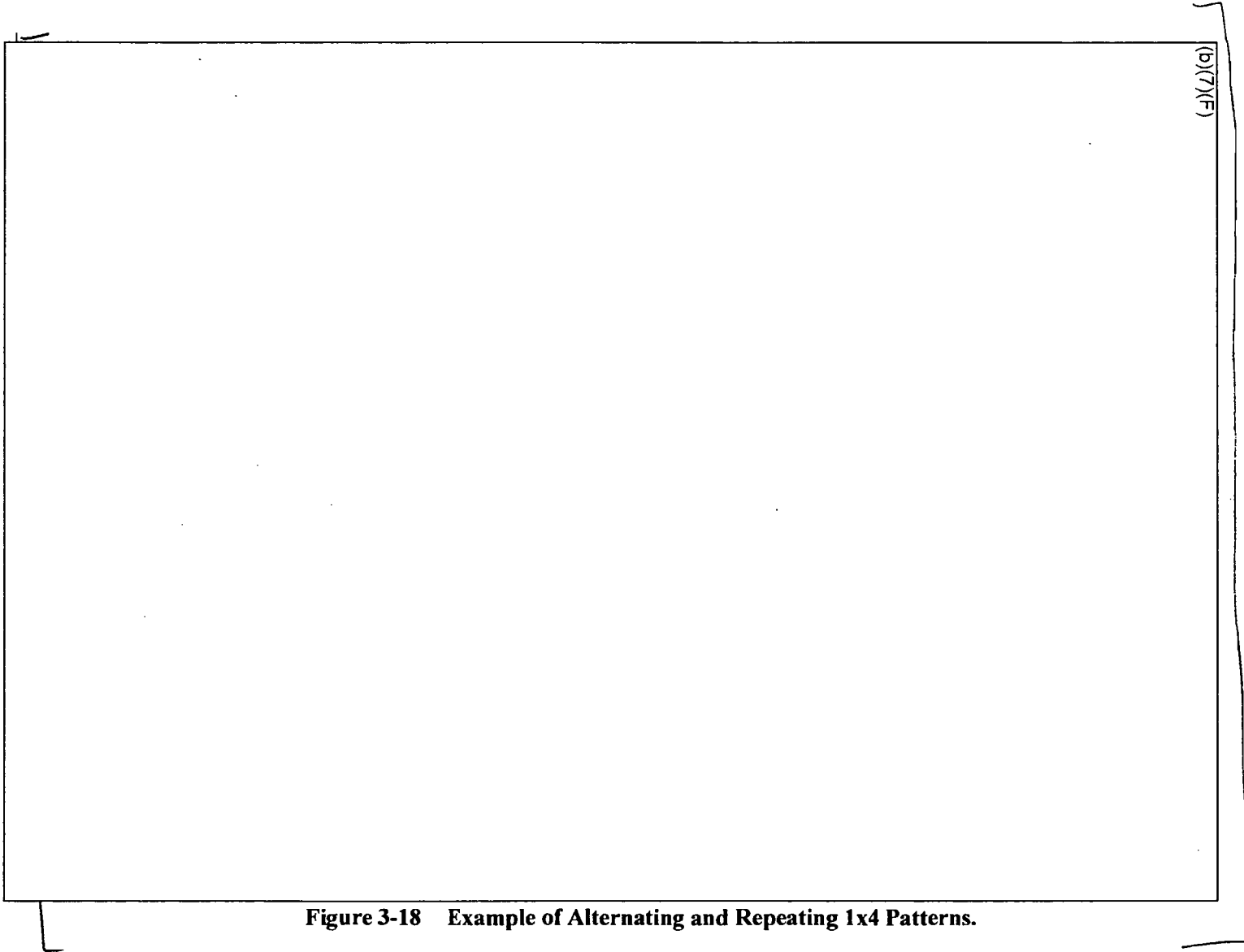
Figure 3-19 shows the cell-wall radiation view factors between the various rings. The resultant view factor specifies the amount of coupling from each region to another. For example, the Ring 1 cells are completely surrounded by Ring 2 cells. Hence, the view factor from Ring 1 to Ring 2 is 1.0. Similarly, Rings 3 and 4 and Rings 5 and 6 are coupled in 1x4 patterns. Due to limitations in the MELCOR radial radiation scheme, only adjacent rings can be thermally coupled. Consequently, the inter-dependent coupling between adjacent rings can not be represented. The resultant assembly patterns only couple the 1x4 patterns in Rings 1 through 6,

<sup>12</sup> Figure 3-18 is an illustration of a well-configured SFP. Similarly, the layout used in the present analysis uses 1x4 patterns with the last offload surrounded by the lowest decay heat assemblies. However, the layout of the (b)(7)(F) assemblies was a simply a checkerboard pattern. Since the new whole pool model was only used to establish inlet boundary conditions for the separate effects models, no further refinement of the assembly or ring layout was performed. It would be relatively straight-forward to change the number of assemblies in each ring and their coupling to adjacent rings.

<sup>13</sup> "Ring" is a MELCOR term for a grouping of assemblies. In MELCOR's typical reactor configuration, the core is geometrically divided into a group of concentric rings. Each assembly in a ring has the same decay heat and thermo-physical properties.

a checkerboard pattern in Rings 7 and 8 and empty cells around the periphery in Ring 9. No other inter-ring couplings are considered.

Within each MELCOR ring, the assembly decay heat is uniform. Table 3-3 summarizes the average assembly decay power in each ring from the individual batches. Consequently, for any given scenario, the decay heat in each ring is adjusted to give the average assembly power. Due to the variable decay factors in the assembly decay heat, the assembly power is conservatively assumed to remain constant for the duration of the scenario.



(b)(7)(F)

Ex 7F

Figure 3-18 Example of Alternating and Repeating 1x4 Patterns.

Table 3-3 Summary of Regions in the MELCOR Whole Pool Model.

(b)(7)(F)

Ex 7F

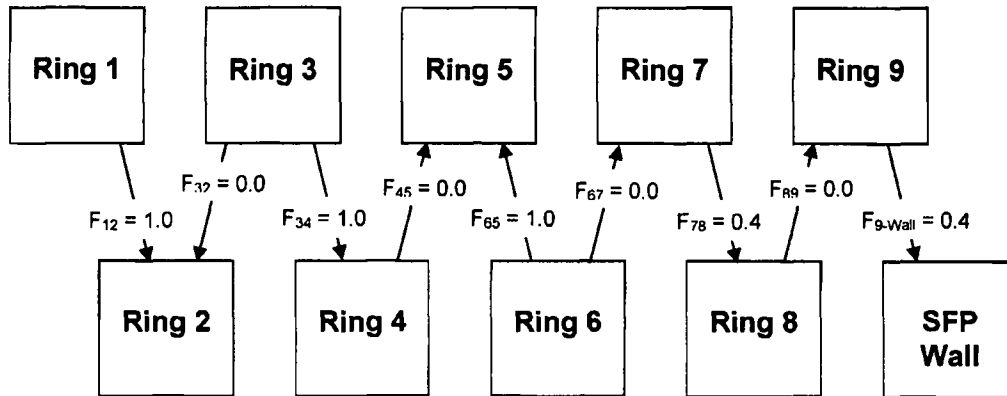


Figure 3-19 The Radial Coupling Scheme as Implemented in MELCOR SFP Model.

### 3.3.1.2 Simplified Refueling Room Model

A complete reactor building was developed as part of the BWR reference plant accident progression model. However, for the present analysis, the reactor building model was simplified to only model the refueling room (i.e., within the red dashed line on Figure 3-20). The SFP nodalization (see Section 3.3) was coupled to the SFP model as shown in Figure 3-20.

A single control volume models the refueling bay. An open hatch in the southeast quadrant (via flow paths) connects the refueling bay to a boundary condition volume representing the lower sections of the building. Nominal reactor building leakage is modeled at the center elevation of the refueling bay. The leakage flow in the simplified model was tuned to match the 100% design in-leakage rate of the detailed reactor building model.

The detailed reactor building model represented many over-pressure failure flow paths within the reactor building. The two most important flow paths for the present calculations were added to the simplified refueling floor model, (1) the blowout panels on the refueling room walls and (2) a pathway representing the structural failure of the reactor building roof. (b)(7)(F)

(b)(7)(F)

Ex 4

Recently, computational fluid dynamic (CFD) simulations of the air flow patterns in a PWR fuel storage building during a complete loss-of-coolant inventory accident guided the development of the model nodalization [Khalil]. The CFD results show a flow pattern of hot air exiting from the assemblies at the top of the racks (see Figure 3-21). The hot gases form a plume which that rises to the building ceiling. Once the plume hits the ceiling, it spreads radially and mixes within the hot gas layer at the top of the room. The room remains thermally stratified as hot gases preferentially leak out the large, open ceiling ventilation units. Meanwhile, cool air enters

Ex 7 F

(b)(7)(F) to replace the exiting hot gases. The cool air fills the lower regions of the building, overflows to the SFP floor elevation, and sinks into the SFP to replace exiting hot gases. The cool air flows underneath the racks from the cask area and then spreads radially under the racks. The hydrostatic pressure difference between the cold gases outside the racks and the hot gases inside the assemblies drives the airflow through the racks.

This flow pattern is similar to that expected in the reference BWR refueling room<sup>14</sup>. By comparing Figure 3-20 and Figure 3-21, (b)(7)(F)

(b)(7)(F)

Ex 9 F

MELCOR does not include models for stratification of hot gases. Each control volume is assumed to be well-mixed and have a single temperature. Large-scale natural circulation flow patterns can be predicted where the bulk temperature differences between adjacent rooms create mixing flows. However, it would be awkward or perhaps impossible to predict complex plume

<sup>14</sup> The PWR refueling building is shown because the CFD code used in that analysis provides superior visualization of the resultant flow patterns than the figures available from the comparable BWR CFD study.

behavior within regions typically modeled with a single control volume (e.g., the room above the SFP). Consequently, the MELCOR calculations are expected to over-predict the amount of thermal mixing within the building. Based on insights from the CFD calculations, the MELCOR refueling room model nodalization included modeling features to minimize excessive mixing.

The refueling room is modeled as a single control volume. (b)(7)(F)

(b)(7)(F)

(b)(7)(F)

In this manner, the cool gases leaving the lower regions of the building are not brought into thermal equilibrium with gases above the SFP. Cross-flow is simulated between CV-300 and CV-301 as observed in Figure 3-21.

[x] F

Finally, no counter-current flow was modeled between CV-301 (see Figure 3-17) and the refueling room (CV-412). CV-301 is connected to the refueling room via flow into the SFP pit. The detailed FLUENT CFD solution shows a hot gas layer near the ceiling of the room above the SFP pit. If the heat removal is inadequate, then the hot gas layer fills the room (i.e., CV-320) and extends down into the lower rooms in the building. MELCOR can not calculate the formation and movement of a hot gas layer. However, when the gas flow into the refueling room (i.e., via FL-300 from the SFP pit) exceeds the leakage from the building, hot air circulates into lower floors through the hatch.<sup>15</sup>

<sup>15</sup> For the present boundary condition calculations, the temperature feedback from the hot gas layer filling the refueling room was not adequately modeled. If the refueling room filled with hot gas, there was not a mechanism to heat the lower floors and draw hotter gas into the SFP. This deficiency will be addressed in future calculations by including a heated gas recirculation path into the SFP.

(b)(7)(F)

Ex 4

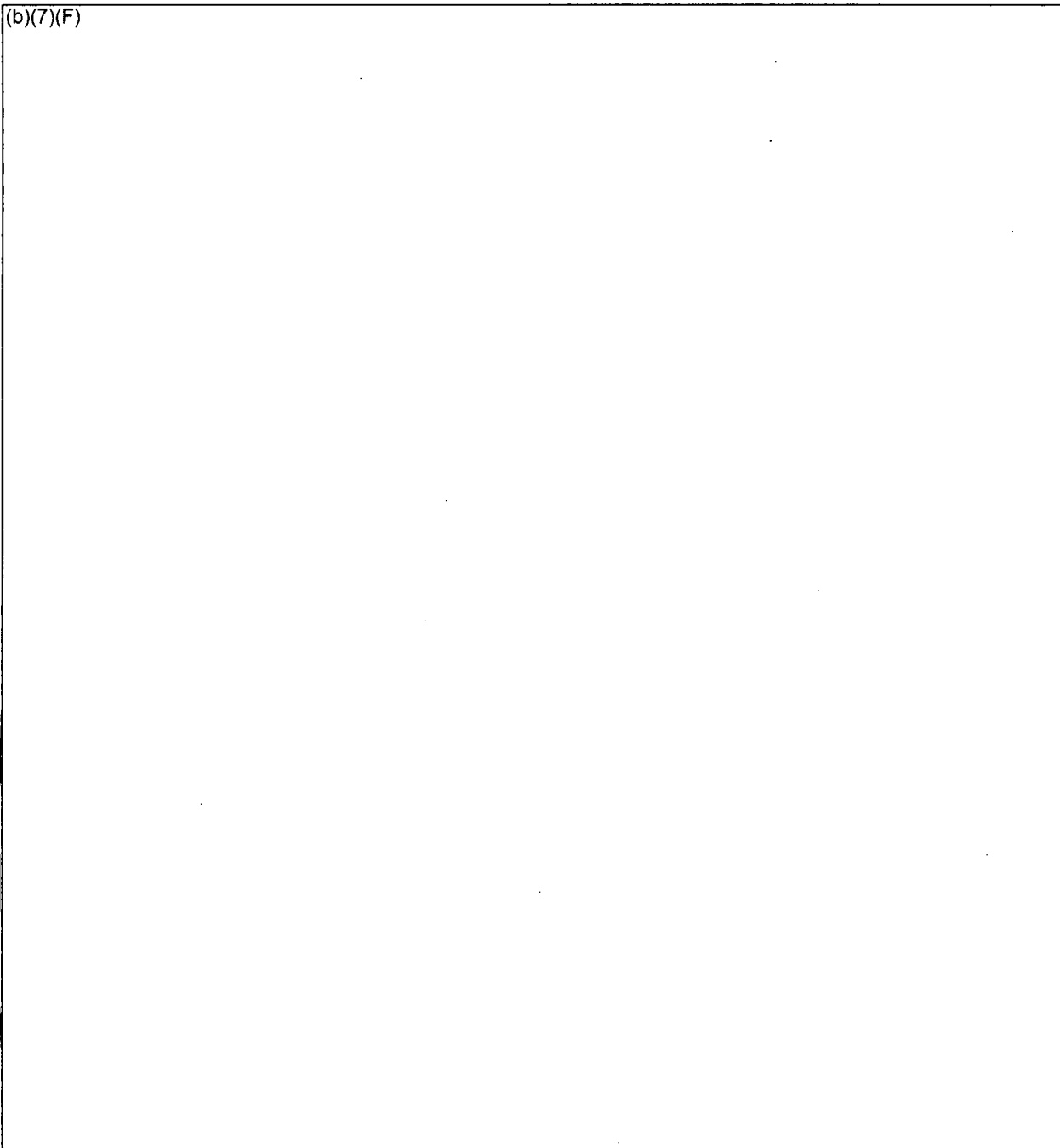


**Figure 3-20 MELCOR Reactor Building Model.**

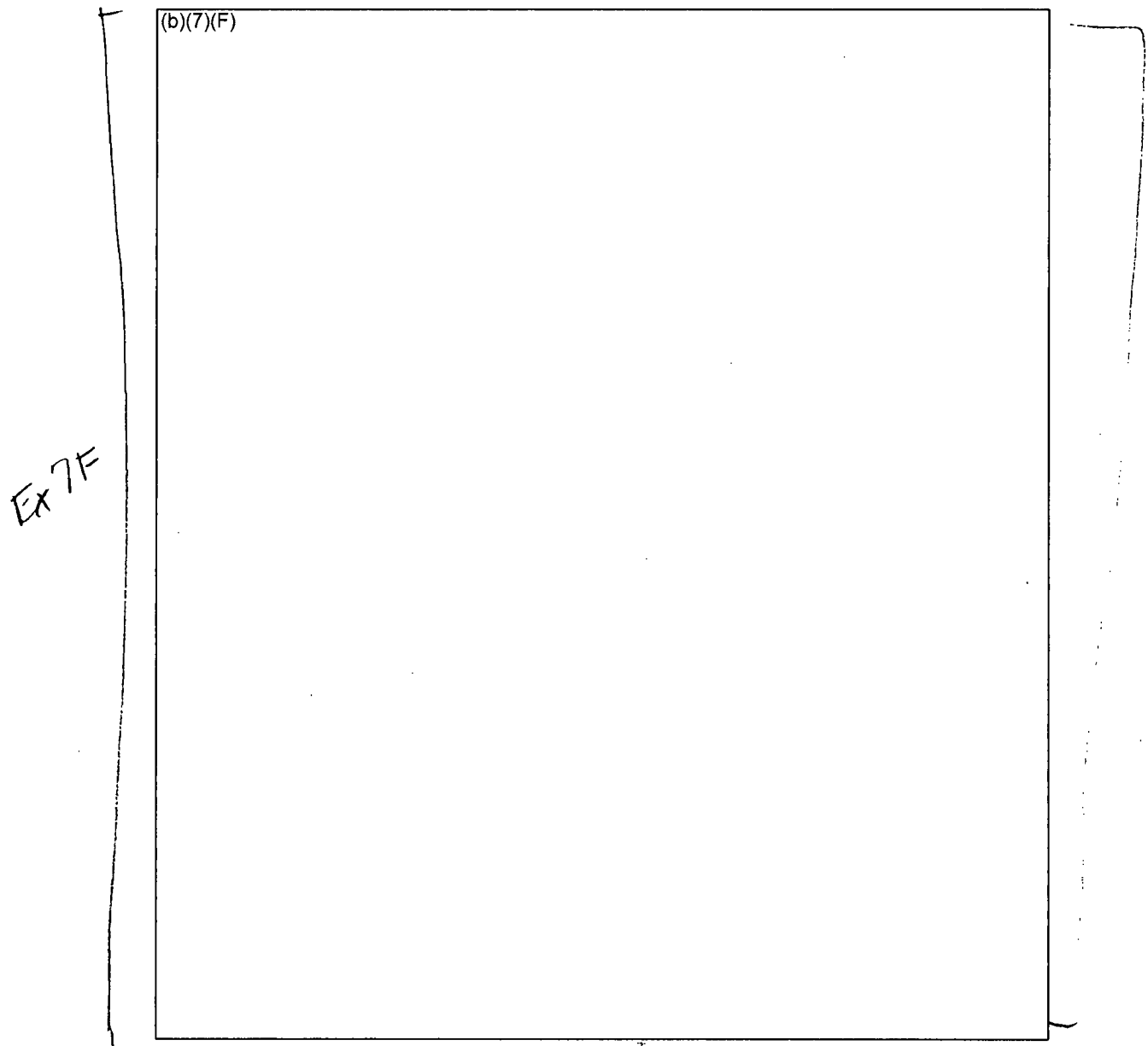


Figure 3-21 Example of Pressurized Water Reactor SFP Building Flow Patterns From FLUENT Calculations

(b)(7)(F)

Ex 7F

### 3.4 Description of the Initial and Boundary Conditions

In most cases, the separate effect BWR SFP models described in Section 3.2 were used to evaluate the fuel thermal response to emergency spray operation. The initial conditions are summarized in Table 3-4. The model was initiated from normal conditions (i.e., 300 K and normal water level). However, the pool heat removal and the building ventilation were assumed disabled. The emergency spray flowrate  $(b)(7)(F)$  across the pool cross-section. Ex 7F  
The spray system response above the SFP racks was modeled in the whole pool model and used MELCOR's spray model.

The focus of the present study was to characterize the fuel response to spray operation. Other uncertainties affecting the response have been examined in a previous BWR separate effects study [Wagner, 2003]. Table 3-5 summarizes the base values of the uncertain and variable values used in the present study. These base modeling parameters were similar to the base values used previously. The last boundary condition was the emergency spray source. It was assumed that the emergency SFP spray system evenly covered the cross-sectional area of the SFP. Once it hit the assemblies in the SFP racks, the water drained into the SFP assemblies. The spray water was introduced as a water source into the control volume representing the upper tieplate.

**Table 3-4 Summary of Base Case SFP Model Initial Conditions for BWR SFP Emergency Spray Calculations.**

Parameter	Value
Pool temperature	300 K
Water level	Normal, 37.75 ft
Pool heat removal	Deactivated
Building ventilation	Deactivated
Spray injection flowrate	$(b)(7)(F)$ Ex 7F
Spray water temperature	300 K
Spray droplet size	Usually 1250 $\mu$ m
Spray initiation time	$(b)(7)(F)$ Ex 7F
Spray nozzle overlap inefficiencies	None
Spray nozzle delivery inefficiencies	None
Notes:	
1.	The spray system is assumed $(b)(7)(F)$ uniformly across the entire SFP cross-section. Ex 7F
2.	Any inefficiencies due to overlap from adjacent spray nozzles or droplets hitting the walls or missing the SFP are not included. To $(b)(7)(F)$ into the pool, the overall system flowrate must be increased. Ex 7F
3.	Only the hybrid and whole pool models simulated the falling spray droplets. The separate effects model simulated the spray as a water pool forming on the upper tieplate of the assembly.

**Table 3-5 Summary of Base Case SFP Model Boundary Conditions for BWR SFP Emergency Spray Calculations.**

Parameter	Value
Decay Heat	Peak assembly power from utility calculation using ANSI/ANS-95 decay heat standard. Low-powered assemblies were at the reference BWR SFP median value (b)(7)(F)
Bernoulli Effect	Not explicitly included
Inlet Temperature and water level	Specified from whole pool model (see Section 5)
Initial Oxide Layer Thickness	25 $\mu\text{m}$ [Lanning]
Viscous Wall Friction Correlation	As measured in SNL experiments.
Flow Restrictions	None unless noted.
Rod Ballooning	Not modeled. <sup>16</sup>
Oxidation Correlation	ANL zircaloy-4 air oxidation kinetics model with breakaway <sup>17</sup> and Urbanic-Heidrich steam oxidation model.
Heat Transfer to surrounding cells or assemblies	Adiabatic boundary in the radial direction. Radial heat transfer was calculated within the checkerboard and 1x4 models between the low- and high-powered assemblies.
Spray water source	Specified as a liquid source to the control volume above the upper tie-plate. For the whole pool and hybrid models, the spray source was modeled using MELCOR's containment spray model [Gauntt].

Ex 71F

(b)(7)(F)

Ex 71F

<sup>17</sup> The pre- and post-breakaway air oxidation kinetics models were based on Zircaloy-4 cladding. The reference BWR assemblies have Zircaloy-2 cladding. It is assumed (and believed) that Zircaloy-4 and Zircaloy-2 will oxidize at the same rate. Due to limited data, MELCOR's breakaway timing model is based on data from both Zircaloy-4 and Zirlo samples.

#### 4. SPRAY MITIGATION HAND CALCULATIONS

Two sets of hand calculations were performed to estimate the heat removal required from the spray system in the reference BWR spent fuel pool. In the first calculation, the spray system was initiated prior to uncover of the fuel and the water leakage location is above the top of the racks. In the second hand calculation, it is assumed that the fuel is uncovered. The hand calculations represent simple straight-forward energy balances that are useful for estimating the required flowrate for a spray system. The hand calculations do not address the complications of radial heat transfer between low- and high-powered assemblies, the effectiveness of heat removal through the bypass region between the canister and the rack wall, or the response when the assumptions are violated (e.g., inadequate cooling). The MELCOR calculations in Section 6 address those phenomena and conditions.

##### 4.1 Leak Above the Top of the Racks

In the first calculation, the spray system was initiated prior to uncover of the fuel and the water leakage location is above the top of the racks. It is assumed that the accident has disabled the SFP heat removal capabilities and the decay heat from the SFP is boiling away the remaining inventory. Depending on the time of the accident, the decay heat varies. Close to the most recent offload of fuel into the SFP, the decay heat is highest (see whole pool decay heat for the reference BWR in Figure 4-1). Figure 4-2 shows the required flow rate to maintain the SFP level.

The calculations for the heat removal requirements at (b)(7)(F) are shown below. (b)(7)(F) Ex 7F  
Ex 7F (b)(7)(F) is required. Since the fuel is covered, a spray system is not technically needed. Rather any water injection system would be sufficient.

##### Assumptions:

1. Reference BWR SFP decay heat data
2. Last offload had (b)(7)(F) since reactor shutdown Ex 7F
3. 80°F spray water
4. Decay heat removal is provided by boiling spray (injection) water
5. Other modes of heat transfer are ignored.

$$\rho = 62.1 \text{ lbm/ft}^3 = 996 \text{ kg/m}^3$$

$$h_{fg} = 970.3 \text{ BTU/lbm} = 2.257 \times 10^6 \text{ J/kg}$$

$$h_{80^\circ\text{F} \rightarrow 212^\circ\text{F}} = 180.18 \text{ BTU/lbm} - 48.13 \text{ BTU/lbm} = 132.05 \text{ BTU/lbm} = 3.072 \times 10^5 \text{ J/kg}$$

$$\Delta h = h_{fg} + h_{80^\circ\text{F} \rightarrow 212^\circ\text{F}} = 1102 \text{ BTU/lbm} = 2.56 \times 10^6 \text{ J/kg}$$

Whole pool decay heat at (b)(7)(F)

Ex 7F

$$\text{Spray Flowrate} = \frac{(b)(7)(F)}{(264.2 \text{ gal/m}^3)} (996 \text{ kg/m}^3 * 2.56 \times 10^6 \text{ J/kg}) * (60 \text{ sec/min})$$

$$= (b)(7)(F)$$

Ex 7F

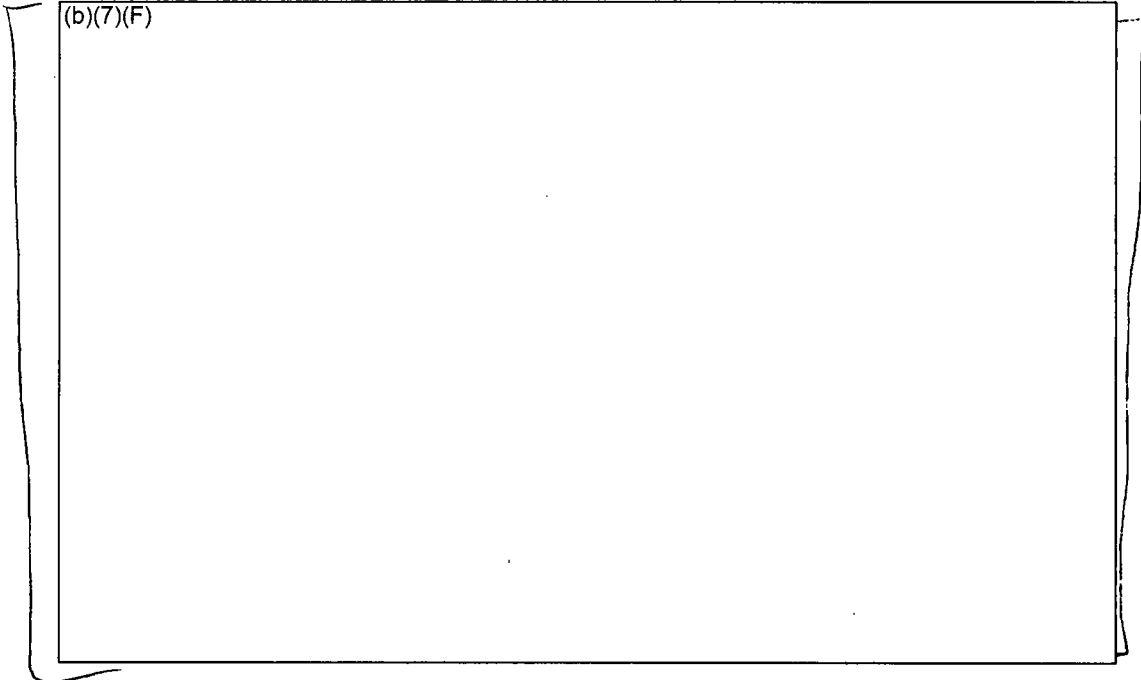


Figure 4-1 Total Decay Heat Power in the Reference BWR SFP.

Ex 7F

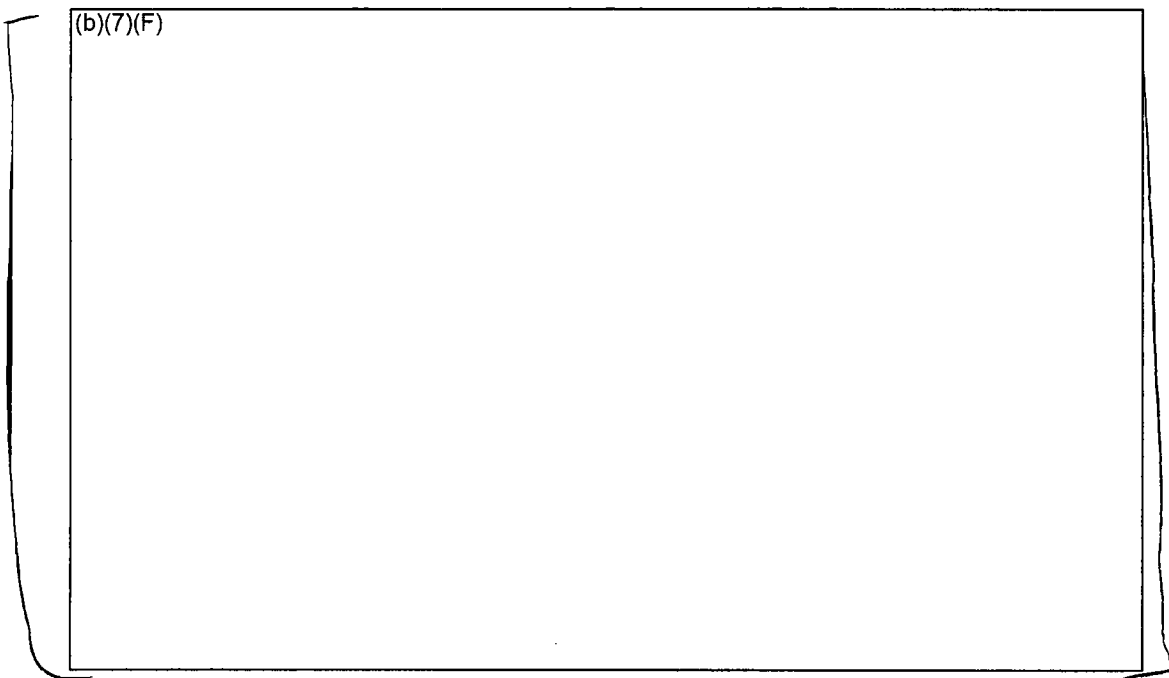


Figure 4-2 Make-up Flowrate for the Reference BWR SFP.

#### 4.2 Leak Below the Top of the Racks

In the second calculation, the spray system was not initiated prior to uncover of the fuel and/or the water leakage location is below the top of the racks. Similar to the previous calculation, the accident has disabled the SFP heat removal capabilities and the decay heat from the SFP is boiling away the remaining inventory. It is assumed that the spray system is initiated before the fuel becomes uncovered. If not, additional spray would be required to remove the sensible heat from the regions of the assembly which has heated (e.g., see Section 4.2.3). Furthermore, if the fuel rods are at high temperature, then the initial mode of spray heat removal would be film boiling, which is less effective than nucleate boiling.

There are several other assumptions that were applied for these calculations. Since the fuel is uncovered, a spray system is required to distribute the water to the individual assemblies. To achieve a uniform coverage, the spray systems would have some inefficiencies due to overlap from the adjacent nozzles and inaccurate delivery (e.g., hitting walls or missing the pool). The magnitude of the total SFP spray flow assumes a 33% spray overlap factor to account for these two inefficiencies. However, the hand calculations assume that the most limiting assembly is not within a zone that has spray overlap. Furthermore, only the spray which enters the assembly canister was considered as effective (i.e., neglect spray into the space between the assembly canister and the rack cell wall). In addition, all other modes of heat transfer are conservatively

neglected. For example, radial heat transfer to adjacent lower powered assemblies was neglected.

Figure 4-3 shows the peak, median, and minimum assembly power in the reference BWR SFP as a function of time after the last offload. (b)(7)(F)

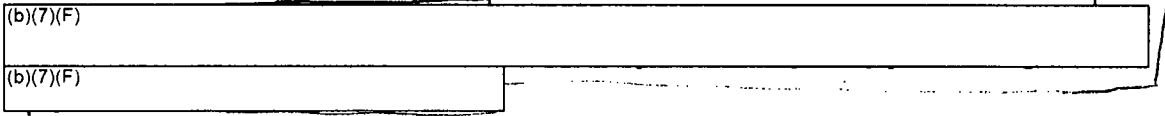
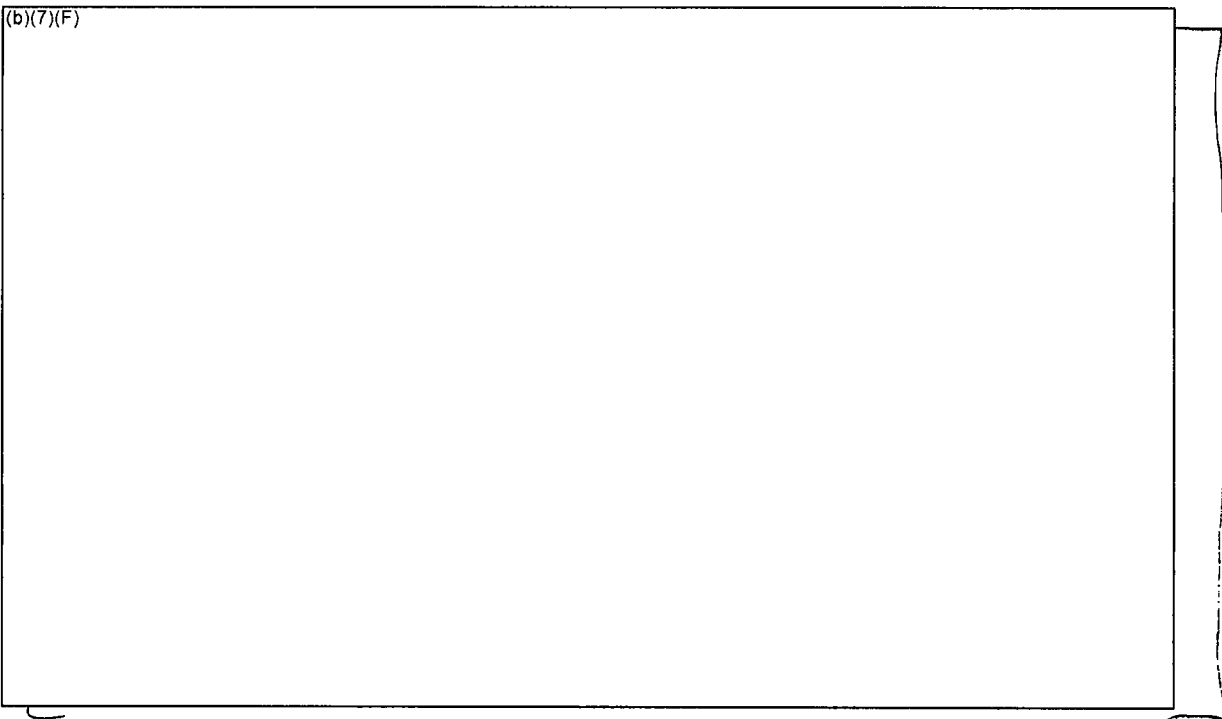


Figure 4-4 shows the required spray rate to provide adequate heat removal from the peak decay heat assembly. For example, (b)(7)(F) Furthermore, a spray system is required to direct the flow into the assemblies. Sample calculations for the heat removal requirements (b)(7)(F) are shown in Section 4.2.1. Some scoping hand calculations suggest that the spray water will be able to penetrate into the assembly (b)(7)(F) (see Section 4.2.2). Finally, the impact of the assembly sensible heat upon the initial spray effectiveness is discussed in Section 4.2.3.

Ex 7F



**Figure 4-3 Comparison of the Peak, Median, and Minimum Assembly Decay Heat Power in the Reference BWR SFP.**

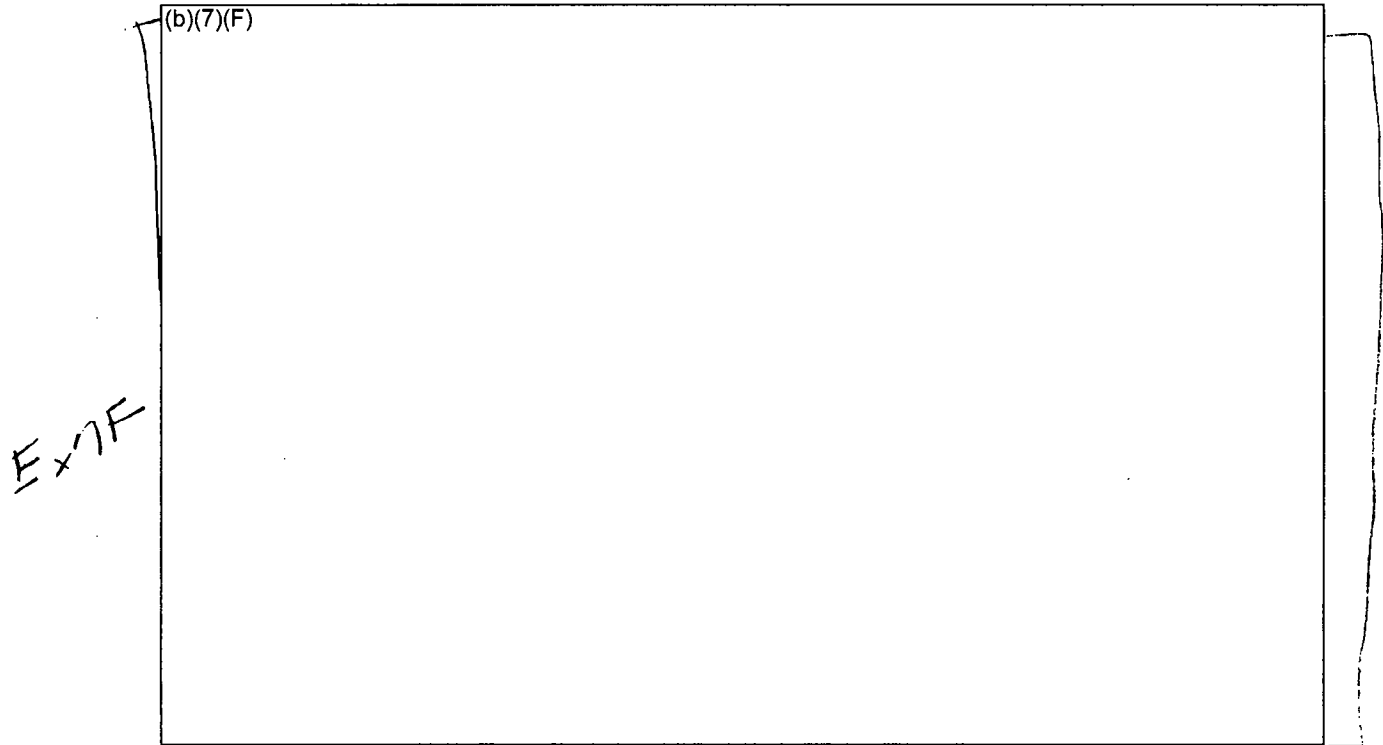


Figure 4-4 Make-up Flowrate for the Reference BWR SFP.

#### 4.2.1 Calculations for One Point on the BWR Spray Chart

Assumptions:

1. Reference BWR SFP data, Ex 7F
2. Peak assembly (b)(7)(F) Ex 7F
3. 80°F spray water
4. 33% spray coverage inefficiency/overlap
5. Only flow within the canister cross-section is effective
6. Make-up based on peak assembly decay heat projected across entire pool

$$\rho = 62.1 \text{ lbm/ft}^3 = 996 \text{ kg/m}^3$$

$$h_{fg} = 970.3 \text{ BTU/lbm} = 2.257 \times 10^6 \text{ J/kg}$$

$$h_{80^\circ\text{F} \rightarrow 212^\circ\text{F}} = 180.18 \text{ BTU/lbm} - 48.13 \text{ BTU/lbm} = 132.05 \text{ BTU/lbm} = 3.072 \times 10^6 \text{ J/kg}$$

$$\Delta h = h_{fg} + h_{80^\circ\text{F} \rightarrow 212^\circ\text{F}} = 1102 \text{ BTU/lbm} = 2.56 \times 10^6 \text{ J/kg}$$

Peak assembly power  $\frac{(b)(7)(F)}{(b)(7)(F)}$

BWR SFP Assembly Pitch = 6.28"  
BWR SFP Canister ID = 5.4

Inside canister area to cell pitch ratio =  $(5.4" \times 5.4") / (6.28" \times 6.28") = 0.739$

Whole Pool Size =  $480" \times 424" = 203,520 \text{ in}^2 = 131.3 \text{ m}^2$  (Cross-sectional area)

Equivalent number of SFP rack cells in entire SFP cross-section  
 $= 203,520 \text{ in}^2 / (6.28" \times 6.28") = 5160$  equivalent cells

Spray Flowrate =  $\frac{(b)(7)(F)}{(264.2 \text{ gal/m}^3)} (996 \text{ kg/m}^3 * 2.56 \times 10^6 \text{ J/kg}) * (60 \text{ sec/min})$   
 $* 1.33 \text{ (overlap)} * 1.35 \text{ (chan ratio)} * 5160 \text{ equiv. cells}$

$\frac{(b)(7)(F)}{(b)(7)(F)}$

#### 4.2.2 Calculations for Counter-Current Flow Limitation (CCFL)

$\frac{(b)(7)(F)}{(b)(7)(F)}$

Ex 7F

Consequently, counter-current flow limiting (CCFL) of water down into the assembly due to the shear forces from the upward steam flow is a concern.

The following terms are needed to calculate the Wallis non-dimensional flooding velocities to evaluate whether CCFL is a concern, assuming a downward liquid velocity  $\frac{(b)(7)(F)}{(b)(7)(F)}$  water and steam properties, and the reference BWR geometry  $\frac{(b)(7)(F)}{(b)(7)(F)}$

Ex 7F

First, calculate the phasic volumetric fluxes [Wallis],

Ex 7F

$$J_i = Q_i / A$$

where,

$J_i$  is the phasic volumetric flux

$Q_i$  is the volumetric flow

$$Q_L = \frac{(b)(7)(F)}{(b)(7)(F)}$$

$$Q_G = \frac{(b)(7)(F)}{(b)(7)(F)}$$

A is the cross-sectional flow area  $\frac{(b)(7)(F)}{(b)(7)(F)}$

So,

$$\frac{J_L}{J_G} = \frac{(b)(7)(F)}{(b)(7)(F)}$$

Next calculate  $J_i^*$  terms,

$$J_i^* = J_i * (\rho_i)^{1/2} / [g * D_H * (\rho_L - \rho_G)]^{1/2}$$

where,

$Q_i$  is the phasic volumetric flux

$$Q_L = \boxed{(b)(7)(F)} \quad E_x$$
$$Q_G = \boxed{(b)(7)(F)} \quad E_x$$

$g$  is gravity ( $9.81 \text{ m/s}^2$ )

$D_H$  is the hydraulic diameter of the upper assembly  $\boxed{(b)(7)(F)} \quad E_x$

$\rho_L$  is the water density ( $996 \text{ kg/m}^3$ )

$\rho_G$  is the steam density ( $0.598 \text{ kg/m}^3$ )

So,

$$J_G^* = \frac{E_y}{J_G} = \frac{\boxed{(b)(7)(F)}}{\boxed{(b)(7)(F)}} \left[ 9.81 \text{ m/s}^2 * \frac{E_x}{\boxed{(b)(7)(F)}} \right] \left[ (996 \text{ kg/m}^3 - 0.598 \text{ kg/m}^3) \right]^{0.5}$$

$$J_L^* = \frac{E_y}{J_L} = \frac{\boxed{(b)(7)(F)}}{\boxed{(b)(7)(F)}} \left[ 9.81 \text{ m/s}^2 * \frac{E_x}{\boxed{(b)(7)(F)}} \right] \left[ (996 \text{ kg/m}^3 - 0.598 \text{ kg/m}^3) \right]^{0.5}$$

Next Grashof Number is calculated as follows,

$$N_L = [ \rho_L \cdot g \cdot D^3 (\rho_L - \rho_G) / \mu_L^2 ]^{1/4}$$

$$N_L = [ 996 \text{ kg/m}^3 * 9.81 \text{ m/s}^2 * \frac{E_y}{\boxed{(b)(7)(F)}} * (996 \text{ kg/m}^3 - 0.598 \text{ kg/m}^3) / (2.82 \times 10^{-4} \text{ kg/m-s}) ]^{1/4}$$

$$N_L = \frac{\boxed{(b)(7)(F)}}{\boxed{(F)}} \quad E_y$$

From the Wallis flooding curve with  $N_L = \frac{\boxed{(b)(7)(F)}}{\boxed{(F)}} \quad E_x$

$$m = \frac{\boxed{(b)(7)(F)}}{\boxed{(F)}} \quad E_x$$

The flooding (CCFL) limit is,

$$(J_G^*)^{0.5} + (J_L^*)^{0.5} = \frac{\boxed{(b)(7)(F)}}{\boxed{(F)}} \quad E_y$$
$$\frac{\boxed{(b)(7)(F)}}{\boxed{(F)}}^{0.5} + \frac{\boxed{(b)(7)(F)}}{\boxed{(F)}}^{0.5} = 0.8 \quad E_x$$

$$\frac{\boxed{(b)(7)(F)}}{\boxed{(F)}} < 0.8, \text{ which is below the flooding limit}$$

Another criterion by Wallis also suggests that the flow conditions are well below the flow reversal limitation,

$$J_G^* = 0.5 \text{ for flow reversal.}$$

In our case,

$$\frac{\boxed{(b)(7)(F)}}{\boxed{(F)}} < 0.5? \quad E_x$$

Ex

$$\frac{(b)(7)(F)}{(F)} < 0.5, \text{ which is also below the flooding limit}$$

It has been acknowledged that the classical Wallis correlations have some limitations due to the diameter effect [Bergles]. Using an alternate Kutaleadze relationship, which represents the ratio of the gas inertial forces acting on the capillary waves,

$$Ku = (J_g) * (\rho_g)^{1/2} / [g \sigma (\rho_L - \rho_G)]^{1/4}$$

where,

Ku is the Kutaleadze Number

$\sigma$  is surface tension between steam and water (0.072 kg/s<sup>2</sup>)

Ex

$$Ku = \frac{(b)(7)(F)}{(F)} * (0.598 \text{ kg/m}^3)^{1/2} / [9.81 \text{ m/s}^2 * 0.073 \text{ kg/s}^2 * (996 \text{ kg/m}^3 - 0.598 \text{ kg/m}^3)]^{1/4}$$

Ex

$$Ku = \frac{(b)(7)(F)}{(F)} < 3.2$$

If the Kutaleadze number is less than 3.2, then there is no CCFL. Hence, all three flooding correlations show CCFL is not expected to be a concern (b)(7)(E) (i.e., peak assembly decay heat power (b)(7)(F) Ex

#### 4.2.3 Impact of Assembly Sensible Heat

The assembly sensible heat has an effect on the spray heat removal effectiveness. If the sprays are started after the assembly begins heating, then a portion of the water's cooling potential removes the sensible heat from the assembly. A high amount of sensible energy (i.e., high temperature) also transitions the rod heat transfer from nucleate boiling to less effective film boiling. If film boiling is not effective, then the fuel would continue to heat.

Assuming that the heat transfer (i.e., whether film or nucleate boiling) is effective enough to boil all the spray water entering the limiting assembly, the impact on the cooling time is shown in Figure 4-5 and Figure 4-6 (b)(7)(F) spray flow, respectively. The amount of time required to cool the assembly to near saturation conditions from various initial temperatures while simultaneously removing decay heat is quantified in these figures. (b)(7)(F) Ex 7F

(b)(7)(F)

(b)(7)(F)

Ex 7F

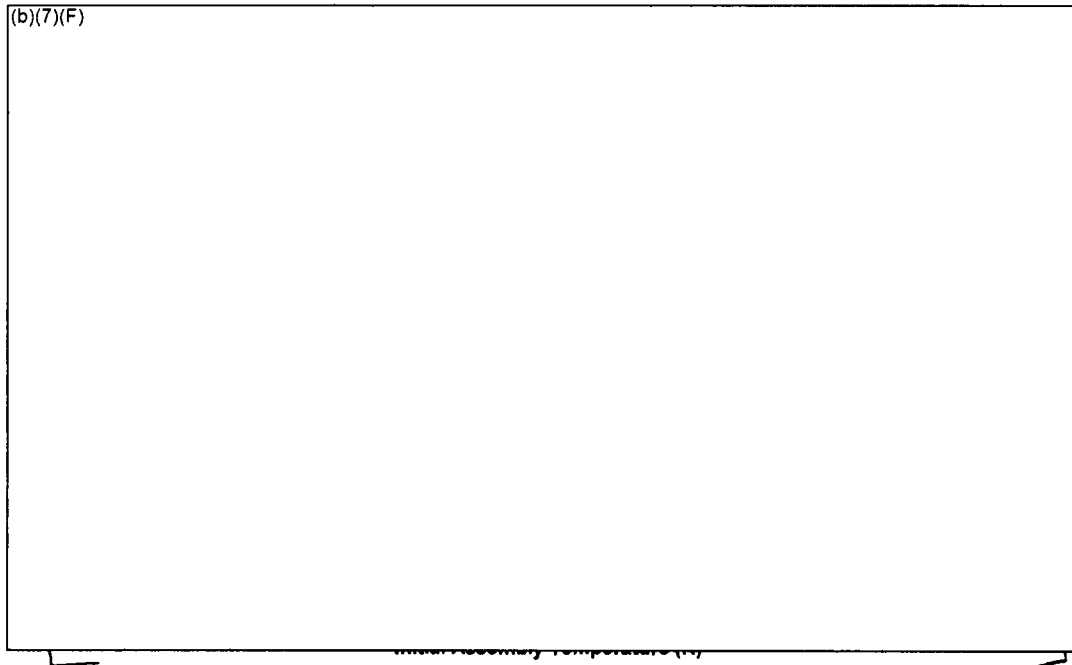


Figure 4-5 Timing Impact of Sensible Heat on Assembly Cooling at (b)(7)(F) for a Uniform Configuration.   
 EOF

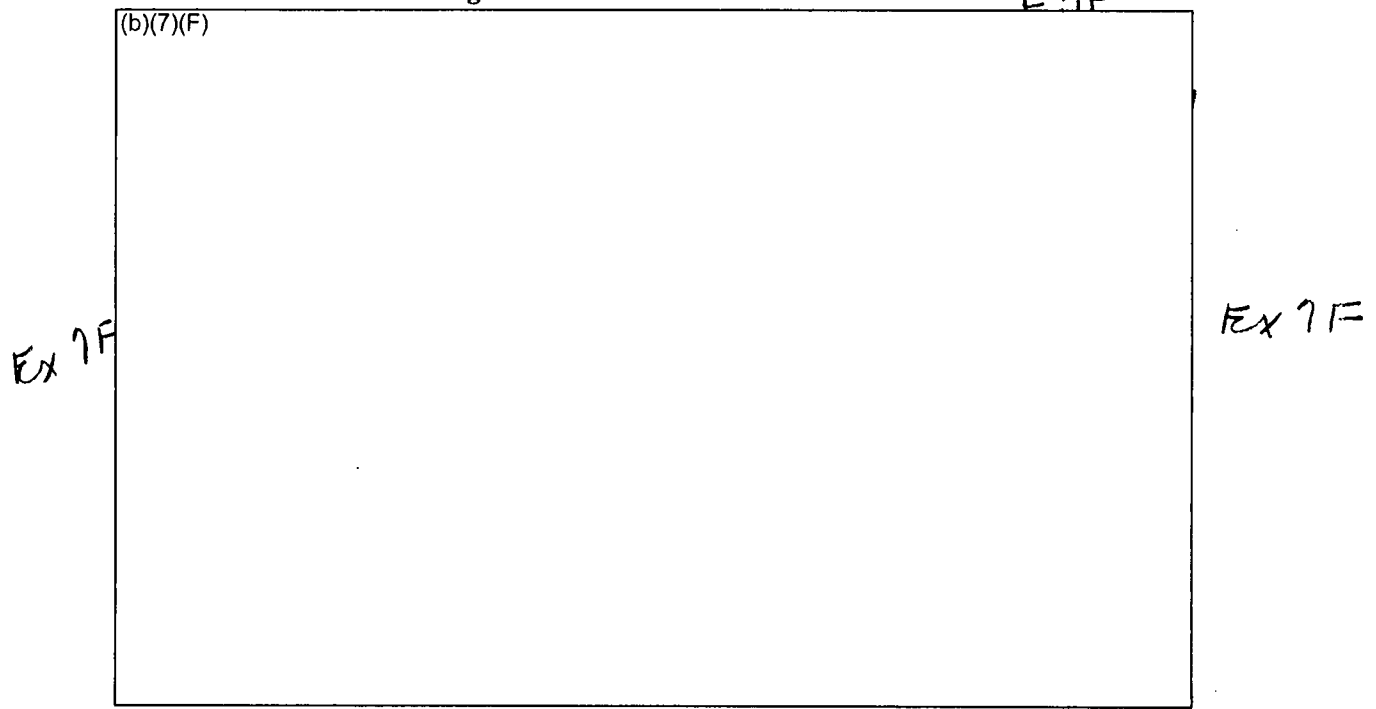


Figure 4-6 Timing Impact of Sensible Heat on Assembly Cooling at (b)(7)(F) for a Uniform Configuration.

### 5. WHOLE POOL MODEL BOUNDARY CONDITION CALCULATIONS

An assortment of whole pool calculations was run using the new whole pool model (see Section 3.3) to establish boundary conditions for the separate effects calculations. Section 5.1 shows typical results (b)(7)(F) equivalent diameter leak with (b)(7)(F). The detailed responses from other cases are not shown but were similar.

The most interesting of these boundary condition values was the resultant water level. (b)(7)(F)

(b)(7)(F)  
(b)(7)(F)

Ex 7F

Table 5-1 summarizes the results from the whole pool calculations. For the range of hole sizes and spray flow rates considered in this study, the long-term water level spanned conditions that would allow air flow (i.e., the inlet is not plugged) versus cases where the inlet would be plugged. (b)(7)(F) hole cases had a relatively high level that would partially cover the bottom of the fuel (a water level of >16"). In contrast, (b)(7)(F) hole had a very low water level and would be ensured to have air natural circulation flow. As discussed in Section 2.2, the phenomena and thermal response for cases with the inlet plugged by the water level is much different than the response when there is air flow in the assembly. Furthermore, it is expected that (b)(7)(F) case with (b)(7)(F) hole might have characteristics of both types of accidents.

Ex 7F

Ex 7F

**Table 5-1 Summary of the Steady-State Water Levels as a Function of Leakage Hole Size and Spray Flow Rate.**

(b)(7)(F)

Ex 7F

5.1 (b)(7)(F) Spray Flow Rate

Ex 7F Figure 5-1 through Figure 5-4 show the boundary conditions taken (b)(7)(F) Ex 7F (b)(7)(F) emergency spray flow. A special boundary condition control volume was created to specify fluid boundary conditions for the separate effects model. The time-dependent data consisted of water level (Figure 5-1), water and gas temperature (Figure 5-2), steam partial pressure (Figure 5-3), non-condensable gas concentrations (Figure 5-5<sup>18</sup>, actually reflects normal atmospheric concentrations of nitrogen and oxygen), and gas pressure (not shown, approximately atmospheric pressure). The blue points on each figure represent the data transferred to the separate effects model.

The whole pool results show expected trends. The water level drops in response to the leakage. Since the boundary condition control volume is only 5 m, Figure 5-1 only shows the level response below 5 m. Figure 5-4 shows the overall model level response. (b)(7)(F) Ex 7F

(b)(7)(F) Since the base plate of the racks is 7.25" off the SFP floor, there was a circulation of natural air into the racks.

The water temperatures initially heated in response to the loss of SFP heat removal. Once the rack uncovered, separate gas and water temperatures are calculated. However, due to spray cooling, the pool under the racks and the gas temperatures remained relatively low (b)(7)(F) Ex 7F (b)(7)(F) Due to boiling of the spray water in the hot assemblies and evaporation, the partial pressure of the steam in the room also steadily increased (Figure 5-3). After 48 hours, the equivalent steam molar concentration was (b)(7)(F) (see Figure 5-5). Ex 7F

Ex 7F Figure 5-6 shows the flow balance between the water leakage flow from the SFP and the emergency spray flow. Initially the water leakage flow was very high due to the large head of water above the leakage location. As the water level dropped, the water leakage flow steadily decreased. (b)(7)(F) Ex 7F emergency spray system was started. However, due to the high leakage flowrate, emergency spray had little impact in slowing the level drop. (b)(7)(F) Ex 7F the water level (b)(7)(F) and the leakage flow is equal to the spray flow. The level remained at this value for the remainder of the calculation.

<sup>18</sup> The data from Figure 5-5 was not used directly. However, it was included to show the relative molar concentrations of steam, oxygen, and nitrogen. To define the gas composition, the steam partial pressure (Figure 5-3) was used with constant non-condensable molar concentrations of oxygen (20%) and nitrogen (80%).

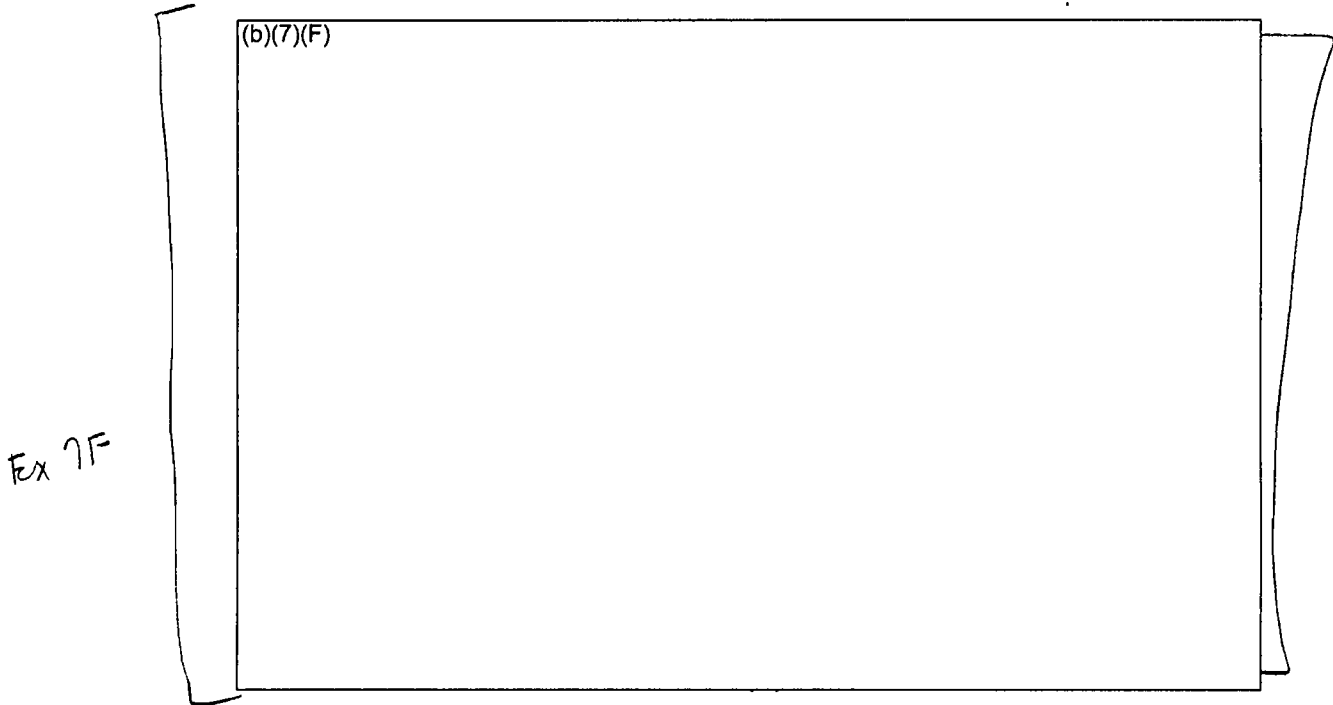


**Figure 5-1** Water Level Boundary Condition from the BWR Whole Pool Model with (b)(7)(F) and a Spray Flow of (b)(7)(F) Ex 7F

Temperature Boundary Condition for SE Model

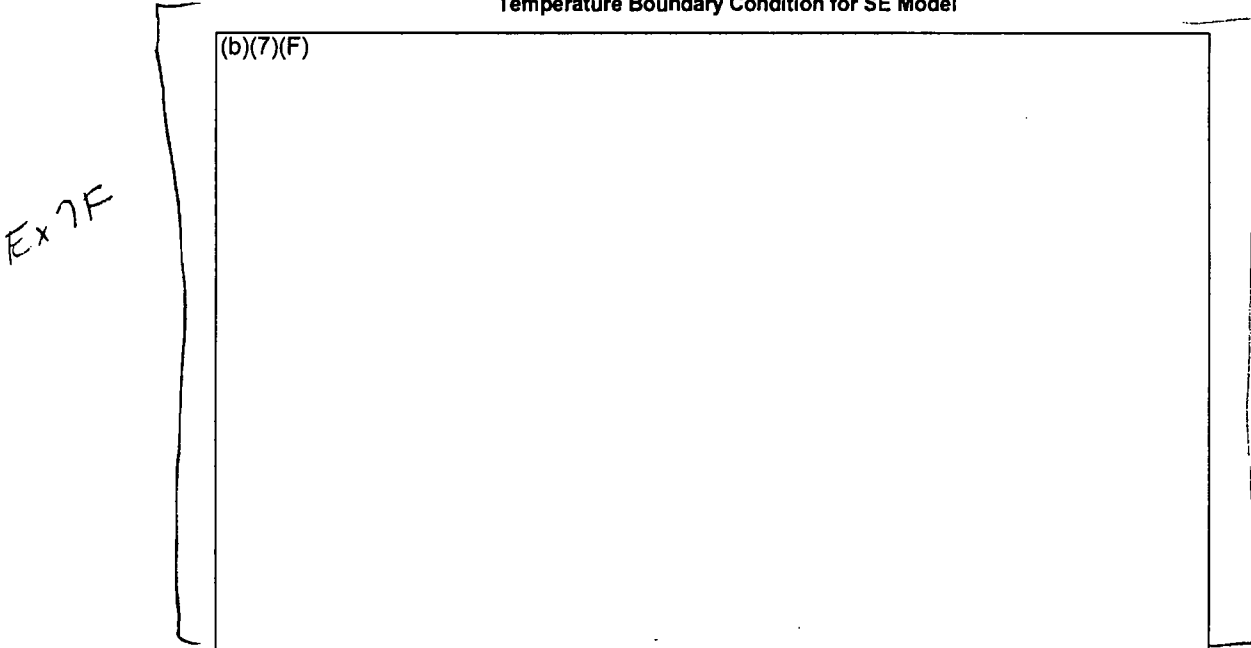


**Figure 5-2** Vapor and Liquid Temperature Boundary Condition from the BWR Whole Pool Model with (b)(7)(F) and a Spray Flow of (b)(7)(F) Ex 7F

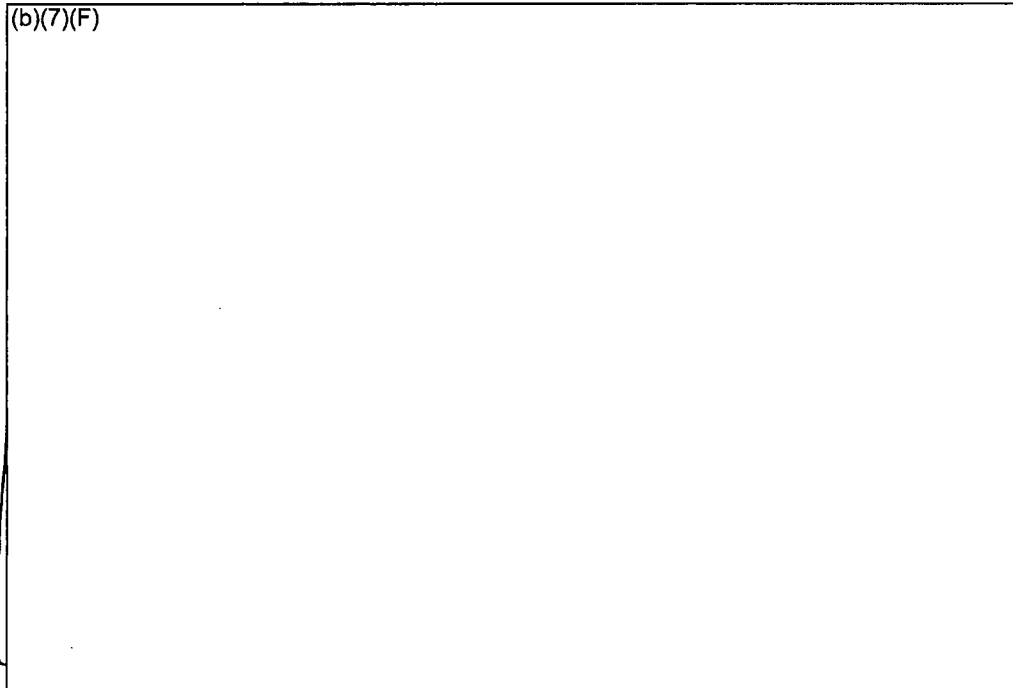


Figure 5-3 Steam Partial Pressure Boundary Condition from the BWR Whole Pool Model with (b)(7)(F) and a Spray Flow of (b)(7)(F)

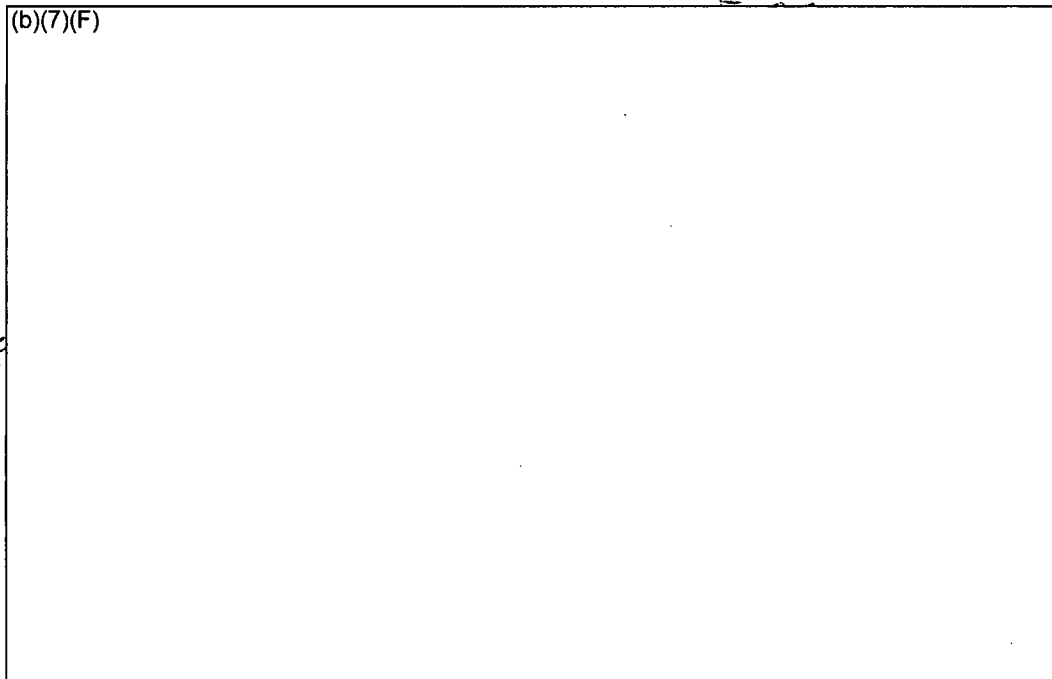
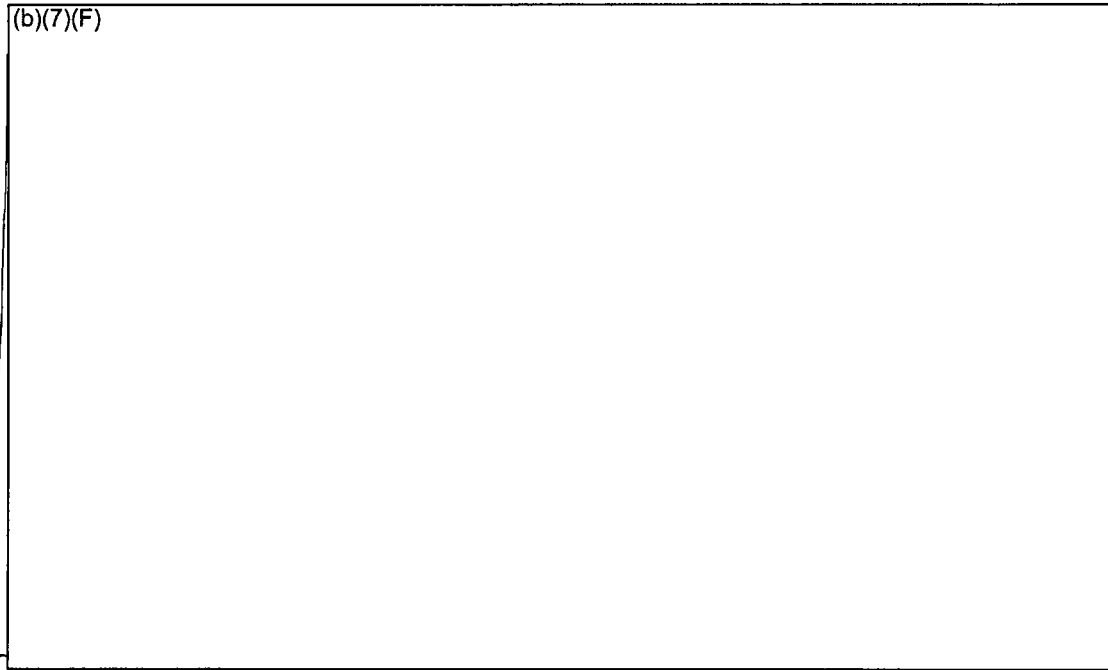


Figure 5-4 Whole Pool Level Response (b)(7)(F) with (b)(7)(F) and a Spray Flow of (b)(7)(F)

Ex 7F

Ex 7F



**Figure 5-5 Gas Concentration in the Refueling Room above the SFP for (b)(7)(F) and a Spray Flow of (b)(7)(F)**

Ex 7F

Ex 7F

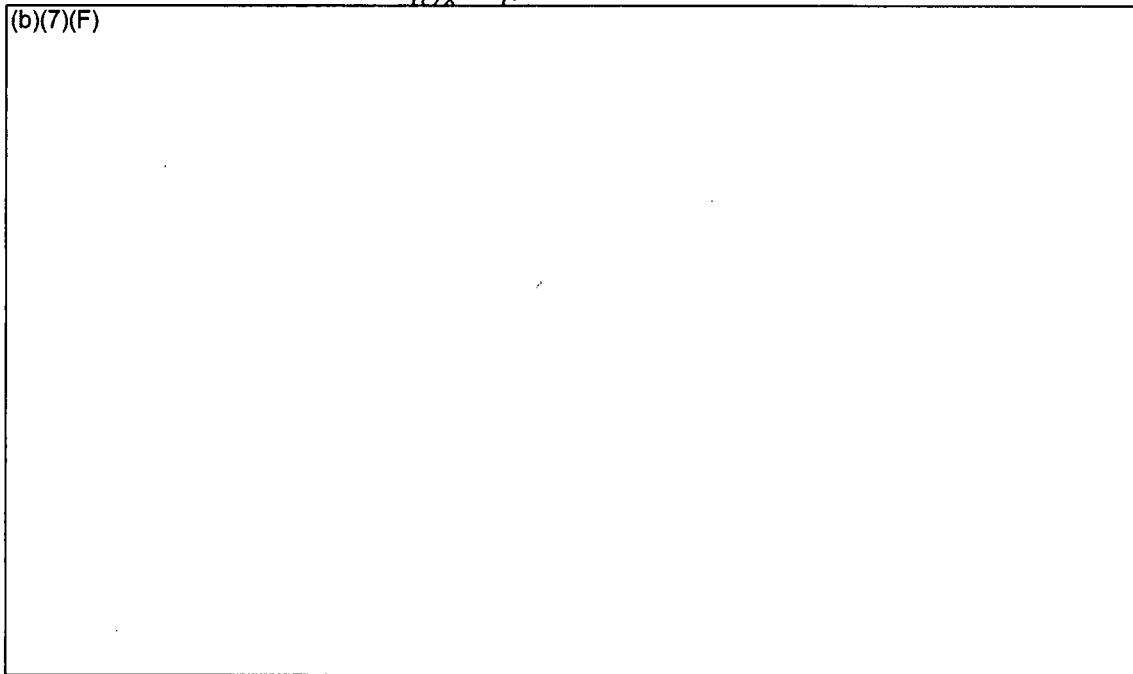


**Figure 5-6 Comparison of the Leak Rate and Spray Flowrate Response from a (b)(7)(F) (b)(7)(F) and a Spray Flow of (b)(7)(F)**

Ex 7F

## 6. MELCOR SEPARATE EFFECTS MODEL RESULTS

Section 6.1 provides a table with a coolability summary of all the separate effects spray calculation. Additional details about the uniform, checkerboard, and 1x4 configuration calculations are provided in Sections 6.2, 6.3, and 6.4, respectively.

### 6.1 Summary of Separate Effect Spray Calculations

Table 6-1 summarizes the results of the spray separate effects calculations. Calculations were performed for the uniform, checkerboard, and 1x4 configurations. For each configuration, parametric calculations were performed with variations in one of the scenario or modeling attributes. The various groups of calculations are separated by bold horizontal lines in the table. The table was intended to provide a quick quantitative summary of the coolability results from the various cases. The variations in the calculations included fuel configuration (uniform, checkerboard, and 1x4), aging time of the peak powered assembly, leak size (b)(7)(F) Ex 7F spray flow rate (b)(7)(F) Ex 7F air flow (some configurations that were expected to have air flow had a sensitivity study where the inlet was plugged with water), and a modeling parameter (MELCOR's flow regime model active or inactive).

The high level results are presented in the last two columns of the table. (b)(7)(F)

(b)(7)(F) Ex 7F

cladding temperature is listed. Additional details about the uniform, checkerboard, and 1x4 configurations are provided in Sections 6.2, 6.3, and 6.4, respectively.

**Table 6-1 Summary of the Spray Calculations**

(b)(7)(F)

Ex 7F

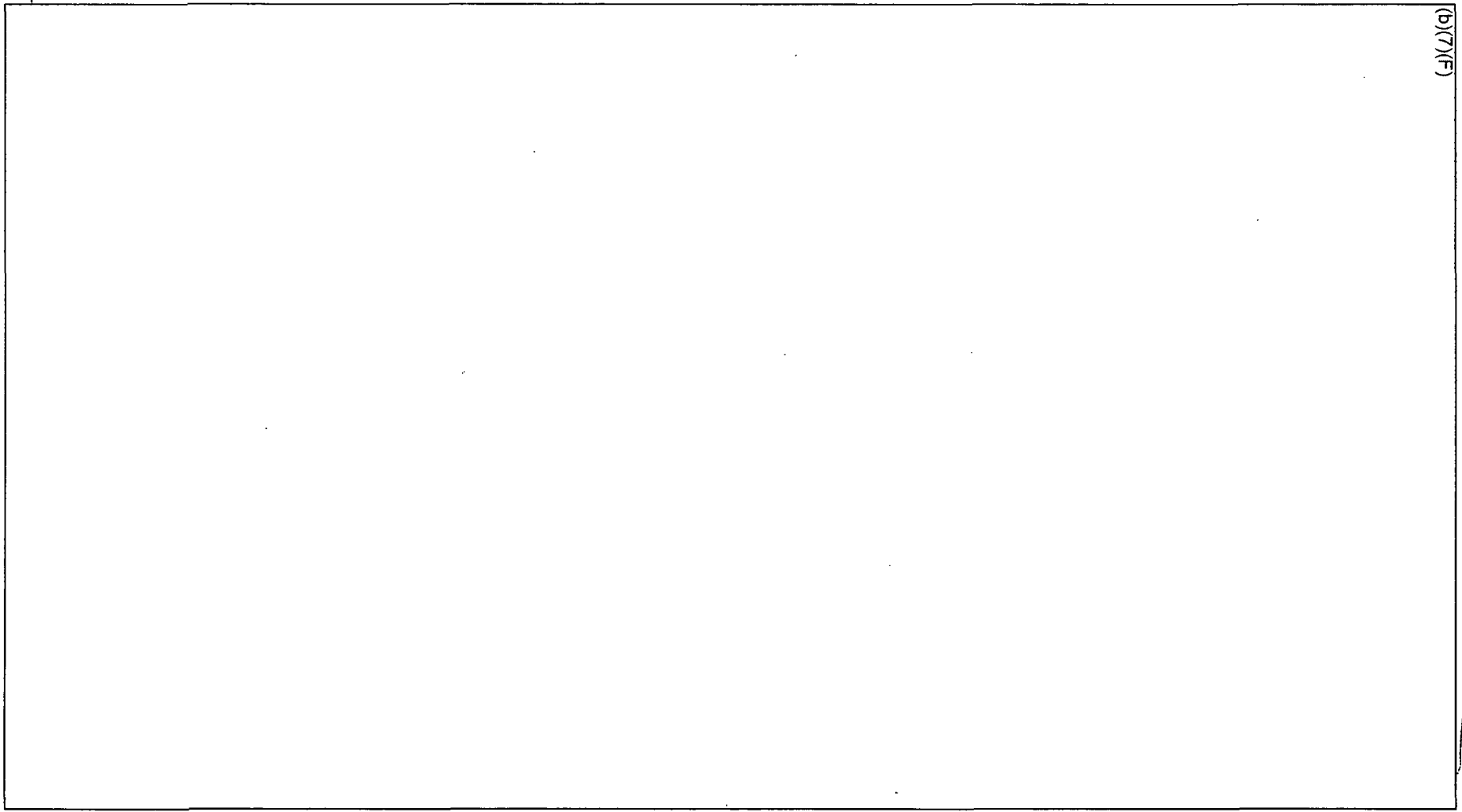
Table 6-1 Summary of the Spray Calculations

(b)(7)(F)

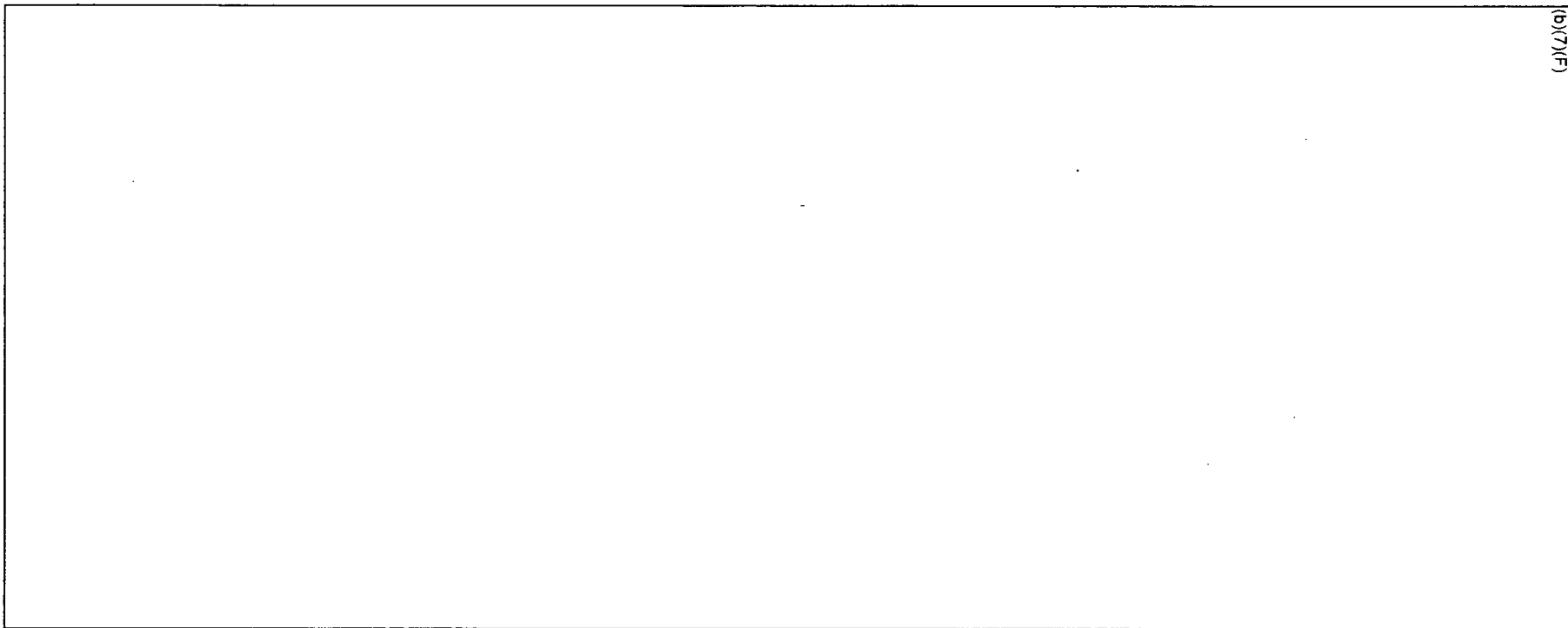
Ex 7F

Ex 7F

Table 6-1 Summary of the Spray Calculations



(b)(7)(F)



(b)(7)(F)

Ex 7F

## 6.2 Separate Effects Spray Model Results for the Uniform Configuration

Section 6.2.1 gives a summary of the 4 cases with (b)(7)(F) leakage hole in a uniform fuel configuration. The four cases examine differences in the response with and without sprays and with and without the flow regime model active (see Section 3.1.4 for a more complete discussion). Section 6.2.2 shows the results of an energy balance on a spray case to illustrate the heat flows. Finally, Sections 6.2.3, 6.2.4, and 6.2.5 show the coolability results as a function of aging for different leakage rates and spray flow rates.

### 6.2.1 Base Calculations for Spray

The S1 and S5 base case configuration calculations simulated a uniform configuration of the highest powered assemblies discharged into the spent fuel pool with (b)(7)(F) since reactor shutdown. The uniform configuration represents the response of an assembly in the center of a region of high-powered assemblies, such that there is negligible radial heat transfer (i.e., an adiabatic condition in the radial direction).

(b)(7)(F)

(b)(7)(F) examined differences in the response with and without sprays and with and without the flow regime model active. When the flow regime model was deactivated, the spray water has a relatively small surface contact area with the cladding. Due to the reduction of heat transfer, the spray flow penetrates more deeply into the assembly before completely evaporating. In addition, a S1 case was run where the inlet of the assembly was plugged by water. As discussed in Section 5, depending upon the hole size and the spray rate, cases were identified where the inlet to the racks could be covered. Consequently, Case S1 and S1p parametrically investigated both conditions. However, it should be noted that the best-estimate level responses (b)(7)(F) with (b)(7)(F) sprays were well below the bottom of the rack baseplate.

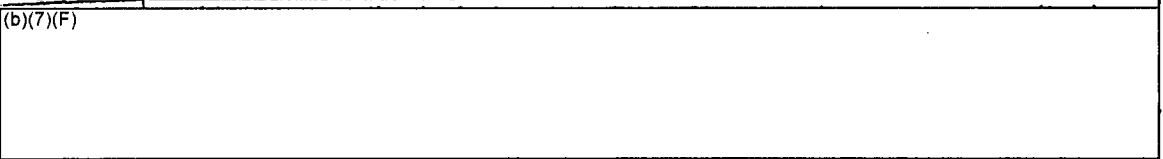
(b)(7)(F)

The axial temperature profiles for the four cases are shown in Figure 6-3 through Figure 6-6.

(b)(7)(F)

correspond to the COR Package nodalization shown in Figure 3-16. For example, COR-TCL.104 corresponds to the COR Package cladding temperature in Ring 1 and Level 4. Level 4 is the bottom of the active fuel and Level 12 is the top of the active fuel. Level 13 is the gas plenum at the top of the fuel rods.

The axial temperature response for the case with the flow regime model inactive is shown in Figure 6-4. (b)(7)(F)



Ex 7F

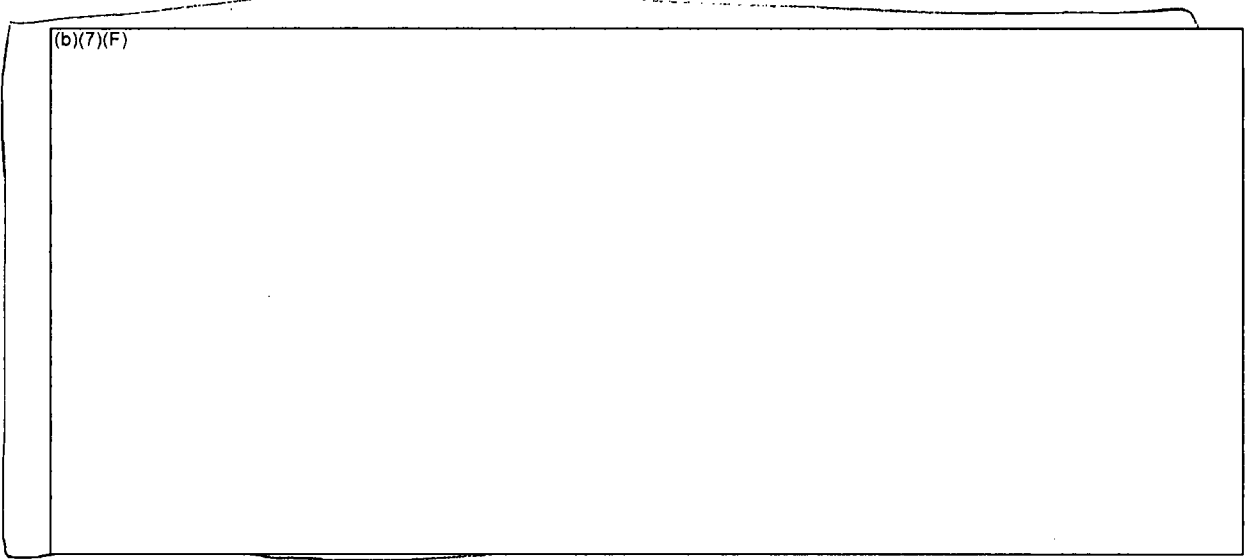
The plugged case (S1p) did not have air cooling. As shown in Figure 6-1 and Figure 6-6, the peak temperature response was similar to Case S1. However, the absence of air in the assembly led to less oxidation heating and a slower heatup at high temperatures. (b)(7)(F) Ex 7F

Ex 7F

Finally, the axial temperature profiles (b)(7)(F) are shown in Figure 6-7 for all four cases. It is interesting to observe that the peak cladding temperature somewhat follows the axial power profile in the case without spray.<sup>19</sup> In contrast, the cases with spray flow are much cooler at the top of the assembly. Both the base case (S1) and the plugged case (S1p) used the flow regime model, which enhanced heat removal at the top of the assembly. However, due to the large mismatch between the heat generation rate and the heat removal (also see Section 6.2.2), the region at the top of the assembly still oscillated between film and nucleate boiling (e.g., see temperature responses in Figure 6-3 and Figure 6-6). Conversely, the non-flow regime case spray was less effective at the top but penetrated deep into the assembly. (b)(7)(F)

Ex 7F

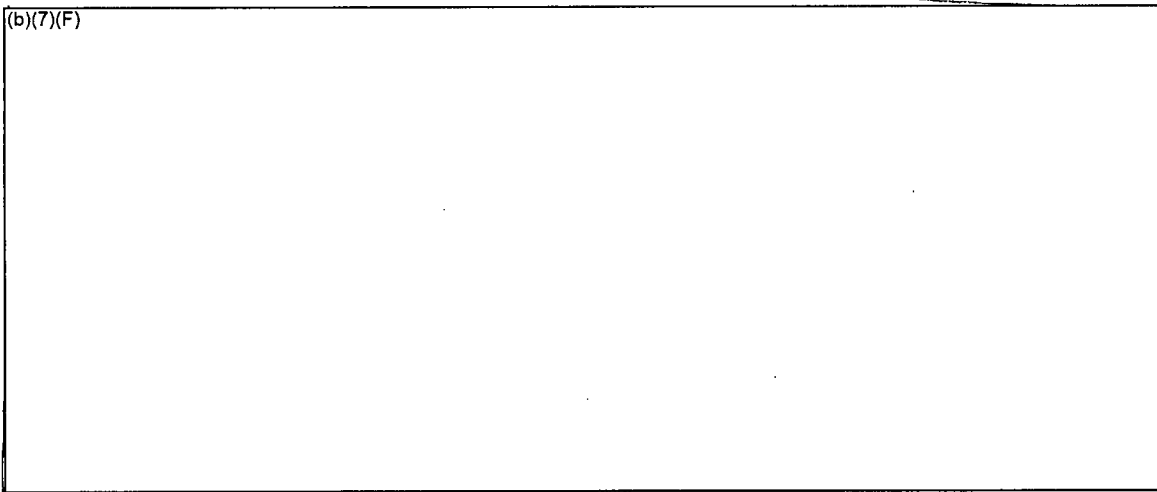
(b)(7)(F) The net effect was to slightly delay heatup relative to the other cases.



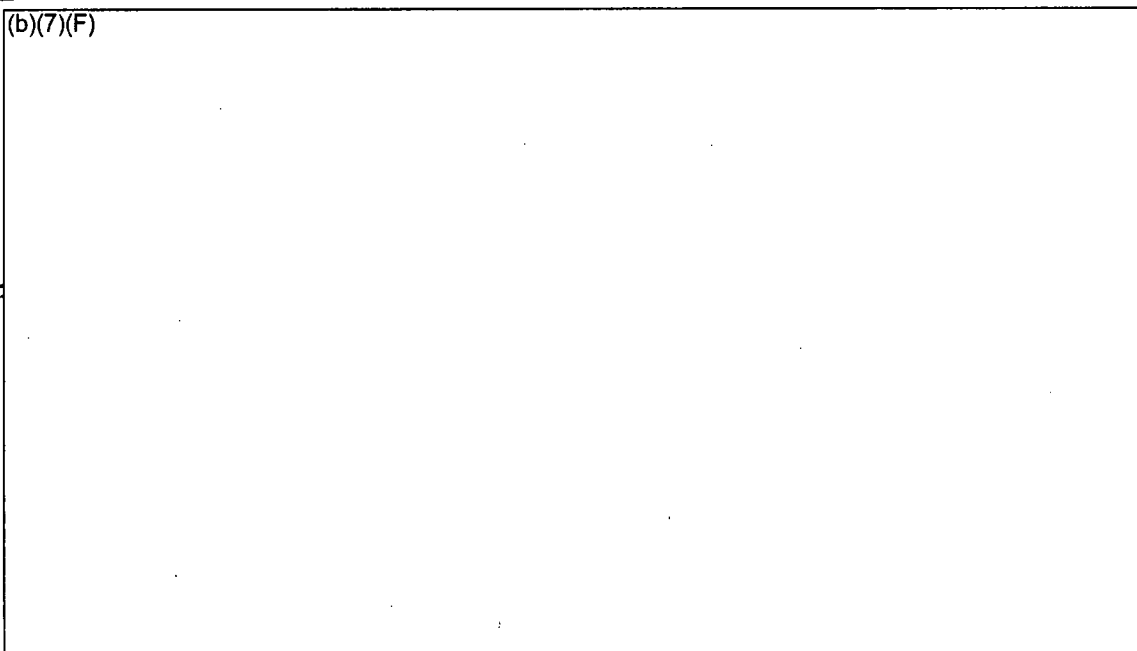
Ex 7F

<sup>19</sup> This axial profile trend will change if the assembly reached a steady state temperature profile or if the heating rate was lower. (b)(7)(F)

Ex 7F



Ex 7F

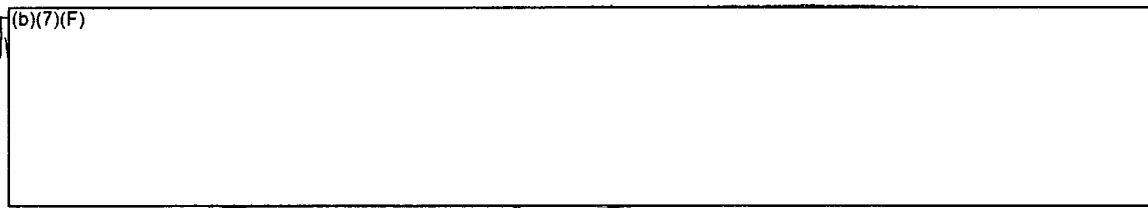


Ex 7F

**Figure 6-1 Comparison of the Peak Cladding Temperatures** (b)(7)(F) **with a Uniform Configuration** with (b)(7)(F) **and a Whole Pool Spray Flow of** (b)(7)(F)

(b)(7)(F)

Ex 7F



Ex 7F

Ex 7F

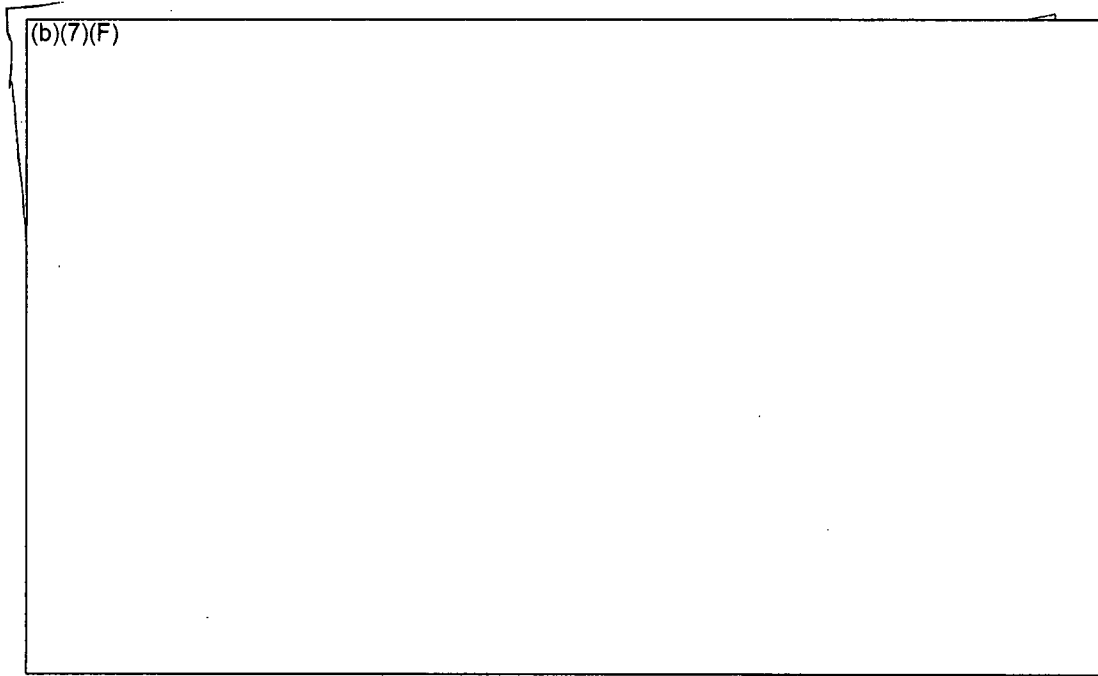


Figure 6-2 Comparison of the Peak Cladding Temperatures (b)(7)(F) with a Uniform Configuration with (b)(7)(F) and a Whole Pool Spray Flow of (b)(7)(F)

(b)(7)(F)

Ex 7F

Ex 7F

Ex 7F

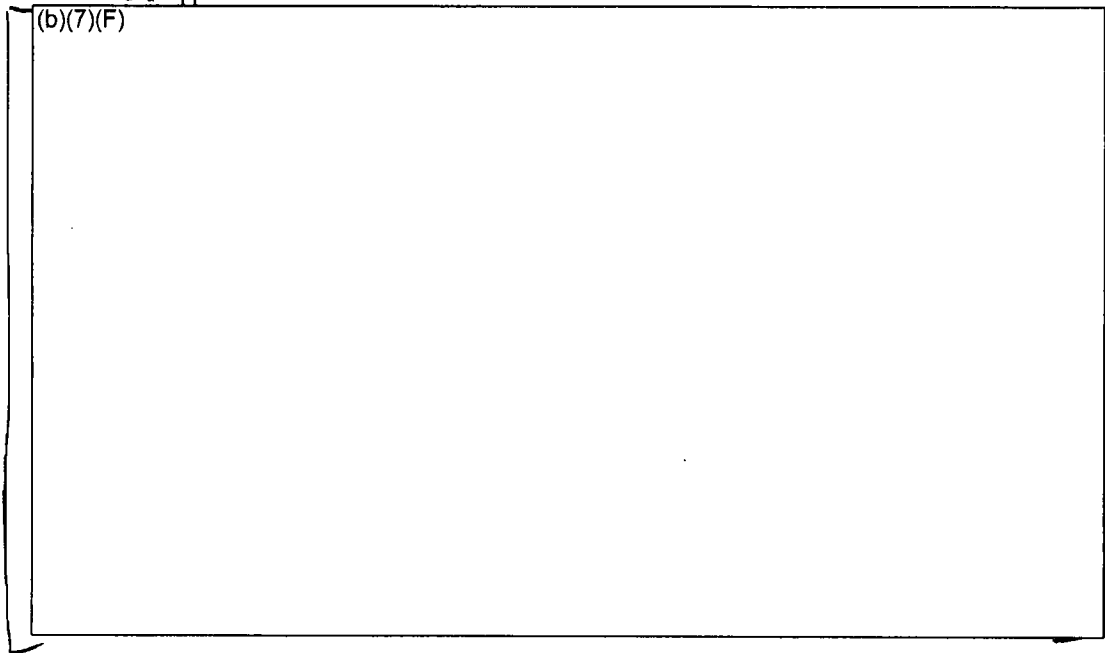
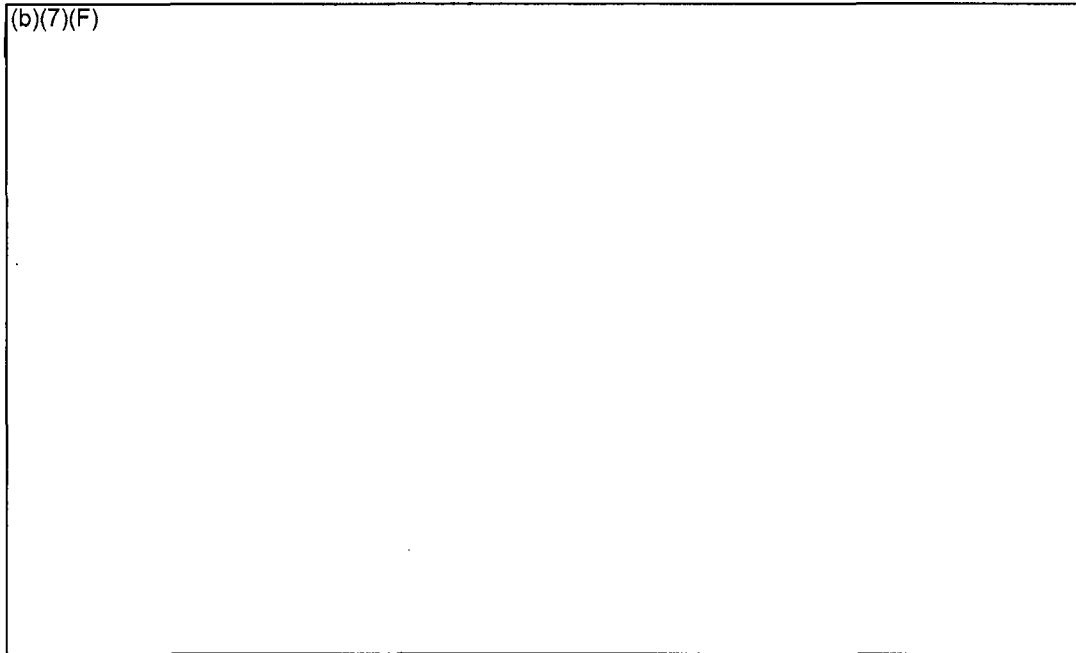


Figure 6-3 Assembly Cladding Temperatures for the Uniform Configuration with (b)(7)(F) Spray Flow (Case S1).

Ex 7F

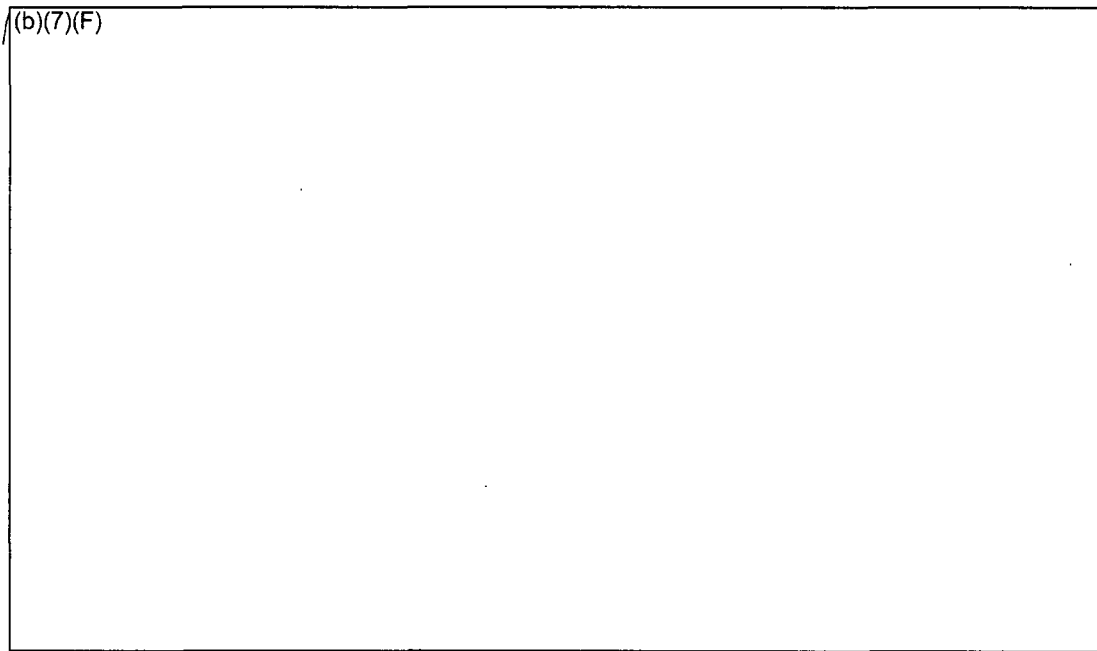
(b)(7)(F)



Ex 7F

Figure 6-4 Assembly Cladding Temperatures for the Uniform Configuration with (b)(7)(F) Spray Flow, and the Flow Regime Model Inactive (Case S1a).

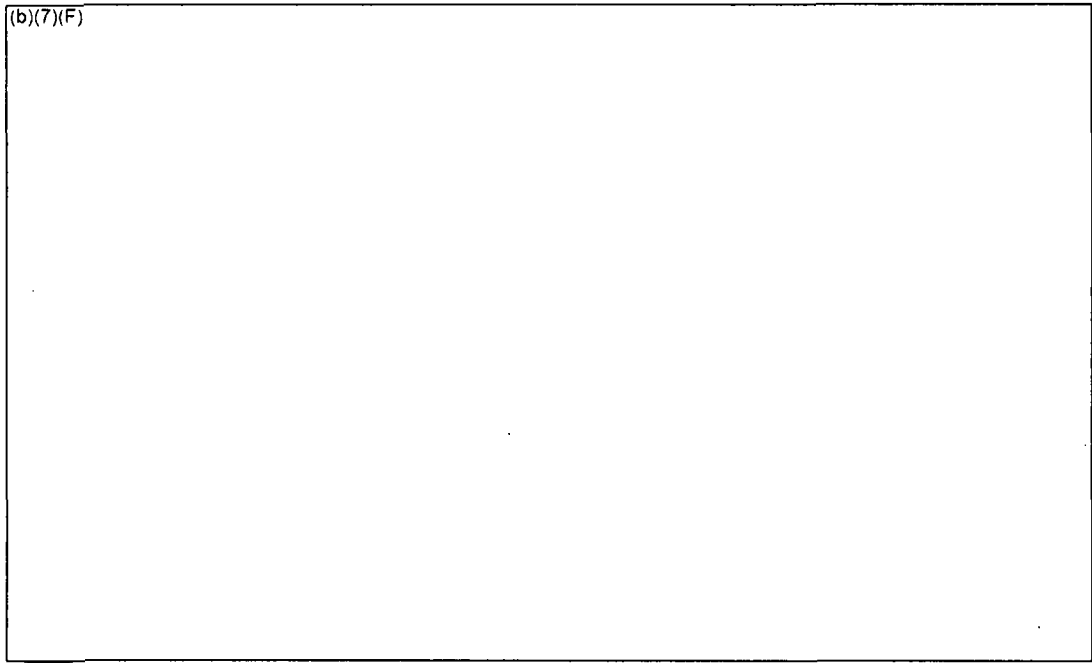
Ex 7F

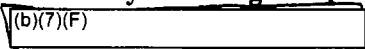


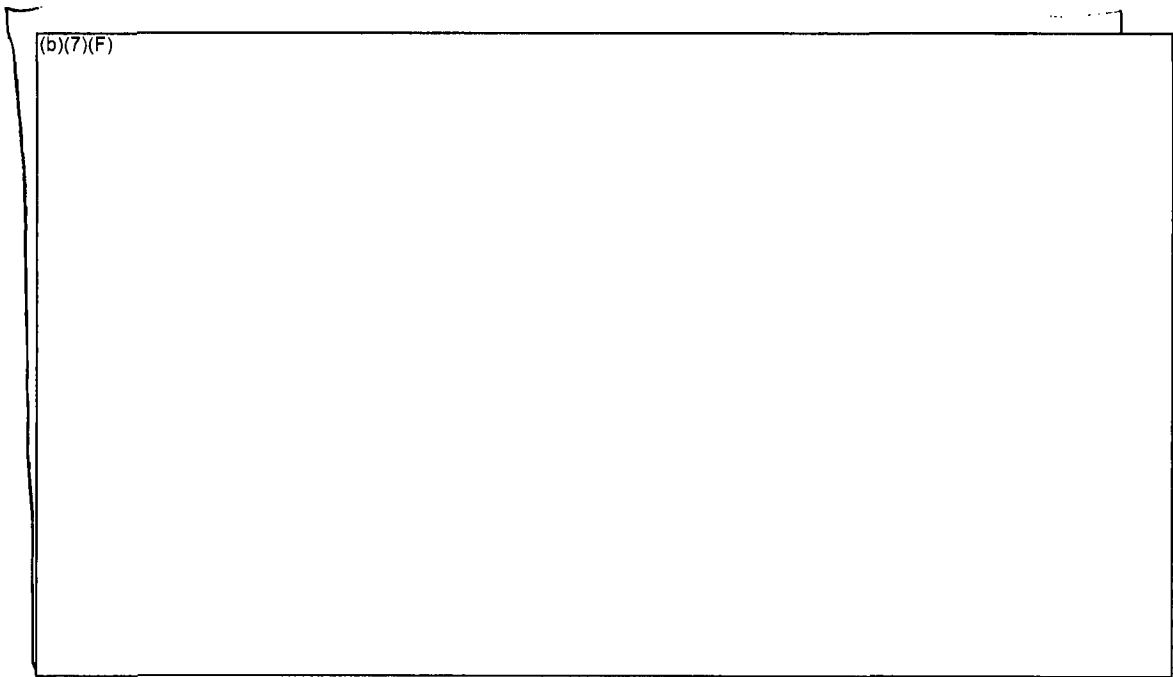
Ex 7F

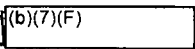
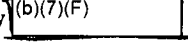
Figure 6-5 Assembly Cladding Temperatures for the Uniform Configuration with (b)(7)(F) and No Spray Flow (Case S1b).

Ex 7F



**Figure 6-6** Assembly Cladding Temperatures for the Uniform Configuration with   Spray Flow and Plugged Inlet (Case S1p).



**Figure 6-7** Axial Cladding Temperature Profiles  Uniform Configuration,  Spray Flow 

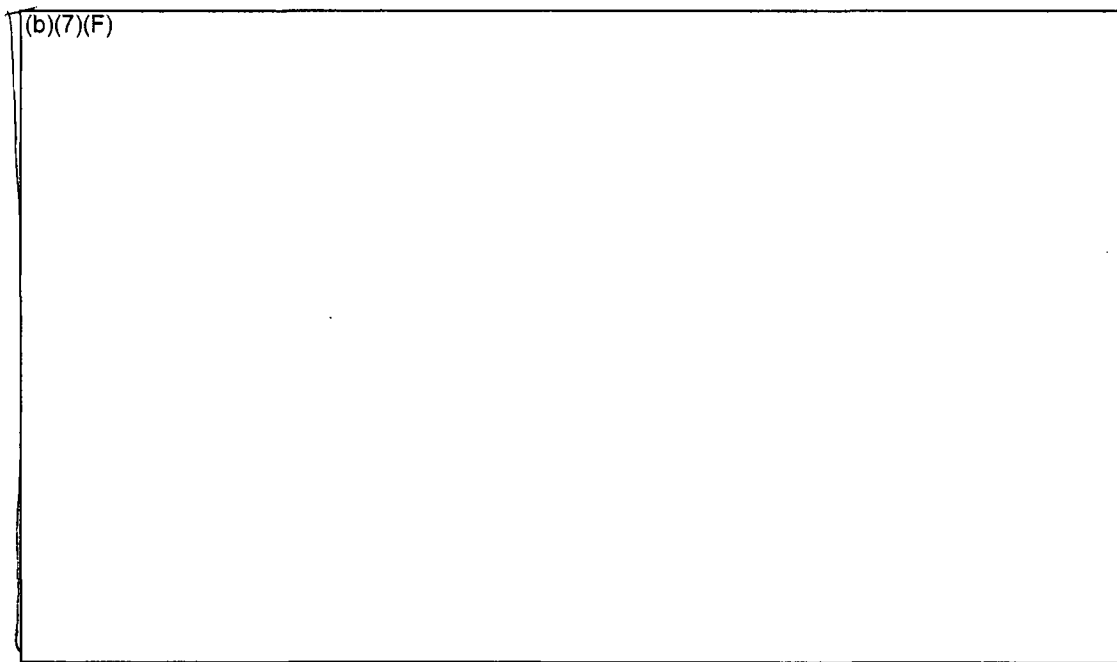


Figure 6-8 Axial Temperature Profiles for the (b)(7)(F) Uniform Configuration, (b)(7)(F) Spray Flow as a Function of Time.

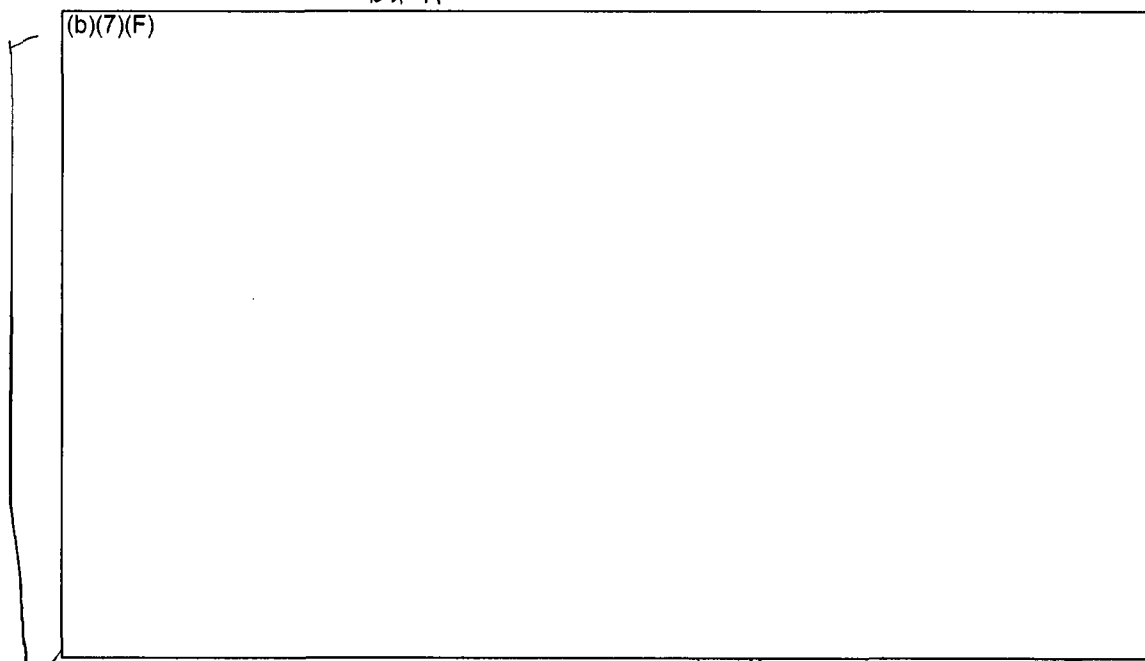


Figure 6-9 Axial Temperature Profiles (b)(7)(F) Uniform Configuration, (b)(7)(F) and No Spray Flow as a Function of Time.

### 6.2.2 Energy Balance on Base Calculation Spray

(b)(7)(F)

Ex 7F

An energy balance was performed on the S1 case with the flow regime model operating. This energy balance is somewhat less useful than the ones done for the checkerboard and 1x4 configurations because the assembly did not reach steady conditions.

(b)(7)(F) Figure 6-10 graphically shows the key heat flows in the model.

(b)(7)(F) Meanwhile, the structure energy is increasing thereby signifying a steady increase in its temperature. The net heat removal by the gas (b)(7)(F) when the exit enthalpy flow diminishes due to the rapid consumption of oxygen and a slight cooling of the exit gases<sup>21</sup>. The net heat balance is the sum of the heat flow terms besides the decay power (i.e., it should be approximately equal to the decay heat power<sup>22</sup>).

Ex 7F

Ex 7F

Ex 7F

The energy balance is reported in Table 6-2 (b)(7)(F) during a period before rapid oxidation (see Figure 6-3). The total power put into the assembly is a combination of the decay heat (b)(7)(F) and oxidation power (b)(7)(F). The resultant distribution of that power (b)(7)(F) of the energy going into the structures and being removed by the gas (i.e., the combination of air flow and steam from boiled spray water). Since the liquid spray flow entering the assembly was completely boiled to steam, liquid component is only adding energy from a phasic enthalpy removal perspective. In summary, there was a large difference between the heat removal (b)(7)(F) and the total heat generation (b)(7)(F).

Ex 7F

(b)(7)(F)

(b)(7)(F)

Ex 7F

Ex 7F

<sup>21</sup> The oxygen concentration exiting the center assembly (b)(7)(F) and all other gas component mass flows (i.e., nitrogen and steam) remained approximately the same. The exit gas temperature (b)(7)(F) because of slightly more effective cooling by the spray flow (i.e., slower gas velocity). The spray cooling effect was more effective than the increased heating near the high oxidation location. Since more mass was entering than leaving and the exit gases were cooled by the spray flow, the net enthalpy decreased.

Ex 7F

Ex 7F

<sup>22</sup> The small transient differences between the net energy balance and the decay power is attributed to limitations in the access of plot quantities of all the subcomponents of the energy flow. However, the major components are shown on the figure. The MELCOR COR Package calculations have very high fidelity. For example, Case S1 had a total energy error of 0.02%.

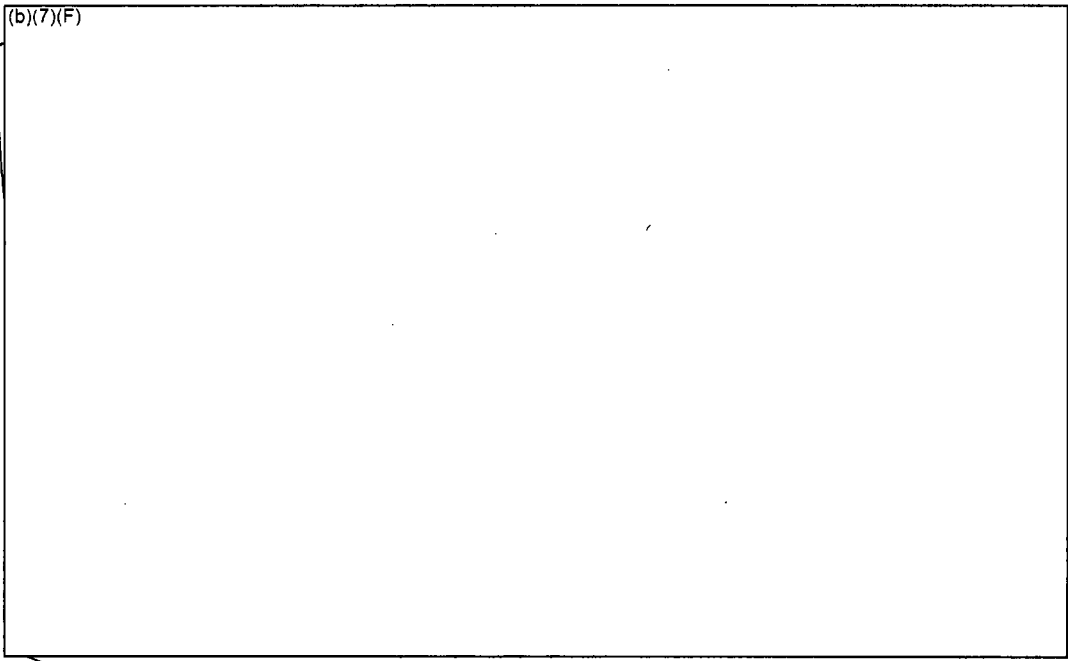


**Figure 6-10** Time-averaged Energy Flow in the Uniform Configuration with (b)(7)(F) *Ex 7F*  
(b)(7)(F) Spray Flow.

**Legend for Figure 6-10:**

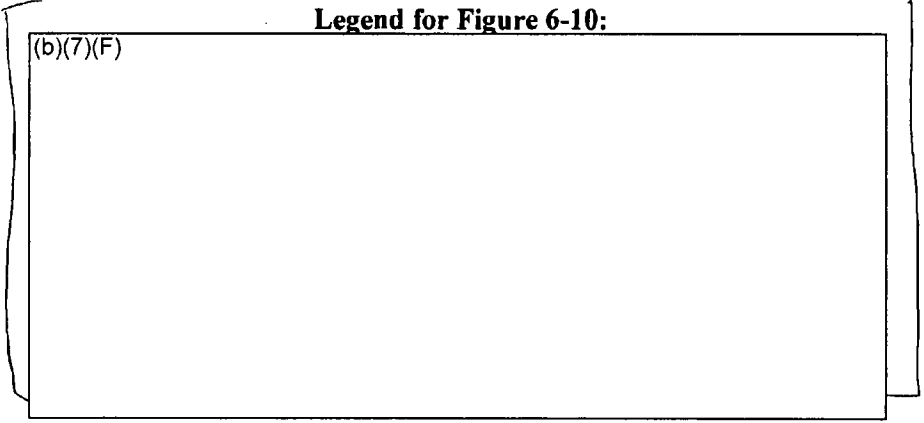
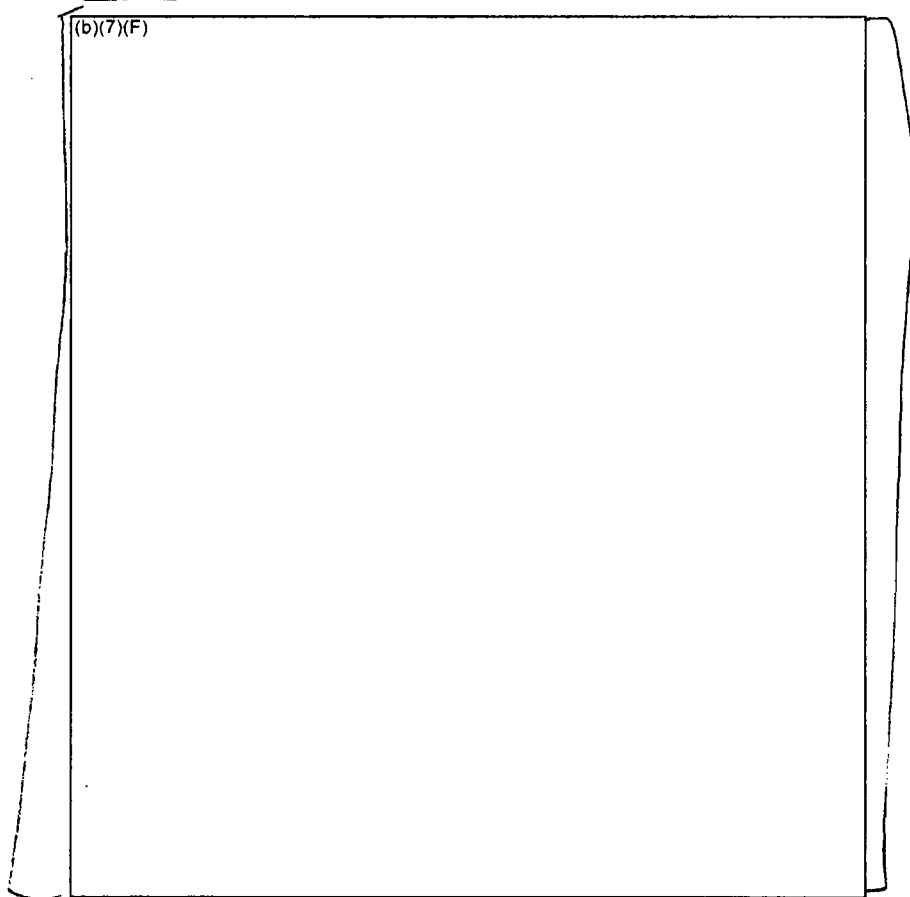


Table 6-2 Energy Balance for the Uniform Assembly Configuration in SFP with Ex 7F Spray.

(b)(7)(F)



(b)(7)(F)

Ex 7F

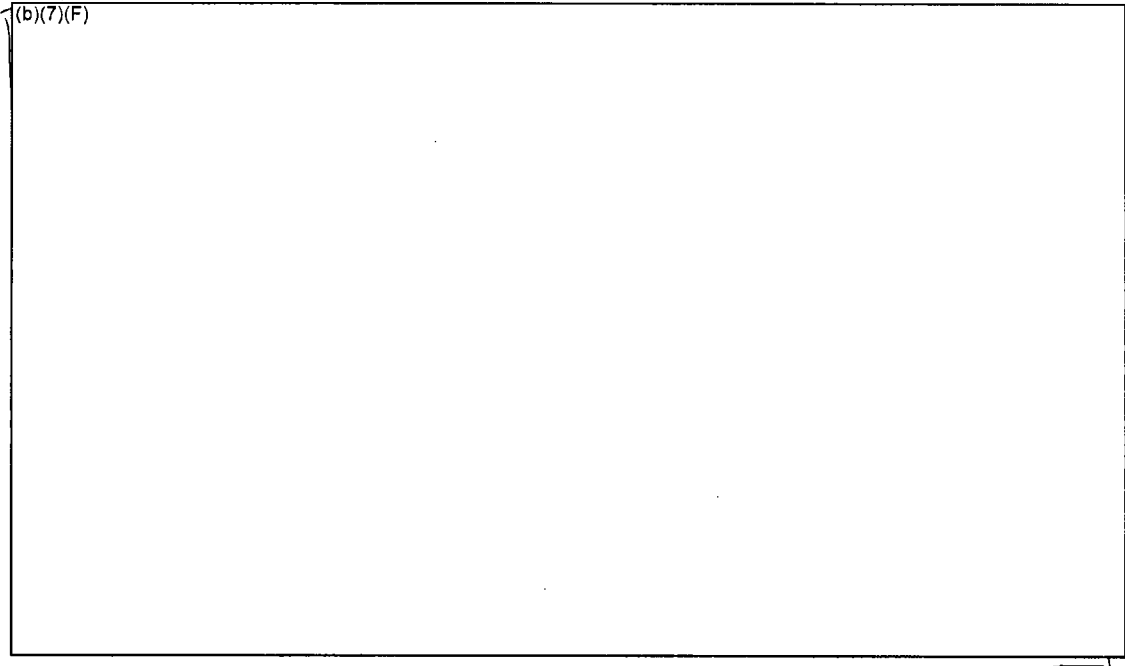
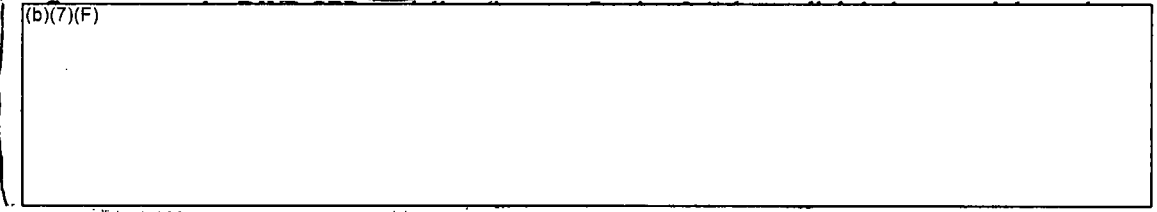
**6.2.3 Coolability Analysis** (b)(7)(F) **Spray Flowrate**

A coolability analysis was done for the uniform configuration with a (b)(7)(F) spray. A set of parametric calculations was performed with aging ranging (b)(7)(F) (b)(7)(F) (b)(7)(F). As shown previously in Section 6.2.1, an aging time (b)(7)(F)

Ex 7F

(b)(7)(F) (b)(7)(F) In previous separate effects calculations for the uniform configuration with air flow but no spray flow [Wagner, 2003], (b)(7)(F)

Ex 7F



Ex 7F

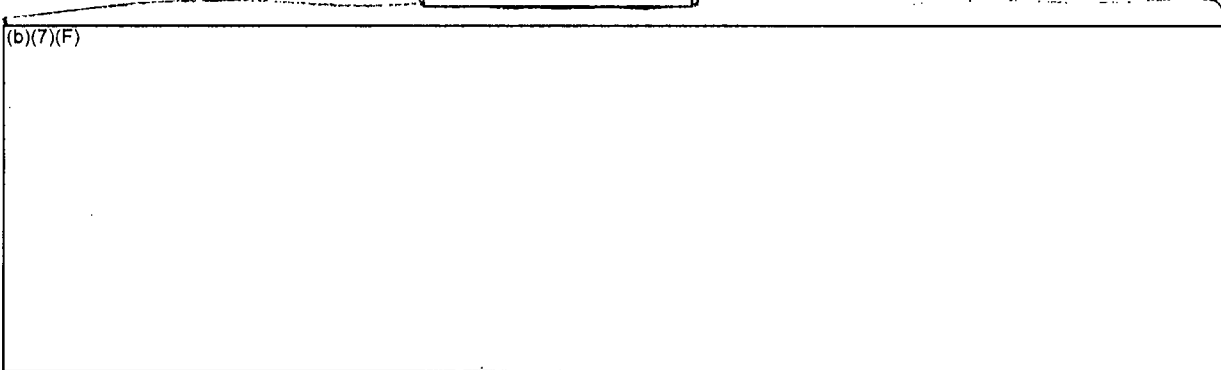
**Figure 6-11 Comparison of the Peak Cladding Temperatures for the Uniform Configuration with Various Aging Periods and a Whole Pool Spray Flow of** (b)(7)(F)

(b)(7)(F) Ex 7F

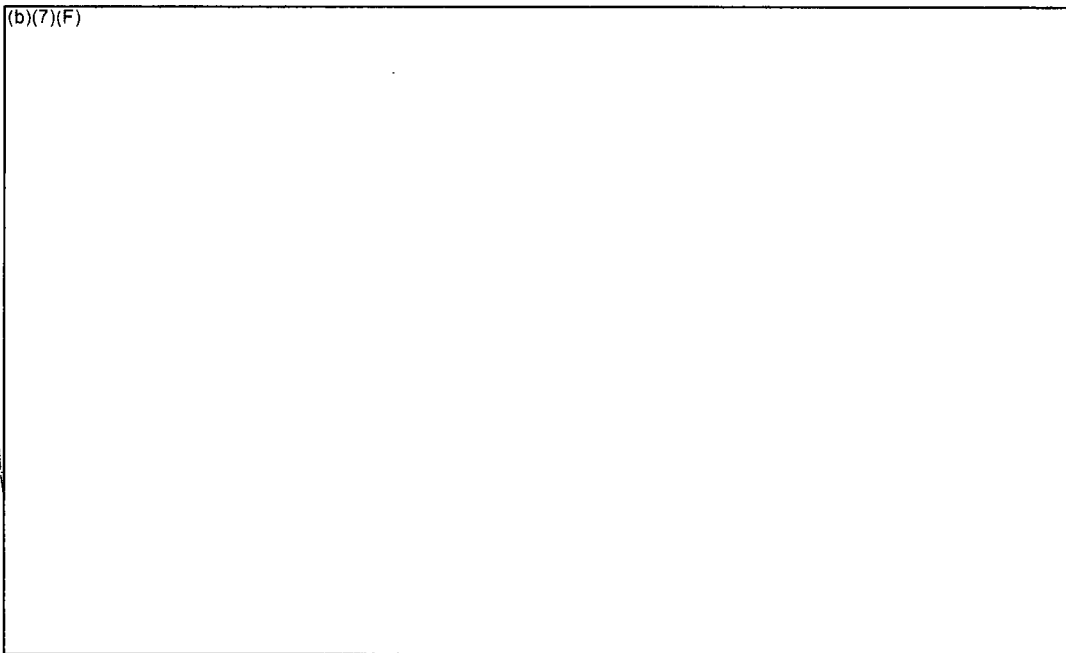
Ex 7F

6.2.4 Coolability Analysis for (b)(7)(F) Spray Flowrate

(b)(7)(F)



(b)(7)(F)



Ex 7F

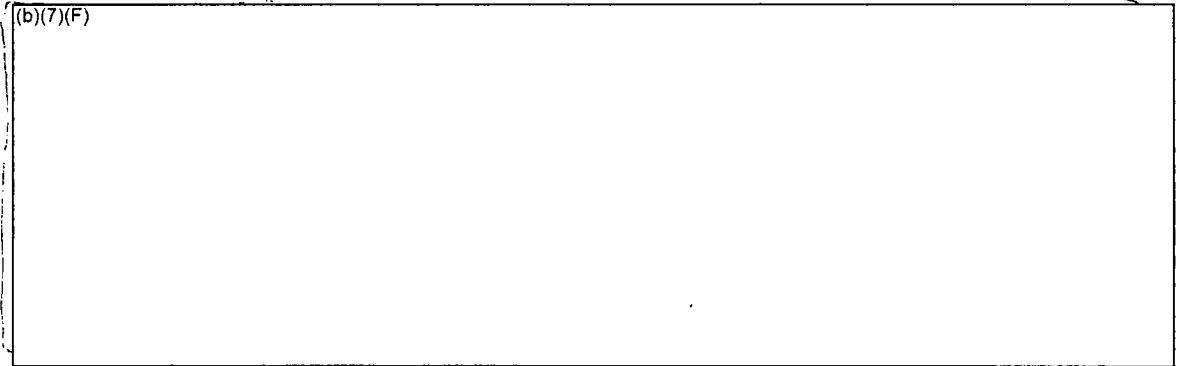
Figure 6-12 Comparison of the Peak Cladding Temperatures for the Uniform Configuration with Various Aging Periods and a Whole Pool Spray Flow of

(b)(7)(F)

Ex 7F

6.2.5 Coolability Analysis (b)(7)(F) Spray Flowrate

Ex 7E



Ex 7F

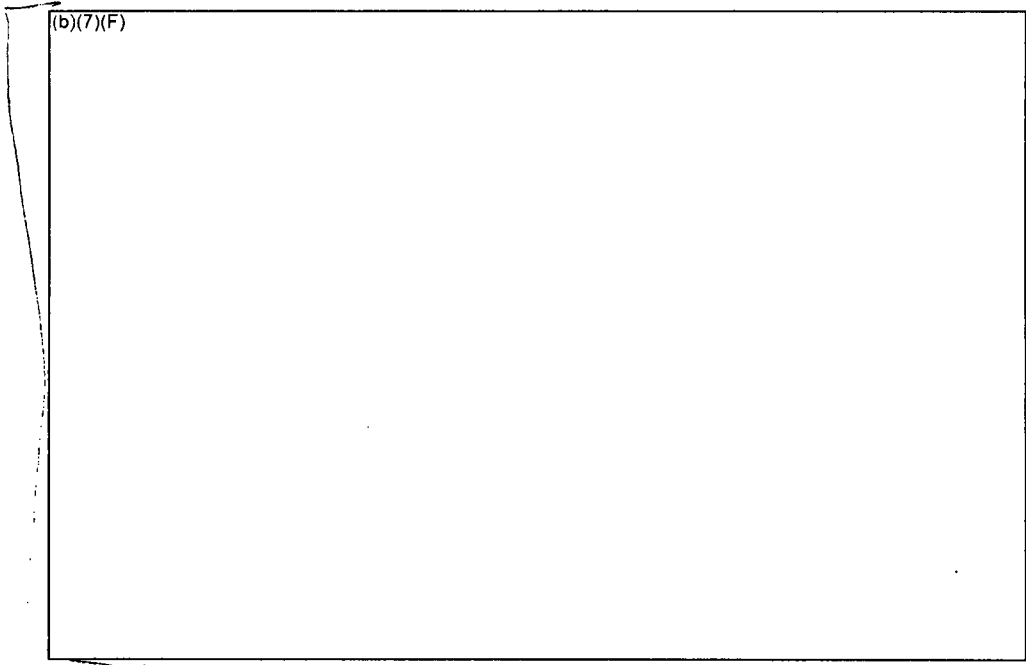


Figure 6-13 Comparison of the Peak Cladding Temperatures for the Uniform Configuration with Various Aging Periods and a Whole Pool Spray Flow of

(b)(7)(F) Ex 7F

### 6.3 Separate Effects Spray Model Results for the Checkerboard Configuration

EX 7F

Section 6.3.1 gives a summary of the 4 cases with (b)(7)(F) hole in a uniform fuel configuration. The four cases examine differences in the response with and without sprays and with and without the flow regime model active (see Section 3.1.4 for a more complete discussion). Section 6.3.2 shows the results of an energy balance (b)(7)(F) spray case to illustrate the heat flows.

#### 6.3.1 Base Calculations (b)(7)(F) Spray

EX 7F

The S3 and S7 configuration calculations simulated a checkerboard configuration of the highest powered assemblies discharged into the spent fuel pool with (b)(7)(F) since reactor shutdown and low-powered assemblies at the median power of the reference BWR SFP

EX 7F

(b)(7)(F) The limiting response in a checkerboard configuration represents the response of the high-powered assembly in a region of alternating high- and low-powered assemblies. Unlike the uniform configuration, the high-powered assemblies benefit from radial heat transfer to adjacent low-powered assemblies. (b)(7)(F)

(b)(7)(F)

EX 7F

The four (b)(7)(F) (i.e., see S3 calculations in Table 6-1) examined differences in the response with and without sprays and with and without the flow regime model active. When the flow regime model was deactivated, the spray water has a relatively small surface contact area with the cladding. Due to the reduction of heat transfer, the spray flow penetrates more deeply into the assembly before completely evaporating. In addition, a S3 case was run where the inlet of the assembly was plugged by water. (b)(7)(F)

EX 7F

(b)(7)(F)

Figure 6-14 and Figure 6-15 show the temperature responses for (b)(7)(F)

(b)(7)(F)

EX 7F

For completeness, the high- and low-powered cladding temperature responses from Cases S3b and S3p are shown in Figure 6-20 through Figure 6-23. In a checkerboard configuration, convective heat removal in the low-powered assemblies is particularly important. Due to radial heat transfer, (b)(7)(F) heat from the high-powered assembly in Case S3 was transferred to the peripheral assembly (see the energy balance in Section 6.3.2 for a full discussion). If the inlet is plugged, the benefit of the peripheral assembly to remove heat is greatly diminished. The peripheral assembly initially stores some of the heat from the center assembly but gradually becomes ineffective as an energy sink without simultaneous convective heat removal. In contrast, the impact of plugging in the uniform assembly configuration is less important because there is no radial heat transfer.

In previous separate effects calculations for the checkerboard configuration with air flow but no spray flow [Wagner, 2003], (b)(7)(F) Subsequent refinements to the BWR SFP modeling (i.e., see Section 3.1) will likely increase that value but have not yet been quantified. (b)(7)(F)

(b)(7)(F) However, if water blocks or limits the air flow through the bottom of the racks, additional spray flow would be necessary to provide cooling.

Finally, the high- and low-powered assembly axial temperature profiles are shown in Figure 6-24 and Figure 6-25 for all four cases, respectively. As observed in the axial temperature profiles for the uniform cases, the impact of the spray flow at the top of the assembly is clearly seen. The cases with the flow regime model active have cooler temperatures until the spray flow is depleted. The case without the flow regime model shows less heat removal at the top of the assembly but more heat removal at the bottom. In general, the temperatures are lower in the low-powered assembly and the spray penetrates deeper. Consequently, there is radial heat transfer from the high-powered assembly to the low-powered assembly. (b)(7)(F)

(b)(7)(F)

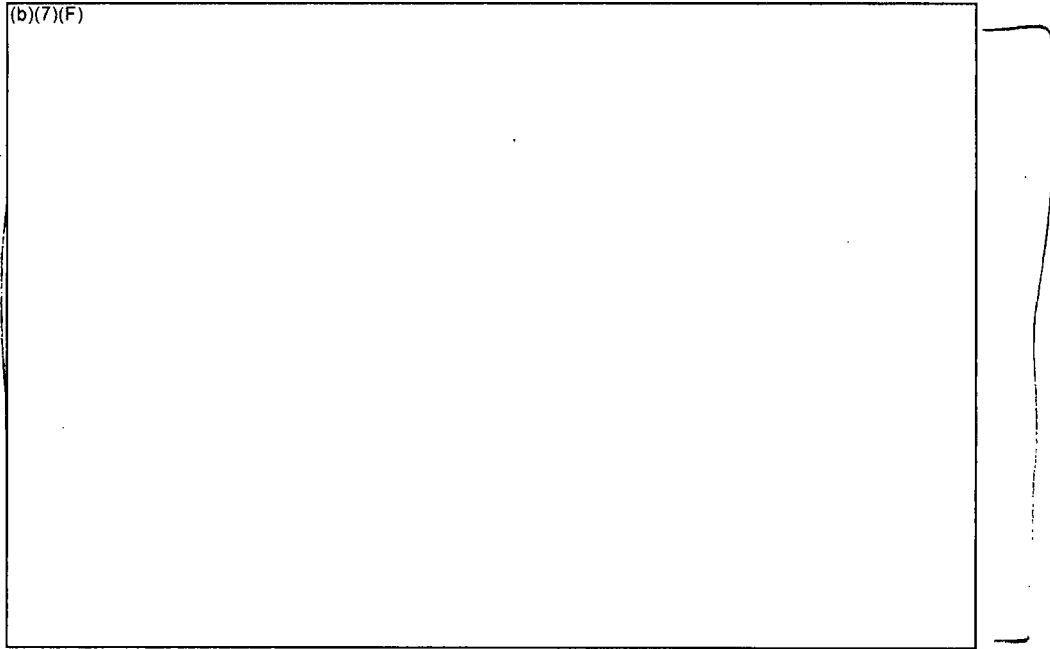


**Figure 6-14** Comparison of the Peak Cladding Temperatures (b)(7)(F) with a Checkerboard Configuration with (b)(7)(F) and a Whole Pool Spray Flow of (b)(7)(F)

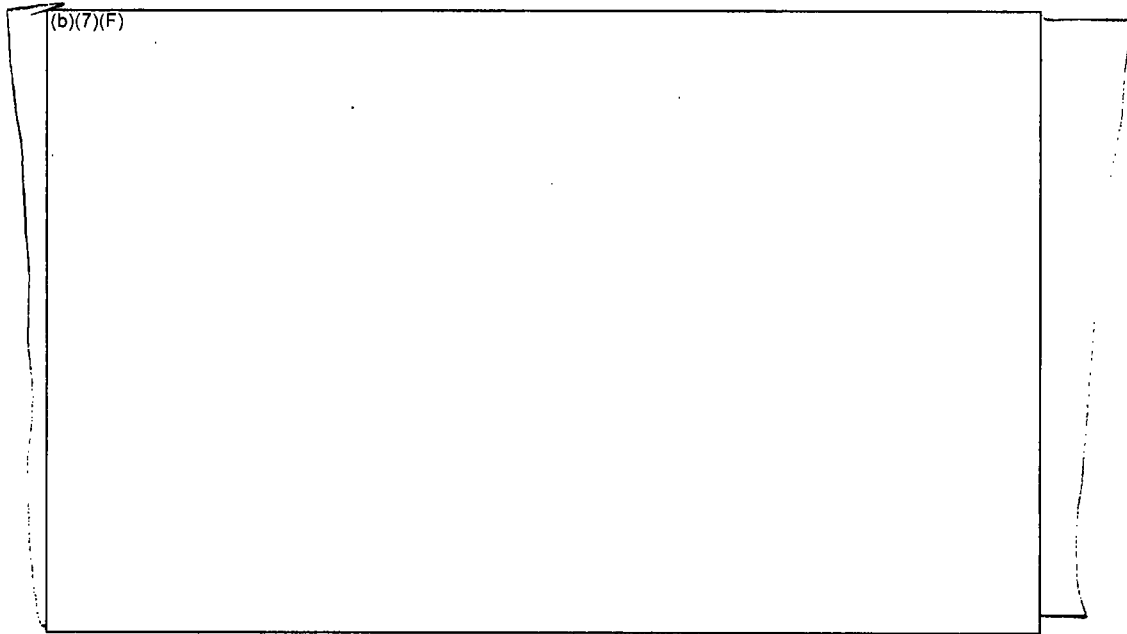


**Figure 6-15** Comparison of the Peak Cladding Temperatures (b)(7)(F) Leak with a Checkerboard Configuration with (b)(7)(F) and a Whole Pool Spray Flow of (b)(7)(F)

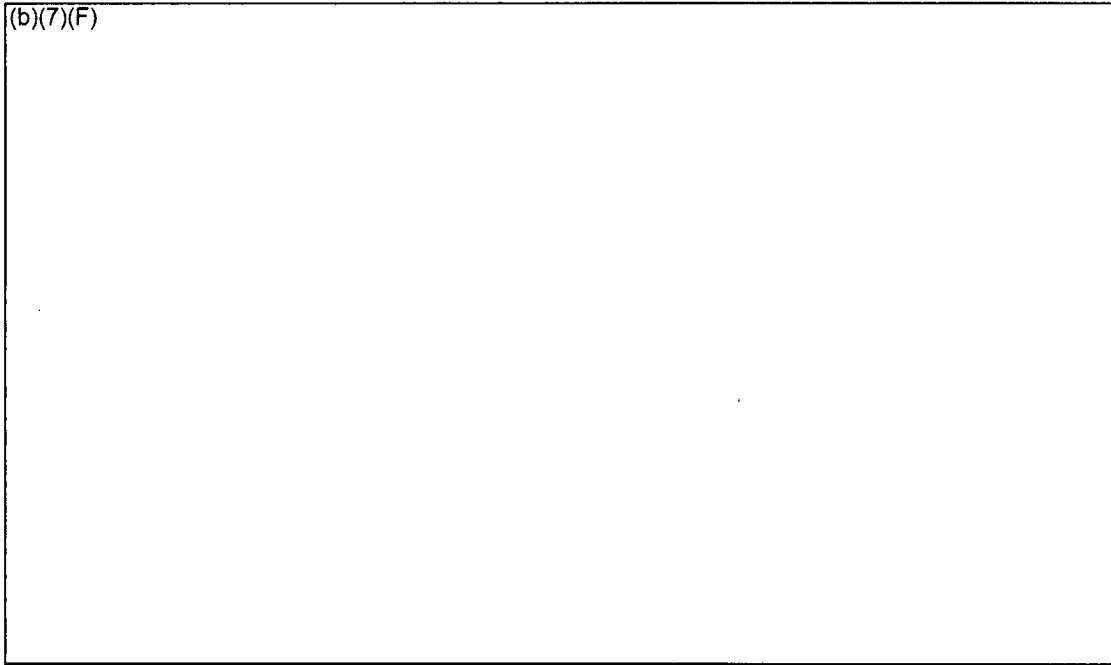


**Figure 6-16 High-Powered Assembly Cladding Temperatures for the Checkerboard Configuration with (b)(7)(F) Spray Flow (Case S3).**

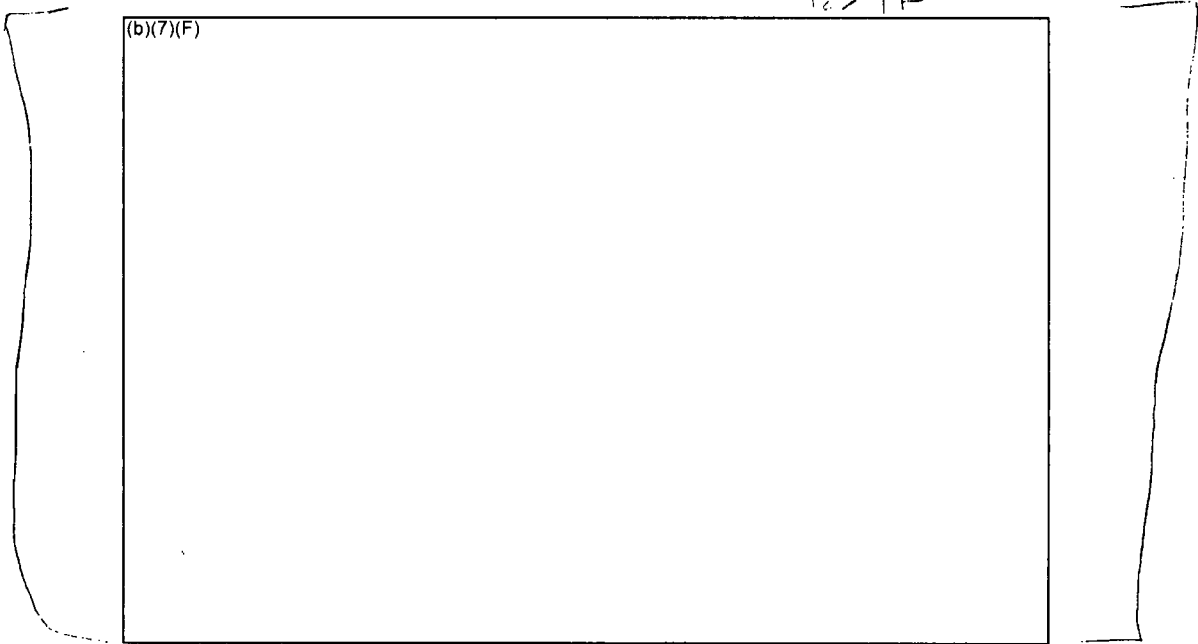


**Figure 6-17 Low-Powered Assembly Cladding Temperatures for the Checkerboard Configuration with (b)(7)(F) Spray Flow (Case S3).**

E27F

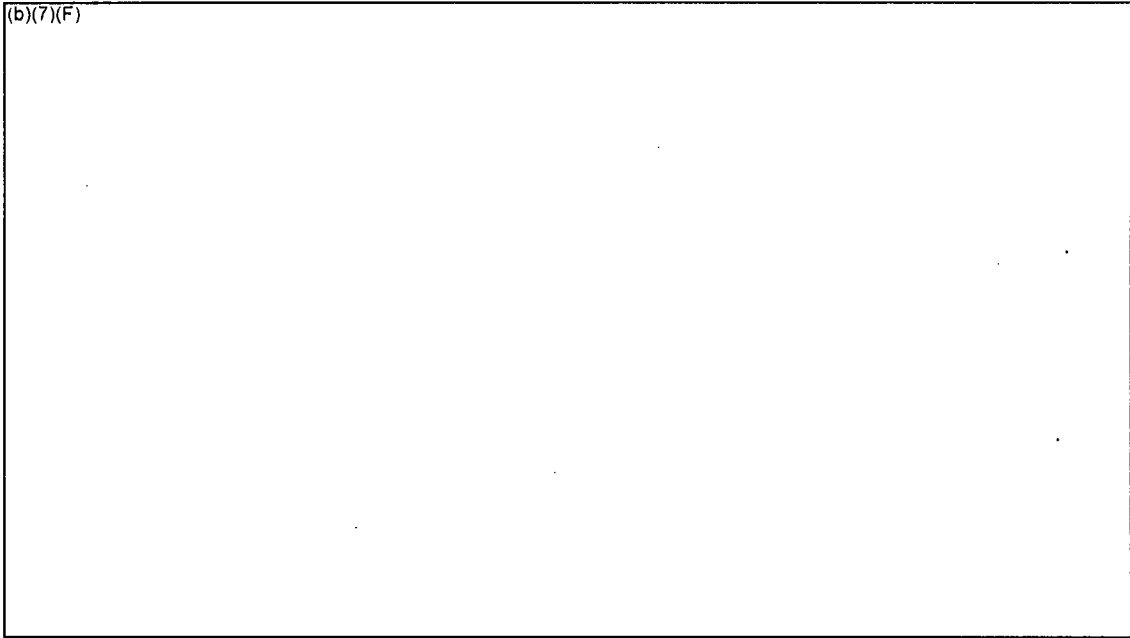


**Figure 6-18 High-Powered Assembly Cladding Temperatures for the Checkerboard Configuration with (b)(7)(F) Spray Flow and the Flow Regime Model Inactive (S3a).** Ex 7F

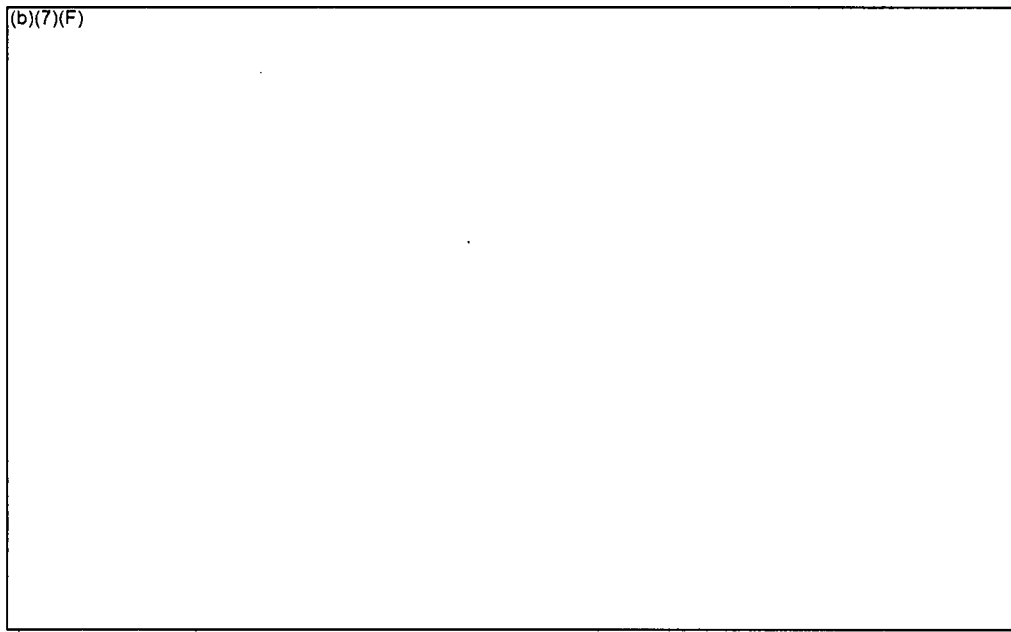


**Figure 6-19 Low-Powered Assembly Cladding Temperatures for the Checkerboard Configuration with (b)(7)(F) Spray Flow and the Flow Regime Model Inactive (S3a).** Ex 7F

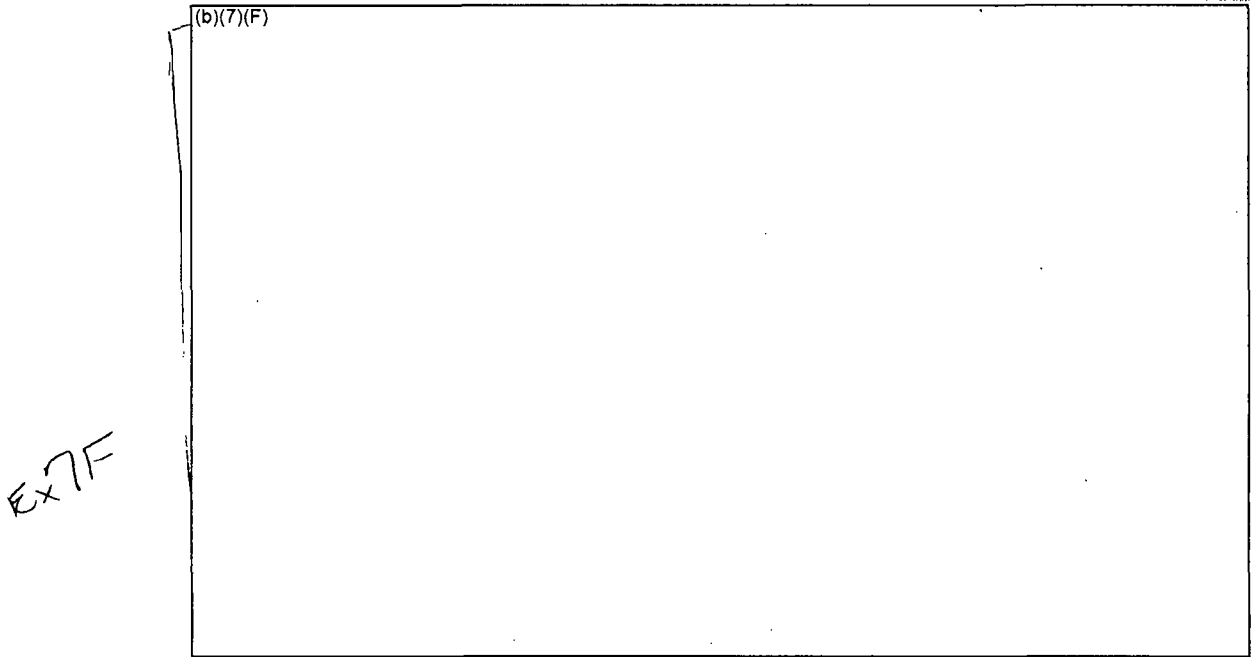


**Figure 6-20 High-Powered Assembly Cladding Temperatures for the Checkerboard Configuration with (b)(7)(F) and No Spray Flow (Case S3b).**

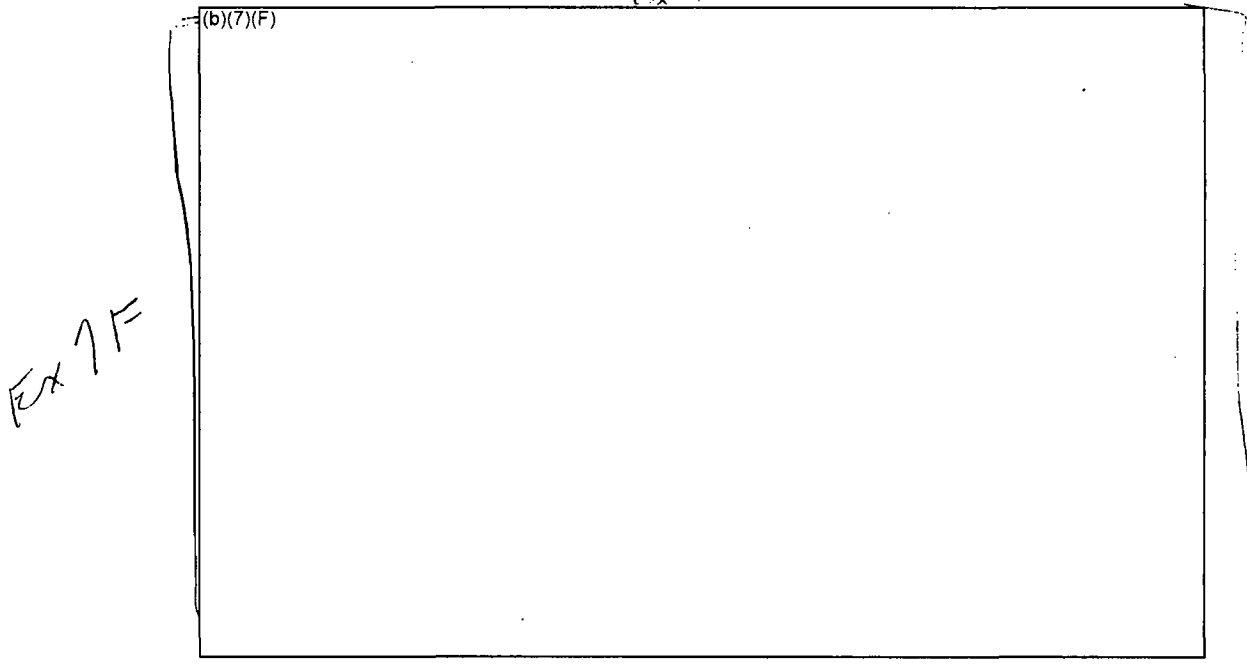


**Figure 6-21 Low-Powered Assembly Cladding Temperatures for the Checkerboard Configuration with (b)(7)(F) and No Spray Flow (Case S3b).**

EX 7F

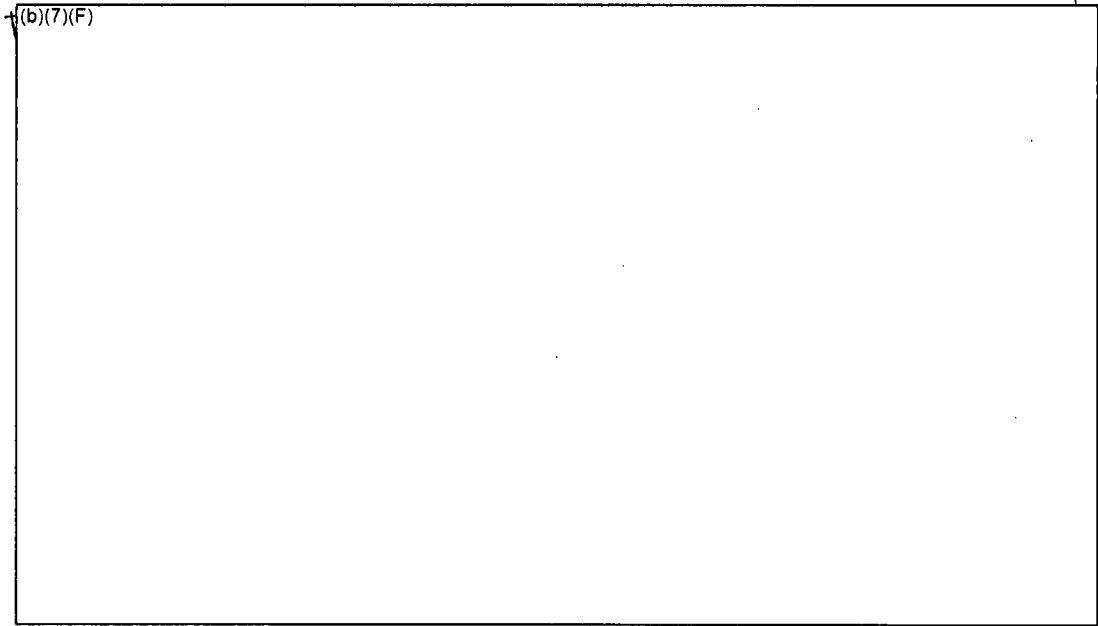


**Figure 6-22 High-Powered Assembly Cladding Temperatures for the Checkerboard Configuration with (b)(7)(F) Spray Flow and Plugged Inlet (Case S3p).**

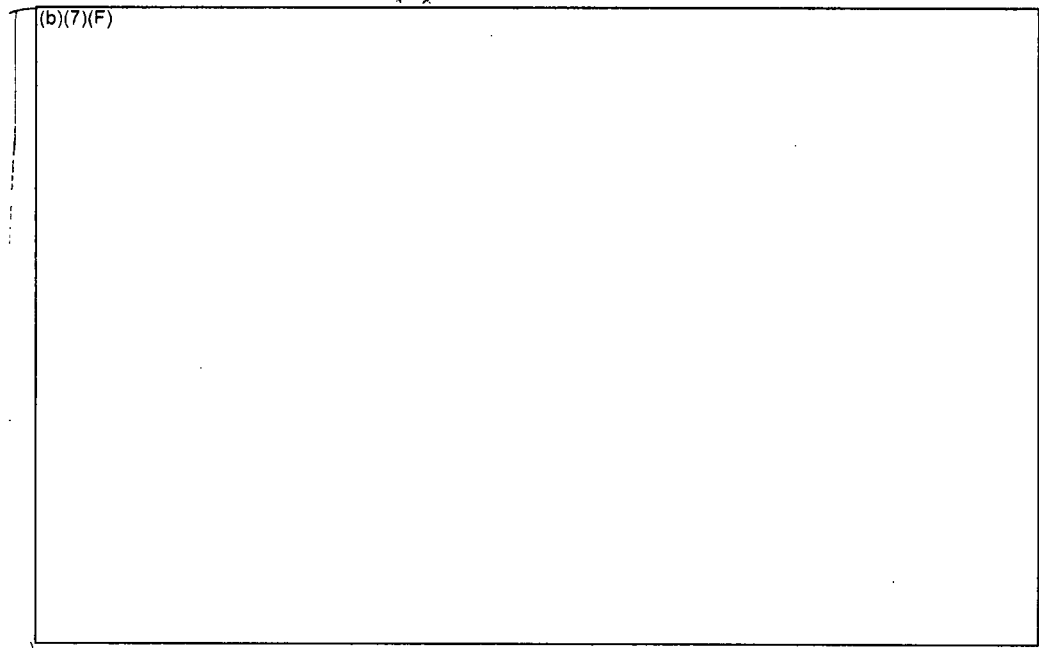


**Figure 6-23 Low-Powered Assembly Cladding Temperatures for the Checkerboard Configuration with (b)(7)(F) Spray Flow and Plugged Inlet (Case S3p).**

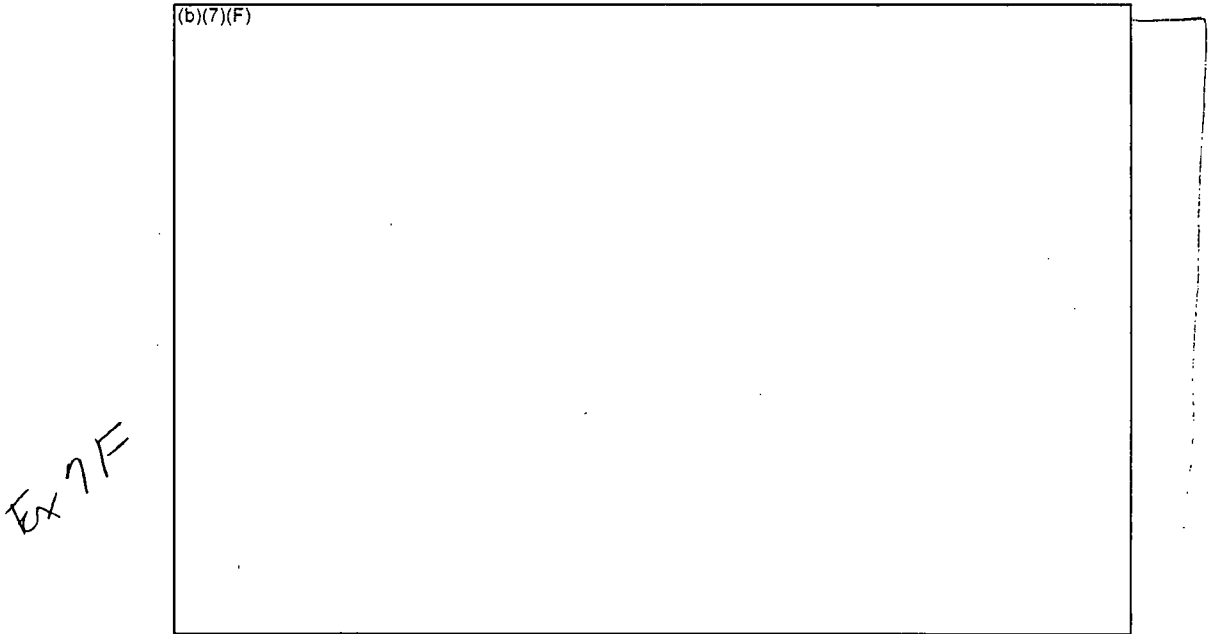


**Figure 6-24 High-Powered Assembly Cladding Temperature Profiles for the Checkerboard Configuration with a** (b)(7)(F)

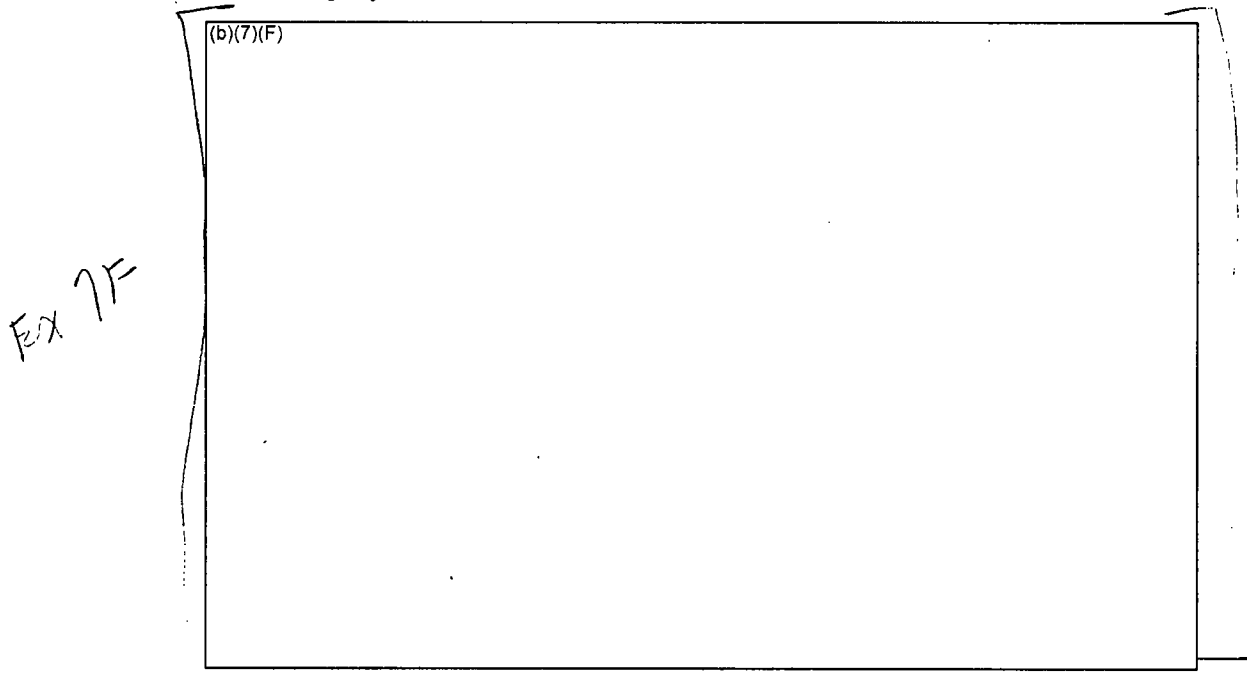


**Figure 6-25 Low-Powered Assembly Cladding Temperature Profiles for the Checkerboard Configuration with a** (b)(7)(F)

6.3.2 Energy Balance on Base Calculation (b)(7)(F)  
Spray

Ex 71

An energy balance was performed on the S3 case with the flow regime model operating. Figure 6-36 graphically shows the key heat flows in the model. After water level drops below the base plate, the power going into the structure steadily decreases to near zero. Meanwhile, due to air and steam convection, the heat removed by the gas in the peripheral assembly gradually increases. The convective heat removal by the center assembly gas is relatively constant after the base plate clearing. In this figure, the decay power includes both the low- and high-powered assemblies. The net heat balance is the sum of the heat flow terms besides the decay power (i.e., it should be approximately equal to the decay heat power<sup>23</sup>).

The energy balance is reported in Table 6-2 based on average conditions (b)(7)(F). The total power put into the checkerboard configuration is a combination of the decay heat for both the high- and low-powered assemblies (b)(7)(F) and oxidation power

(b)(7)(F) (b)(7)(F) The resultant distribution of energy generated in the center represented (b)(7)(F) of the decay power and (b)(7)(F) oxidation energy (b)(7)(F) of the power in the high-powered assembly is removed by convective gas flow and the remaining (b)(7)(F) of the energy is radially transferred to the peripheral assembly. The decay heat power in the peripheral assembly is relatively small (b)(7)(F) However, the addition of the radial heat load from the center assembly increases the effective peripheral assembly heat load (b)(7)(F) that heat load is convectively removed by the gas and a small amount (b)(7)(F) goes into slowly heating portions of the assembly and heat removal by spray water out of the bottom.

Ex 71

<sup>23</sup> The small transient differences between the net energy balance and the decay power is attributed to limitations in the access of plot quantities available to the user to access all the subcomponents of the energy flow. However, the major components are shown on the figure. The internal MELCOR core calculations have very high fidelity.

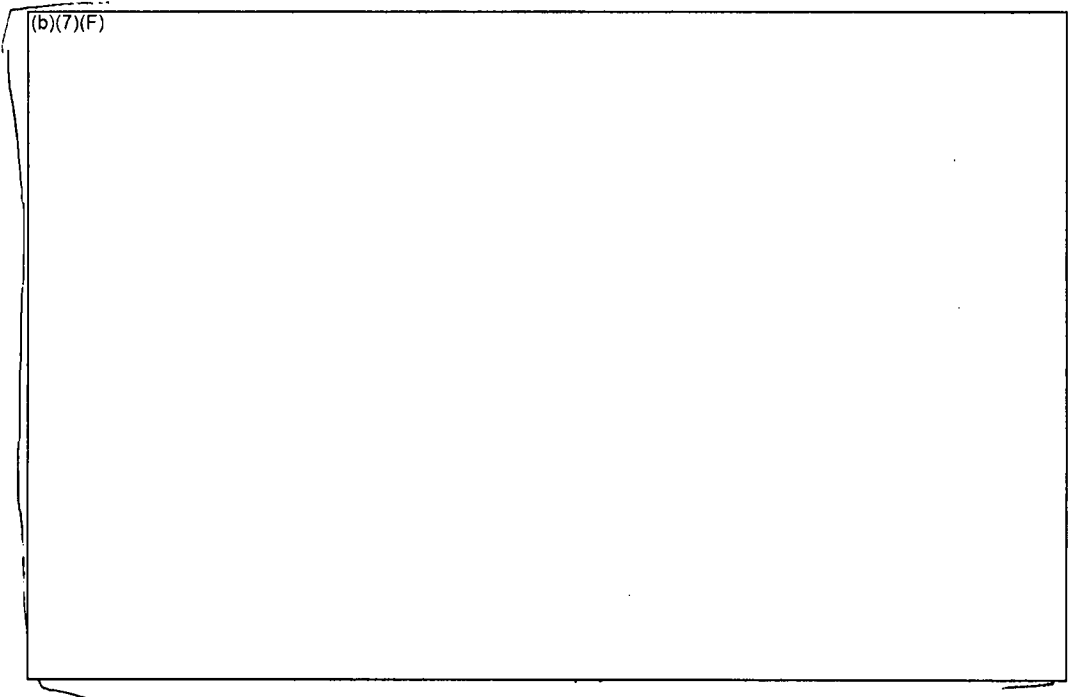


**Figure 6-26 Time-average Energy Flow in the Checkerboard Configuration** with (b)(7)(F)

Ex 7F

(b)(7)(F) Spray Flow (b)(7)(F)

**Legend for Figure 6-26:**

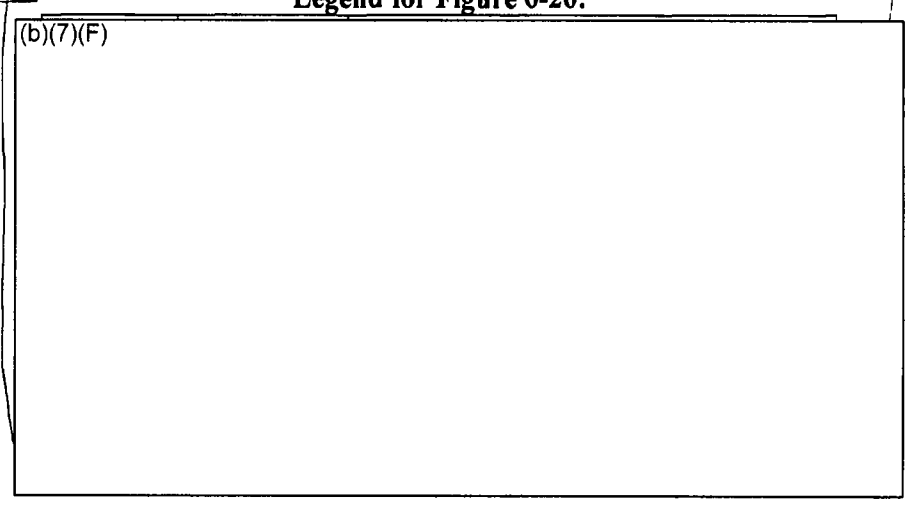
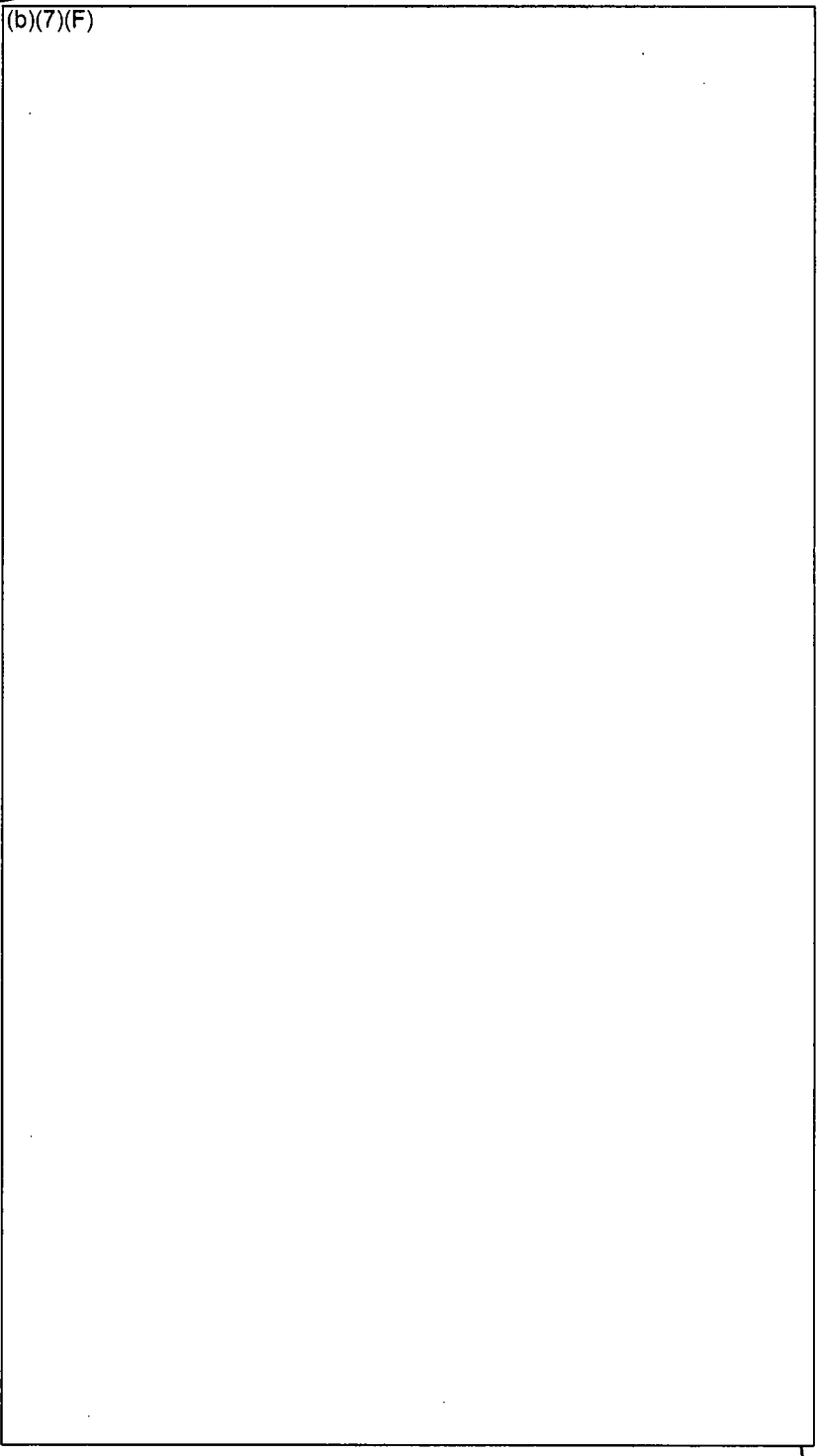


Table 6-3 Energy Balance for the Checkerboard Assembly Configuration in SFP with (b)(7)(F) Spray.

(b)(7)(F)



F-7F

### 6.4 Separate Effects Spray Model Results for the 1x4 Configuration Cases

Section 6.4.1 gives a summary of the 4 cases with (b)(7)(F) and (b)(7)(F) hole in a 1x4 fuel configuration. The four cases examine differences in the response with and without sprays and with and without the flow regime model active (see Section 3.1.4 for a more complete discussion). Finally, Section 6.3.2 shows the results of an energy balance on (b)(7)(F) case with sprays to illustrate the heat flows.

#### 6.4.1 Base Calculations (b)(7)(F) Spray

The S4 and S8 configuration calculations simulated a 1x4 configuration of the highest powered assemblies discharged into the spent fuel pool (b)(7)(F) since reactor shutdown surrounded by four low-powered assemblies at the median power with the reference BWR SFP (b)(4). The limiting response in a 1x4 configuration represents the response of a repeating pattern of 1x4 assemblies (e.g., see Figure 3-18). Similar to the checkerboard configuration, the high-powered assemblies benefit from radial heat transfer to adjacent low-powered assemblies. The transient is initiated with (b)(7)(F)

(b)(7)(F)

The four (b)(7)(F) (i.e., see S4 calculations in Table 6-1) examined differences in the response with and without sprays and with and without the flow regime model active. When the flow regime model was deactivated, the spray water has a relatively small surface contact area with the cladding. Due to the reduction of heat transfer, the spray flow penetrates more deeply into the assembly before completely evaporating. In addition, a S4 case was run where the inlet of the assembly was plugged by water. As discussed in Section 5, depending upon the size hole and the spray rate, cases were identified where the inlet to the racks could be covered.

Consequently, Case S4 and S4p parametrically investigated both conditions. (b)(7)(F)

(b)(7)(F)

Figure 6-27 and Figure 6-28 show the temperature responses for the (b)(7)(F) respectively. (b)(7)(F)

(b)(7)(F) Similar to the uniform and checkerboard results, the disabled flow regime model cases were more effective at providing spray cooling to the middle of the assembly. (b)(7)(F) cases with the flow regime model off were (b)(7)(F) cooler than when the model was active. The effect was more dramatic in the checkerboard cases (b)(7)(F) because the peak cladding temperatures in the flow regime cases were more greatly affected by the breakaway oxidation kinetics. In the cases with flow regime model active, there is very effective cooling of the top region of the fuel. (b)(7)(F)

(b)(7)(F)

(b)(7)(F) In both cases, the peripheral assemblies were well coated.

Figure 6-29 and Figure 6-30 show the axial temperature response in the center and peripheral assemblies for Case S4 with the flow regime model. (b)(7)(F)

(b)(4) The center assembly is cooled by gas convection, which is enhanced by the spray flow and radial heat transfer (b)(7)(F) see the energy balance in Section 6.4.2 for a full discussion). In the peripheral assemblies, gas convection out the top of the assembly removed most of the effective heat load from the peripheral assembly decay heat power and the radial heat flow from the center assembly. In addition, spray water flows out the bottom of the peripheral assemblies (b)(7)(F) of the total decay heat power.

Similar to the previous configurations, the calculation with the flow regime model inactive (i.e., Case 4a in Figure 6-31 and Figure 6-32) had a slightly lower peak temperature than when the flow regime model was active.

The high- and low-powered cladding temperature responses from Cases S4b and S4p are shown in Figure 6-33 through Figure 6-36. (b)(7)(F)

Ex 7F

(b)(7)(F) In previous separate effects calculations for the 1x4 configuration with air flow but no spray flow [Wagner, 2003], (b)(7)(F)

(b)(7)(F)

Ex 7F

(b)(7)(F)

(b)(7)(F) Similar to the checkerboard configuration, the convective heat removal in the low-powered assemblies is important. However, the 1x4 configuration has four low-powered assemblies surrounding the high-powered assembly. Although the convective gas flow was limited, the convective removal in the center assembly by boiling the spray water as well as removal in the liquid flow out the bottom of the four peripheral assemblies provided sufficient heat removal to keep the configuration cool.

Finally, the center and peripheral assembly axial temperature profiles are shown in Figure 6-37 and Figure 6-38 for all four cases, respectively. As observed in the axial temperature profiles for the uniform and checkerboard cases, the impact of the spray flow at the top of the assembly is clearly seen. The cases with the flow regime model active have cooler temperatures until the spray flow is depleted. The case without the flow regime model shows less heat removal at the top of the assembly but more heat removal at the bottom. (b)(7)(F)

Ex 7F

(b)(7)(F)

Consequently, the center assembly spray flow removed much of the decay heat at the top of the assembly whereas the spray flow in the peripheral assemblies helped removed the decay power in the lower portion of the assembly for the plugged case.

Ex 7F

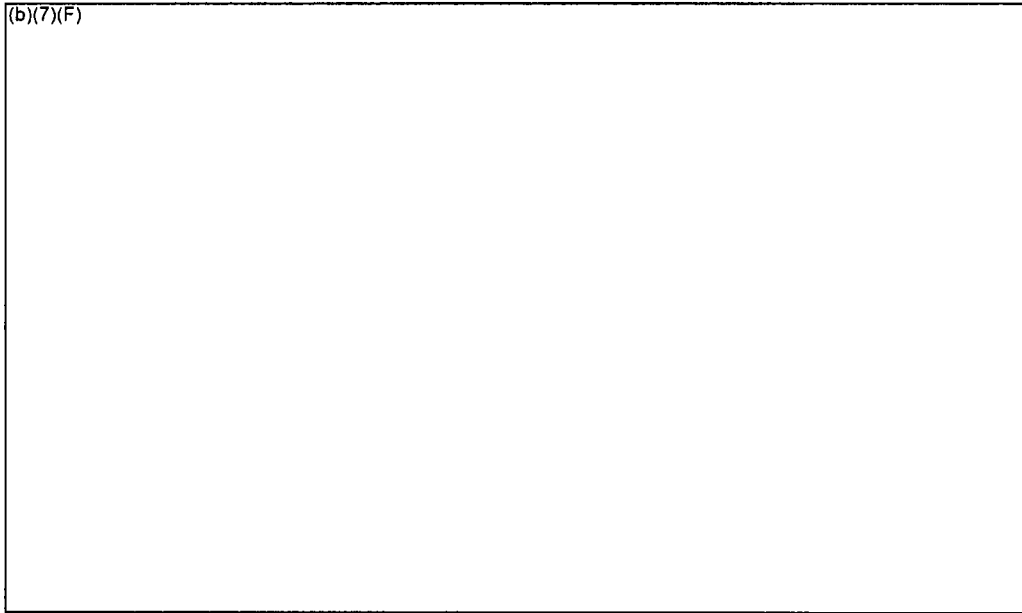


**Figure 6-27** Comparison of the Peak Cladding Temperatures (b)(7)(F) with a 1x4 Configuration with (b)(7)(F) and a Whole Pool Spray Flow of (b)(7)(F)



**Figure 6-28** Comparison of the Peak Cladding Temperatures (b)(7)(F) with a 1x4 Configuration with (b)(7)(F) and a Whole Pool Spray Flow of (b)(7)(F)

Ex 7F

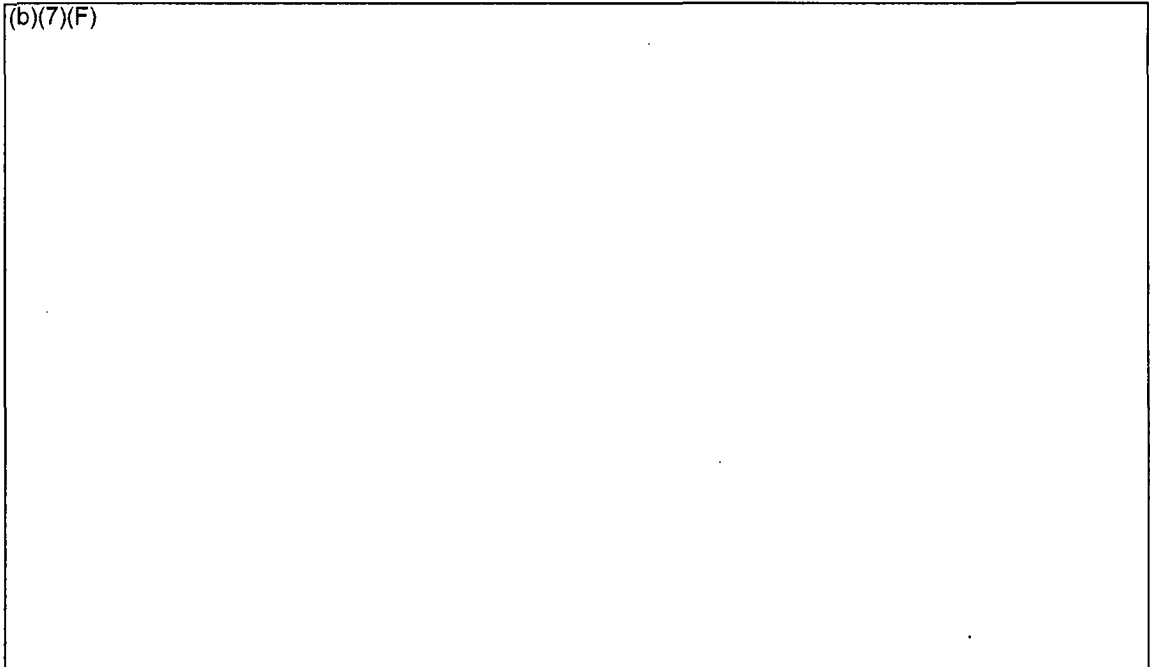


**Figure 6-29 Center Assembly Cladding Temperatures for the 1x4 Configuration with**  
**(b)(7)(F) Spray Flow (Case S4).**

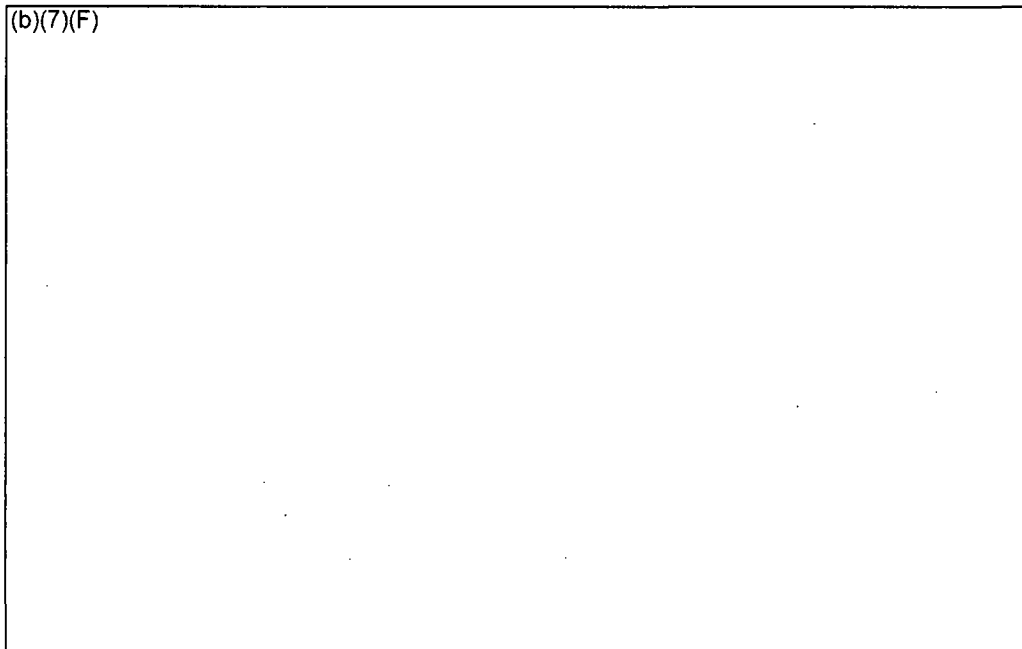


**Figure 6-30 Peripheral Assembly Cladding Temperatures for the 1x4 Configuration with**  
**(b)(7)(F) Spray Flow (Case S4).**

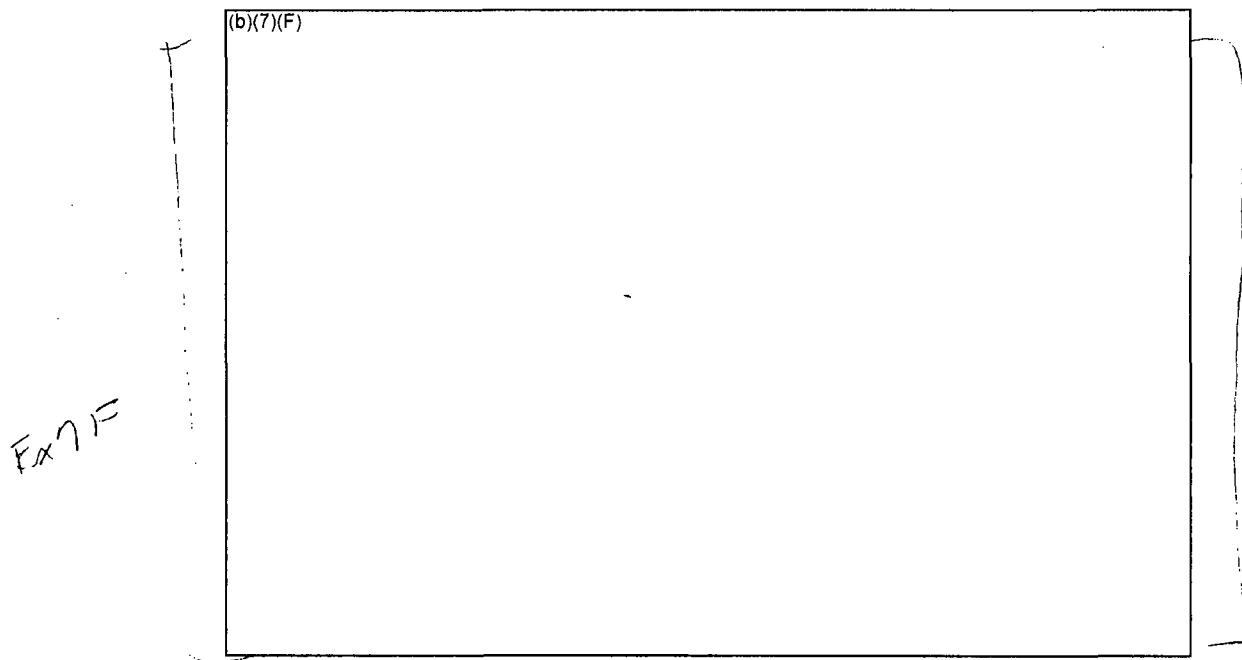


**Figure 6-31 Center Assembly Cladding Temperatures for the 1x4 Configuration with** (b)(7)(F) **Spray and the Flow Regime Model Inactive (Case S4a).**

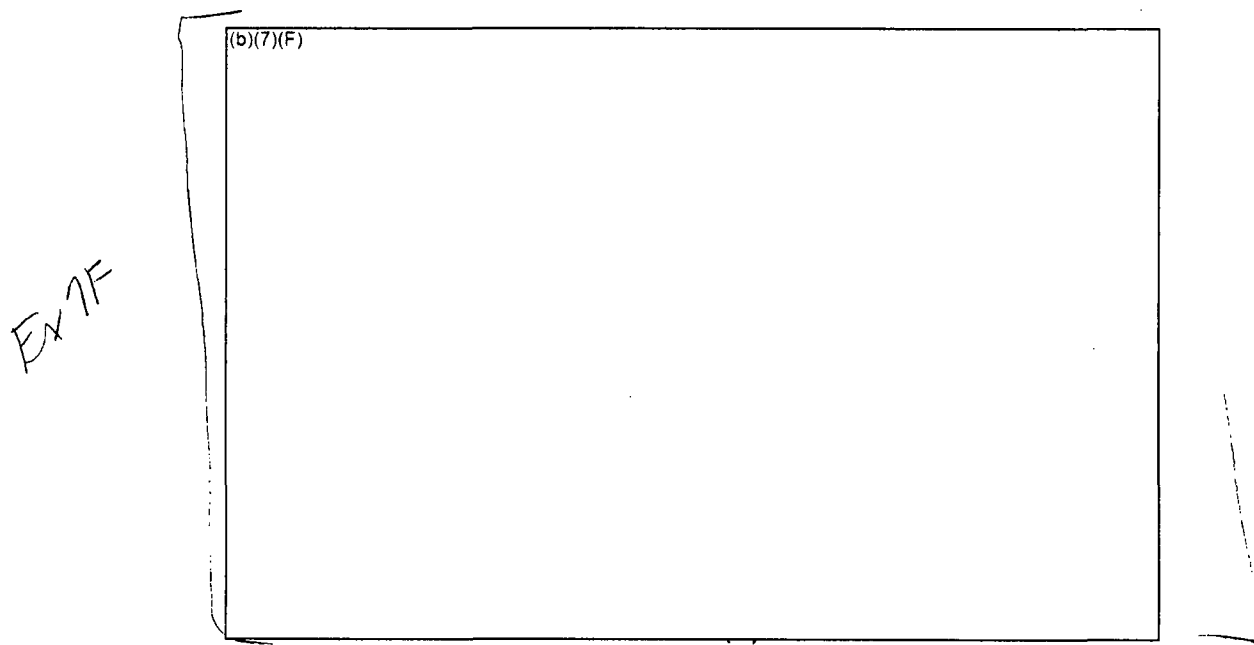


**Figure 6-32 Peripheral Assembly Cladding Temperatures for the 1x4 Configuration with** (b)(7)(F) **Spray and the Flow Regime Model Inactive (Case S4a).**

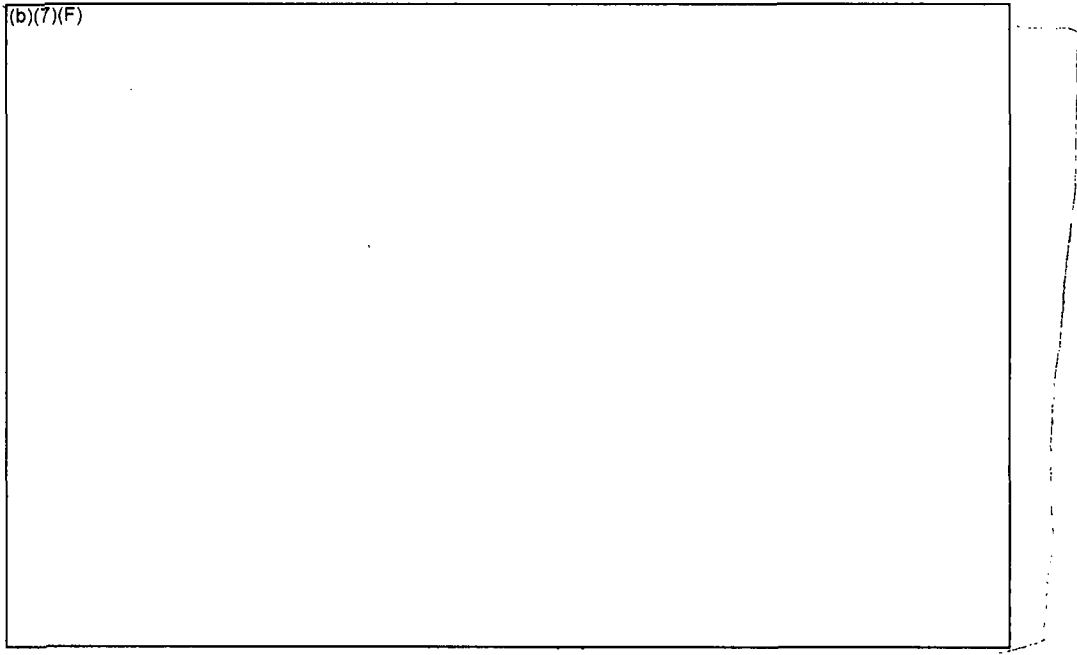


**Figure 6-33 Center Assembly Cladding Temperatures for the 1x4 Configuration with** (b)(7)(F) **and No Sprays (Case S4b).**

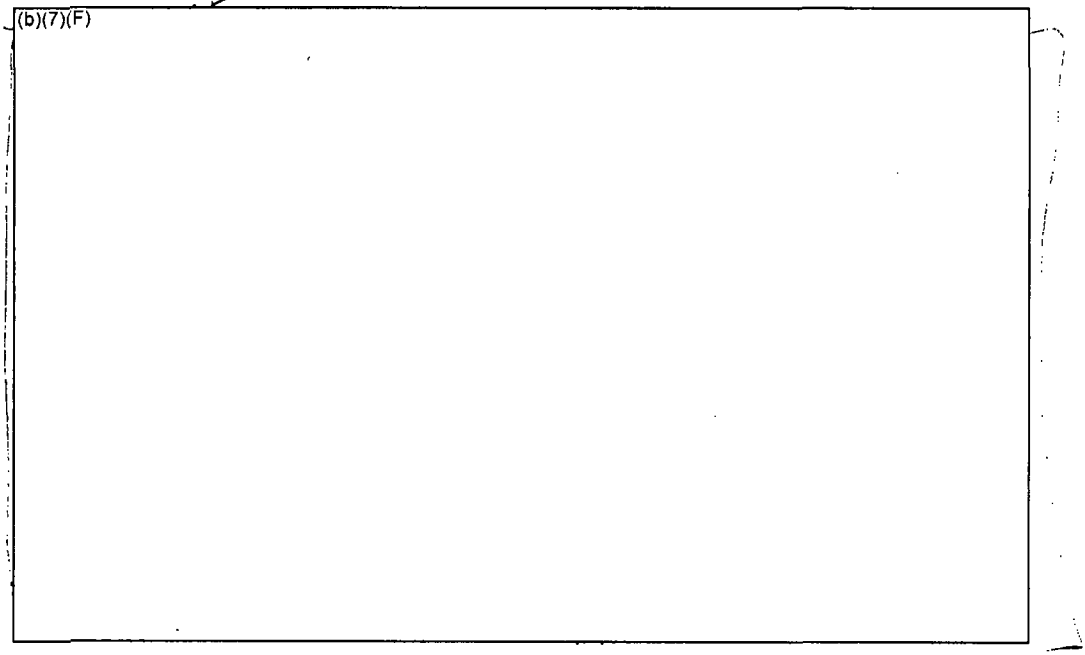


**Figure 6-34 Peripheral Assembly Cladding Temperatures for the 1x4 Configuration with** (b)(7)(F) **and No Spray Flow (Case S4b).**

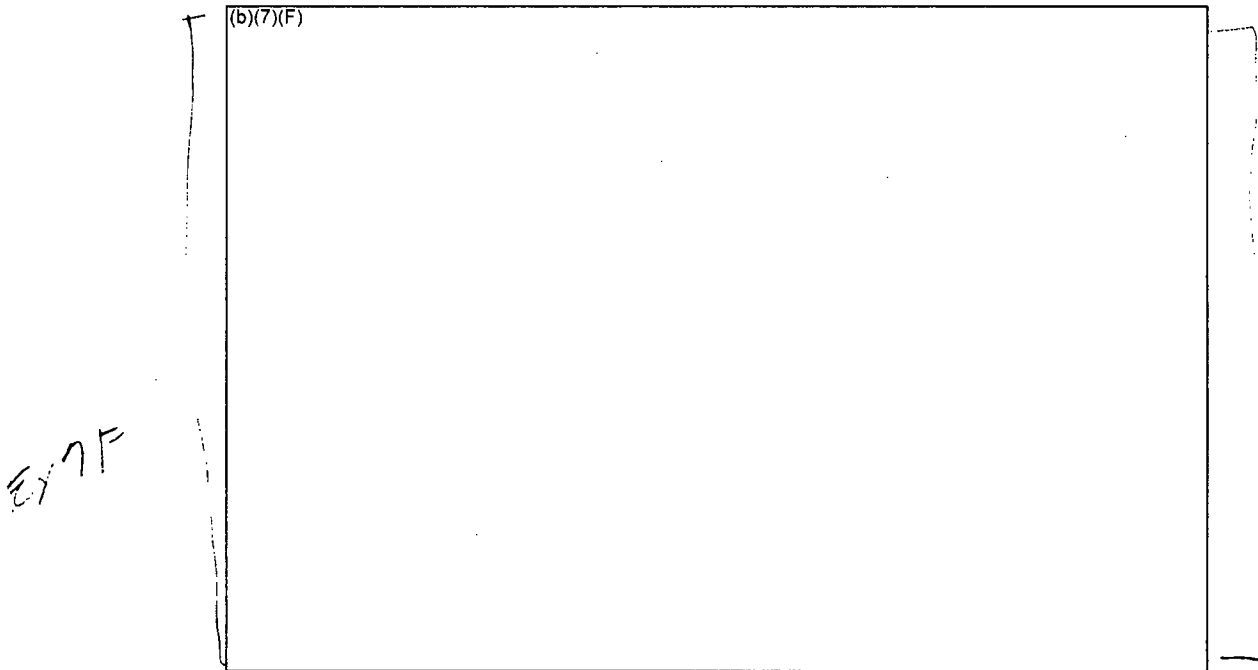


**Figure 6-35 Center Assembly Cladding Temperatures for the 1x4 Configuration with**  
**Spray Flow and Plugged Inlet (Case S4p).**

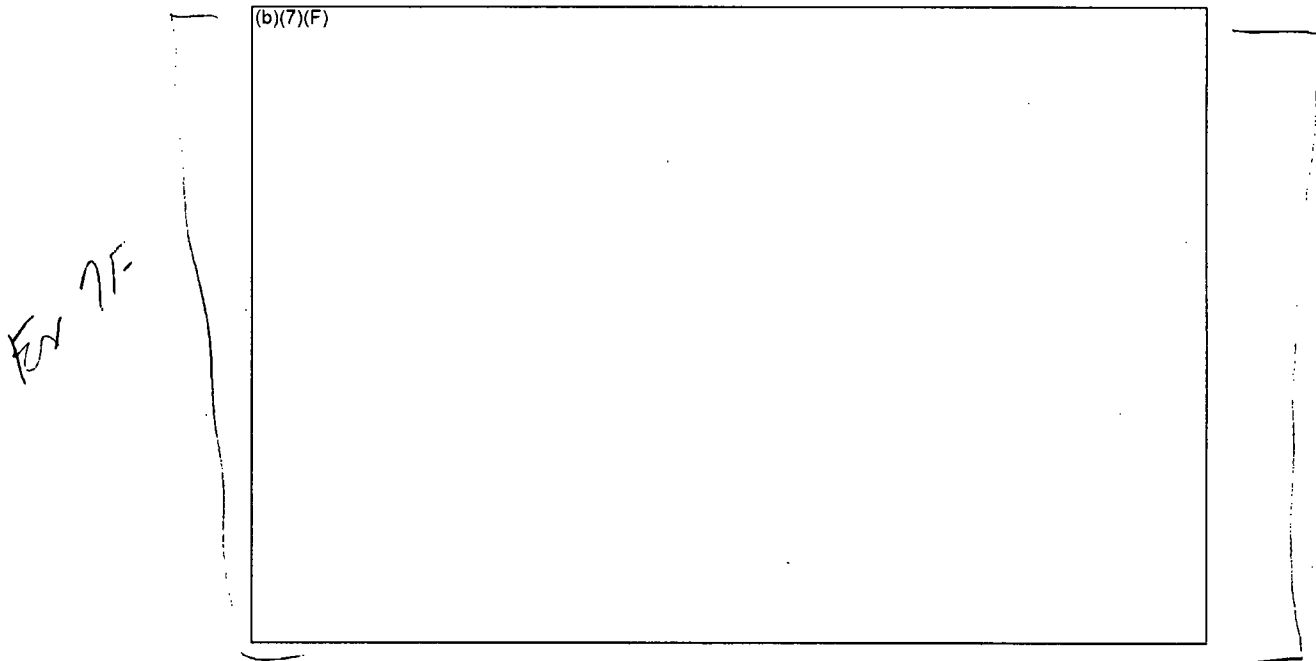


**Figure 6-36 Peripheral Assembly Cladding Temperatures for the 1x4 Configuration with**  
**Spray Flow and Plugged Inlet (Case S4p).**

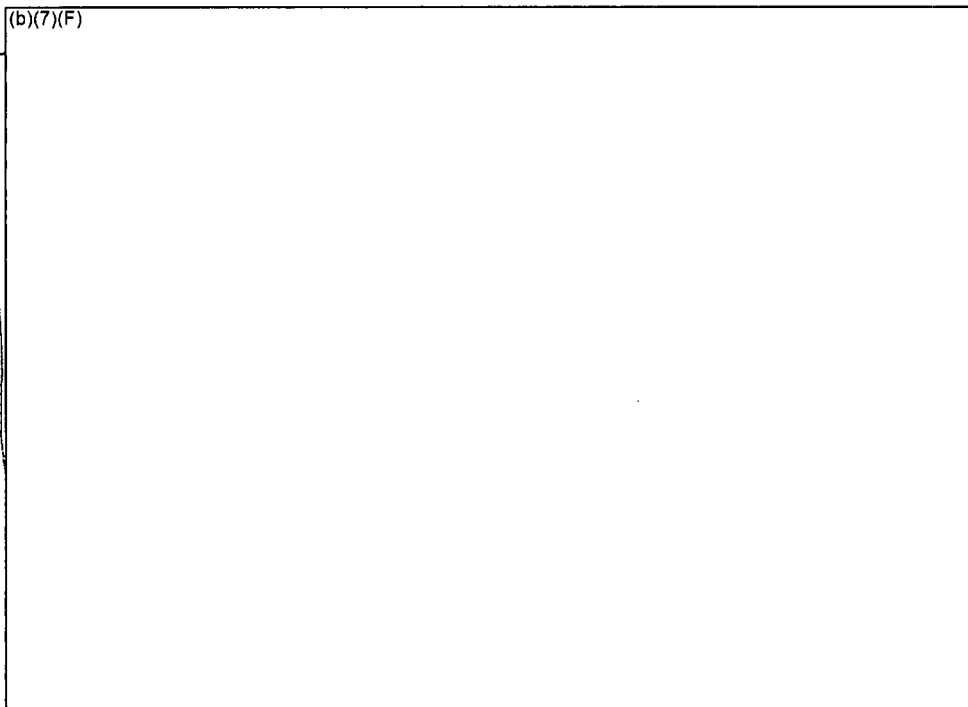


Figure 6-37 **Center Assembly Axial Cladding Temperatures for the 1x4 Configuration with a** (b)(7)(F) **Spray Flow.**

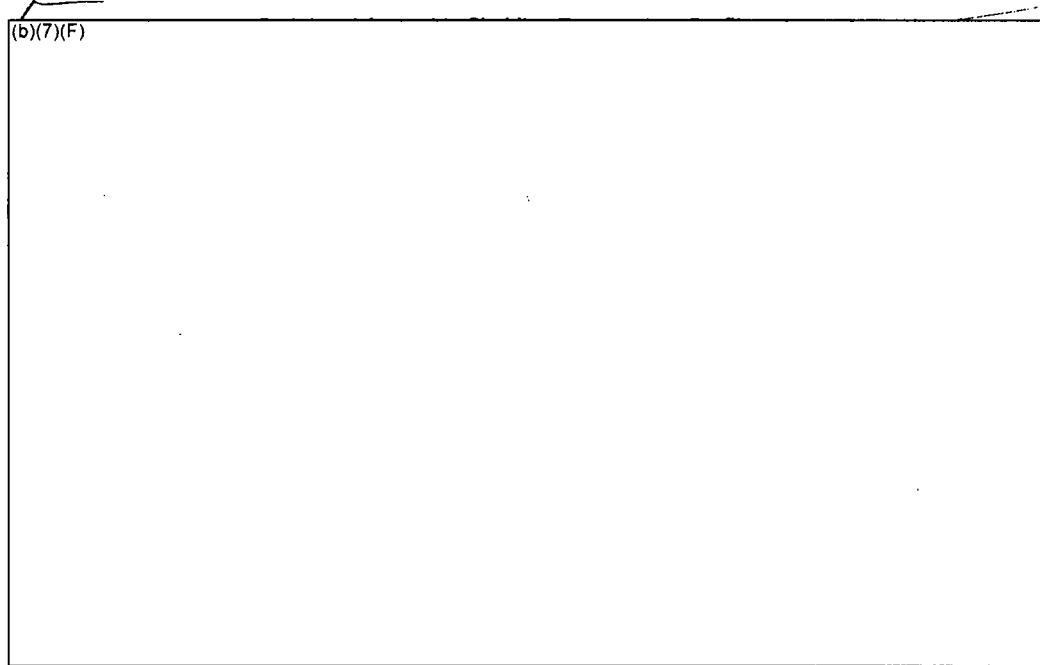


Figure 6-38 **Peripheral Assembly Axial Cladding Temperatures for the 1x4 Configuration with a** (b)(7)(F) **Spray Flow.**

Ex 7F

6.4.2 Energy Balance on Base Calculation (b)(7)(F)  
Spray EX 7F

An energy balance was performed on the S4 case with the flow regime model operating (Case S4). Figure 6-39 graphically shows the key heat flows in the model. After water level drops below the base plate, the power going into the structure steadily decreases to near zero. Meanwhile, due to air and steam convection, the heat removed by the gas in the peripheral assembly gradually increases. The convective heat removal by the center assembly gas is relatively constant after the base plate clearing. In this figure, the decay power includes both the low- and high-powered assemblies. The net heat balance is the sum of the heat flow terms besides the decay power (i.e., it should be approximately equal to the decay heat power<sup>24</sup>).

The energy balance is reported in Table 6-4. The total power put into the 1x4 configuration is a combination of the decay heat for both the high- and low-powered assemblies (b)(7)(F)

(b)(7)(F) Due to the relatively low temperatures in all five assemblies, there was (b)(7)(F) oxidation power. (b)(7)(F) of the power in the center assembly was removed by convection and (b)(7)(F) by radial heat transfer to the peripheral assemblies. In the peripheral assemblies, (b)(7)(F) of the net heat load from the peripheral assembly decay powers and the radial heat transfer was removed by gas convection out the top of the assembly. (b)(7)(F) of the power in the peripheral assemblies was carried away by liquid spray flow out the bottom of the assembly.

(b)(7)(F)  
(b)(7)(F)  
(b)(7)(F) EX 7F

(b)(7)(F)

<sup>24</sup> The small transient differences between the net energy balance and the decay power is attributed to limitations in the access of plot quantities available to the user to access all the subcomponents of the energy flow. However, the major components are shown on the figure. The internal MELCOR core calculations have very high fidelity.

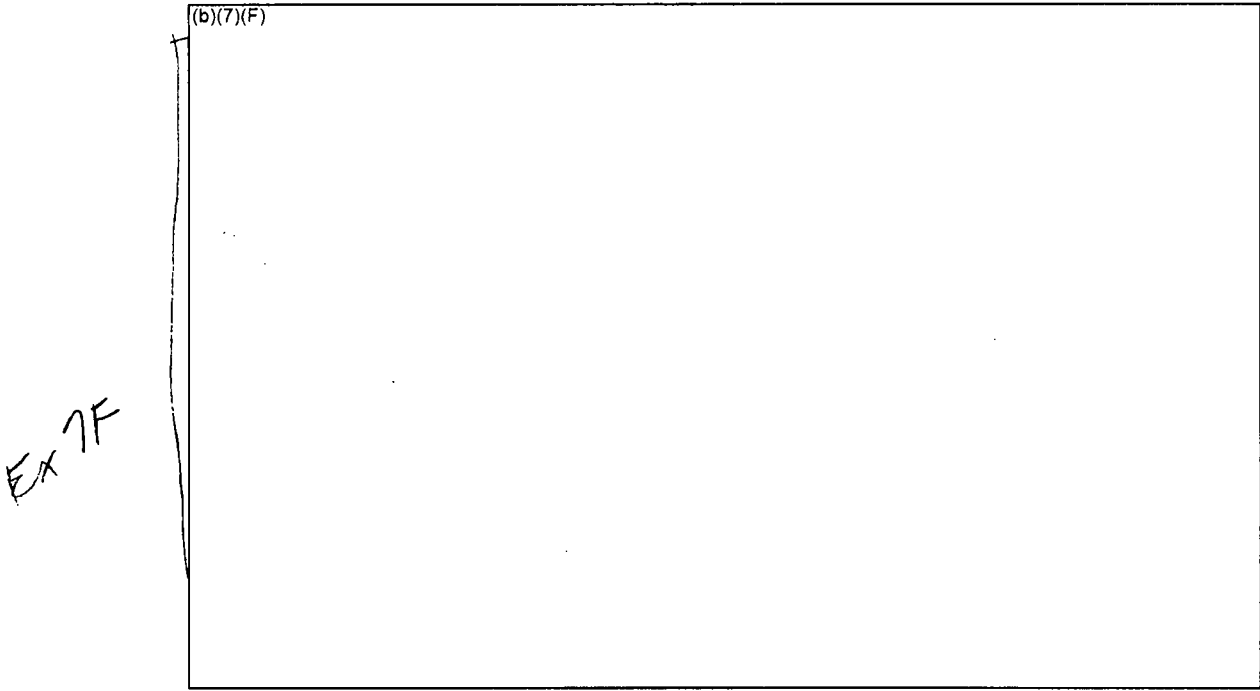


**Figure 6-39 Time-averaged Energy Flow in the 1x4 Configuration with** (b)(7)(F)  
**and a Whole Pool Spray Flow of** (b)(7)(F)

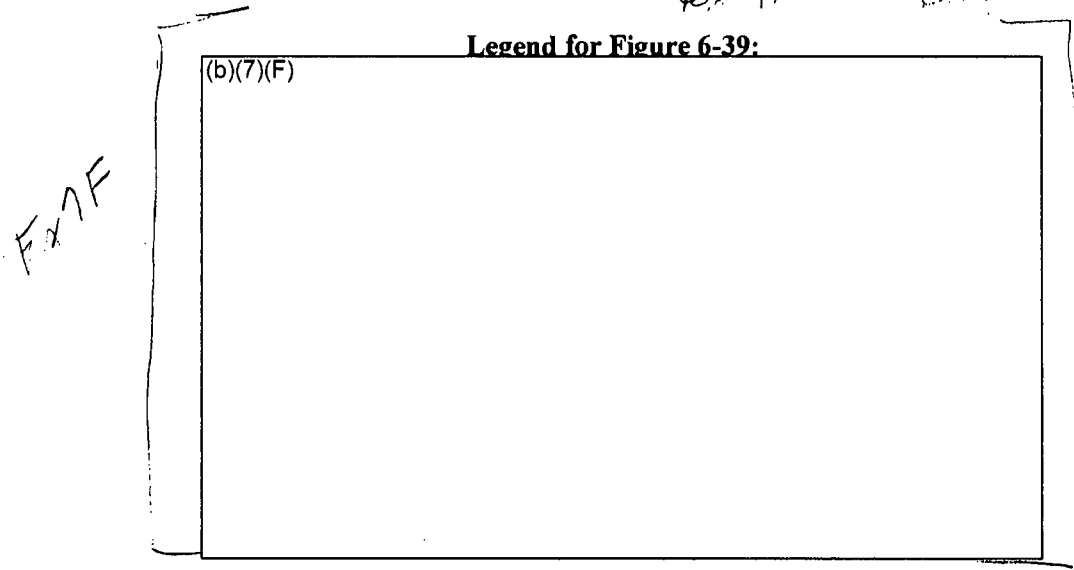


Table 6-4 Energy Balance for 1x4 Assembly Configuration in SFP with (b)(7)(F) Spray.

(b)(7)(F)

Ex 7F

## 7. REFERENCES

- Bergles, A. E., et al., Two-Phase Flow and Heat Transfer in the Power and Process Industries, McGraw-Hill Book Company, 1981.
- Boyd, C., "Predictions of Spent Fuel Heatup after a Complete Loss of-Coolant Accident," NUREG-1726, July 2000.
- Collins, T. E., and Hubbard, G., "Technical Study of Spent Fuel Pool Accident Risk at Decommissioning Nuclear Power Plants," NUREG-1738, February, 2001.
- Curbin, S., "Hydraulic Analysis of the Spent Fuel Pool Experiment," Revision 4, Sandia National Laboratories Internal Memo dated 11/21/05.
- Gauntt, R. O. et al, "MELCOR Computer Code Manuals, Reference Manual, Version 1.8.5, Vol. 2, Rev. 2", Sandia National Laboratories, NUREG/CR-6119, SAND2000-2417/1.
- Shalil, I., and Webb, S., "Simulations of Natural Convection Airflow in a Completely Drained Pressurized Water Reactor Spent Fuel Pool using FLUENT," Sandia National Laboratories, Letter Report, Revision 1, October 2005.
- Lanning, D. D., Beyer, C. E., Geelhood, and K.J., FRAPCON-3 Updates, Including Mixed-Oxide Fuel Properties," NUREG/CR-6534, Vol. 4, PNNL-11513, Pacific Northwest National Laboratory, May 2005.
- Lipinski, R. J., "A Model for Boiling and Dryout in Particle Beds," Sandia National Laboratories, SAND82-0765, NUREG/CR-2646, June 1982.
- Natesan, K., and Soppet, W.K., "Air Oxidation Kinetics for Zr-Based Alloys," NUREG/CR-6846, Argonne National Laboratories, June 2004.
- Nuclear Regulatory Commission, "Accident Source Terms for Light-Water Nuclear Power Plants," NUREG-1465, February 1995.
- Ross, K. W., Wagner, KC, and Gauntt, R. O., "Analysis of Spent Fuel Pool Flow Patterns Using Computational Fluid Dynamics: Part 2 - Partial Water Cases," Sandia National Laboratories, Informal Report, April 2003.
- Wagner, K. C., and Gauntt, R. O., "MELCOR 1.8.5 Separate Effect Analyses of Spent Fuel Pool Assembly Accident Response," Sandia National Laboratories, Draft Informal Report, Revision 0, June 2003.
- Wagner, K. C., and Gauntt, R. O., "Evaluation of a BWR Spent Fuel Pool Accident Response to Loss-of-Coolant Inventory Scenarios Using MELCOR 1.8.5," Sandia National Laboratories, Draft Informal Report, Revision 2, December 2004.

Wagner, K. C., and Gauntt, R. O., “Analysis of BWR Spent Fuel Pool Flow Patterns Using Computation Fluid Dynamics: Supplemental Air Cases,” Sandia National Laboratories, Draft Informal Report, Revision 2, October 2005.

Wagner, K. C. , Dallman, R. J., and Annon, M.C., “Best-Estimate Evaluation Of Loss-Of-Coolant Inventory In A Nuclear Power Plant Spent Fuel Pool,” *International Meeting on Best-Estimate Methods in Nuclear Installation Safety Analysis (BE-2000)*, Washington, DC, November, 2000.

Wallis, G. B., One-Dimensional Two-phase Flow, McGraw-Hill Book Company, 1969.

**SANDIA LETTER REPORT**

Revision 2 Completed: January 2008

# **Analysis of Emergency Spray Mitigation of Spent Fuel Pool Loss-of-Coolant Inventory Accidents**

K. C. Wagner  
R. O. Gauntt

Prepared by  
Sandia National Laboratories  
Albuquerque, New Mexico 87185 and Livermore, California 94550

Sandia is a multiprogram laboratory operated by Sandia Corporation,  
a Lockheed Martin Company, for the United States Department of Energy's  
National Nuclear Security Administration under Contract DE-AC04-94AL85000.



Issued by Sandia National Laboratories, operated for the United States Department of Energy by Sandia Corporation.

**NOTICE:** This report was prepared as an account of work sponsored by an agency of the United States Government. Neither the United States Government, nor any agency thereof, nor any of their employees, nor any of their contractors, subcontractors, or their employees, make any warranty, express or implied, or assume any legal liability or responsibility for the accuracy, completeness, or usefulness of any information, apparatus, product, or process disclosed, or represent that its use would not infringe privately owned rights. Reference herein to any specific commercial product, process, or service by trade name, trademark, manufacturer, or otherwise, does not necessarily constitute or imply its endorsement, recommendation, or favoring by the United States Government, any agency thereof, or any of their contractors or subcontractors. The views and opinions expressed herein do not necessarily state or reflect those of the United States Government, any agency thereof, or any of their contractors.



SANDIA Letter Report  
Revision 2, January 2008

# **Analysis of Emergency Spray Mitigation of Spent Fuel Pool Loss-of-Coolant Inventory Accidents**

K. C. Wagner  
R. O. Gauntt

Reactor Modeling and Analysis Division  
Sandia National Laboratories  
P.O. Box 5800  
Albuquerque, New Mexico 87185-MS-0748

## **ABSTRACT**

This report describes calculations to analyze the effectiveness of emergency spray mitigation of spent fuel pool (SFP) loss-of-coolant inventory accidents. The data used to perform these calculations were developed from an operating boiling water reactor. This report is a supplement to earlier studies, which also examined the BWR SFP accident response without spray mitigation. The MELCOR 1.8.5 severe accident computer code was the primary tool used to simulate the SFP accident response. The emergency spray mitigation calculations include separate effects calculations of one or a few assemblies in the spent fuel pool and the whole pool response. Some hand calculations are also included to illustrate the basic energy balances.

**REVISION HISTORY**

<b>Revision</b>	<b>Issue date</b>	<b>Description</b>
Draft	April 2006	Original issue
Revision 1	May 2006	Substantial editorial and technical updates
Revision 2	January 2008	2 minor typographic corrections. Reformat to standard SNL letter format.

**Revision 3 Error Correction Summary**

<b>Location</b>	<b>Correction</b>
Table ES-1	Third 1x4 result should be <span style="border: 1px solid black; padding: 2px;">(b)(7)(F)</span>
Table 5-1	For the second and fourth rows, '4.3 h' should be '1.5 h'

Ev 7F  
P

## EXECUTIVE SUMMARY

In 2001, United State Nuclear Regulatory Commission (NRC) staff performed an evaluation of the potential accident risk in a spent fuel pool (SFP) at decommissioning plants in the United States [NUREG-1738]. The study was prepared to provide a technical basis for decommissioning rulemaking for permanently shutdown nuclear power plants. The study described a modeling approach of a typical decommissioning plant with design assumptions and industry commitments; the thermal-hydraulic analyses performed to evaluate spent fuel stored in the spent fuel pool at decommissioning plants; the risk assessment of spent fuel pool accidents; the consequence calculations; and the implications for decommissioning regulatory requirements. It was known that some of the assumptions in the accident progression in NUREG-1738 were necessarily conservative, especially the estimation of the fuel damage. Subsequently, the NRC desired to expand the study to include accidents in the spent fuel pools of operating power plants. Consequently, the NRC has continued spent fuel pool accident research by applying best-estimate computer codes to predict the severe accident progression following various postulated accident initiators. This report describes the effectiveness of emergency sprays systems for mitigating spent fuel pool accidents.

The data used to perform these calculations were developed from an operating boiling water reactor (BWR). The reference plant is typical of many BWRs with fuel in the SFP from several decades old to the most recent offload. This reference plant has a two-year fuel cycle and roughly discharges one-third of the reactor fuel (b)(7)(F) each outage. The plant removes an equivalent amount of various aged fuel between outages for storage in dry casks, thereby maintaining a relatively constant number of assemblies in the SFP. Hence, the SFP has a wide variety of different aged fuel. In addition, the SFP racks have enough empty cell locations (b)(7)(F) to permit a complete emergency reactor offload as well as store all the refueling blade guides. A schematic of the reference BWR spent fuel pool storage building is shown in Figure ES-1.

The MELCOR 1.8.5 severe accident computer code [Gauntt] with enhancements through Version RP was used to simulate the SFP accident response. MELCOR includes fuel degradation models for pressurized water reactor (PWR) and BWR fuel, radiation, convection, and conduction heat transfer models, air and steam oxidation models, hydrogen burn models, two-phase thermal-hydraulic models, and fission product release and transport models. Therefore, it contains the basic models to address questions and phenomena expected during a spent fuel pool accident.

Version RP includes three recent modeling enhancements applicable to BWR SFP modeling, (1) a new rack component, which permits better modeling of a SFP rack, (2) a new oxidation kinetics model, and (3) a simplified flow regime model. The new BWR spent fuel pool rack component permits proper radiative modeling of the SFP rack between groups of different assemblies. The new oxidation kinetics model predicts the transition to breakaway oxidation in air environments on a node-by-node basis. The simplified flow regime model and an expanded axial CVH nodalization corresponding to a 1:1 matching of the COR nodalization permitted simulation of liquid films draining down the BWR fuel assemblies during spray operation.

The purpose of the study is to evaluate the effectiveness of emergency spray mitigation during a loss-of-coolant inventory accident. The accidents are initiated with a leak in the SFP. Once the water level has reached roughly the fuel [redacted] there would be inadequate cooling. Most calculations assumed a [redacted] until an emergency spray system could be activated. In a complete loss-of-coolant inventory accident, the leak is located at the bottom of the SFP on the side wall. An air natural circulation pattern can be established through the assemblies if the level drains below the bottom of the racks. If the fuel heats to high temperatures, then rapid exothermic oxidation of the zirconium cladding and canisters occurs using the oxygen in the air. If water from the spray system fills the bottom of the pool above the bottom of the racks, the accident will progress without convective air cooling.

Ex 7F

Two sets of hand calculations were performed to estimate the heat removal required from the spray system in the reference BWR spent fuel pool. The hand calculations represent simple straight-forward energy balances that are useful for estimating the required flowrate for a spray system. In the first calculation, the spray system was initiated prior to uncovering of the fuel and the water leakage location is above the top of the racks. [redacted]

Ex 7F

Ex 7F

of [redacted] Since the fuel is covered, a spray system is not technically needed. Rather any water injection system would be sufficient. In the second hand calculation, it is assumed that the fuel is substantially uncovered. [redacted]

Ex 7F

[redacted] Since the fuel is uncovered, a spray system is required to distribute the water to the individual assemblies. The flowrate estimate includes factors to account for inefficiencies due to overlap from the adjacent nozzles and flow into the region between the fuel canister and rack walls. The hand calculations also assume no radial heat transfer between assemblies, which effectively represents conditions corresponding to uniform loading of the most recently discharged fuel.

Recognizing that the above hand calculations for an uncovered pool were potentially conservative, a series of whole pool and detailed separate effects MELCOR calculations were performed. First, a BWR whole pool model was developed to establish boundary conditions for the separate effects calculations.<sup>1</sup> The most important output from the whole pool calculations was the steady state water level. For the range of hole sizes and spray flow rates considered in this study, the long-term water level spanned conditions that would allow air flow (i.e., the water level is not above the inlet to the racks or "plugged" by the water) versus cases where the inlet would be plugged. [redacted]

Ex 7F

Previous calculations have shown that the phenomena and thermal response for cases with the inlet plugged by the water level are different than the response when there is air flow in the assembly. Most importantly, the blocked inlet configuration substantially decreases the assembly heat removal. However, the spray calculations with a plugged inlet showed a much

<sup>1</sup> As will be discussed in the report, it was computationally impractical to include a sufficiently detailed nodalization to track spray behavior within the fuel assemblies in the whole spent pool and building model. Hence, the whole pool model was used to establish global boundary conditions for the separate effects calculations.

less significant impact after the spray initiation. The spray flow source provided an active heat removal mechanism that reduced the necessity of convective air flow.

Table ES-1 summarizes the highlights of separate effects spray calculations. Calculations were performed for the uniform, checkerboard, and 1x4 configurations. For each configuration, parametric calculations were performed with variations in one or more of the scenario or modeling attributes. The variations in the calculations included fuel configuration (uniform, checkerboard, and 1x4), aging time of the peak powered assembly, leak size (b)(7)(F) Ex 7F, spray flow rate (b)(7)(F) Ex 7F, air flow (some configurations that were expected to have air flow had a sensitivity study where the inlet was plugged with water), and a modeling parameter (MELCOR's flow regime model active or inactive).

Ex 7F For fuel which has been favorably configured (i.e., a 1x4 or checkerboard pattern), a spray flow rate of (b)(7)(F) is adequate for cooling the fuel (b)(7)(F) Ex 7F

(b)(7)(F)

**Table ES-1 Summary of Separate Effects Spray Calculation Results.**

(b)(7)(F)

Ex 7F

(b)(7)(F)

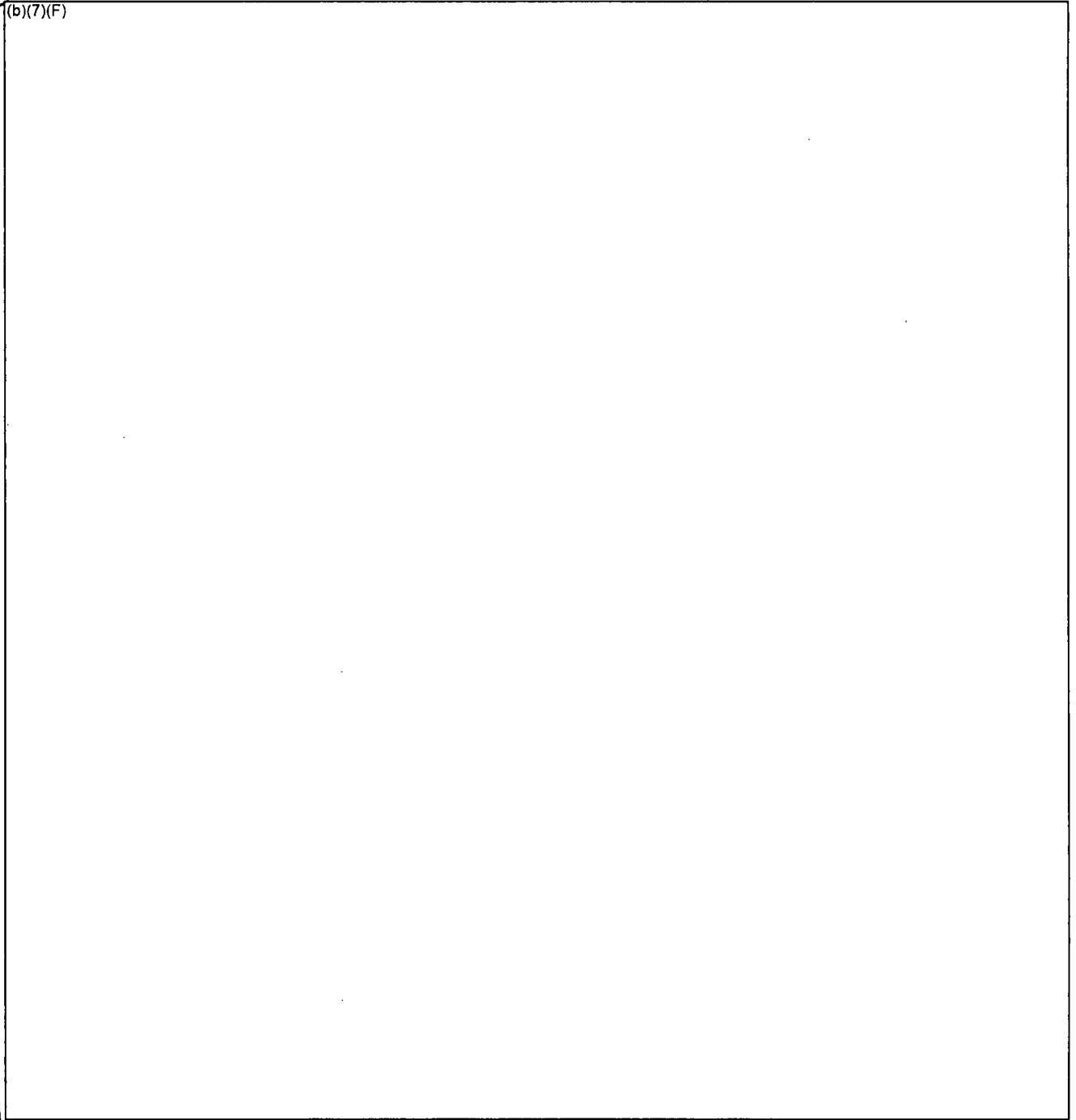


**Figure ES-1 Schematic of a BWR Reactor Building Showing the Refueling Room and Spent Fuel Pool.**

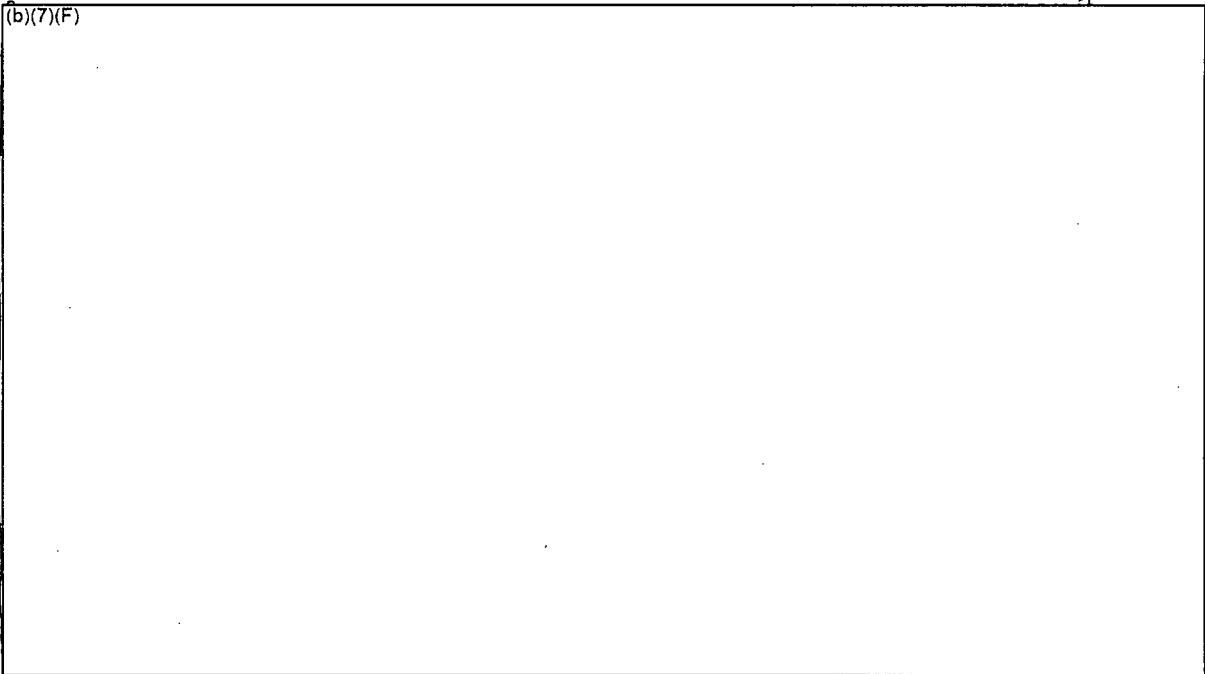


**Figure ES-2 Hand Calculations to Estimate Spray Heat Removal Requirements for Leaks Above and Below the Top of the Racks.**

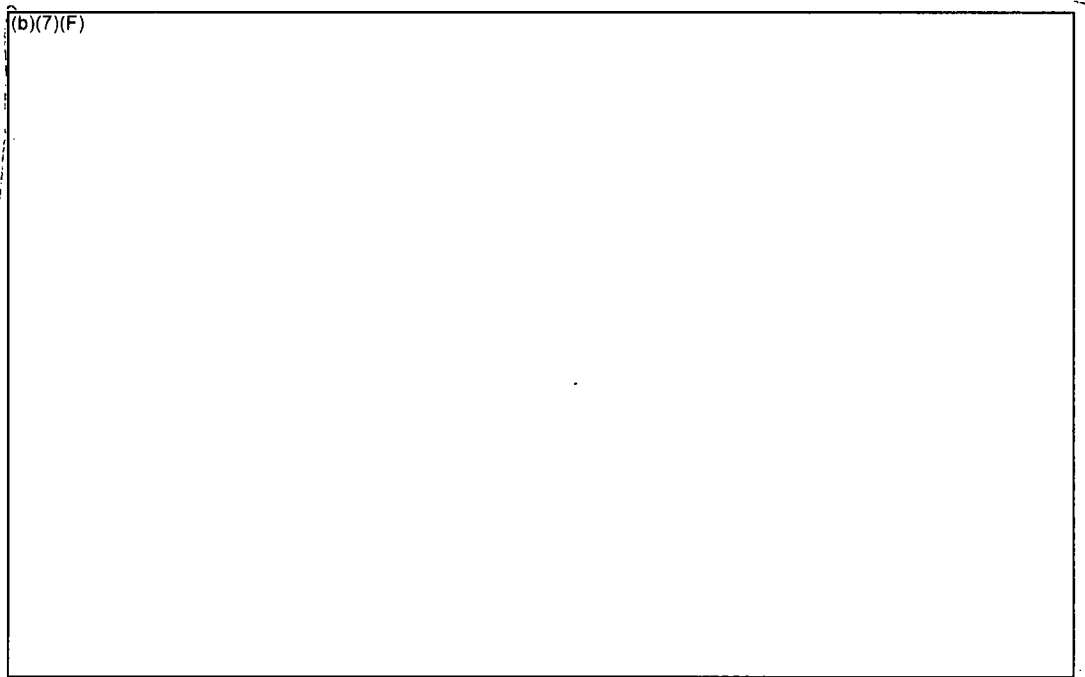


**Figure ES-3 Comparison of the Peak Cladding Temperatures for the Uniform Configuration with Various Aging Periods and a Whole Pool Spray Flow of**

E, 7F

(b)(7)(F)

TABLE OF CONTENTS

ABSTRACT..... iii

REVISION HISTORY ..... iv

1. INTRODUCTION..... 1

2. BACKGROUND ..... 2

    2.1 Description of the Spent Fuel Pool ..... 2

    2.2 SFP Accident Scenarios..... 6

        2.2.1 Complete Loss-of-Coolant Inventory Accident ..... 6

        2.2.2 Partial Loss-of-Coolant Accident..... 7

3. ANALYSIS METHODOLOGY ..... 9

    3.1 New BWR SFP Modeling ..... 9

        3.1.1 New BWR SFP Model..... 9

        3.1.2 Breakaway Air Oxidation Model..... 13

        3.1.3 New Hydraulic Resistance Model ..... 17

        3.1.4 Spray Modeling in MELCOR..... 23

    3.2 MELCOR Separate Effects Model..... 26

    3.3 Whole Pool Model..... 31

        3.3.1.1 Radial Thermal Coupling..... 33

        3.3.1.2 Simplified Refueling Room Model..... 37

    3.4 Description of the Initial and Boundary Conditions ..... 41

4. SPRAY MITIGATION HAND CALCULATIONS ..... 43

    4.1 Leak Above the Top of the Racks..... 43

    4.2 Leak Below the Top of the Racks ..... 45

        4.2.1 Calculations for One Point on the BWR Spray Chart..... 47

        4.2.2 Calculations for Counter-Current Flow Limitation (CCFL)..... 48

        4.2.3 Impact of Assembly Sensible Heat..... 50

5. WHOLE POOL MODEL BOUNDARY CONDITION CALCULATIONS..... 52

    5.1 (b)(7)(F) Spray Flow Rate..... 53

6. MELCOR SEPARATE EFFECTS MODEL RESULTS ..... 57

    6.1 Summary of Separate Effect Spray Calculations ..... 57

    6.2 Separate Effects Spray Model Results for the Uniform Configuration..... 62

        6.2.1 Base Calculations (b)(7)(F) Spray ..... 62

        6.2.2 Energy Balance on Base Calculator (b)(7)(F) Spray ..... 69

        6.2.3 Coolability Analysis (b)(7)(F) Spray Flowrate ..... 72

        6.2.4 Coolability Analysis (b)(7)(F) Spray Flowrate ..... 73

Ex 7F

Ex 7F  
Ex 7F

6.2.5	Coolability Analysis	(b)(7)(F)	Spray Flowrate	74	Ex 7F
6.3	<b>Separate Effects Spray Model Results for the Checkerboard Configuration</b>				75
6.3.1	Base Calculations	(b)(7)(F)	Spray	75	Ex 7F
6.3.2	Energy Balance on Base Calculation	(b)(7)(F)	Spray	83	
6.4	<b>Separate Effects Spray Model Results for the 1x4 Configuration Cases</b>				86
6.4.1	Base Calculations	(b)(7)(F)	Spray	86	Ex 7F
6.4.2	Energy Balance on Base Calculation	(b)(7)(F)	Spray	94	
7.	<b>REFERENCES</b>				97

**List of Tables**

Table 2-1	Spent Fuel Pool Data			4	
Table 2-2	Fuel Assembly Data			4	
Table 2-3	Spent Fuel Pool Rack Data			4	
Table 2-4	Fuel Assembly and Rack Flow Area Data			5	
Table 3-1	MELCOR Fit of the Timings for Transition from Pre-Breakaway to Post-Breakaway Oxidation Reaction Kinetics for Zirlo and Zircaloy-4 in the ANL Experiments [Natesan, 2004]			15	
Table 3-2	SLAM And k Coefficients for the Unblocked Water Rod Assembly Assuming All Flow Passes Through the Bundle			19	
Table 3-3	Summary of Regions in the MELCOR Whole Pool Model			36	
Table 3-4	Summary of Base Case SFP Model Initial Conditions for BWR SFP Emergency Spray Calculations			41	
Table 3-5	Summary of Base Case SFP Model Boundary Conditions for BWR SFP Emergency Spray Calculations			42	
Table 5-1	Summary of the Steady-State Water Levels as a Function of Leakage Hole Size and Spray Flow Rate			52	
Table 6-1	Summary of the Spray Calculations			58	
Table 6-2	Energy Balance for the Uniform Assembly Configuration in SFP with	(b)(7)(F)	Spray	71	Ex 7F
Table 6-3	Energy Balance for the Checkerboard Assembly Configuration in SFP with	(b)(7)(F)	Spray	85	Ex 7F
Table 6-4	Energy Balance for 1x4 Assembly Configuration in SFP with	(b)(7)(F)	Spray	96	Ex 7F

List of Figures

Figure 2-1 Spent Fuel Pool Rack Layout..... 3  
Figure 2-2 Typical Spent Fuel Pool Rack Cut-away Cross-Section Showing the Fuel Assembly..... 6  
Figure 3-1 MELCOR Modeling of a BWR Assembly in the Reactor Core. .... 10  
Figure 3-2 Original MELCOR Modeling of BWR Assemblies in a 1x4 SFP Configuration. .... 11  
Figure 3-3 Heat Flow for the Original MELCOR Modeling of a BWR Assemblies in a 1x4 SFP Configuration. .... 11  
Figure 3-4 New MELCOR Modeling of BWR Assemblies in a 1x4 SFP Configuration. 12  
Figure 3-5 Heat Flow for the New MELCOR Modeling of BWR Assemblies in a 1x4 SFP Configuration. .... 13  
Figure 3-6 Comparison of the MELCOR Breakaway Timing Fit to the Zirlo and Zr-4 Data from the ANL Air Oxidation Tests. .... 14  
Figure 3-7 Parabolic Reaction Kinetics Coefficients for Zr-4 Oxidation..... 16  
Figure 3-8 BWR Assembly Experimental Apparatus used in the Hydraulic Resistance Testing..... 20  
Figure 3-9 Measured Pressure Drop over the Full, Partial, and Total Assembly Regions. .... 21  
Figure 3-10 Comparison of the Calculated and Measured Bypass Flow. .... 22  
Figure 3-11 Axial Temperature Profile in the Assembly with Spray Flow..... 24  
Figure 3-12 Core Package Representation of Spray Flow..... 25  
Figure 3-13 CVH Package Representation of Spray Flow. .... 25  
Figure 3-14 Repeating Patterns Found in the MELCOR Separate Effects Models..... 26  
Figure 3-15 Schematic of the 1x4 Configuration. .... 29  
Figure 3-16 MELCOR Nodalization of the 5 Assembly Separate Effects Model..... 30  
Figure 3-17 Schematic of the Whole Pool Model Configuration..... 32  
Figure 3-18 Example of Alternating and Repeating 1x4 Patterns. .... 35  
Figure 3-19 The Radial Coupling Scheme as Implemented in MELCOR SFP Model. .... 36  
Figure 3-20 MELCOR Reactor Building Model. .... 39  
Figure 3-21 Example of Pressurized Water Reactor SFP Building Flow Patterns From FLUENT Calculations With An Open Roll Door. .... 40  
Figure 4-1 Total Decay Heat Power in the Reference BWR SFP. .... 44  
Figure 4-2 Make-up Flowrate for the Reference BWR SFP. .... 45  
Figure 4-3 Comparison of the Peak, Median, and Minimum Assembly Decay Heat Power in the Reference BWR SFP. .... 46  
Figure 4-4 Make-up Flowrate for the Reference BWR SFP. .... 47  
Figure 4-5 Timing Impact of Sensible Heat on Assembly Cooling  $\left[ \frac{(b)(7)(F)}{F} \right]$  for a  $F \times 7F$  Uniform Configuration..... 51  
Figure 4-6 Timing Impact of Sensible Heat on Assembly Cooling  $\left[ \frac{(b)(7)(F)}{F} \right]$  for a  $F \times 7F$  Uniform Configuration..... 51  
Figure 5-1 Water Level Boundary Condition from the BWR Whole Pool Model with  $\left[ \frac{(b)(7)(F)}{F} \right]$  and a Spray Flow of  $\left[ \frac{(b)(7)(F)}{F} \right]$  ..... 54  
Figure 5-2 Vapor and Liquid Temperature Boundary Condition from the BWR Whole Pool Model with  $\left[ \frac{(b)(7)(F)}{F} \right]$  and a Spray Flow of  $\left[ \frac{(b)(7)(F)}{F} \right]$  ..... 54

Figure 5-3 *Ex 7F* Steam Partial Pressure Boundary Condition from the BWR Whole Pool Model with (b)(7)(F) and a Spray Flow of (b)(7)(F) ..... 55

Figure 5-4 *Ex 7F* Whole Pool Level Response (b)(7)(F) with (b)(7)(F) and a Spray Flow of (b)(7)(F) ..... 55

Figure 5-5 *Ex 7F* Gas Concentration in the Refueling Room above the SFP for (b)(7)(F) and a Spray Flow (b)(7)(F) ..... 56

Figure 5-6 *Ex 7F* Comparison of the Leak Rate and Spray Flowrate Response (b)(7)(F) (b)(7)(F) with (b)(7)(F) and a Spray Flow of (b)(7)(F) ..... 56

Figure 6-1 *Ex 7F* Comparison of the Peak Cladding Temperatures (b)(7)(F) with a Uniform Configuration with (b)(7)(F) and a Whole Pool Spray Flow of (b)(7)(F) ..... 64

Figure 6-2 *Ex 7F* Comparison of the Peak Cladding Temperatures (b)(7)(F) with a Uniform Configuration with (b)(7)(F) and a Whole Pool Spray Flow of (b)(7)(F) ..... 65

Figure 6-3 *Ex 7F* Assembly Cladding Temperatures for the Uniform Configuration with (b)(7)(F) Spray Flow (Case S1) ..... 65

Figure 6-4 *Ex 7F* Assembly Cladding Temperatures for the Uniform Configuration with (b)(7)(F) Spray Flow, and the Flow Regime Model Inactive (Case S1a) ..... 66

Figure 6-5 *Ex 7F* Assembly Cladding Temperatures for the Uniform Configuration with (b)(7)(F) and No Spray Flow (Case S1b) ..... 66

Figure 6-6 *Ex 7F* Assembly Cladding Temperatures for the Uniform Configuration with (b)(7)(F) Spray Flow and Plugged Inlet (Case S1p) ..... 67

Figure 6-7 *Ex 7F* Axial Cladding Temperature Profiles (b)(7)(F) Uniform Configuration (b)(7)(F) Spray Flow (b)(7)(F) ..... 67

Figure 6-8 *Ex 7F* Axial Temperature Profiles (b)(7)(F) Uniform Configuration, (b)(7)(F) Spray Flow as a Function of Time ..... 68

Figure 6-9 *Ex 7F* Axial Temperature Profiles (b)(7)(F) Uniform Configuration, (b)(7)(F) and No Spray Flow as a Function of Time ..... 68

Figure 6-10 *Ex 7F* Time-averaged Energy Flow in the Uniform Configuration with (b)(7)(F) Spray Flow ..... 70

Figure 6-11 *Ex 7F* Comparison of the Peak Cladding Temperatures for the Uniform Configuration with Various Aging Periods and a Whole Pool Spray Flow of (b)(7)(F) ..... 72

Figure 6-12 *Ex 7F* Comparison of the Peak Cladding Temperatures for the Uniform Configuration with Various Aging Periods and a Whole Pool Spray Flow of (b)(7)(F) ..... 73

Figure 6-13 *Ex 7F* Comparison of the Peak Cladding Temperatures for the Uniform Configuration with Various Aging Periods and a Whole Pool Spray Flow of (b)(7)(F) ..... 74

Figure 6-14 *Ex 7F* Comparison of the Peak Cladding Temperatures (b)(7)(F) with a Checkerboard Configuration with (b)(7)(F) and a Whole Pool Spray Flow of (b)(7)(F) ..... 77

Figure 6-15 Comparison of the Peak Cladding Temperatures (b)(7)(F) with a Checkerboard Configuration with (b)(7)(F) and a Whole Pool Spray Flow of (b)(7)(F) ..... 77

Ex 7F Figure 6-16 High-Powered Assembly Cladding Temperatures for the Checkerboard Configuration with (b)(7)(F) Spray Flow (Case S3)..... 78

Ex 7F Figure 6-17 Low-Powered Assembly Cladding Temperatures for the Checkerboard Configuration with (b)(7)(F) Spray Flow (Case S3)..... 78

Ex 7F Figure 6-18 High-Powered Assembly Cladding Temperatures for the Checkerboard Configuration with (b)(7)(F) Spray Flow and the Flow Regime Model Inactive (S3a)..... 79

Ex 7F Figure 6-19 Low-Powered Assembly Cladding Temperatures for the Checkerboard Configuration with (b)(7)(F) Spray Flow and the Flow Regime Model Inactive (S3a)..... 79

Ex 7F Figure 6-20 High-Powered Assembly Cladding Temperatures for the Checkerboard Configuration with (b)(7)(F) and No Spray Flow (Case S3b)..... 80

Ex 7F Figure 6-21 Low-Powered Assembly Cladding Temperatures for the Checkerboard Configuration with (b)(7)(F) and No Spray Flow (Case S3b)..... 80

Ex 7F Figure 6-22 High-Powered Assembly Cladding Temperatures for the Checkerboard Configuration with (b)(7)(F) Spray Flow and Plugged Inlet (Case S3p)..... 81

Ex 7F Figure 6-23 Low-Powered Assembly Cladding Temperatures for the Checkerboard Configuration with (b)(7)(F) Spray Flow and Plugged Inlet (Case S3p)..... 81

Ex 7F Figure 6-24 High-Powered Assembly Cladding Temperature Profiles for the Checkerboard Configuration with a (b)(7)(F) and (b)(7)(F) Spray Flow..... 82

Ex 7F Figure 6-25 Low-Powered Assembly Cladding Temperature Profiles for the Checkerboard Configuration with a (b)(7)(F) Spray Flow..... 82

Ex 7F Figure 6-26 Time-average Energy Flow in the Checkerboard Configuration with (b)(7)(F) Aging and a Whole Pool Spray Flow of (b)(7)(F)..... 84

Ex 7F Figure 6-27 Comparison of the Peak Cladding Temperatures (b)(7)(F) with a 1x4 Configuration with (b)(7)(F) and a Whole Pool Spray Flow of (b)(7)(F)..... 88

Ex 7F Figure 6-28 Comparison of the Peak Cladding Temperatures (b)(7)(F) with a 1x4 Configuration with (b)(7)(F) and a Whole Pool Spray Flow (b)(7)(F)..... 88

Ex 7F Figure 6-29 Center Assembly Cladding Temperatures for the 1x4 Configuration with (b)(7)(F) Spray Flow (Case S4)..... 89

Ex 7F Figure 6-30 Peripheral Assembly Cladding Temperatures for the 1x4 Configuration with (b)(7)(F) Spray Flow (Case S4)..... 89

Ex 7F Figure 6-31 Center Assembly Cladding Temperatures for the 1x4 Configuration with (b)(7)(F) Spray and the Flow Regime Model Inactive (Case S4a)..... 90

EX 7F

Figure 6-32 **Peripheral Assembly Cladding Temperatures for the 1x4 Configuration with** (b)(7)(F) **Spray and the Flow Regime Model Inactive** (with (b)(7)(F)) (Case S4a). ..... 90

EX 7F  
Figure 6-33 **Center Assembly Cladding Temperatures for the 1x4 Configuration with** (b)(7)(F) **and No Sprays (Case S4b).** ..... 91

EX 7F  
Figure 6-34 **Peripheral Assembly Cladding Temperatures for the 1x4 Configuration with** (b)(7)(F) **and No Spray Flow (Case S4b).** ..... 91

EX 7F  
Figure 6-35 **Center Assembly Cladding Temperatures for the 1x4 Configuration with** (b)(7)(F) **Spray Flow and Plugged Inlet (Case S4p).** ..... 92

EX 7F  
Figure 6-36 **Peripheral Assembly Cladding Temperatures for the 1x4 Configuration with** (b)(7)(F) **Spray Flow and Plugged Inlet (Case S4p).** ..... 92

EX 7F  
Figure 6-37 **Center Assembly Axial Cladding Temperatures for the 1x4 Configuration** with a (b)(7)(F) **Spray Flow.** ..... 93

Figure 6-38 **Peripheral Assembly Axial Cladding Temperatures for the 1x4 Configuration with a** (b)(7)(F) **with** (b)(7)(F) **Spray Flow.** ..... 93

Figure 6-39 **Time-averaged Energy Flow in the 1x4 Configuration with** (b)(7)(F) **and a Whole Pool Spray Flow of** (b)(7)(F) ..... 95

EX 7F

## Analysis of Emergency Spray Mitigation of Spent Fuel Pool Loss-of-Coolant Inventory Accidents

### 1. INTRODUCTION

In 2001, United State Nuclear Regulatory Commission (NRC) staff performed an evaluation of the potential accident risk in a spent fuel pool (SFP) at decommissioning plants in the United States [NUREG-1738]. The study was prepared to provide a technical basis for decommissioning rulemaking for permanently shutdown nuclear power plants. The study described a modeling approach of a typical decommissioning plant with design assumptions and industry commitments; the thermal-hydraulic analyses performed to evaluate spent fuel stored in the spent fuel pool at decommissioning plants; the risk assessment of spent fuel pool accidents; the consequence calculations; and the implications for decommissioning regulatory requirements. It was known that some of the assumptions in the accident progression in NUREG-1738 were necessarily conservative, especially the estimation of the fuel damage. Subsequently, the NRC desired to expand the study to include accidents in the spent fuel pools of operating power plants. Consequently, the NRC has continued spent fuel pool accident research by applying best-estimate computer codes to predict the severe accident progression following various postulated accident initiators. This report describes the effectiveness of emergency sprays systems for mitigating spent fuel pool accidents.

The data used to perform these calculations were developed from an operating boiling water reactor (BWR). The reference plant is typical of many BWRs with fuel in the SFP from several decades old to the most recent offload. This reference plant has a two-year fuel cycle and roughly discharges one-third of the reactor fuel (b)(7)(F) each outage. The plant removes an equivalent amount of various aged fuel between outages for storage in dry casks, thereby maintaining a relatively constant number of assemblies in the SFP. Hence, the SFP has a wide variety of different aged fuel. In addition, the SFP racks have enough empty cell locations (b)(7)(F) to permit a complete emergency reactor offload as well as store all the refueling blade guides.

The MELCOR 1.8.5 severe accident computer code [Gauntt] with enhancements through Version RP is used to simulate the SFP accident response. MELCOR includes fuel degradation models for pressurized water reactor (PWR) and BWR fuel, radiation, convection, and conduction heat transfer models, air and steam oxidation models, hydrogen burn models, two-phase thermal-hydraulic models, and fission product release and transport models. Therefore, it contains the basic models to address questions and phenomena expected during a spent fuel pool accident.

Version RP includes three recent modeling enhancements applicable to BWR SFP modeling, (1) a new rack component, which permits better modeling of a SFP rack, (2) a new oxidation kinetics model, and (3) a simplified flow regime model. The new BWR spent fuel pool rack component permits proper radiative modeling of the SFP rack between groups of different assemblies. The new oxidation kinetics model predicts the transition to breakaway oxidation in

air environments on a node-by-node basis.<sup>2</sup> The simplified flow regime model and an expanded axial CVH nodalization corresponding to a 1:1 matching of the COR nodalization permitted simulation of liquid films draining down the BWR fuel assemblies during spray operation.

## 2. BACKGROUND

The reference plant for the SFP analysis is a large BWR. Like most other nuclear plants, the reference plant has installed high-density racks to maximize the storage of fuel in the SFP. A description of the reference plant SFP is given in 2.1. The accidents considered in the present study consist of a loss-of-coolant inventory. A description of the accident progression is provided in Section 2.2.

### 2.1 Description of the Spent Fuel Pool

CEX The spent fuel pool, 40 feet wide by 35.3 feet long by 38 feet deep, is located on the refueling floor (b)(7)(F) of the reactor building. The pool is constructed of reinforced concrete with a wall and floor lining of 1/4-inch thick stainless steel. The walls and the floor of the spent fuel pool are approximately 6'. In the northeast corner of the SFP is a cask area of 10' square (see Figure 2-1). The general attributes of the spent fuel pool, the BWR fuel assemblies, the spent fuel pool racks, and the assembly and rack flow areas are described in Table 2-1, Table 2-2, Table 2-3, and Table 2-4, respectively.

The high density SFP racks provide spent fuel storage at the bottom of the fuel pool. The fuel storage racks are normally covered with about 23 ft of water for radiation shielding. The SFP racks are freestanding, full length, top entry and are designed to maintain the spent fuel in a spaced geometry, which precludes the possibility of criticality under any condition.

(b)(7)(F) CEX The high-density SFP racks are of the "poison" type utilizing a neutron absorbing material to maintain a subcritical fuel array. The racks are rectilinear in shape and are of nine different sizes. A total of [redacted] storage locations are provided in the pool. The racks are constructed of stainless steel materials and each rack module is composed of cell assemblies, a base plate, and base support assemblies. Each cell is composed of (a) a full-length enclosure constructed of 0.075" thick stainless steel, (b) sections of Bisco Boraflex, which is a neutron absorbing material, and (c) wrapper plates constructed of 0.020" tick stainless steel. The inside square dimension of a cell enclosure is 6.07". The cell pitch is 6.28".

The base plate is a 0.5" thick stainless steel with 3.8" chamfered through holes centered at each storage location, which provides a seating surface for the fuel assemblies. These holes also provide passage for coolant flow.

Each rack module has base support assemblies (i.e., 'rack feet') located at the center of the corner cells within the module and at interior locations<sup>3</sup> to distribute the pool floor loading (e.g., see Figure 2-2). Each base assembly is composed of a level block assembly, a leveling screw,

<sup>2</sup> It should be noted that the steam oxidation model does not use a breakaway kinetics model. Steam-zircaloy oxidation is based on the default Urbanic-Heidrich model [Gauntt].

<sup>3</sup> There are several different rack sizes in the SFP. However, for a 19x10 size rack, there are 18 base support assemblies, 14 on the perimeter and 4 in the interior.

and a support pad. The top of the leveling block assembly is welded to the bottom of the base plate. SFP fuel cells are located above each rack foot. Four 1" holes are drilled into the side of the support pad. The interior of the support pad is hollow and permits flow to the opening in the base plate.

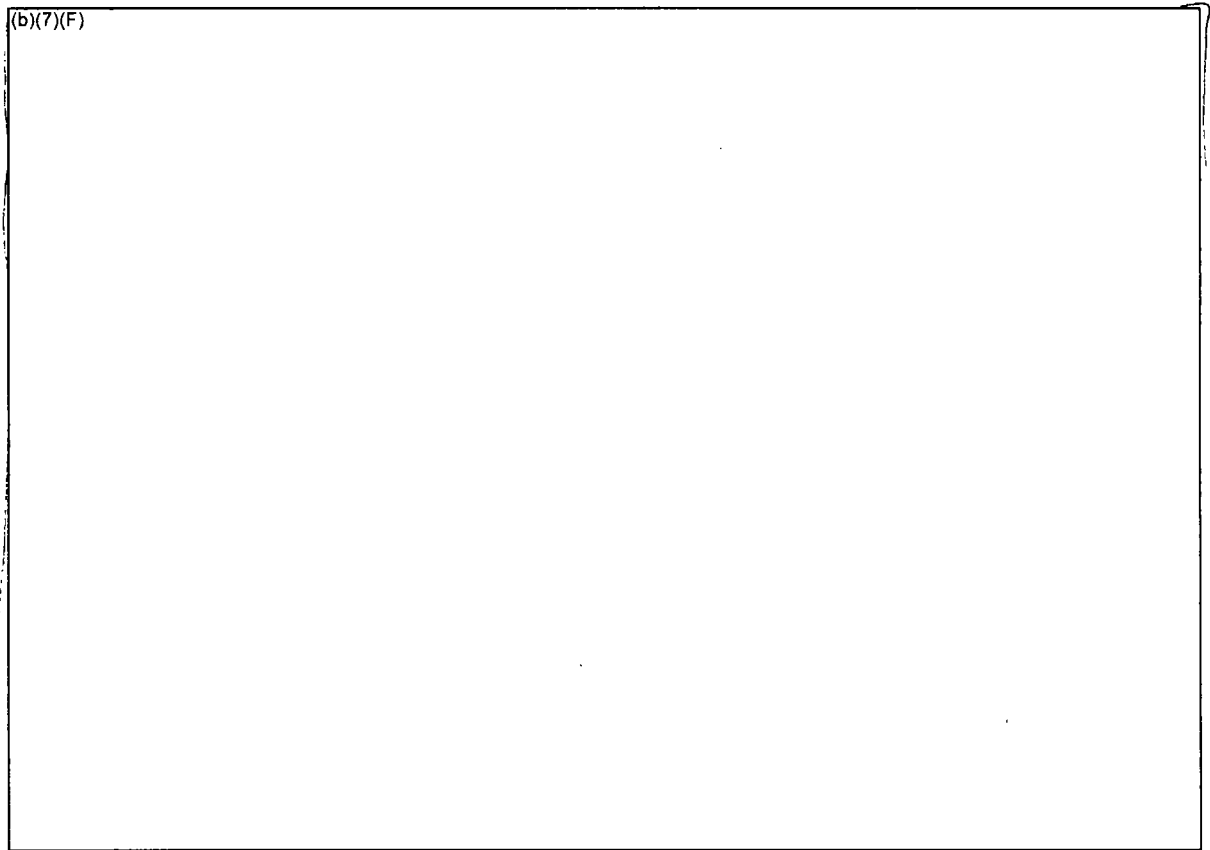


**Figure 2-1 Spent Fuel Pool Rack Layout.**

Table 2-1 Spent Fuel Pool Data.

SFP Pool Characteristics	Description or Dimensions
Dimensions	480" x 424" 10 ft square Cask Area in NW corner 39' high walls
Concrete thickness	~6 feet
SFP Volume	53,350 ft <sup>3</sup> (399,000 gal)
Number of storage locations	(b)(7)(F)

Table 2-2 Fuel Assembly Data.

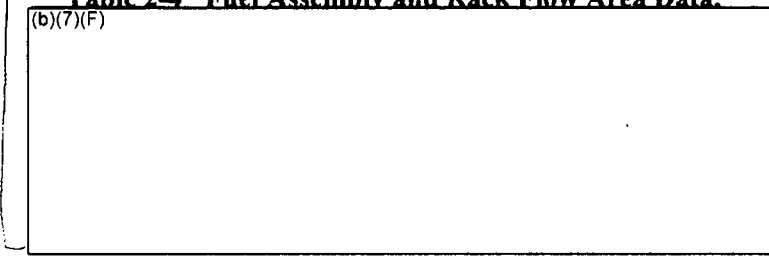
Assembly Characteristics	Description or Dimensions
Fuel Type	GE 9x9
Number of Fuel Rods	74
Fuel Pitch	0.566"
Fuel Rod Dimensions	0.44" OD 0.028" Cladding 146" Active Length
Maximum Initial Enrichment	4% U-235 by weight
Number of Water Rods	2
Water Rod Dimensions	0.98" OD Zircaloy

Table 2-3 Spent Fuel Pool Rack Data.

SFP Rack Characteristics	Description or Dimensions
Rack Height Above the Base Plate	169"
Baseplate Thickness	0.5"
Support Leg Height	7.25"
Poison Material	Boraflex
Cell Pitch	6.28
Cell Construction	0.075" (Gage14) 304 stainless steel walls with Bisco Boraflex B <sub>4</sub> C particles clad in a non-metallic binder (0.081") with 0.020" stainless wrapper

**Table 2-4 Fuel Assembly and Rack Flow Area Data.**

(b)(7)(F)



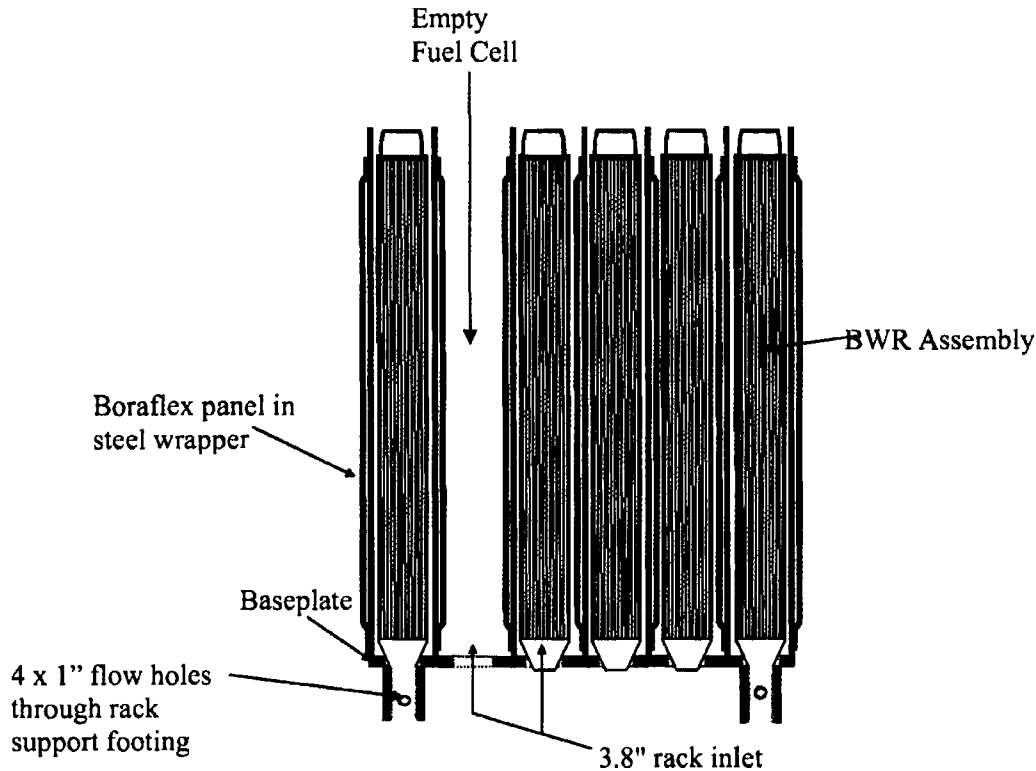


**Figure 2-2 Typical Spent Fuel Pool Rack Cut-away Cross-Section Showing the Fuel Assembly.**

## 2.2 SFP Accident Scenarios

From a natural circulation flow perspective, the SFP accidents are broken down into two categories; scenarios with water above the base plate of the racks and scenarios with a completely drained SFP. Each accident is described next.

### 2.2.1 Complete Loss-of-Coolant Inventory Accident

In the "air" flow case, the accident is initiated with a complete loss-of-coolant accident (see Figure ES-1 for pre-accident building configuration and Figure 2-2 for the rack configuration). Due to the removal of the water, a heat-up of the fuel rods ensues. The fuel rods heat the air in the assemblies, which creates a natural circulation pattern. Complex flow patterns develop above and around the SFP racks and in the refueling room due to the interaction between the hot rising plume and descending cool air. After the hot plume exits the SFP, the plume will rise to the ceiling and spread radially within the hot gas layer at the top of the refueling room. The degree of heating in the spent fuel storage building and behavior of the hot gas layer depends on many factors including the rate of ventilation (e.g., ventilation system operation, openings or

leakage, and/or structural failures), the heat loss through the building walls and ceiling, and other accident thermal effects (e.g., fire).

The flow patterns of the gases under the racks are also complicated. The regions of down flow include the space between the rack and walls, some of the empty rack slots, and the cask region or other open areas. If a high speed flow region develops under the racks, then there can be a Bernoulli Effect. For example, if the air to the SFP cells is preferentially provided through the cask area, a high speed flow (i.e., 3 m/s) can develop under the rack cells adjacent to the cask area. The high speed flow reduces the upflow of gases into the affected assemblies, which leads to less heat removal and a faster heat-up (e.g., see [Wagner, 2000]).

If inadequate cooling is provided, then the fuel cladding will heat up and the Zircaloy cladding will rapidly oxidize (i.e., burn) and to a lesser extent, nitride (i.e., combine with nitrogen if no oxygen or steam are available). Since the oxidation and nitride processes are exothermic, the fuel rods could heat to melting conditions and structurally degrade. Meanwhile, the steel racks supporting the fuel assemblies will also heat due to convection and radiation from the fuel assemblies. The timing of the degradation of the specific fuel assemblies and racks are affected by the decay heat level (i.e., burn-up, power history, enrichment, and time since discharge), the assembly inlet temperature, convective and conductive heat removal rates, and the heat transfer rate from/to adjacent assemblies. Finally, and most importantly, the degradation of the fuel rods can lead to fission product releases.

An accurate analysis of the SFP response requires consideration of the aforementioned phenomena. As evidenced by the accident description, there is a large range of geometric length scales and modeling requirements. The length scales range from details of the individual assembly heat generation and flow patterns (e.g., also including multi-dimensional flow within an assembly, see [Ross, 2003]), intra-assembly heat transfer, large scale flow patterns above, below, and through the racks, and the building response (e.g., ventilation, heat loss, structural failures, etc.). The relevant physics and phenomena include heat transfer (convection, conduction, and radiation), fluid flow (small scale to large scale), chemical reactions (i.e., oxidation), severe accident fuel degradation behavior, and fission product release and transport.

### **2.2.2 Partial Loss-of-Coolant Accident**

In the second type of accident, the SFP is partially drained (i.e., due to partial drain or boil-off) and does not include recirculation of hot gases through the bottom of racks. Consequently, the gas in the fuel assemblies above the pool level is relatively stagnant (i.e., except for steam flow from boiling). In this condition, steam cooling and/or a level swell from the boiling will keep the fuel rods cool unless the pool level drops too far. However, once the level drops below roughly one-half of the fuel height, the top of the fuel rods will heat-up and degrade.

If the top of the fuel is uncovered, then several new phenomena occur in a partial loss-of-coolant accident. First, the convective flows are much smaller than a complete loss-of-coolant accident. In the complete loss-of-coolant accident, there was ample air flow as the assembly heated. However, in a partial loss-of-coolant accident, the fluid in the assembly is relatively stagnant because the pool blocks the bottom of the racks. The primary source of cooling comes from

steam flow due to boiling below the water level. Hence, there are competing effects of the lack of a strong convective flow versus the benefits of some steam cooling and axial conduction to the water. In summary, the scenarios with water include (a) two-phase boiling, (b) an assembly flow rate that is strongly affected by the amount of boiling below the water surface, and (c) gas inlet temperature that is limited to the boiling point of water (i.e., the air cases are not similarly constrained).

The rate of oxidation of the Zircaloy cladding is the second key difference expected in a partial loss-of-coolant accident. In particular, the fluid next to the Zircaloy cladding will be steam rather than air. Steam also reacts exothermically with Zircaloy but at a slower rate than with air. Furthermore, the byproduct of this reaction is hydrogen. The hydrogen will replace the steam and retard or stop the Zircaloy/steam reaction. Consequently, the reaction could become "steam starved" and controlled by the rate of steam production by boiling below the pool level, which is expected to be very low for aged spent fuel. If there is adequate steam when the Zircaloy reaches high temperatures (i.e.,  $>1500$  K), the power from metal water reactions can be much larger than decay heat. Therefore, there are two competing effects on the rate of fuel degradation relative to the complete loss-of-inventory accident scenario (i.e., as described in Section 2.2.1), (1) a lower, controlled oxidation effect (i.e., due to steam starvation) and (2) a much lower convective cooling rate (i.e., because the bottom of the racks are "plugged" with water).

Finally, a third new difference in the partial loss-of-coolant accident is the behavior of the hydrogen. As hydrogen is produced during fuel degradation, the hydrogen may collect and mix with oxygen in the air above the pool. Given the appropriate conditions, the hydrogen could ignite and possibly cause structural damage to the reactor building. Any damage or enhanced leakage caused by the pressurization from the hydrogen burn could increase the release of fission products and their associated adverse consequences.

As will be discussed in Section 5, spray operation complicates the potential for water plugging the inlet to the racks. For appropriate combinations of leakage and sprays rates and leakage location, the spray flow can maintain a water level above the base plate of the racks. Consequently, spray operation in some circumstances will stop air natural circulation. Depending upon the relative magnitudes of the spray flow and decay heat power, the resultant configuration may be less effectively cooled.

### 3. ANALYSIS METHODOLOGY

Based on the information supplied by the reference plant staff, MELCOR models were developed to perform accident analyses (e.g., see [Wagner, 2003] and [Wagner, 2004]). Since those analyses were performed, there have been several significant improvements in the modeling of the SFPs. Section 3.1 summarizes those improvements. Several different models were used for the detailed evaluations of the fuel response to emergency spray. A description of the MELCOR separate effects models are presented in Section 3.2. The separate effects models were used to simulate the details of the spray penetration into the assemblies. Next, the whole pool models are described in Section 3.3. The whole pool models were used to calculate boundary conditions for the separate effects models as well as calculate the spray scrubbing efficiency and the source term behavior.

#### 3.1 New BWR SFP Modeling

Since the last report on BWR SFP modeling, there have been a number of improvements in MELCOR's modeling capabilities. Section 3.1.1 describes the new BWR-SFP Core Package model with the new Rack component. Next, Section 3.1.2 describes the new breakaway oxidation kinetics model based on experiments at Argonne National Laboratory. The fuel geometric model was completely updated to include partial fuel rods, the hydraulic effects of water rod flow, and other detailed weight and geometric information from GNF hardware used in the SNL SFP experiments. In addition, a new flow resistance model was implemented based on detailed flow tests. The pertinent results from the SNL experimental program are described in Section 3.1.3. Finally, a technique to model the spray thermal-hydraulic response in MELCOR was developed and is described in Section 3.1.4.

##### 3.1.1 New BWR SFP Model

Previous MELCOR BWR SFP calculations were performed using the "BWR" model designation in the COR Package input (i.e., [Wagner, 2003] and [Wagner 2004]). Once the model designation is selected, certain fixed geometry specifications are made. At the time of the original calculations, only the BWR and PWR model designations were available. The BWR designation assumes the BWR fuel rods are surrounded by a BWR canister. Outside the canister is a control blade (see Figure 3-1). Typically in a MELCOR reactor application, concentric rings are used to model the fuel in the core. Ring 1 would represent the center of the core and successive, concentric rings would represent annular regions of assemblies with increasing radii to the edge of the core.

**MELCOR 1.8.5 BWR Model**  
**("Blade" is enclosed inside the ring)**

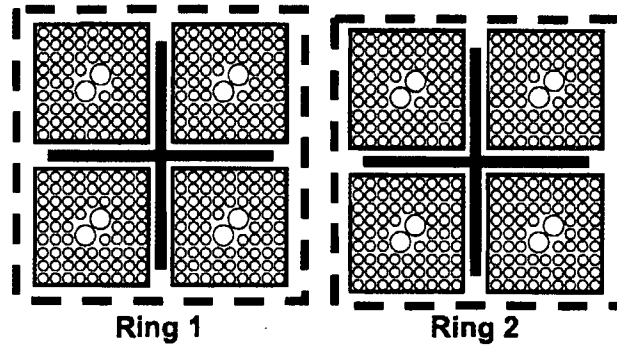


**Figure 3-1 MELCOR Modeling of a BWR Assembly in the Reactor Core.**

For application to the SFP geometry, it was not possible to explicitly model the SFP rack. The only components available are those shown Figure 3-1, i.e., the fuel and cladding, the canister, and the control blade. For the original SFP BWR calculations, the control blade component was used to model the rack. The SFP BWR 1x4 configuration is shown in Figure 3-2. Although the rack walls are contained internally within a ring, the appropriate surface area and mass was properly conserved. From a radiation heat transfer perspective, heat flows from adjacent rings between the canister walls. In particular, the radiation heat transfer from Ring 1 to Ring 2 in Figure 3-2 occurs from the canister of Ring 1 to the canister of Ring 2 (i.e., see Figure 3-3). Simultaneously, radiative exchange is also calculated within each ring from the canister wall to the rack wall (i.e., see summary in Figure 3-3). Consequently, from a radiation perspective, the rack wall is not correctly represented between the adjacent rings of fuel assemblies. Similarly, the surface areas for convection are preserved. However, the adjacent fluid temperature for the racks is characteristic of the region within a ring (i.e., the bypass fluid region outside the canister) rather than the Ring 1 bypass on interior side and the Ring 2 bypass on the exterior side.

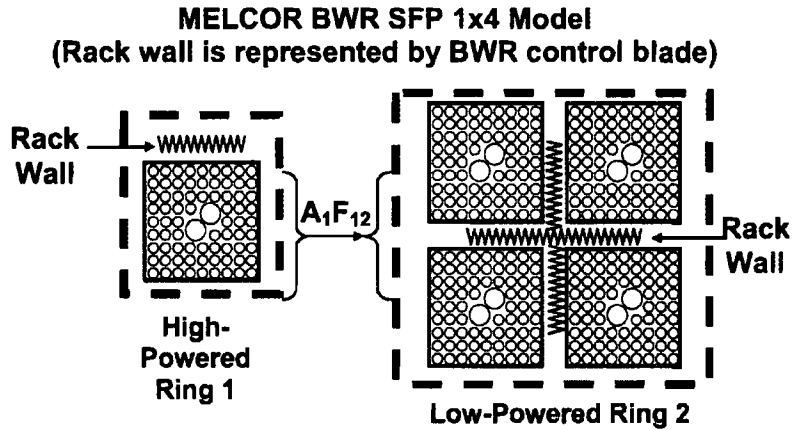
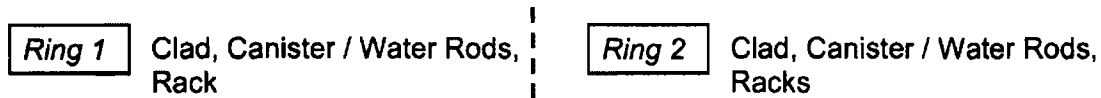
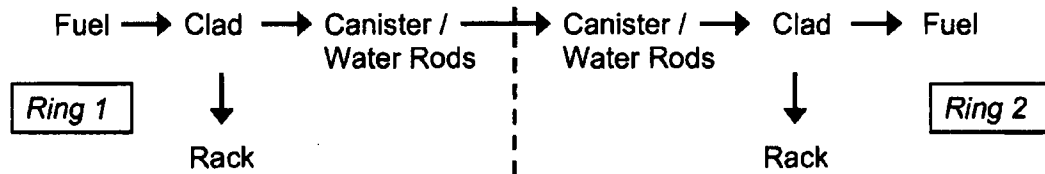


Figure 3-2 Original MELCOR Modeling of BWR Assemblies in a 1x4 SFP Configuration.<sup>4</sup>

**Convective Heat Transfer Surfaces:**



**Radiative Heat Transfer Flow Path:**



- Rack is modeled via a Control Rod Blade component

Figure 3-3 Heat Flow for the Original MELCOR Modeling of a BWR Assemblies in a 1x4 SFP Configuration.

During and subsequent to the original BWR SFP separate effects calculations, additional scoping work was done to estimate the impact of the aforementioned heat transfer limitation. For the configuration of a single assembly in a uniform decay heat region (i.e., the configuration for many of the calculation), the heat transfer rate from the fuel would be too high prior to achieving steady state conditions because heat was simultaneously transferring directly to the rack wall and the canister. However, due to the efficiency of high temperature radiation from thin structures with large surface areas the thermal coupling between the fuel rods and the rack wall was

<sup>4</sup> The rack wall is shown in a zigzag pattern to only emphasize the correct surface and mass was preserved while wholly containing the rack wall on the inside of Rings 1 and 2.

expected to be very close<sup>5</sup>. The greatest impact was expected to occur in a 1x4 configuration where radiative heat transfer from a high-powered center assembly to four adjacent peripheral assemblies. In this configuration, the rack wall would be a radiation barrier between the center assembly and the peripheral assemblies. Hence, the thermal coupling shown in Figure 3-2 and Figure 3-3 would be over-estimated.

Subsequent to the release of the original MELCOR BWR separate effects report ([Wagner, 2003]), MELCOR was modified to include "SFP-BWR" and "SFP-PWR" model types. The new designator specified the geometry as shown in Figure 3-4 for the 1x4 configuration and the radiation and convection solution as shown in Figure 3-5. Consequently, the rack wall around Ring 1 is properly placed between the Ring 1 and Ring 2 assemblies. The remaining rack walls for the four peripheral assemblies in Ring 2 is placed at the outer boundary of Ring 2, which is an adiabatic boundary condition for the 1x4 simulations. Similar to previous models, the rack wall was comprised of steel and control material. The MELCOR models described in Section 3.2 and 3.3 used this designation.

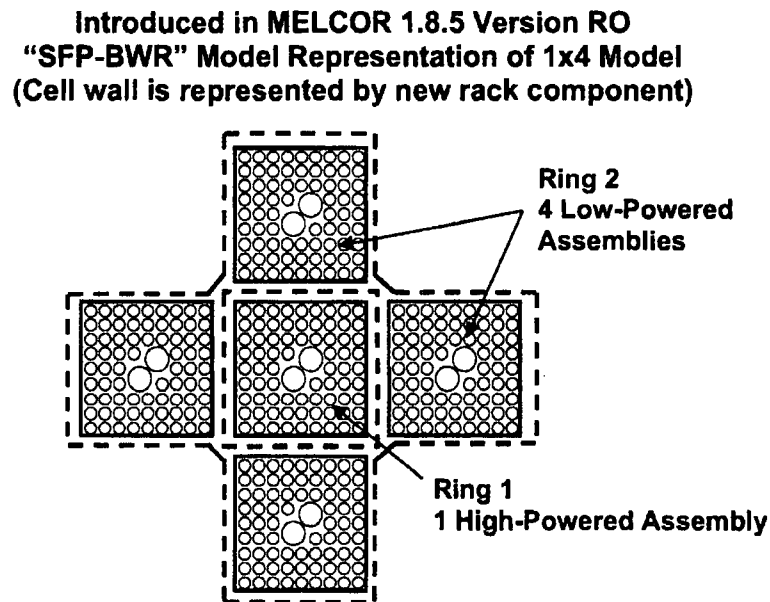


**Figure 3-4 New MELCOR Modeling of BWR Assemblies in a 1x4 SFP Configuration.**

<sup>5</sup> These limitations were recognized early and have been steadily examined with increasingly sophisticated approaches. Initially, the MELCOR heat structure components were used to examine the heat flow for a uniform configuration. Subsequently, three-dimensional COBRA-SFS calculations were performed for the 1x4 configuration. Next, MELCOR was modified as described in this section to properly represent the geometric location of the rack wall and the radiative exchange in a 1x4 configuration. Most recently, analysis of experimental work is being done with the new SFP-BWR configuration. Each of the complimentary analyses has confirmed the goodness of this assumption. The more accurate SFP-BWR 1x4 model only shows a minor degradation of radial radiative heat transfer at high temperatures.



A new oxidation model was implemented in MELCOR by adding a breakaway lifetime calculation. The model calculates an oxidation "lifetime" value for Zircaloy components in each cell using the local Zircaloy cladding temperature. Figure 3-6 shows the breakaway timing data from the ANL tests. As the specimen temperature increased, the amount of time until breakaway became shorter.

For implementation into MELCOR, the ANL data was curve fit as follows,

$$LF = \int_0^{t'} \frac{t'}{\tau(T)} \quad (\text{Eqn. 2.2})$$

where,  $\tau(T)$  is

$$\tau(T) = 10^{P_{LOX}} \quad (\text{Eqn. 2.3})$$

and  $P_{LOX}$

$$P_{LOX} = -12.528 \cdot \log_{10} T + 42.038 \quad (\text{Eqn. 2.4})$$

A comparison of the data with Equation 2.4 is shown in Figure 3-6. For reference, specific values of the breakaway timing are provided in Table 3-1.

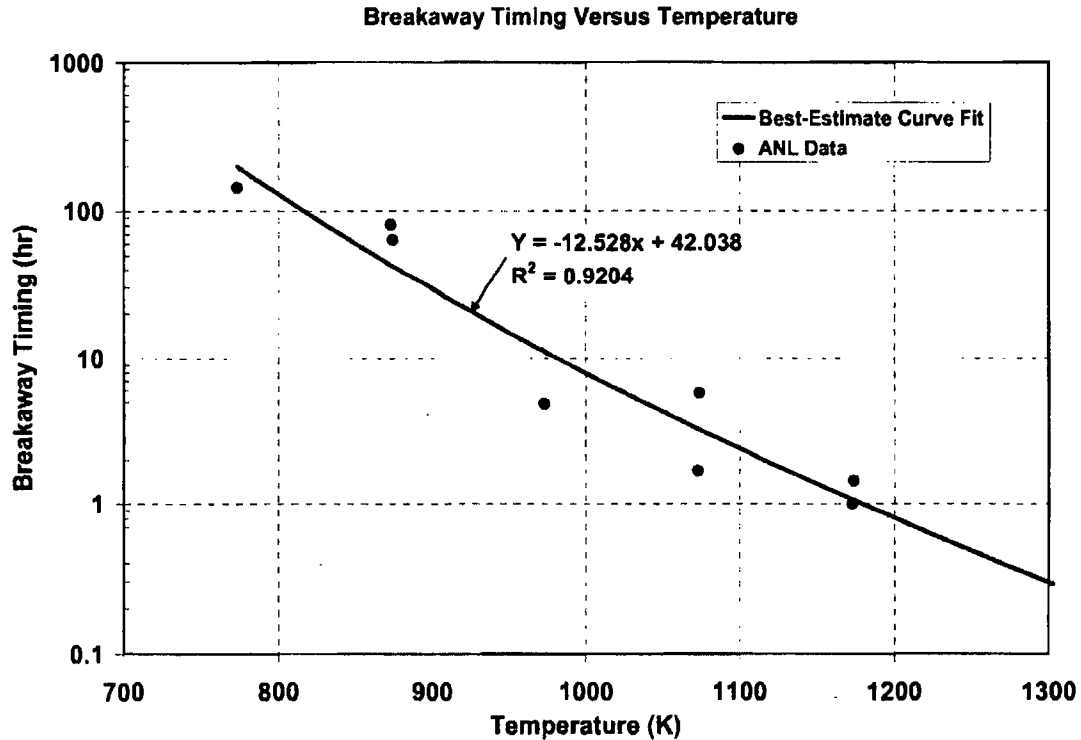


Figure 3-6 Comparison of the MELCOR Breakaway Timing Fit to the Zirlo and Zr-4 Data from the ANL Air Oxidation Tests.

The new MELCOR breakaway oxidation model calculates the lifetime function at every node in the MELCOR model with Zircaloy cladding. The oxidation kinetics linearly transitions from the pre-breakaway correlation at  $LF = 1$  to post-breakaway kinetics at  $LF = 1.25$ . Hence, only nodes that have exceeded the lifetime function will have the higher post-breakaway oxidation kinetics.

The ANL pre- and post-breakaway Zr-4 oxidation correlations<sup>6</sup> are summarized below,

- Steam pre-oxidized, wide-temperature pre-breakaway Zr-4 oxidation correlation (red line on Figure 3-7)

$$K(T) = 26.7 \exp (-17,490 / T) \text{ [kg}^2/\text{m}^4\text{-s]} \quad (\text{Eqn 6.6 in [Natesan, 2004]})$$

- Steam pre-oxidized, wide-temperature post-breakaway Zr-4 oxidation correlation (black line on Figure 3-7)

$$K(T) = 2.97\text{e}4 \exp (-19,680 / T) \text{ [kg}^2/\text{m}^4\text{-s]} \quad (\text{Eqn 6.7 in [Natesan, 2004]})$$

**Table 3-1 MELCOR Fit of the Timings for Transition from Pre-Breakaway to Post-Breakaway Oxidation Reaction Kinetics for Zirlo and Zircaloy-4 in the ANL Experiments [Natesan, 2004].**

Specimen Temperature	Breakaway Timing (Eqn. 2.4)	ANL Data Used in Curve Fit (See Figure 3-6)
400°C (673 K)	1125 hr (Extrapolated)	-
450°C (723 K)	458 hr (Extrapolated)	-
500°C (773 K)	198 hr	144 hr
550°C (823 K)	90 hr	-
600°C (873 K)	43 hr	64 and 81hr
650°C (923 K)	22 hr	-
700°C (973 K)	11 hr	4.8 hr
750°C (1023 K)	5.9 hr	-
800°C (1073 K)	3.3 hr	1.7 hr and 5.8 hr
850°C (1123 K)	1.8 hr	-
900°C (1173 K)	1.1 hr	1 hr and 1.4 hr

<sup>6</sup> Note that the form of the leading coefficient of these correlations were adjusted to MELCOR input requirements, which uses  $K(T)$  is a function of Zircaloy oxidized versus oxide weight gain.

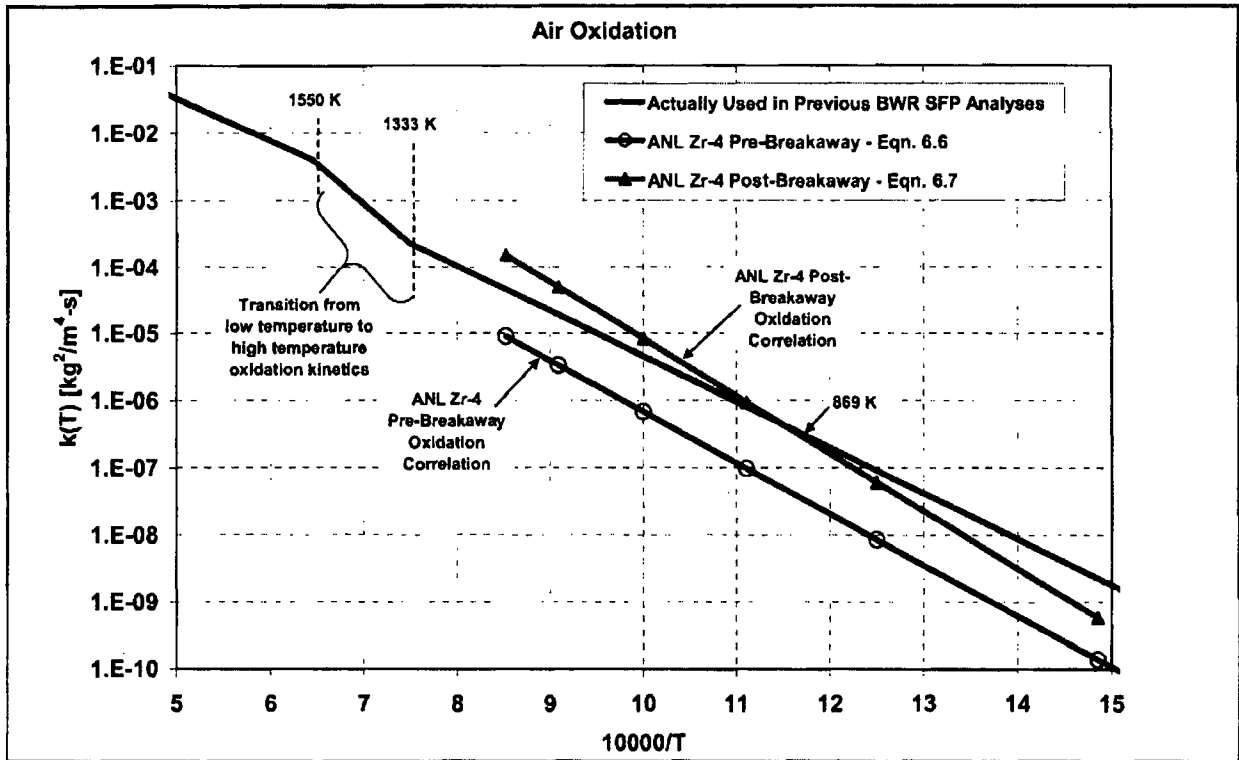


Figure 3-7 Parabolic Reaction Kinetics Coefficients for Zr-4 Oxidation.

### 3.1.3 New Hydraulic Resistance Model

Recently, hydraulic resistance measurements were performed on a Global Nuclear Fuel (GNF) 9x9 BWR assembly at Sandia National Laboratories [Durbin]. Commercial components were purchased to create the assembly including the top and bottom tie plates, spacers, water rods, channel box, and all related assembly hardware. Stainless steel conduit was substituted for the fuel pins for hydraulic testing. The stainless steel mock fuel pins were fabricated based on drawings and physical examples supplied by GNF.

Figure 3-8 shows the layout of the BWR pressure drop experimental assembly, including the 18 pressure port locations. Two Paroscientific Digiquartz differential pressure transducers were plumbed directly to the desired pressure ports. These pressure gauges use a highly sensitive quartz crystal to measure slight changes in differential pressure (resolution ~ 0.02 Pa). Measurements were recorded directly to the hard drive of a PC-based data acquisition system every 3 seconds using a LabView 7.1 interface. These measurements included the air flow rate through the assembly, ambient air temperature, ambient air pressure, and the assembly pressure drops.

Three primary series of experimental runs were performed. In the first two sets of experimental runs, the flow holes in the water rods were either blocked or unblocked. The bypass holes on the inlet nozzle assembly were blocked for these tests. In the final tests, the bypass holes were opened. In the assembly's prototypical configuration, the water rods are un-blocked and the bypass holes are unplugged. The subsequent analysis of the data calculated a wide range of parameters including the flow through the water rods and bypass holes as well as the corresponding local and total pressure drops for a Reynolds Numbers range of 70 to 900

Ex (b)(7)(F) In all configurations, the tests were repeated several times and alternate primary measurements were performed to verify the assembly flowrate and overall pressure drop. From the pressure drop data, the laminar flow resistance terms were processed in terms of inputs for the MELCOR code (i.e., see below,  $S_{LAM}$  and  $k$ ). An error analysis of the measurements revealed an uncertainty of hydraulic resistance values for input into MELCOR to be very small (b)(7)(F) Ex 2F

(b)(7)(F) Ex 1F MELCOR, like other control volume codes, includes constitutive relationships to specify form losses (i.e., minor losses) and wall friction losses (i.e., major or viscous) along a flow path as a hydraulic flow loss term to the momentum equation. The format of the user-specified input for MELCOR is defined from the sum of the local viscous and major pressure drops,

$$\Delta P = \frac{1}{2} \rho v^2 (fL/D + k) \quad \text{Eqn. 3.1}$$

The laminar friction factor ( $f$ ) for laminar flow is written explicitly as,

$$f = S_{LAM} / Re \quad \text{Eqn. 3.2}$$

where,

$S_{LAM} = 64$  for pipe flow (and  $S_{LAM} = 100$  for bundle flow in the BWR SFP model in [Boyd], [Wagner, 2003], and [Wagner, 2004])

Re = Reynolds Number or  $(\rho v d_H) / \mu$

$\rho$  = local density

$v$  = local velocity

$\mu$  = local fluid viscosity

$d_H$  = local hydraulic diameter (defined as  $4 A / P_w$ )

A = local flow area

$P_w$  = wetted perimeter

As shown in Figure 3-8, the BWR fuel assembly (b)(7)(F) grid spacers, upper and lower tie-plates, full and partial rod regions, two water rods, and an inlet nozzle. It is not practical to include a detailed representation of all the geometry changes in the MELCOR model. In addition, the MELCOR code includes some hard-wired geometry models that further limit the modeling of the two large water rods inside the assembly and their associated flow. Consequently, modeling choices are required to represent the geometry of the BWR assembly. Relative to the hydraulic modeling in the BWR SFP MELCOR model, the experimental data are used in the following manner,

- Based on the hydraulic impact of the fully populated versus the partial regions, the control volume boundaries were specified to span uniform geometry regions. Control volume boundaries were placed at the bottom of the lower tieplate, the transition from the fully populated rod region to the partial region, and at the top of the upper tieplate. By spatially dividing the two regions, the distinct flow loss effects can be extended to heated conditions, where the flow will accelerate along the length of the assembly.
- The flow resistance in a flow path spans the region from cell-center of the lower control volume to cell-center of the upper control volume. Hence, the pressure in a given control volume represents the pressure in the center of the control volume. A single flow path may span more than one grid spacer and perhaps a tieplate. Segment data on a particular flow path defines the form and wall friction losses along the geometric regions encompassed in the flow path length. Several flow paths had multiple flow segments due to geometry changes within the flow path range. The net effects of varying flow resistance are calculated by the code.

(b)(7)(F)

(b)(7)(F)

- For the application to the emergency BWR SFP spray analysis, the results from Table 3-2 were used, which includes prototypical water rod flow effects. For the flow segments in the fully populated tube region, a  $S_{LAM}$  of (b)(7)(F) was used and k losses of (b)(7)(F) were used for each spacer included in the range of the flow path. The flow area and hydraulic diameters were preserved. The total length across all flow paths in the fully populated region (b)(7)(F) and the total k (b)(7)(F). Therefore, the total flow losses (b)(7)(F) were exactly preserved, including the effect of flow within the water rods. Similarly, the partially populated tube region used (b)(7)(F) per spacer in the range of the flow path. The total length across all flow paths in the fully populated region (b)(7)(F) and the total k (b)(7)(F)

EX 7F  
EX 7F  
EX 7F  
EX 7F

(b)(7)(F) Ex 7F The flow path segments in the partial rod region used the larger flow area and hydraulic diameter as specified in 2-8 from Table 3-2. For reference, the overall resistance was of a (b)(7)(F)  $S_{LAM}$  of (b)(7)(F) and k losses of (b)(7)(F). In comparison, the previous BWR analysis used  $S_{LAM}$  of (b)(7)(F) Ex 7F and k losses of (b)(7)(F) across the same region (i.e., not including the inlet nozzle).

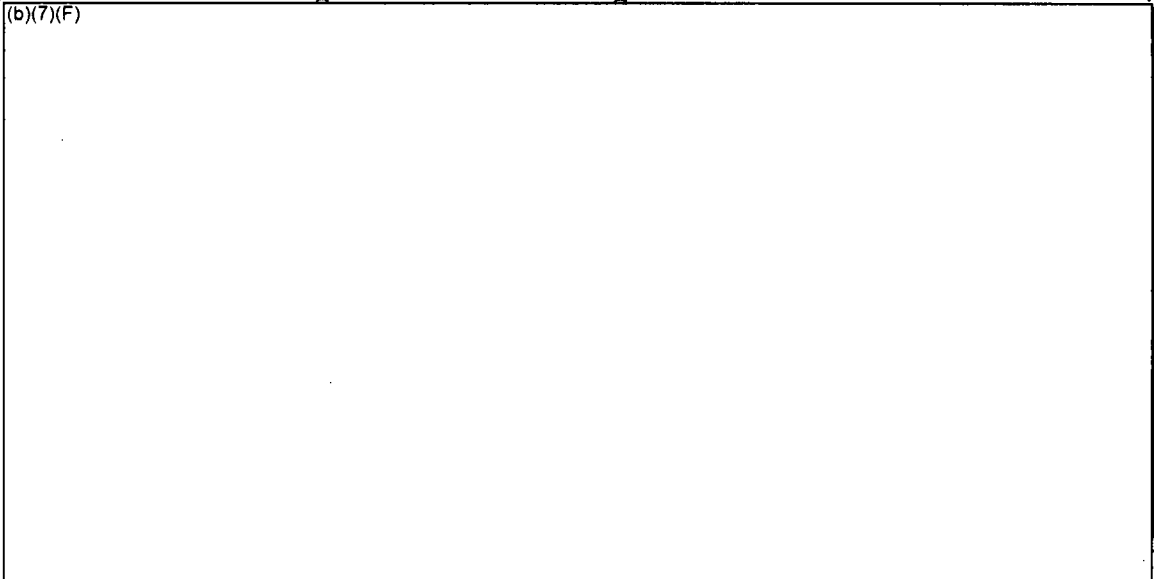
- Table 3-2 was also used to specify the pressure drop across the upper tieplate (b)(7)(F) and lower tieplates and the inlet region (b)(7)(F) Ex 7F. Similar to above, the appropriate flow areas and hydraulic diameters for these regions were used.
- Finally, the results from Figure 3-10 were used to specify the flow loss terms for the inlet nozzle leakage to the interstitial bypass region. The form losses in the MELCOR model were adjusted to match the measured total to bypass flow split.

Until this hydraulic data was available, the previous BWR SFP MELCOR analyses did not include the sophistication of separate flow resistances for the partial and fully populated regions of the BWR bundle.

The results analysis in Table 3-2 precisely satisfies the model input requirements for MELCOR, as well as other control volume codes. The linear (i.e.,  $S_{LAM}$ ) and quadratic (i.e., the k term) hydraulic loss coefficients are easily put into the MELCOR input format and will replicate the measured flow losses across the Reynolds number range of 70 to 900, including the overall nonlinear hydraulic effects from (a) flow development regions, (b) the grid spacer entrance, internal, and exit effects, (c) the inlet and exit flows to the water rods, and (d) the transition from the fully to partially populated tubes regions.

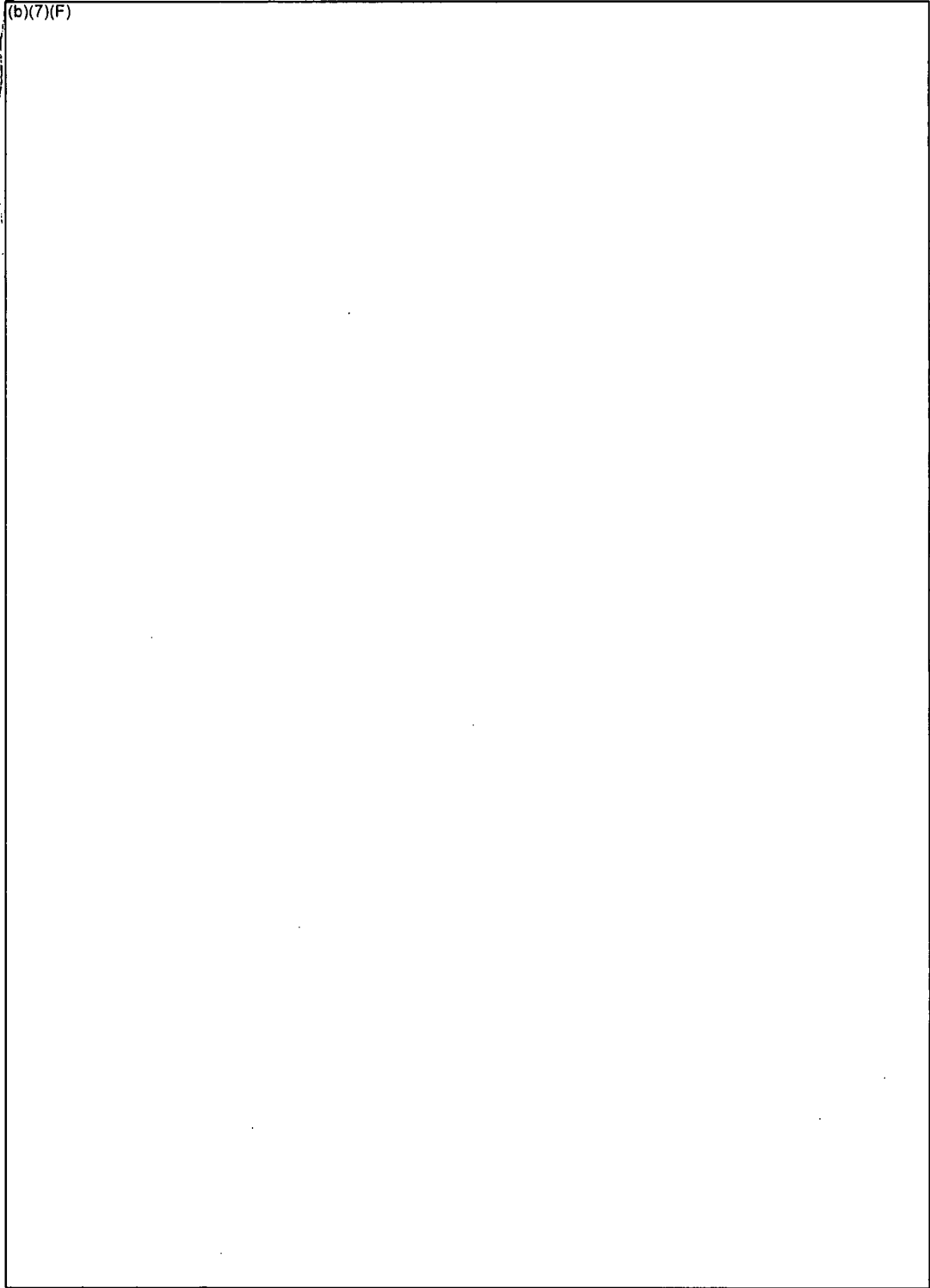
**Table 3-2  $S_{LAM}$  And k Coefficients for the Unblocked Water Rod Assembly Assuming All Flow Passes Through the Bundle.**

(b)(7)(F)



(b)(7)(F)

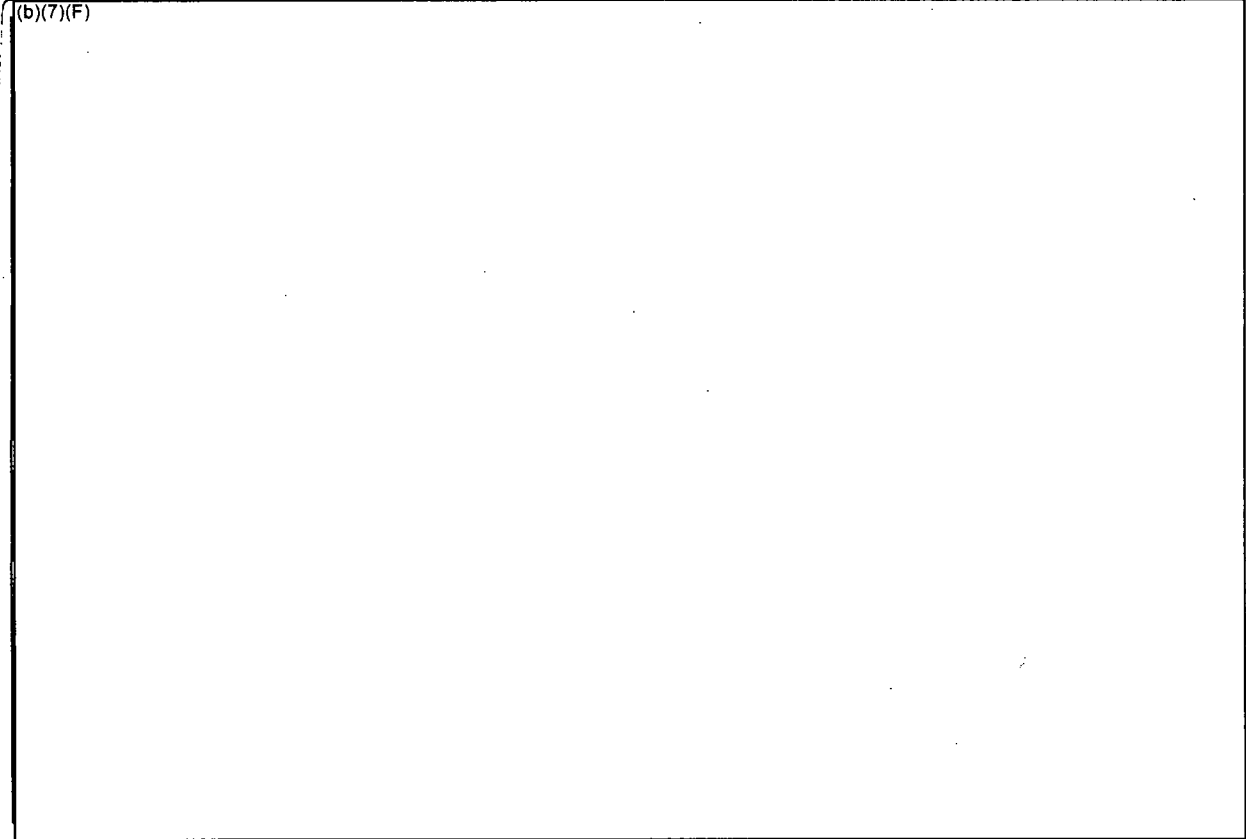
(b)(7)(F)



Ex

Figure 3-8 BWR Assembly Experimental Apparatus used in the Hydraulic Resistance Testing.

(b)(7)(F)



1.9F

Figure 3-9 Measured Pressure Drop over the Full, Partial, and Total Assembly Regions.

MELCOR Correlation to Experimental Data on Bypass Flow

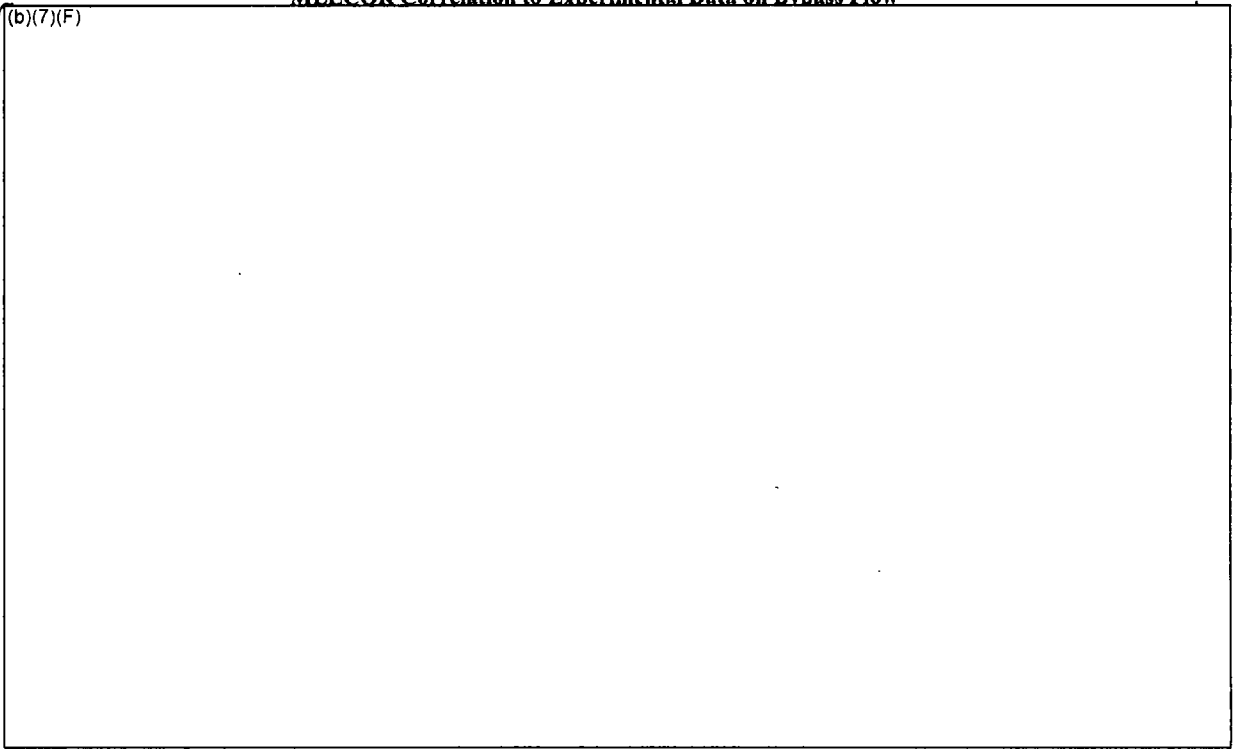


Figure 3-10 Comparison of the Calculated and Measured Bypass Flow.

### 3.1.4 Spray Modeling in MELCOR

The spray modeling was performed in two ways. For the whole pool calculations, the MELCOR containment spray model was used. The MELCOR containment spray package includes calculations for spray droplet heat and mass transfer and fission product removal [Gauntt]. A droplet size of 1250 microns was used unless otherwise noted.<sup>7</sup> The droplets were directed into the assemblies and open spaces based on their respective cross-sectional areas. Upon entering the assemblies, the thermal-hydraulic calculations were performed by MELCOR's CVH package as described below.

Generally, the separate effects models were used to resolve the spray performance. Boundary conditions for the inlet and exit of the separate assembly model were provided by whole pool calculations (see Section 3.3 for a description of the models). A spray water source was specified to the top of the assembly according to the relative cross-sectional area. For example, spray water was added to CV-119, CV-129, CV-219, and CV-229 in the 1x4 SE model (see Figure 3-16). The flow area and resistance representing the upper tie-plate is represented in the next downward flowpath. The penetration of the spray water into the assembly is controlled by MELCOR's interphase momentum model, which replicates the Wallis flooding curve [Gauntt].

Once the spray water enters the assembly, the spray is assumed to form a thin film on the fuel structures in the assembly, which drains downward. The new COR Package simplified flow regime model identifies the spray flow as a film in contact with the fuel rods (see Figure 3-12). Heat transfer takes place between the fuel rods and water in core cells where the flow regime model is active. Nucleate or film boiling heats the water film to saturation conditions as it drains down the assembly. Simultaneous heat transfer from the rods and surrounding gas causes the spray flow to boil. The spray film travels downward in contact with the fuel rods until the local CVH void fraction becomes greater than 99.8% (i.e.,  $\alpha > 0.998$ ). Due to numerical considerations, the residual water is converted into a shallow pool where the liquid heat transfer area is apportioned by the depth of the pool in the control volume.<sup>8</sup> Typically, the remaining water boils away in the first core cell after the flow regime model is disabled.

A detailed CVH/COR nodalization was used to track the water as it penetrates into the assembly (see Figure 3-15). The detailed nodalization permits a better local representation of the fluid conditions and the location of the spray dryout. The calculated results show a steadily decreasing flowrate and increasing void fraction as the liquid spray penetrates into the assembly. For example, Figure 3-11 shows the axial temperature response in an assembly with spray cooling using the new flow regime model. (b)(7)(F)

(b)(7)(F)

Lx. 7F

<sup>7</sup> A 1250  $\mu\text{m}$  droplet size was selected based on reviewing design specifications from some pressurized water reactor containment spray systems.

<sup>8</sup> If the flow regime model was used until the flow disappears, very small timesteps are needed to resolve the large heat transfer rates to negligible water mass. When the surface area in contact with water is partitioned by the pool depth, a larger timestep can be used which just boils the water dry in the first or next CVH volume. The residual heat removal for void fractions greater than 0.998 is relatively small.

(b)(7)(F)

Ex. 7F

It should be noted that the CVH package interprets the liquid film as small pools at the bottom of each CVH volume (see Figure 3-13). Due to the high void fraction, the phasic resistance of the steam or air flowing through the pool is relatively insignificant, which is the expected impact of a liquid film. Similarly, the depth of the spray water penetration is controlled by the COR heat transfer rate rather than the momentum solution. Axial, stepwise heat transfer from the core cells limits how far the spray water penetrates into the assembly.

A possible limitation of the CVH representation is the relatively small heat transfer area between the two phases (i.e., heat transfer through the pool and the surface versus a film). However, the rate of heat transfer from the gas to the water film is minor in comparison to the nucleate and film boiling heat transfer on the surface of the fuel rods. In addition, MELCOR's quenching model is relatively ineffective. The model accurately calculates separate quenched and un-quenched temperatures in each COR cell that is in film boiling. However, it assumes the unquenched portion is at the top of the cell. Hence, any axial condition benefit from a downward moving quench front is not realized. The impact from this limitation is not expected to be too significant due to the relative magnitudes of the surface heat transfer rate relative to any axial conduction effects.

(b)

(b)(7)(F)

Ex. 7F

Figure 3-11 Axial Temperature Profile in the Assembly with Spray Flow.

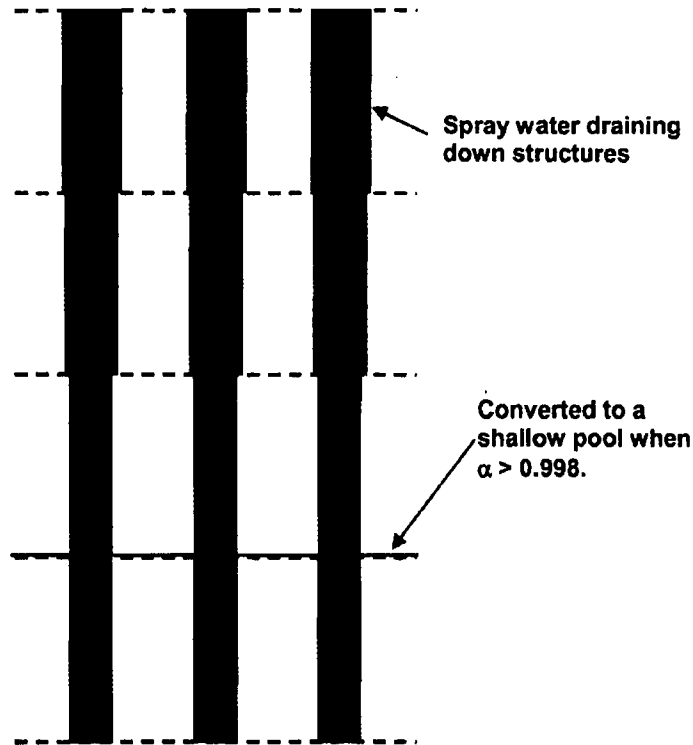


Figure 3-12 Core Package Representation of Spray Flow.

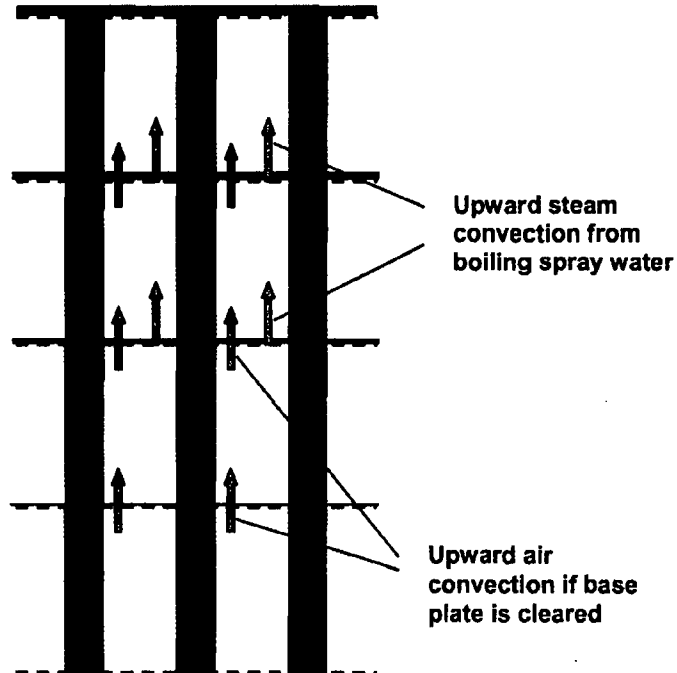
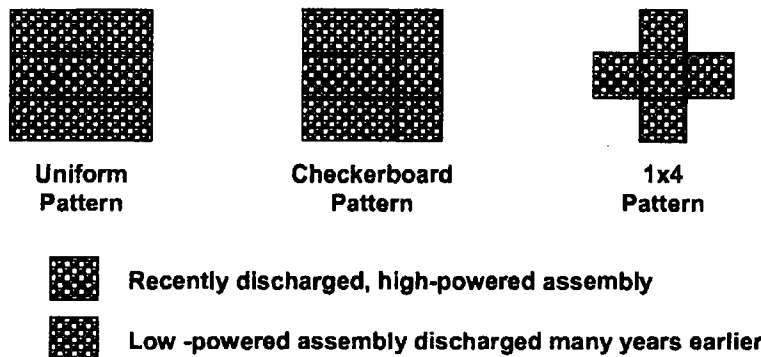


Figure 3-13 CVH Package Representation of Spray Flow.

### 3.2 MELCOR Separate Effects Model

Three intact configuration separate effect models were developed to analyze the spent fuel pool response to emergency spray mitigation of loss-of-coolant inventory accident conditions. The models simulate uniform, checkerboard, and 1x4 patterns. For implementation into MELCOR, the uniform pattern model was represented by a single, high-powered assembly with an adiabatic radial boundary or a 1x4 model with equal power in all five assemblies. The checkerboard pattern was represented with a high-powered and a low-powered assembly (i.e., taken as having the median assembly on the reference BWR spent fuel pool) with the appropriate adjoining wall area. Hence, radial heat transfer was possible from the high-powered assembly to the low-powered assembly. Similarly, a 1x4 pattern model was developed, which had one high-powered assembly surrounded by four low-powered assemblies. The MELCOR models represent the coupled thermal response of repeating pattern for each configuration (e.g., see Figure 3-18 for an example of a repeat 1x4 pattern). An adiabatic boundary was specified on the outer radial face of each model.

For reference purposes, the 1x4 intact configuration separate effects model will be described. The checkerboard model was a variation of the 1x4 model. However, the number of low-powered assemblies was reduced to one and the adjoining area between the two assemblies was adjusted accordingly. Finally, two types of uniform pattern models were used. First, the 1x4 model was used; however, all assemblies were specified to have the same power. However, to improve runtime on more difficult calculations, a dedicated separate effects model was developed with one assembly and an adiabatic outer boundary.



**Figure 3-14 Repeating Patterns Found in the MELCOR Separate Effects Models.**

As described above, the 1x4 separate effects model contains 5 spent fuel assemblies (see Figure 3-15). The five assemblies are divided into two radial rings and are modeled using the MELCOR “SFP-BWR” designation (see Section 3.1.1 for further discussion). The inner assembly is in Ring 1 and the four adjacent assemblies are in Ring 2 (see Figure 3-15). The outer boundary of Ring 2 is modeled as adiabatic. In the various calculations, the power is sometimes varied independently from Ring 1 and Ring 2. Each ring has 9 axial control volumes, which represent the fluid volume within the fuel assembly.

The interstitial area between the canister wall and the rack wall is modeled as the BWR bypass region. The bypass uses the same 9 control volume axial nodalization as the channel region. Nine radial cross-flow paths are located between the bypass and channel region. The cross-flow paths are controlled by the COR package and open if the canister wall should fail. A control volume represents the region below the assemblies. Another control volume represents the bulk pool conditions above the separate effects model.

The hydraulic resistance was specified using the results from the SNL experimental test program (see Section 3.1.3). The flow resistance under the racks was represented using typical contraction inertial loss coefficients and viscous losses consistent with a flow length to the center of the SFP.<sup>9</sup>

The BWR assembly canister is modeled with the MELCOR canister component. The rack walls are modeled with the new rack component (see Section 3.1.1) with stainless steel and Boraflex. MELCOR does not include an option to model the two large water rods in the assembly. Consequently, the water rod mass and surface area was included in the canister wall.

The axial and canister wall blockage models were active and controlled the resistance in the respective flow paths. The blockage model monitors the porosity of the materials in the various core regions. If a debris bed forms, the flow resistance is adjusted via an Ergun flow resistance model [Gaunt]. The canister wall radial blockage model controls flow paths between the bypass region and the assembly. Initially, the canister wall precludes flow. However, if the canister fails, a radial flow path is activated that permits flow between the two regions. Similar to the axial blockage model, the flow resistance is adjusted based on the local debris porosity.

The BWR fuel assembly is represented by 14 axial levels in the COR Package,

- Level 1 is the region below the core,
- Level 2 is the base plate
- Level 3 is the inlet region between the inlet nozzle and the lower tieplate
- Level 4 is the start of the active fuel region
- Level 8 is the top of the partial rod active fuel region
- Level 9 represents the region of the plenum of partial rods
- Level 12 is the top of the full length rod active fuel region
- Level 13 represents the plenum region of the full-length rods
- Level 14 represents the region between the upper tieplate and the top of the racks

The upper and lower tieplates are modeled as supporting plate structures, made of stainless steel. The 0.5" rack support plate at Level 2 is also modeled as a stainless-steel supporting structure.

The assembly ring-to-ring radiation is modeled (described in Section 3.1.1) between the outer surfaces of the Ring 1 rack wall to the outer surface of the canister in the adjacent ring. Radiative coupling was enabled for all calculations. In cases of a uniform configuration (i.e., a region where all assemblies have the same power), the ring-to-ring thermal radiative coupling did not have an effect because all 5 assemblies had the same decay power and thermal response.

<sup>9</sup> CFD calculations show the flow resistance under the racks is relatively small [Chiffelle].

(b)(7)(F)

Ex

The assembly decay heat is specified separately for each core ring. The decay heat load is primarily deposited in the fuel. However, as calculated by the gamma heating model, a small fraction of the decay heat is deposited directly in the cladding, canister, and surrounding structures (i.e., the rack wall). The outer boundary heat structures (i.e., ordinarily modeling the core barrel) outside Ring 2 were modeled as adiabatic (i.e., do not absorb any energy from Ring 2).

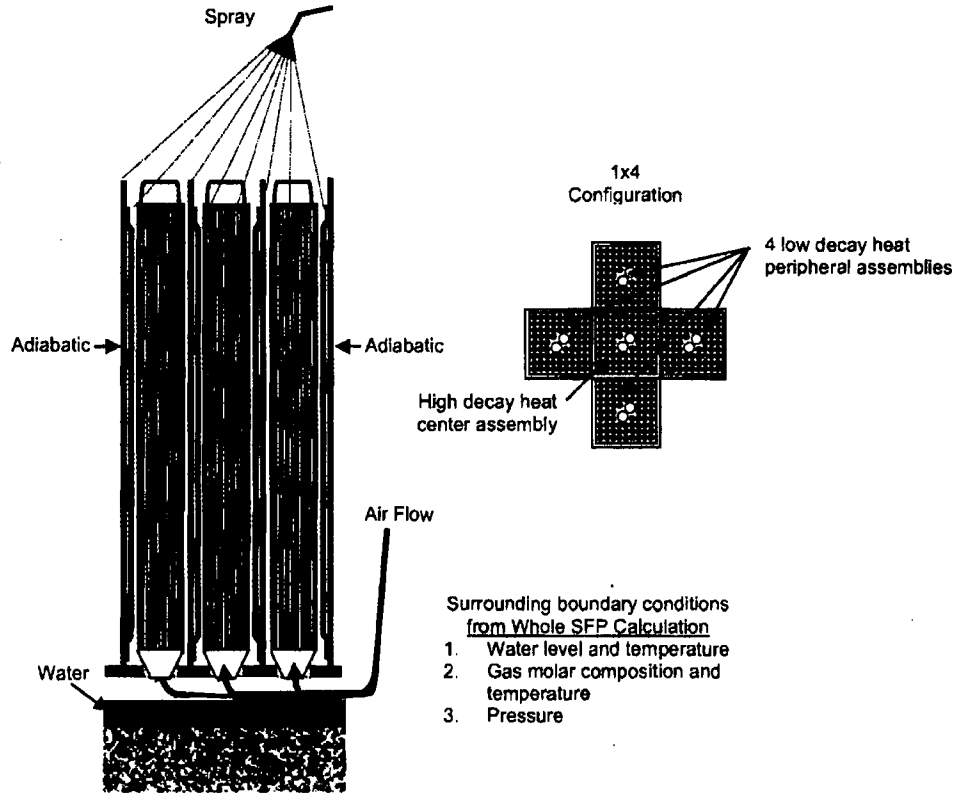


Figure 3-15 Schematic of the 1x4 Configuration.

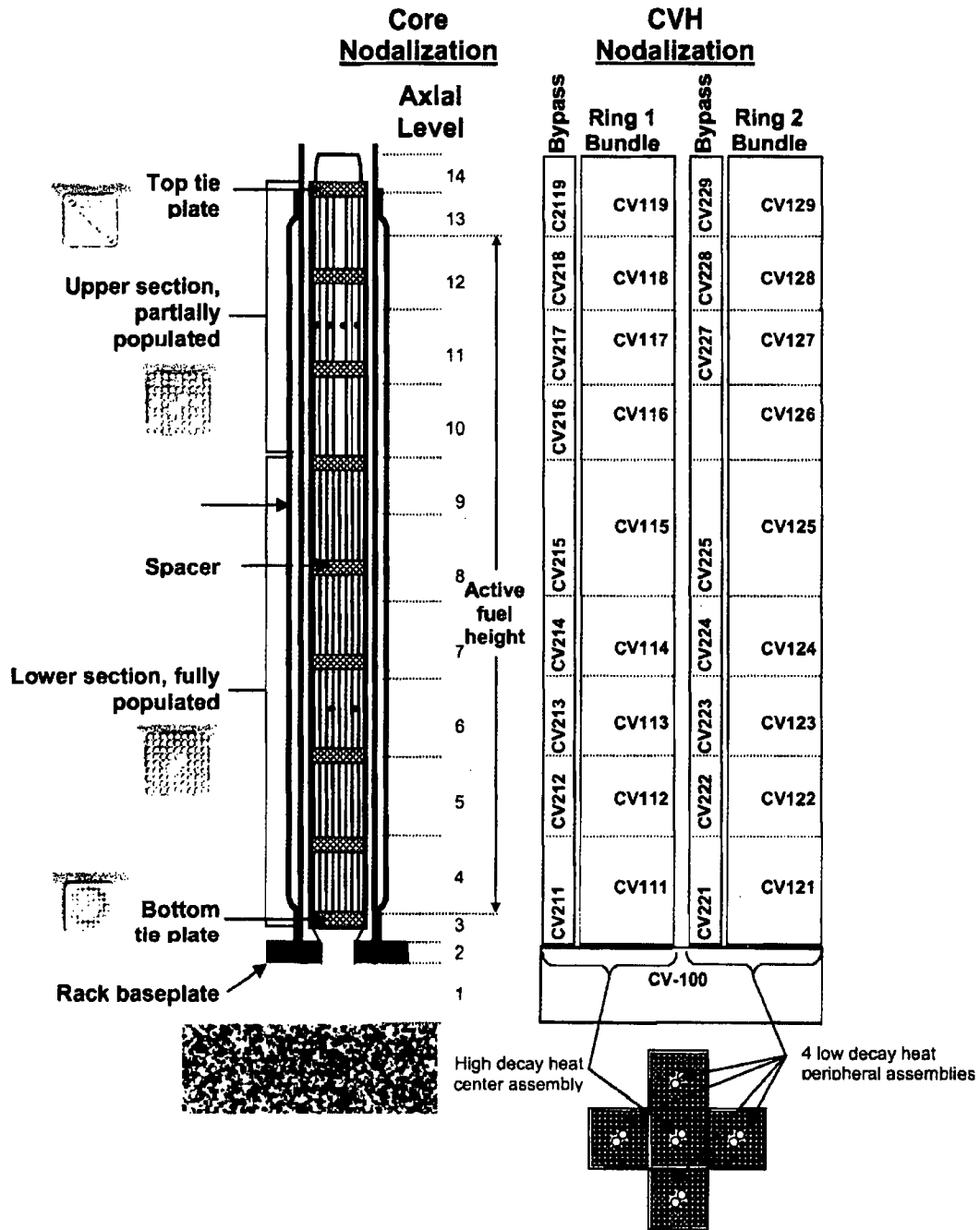


Figure 3-16 MELCOR Nodalization of the 5 Assembly Separate Effects Model.<sup>10</sup>

<sup>10</sup> Only the center assembly is shown for the Core Package nodalization shown in the left-hand side of this figure. However, the four peripheral assemblies are lumped together and have an identical 14 level axial nodalization. Both the CVH nodalizations for the center (Ring 1) and four peripheral assemblies (Ring 2) are shown on the right-hand side.

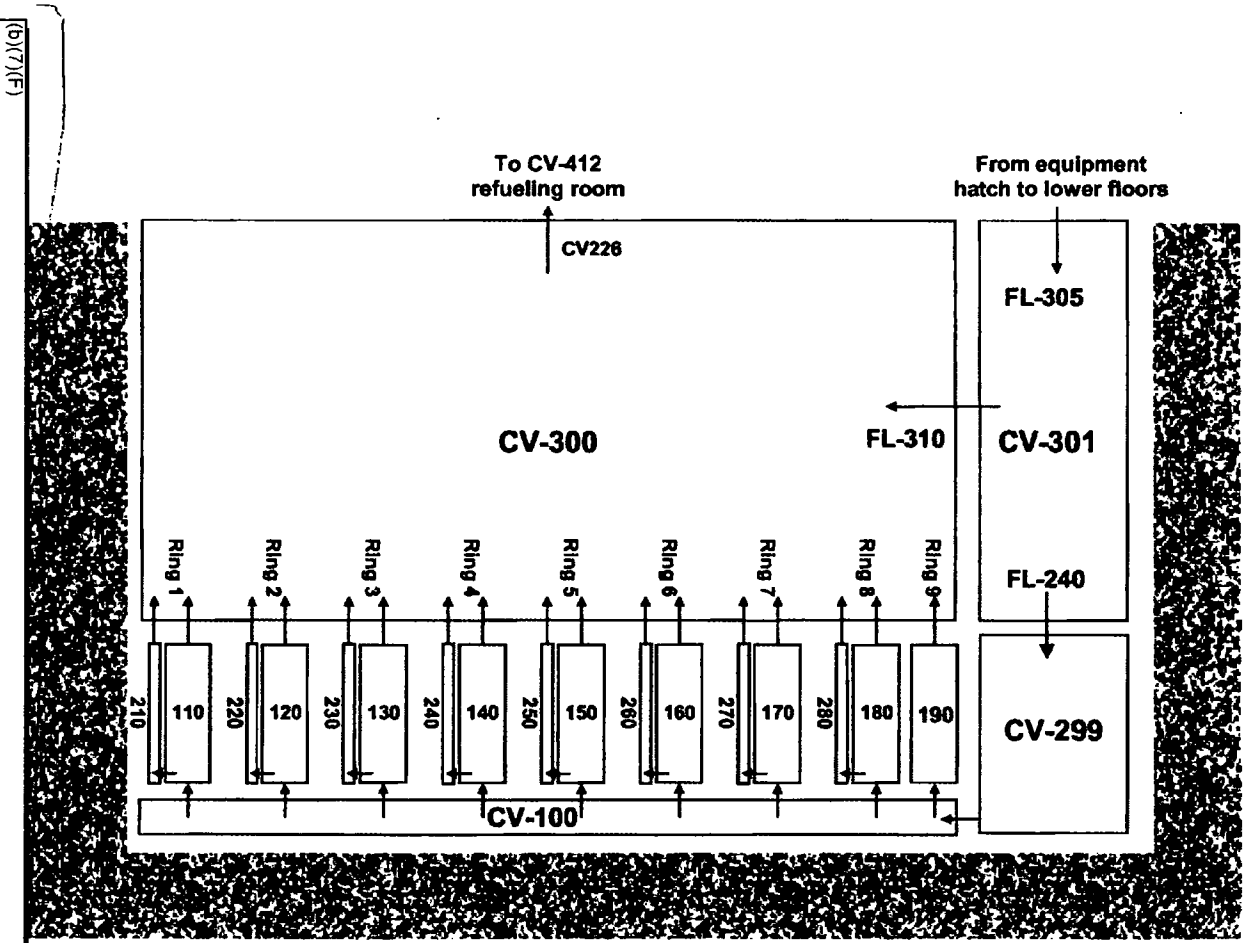
### 3.3 Whole Pool Model

A whole pool model was previously developed to perform source term calculations (see [Wagner, 2004] for a description). The scope of the whole pool model included the entire spent fuel pool including all the assemblies and the surrounding reactor building. However, the original BWR whole pool model did not include the new features described in Section 3.1. Consequently, a new simplified whole pool model was used to specify the boundary conditions for the separate effects model. The new BWR whole pool model includes all the new features described in Section 3.1 except the more detailed COR/CVH nodalization for tracking spray front.<sup>11</sup> The fuel assemblies and empty rack cells are represented in 9 rings in the MELCOR model. The new whole pool model uses the same 14-axial level COR Package described in the separate effects model (see Section 3.3). However, for improved computational runtime, only one control is used for the bundle region and one for the bypass region per COR package ring.

Figure 3-17 shows the CVH nodalization of the SFP region of the new simplified whole pool model. The lower SFP was divided into ten regions. CV-299 represents all the open regions in the SFP around the racks and including the cask area. The racks are divided into 9 regions. CV-110 and CV-210 represent the assembly and bypass regions of the first ring. Similarly, COR Rings 2 through 8 contain assembly and bypass regions. Ring 9 represents (b)(7)(F) empty rack cells. Hence, CV-190 only contains empty cells (i.e., no assemblies or bypass regions). The axial volume, flow area, and resistance are represented as described in Section 3.1.3. The region above the pool is divided into two control volumes. Typically, flow goes down CV-301 and CV-299 and rises through CV-300. The flow enters the bottom of the racks through CV-100. A 14 level COR nodalization is used as described in Section 3.2.

---

<sup>11</sup> A detailed COR/CVH nodalization in the framework of a multi-ring model is too computationally intensive for the present application. The simplified whole pool model is used to calculate global boundary conditions for the more detailed separate effect models described in Section 3.1.



(b)(7)(F)

Figure 3-17 Schematic of the Whole Pool Model Configuration.

### 3.3.1.1 Radial Thermal Coupling

The reference plant for the SFP analysis is a large BWR. The SFP is representative of a modern, high-density SFP. The plant has begun a dry or off-site fuel storage program. As fuel assemblies are added to the SFP, a similar number are removed for dry storage. Consequently, the number of assemblies in the SFP is kept approximately constant. For the present analyses, the layout of the fuel was specified to be representative of a well-configured SFP. In particular, the assembly layout was specified to enhance radial heat transfer from recently discharged, high-powered assemblies to low-powered assemblies. Figure 3-18 shows an example of a well-configured SFP layout. The most recently discharged "orange" and "red" assemblies are surrounded by the older "blue" assemblies in the SFP in 1x4 patterns. (b)(7)(F)

(b)(7)(F)

Ex. 7F

The layout of the assemblies from the last offload for the new MELCOR whole pool model conceptually followed the example shown in Figure 3-18.<sup>12</sup> The assemblies in the reference PWR SFP were grouped into 9 types or "rings" by decay heat power and time of discharge.<sup>13</sup> The ring layout assumed in this analysis is shown in Table 3-3. The last assembly offload from the reference plant (b)(7)(F) assemblies. (b)(7)(F) assemblies were subdivided into Rings 1, 3, and 5. By using three rings to represent the last core offload, the relative powers of the assemblies were accurately characterized into high, medium, and low-powered groups. Surrounding each of those groups in Rings 2, 4, and 6 were the lowest-powered assemblies in the SFP. There were four low-powered assemblies in Rings 2, 4, and 6 for each high-powered assembly in Rings 1, 3, and 5, respectively. This 1x4 pattern utilized (b)(7)(F) the lowest powered assemblies. The remaining mid-powered assemblies were placed in an approximate checkerboard pattern with the next lowest powered (b)(7)(F) in Ring 7 interspersed amongst (b)(7)(F) of Ring 8. Finally, (b)(7)(F) empty cells were placed around the outside of the SFP to ensure open air downflow regions into the SFP in the event of a complete loss-of-coolant inventory accident.

7F

7F

Ex 7F

Figure 3-19 shows the cell-wall radiation view factors between the various rings. The resultant view factor specifies the amount of coupling from each region to another. For example, the Ring 1 cells are completely surrounded by Ring 2 cells. Hence, the view factor from Ring 1 to Ring 2 is 1.0. Similarly, Rings 3 and 4 and Rings 5 and 6 are coupled in 1x4 patterns. Due to limitations in the MELCOR radial radiation scheme, only adjacent rings can be thermally coupled. Consequently, the inter-dependent coupling between adjacent rings can not be represented. The resultant assembly patterns only couple the 1x4 patterns in Rings 1 through 6,

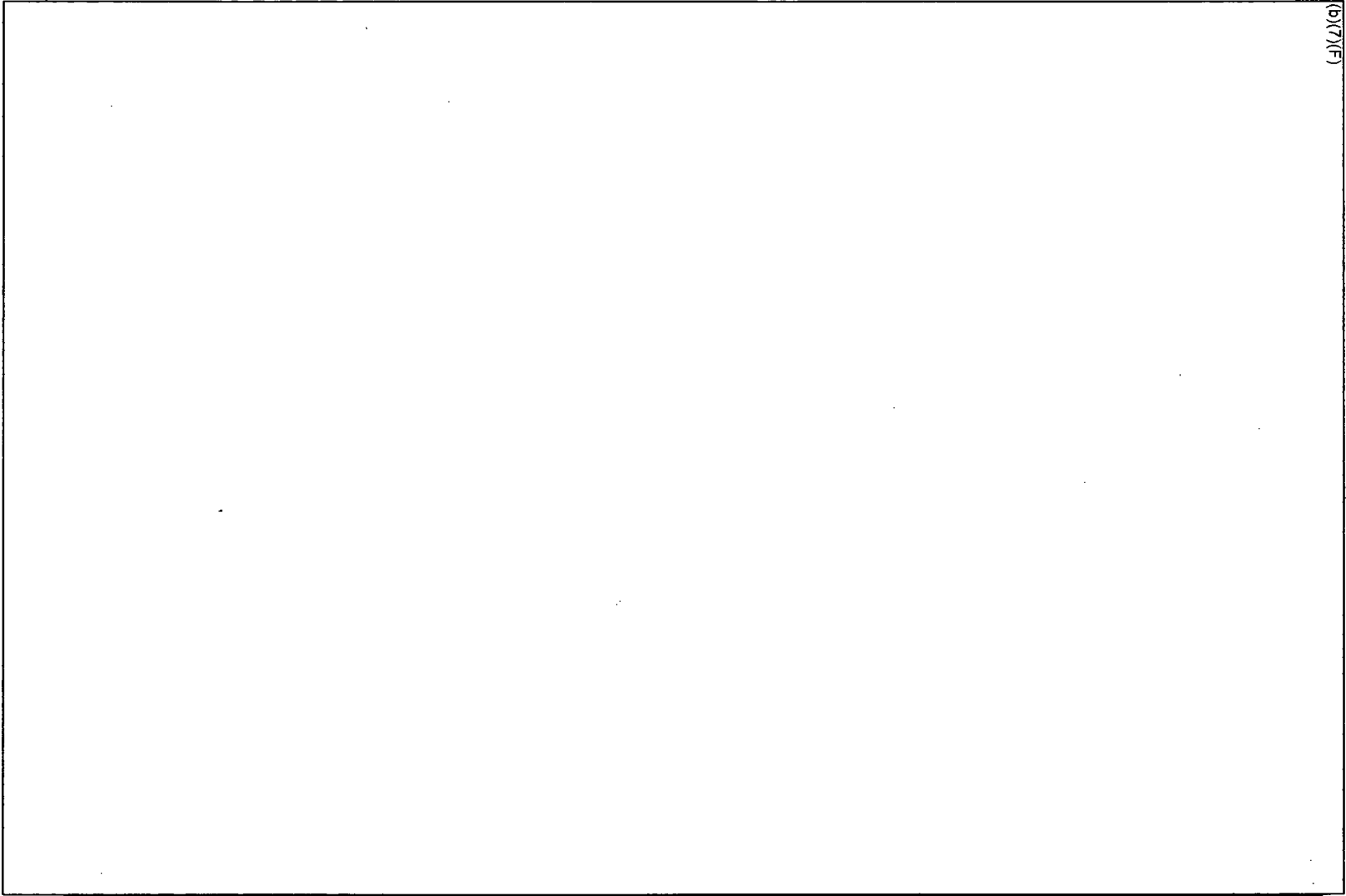
<sup>12</sup> Figure 3-18 is an illustration of a well-configured SFP. Similarly, the layout used in the present analysis uses 1x4 patterns with the last offload surrounded by the lowest decay heat assemblies. However, the layout of the (b)(7)(F) assemblies was a simply a checkerboard pattern. Since the new whole pool model was only used to establish inlet boundary conditions for the separate effects models, no further refinement of the assembly or ring layout was performed. It would be relatively straight-forward to change the number of assemblies in each ring and their coupling to adjacent rings.

Ex 7F

<sup>13</sup> "Ring" is a MELCOR term for a grouping of assemblies. In MELCOR's typical reactor configuration, the core is geometrically divided into a group of concentric rings. Each assembly in a ring has the same decay heat and thermo-physical properties.

a checkerboard pattern in Rings 7 and 8 and empty cells around the periphery in Ring 9. No other inter-ring couplings are considered.

Within each MELCOR ring, the assembly decay heat is uniform. Table 3-3 summarizes the average assembly decay power in each ring from the individual batches. Consequently, for any given scenario, the decay heat in each ring is adjusted to give the average assembly power. Due to the variable decay factors in the assembly decay heat, the assembly power is conservatively assumed to remain constant for the duration of the scenario.



(b)(7)(F)

Ex 41

Figure 3-18 Example of Alternating and Repeating 1x4 Patterns.

Table 3-3 Summary of Regions in the MELCOR Whole Pool Model.

(b)(7)(F)

EJ TF

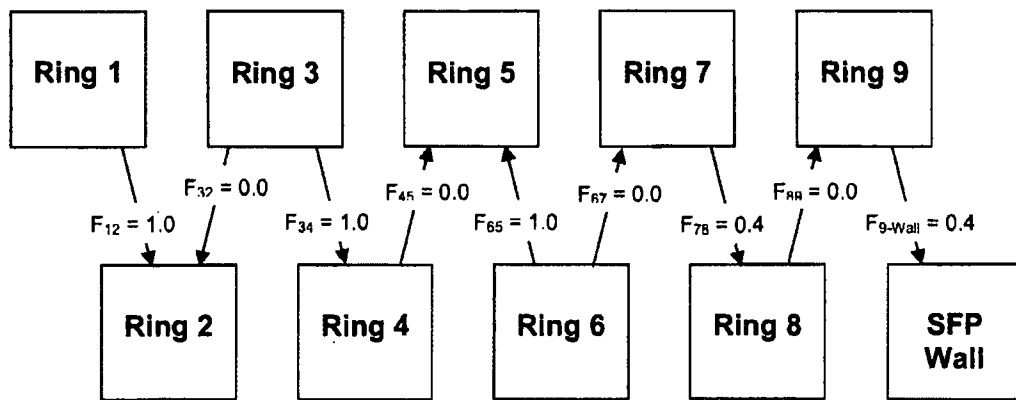


Figure 3-19 The Radial Coupling Scheme as Implemented in MELCOR SFP Model.

### 3.3.1.2 Simplified Refueling Room Model

A complete reactor building was developed as part of the BWR reference plant accident progression model. However, for the present analysis, the reactor building model was simplified to only model the refueling room (i.e., within the red dashed line on Figure 3-20). The SFP nodalization (see Section 3.3) was coupled to the SFP model as shown in Figure 3-20.

A single control volume models the refueling bay. An open hatch in the southeast quadrant (via flow paths) connects the refueling bay to a boundary condition volume representing the lower sections of the building. Nominal reactor building leakage is modeled at the center elevation of the refueling bay. The leakage flow in the simplified model was tuned to match the 100% design in-leakage rate of the detailed reactor building model.

The detailed reactor building model represented many over-pressure failure flow paths within the reactor building. The two most important flow paths for the present calculations were added to the simplified refueling floor model, (1) the blowout panels on the refueling room walls and (2) a pathway representing the structural failure of the reactor building roof. (b)(7)(F)

(b)(7)(F)

Ex. 7F

Recently, computational fluid dynamic (CFD) simulations of the air flow patterns in a PWR fuel storage building during a complete loss-of-coolant inventory accident guided the development of the model nodalization [Khalil]. The CFD results show a flow pattern of hot air exiting from the assemblies at the top of the racks (see Figure 3-21). The hot gases form a plume which that rises to the building ceiling. Once the plume hits the ceiling, it spreads radially and mixes within the hot gas layer at the top of the room. The room remains thermally stratified as hot gases preferentially leak out the large, open ceiling ventilation units. Meanwhile, cool air enters (b)(7)(F) to replace the exiting hot gases. The cool air fills the lower regions of the building, overflows to the SFP floor elevation, and sinks into the SFP to replace exiting hot gases. The cool air flows underneath the racks from the cask area and then spreads radially under the racks. The hydrostatic pressure difference between the cold gases outside the racks and the hot gases inside the assemblies drives the airflow through the racks.

Ex. 7F

This flow pattern is similar to that expected in the reference BWR refueling room<sup>14</sup>. By comparing Figure 3-20 and Figure 3-21 (b)(7)(F)

(b)(7)(F)

Ex. 7F

MELCOR does not include models for stratification of hot gases. Each control volume is assumed to be well-mixed and have a single temperature. Large-scale natural circulation flow patterns can be predicted where the bulk temperature differences between adjacent rooms create mixing flows. However, it would be awkward or perhaps impossible to predict complex plume

<sup>14</sup> The PWR refueling building is shown because the CFD code used in that analysis provides superior visualization of the resultant flow patterns than the figures available from the comparable BWR CFD study.

behavior within regions typically modeled with a single control volume (e.g., the room above the SFP). Consequently, the MELCOR calculations are expected to over-predict the amount of thermal mixing within the building. Based on insights from the CFD calculations, the MELCOR refueling room model nodalization included modeling features to minimize excessive mixing.

The refueling room is modeled as a single control volume. (b)(7)(F)

(b)(7)(F)

(b)(7)(F)

In this manner, the cool gases leaving the lower regions of the building are not brought into thermal equilibrium with gases above the SFP. Cross-flow is simulated between CV-300 and CV-301 as observed in Figure 3-21.

Ex 7P

Finally, no counter-current flow was modeled between CV-301 (see Figure 3-17) and the refueling room (CV-412). CV-301 is connected to the refueling room via flow into the SFP pit. The detailed FLUENT CFD solution shows a hot gas layer near the ceiling of the room above the SFP pit. If the heat removal is inadequate, then the hot gas layer fills the room (i.e., CV-320) and extends down into the lower rooms in the building. MELCOR can not calculate the formation and movement of a hot gas layer. However, when the gas flow into the refueling room (i.e., via FL-300 from the SFP pit) exceeds the leakage from the building, hot air circulates into lower floors through the hatch.<sup>15</sup>

<sup>15</sup> For the present boundary condition calculations, the temperature feedback from the hot gas layer filling the refueling room was not adequately modeled. If the refueling room filled with hot gas, there was not a mechanism to heat the lower floors and draw hotter gas into the SFP. This deficiency will be addressed in future calculations by including a heated gas recirculation path into the SFP.

(b)(4)

Ex 7 F

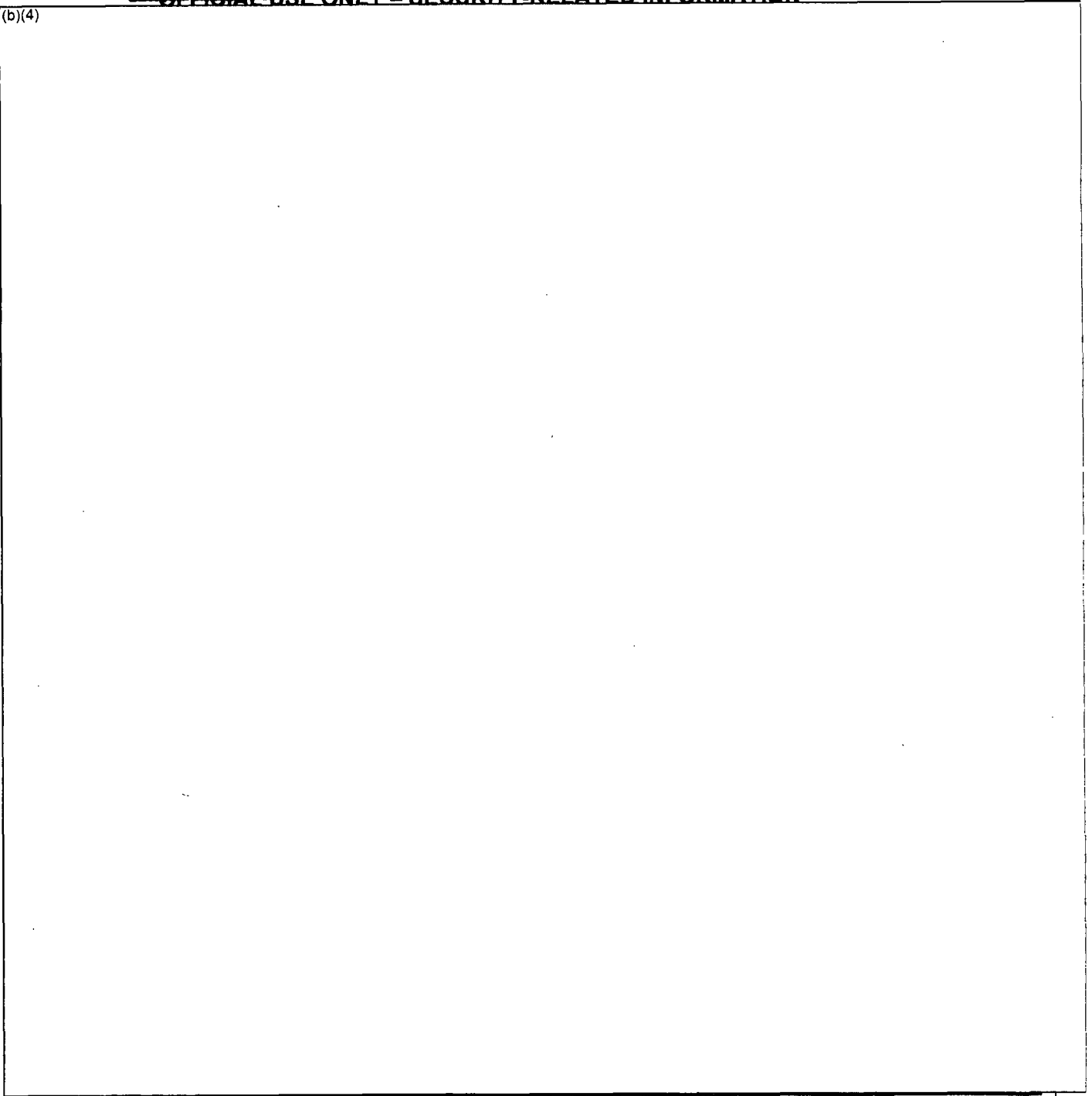


Figure 3-20 MELCOR Reactor Building Model.

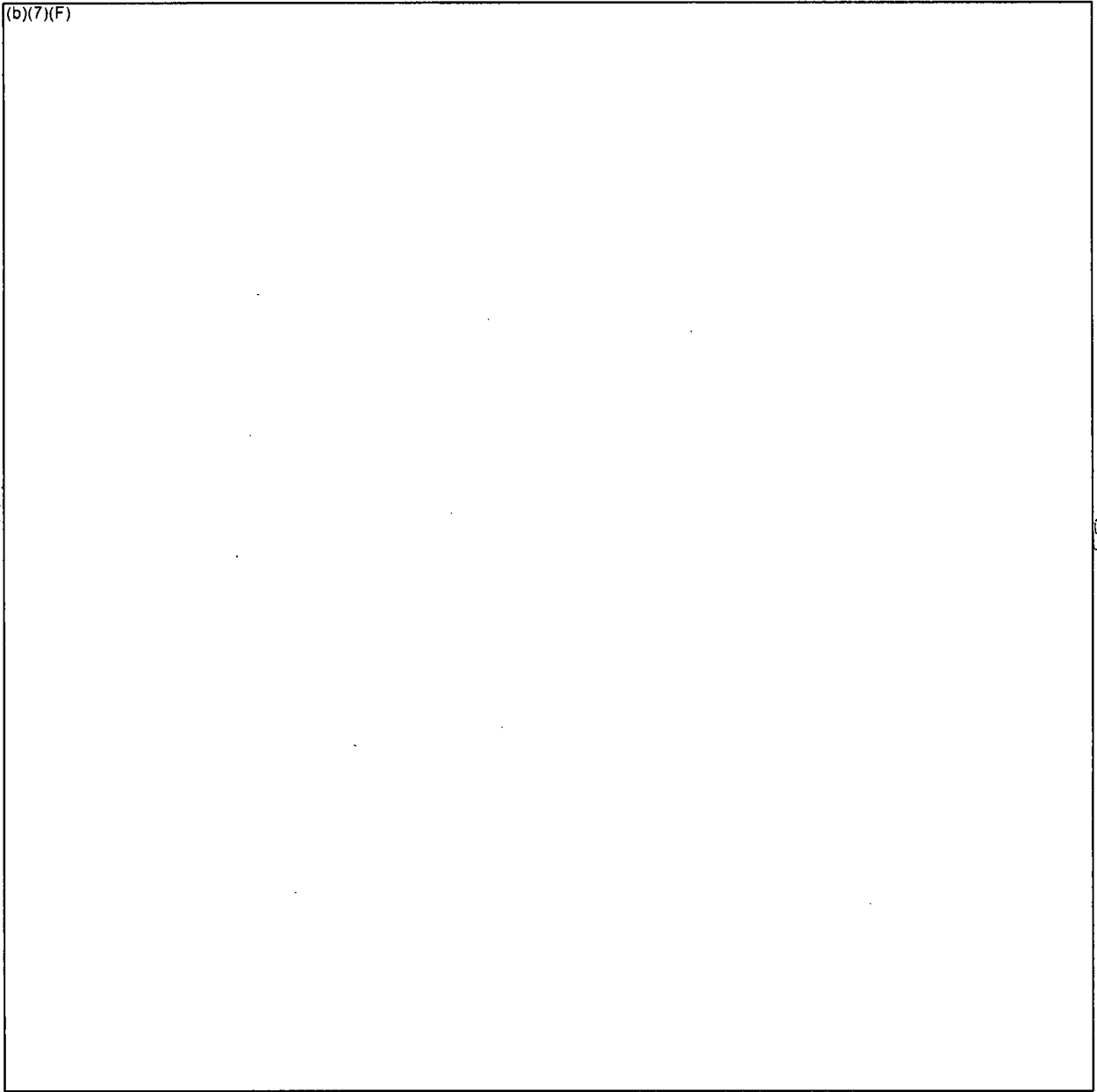


Figure 3-21 Example of Pressurized Water Reactor SFP Building Flow Patterns From FLUENT Calculations With (b)(7)(F) Ex 7F

### 3.4 Description of the Initial and Boundary Conditions

In most cases, the separate effect BWR SFP models described in Section 3.2 were used to evaluate the fuel thermal response to emergency spray operation. The initial conditions are summarized in Table 3-4. The model was initiated from normal conditions (i.e., 300 K and normal water level). However, the pool heat removal and the building ventilation were assumed disabled. The emergency spray flowrate (b)(7)(F) across the pool cross-section. Ex 7F  
The spray system response above the SFP racks was modeled in the whole pool model and used MELCOR's spray model.

The focus of the present study was to characterize the fuel response to spray operation. Other uncertainties affecting the response have been examined in a previous BWR separate effects study [Wagner, 2003]. Table 3-5 summarizes the base values of the uncertain and variable values used in the present study. These base modeling parameters were similar to the base values used previously. The last boundary condition was the emergency spray source. It was assumed that the emergency SFP spray system evenly covered the cross-sectional area of the SFP. Once it hit the assemblies in the SFP racks, the water drained into the SFP assemblies. The spray water was introduced as a water source into the control volume representing the upper tieplate.

**Table 3-4 Summary of Base Case SFP Model Initial Conditions for BWR SFP Emergency Spray Calculations.**

Parameter	Value
Pool temperature	300 K
Water level	Normal, 37.75 ft
Pool heat removal	Deactivated
Building ventilation	Deactivated
Spray injection flowrate	<span style="border: 1px solid black; padding: 0 20px;">(b)(7)(F)</span>
Spray water temperature	300 K
Spray droplet size	Usually 1250 $\mu\text{m}$
Spray initiation time	<span style="border: 1px solid black; padding: 0 20px;">(b)(7)(F)</span>
Spray nozzle overlap inefficiencies	None
Spray nozzle delivery inefficiencies	None
Notes:	
1.	The spray system is assumed <span style="border: 1px solid black; padding: 0 20px;">(b)(7)(F)</span> uniformly across the entire SFP cross-section. Ex 7F
2.	Any inefficiencies due to overlap from adjacent spray nozzles or droplets hitting the walls or missing the SFP are not included. To <span style="border: 1px solid black; padding: 0 20px;">(b)(7)(F)</span> into the pool, the overall system flowrate must be increased. Ex 7F
3.	Only the hybrid and whole pool models simulated the falling spray droplets. The separate effects model simulated the spray as a water pool forming on the upper tieplate of the assembly.

Table 3-5 Summary of Base Case SFP Model Boundary Conditions for BWR SFP Emergency Spray Calculations.

Parameter	Value
Decay Heat	Peak assembly power from utility calculation using ANSI/ANS-95 decay heat standard. Low-powered assemblies were at the reference BWR SFP median value (b)(7)(F)
Bernoulli Effect	Not explicitly included
Inlet Temperature and water level	Specified from whole pool model (see Section 5)
Initial Oxide Layer Thickness	25 $\mu\text{m}$ [Lanning]
Viscous Wall Friction Correlation	As measured in SNL experiments.
Flow Restrictions	None unless noted.
Rod Ballooning	Not modeled. <sup>16</sup>
Oxidation Correlation	ANL zircaloy-4 air oxidation kinetics model with breakaway <sup>17</sup> and Urbanic-Heidrich steam oxidation model.
Heat Transfer to surrounding cells or assemblies	Adiabatic boundary in the radial direction. Radial heat transfer was calculated within the checkerboard and 1x4 models between the low- and high-powered assemblies.
Spray water source	Specified as a liquid source to the control volume above the upper tie-plate. For the whole pool and hybrid models, the spray source was modeled using MELCOR's containment spray model [Gauntt].

Ex. 7F

(b)(7)(F)

Ex. 7F

<sup>16</sup>The pre- and post-breakaway air oxidation kinetics models were based on Zircaloy-4 cladding. The reference BWR assemblies have Zircaloy-2 cladding. It is assumed (and believed) that Zircaloy-4 and Zircaloy-2 will oxidize at the same rate. Due to limited data, MELCOR's breakaway timing model is based on data from both Zircaloy-4 and Zirlo samples.

#### 4. SPRAY MITIGATION HAND CALCULATIONS

Two sets of hand calculations were performed to estimate the heat removal required from the spray system in the reference BWR spent fuel pool. In the first calculation, the spray system was initiated prior to uncover of the fuel and the water leakage location is above the top of the racks. In the second hand calculation, it is assumed that the fuel is uncovered. The hand calculations represent simple straight-forward energy balances that are useful for estimating the required flowrate for a spray system. The hand calculations do not address the complications of radial heat transfer between low- and high-powered assemblies, the effectiveness of heat removal through the bypass region between the canister and the rack wall, or the response when the assumptions are violated (e.g., inadequate cooling). The MELCOR calculations in Section 6 address those phenomena and conditions.

##### 4.1 Leak Above the Top of the Racks

In the first calculation, the spray system was initiated prior to uncover of the fuel and the water leakage location is above the top of the racks. It is assumed that the accident has disabled the SFP heat removal capabilities and the decay heat from the SFP is boiling away the remaining inventory. Depending on the time of the accident, the decay heat varies. Close to the most recent offload of fuel into the SFP, the decay heat is highest (see whole pool decay heat for the reference BWR in Figure 4-1). Figure 4-2 shows the required flow rate to maintain the SFP level.

The calculations for the heat removal requirements (b)(7)(F) are shown below. (b)(7)(F) Ex 7F (b)(7)(F) is required. Since the fuel is covered, a spray system is not technically needed. Rather any water injection system would be sufficient.

##### Assumptions:

1. Reference BWR SFP decay heat data
2. Last offload had (b)(7)(F) since reactor shutdown Ex 7F
3. 80°F spray water
4. Decay heat removal is provided by boiling spray (injection) water
5. Other modes of heat transfer are ignored.

$$\rho = 62.1 \text{ lbm/ft}^3 = 996 \text{ kg/m}^3$$

$$h_{fg} = 970.3 \text{ BTU/lbm} = 2.257 \times 10^6 \text{ J/kg}$$

$$h_{80^\circ\text{F} \rightarrow 212^\circ\text{F}} = 180.18 \text{ BTU/lbm} - 48.13 \text{ BTU/lbm} = 132.05 \text{ BTU/lbm} = 3.072 \times 10^5 \text{ J/kg}$$

$$\Delta h = h_{fg} + h_{80^\circ\text{F} \rightarrow 212^\circ\text{F}} = 1102 \text{ BTU/lbm} = 2.56 \times 10^6 \text{ J/kg}$$

Whole pool decay heat at  $\boxed{(b)(7)(F)}$   $\times \gamma F$

Spray Flowrate  $\gamma F = \frac{\boxed{(b)(7)(F)}}{(264.2 \text{ gal/m}^3)} (996 \text{ kg/m}^3 * 2.56 \times 10^6 \text{ J/kg}) * (60 \text{ sec/min})$

$\boxed{(b)(7)(F)}$   $\times \gamma F$



Figure 4-1 Total Decay Heat Power in the Reference BWR SFP.

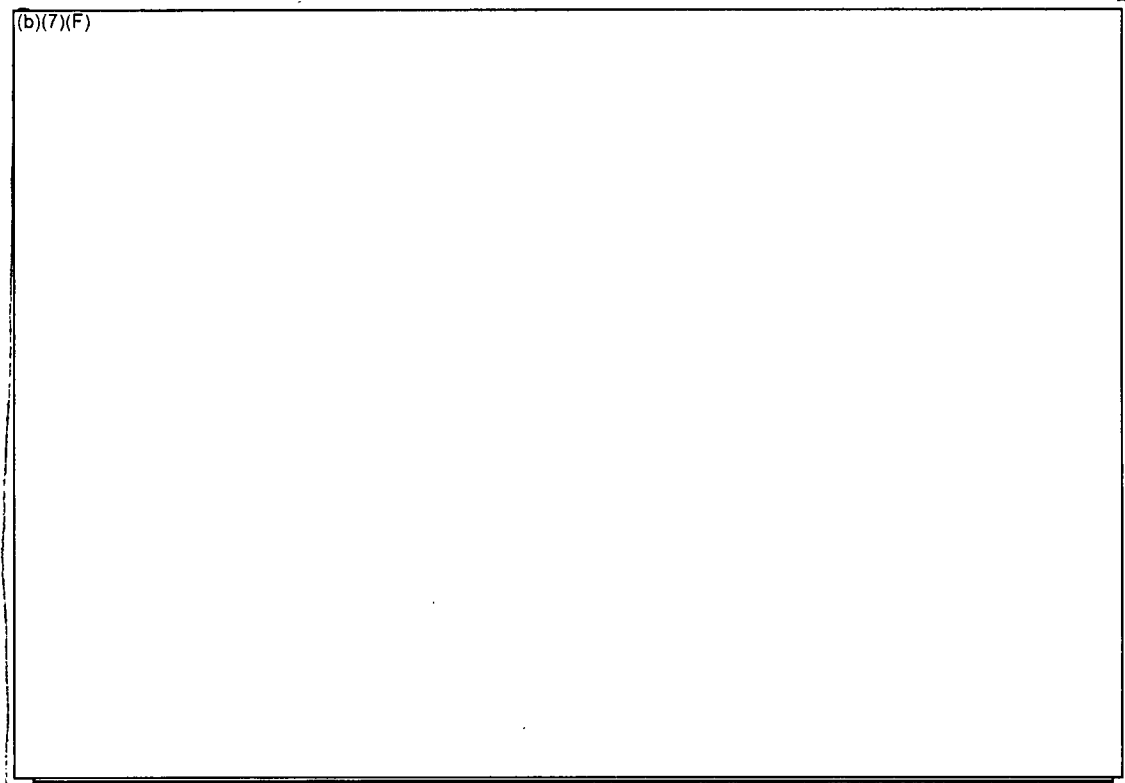


Figure 4-2 Make-up Flowrate for the Reference BWR SFP.

#### 4.2 Leak Below the Top of the Racks

In the second calculation, the spray system was not initiated prior to uncover of the fuel and/or the water leakage location is below the top of the racks. Similar to the previous calculation, the accident has disabled the SFP heat removal capabilities and the decay heat from the SFP is boiling away the remaining inventory. It is assumed that the spray system is initiated before the fuel becomes uncovered. If not, additional spray would be required to remove the sensible heat from the regions of the assembly which has heated (e.g., see Section 4.2.3). Furthermore, if the fuel rods are at high temperature, then the initial mode of spray heat removal would be film boiling, which is less effective than nucleate boiling.

There are several other assumptions that were applied for these calculations. Since the fuel is uncovered, a spray system is required to distribute the water to the individual assemblies. To achieve a uniform coverage, the spray systems would have some inefficiencies due to overlap from the adjacent nozzles and inaccurate delivery (e.g., hitting walls or missing the pool). The magnitude of the total SFP spray flow assumes a 33% spray overlap factor to account for these two inefficiencies. However, the hand calculations assume that the most limiting assembly is not within a zone that has spray overlap. Furthermore, only the spray which enters the assembly canister was considered as effective (i.e., neglect spray into the space between the assembly canister and the rack cell wall). In addition, all other modes of heat transfer are conservatively

neglected. For example, radial heat transfer to adjacent lower powered assemblies was neglected.

Figure 4-3 shows the peak, median, and minimum assembly power in the reference BWR SFP as a function of time after the last offload. (b)(7)(F)

(b)(7)(F)

Figure 4-4 shows the required spray rate to provide adequate heat removal from the peak decay heat assembly. For example (b)(7)(F) Furthermore, a spray system is required to direct the flow into the assemblies. Sample calculations for the heat removal requirements (b)(7)(F) are shown in Section 4.2.1. Some scoping hand calculations suggest that the spray water will be able to penetrate into the assembly (b)(7)(F) see Section 4.2.2). Finally, the impact of the assembly sensible heat upon the initial spray effectiveness is discussed in Section 4.2.3.

Ex 7F  
Ex 7F

Ex 7F

Ex 7F

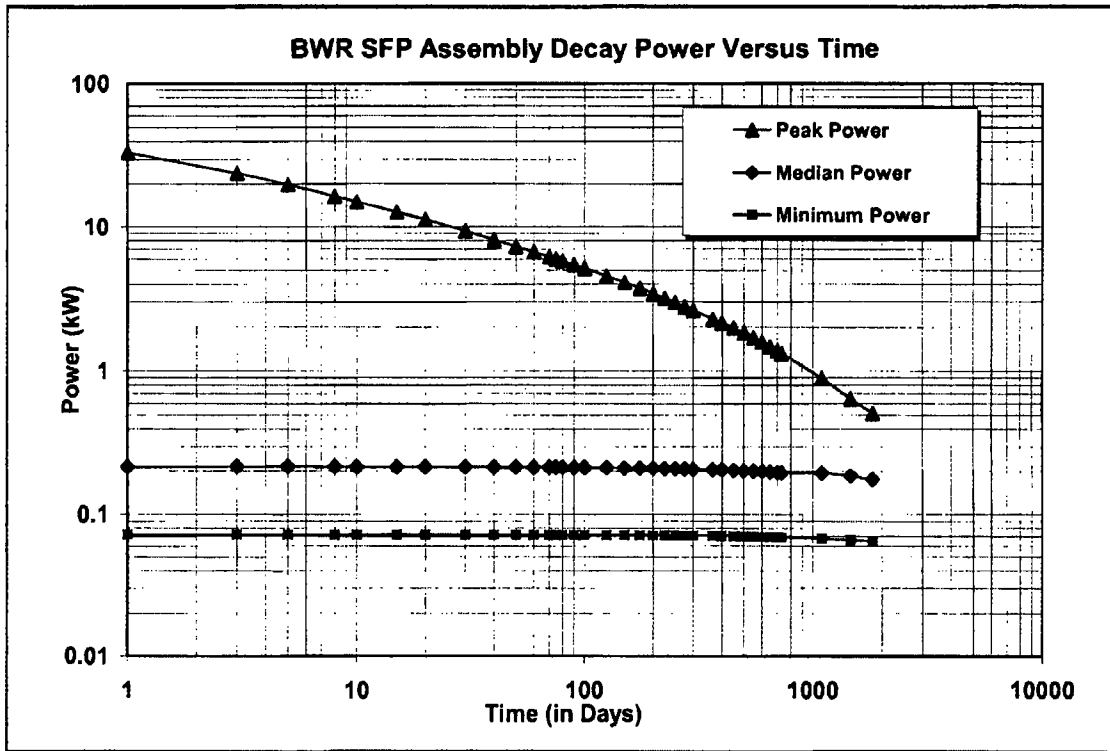


Figure 4-3 Comparison of the Peak, Median, and Minimum Assembly Decay Heat Power in the Reference BWR SFP.

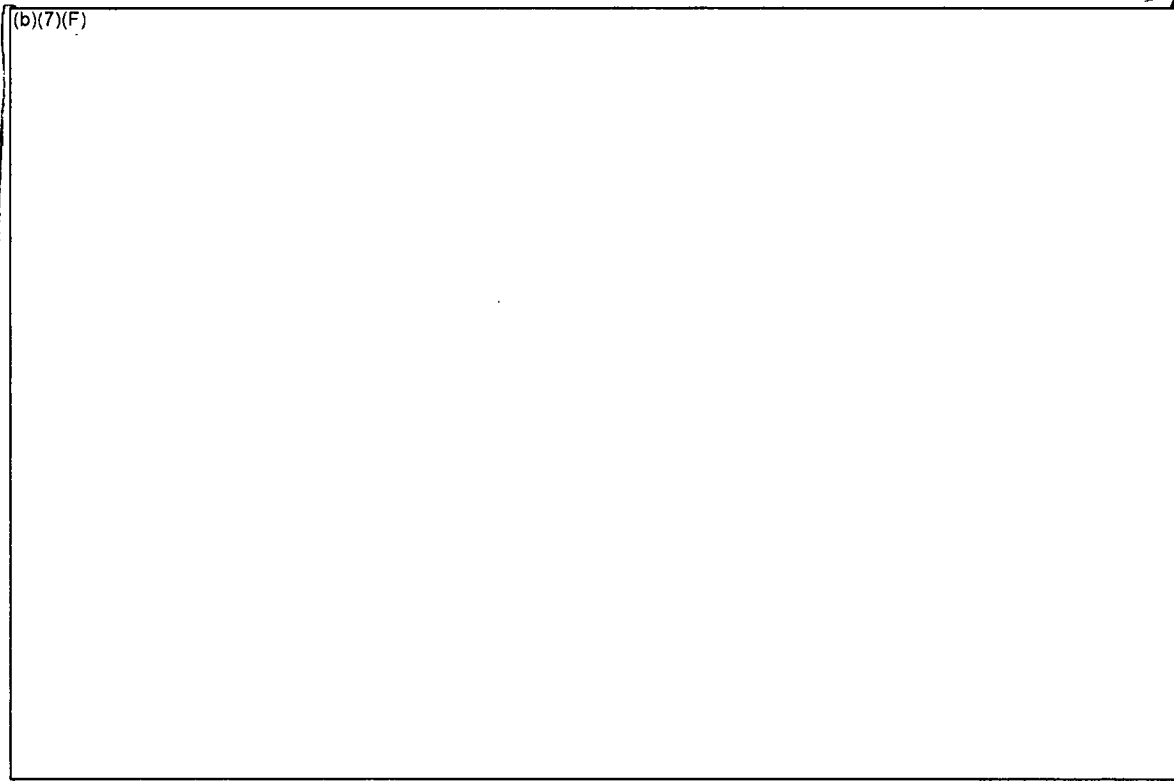


Figure 4-4 Make-up Flowrate for the Reference BWR SFP.

#### 4.2.1 Calculations for One Point on the BWR Spray Chart

Assumptions:

1. Reference BWR SFP data
2. Peak assembly (b)(7)(F) *Ex 7F*
3. 80°F spray water
4. 33% spray coverage inefficiency/overlap
5. Only flow within the canister cross-section is effective
6. Make-up based on peak assembly decay heat projected across entire pool

$$\rho = 62.1 \text{ lbm/ft}^3 = 996 \text{ kg/m}^3$$

$$h_{fg} = 970.3 \text{ BTU/lbm} = 2.257 \times 10^6 \text{ J/kg}$$

$$h_{80^\circ\text{F} \rightarrow 212^\circ\text{F}} = 180.18 \text{ BTU/lbm} - 48.13 \text{ BTU/lbm} = 132.05 \text{ BTU/lbm} = 3.072 \times 10^6 \text{ J/kg}$$

$$\Delta h = h_{fg} + h_{80^\circ\text{F} \rightarrow 212^\circ\text{F}} = 1102 \text{ BTU/lbm} = 2.56 \times 10^6 \text{ J/kg}$$

Peak assembly power  $\frac{(b)(7)(F)}{(b)(7)(F)}$  Ex 7F

BWR SFP Assembly Pitch = 6.28"  
BWR SFP Canister ID = 5.4

Inside canister area to cell pitch ratio =  $(5.4'' \times 5.4'') / (6.28'' \times 6.28'') = 0.739$

Whole Pool Size =  $480'' \times 424'' = 203,520 \text{ in}^2 = 131.3 \text{ m}^2$  (Cross-sectional area)

Equivalent number of SFP rack cells in entire SFP cross-section  
 $= 203,520 \text{ in}^2 / (6.28'' \times 6.28'') = 5160$  equivalent cells

Spray Flowrate =  $\frac{(b)(7)(F)}{(264.2 \text{ gal/m}^3)} \times 996 \text{ kg/m}^3 \times 2.56 \times 10^6 \text{ J/kg} \times (60 \text{ sec/min}) \times 1.33 \text{ (overlap)} \times 1.35 \text{ (chan ratio)} \times 5160 \text{ equiv. cells}$  Ex 7F  
 $\frac{(b)(7)(F)}{}$  Ex 7F

#### 4.2.2 Calculations for Counter-Current Flow Limitation (CCFL)

$(b)(7)(F)$   
 $(b)(7)(F)$  Ex 7F

Consequently, counter-current flow limiting (CCFL) of water down into the assembly due to the shear forces from the upward steam flow is a concern.

The following terms are needed to calculate the Wallis non-dimensional flooding velocities to evaluate whether CCFL is a concern, assuming a downward liquid velocity  $(b)(7)(F)$  water and steam properties, and the reference BWR geometry  $(b)(7)(F)$  Ex 7F

Ex 4

$(b)(7)(F)$  First, calculate the phasic volumetric fluxes [Wallis], Ex 4

$$J_i = Q_i / A$$

where,

$J_i$  is the phasic volumetric flux

$Q_i$  is the volumetric flow

$$\frac{Q_L}{Q_G} = \frac{(b)(7)(F)}{(b)(7)(F)}$$
 Ex 7F

A is the cross-sectional flow area  $(b)(7)(F)$  Ex 4

So,

$$\frac{J_L}{J_G} = \frac{(b)(7)(F)}{(b)(7)(F)}$$
 Ex 7F

Next calculate  $J_i^*$  terms,

$$J_i^* = J_i \cdot (\rho_i)^{1/2} / [g \cdot D_H \cdot (\rho_L - \rho_G)]^{1/2}$$

where,

$Q_i$  is the phasic volumetric flux

$$Q_L = \frac{(b)(7)(F)}{Ex \ 7F}$$

$$Q_G = \frac{(b)(7)(F)}{Ex \ 7F}$$

$g$  is gravity ( $9.81 \text{ m/s}^2$ )

$D_H$  is the hydraulic diameter of the upper assembly  $\frac{(b)(7)(F)}{Ex}$

$\rho_L$  is the water density ( $996 \text{ kg/m}^3$ )

$\rho_G$  is the steam density ( $0.598 \text{ kg/m}^3$ )

So,

$$J_G^* = \frac{(b)(7)(F)}{Ex \ 7F} / [9.81 \text{ m/s}^2 * \frac{(b)(7)(F)}{Ex} * (996 \text{ kg/m}^3 - 0.598 \text{ kg/m}^3)]^{0.5}$$
$$J_G^* = 0.049$$

$$J_L^* = \frac{(b)(7)(F)}{Ex \ 7F} / [9.81 \text{ m/s}^2 * \frac{(b)(7)(F)}{Ex} * (996 \text{ kg/m}^3 - 0.598 \text{ kg/m}^3)]^{0.5}$$
$$J_L^* = 0.001$$

Next Grashof Number is calculated as follows,

$$N_L = [ \rho_L g D^3 (\rho_L - \rho_G) / \mu_L^2 ]^{1/4}$$

$$N_L = [ 996 \text{ kg/m}^3 * 9.81 \text{ m/s}^2 * \frac{(b)(7)(F)}{Ex} * (996 \text{ kg/m}^3 - 0.598 \text{ kg/m}^3) / (2.82 \times 10^{-4} \text{ kg/m-s}) ]^{1/4}$$

$$N_L = \frac{(b)(7)(F)}{Ex \ 7F}$$

From the Wallis flooding curve with  $N_L = \frac{(b)(7)(F)}{Ex \ 7F}$

$$m = \frac{(b)(7)(F)}{Ex \ 7F}$$
$$C = \frac{(b)(7)(F)}{Ex \ 7F}$$

The flooding (CCFL) limit is,

$$(J_G^*)^{0.5} + (J_L^*)^{0.5} = \frac{(b)(7)(F)}{Ex \ 7F}$$

$$\frac{(b)(7)(F)}{Ex \ 7F}^{0.5} + \frac{(b)(7)(F)}{Ex \ 7F}^{0.5} = 0.8$$

$$\frac{(b)(7)(F)}{Ex \ 7F} = 0.8, \text{ which is below the flooding limit}$$

Another criterion by Wallis also suggests that the flow conditions are well below the flow reversal limitation,

$$J_G^* = 0.5 \text{ for flow reversal.}$$

In our case,

$$\frac{(b)(7)(F)}{Ex \ 7F} < 0.5?$$

F x 7F

$\frac{(b)(7)(F)}{(F)} < 0.5$ , which is also below the flooding limit

It has been acknowledged that the classical Wallis correlations have some limitations due to the diameter effect [Bergles]. Using an alternate Kutaleadze relationship, which represents the ratio of the gas inertial forces acting on the capillary waves,

$Ku = (J_g) * (\rho_g)^{1/2} / [g \sigma (\rho_L - \rho_G)]^{1/4}$

where,

Ku is the Kutaleadze Number

$\sigma$  is surface tension between steam and water (0.072 kg/s<sup>2</sup>)

F x 7F

$Ku = \frac{(b)(7)(F)}{(F)} * (0.598 \text{ kg/m}^3)^{1/2} / [9.81 \text{ m/s}^2 * 0.073 \text{ kg/s}^2 * (996 \text{ kg/m}^3 - 0.598 \text{ kg/m}^3)]^{1/4}$

E x 7F

$Ku = \frac{(b)(7)(F)}{(F)} \ll 3.2$

E x 7F

If the Kutaleadze number is less than 3.2, then there is no CCFL. Hence, all three flooding correlations show CCFL is not expected to be a concern  $\frac{(b)(7)(F)}{(F)}$  (i.e., peak assembly decay heat power of  $\frac{(b)(7)(F)}{(F)}$ )

### 4.2.3 Impact of Assembly Sensible Heat

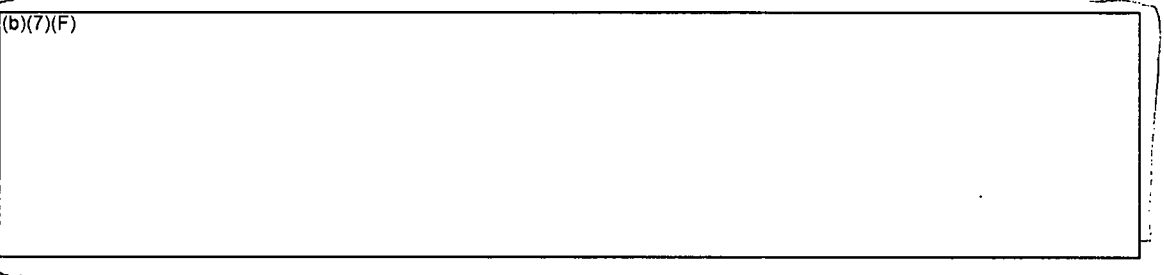
The assembly sensible heat has an effect on the spray heat removal effectiveness. If the sprays are started after the assembly begins heating, then a portion of the water's cooling potential removes the sensible heat from the assembly. A high amount of sensible energy (i.e., high temperature) also transitions the rod heat transfer from nucleate boiling to less effective film boiling. If film boiling is not effective, then the fuel would continue to heat.

E x 7F

E x 7F

Assuming that the heat transfer (i.e., whether film or nucleate boiling) is effective enough to boil all the spray water entering the limiting assembly, the impact on the cooling time is shown in Figure 4-5 and Figure 4-6  $\frac{(b)(7)(F)}{(F)}$  spray flow, respectively. The amount of time required to cool the assembly to near saturation conditions from various initial temperatures while simultaneously removing decay heat is quantified in these figures.  $\frac{(b)(7)(F)}{(F)}$  spray

flow  $\frac{(b)(7)(F)}{(F)}$



F x 7F

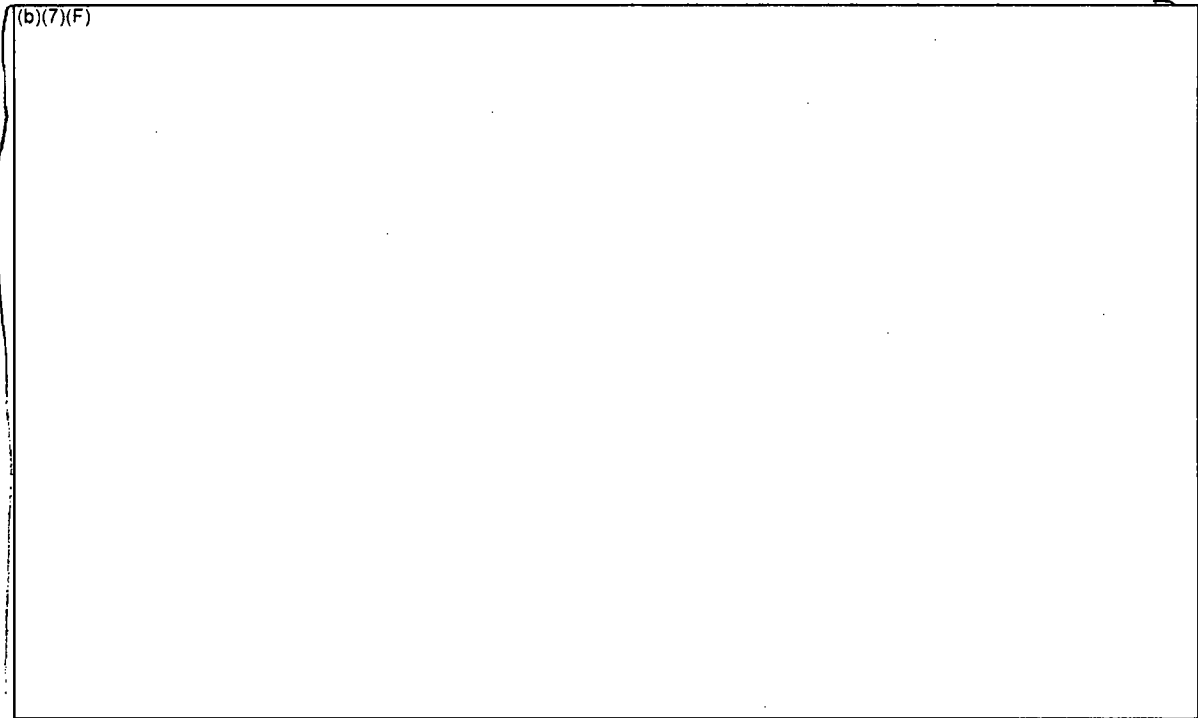


Figure 4-5 Timing Impact of Sensible Heat on Assembly Cooling (b)(7)(F) for a E. 7F  
Uniform Configuration.

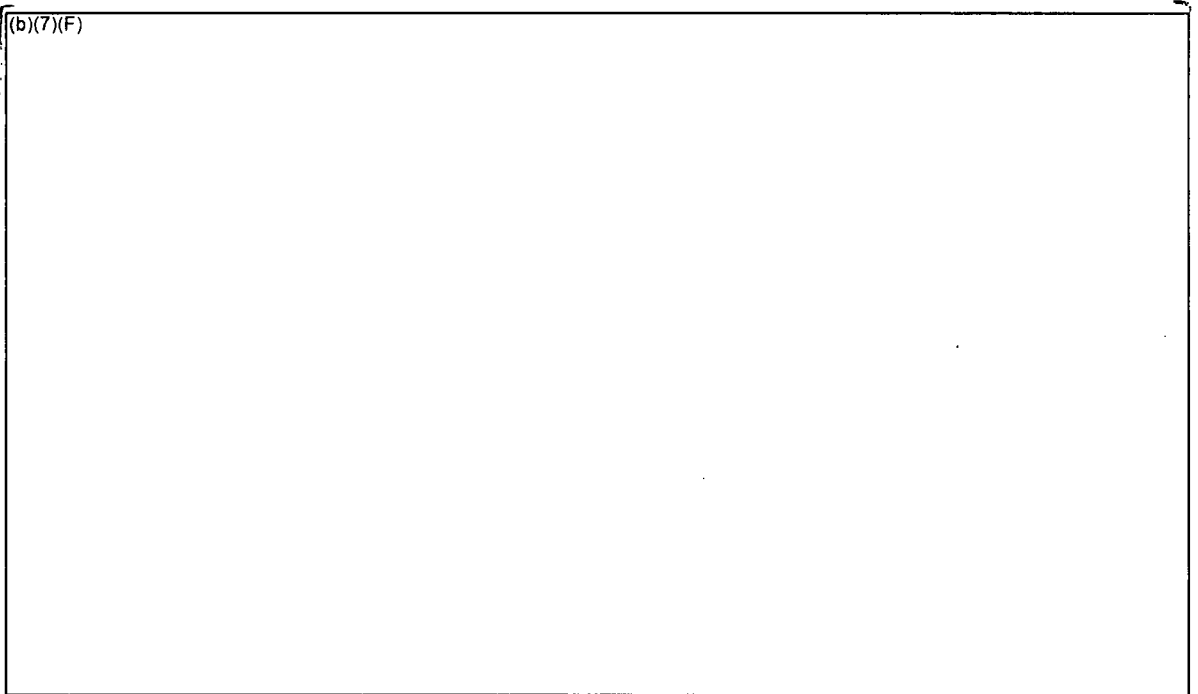


Figure 4-6 Timing Impact of Sensible Heat on Assembly Cooling (b)(7)(F) for a E. 7F  
Uniform Configuration.

**5. WHOLE POOL MODEL BOUNDARY CONDITION CALCULATIONS**

An assortment of whole pool calculations was run using the new whole pool model (see Section 3.3) to establish boundary conditions for the separate effects calculations. Section 5.1 shows typical results (b)(7)(F) equivalent diameter leak with (b)(7)(F). The detailed responses from other cases are not shown but were similar.

EX 7F

Ex 5

The most interesting of these boundary condition values was the resultant water level. (b)(7)(F)

(b)(7)(F)

EX 7F

(b)(7)(F) Table 5-1 summarizes the results from the whole pool calculations. For the range of hole sizes and spray flow rates considered in this study, the long-term water level spanned conditions that would allow air flow (i.e., the inlet is not plugged) versus cases where the inlet would be plugged. (b)(7)(F) hole cases had a relatively high level that would partially cover the bottom of the fuel (a water level of >16"). In contrast, (b)(7)(F) hole had a very low water level and would be ensured to have air natural circulation flow. As discussed in Section 2.2, the phenomena and thermal response for cases with the inlet plugged by the water level is much different than the response when there is air flow in the assembly. Furthermore, it is expected that (b)(7)(F) case with (b)(7)(F) hole might have characteristics of both types of accidents.

EX 7F

7F

7F

**Table 5-1 Summary of the Steady-State Water Levels as a Function of Leakage Hole Size and Spray Flow Rate.**

(b)(7)(F)

7F

OFFICIAL USE ONLY – SECURITY-RELATED INFORMATION

5.1 (b)(7)(F) Spray Flow Rate 7F

Figure 5-1 through Figure 5-4 show the boundary conditions taken (b)(7)(F) of (b)(7)(F) with a (b)(7)(F) emergency spray flow. A special boundary condition control volume was created to specify fluid boundary conditions for the separate effects model. The time-dependent data consisted of water level (Figure 5-1), water and gas temperature (Figure 5-2), steam partial pressure (Figure 5-3), non-condensable gas concentrations (Figure 5-5<sup>18</sup>, actually reflects normal atmospheric concentrations of nitrogen and oxygen), and gas pressure (not shown, approximately atmospheric pressure). The blue points on each figure represent the data transferred to the separate effects model.

The whole pool results show expected trends. The water level drops in response to the leakage. Since the boundary condition control volume is only 5 m, Figure 5-1 only shows the level response below 5 m. Figure 5-4 shows the overall model level response. (b)(7)(F)

(b)(7)(F). Since the base plate of the racks is 7.25" off the SFP floor, there was a circulation of natural air into the racks.

The water temperatures initially heated in response to the loss of SFP heat removal. Once the rack uncovered, separate gas and water temperatures are calculated. However, due to spray cooling, the pool under the racks and the gas temperatures remained relatively low. (b)(7)(F) Due to boiling of the spray water in the hot assemblies and evaporation, the partial pressure of the steam in the room also steadily increased (Figure 5-3). (b)(7)(F) the equivalent steam molar concentration was (b)(7)(F) (see Figure 5-5).

Figure 5-6 shows the flow balance between the water leakage flow from the SFP and the emergency spray flow. Initially the water leakage flow was very high due to the large head of water above the leakage location. As the water level dropped, the water leakage flow steadily decreased. (b)(7)(F) emergency spray system was started. However, due to the high leakage flow rate, emergency spray had little impact in slowing the level drop. (b)(7)(F) the water level (b)(7)(F) and the leakage flow is equal to the spray flow. The level remained at this value for the remainder of the calculation.

<sup>18</sup> The data from Figure 5-5 was not used directly. However, it was included to show the relative molar concentrations of steam, oxygen, and nitrogen. To define the gas composition, the steam partial pressure (Figure 5-3) was used with constant non-condensable molar concentrations of oxygen (20%) and nitrogen (80%).

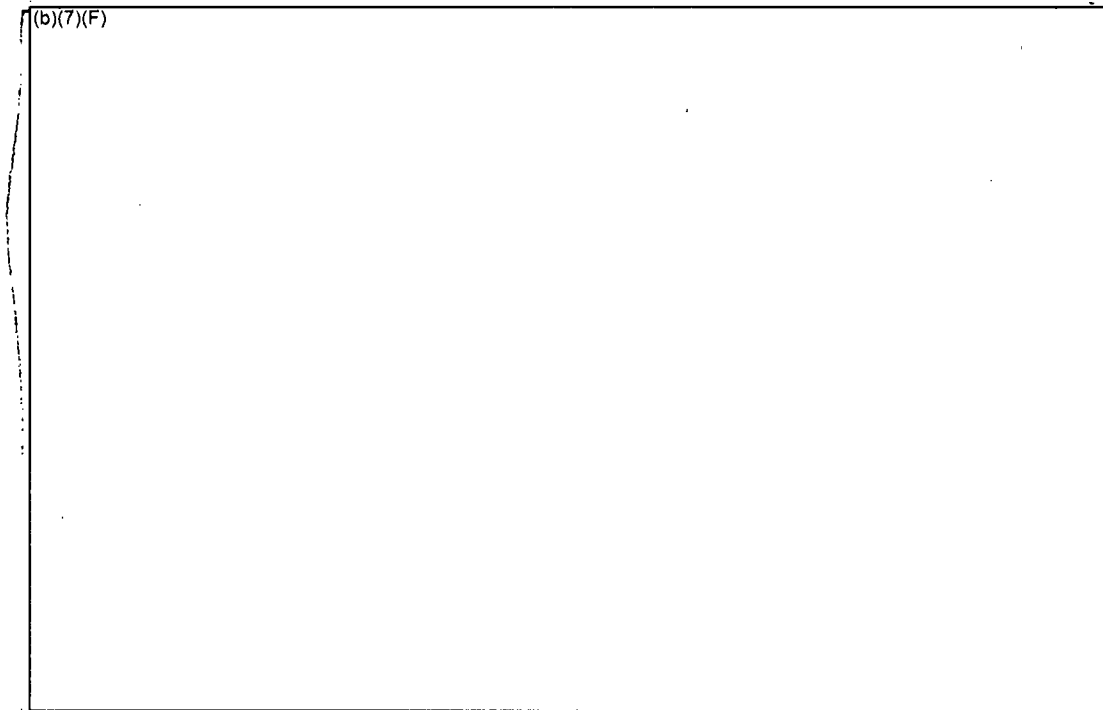


Figure 5-1 Water Level Boundary Condition from the BWR Whole Pool Model with  $(b)(7)(F)$  and a Spray Flow of  $(b)(7)(F)$

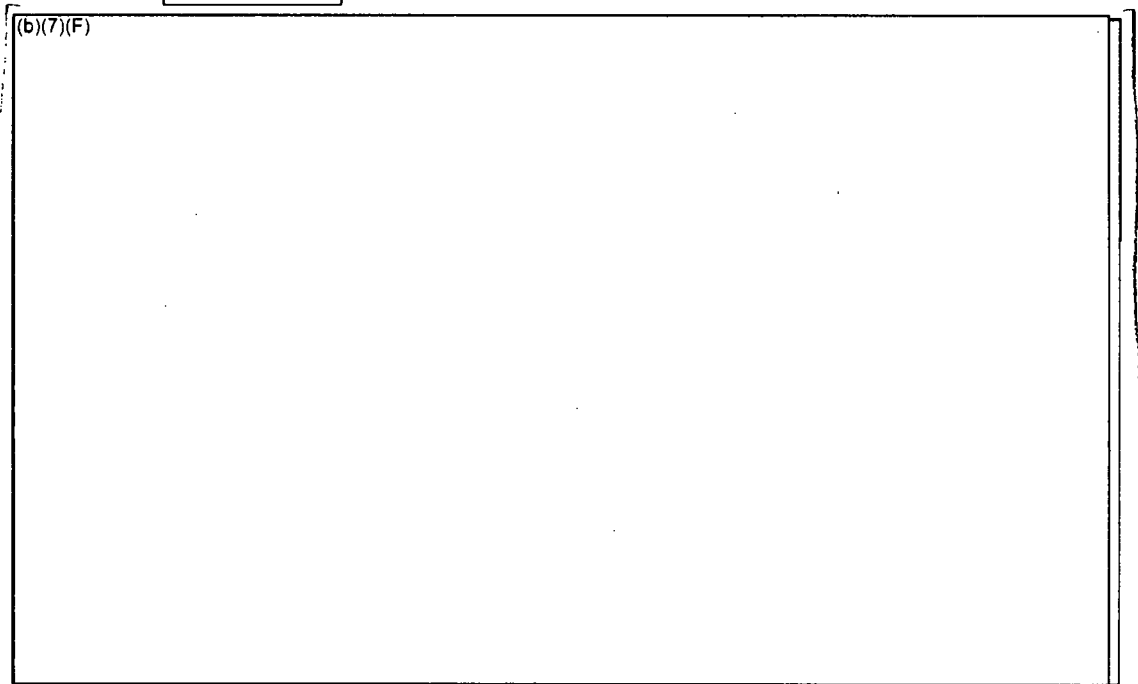
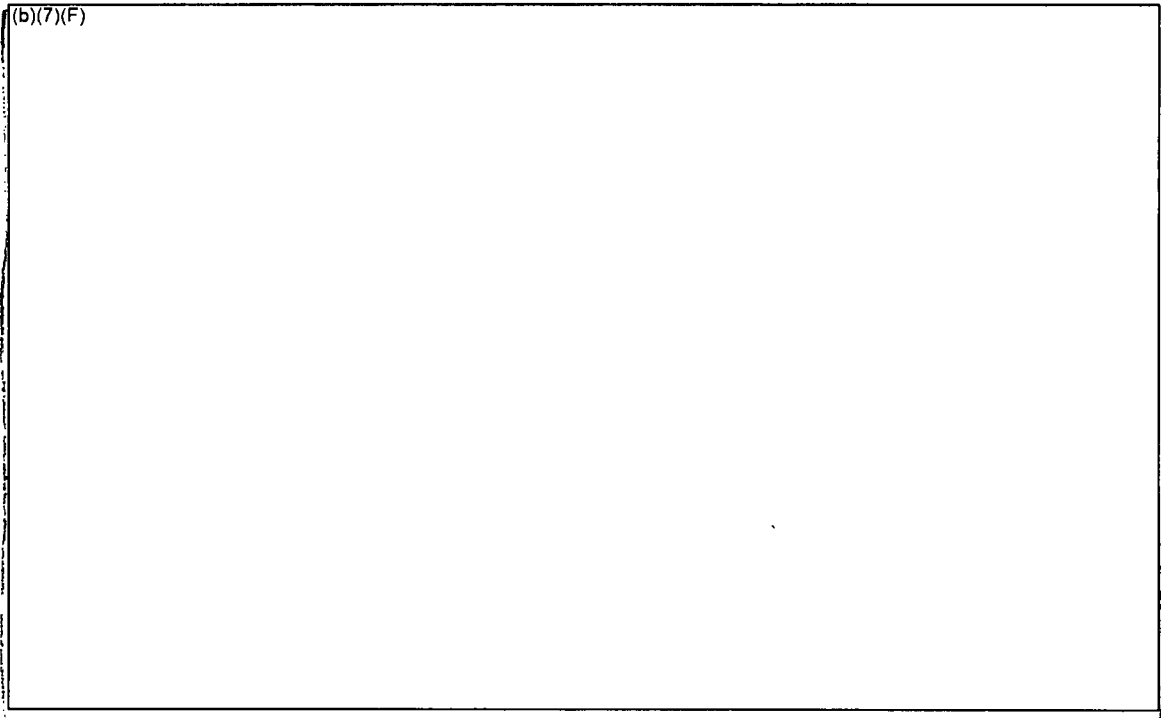
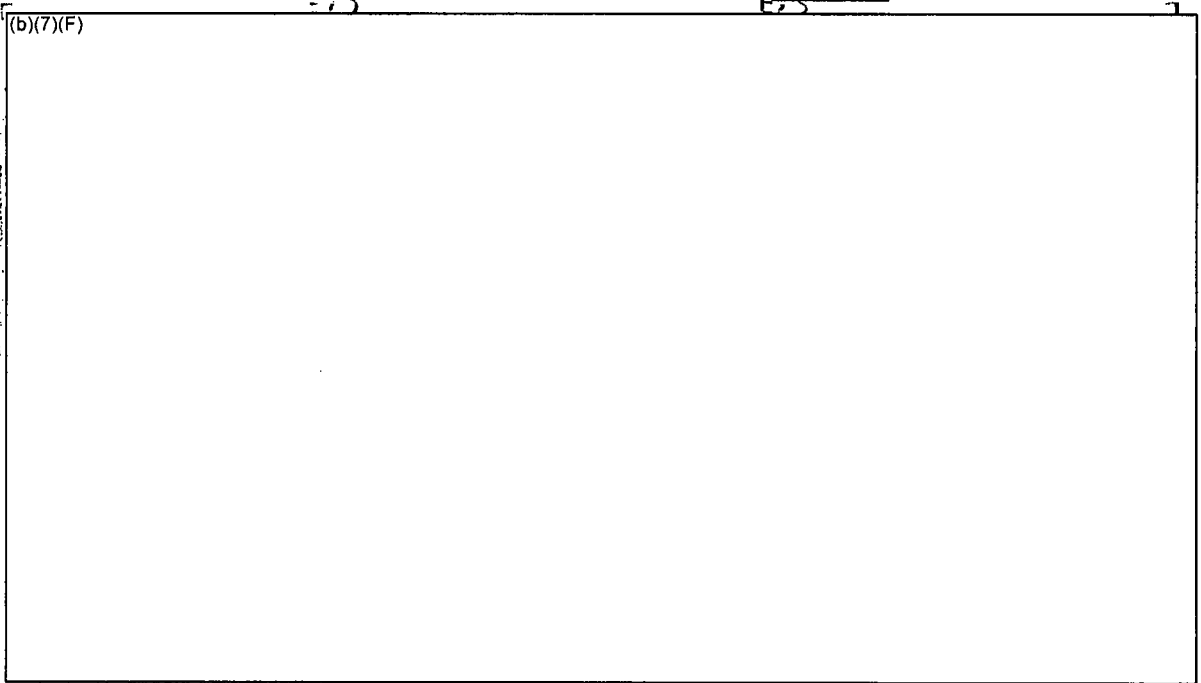


Figure 5-2 Vapor and Liquid Temperature Boundary Condition from the BWR Whole Pool Model with  $(b)(7)(F)$  and a Spray Flow of  $(b)(7)(F)$



E.7F

**Figure 5-3** Steam Partial Pressure Boundary Condition from the BWR Whole Pool Model with (b)(7)(F) and a Spray Flow of (b)(7)(F)



E.7F

**Figure 5-4** Whole Pool Level Response (b)(7)(F) with (b)(7)(F) and a Spray Flow of (b)(7)(F)

E.7F

E.7F

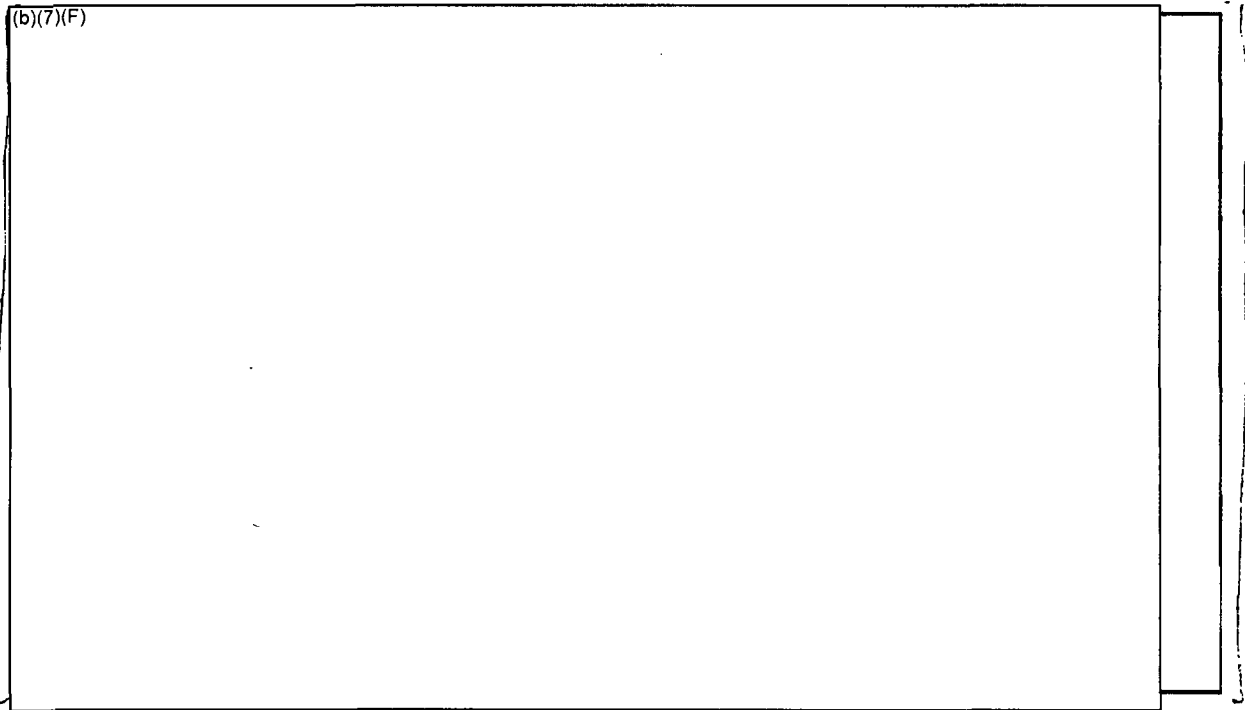


Figure 5-5 Gas Concentration in the Refueling Room above the SFP [redacted] and a Spray Flow of [redacted] Ex 7F

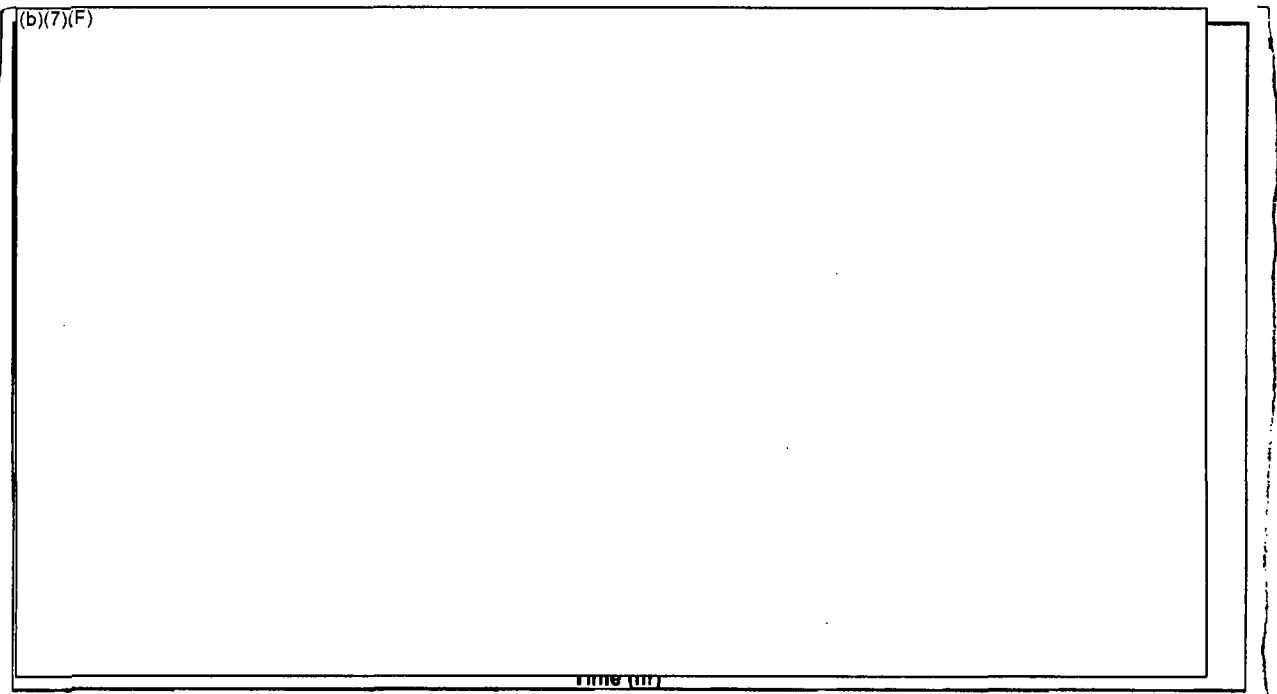


Figure 5-6 Comparison of the Leak Rate and Spray Flowrate Response [redacted] with [redacted] and a Spray Flow of [redacted] Ex 7F

## 6. MELCOR SEPARATE EFFECTS MODEL RESULTS

Section 6.1 provides a table with a coolability summary of all the separate effects spray calculation. Additional details about the uniform, checkerboard, and 1x4 configuration calculations are provided in Sections 6.2, 6.3, and 6.4, respectively.

### 6.1 Summary of Separate Effect Spray Calculations

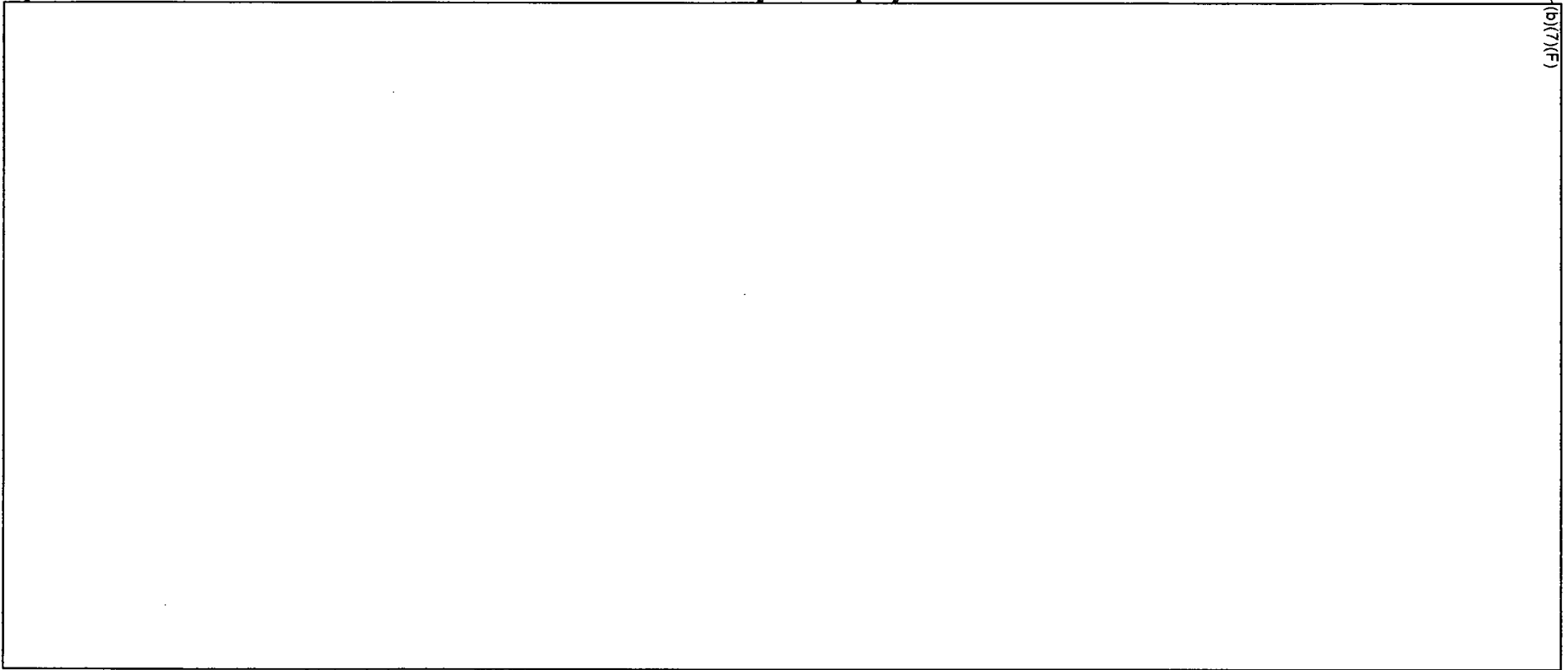
Table 6-1 summarizes the results of the spray separate effects calculations. Calculations were performed for the uniform, checkerboard, and 1x4 configurations. For each configuration, parametric calculations were performed with variations in one of the scenario or modeling attributes. The various groups of calculations are separated by bold horizontal lines in the table. The table was intended to provide a quick quantitative summary of the coolability results from the various cases. The variations in the calculations included fuel configuration (uniform checkerboard, and 1x4), aging time of the peak powered assembly, leak size (b)(7)(F), spray flow rate (b)(7)(F), air flow (some configurations that were expected to have air flow had a sensitivity study where the inlet was plugged with water), and a modeling parameter (MELCOR's flow regime model active or inactive).

The high level results are presented in the last two columns of the table. (b)(7)(F)

(b)(7)(F)

(b)(7)(F). Additional details about the uniform, checkerboard, and 1x4 configurations are provided in Sections 6.2, 6.3, and 6.4, respectively.

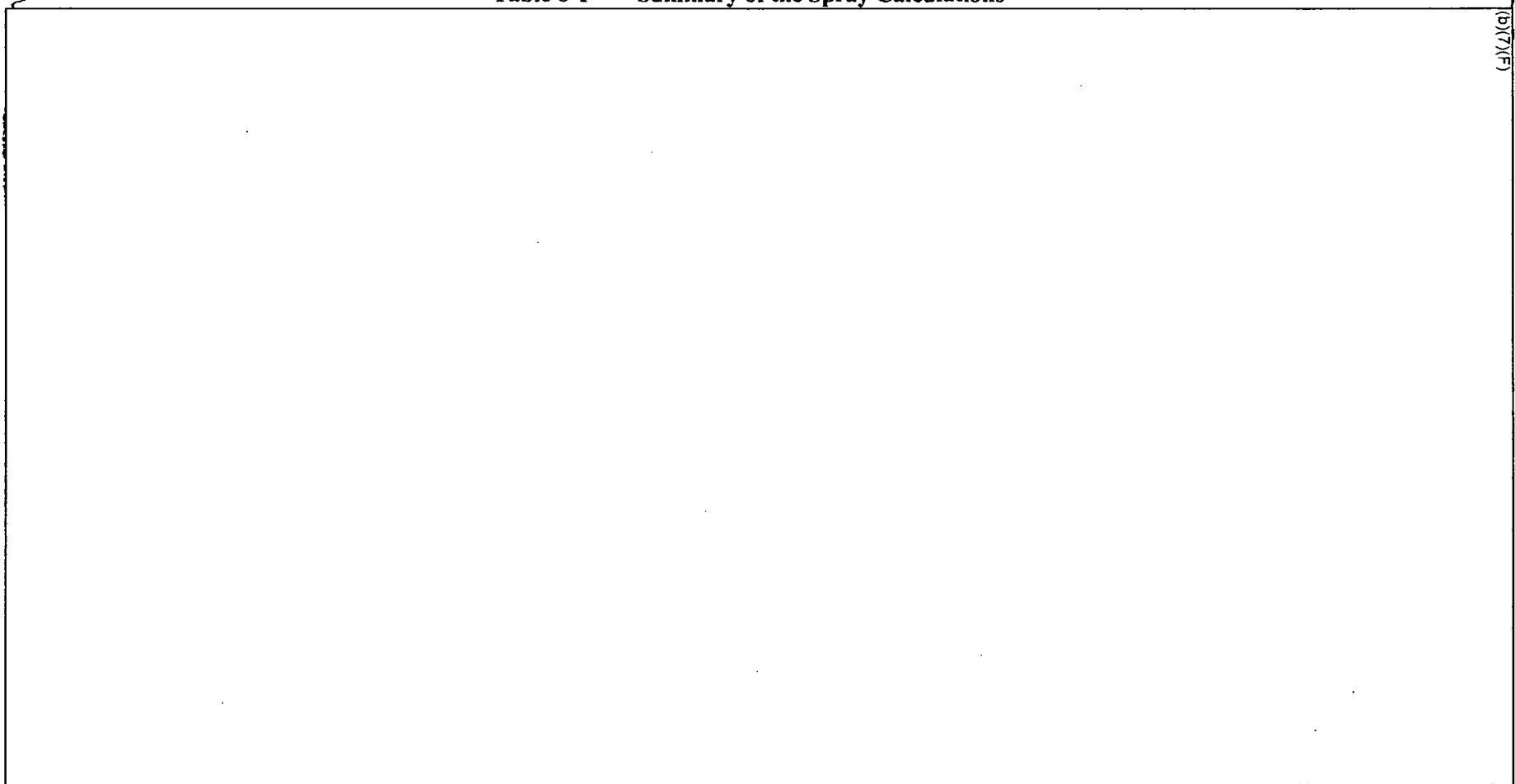
Table 6-1 Summary of the Spray Calculations



(b)(7)(F)

Exif

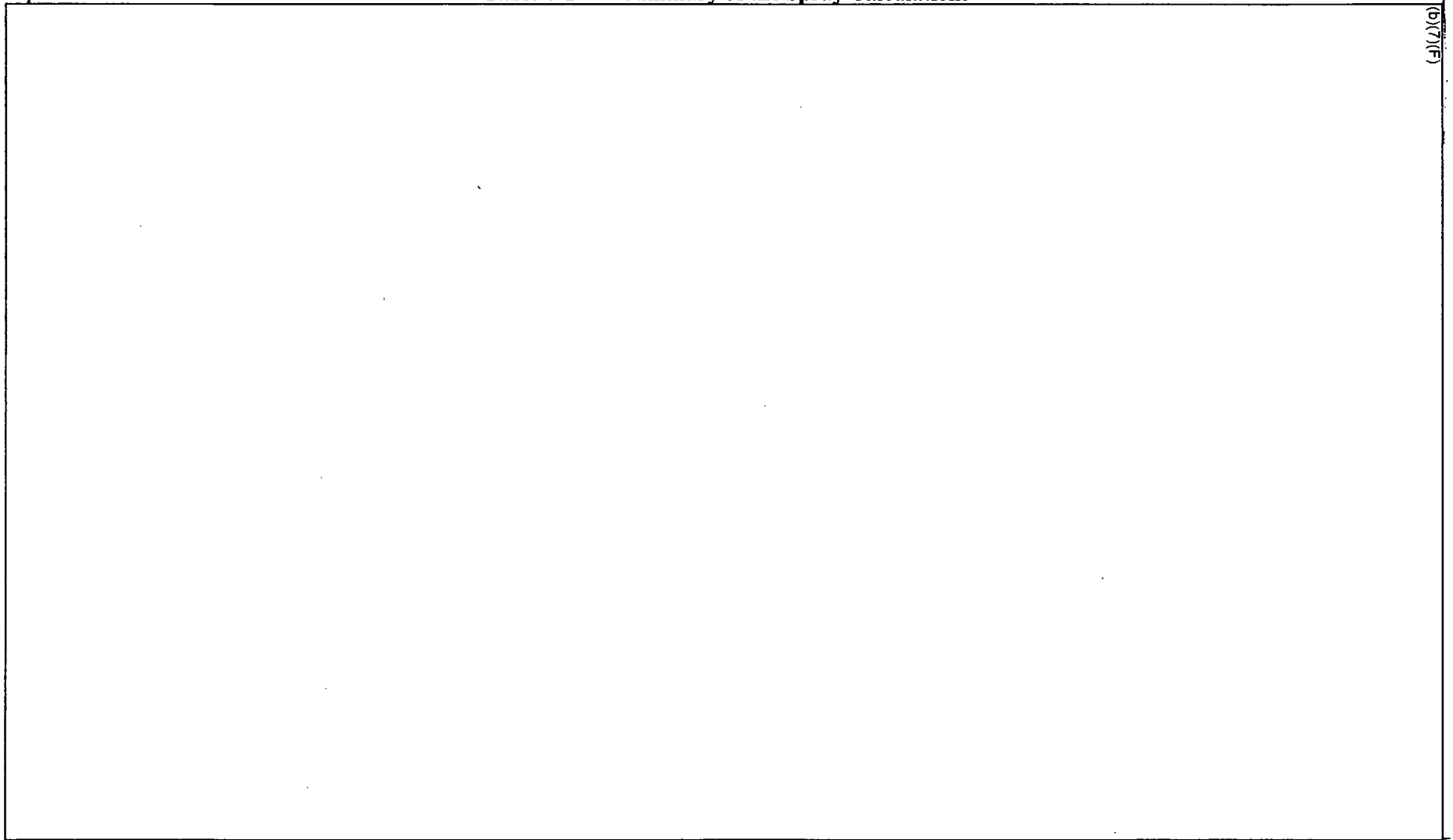
Table 6-1 Summary of the Spray Calculations



(b)(7)(X)(F)

X7F

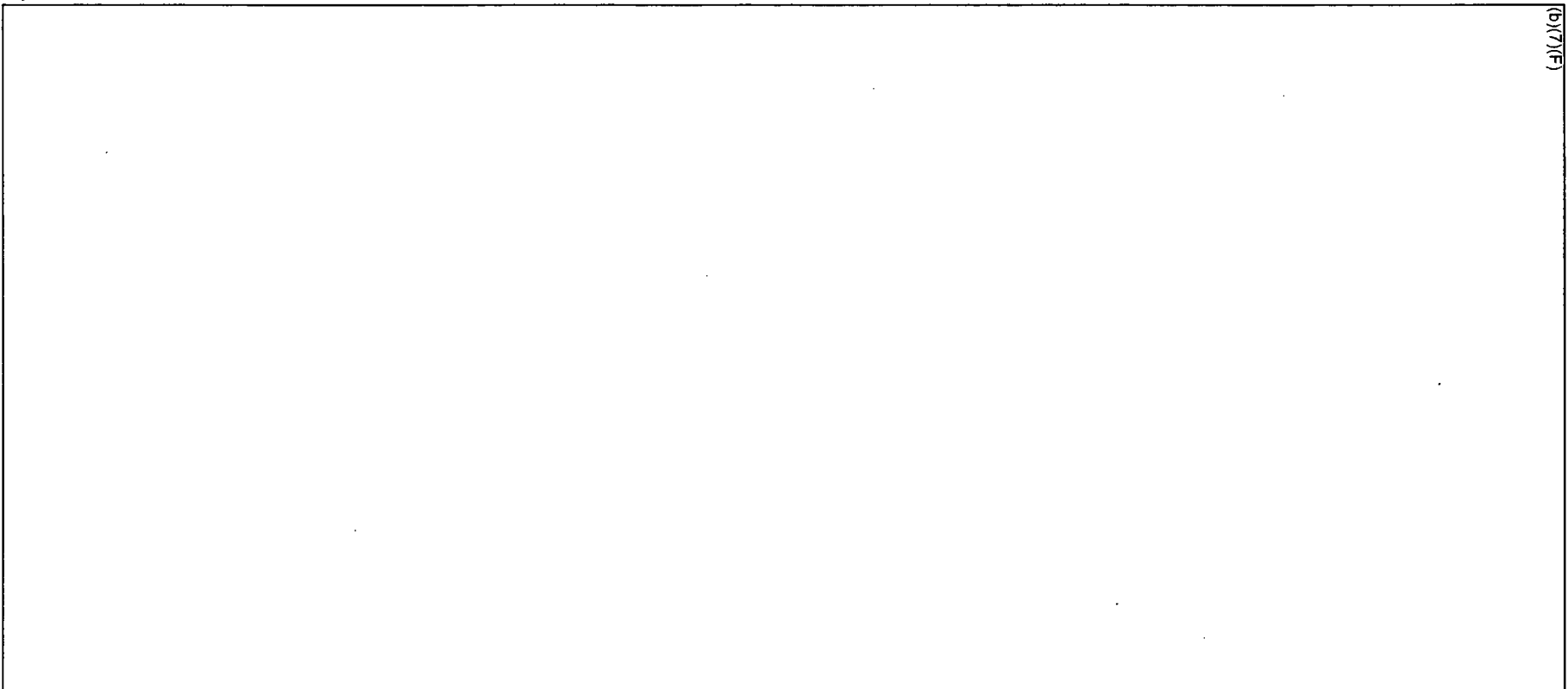
Table 6-1 Summary of the Spray Calculations



(b)(7)(F)

Ex 7F

~~OFFICIAL USE ONLY - SECURITY-RELATED INFORMATION~~



(b)(7)(F)

Ex 7F

~~OFFICIAL USE ONLY - SECURITY-RELATED INFORMATION~~

## 6.2 Separate Effects Spray Model Results for the Uniform Configuration

Section 6.2.1 gives a summary of the 4 cases with (b)(7)(F) (b)(7)(F) leakage hole in a uniform fuel configuration. The four cases examine differences in the response with and without sprays and with and without the flow regime model active (see Section 3.1.4 for a more complete discussion). Section 6.2.2 shows the results of an energy balance on (b)(7)(F) spray case to illustrate the heat flows. Finally, Sections 6.2.3, 6.2.4, and 6.2.5 show the coolability results as a function of aging for different leakage rates and spray flow rates.

### 6.2.1 Base Calculations

(b)(7)(F)

Spray

The S1 and S5 base case configuration calculations simulated a uniform configuration of the highest powered assemblies discharged into the spent fuel pool (b)(7)(F) since reactor shutdown. The uniform configuration represents the response of an assembly in the center of a region of high-powered assemblies, such that there is negligible radial heat transfer (i.e., an adiabatic condition in the radial direction). (b)(7)(F)

(b)(7)(F)

(b)(7)(F)

Ex 7F examined differences in the response with and without sprays and with and without the flow regime model active. When the flow regime model was deactivated, the spray water has a relatively small surface contact area with the cladding. Due to the reduction of heat transfer, the spray flow penetrates more deeply into the assembly before completely evaporating. In addition, a S1 case was run where the inlet of the assembly was plugged by water. As discussed in Section 5, depending upon the hole size and the spray rate, cases were identified where the inlet to the racks could be covered. Consequently, Case S1 and S1p parametrically investigated both conditions. However, it should be noted that the best-estimate level responses (b)(7)(F) with (b)(7)(F) sprays were well below the bottom of the rack baseplate.

(b)(7)(F)

The axial temperature profiles for the four cases are shown in Figure 6-3 through Figure 6-6.

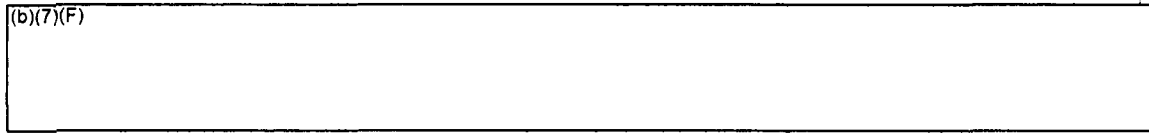
(b)(7)(F)

(b)(7)(F)

The designators in the figure legend

correspond to the COR Package nodalization shown in Figure 3-16. For example, COR-TCL.104 corresponds to the COR Package cladding temperature in Ring 1 and Level 4. Level 4 is the bottom of the active fuel and Level 12 is the top of the active fuel. Level 13 is the gas plenum at the top of the fuel rods.

The axial temperature response for the case with the flow regime model inactive is shown in Figure 6-4. (b)(7)(F)

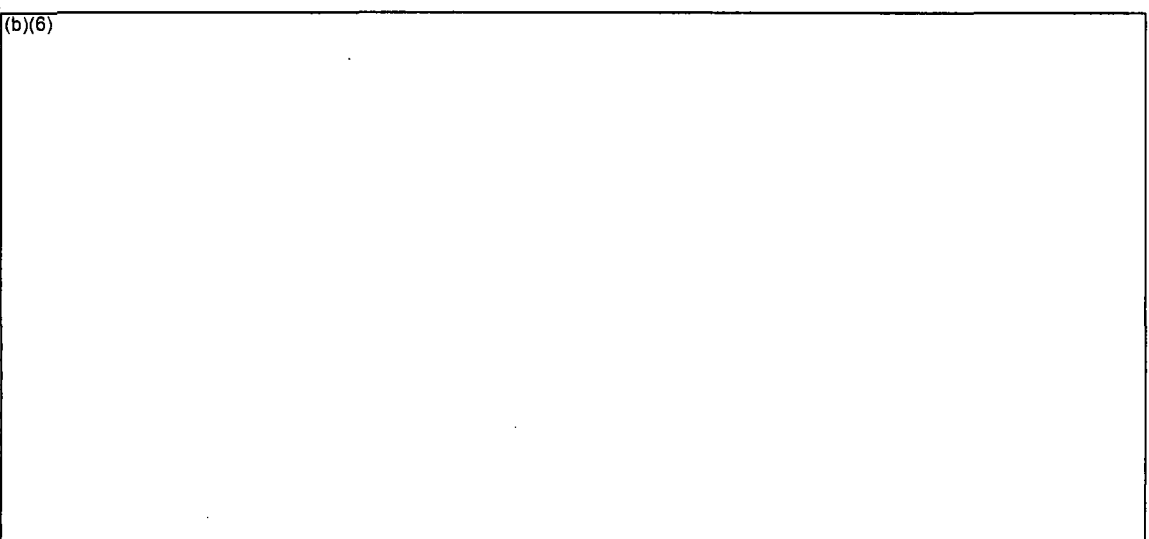


1 x 7F

The plugged case (S1p) did not have air cooling. As shown in Figure 6-1 and Figure 6-6, the peak temperature response was similar to Case S1. However, the absence of air in the assembly led to less oxidation heating and a slower heatup at high temperatures (b)(7)(F) 7F

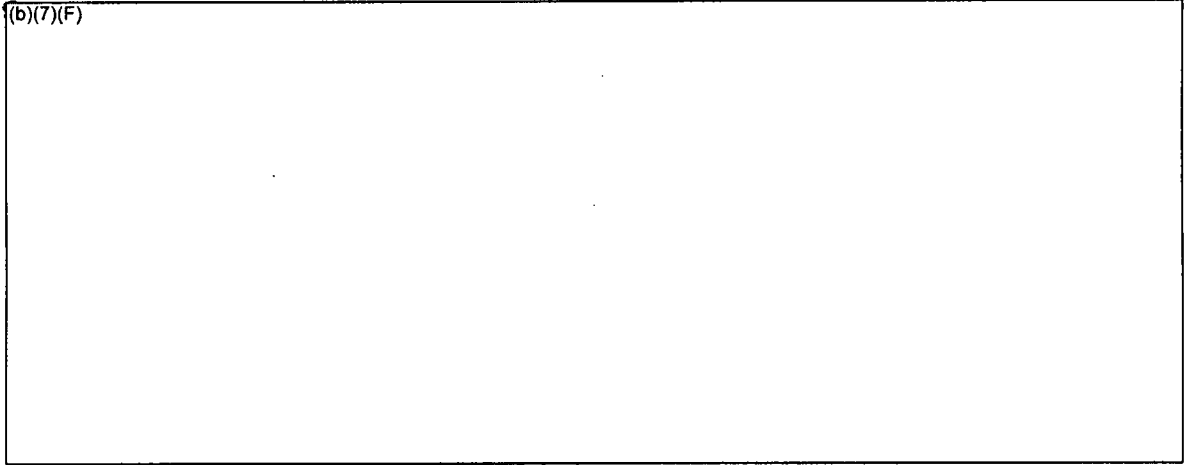
Finally, the axial temperature profiles (b)(7)(F) are shown in Figure 6-7 for all four cases. It is interesting to observe that the peak cladding temperature somewhat follows the axial power profile in the case without spray.<sup>19</sup> In contrast, the cases with spray flow are much cooler at the top of the assembly. Both the base case (S1) and the plugged case (S1p) used the flow regime model, which enhanced heat removal at the top of the assembly. However, due to the large mismatch between the heat generation rate and the heat removal (also see Section 6.2.2), the region at the top of the assembly still oscillated between film and nucleate boiling (e.g., see temperature responses in Figure 6-3 and Figure 6-6). Conversely, the non-flow regime case spray was less effective at the top but penetrated deep into the assembly (b)(7)(F) 7F

(b)(7)(F) The net effect was to slightly delay heatup relative to the other cases.



7F

<sup>19</sup> This axial profile trend will change if the assembly reached a steady state temperature profile or if the heating rate was lower. (b)(7)(F) 7F



(b)(7)(F)

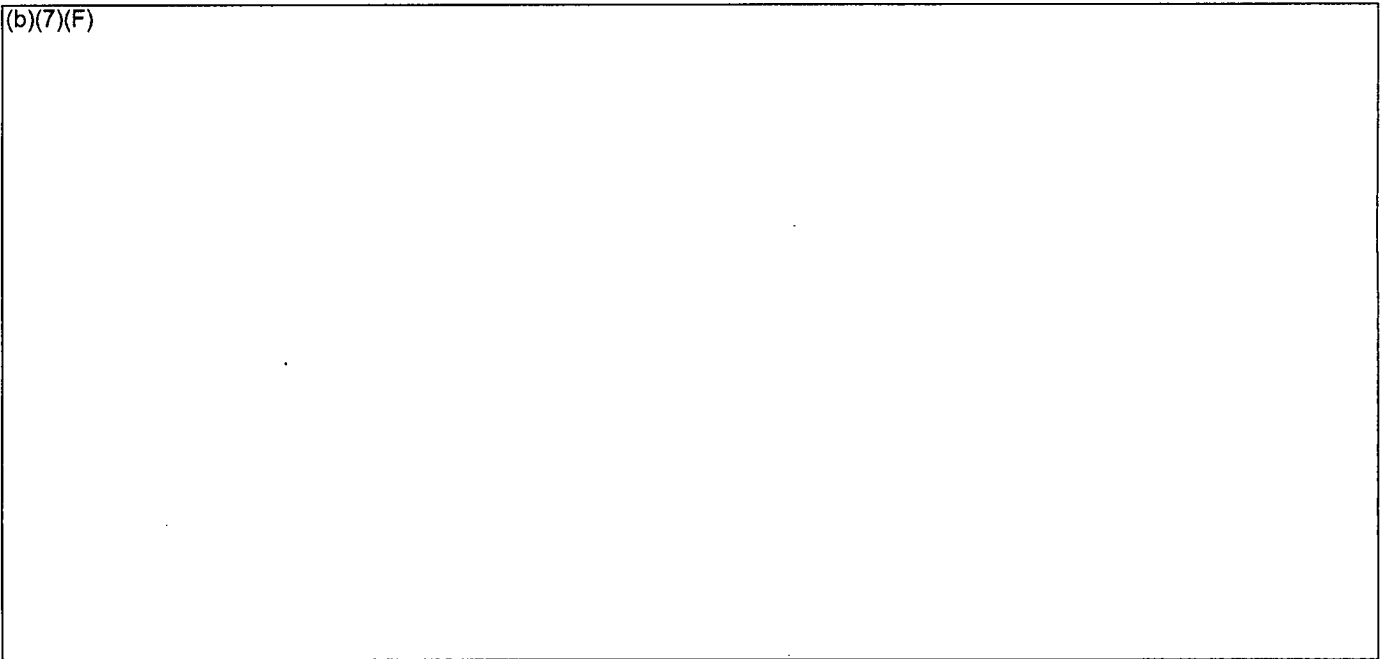
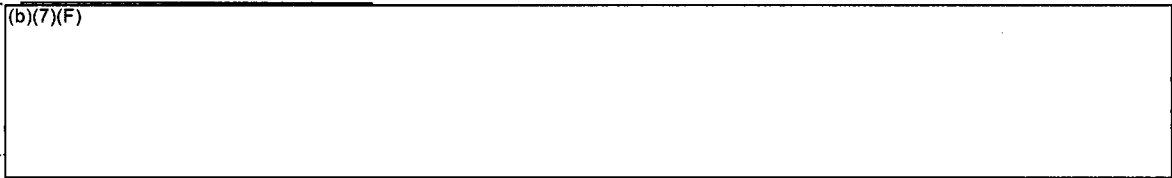
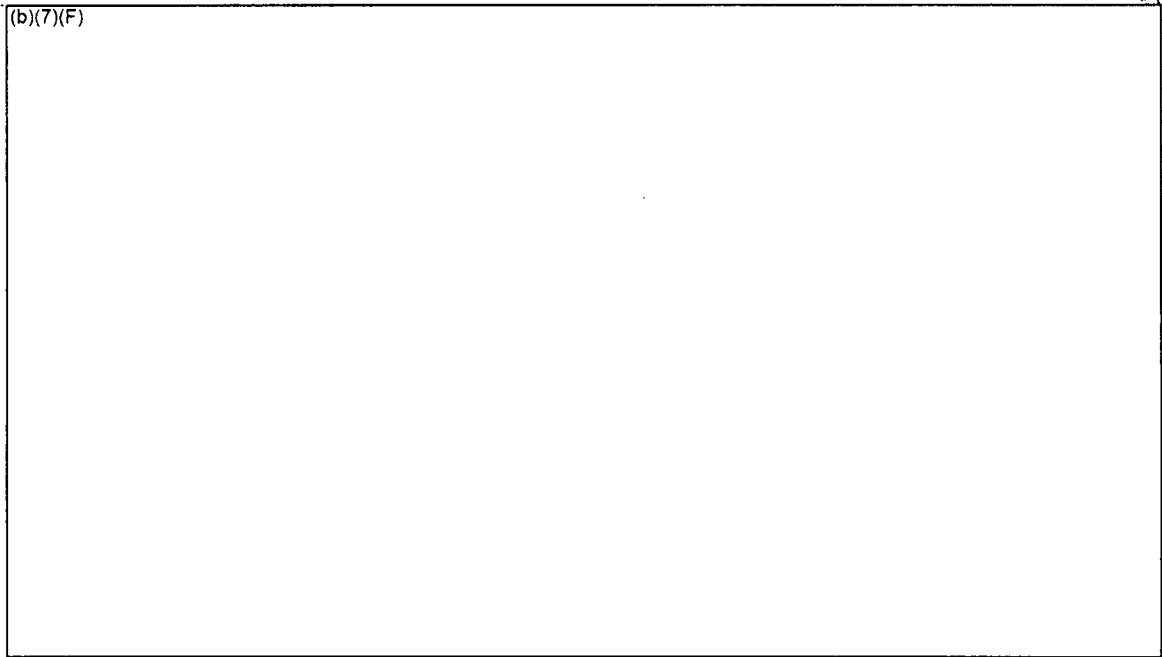


**Figure 6-1** Comparison of the Peak Cladding Temperatures (b)(7)(F) with a Uniform Configuration with (b)(7)(F) and a Whole Pool Spray Flow of (b)(7)(F)

(b)(7)(F)



(b)(7)(F)



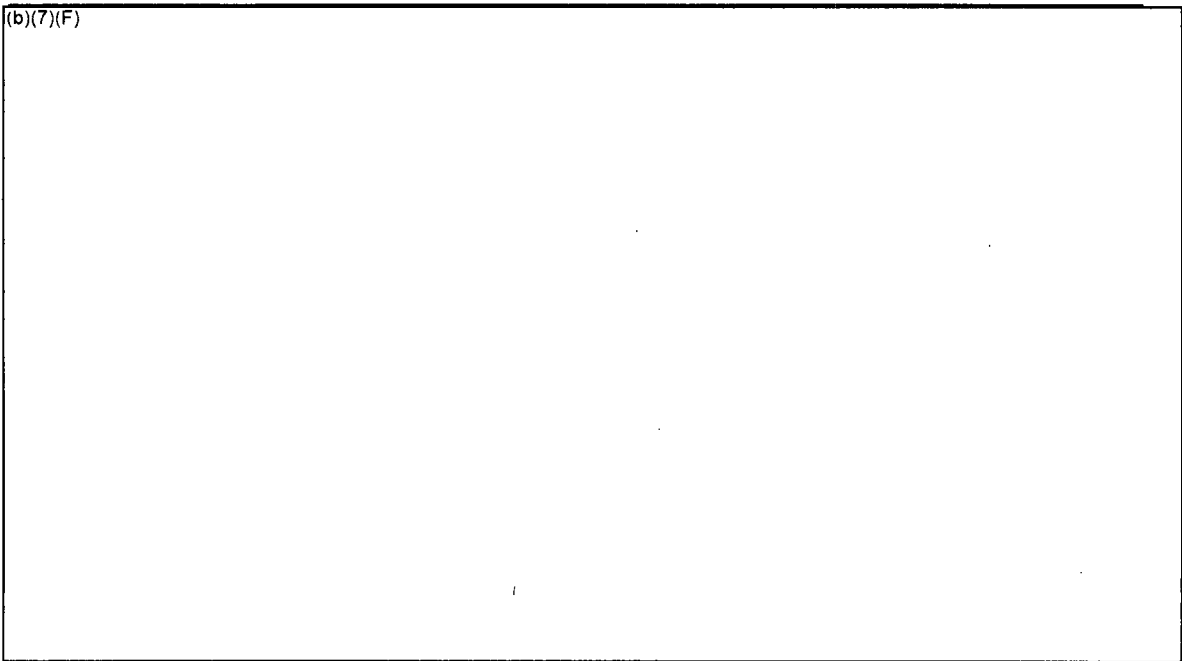
.7F

Figure 6-2 Comparison of the Peak Cladding Temperatures (b)(7)(F) with a Uniform Configuration with (b)(7)(F) and a Whole Pool Spray Flow of (b)(7)(F)

.7F

(b)(7)(F)

x .7F



3.7F

Figure 6-3 Assembly Cladding Temperatures for the Uniform Configuration with (b)(7)(F) Spray Flow (Case S1).

3.7F

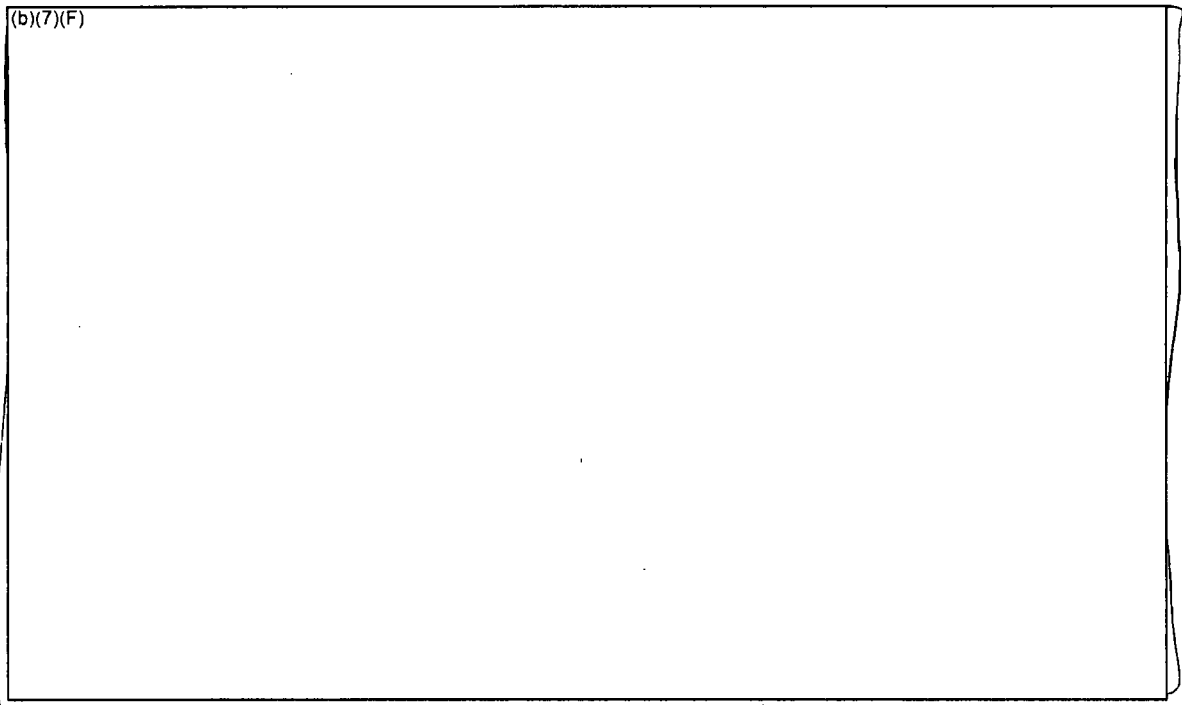


Figure 6-4 Assembly Cladding Temperatures for the Uniform Configuration with (b)(7)(F) Spray Flow, and the Flow Regime Model Inactive (Case S1a). Ex 7F

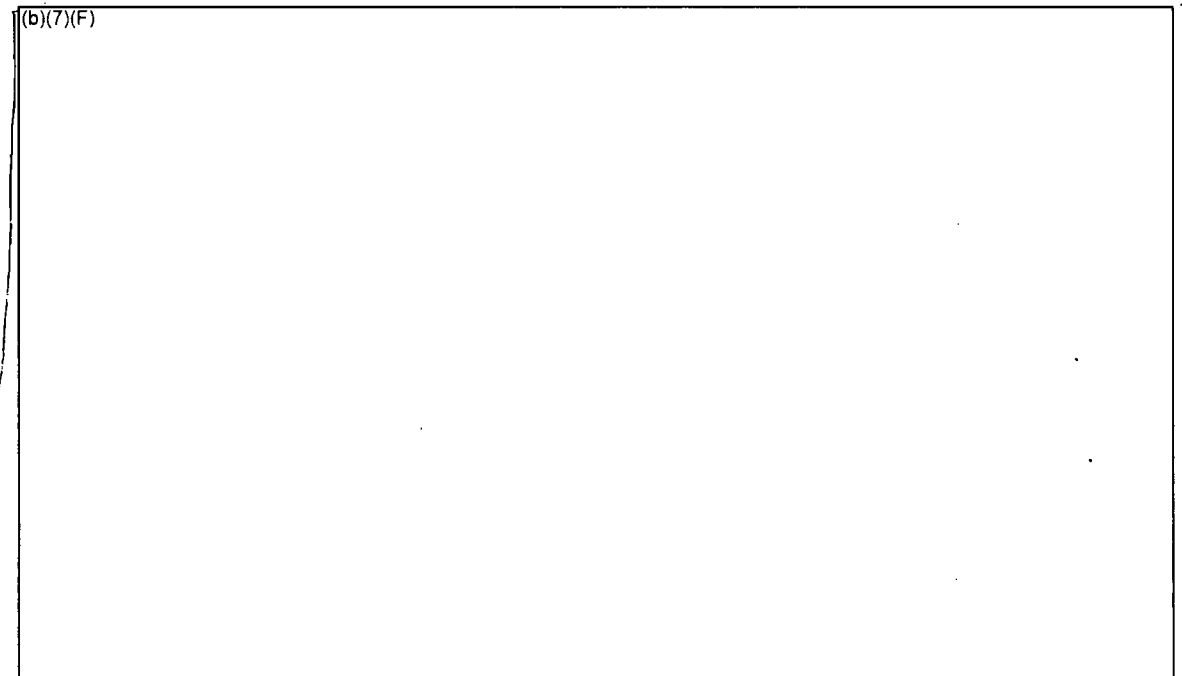
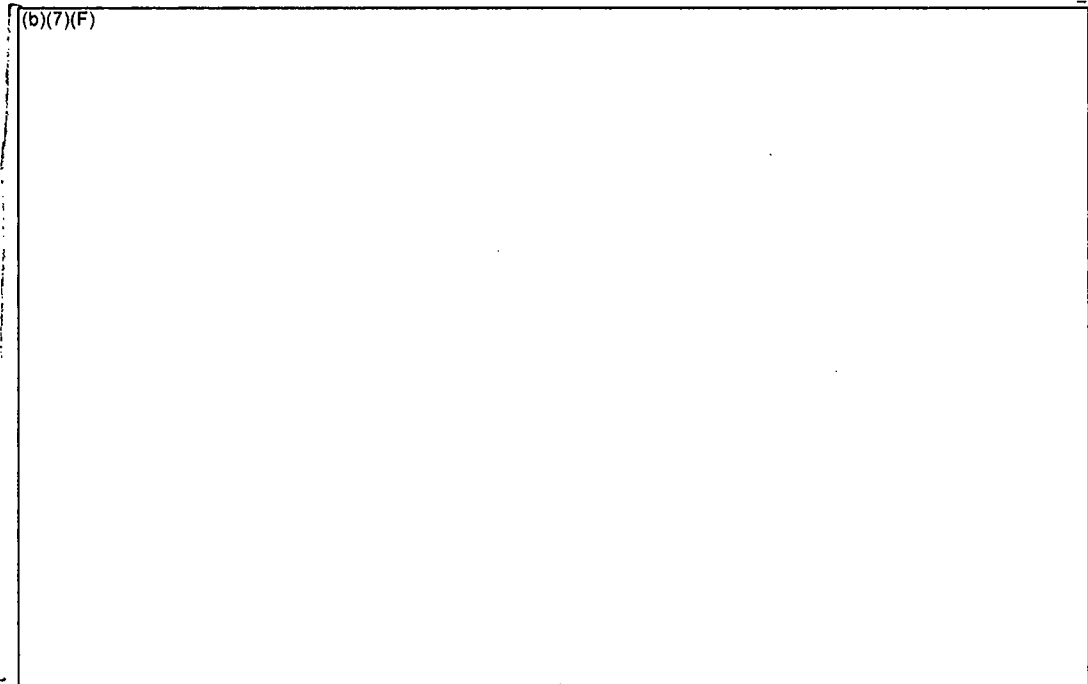
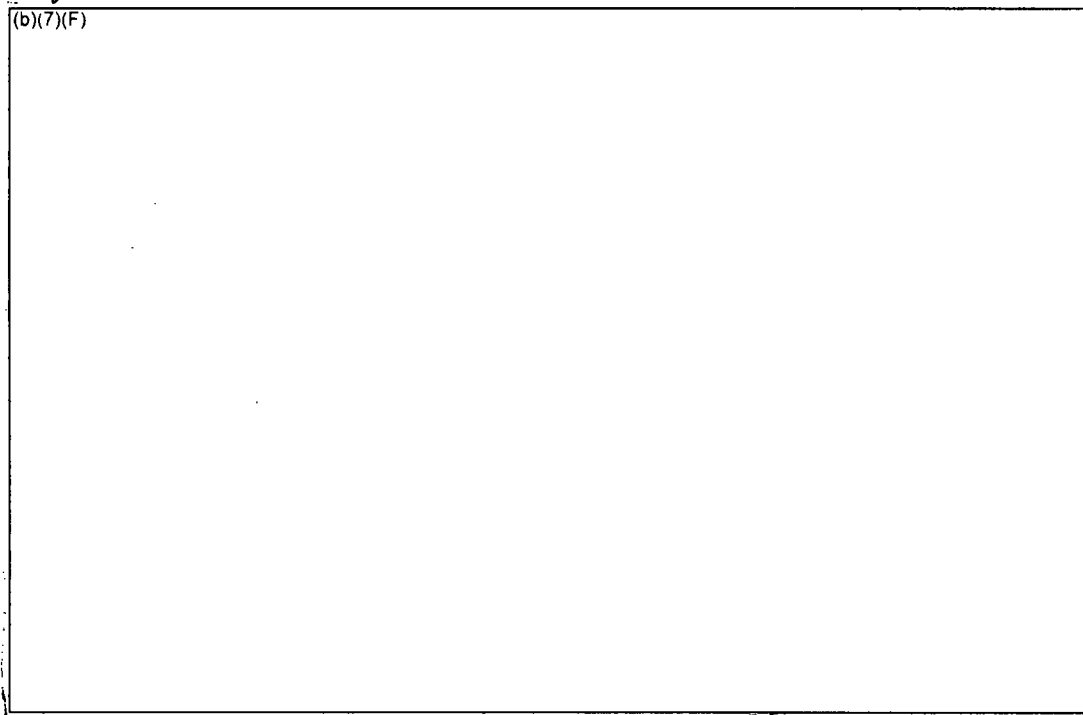


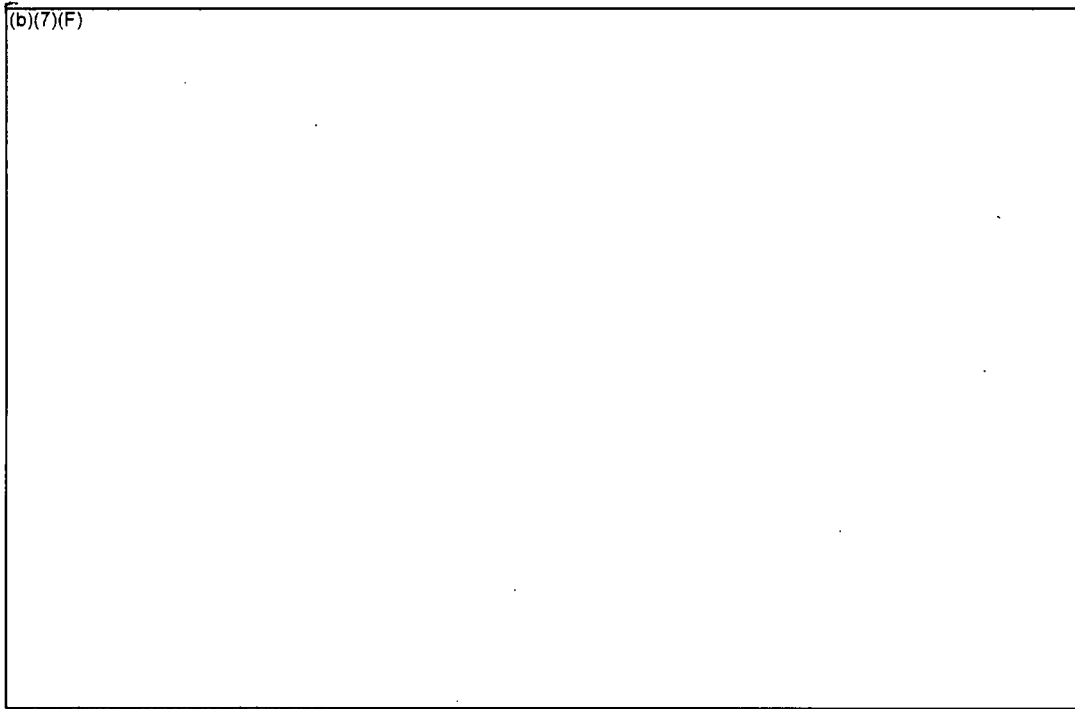
Figure 6-5 Assembly Cladding Temperatures for the Uniform Configuration with (b)(7)(F) and No Spray Flow (Case S1b). Ex 7F



*Ex 7F*  
**Figure 6-6 Assembly Cladding Temperatures for the Uniform Configuration with**  
**(b)(7)(F) Spray Flow and Plugged Inlet (Case S1p).**

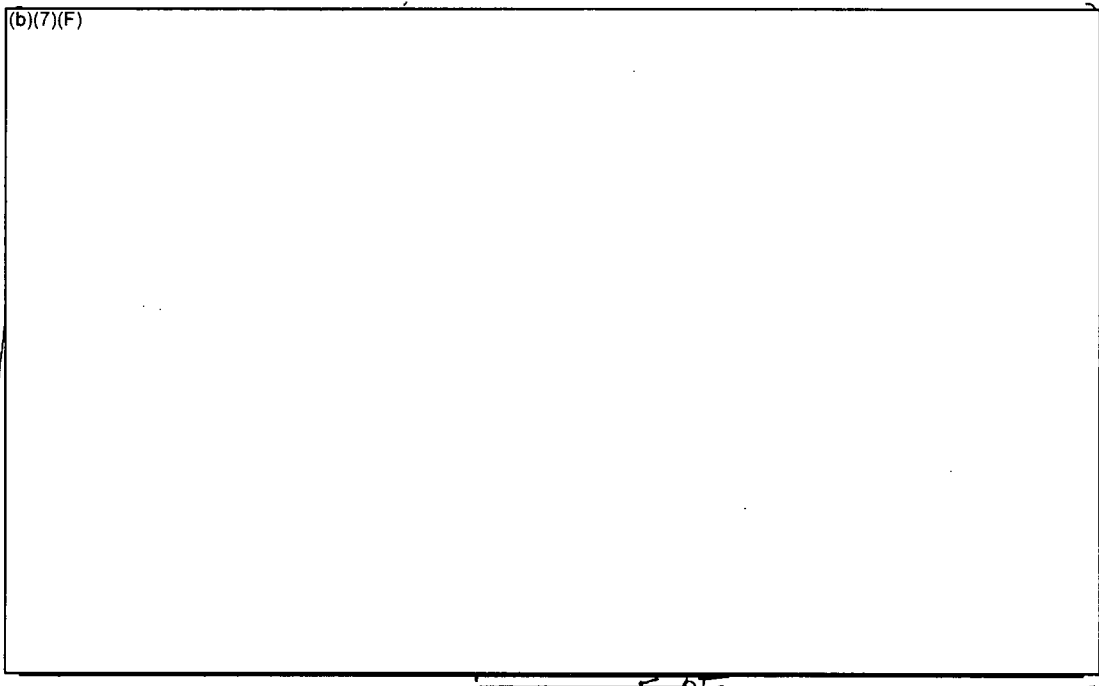


**Figure 6-7 Axial Cladding Temperature Profiles** **(b)(7)(F)** **Uniform**  
**Configuration, (b)(7)(F) Spray Flow (b)(7)(F)**  
*Ex 7F* *Ex 7F*



Ex 7F

Figure 6-8 Axial Temperature Profiles (b)(7)(F) Uniform Configuration, (b)(7)(F) Spray Flow as a Function of Time.



Ex 7F

Figure 6-9 Axial Temperature Profiles (b)(7)(F) Uniform Configuration, (b)(7)(F) and No Spray Flow as a Function of Time.

Ex 7F

6.2.2 Energy Balance on Base Calculation Spray

(b)(7)(F)

Ex 7F

An energy balance was performed on the S1 case with the flow regime model operating. This energy balance is somewhat less useful than the ones done for the checkerboard and 1x4 configurations because the assembly did not reach steady conditions.

(b)(7)(F)

Ex 7F

Figure 6-10 graphically shows the key heat flows in the model.

Meanwhile, the structure energy is increasing thereby signifying a steady increase in its temperature. The net heat removal by the gas

(b)(7)(F)

Ex 7F

when the exit enthalpy flow diminishes due to the rapid consumption of oxygen and a slight cooling of the exit gases<sup>21</sup>. The net heat balance is the sum of the heat flow terms besides the decay power (i.e., it should be approximately equal to the decay heat power<sup>22</sup>).

The energy balance is reported in Table 6-2 during a period before rapid oxidation (see Figure 6-3). The total power put into the assembly is a

(b)(7)(F)

Ex 7F

combination of the decay heat

(b)(7)(F)

Ex 7F

and oxidation power. The resultant distribution of that power is of the energy going into the structures and being removed by the gas (i.e., the combination of air flow and steam from boiled spray water).

(b)(7)(F)

Ex 7F

Since the liquid spray flow entering the assembly was completely boiled to steam, liquid component is only adding energy from a phasic enthalpy removal perspective. In summary, there was a large difference between the heat removal and the total heat generation

(b)(7)(F)

Ex 7F

(b)(7)(F)

Ex 7F

(b)(7)(F)

Ex 7F

<sup>21</sup> The oxygen concentration exiting the center assembly and all other gas component mass flows (i.e., nitrogen and steam) remained approximately the same. The exit gas temperature, because of slightly more effective cooling by the spray flow (i.e., slower gas velocity). The spray cooling effect was more effective than the increased heating near the high oxidation location. Since more mass was entering than leaving and the exit gases were cooled by the spray flow, the net enthalpy decreased.

(b)(6)

Ex 7F

(b)(6)

Ex 7F

Ex 7F

<sup>22</sup> The small transient differences between the net energy balance and the decay power is attributed to limitations in the access of plot quantities of all the subcomponents of the energy flow. However, the major components are shown on the figure. The MELCOR COR Package calculations have very high fidelity. For example, Case S1 had a total energy error of 0.02%.

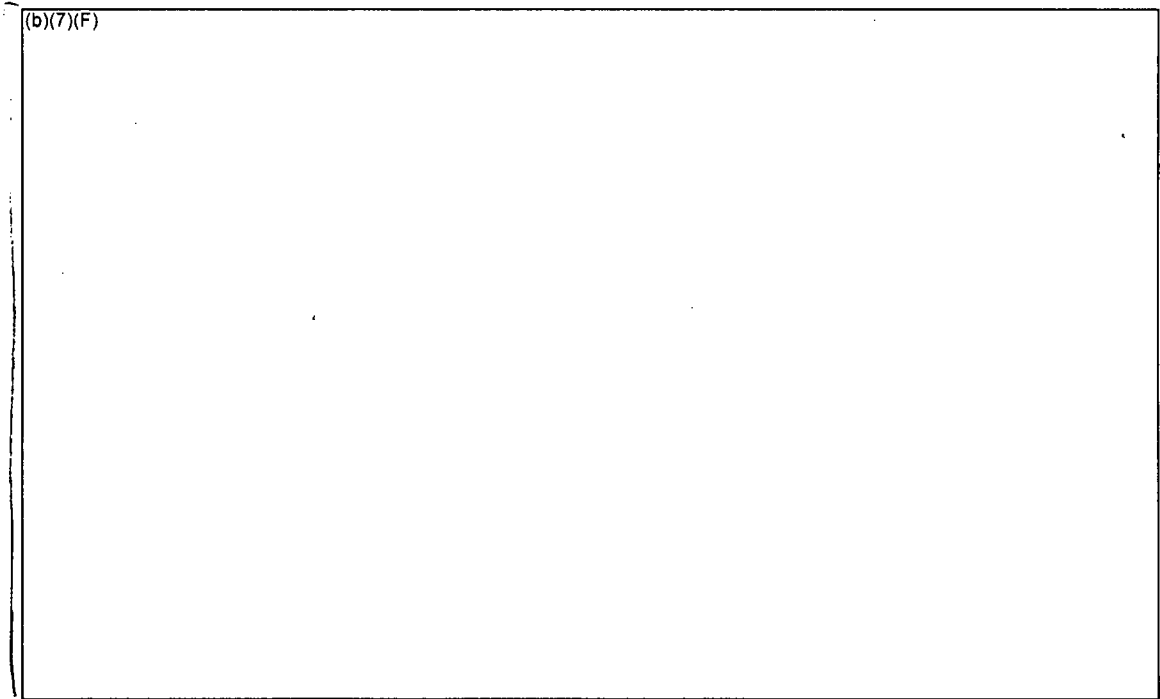


**Figure 6-10** Time-averaged Energy Flow in the Uniform Configuration with (b)(7)(F) *Ex 7F*  
(b)(7)(F) Spray Flow.

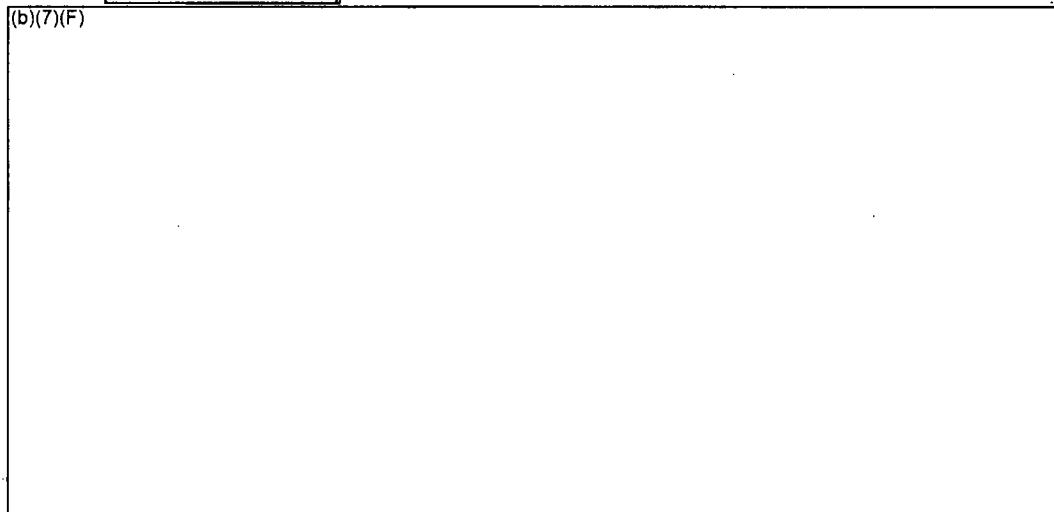
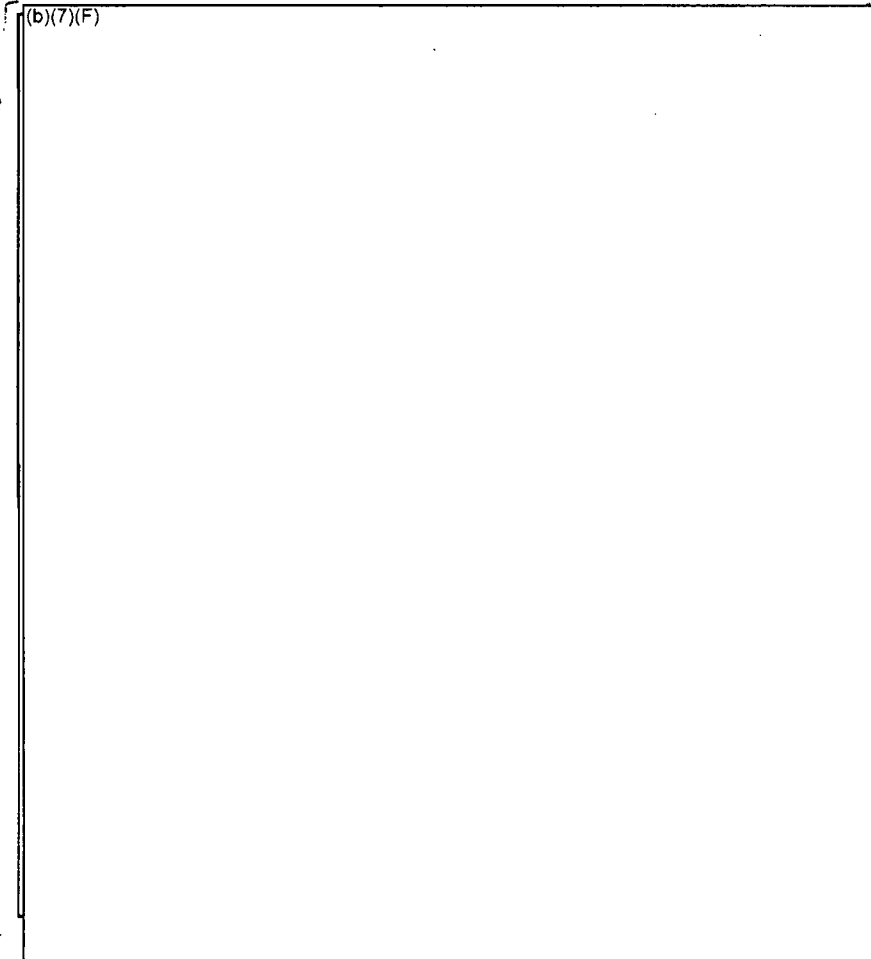


Table 6-2

Energy Balance for the Uniform Assembly Configuration in SFP with (b)(7)(F) Spray.

Ex 7F

(b)(7)(F)



Ex 7F

Ex 7F

6.2.3 Coolability Analysis (b)(7)(F) with (b)(7)(F) Spray Flowrate

A coolability analysis was done for the uniform configuration with a (b)(7)(F) spray.

A set of parametric calculations was performed with aging ranging (b)(7)(F)

(b)(7)(F) As shown previously in Section 6.2.1, an aging time (b)(7)(F)

(b)(7)(F)

(b)(7)(F) In previous separate effects calculations for the uniform configuration with air flow

but no spray flow [Wagner, 2003], (b)(7)(F)

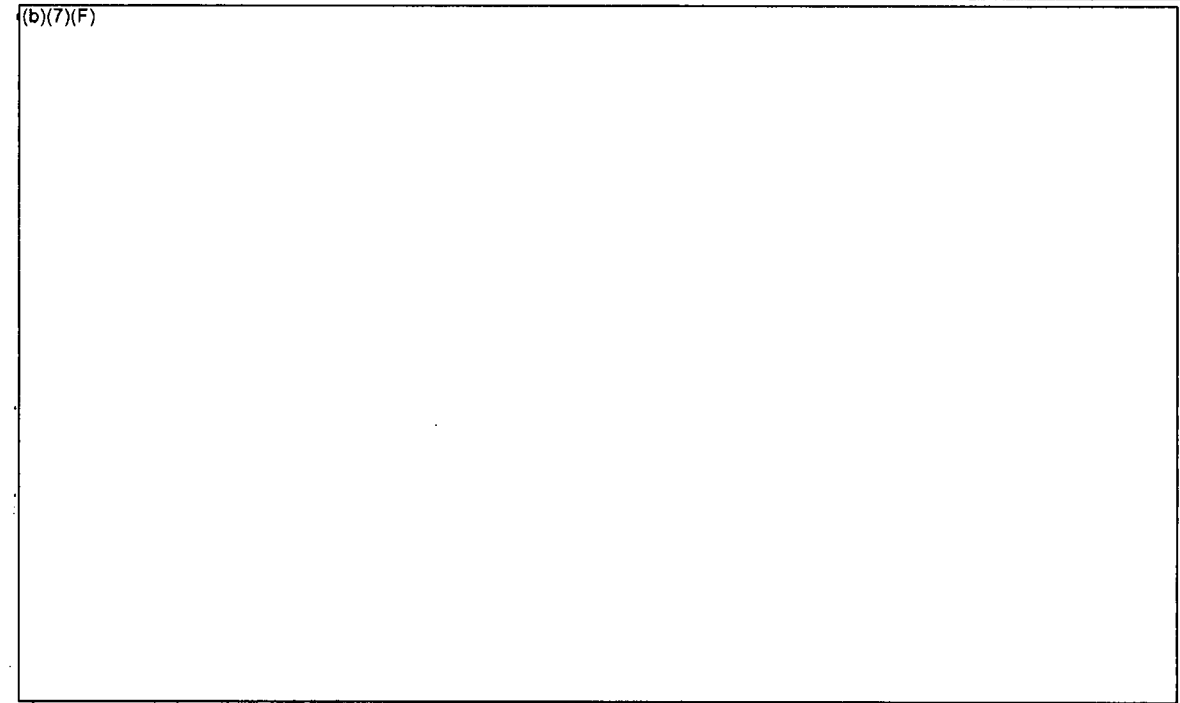
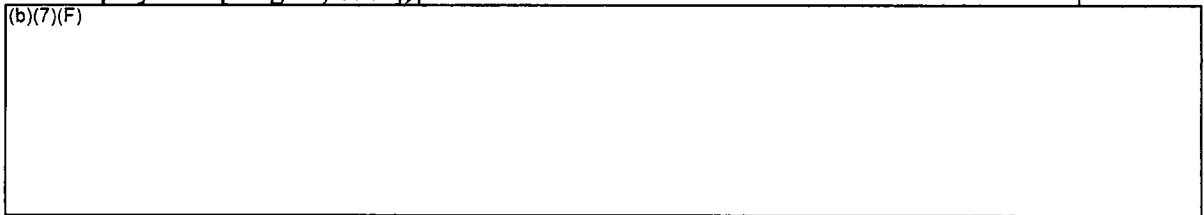
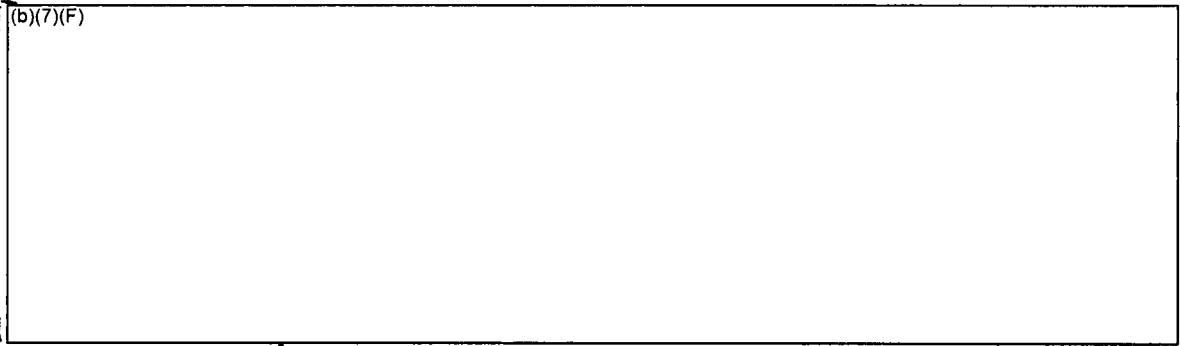


Figure 6-11 Comparison of the Peak Cladding Temperatures for the Uniform Configuration with Various Aging Periods and a Whole Pool Spray Flow of

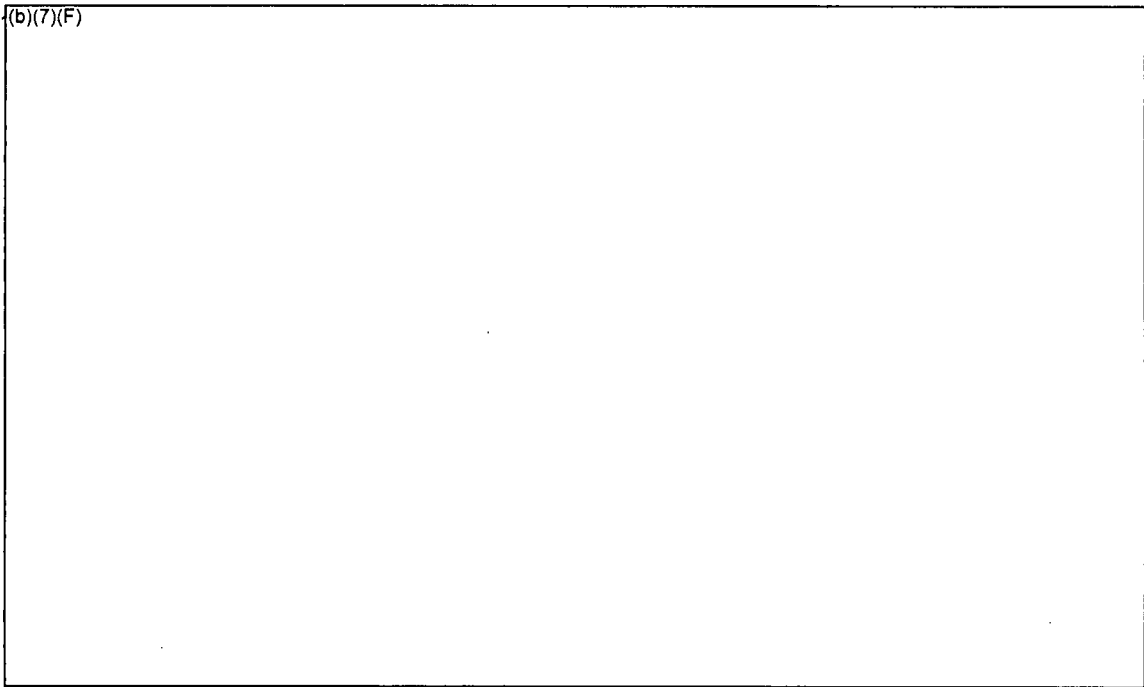
(b)(7)(F) Ex 7F

6.2.4 Coolability Analysis (b)(7)(F) with (b)(7)(F) Spray Flowrate

Ex 7F



7F



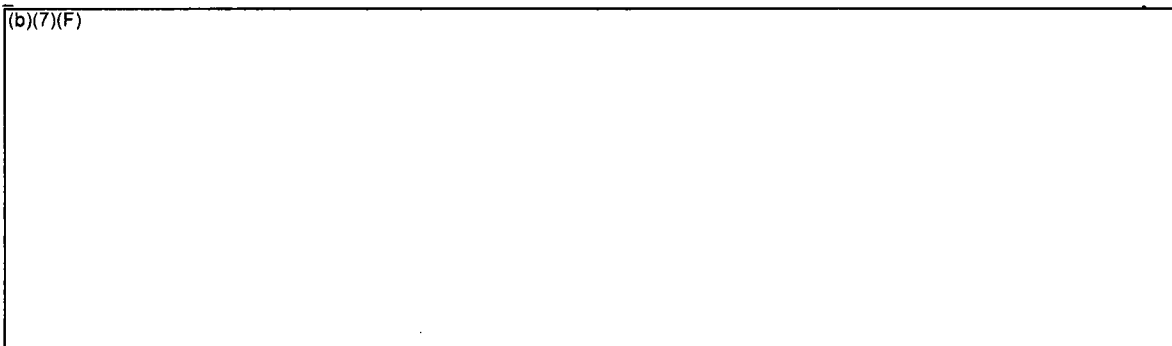
x 7F

Figure 6-12 Comparison of the Peak Cladding Temperatures for the Uniform Configuration with Various Aging Periods and a Whole Pool Spray Flow of

(b)(7)(F)

7F

6.2.5 Coolability Analysis (b)(7)(F) with (b)(7)(F) Spray Flowrate 7F



7F



x 7F

**Figure 6-13 Comparison of the Peak Cladding Temperatures for the Uniform Configuration with Various Aging Periods and a Whole Pool Spray Flow of**

(b)(7)(F) 7F

**6.3 Separate Effects Spray Model Results for the Checkerboard Configuration**

Section 6.3.1 gives a summary of the 4 cases with (b)(7)(F) hole in a uniform fuel configuration. The four cases examine differences in the response with and without sprays and with and without the flow regime model active (see Section 3.1.4 for a more complete discussion). Section 6.3.2 shows the results of an energy balance on a (b)(7)(F) spray case to illustrate the heat flows.

Ex 7F

Ex 7F

**6.3.1 Base Calculations** (b)(7)(F) Spray

Ex 7F

The S3 and S7 configuration calculations simulated a checkerboard configuration of the highest powered assemblies discharged into the spent fuel pool with (b)(7)(F) since reactor shutdown and low-powered assemblies at the median power of the reference BWR SFP (b)(7)(F). The limiting response in a checkerboard configuration represents the response of the high-powered assembly in a region of alternating high- and low-powered assemblies. Unlike the uniform configuration, the high-powered assemblies benefit from radial heat transfer to adjacent low-powered assemblies. (b)(7)(F)

(b)(7)(F)

Ex 7F

(b)(7)(F) 7F

The four (b)(7)(F) (i.e., see S3 calculations in Table 6-1) examined differences in the response with and without sprays and with and without the flow regime model active. When the flow regime model was deactivated, the spray water has a relatively small surface contact area with the cladding. Due to the reduction of heat transfer, the spray flow penetrates more deeply into the assembly before completely evaporating. In addition, a S3 case was run where the inlet of the assembly was plugged by water. (b)(7)(F)

7F

(b)(7)(F)

Figure 6-14 and Figure 6-15 show the temperature responses (b)(7)(F)

(b)(7)(F)

7F

C. 7F For completeness, the high- and low-powered cladding temperature responses from Cases S3b and S3p are shown in Figure 6-20 through Figure 6-23. In a checkerboard configuration, convective heat removal in the low-powered assemblies is particularly important. Due to radial heat transfer, (b)(7)(F) heat from the high-powered assembly in Case S3 was transferred to the peripheral assembly (see the energy balance in Section 6.3.2 for a full discussion). If the inlet is plugged, the benefit of the peripheral assembly to remove heat is greatly diminished. The peripheral assembly initially stores some of the heat from the center assembly but gradually becomes ineffective as an energy sink without simultaneous convective heat removal. In contrast, the impact of plugging in the uniform assembly configuration is less important because there is no radial heat transfer.

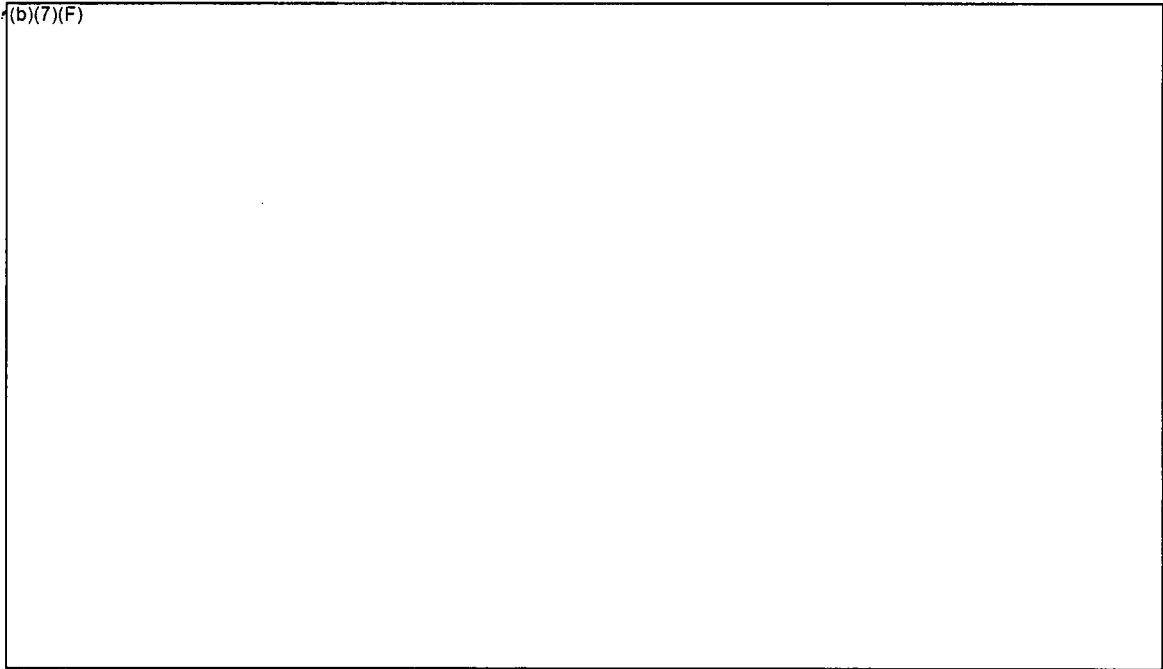
In previous separate effects calculations for the checkerboard configuration with air flow but no spray flow [Wagner, 2003], (b)(7)(F). Subsequent refinements to the BWR SFP modeling (i.e., see Section 3.1) will likely increase that value but have not yet been quantified. (b)(7)(F) (b)(7)(F). However, if water blocks or limits the air flow through the bottom of the racks, additional spray flow would be necessary to provide cooling.

7F  
7F

Finally, the high- and low-powered assembly axial temperature profiles are shown in Figure 6-24 and Figure 6-25 for all four cases, respectively. As observed in the axial temperature profiles for the uniform cases, the impact of the spray flow at the top of the assembly is clearly seen. The cases with the flow regime model active have cooler temperatures until the spray flow is depleted. The case without the flow regime model shows less heat removal at the top of the assembly but more heat removal at the bottom. In general, the temperatures are lower in the low-powered assembly and the spray penetrates deeper. Consequently, there is radial heat transfer from the high-powered assembly to the low-powered assembly. (b)(7)(F)

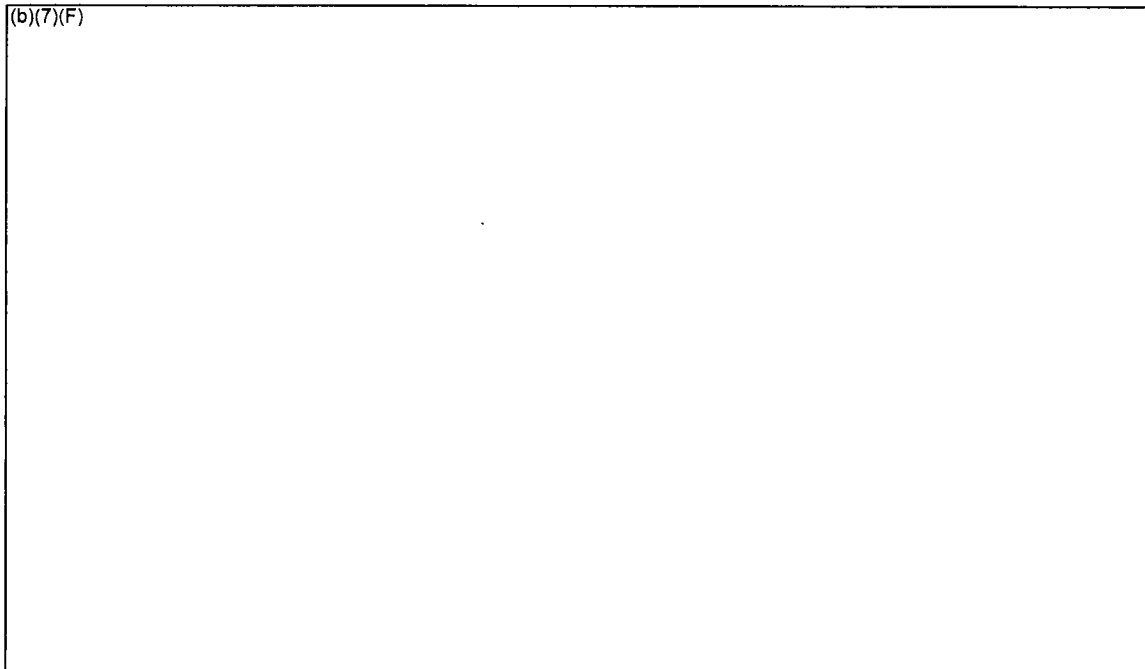
7F

(b)(7)(F)



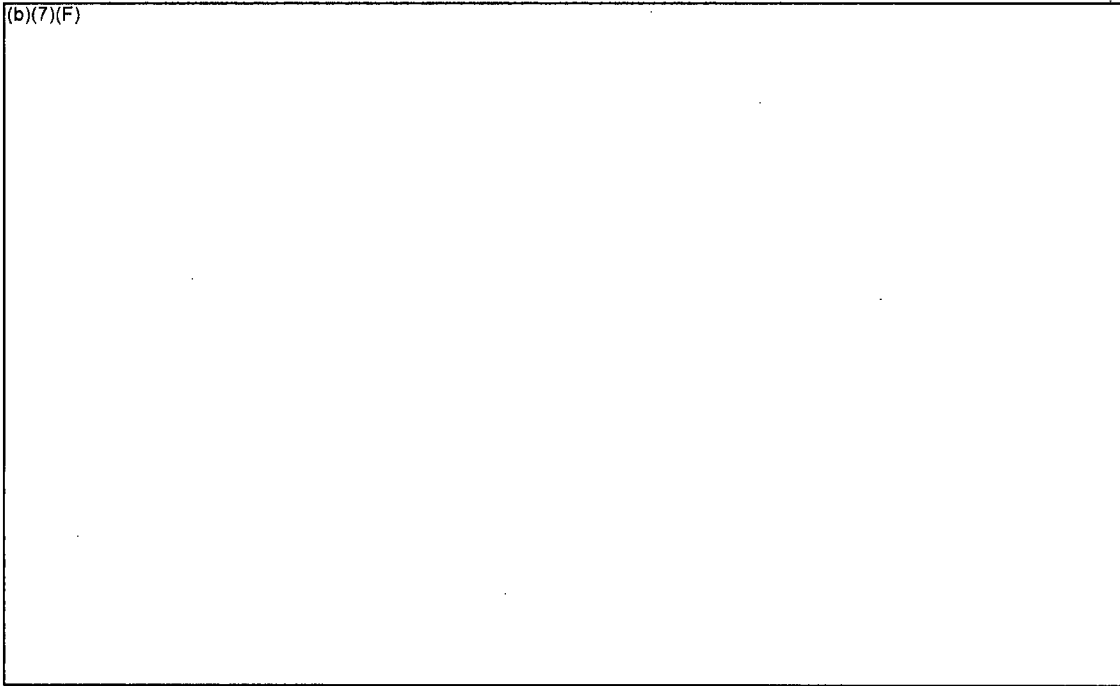
Ex 7F

**Figure 6-14** Comparison of the Peak Cladding Temperatures (b)(7)(F) with a Checkerboard Configuration with (b)(7)(F) and a Whole Pool Spray Flow of (b)(7)(F). Ex 7F Ex 7F



Ex 7F

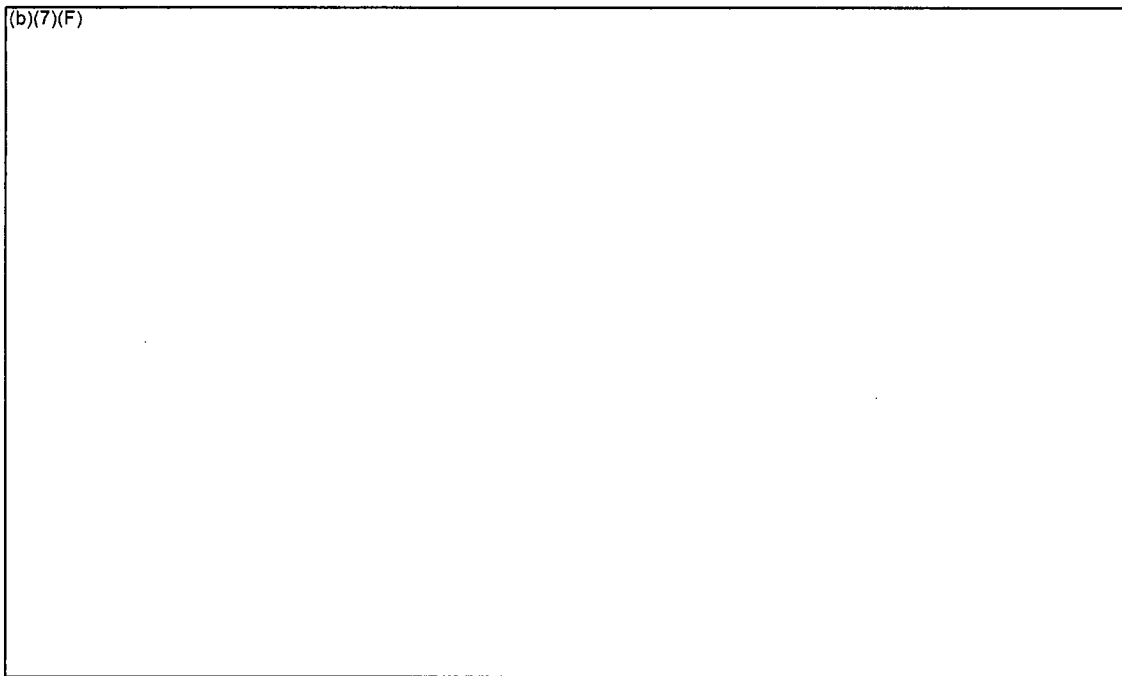
**Figure 6-15** Comparison of the Peak Cladding Temperatures (b)(7)(F) with a Checkerboard Configuration with (b)(7)(F) and a Whole Pool Spray Flow of (b)(7)(F). Ex 7F Ex 7F



Ex 7F

**Figure 6-16 High-Powered Assembly Cladding Temperatures for the Checkerboard Configuration with (b)(7)(F) Spray Flow (Case S3).**

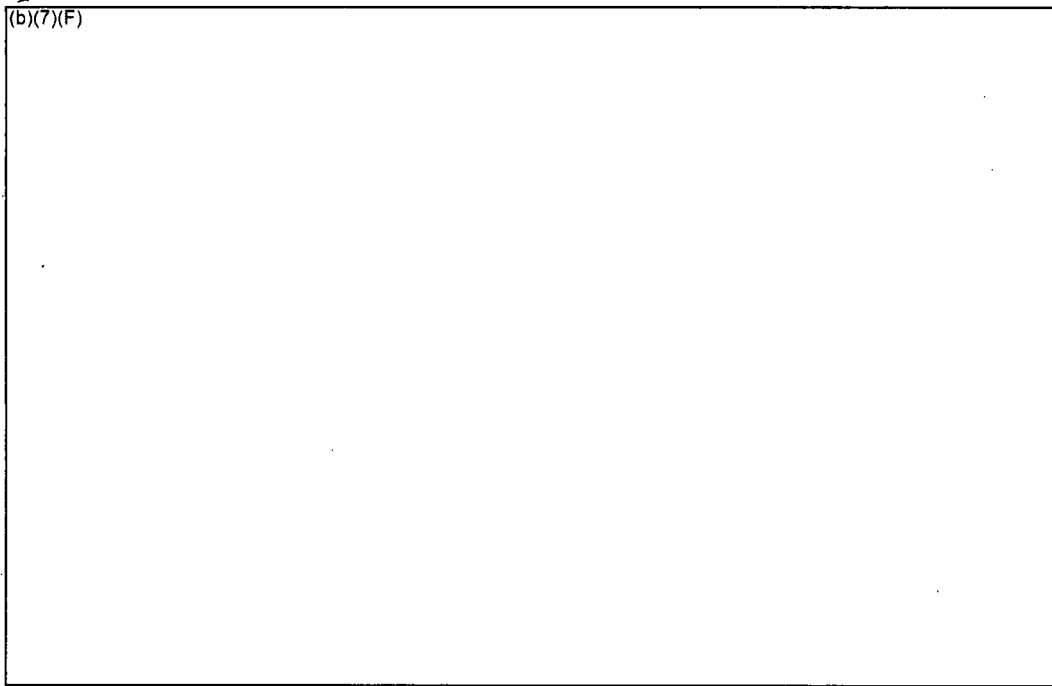
Ex 7F



Ex 7F

**Figure 6-17 Low-Powered Assembly Cladding Temperatures for the Checkerboard Configuration with (b)(7)(F) Spray Flow (Case S3).**

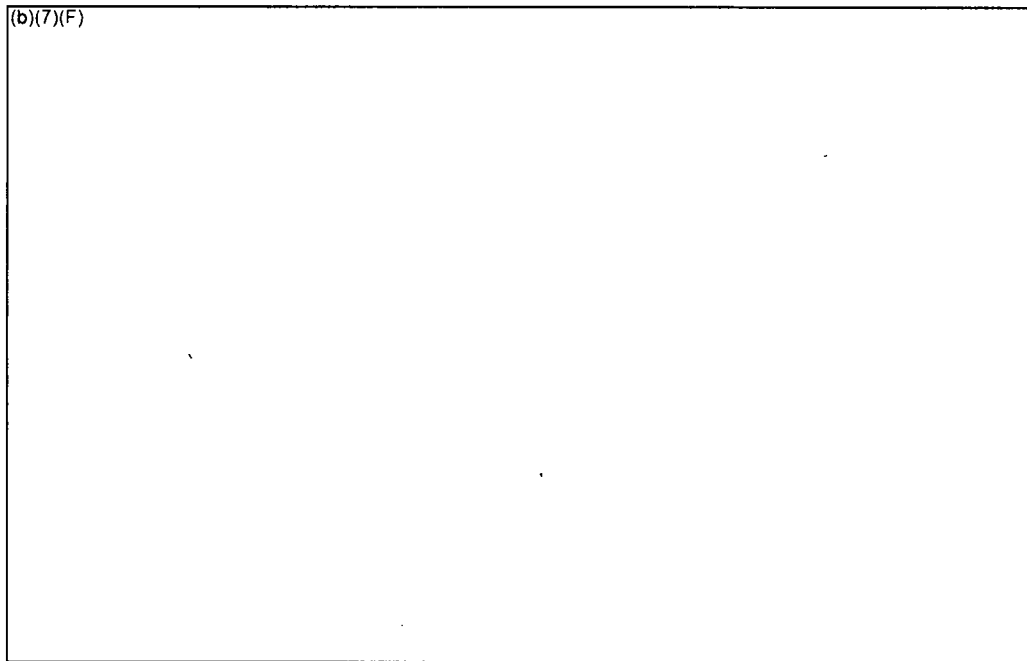
Ex 7F



7F

**Figure 6-18 High-Powered Assembly Cladding Temperatures for the Checkerboard Configuration with (b)(7)(F) Spray Flow and the Flow Regime Model Inactive (S3a).**

7F



7F

**Figure 6-19 Low-Powered Assembly Cladding Temperatures for the Checkerboard Configuration with (b)(7)(F) Spray Flow and the Flow Regime Model Inactive (S3a).**

7F

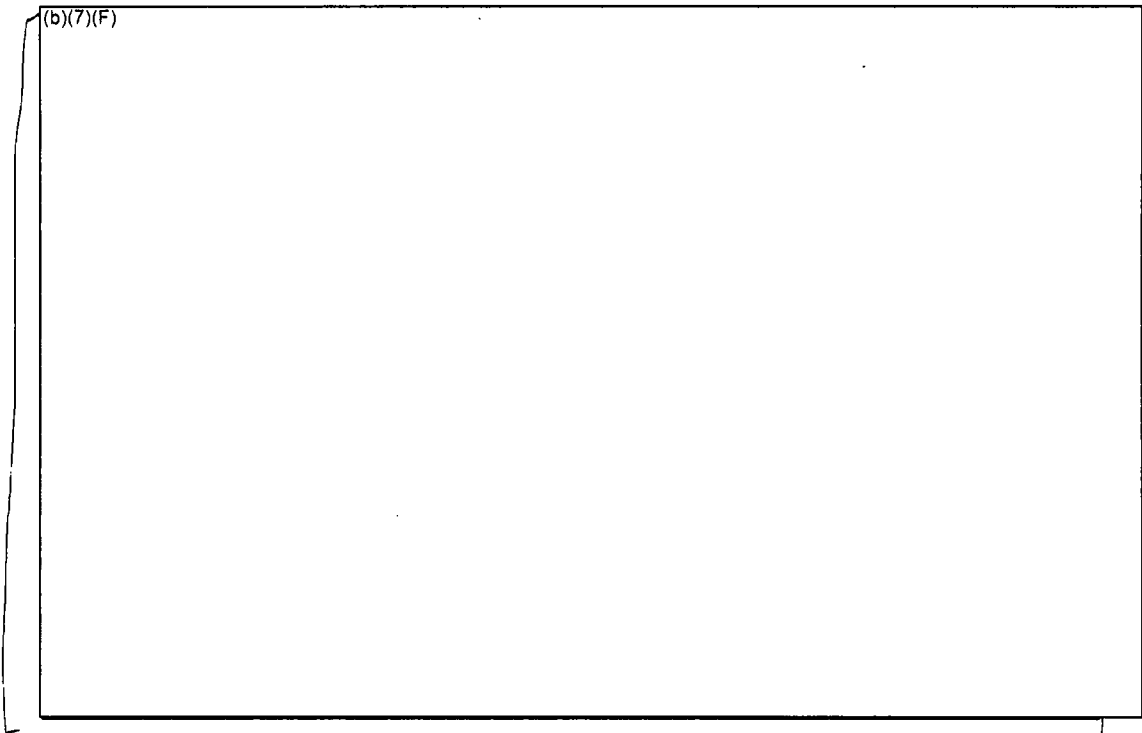


Figure 6-20 High-Powered Assembly Cladding Temperatures for the Checkerboard Configuration with (b)(7)(F) and No Spray Flow (Case S3b).

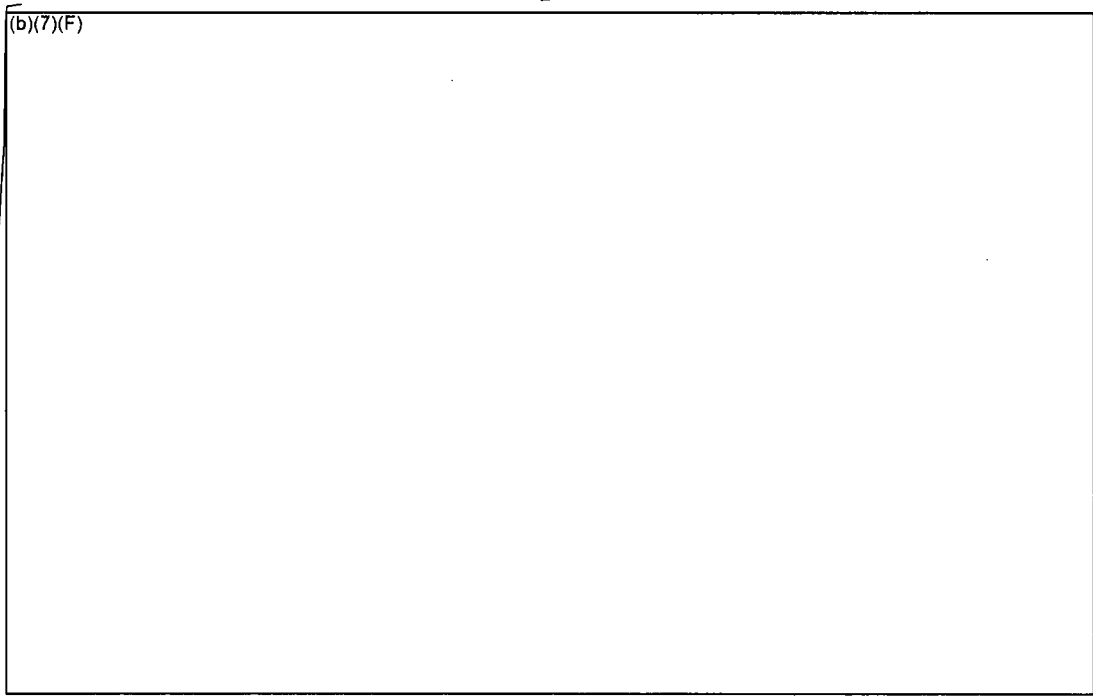
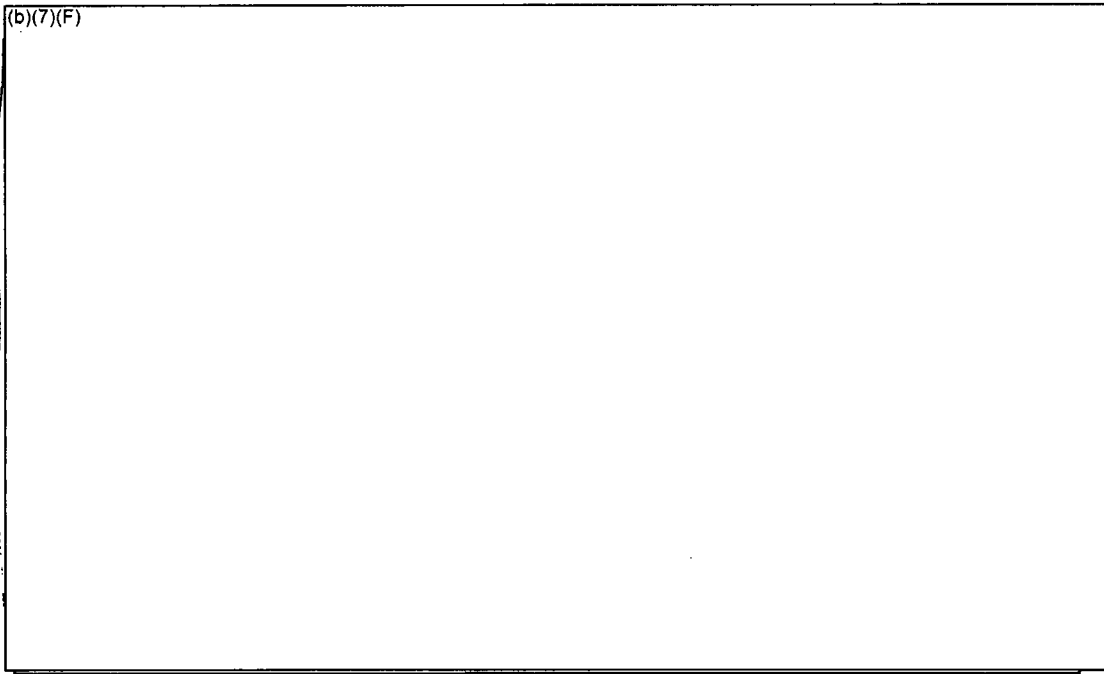


Figure 6-21 Low-Powered Assembly Cladding Temperatures for the Checkerboard Configuration with (b)(7)(F) and No Spray Flow (Case S3b).

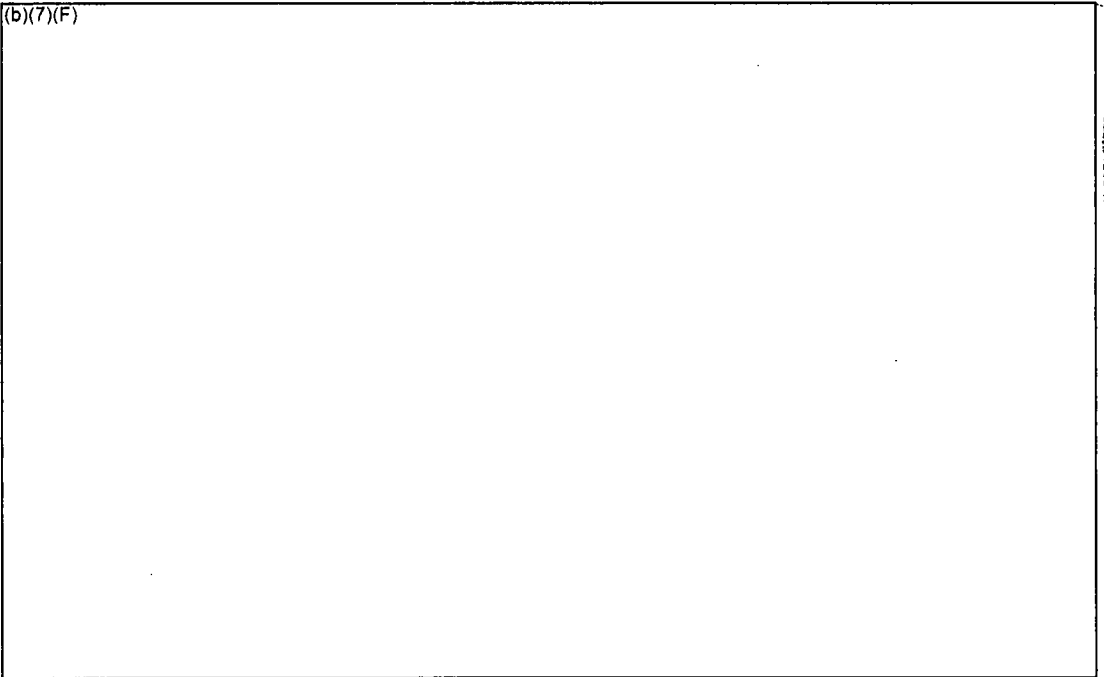
*EMK*



0.7F

**Figure 6-22 High-Powered Assembly Cladding Temperatures for the Checkerboard Configuration with (b)(7)(F) Spray Flow and Plugged Inlet (Case S3p).**

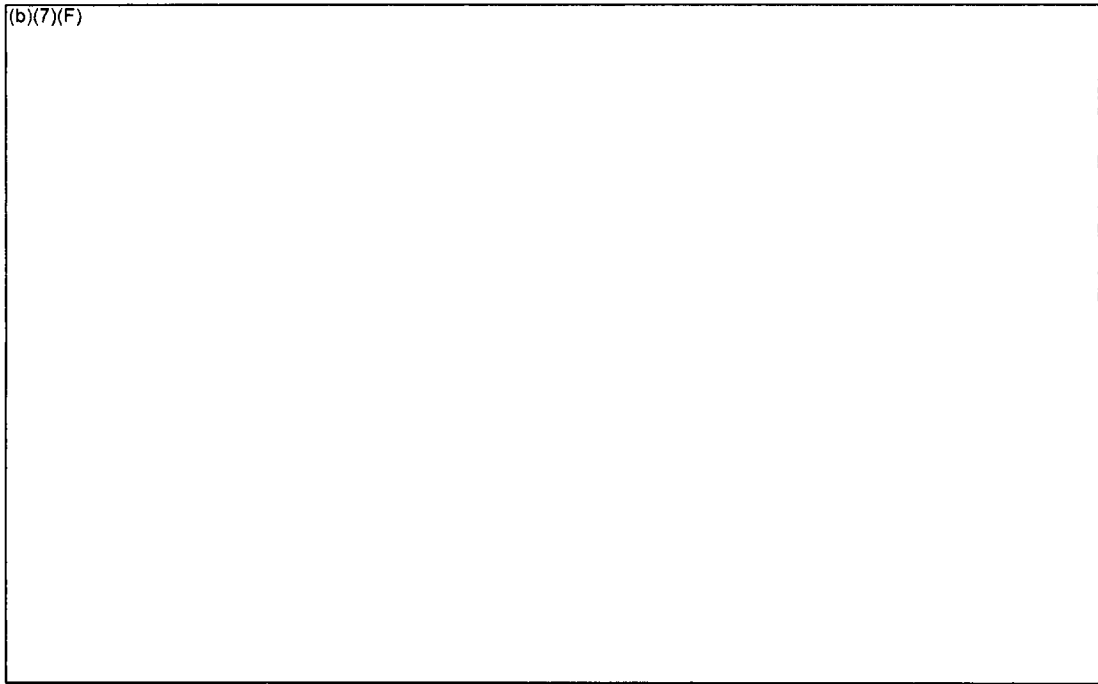
0.7F



0.7F

**Figure 6-23 Low-Powered Assembly Cladding Temperatures for the Checkerboard Configuration with (b)(7)(F) Spray Flow and Plugged Inlet (Case S3p).**

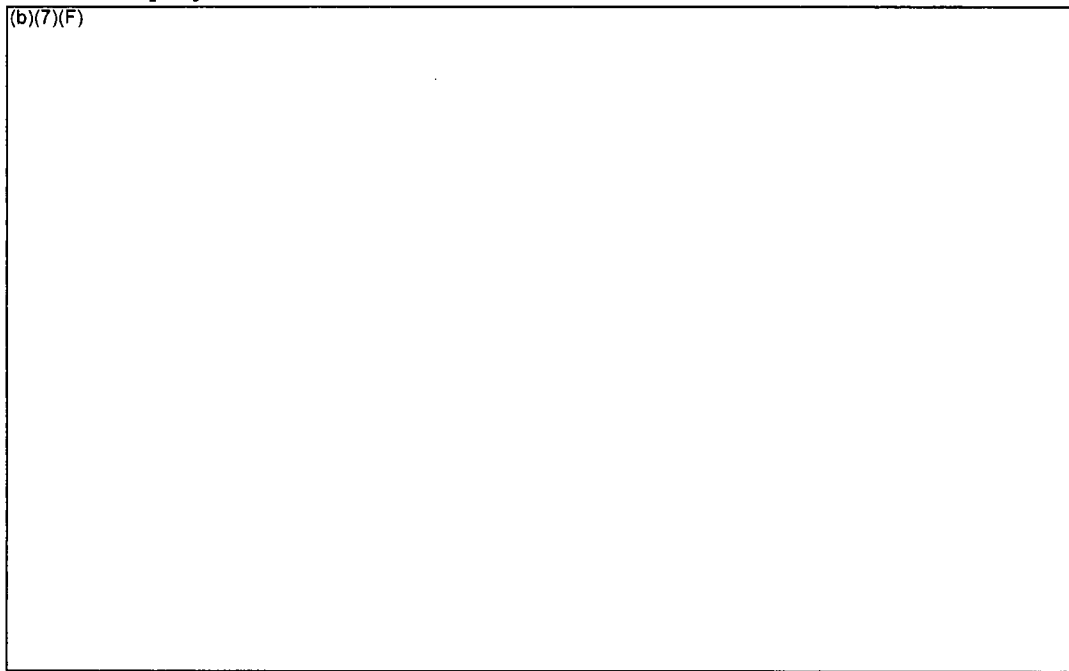
0.7F



7F

**Figure 6-24 High-Powered Assembly Cladding Temperature Profiles for the Checkerboard Configuration with a** (b)(7)(F) **Spray Flow.**

7F



7F

**Figure 6-25 Low-Powered Assembly Cladding Temperature Profiles for the Checkerboard Configuration with a** (b)(7)(F) **Spray Flow.**

7F

6.3.2 Energy Balance on Base Calculation Spray

(b)(7)(F)

x 7F

An energy balance was performed on the S3 case with the flow regime model operating. Figure 6-36 graphically shows the key heat flows in the model. After water level drops below the base plate, the power going into the structure steadily decreases to near zero. Meanwhile, due to air and steam convection, the heat removed by the gas in the peripheral assembly gradually increases. The convective heat removal by the center assembly gas is relatively constant after the base plate clearing. In this figure, the decay power includes both the low- and high-powered assemblies. The net heat balance is the sum of the heat flow terms besides the decay power (i.e., it should be approximately equal to the decay heat power<sup>23</sup>).

The energy balance is reported in Table 6-2 based on average conditions (b)(7)(F). The total power put into the checkerboard configuration is a combination of the decay heat for both the high- and low-powered assemblies (b)(7)(F) and oxidation power (b)(7)(F). The resultant distribution of energy generated in the center represented (b)(7)(F) of the decay power and (b)(7)(F) oxidation energy. (b)(7)(F) of the power in the high-powered assembly is removed by convective gas flow and the remaining (b)(7)(F) of the energy is radially transferred to the peripheral assembly. The decay heat power in the peripheral assembly is relatively small (b)(7)(F). However, the addition of the radial heat load from the center assembly increases the effective peripheral assembly heat load (b)(7)(F) that heat load is convectively removed by the gas and a small amount (b)(7)(F) goes into slowly heating portions of the assembly and heat removal by spray water out of the bottom.

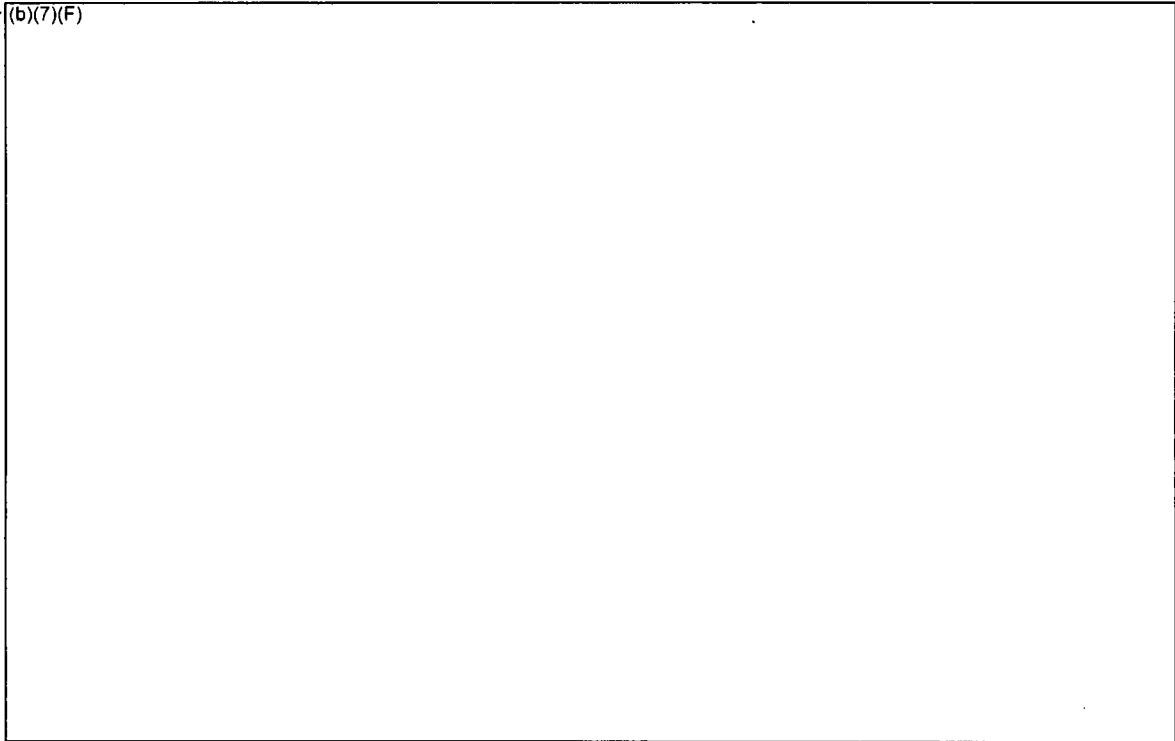
E x 7F  
(b)(7)(F)

7F  
7F  
7F  
7F

E x 7F  
(b)(7)(F)

7F  
7F

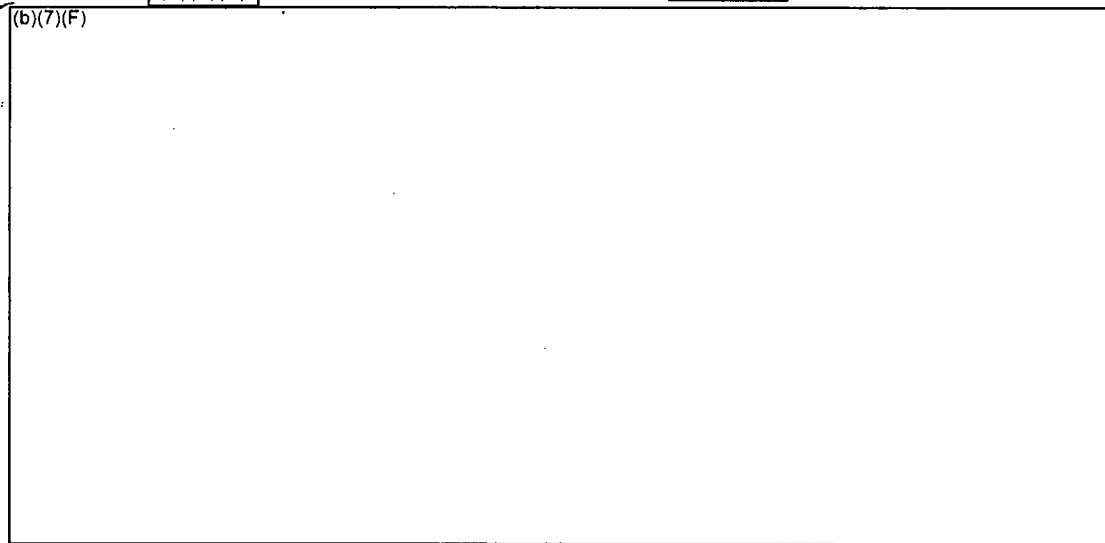
<sup>23</sup> The small transient differences between the net energy balance and the decay power is attributed to limitations in the access of plot quantities available to the user to access all the subcomponents of the energy flow. However, the major components are shown on the figure. The internal MELCOR core calculations have very high fidelity.



7F

Figure 6-26 Time-average Energy Flow in the Checkerboard Configuration, with (b)(7)(F) and a Whole Pool Spray Flow of (b)(7)(F)

7F



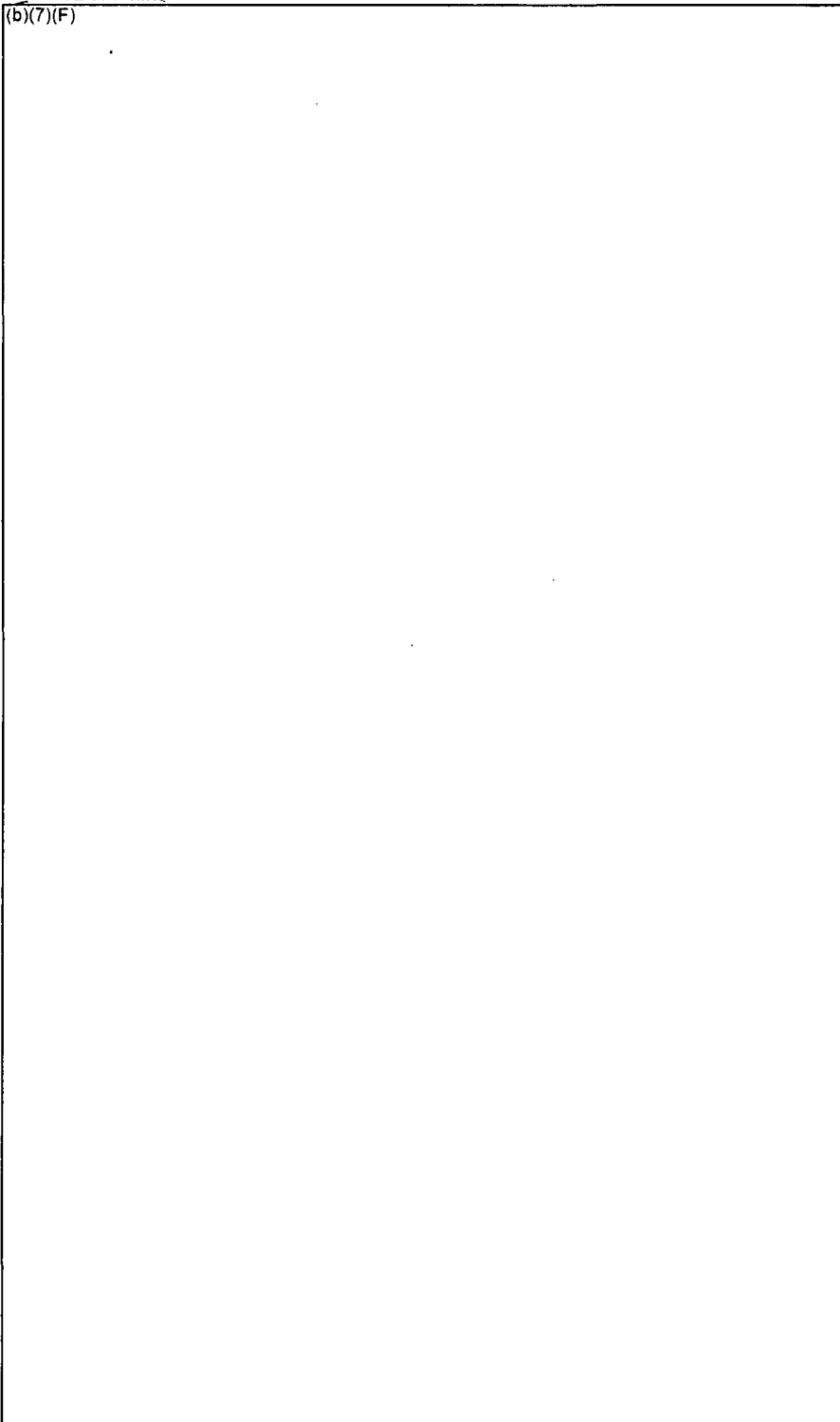
x 7F

7F

Table 6-3 **Energy Balance for the Checkerboard Assembly Configuration in SFP with** (b)(7)(F) **Spray.**

7F

(b)(7)(F)



7F

#### 6.4 Separate Effects Spray Model Results for the 1x4 Configuration Cases

Section 6.4.1 gives a summary of the 4 cases with <sup>EX5</sup> (b)(7)(F) <sup>EX5</sup> hole in a 1x4 fuel configuration. The four cases examine differences in the response with and without sprays and with and without the flow regime model active (see Section 3.1.4 for a more complete discussion). Finally, Section 6.3.2 shows the results of an energy balance on (b)(7)(F) case with sprays to illustrate the heat flows. 7F

##### 6.4.1 Base Calculations (b)(7)(F) Spray 7F

The S4 and S8 configuration calculations simulated a 1x4 configuration of the highest powered assemblies discharged into the spent fuel pool with (b)(7)(F) since reactor shutdown surrounded by four low-powered assemblies at the median power with the reference BWR SFP (b)(7)(F) 7F. The limiting response in a 1x4 configuration represents the response of a repeating pattern of 1x4 assemblies (e.g., see Figure 3-18). Similar to the checkerboard configuration, the high-powered assemblies benefit from radial heat transfer to adjacent low-powered assemblies. The transient is initiated with (b)(7)(F) 7F

The four (b)(7)(F) (i.e., see S4 calculations in Table 6-1) examined differences in the response with and without sprays and with and without the flow regime model active. When the flow regime model was deactivated, the spray water has a relatively small surface contact area with the cladding. Due to the reduction of heat transfer, the spray flow penetrates more deeply into the assembly before completely evaporating. In addition, a S4 case was run where the inlet of the assembly was plugged by water. As discussed in Section 5, depending upon the size hole and the spray rate, cases were identified where the inlet to the racks could be covered. Consequently, Case S4 and S4p parametrically investigated both conditions. (b)(7)(F) 7F

Figure 6-27 and Figure 6-28 show the temperature responses (b)(7)(F) cases, respectively. (b)(7)(F) 7F

(b)(7)(F) Similar to the uniform and checkerboard results, the disabled flow regime model cases were more effective at providing spray cooling to the middle of the assembly. (b)(7)(F) cases with the flow regime model off were (b)(7)(F) 7F cooler than when the model was active. The effect was more dramatic in the checkerboard cases (b)(7)(F) because the peak cladding temperatures in the flow regime cases were more greatly affected by the breakaway oxidation kinetics. In the cases with flow regime model active, there is very effective cooling of the top region of the fuel. (b)(7)(F) 7F

(b)(7)(F)

(b)(7)(F) In both cases, the peripheral assemblies were well cooled.

7F

Figure 6-29 and Figure 6-30 show the axial temperature response in the center and peripheral assemblies for Case S4 with the flow regime model. (b)(7)(F)

7F

(b)(7)(F) The center assembly is cooled by gas convection, which is enhanced by the spray flow and radial heat transfer (b)(7)(F) see the energy balance in Section 6.4.2 for a full discussion). In the peripheral assemblies, gas convection out the top of the assembly removed most of the effective heat load from the peripheral assembly decay heat power and the radial heat flow from the center assembly. In addition, spray water flows out the bottom of the peripheral assemblies (b)(7)(F) of the total decay heat power.

7F

7F

Similar to the previous configurations, the calculation with the flow regime model inactive (i.e., Case 4a in Figure 6-31 and Figure 6-32) had a slightly lower peak temperature than when the flow regime model was active.

The high- and low-powered cladding temperature responses from Cases S4b and S4p are shown in Figure 6-33 through Figure 6-36. (b)(7)(F)

7F

(b)(7)(F) In previous separate effects calculations for the 1x4 configuration with air flow but no spray flow [Wagner, 2003], (b)(7)(F)

7F

(b)(7)(F)

(b)(7)(F) Similar to the checkerboard configuration, the convective heat removal in the low-powered assemblies is important. However, the 1x4 configuration has four low-powered assemblies surrounding the high-powered assembly. Although the convective gas flow was limited, the convective removal in the center assembly by boiling the spray water as well as removal in the liquid flow out the bottom of the four peripheral assemblies provided sufficient heat removal to keep the configuration cool.

7F

Finally, the center and peripheral assembly axial temperature profiles are shown in Figure 6-37 and Figure 6-38 for all four cases, respectively. As observed in the axial temperature profiles for the uniform and checkerboard cases, the impact of the spray flow at the top of the assembly is clearly seen. The cases with the flow regime model active have cooler temperatures until the spray flow is depleted. The case without the flow regime model shows less heat removal at the top of the assembly but more heat removal at the bottom. (b)(7)(F)

(b)(7)(F)

7F

Consequently, the center assembly spray flow removed much of the decay heat at the top of the assembly whereas the spray flow in the peripheral assemblies helped removed the decay power in the lower portion of the assembly for the plugged case.

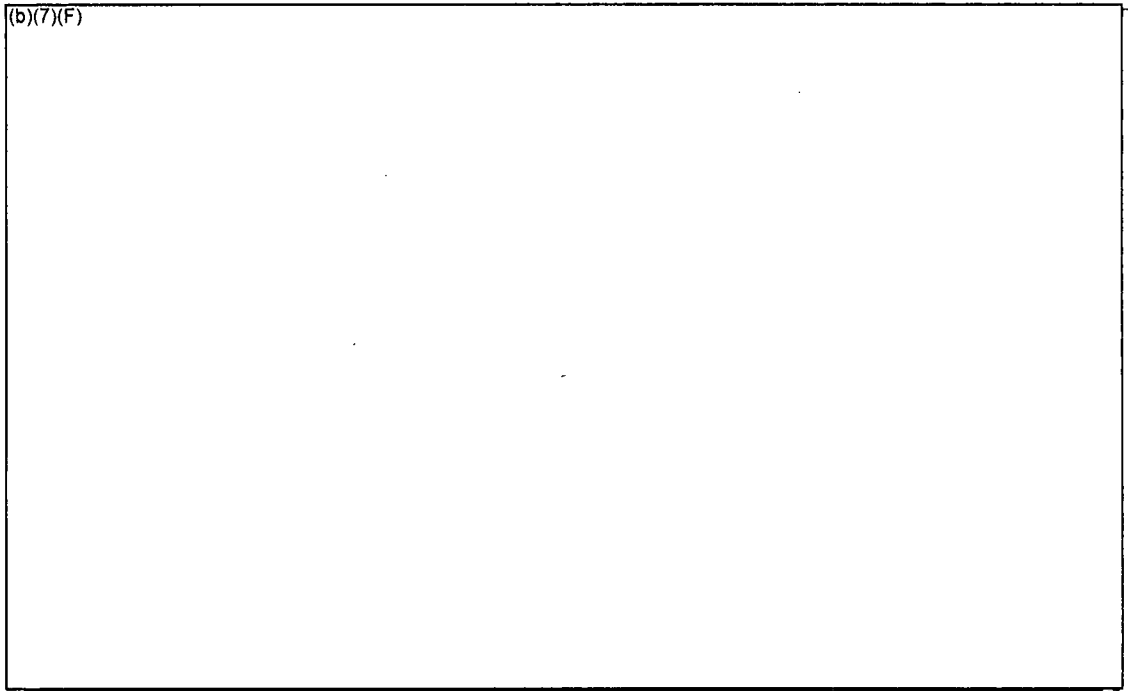


Figure 6-27 Comparison of the Peak Cladding Temperatures (b)(7)(F) with a 1x4 Configuration with (b)(7)(F) and a Whole Pool Spray Flow of (b)(7)(F)

7F  
7F  
7F

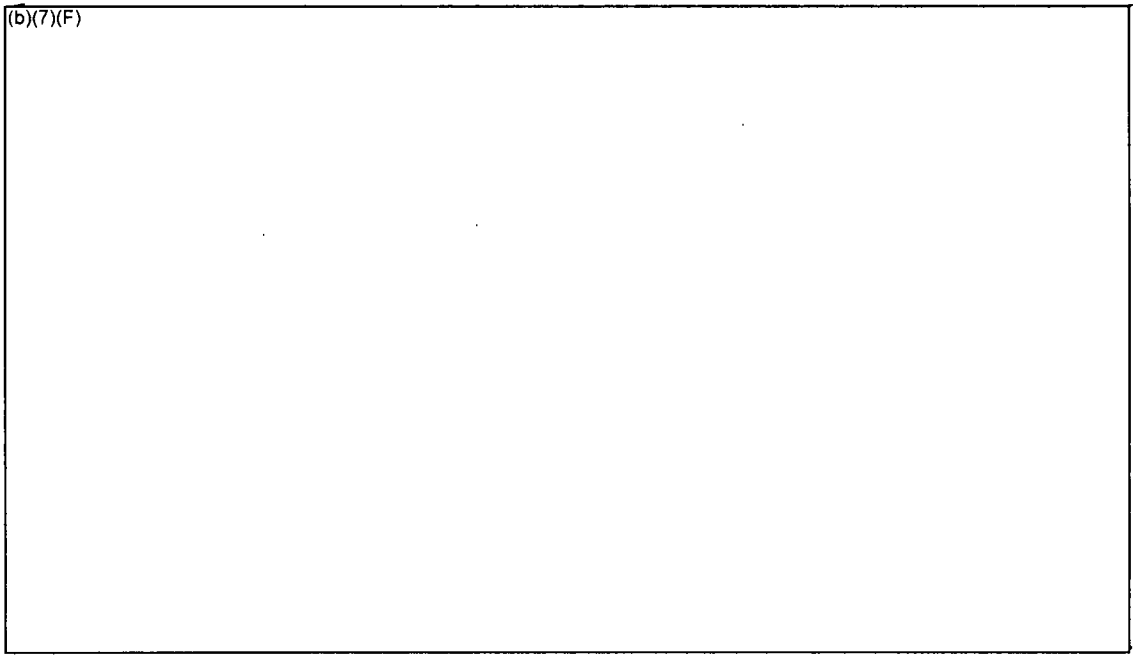
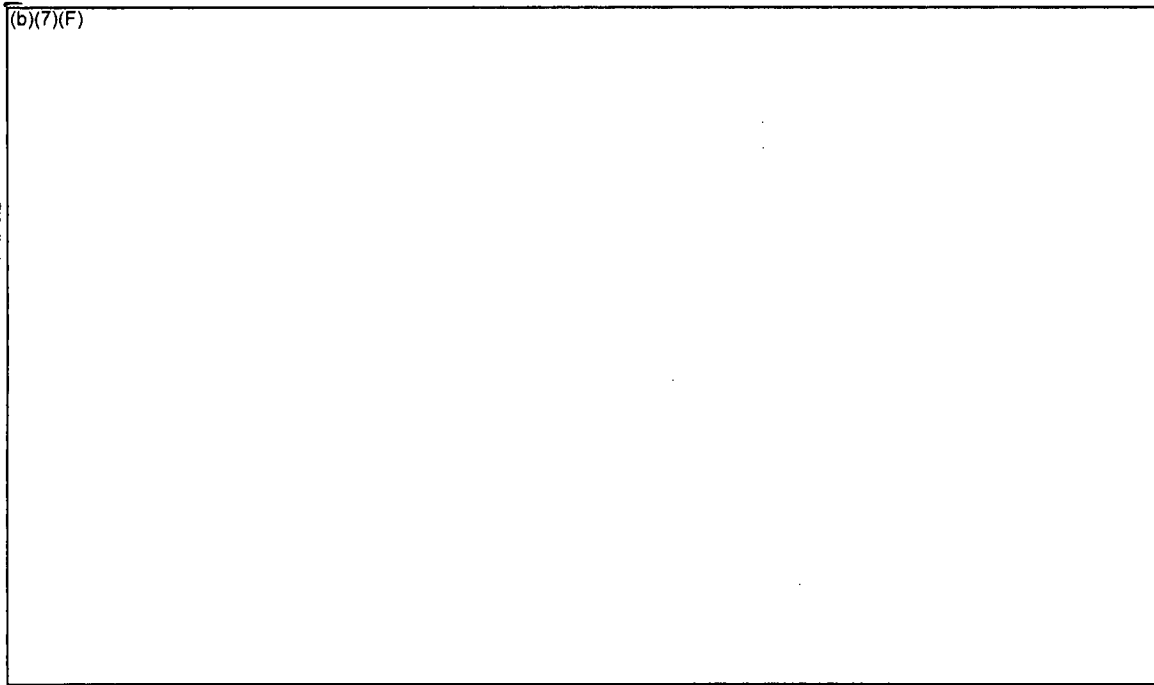


Figure 6-28 Comparison of the Peak Cladding Temperatures (b)(7)(F) with a 1x4 Configuration with (b)(7)(F) and a Whole Pool Spray Flow of (b)(7)(F)

7F  
7F

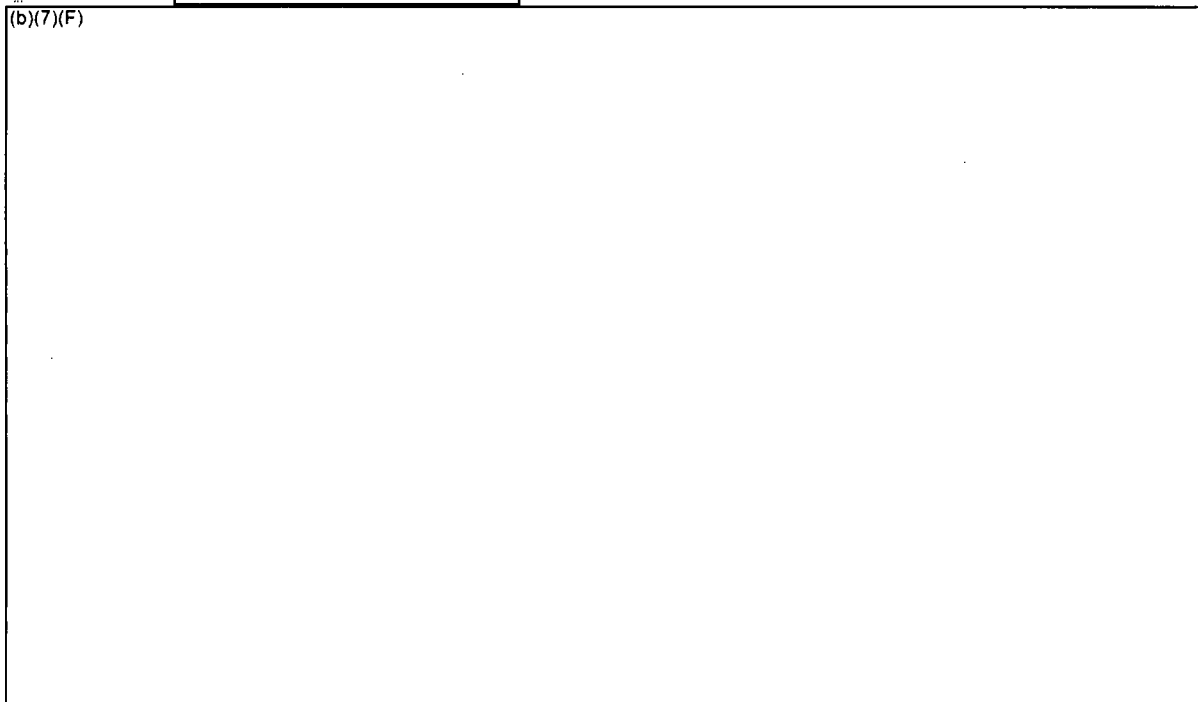


7F

**Figure 6-29 Center Assembly Cladding Temperatures for the 1x4 Configuration with**  
**Spray Flow (Case S4).**

7F

(b)(7)(F)

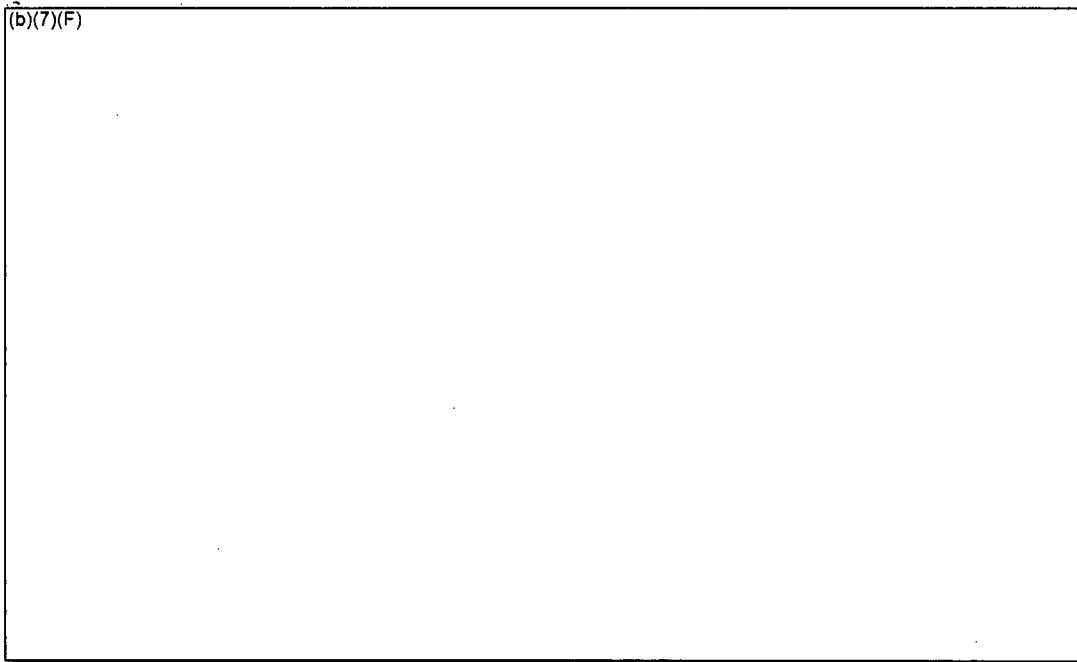


7F

**Figure 6-30 Peripheral Assembly Cladding Temperatures for the 1x4 Configuration with**  
**Spray Flow (Case S4).**

x 7F

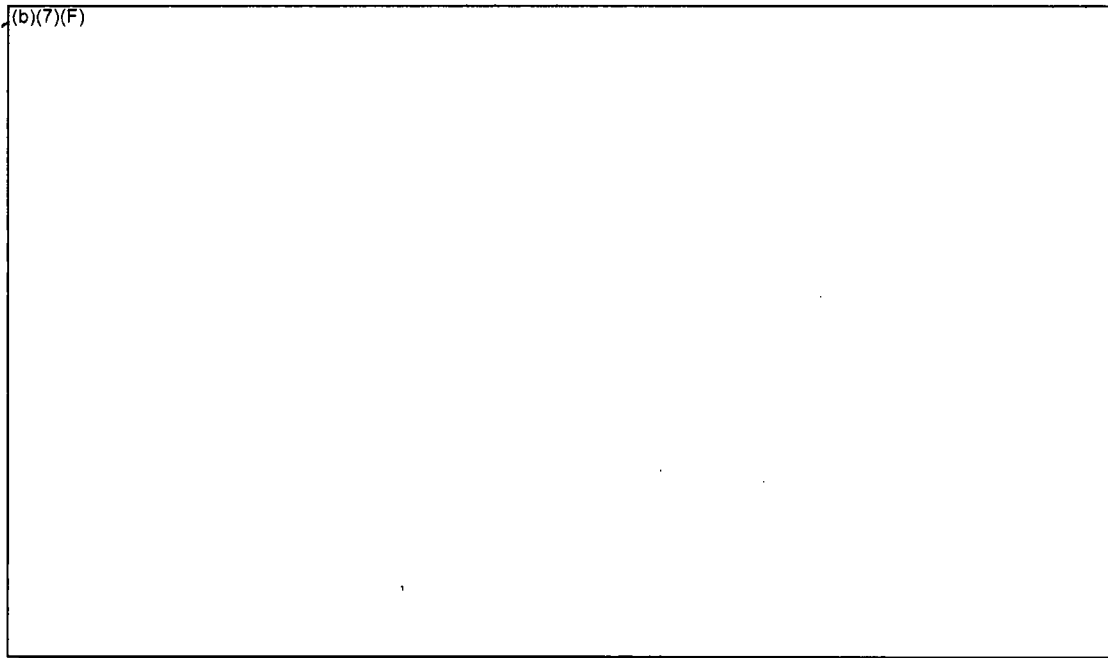
(b)(7)(F)



x7F

**Figure 6-31 Center Assembly Cladding Temperatures for the 1x4 Configuration with**  
**(b)(7)(F) Spray and the Flow Regime Model Inactive**  
**(Case S4a).**

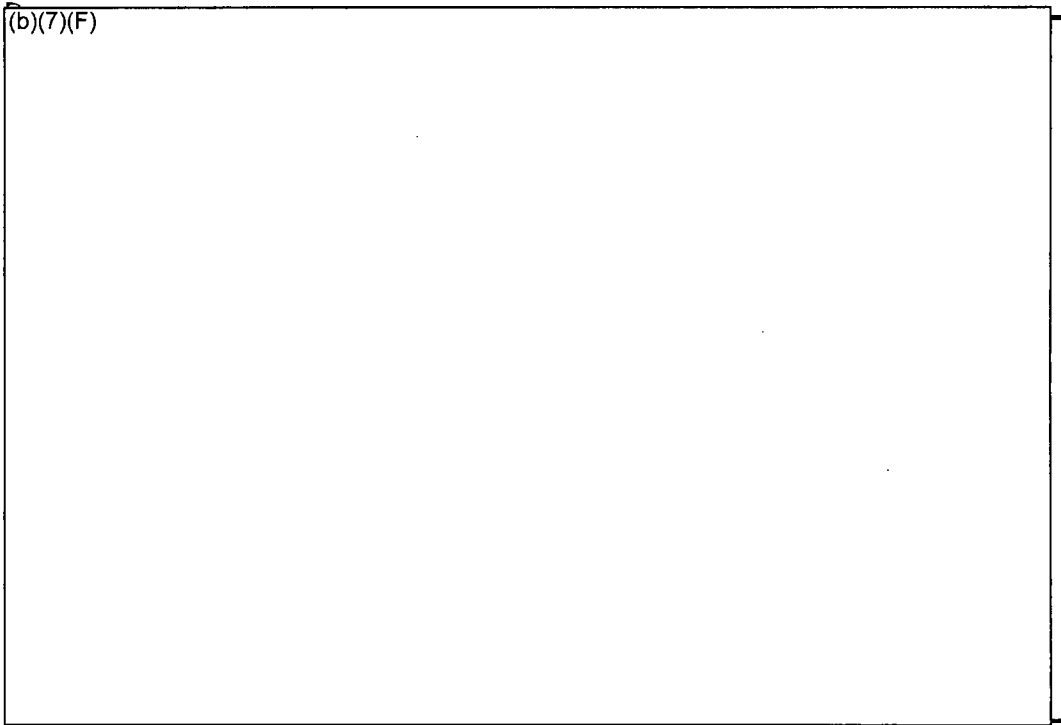
7F



7F

**Figure 6-32 Peripheral Assembly Cladding Temperatures for the 1x4 Configuration with**  
**(b)(7)(F) Spray and the Flow Regime Model Inactive**  
**(Case S4a).**

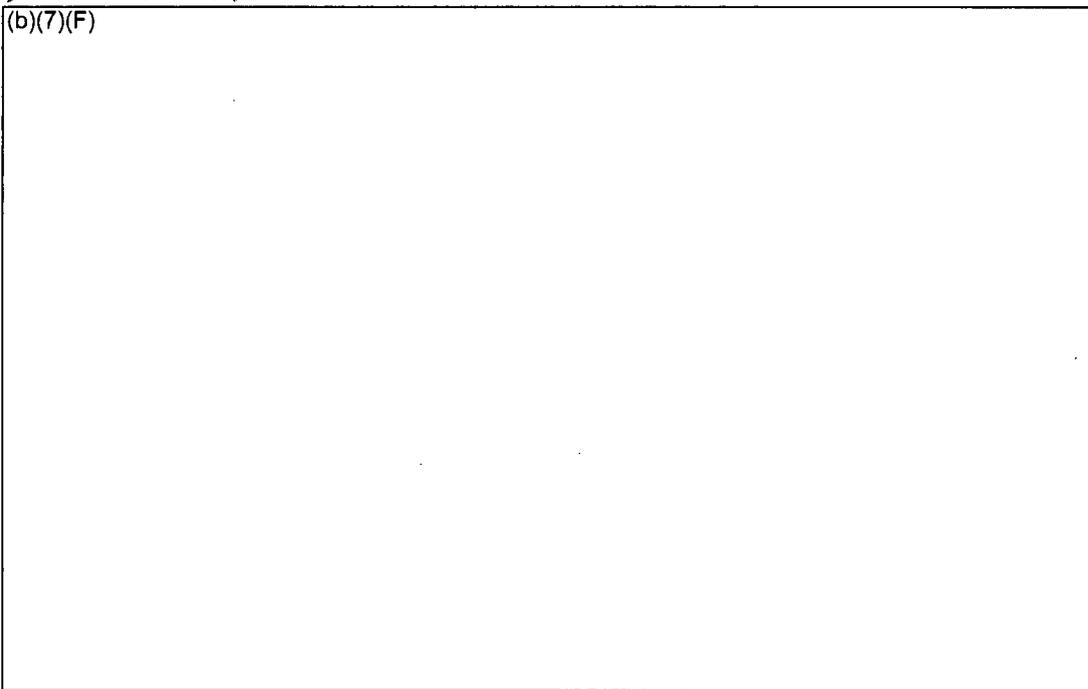
7F



.7F

**Figure 6-33** Center Assembly Cladding Temperatures for the 1x4 Configuration with (b)(7)(F) and No Sprays (Case S4b).

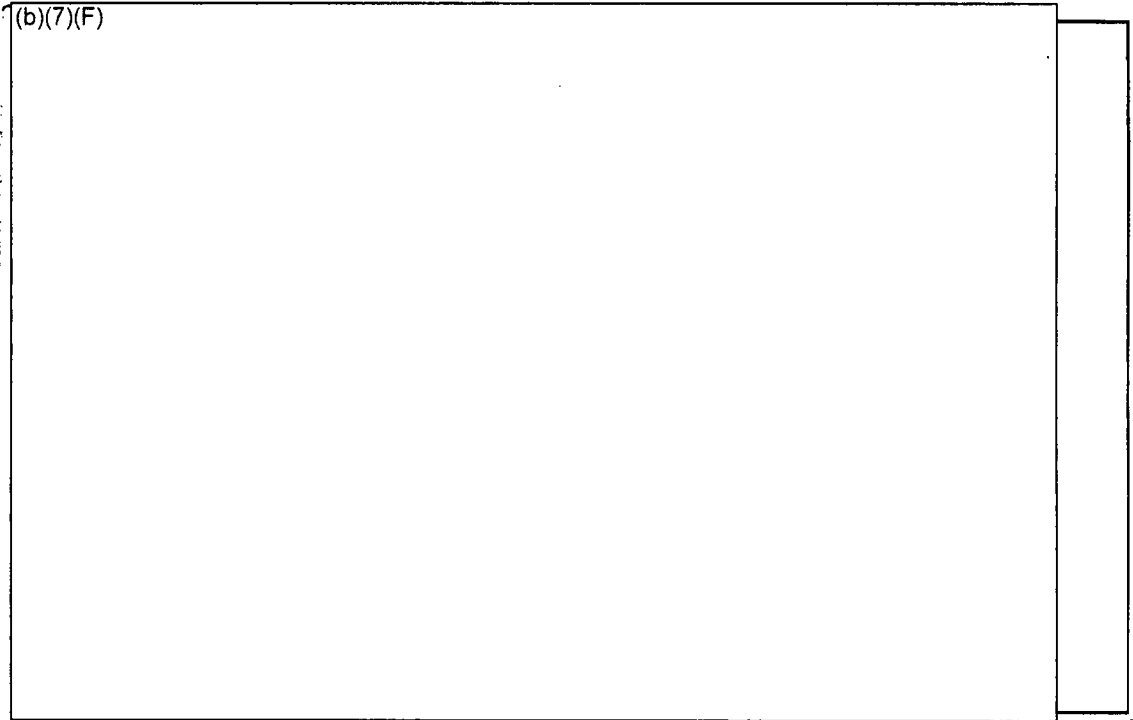
.7F



.7F

**Figure 6-34** Peripheral Assembly Cladding Temperatures for the 1x4 Configuration with (b)(7)(F) and No Spray Flow (Case S4b).

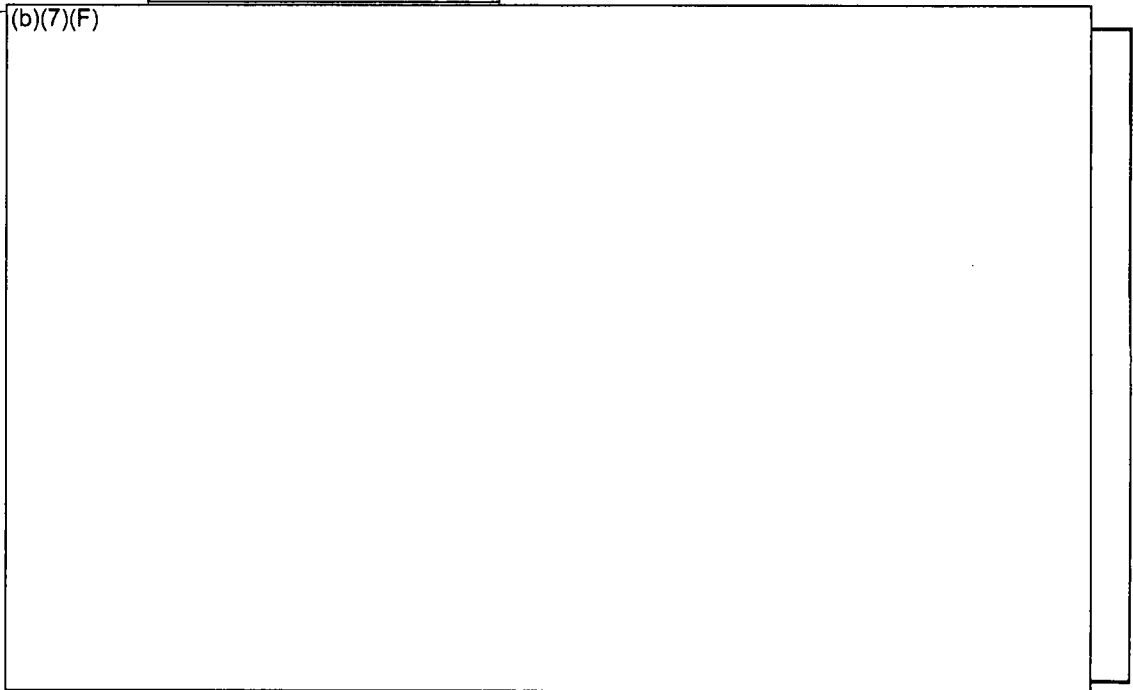
.7F



7F

Figure 6-35 Center Assembly Cladding Temperatures for the 1x4 Configuration with (b)(7)(F) Spray Flow and Plugged Inlet (Case S4p).

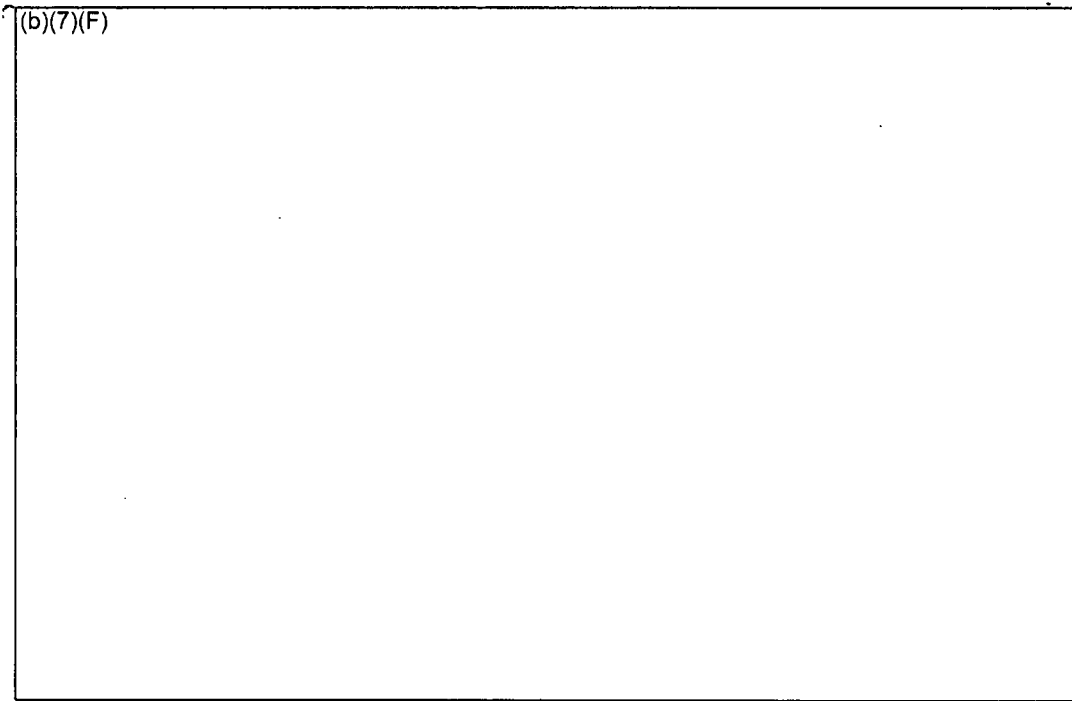
7F



7F

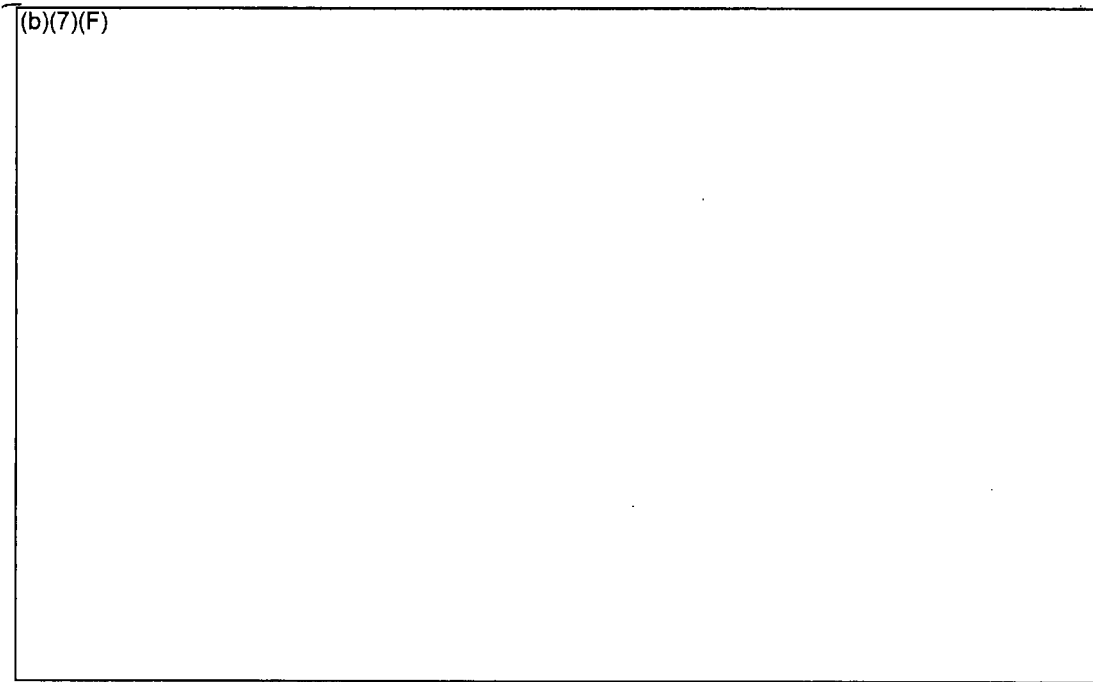
Figure 6-36 Peripheral Assembly Cladding Temperatures for the 1x4 Configuration with (b)(7)(F) Spray Flow and Plugged Inlet (Case S4p).

7F



7F

Figure 6-37 Center Assembly Axial Cladding Temperatures for the 1x4 Configuration with a (b)(7)(F) Spray Flow. 7F



7F

Figure 6-38 Peripheral Assembly Axial Cladding Temperatures for the 1x4 Configuration with a (b)(7)(F) with (b)(7)(F) Spray Flow. x 7F

6.4.2 Energy Balance on Base Calculation, Spray

(b)(7)(F)

7F

An energy balance was performed on the S4 case with the flow regime model operating (Case S4). Figure 6-39 graphically shows the key heat flows in the model. After water level drops below the base plate, the power going into the structure steadily decreases to near zero. Meanwhile, due to air and steam convection, the heat removed by the gas in the peripheral assembly gradually increases. The convective heat removal by the center assembly gas is relatively constant after the base plate clearing. In this figure, the decay power includes both the low- and high-powered assemblies. The net heat balance is the sum of the heat flow terms besides the decay power (i.e., it should be approximately equal to the decay heat power<sup>24</sup>).

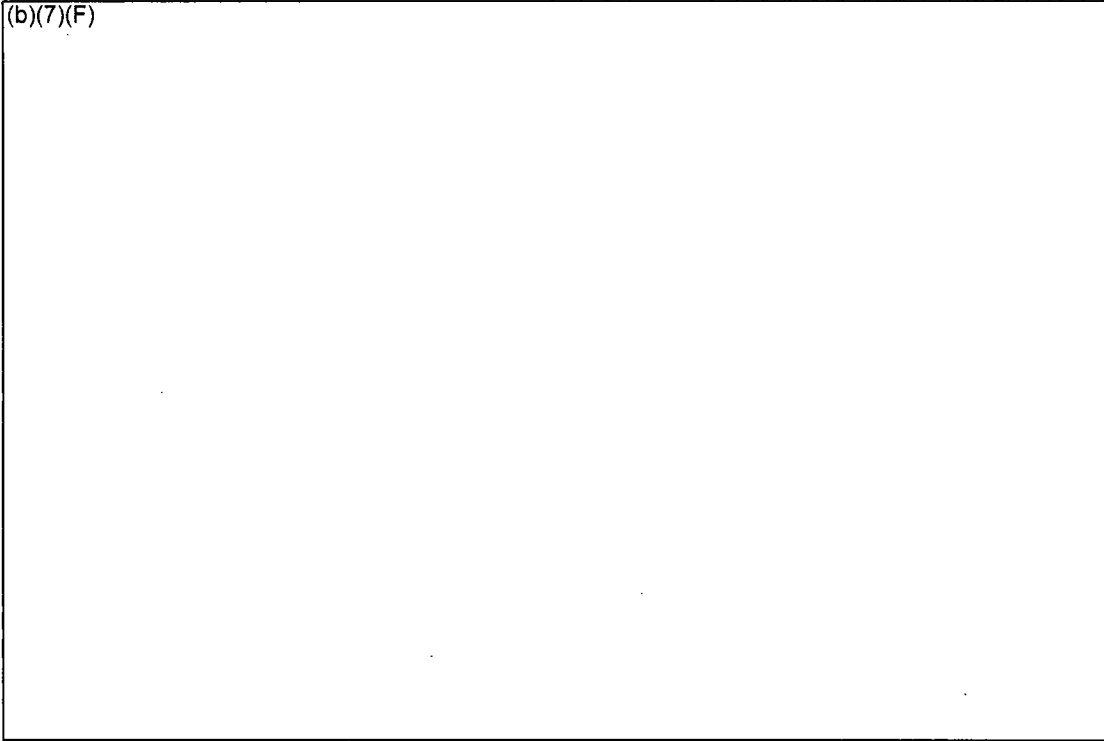
The energy balance is reported in Table 6-4. The total power put into the 1x4 configuration is a combination of the decay heat for both the high- and low-powered assemblies (b)(7)(F)

(b)(7)(F). Due to the relatively low temperatures in all five assemblies, there (b)(7)(F) (b)(7)(F) oxidation power. (b)(7)(F) of the power in the center assembly was removed by convection and (b)(7)(F) by radial heat transfer to the peripheral assemblies. In the peripheral assemblies, (b)(7)(F) of the net heat load from the peripheral assembly decay powers and the radial heat transfer was removed by gas convection out the top of the assembly. (b)(7)(F) of the power in the peripheral assemblies was carried away by liquid spray flow out the bottom of the assembly.

(b)(7)(F) x 7F  
(b)(7)(F) x 7F  
(b)(7)(F) x 7F

x 7F  
x 7F  
x 7F  
(b)(7)(F)

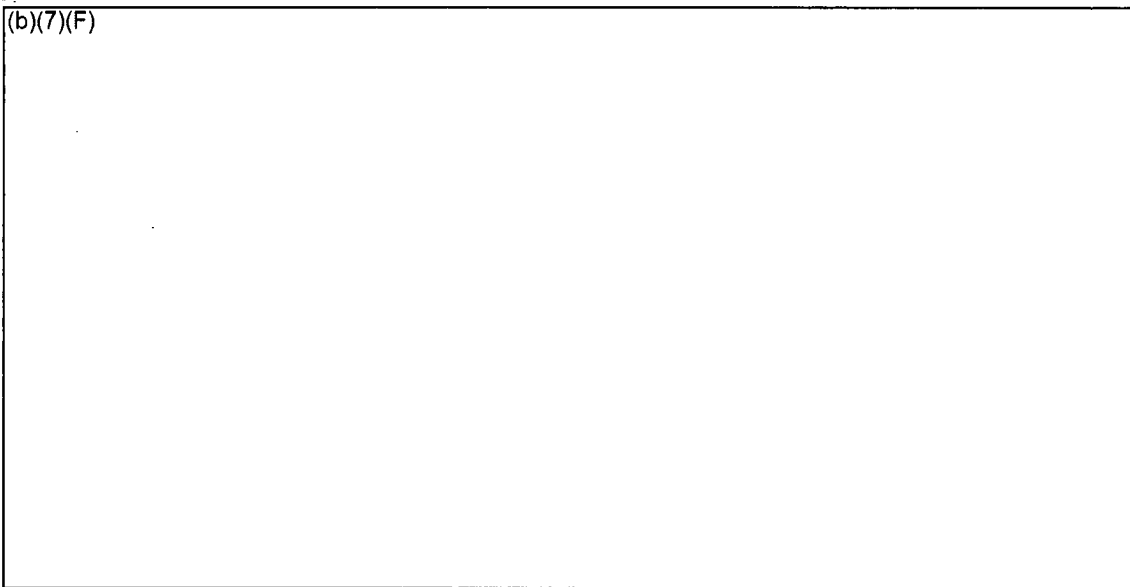
<sup>24</sup> The small transient differences between the net energy balance and the decay power is attributed to limitations in the access of plot quantities available to the user to access all the subcomponents of the energy flow. However, the major components are shown on the figure. The internal MELCOR core calculations have very high fidelity.



7F

**Figure 6-39 Time-averaged Energy Flow in the 1x4 Configuration with** (b)(7)(F)  
**and a Whole Pool Spray Flow of** (b)(7)(F) 7F

7F

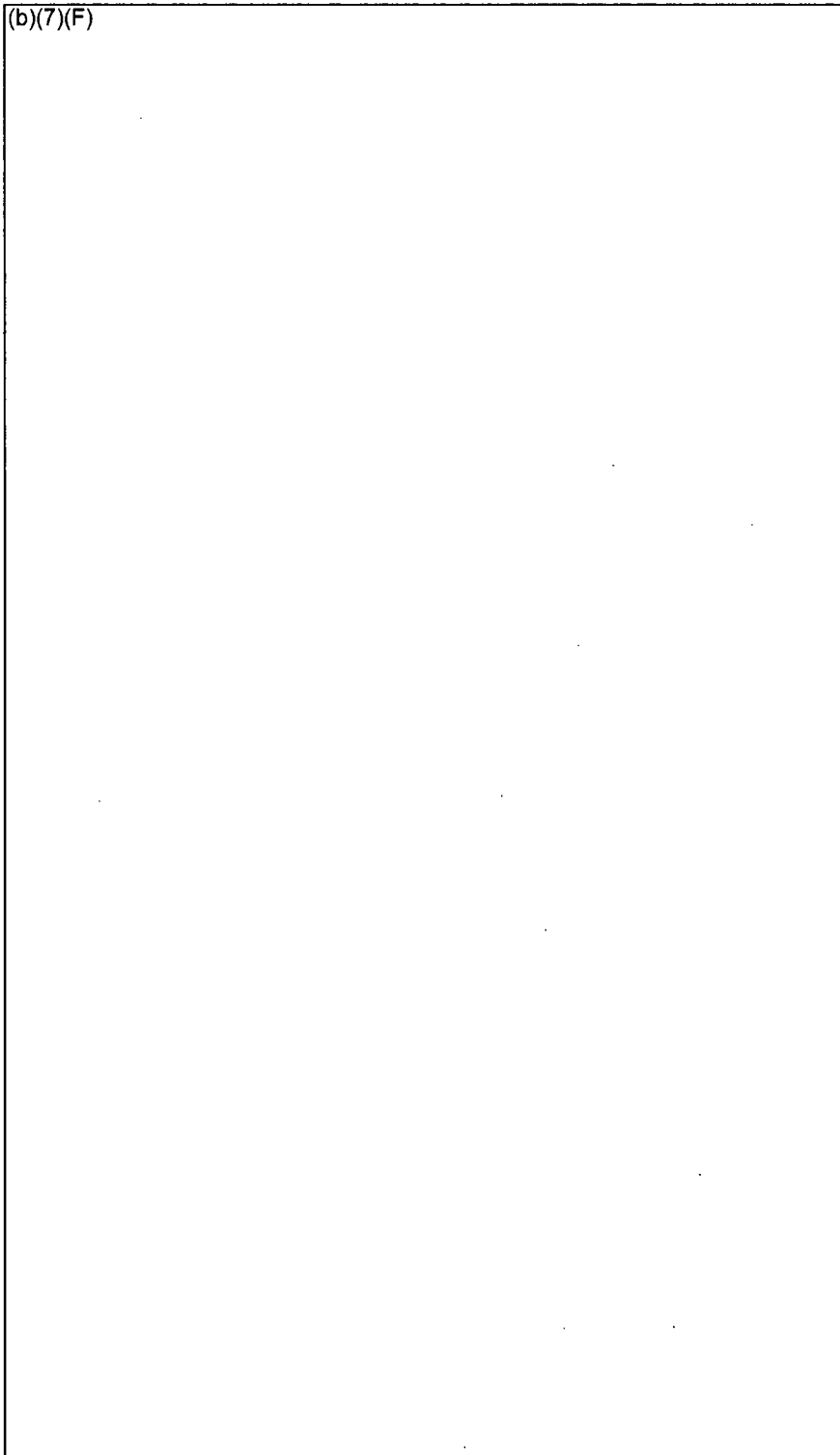


7F

Table 6-4 Energy Balance for 1x4 Assembly Configuration in SFP with (b)(7)(F) Spray.

7F

(b)(7)(F)



7F

## 7. REFERENCES

- Bergles, A. E., et al., Two-Phase Flow and Heat Transfer in the Power and Process Industries, McGraw-Hill Book Company, 1981.
- Boyd, C., "Predictions of Spent Fuel Heatup after a Complete Loss of-Coolant Accident," NUREG-1726, July 2000.
- Collins, T. E., and Hubbard, G., "Technical Study of Spent Fuel Pool Accident Risk at Decommissioning Nuclear Power Plants," NUREG-1738, February, 2001.
- Durbin, S., "Hydraulic Analysis of the Spent Fuel Pool Experiment," Revision 4, Sandia National Laboratories Internal Memo dated 11/21/05.
- Gauntt, R. O. et al, "MELCOR Computer Code Manuals, Reference Manual, Version 1.8.5, Vol. 2, Rev. 2", Sandia National Laboratories, NUREG/CR-6119, SAND2000-2417/1.
- Khalil, I., and Webb, S., "Simulations of Natural Convection Airflow in a Completely Drained Pressurized Water Reactor Spent Fuel Pool using FLUENT," Sandia National Laboratories, Letter Report, Revision 1, October 2005.
- Lanning, D. D., Beyer, C. E., Geelhood, and K.J., FRAPCON-3 Updates, Including Mixed-Oxide Fuel Properties," NUREG/CR-6534, Vol. 4, PNNL-11513, Pacific Northwest National Laboratory, May 2005.
- Lipinski, R. J., "A Model for Boiling and Dryout in Particle Beds," Sandia National Laboratories, SAND82-0765, NUREG/CR-2646, June 1982.
- Natesan, K., and Soppet, W.K., "Air Oxidation Kinetics for Zr-Based Alloys," NUREG/CR-6846, Argonne National Laboratories, June 2004.
- Nuclear Regulatory Commission, "Accident Source Terms for Light-Water Nuclear Power Plants," NUREG-1465, February 1995.
- Ross, K. W., Wagner, KC, and Gauntt, R. O., "Analysis of Spent Fuel Pool Flow Patterns Using Computational Fluid Dynamics: Part 2 – Partial Water Cases," Sandia National Laboratories, Informal Report, April 2003.
- Wagner, K. C., and Gauntt, R. O., "MELCOR 1.8.5 Separate Effect Analyses of Spent Fuel Pool Assembly Accident Response," Sandia National Laboratories, Draft Informal Report, Revision 0, June 2003.
- Wagner, K. C., and Gauntt, R. O., "Evaluation of a BWR Spent Fuel Pool Accident Response to Loss-of-Coolant Inventory Scenarios Using MELCOR 1.8.5," Sandia National Laboratories, Draft Informal Report, Revision 2, December 2004.

Wagner, K. C., and Gauntt, R. O., "Analysis of BWR Spent Fuel Pool Flow Patterns Using Computation Fluid Dynamics: Supplemental Air Cases," Sandia National Laboratories, Draft Informal Report, Revision 2, October 2005.

Wagner, K. C. , Dallman, R. J., and Annon, M.C., "Best-Estimate Evaluation Of Loss-Of-Coolant Inventory In A Nuclear Power Plant Spent Fuel Pool," *International Meeting on Best-Estimate Methods in Nuclear Installation Safety Analysis (BE-2000)*, Washington, DC, November, 2000.

Wallis, G. B., One-Dimensional Two-phase Flow, McGraw-Hill Book Company, 1969.